Virtual Nonlinear Multibody Systems

NATO Advanced Study Institute

Volume II

Edited by

Werner Schiehlen and Michael Valášek

Prague, June 23 – July 3, 2002

20030110 023

REPORT DOCUMENTATION PAGE		Form Approved OMB No. 0704-0188

1. AGENCY USE ONLY (Leave blank)	2. REPORT DATE 2002	3. REPORT TYPE AND DATES COVERED Advanced Study Institute, 23 June – 3 July 2002

4. TITLE AND SUBTITLE Virtual Nonlinear Multibody Systems, Volume 2	5. FUNDING NUMBERS N62358-02-M-6031
6. AUTHOR(S)	

7. PERFORMING ORGANIZATION NAME(S) AND ADDRESS(ES) University of Stuttgart, Germany	

9. SPONSORING/MONITORING AGENCY NAME(S) AND ADDRESS(ES USARDSG-UK, Fiscal Office, Edison House, 223 Old Marylebone Road, London NW1 5th, UK	10. SPONSORING/MONITORING AGENCY REPORT NUMBER R&D 9315-AN-02

11. SUPPLEMENTARY NOTES

12a. DISTRIBUTION/AVAILABILITY STATEMENT Approved for Public Release.	12b. DISTRIBUTION CODE A

ABSTRACT (Maximum 200 words)

Multibody system dynamics is based on classical mechanics and its engineering applications ranging from mechanisms, gyroscopes, satellites and robots to biomechanics and vehicle engineering. Multibody systems dynamics is characterized by algorithms or formalisms, respectively, ready for computer implementation. The simulation of multibody systems demands for adequate dynamic models and takes into account various phenomena. Classical dynamics does not regard all nonlinear effects that appear as a result of the action of multibody systems, as well as their mutual interaction. The virtual prototyping and dynamic modeling of such systems are, from an economical point of view, perspective fields of scientific investigations having in mind the huge expenses for their design and manufacturing. Complex multibody systems composed of rigid and flexible bodies performing spatial motion and various complex tasks are up-to-date objects of virtual prototyping. As a result simulation and animation featuring virtual reality are most important. Recent research fields in multibody dynamics include standardization of data, coupling with CAD systems, parameter identification, real-time animation, contact and impact problems, extension to electronic and mechatronic systems, optimal system design, strength analysis and interaction with fluids. Further, there is a strong interest on multibody systems in analytical and numerical mathematics resulting in reduction methods for the rigorous treatment of simple models and special integration codes for Ordinary Differential Equation (ODE) and Differential Algebraic Equation (DAE) representations supporting the numerical efficiency. New software engineering tools with modular approaches improve the efficiency still required for the more demanding needs in biomechanics, robotics and vehicle dynamics. The scientific research in multibody system dynamics is devoted to improvements in modeling considering nonholonomic constraints flexibility, friction, contact, impact and control. New methods evolved with respect to simulation by recursive formalism, to closed kinematic loops, reaction forces and torques, and pre- and post-processing by data models, CAD coupling, signal analysis, animation and strength evaluation. Multibody system dynamics is applied to a broad variety of engineering problems from aerospace to civil engineering, from vehicle design to micromechanical analysis, from robotics to biomechanics. In particular, multibody dynamics is considered as the basis of mechatronics, e.g. controlled mechanical systems. These challenging applications are subject to fundamental research topics which were presented at the NATO ASI on Virtual Nonlinear Multibody Systems.

14. SUBJECT TERMS US Army Research, Czech Republic, Multibody system dynamics, Virtual prototyping, Dynamic modeling, Data models, CAD coupling, Parameter identification, Real-time animation evaluation, Strength evaluation, Software engineering, Signal analysis, Mechatronics			15. NUMBER OF PAGES
			16. PRICE CODE

17. SECURITY CLASSIFICATION OF REPORT Unclassified	18. SECURITY CLASSIFICATION OF THIS PAGE Unclassified	19. SECURITY CLASSIFICATION OF ABSTRACT Unclassified	20. LIMITATION OF ABSTRACT Unlimited

NATO Advanced Study Institute on
Virtual Nonlinear Multibody Systems
Prague, Czech Republic, 23 June - 3 July 2002

Scientific Abstract

Multibody system dynamics is based on classical mechanics and its engineering applications ranging from mechanisms, gyroscopes, satellites and robots to biomechanics and vehicle engineering. Multibody systems dynamics is characterized by algorithms or formalisms, respectively, ready for computer implementation. The simulation of multibody systems demands for adequate dynamic models and takes into account various phenomena. Classical dynamics does not regard all nonlinear effects that appear as a result of the action of multibody systems, as well as their mutual interaction. The virtual prototyping and dynamic modeling of such systems are, from an economical point of view, perspective fields of scientific investigations having in mind the huge expenses for their design and manufacturing. Complex multibody systems composed of rigid and flexible bodies performing spatial motion and various complex tasks are up-to-date objects of virtual prototyping. As a result simulation and animation featuring virtual reality are most important. Recent research fields in multibody dynamics include standardization of data, coupling with CAD systems, parameter identification, real-time animation, contact and impact problems, extension to electronic and mechatronic systems, optimal system design, strength analysis and interaction with fluids. Further, there is a strong interest on multibody systems in analytical and numerical mathematics resulting in reduction methods for the rigorous treatment of simple models and special integration codes for Ordinary Differential Equation (ODE) and Differential Algebraic Equation (DAE) representations supporting the numerical efficiency. New software engineering tools with modular approaches improve the efficiency still required for the more demanding needs in biomechanics, robotics and vehicle dynamics. The scientific research in multibody system dynamics is devoted to improvements in modeling considering nonholonomic constraints flexibility, friction, contact, impact and control. New methods evolved with respect to simulation by recursive formalism, to closed kinematic loops, reaction forces and torques, and pre- and post-processing by data models, CAD coupling, signal analysis, animation and strength evaluation. Multibody system dynamics is applied to a broad variety of engineering problems from aerospace to civil engineering, from vehicle design to micromechanical analysis, from robotics to biomechanics. In particular, multibody dynamics is considered as the basis of mechatronics, e.g. controlled mechanical systems. These challenging applications are subject to fundamental research topics which were presented at the NATO ASI on Virtual Nonlinear Multibody Systems.

1. Datamodels

Within the multibody system community many computer codes have been developed, however, they differ widely in terms of model description, choice of basic principles of mechanics and topological structure so that a uniform description of models does not exist. The data exchange permits the alternate use of validated multibody system models with different simulation systems.

2. Parameter identification

The parameter identification is an essential part of multibody dynamics. The equations of motion of mechanical systems undergoing large displacements are highly nonlinear, however, they remain linear with respect to the system parameters.

3. Optimal design

Due to development of faster computing facilities the multibody system approach is changing from a purely analyzing method to a more synthesizing tool. Optimization methods are applied to optimize multibody systems with respect to their dynamic behaviour.

4. Dynamic strength analysis

The results obtained in research on strength analysis of material bodies can be applied and combined with the multibody system approach.

5. Contact and impact problems

Rigid and/or flexible bodies moving in space are subject to collisions what mechanically means impact and contact. Contact problems usually include friction phenomena which are modelled by Coulomb's law.

6. Extension to control and mechatronics

The applied forces and torques acting on multibody systems may be subject to control. Then, the multibody system is considered as the plant for which the controller has to be designed. Today, mechatronics is understood as an interdisciplinary approach to controlled mechanical systems usually modelled as multibody systems.

7. Nonholonomic systems

The nonholonomic systems are of engineering interest in vehicle dynamics and mobile robots.

8. Integration codes

The dynamic equations of motion are presented as ODE or DAE. Efficient algorithms for numerical integration of these equations are of major importance.

9. Real time simulation and animation

Efficient and fast simulation is always desirable in computational dynamics but it is really necessary for hardware-in-the loop and operator-in-the-loop applications. There are two approaches to achieve real time simulation: high speed hardware and efficient software. Multibody system dynamics contributes to the efficiency of the software by recursive and/or symbolic formalism and fast integration codes.

10. Challenging applications

Multibody system dynamics has a broad variety of applications. In biomechanics the walking motion is an important topic. However, there are much more problem in biomechanics which can be modeled and solved by multibody dynamics. The applications are ranging from vehicle occupants to sport sciences. Multibody dynamics is also a solid basis for nonlinear dynamics. In particular, impact and friction induced vibrations show chaotic behaviour. The control aspects in multibody dynamics are getting more and more important. Vehicle, aircraft and spaceship dynamics and reliability have always been challenging applications. With respect to transportation systems a challenging application of multibody dynamics is the structural and occupant crashworthiness.
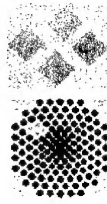
The NATO Science Programme

NATO Advanced Study Institute on

Virtual Nonlinear Multibody Systems

Prague, Czech Republic

June 23-July 3, 2002

University of Stuttgart   Czech Technical University in Prague

Institute B of Mechanics   Department of Mechanics

http://mechatronic.fsik.cvut.cz/ASI_NATO

NATO Advanced Study Institute (ASI) on Virtual Nonlinear Multibody Systems Prague June 23-July 3, 2002

Place: Hotel Krystal, Czech Technical University in Prague, Prague, Czech Republic

Organizing commitee:

Chairman: Prof. W. Schiehlen, University of Stuttgart, Stuttgart, Germany
Co-chairman: Prof. M. Valášek, Czech Technical University in Prague, Prague, Czech Republic

Members:

Prof. A. Shabana University of Illinois at Chicago, Illinois, USA

Prof. E. Kreuzer Technical University Hamburg-Harburg, Hamburg, Germany

Prof. J. Ambrosio IDMEC/IST, Instituto Superior Tecnico, Lisboa, Portugal

Prof. J. McPhee University of Waterloo, Ontario, Canada

Deadlines:

Paper abstract submission: January 31, 2002
Application for financial support: January 31, 2002
Paper acceptance: February 28, 2002
Financial support decision: February 28, 2002
Application for participation only: April 30, 2002
Full paper submission: May 15, 2002
NATO ASI: June 23 - July 3, 2002

Web: http://mechatronic.fsik.cvut.cz/ASI_NATO

Advanced Study Institute description

While not yet in the dictionary, the term "virtual reality" has taken on the meaning of the "computer generated perception of reality on the part of an involved human. The term "virtual reality" motivated the emerging use of the term "virtual prototype", suggesting both computer and human involvement in the process of design and testing of the prototype that do not exist as real object.

The complex multibody systems, that are composed of rigid and flexible bodies achieving spatial motion and various complex tasks, are up-to date objects of the virtual prototyping. The real simulation of the multibody system action takes into account various phenomena and particular properties. The classical dynamics do not regard various nonlinear effects that appear as a result of the action of multibody systems, as well as their mutual interaction. The virtual prototyping and dynamic modeling of such systems are, from economical point of view, perspective realms of scientific investigations having in mind the huge expenses for their design and manufacturing.

Future research fields in multibody dynamics are identified as standardisation of data, coupling with CAD systems, parameter identification, real-time animation, contact and impact problems, extension to electronic and mechatronic systems, optimal system design, strength analysis and interaction with fluids.

Objectives of the Advanced Study Institute:

- To meet leading scientists in the field of nonlinear multibody system dynamics

- To create conditions for exchange of ideas and development of collaborative applied projects

- To give possibilities for perspective young researchers to present their achievements and to establish professional contacts

- Emphasise will be given to analysis, synthesis and stability of large flexible systems and problems related to vehicles, aircraft, spaceships, manipulators, robots and constructions imposed on action of earthquakes.

This long course (10 days) is intended to provide a comprehensive coverage of the whole subject in its multidisciplinary aspects. The course is intended for PhD holders and advanced PhD students as well. Some background is assumed in applied dynamics and control.

The possible presentation of contributed papers of the participants is assumed.

NATO ASI on
Virtual Nonlinear Multibody Systems
Prague June 23-July 3, 2002

Family name:

First name: Title:

Organisation:

Address:

Country:

Phone:

Fax:

E-mail:

I intend to submit a paper YES ☐   NO ☐
Tentative title of the paper:

Please return to the NATO ASI secretariat:

Address: Prof. Michael Valasek, NATO ASI,
Dept. of Mechanics, Karlovo nam. 13, Praha 2,
121 35, Czech Republic

Fax: +420-2-24916709
E-mail: natoasi@felber.fsik.cvut.cz

Topics:
- Nonlinear dynamics models
- Unilateral constraints and contact
- Stability analysis and chaotic motions
- Data processing and visualization
- Control and optimization

Invited Lectures:
W. Schiehlen: Contact Problems And Wave Propagation In Nonlinear Multibody Systems

A. Shabana: Nonlinear Dynamics Of Multibody Systems With Generalized And Non-Generalized Coordinates

F.L. Chernousko: Snake-like Locomotions of Multilink Systems

J. Ambrosio: Impact of Rigid and Flexible Multibody Systems: Implications on the deformation description and contact models

M. Pascal: Numerical Simulation of Flexible Multibody Systems By Using A Virtual Rigid Body Model

P. Nikravesh: Flexible Body Model Reduction Techniques In Multibody Dynamics

F. Pfeiffer: Unilateral Multibody Dynamics

V. Berbyuk: Control And Optimization of The Semi-Passively Actuated Multibody Systems

M. Pereira: Optimization of Rigid-Flexible Multibody Systems With Application to Vehicle Dynamics and Crashworthiness

M. Lankarani: Analysis of External and Internal Impacts in Multibody Systems

E. Kreuzer: Multibody System Dynamics in Ocean Engineering

J. McPhee: Graph-Theoretic Modelling of Multibody Systems

E.J. Haug: Vehicle Virtual Proving Grounds

M. Valasek: Nonlinear Control Synthesis For Nonlinear Multibody Systems

W. Blajer: Geometrical Interpretation of Multibody Dynamics: Theory and Implementations

D. Bestle: Kinematic and Kinetic Analysis of Dynamic Systems, Optimization of Passive and Active Dynamic Systems

E. Zahariev: Modeling of Multibody System Contact Dynamics

P. Eberhard: Contact Formulations for Finite Elements and Multibody Systems

Registration:
If you want to participate at the NATO ASI you must register at the NATO ASI secretariat. If you want to present a paper you must submit an abstract at the NATO ASI secretariat. If you need a financial support, you must fill in an application form and send it to the NATO ASI secreatriat. Please take into account deadlines of the NATO ASI.
It is also possible to register on-line.

Grants:
Special grants are available for students from NATO and Partner countries. Travel, accomodation and subsistence will be supported. Applications should be sent conference secretariat before January 31, 2002.

Accommodation:
Hotel, where accomodation and full board for participants is arranged, is located near the path from the Prague's airport into the city center. It is also close to the Conference center where the NATO ASI will be hold. There are both single rooms (30 Euro/day) and double rooms (45 Euro/day) with full board available.

The participants of NATO ASI should book accomodation at the NATO ASI secretariat.

Contact Information:
NATO ASI secretariat can be reached by following means:

Telephone: +420-2-24357491
Fax: +420-2-24916709
E-mail: natoasi@felber.fsik.cvut.cz
Web: http://mechatronic.fsik.cvut.cz/ASI_NATO

Address: Prof. Michael Valasek, NATO ASI, Dept. of Mechanics, Karlovo nam. 13, Praha 2, 121 35, Czech Republic

Preprints of the
NATO Advanced Study Institute
on

Virtual Nonlinear Multibody Systems

Volume II

Edited by

Werner Schiehlen and Michael Valášek

Supported by the
European Research Office of the US Army

Czech Technical University in Prague
Prague, June 23 – July 3, 2002

AQ F03-02-0376

Table of Contents

Dynamics and Control of a Vehicle with Expanding Wheels Using Differential Flatness

Sunil K. Agrawal*, Jin Yan†, Jaume Franch**

* Professor, Department of Mechanical Engineering
† Graduate Student, Department of Mechanical Engineering
University of Delaware, Newark, DE 19716, USA
e-mail: agrawal@me.udel.edu

** Departament de Matematica Aplicada IV
Jordi Girona 1-3, Modul C-3, Campus Nord
UPC, 08034-Barcelona, Spain
e-mail: jfranch@mat.upc.es

Abstract

This paper describes analytics and experiments on a novel 4-wheel vehicle. The vehicle has back wheel drive and steering in addition to wheels that can expand and change radius. The motivation for this design is to attain added navigation capability by expanding the wheels according to the requirements of the terrain. In this paper, we discuss the motion of the vehicle on a flat floor. The steering angle is kept at zero so that the vehicle has a planar motion. The contact point of the wheel with the ground is assumed to be directly underneath the center of the wheel and has no slip.

The rolling constraints are nonholonomic, i.e., are non-integrable. The rate constraints are written in an input-affine drift-less control system. The structure of this drift-less control system allows to determine the differentially flat outputs of the system. Motion planning of the vehicle between two configurations is achieved through planning of these differentially flat outputs. These trajectories are then used to determine a feedback controller. A dynamic simulation is performed using MATLAB. The motions are currently being implemented on the physical hardware using a dSPACE control system.

Figure 1: A photograph of the vehicle with expanding wheels.

feature of the vehicle in our design is that its wheels can expand and change radius. The motivation for this design is to attain added navigation capability by expanding the wheels according to the requirements of the terrain. This paper addresses the analytics and other details of motion planning and control of this vehicle.

1 Introduction

Conventional four-wheel vehicles are either back wheel or front wheel drive. There are numerous reported literature on design, motion planning, and control of such unmanned vehicles. A mobile robot NOMAD was designed and built for remote operations in Antarctica [9]. This vehicle features a transforming chassis that can expand or compact by driving two pairs of four-bar linkages on each side of the robot. The unique

2 Description of the Vehicle

A photograph of the vehicle is shown in Fig. 1. The vehicle is built on a chassis constructed of half-inch aluminum plates. The rear wheels are driven by an a.c. Kollmorgen servomotor through a gearbox and chain drive system. The front wheels are steered by an identical a.c. servomotor connected to a four-bar mecha-
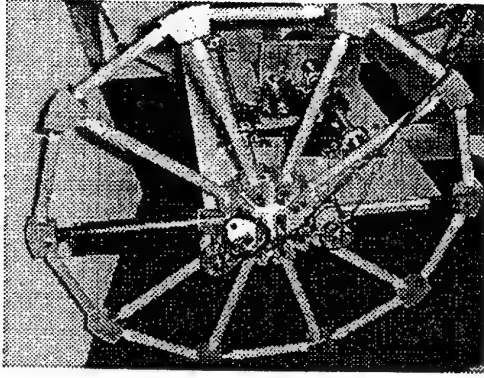
Figure 2: A photograph of the wheel of the vehicle.

Figure 3: A schematic of the vehicle with wheels during planar motion.

nism. In addition, the vehicle consists of four wheels that can expand and change radius as shown in Fig. 2. The design of the wheels of the vehicle is based on polyhedral single degree-of-freedom expanding structures using prismatic joints [1]. Kinematically, each wheel has a single degree-of-freedom during expansion and contraction. In the design, each of the four circular wheels is approximated by a polygon with ten sides and ten radial spokes. The wheels use aluminum decagons as hubs, with composite air cylinders acting as telescoping (or prismatic) joints along each edge and each spoke. The spokes and edges are joined using aluminum nodes cut along three sides to match interior angles, and rounded on the outsides to provide smooth rolling while the node is in contact with the ground. Each vertex of the polygon lying on the circumference has the curvature of a circular wheel. The wheels are actuated using a pair of d.c. linear actuators which replace two spokes and are set opposite each other. A single control signal is sent to both actuators, and position feedback is read from a potentiometer which is connected to one actuator on each wheel.

3 Model of the System

In this paper, we are modeling the motion of the vehicle in the plane as the steering angle is kept constant at zero. The kinematic model of the vehicle has two wheels with different radii in a plane connected by a rod in between, as shown in Fig. 3. We describe the configuration of the vehicle using the following variables: (x_1, y_1) and (x_2, y_2) are respectively the centers of the rear and front wheels in the inertial coordinate frame, θ_1 and θ_2 are respectively the clockwise angular rotations of the spoke 1 of the rear and front wheels with respect to the x-axis of the inertial coordinate
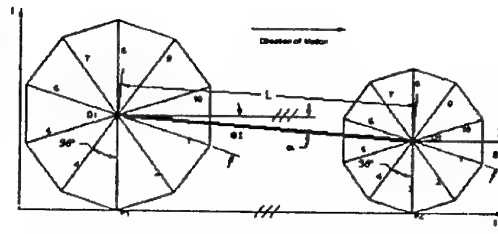
frame which we denote by $\hat{\mathbf{i}}$. Let r_1 and r_2 be respectively the radii of the rear and front wheels. α represents the clockwise angular rotation of the connecting rod with respect to $\hat{\mathbf{i}}$ of the inertial frame.

In the design, a circular wheel has been approximated by a polygon with ten sides and ten spokes. The vertices of the polygon have been fabricated to approximate the curvature of a circle. As the number of sides of the polygon is increased, the polygon better approximates the circular wheel. In the first model of rolling kinematics of the wheel, we assume that it is circular and the contact point of the wheel with the ground is vertically underneath the center of the wheel. This assumption will be relaxed in future models of the vehicle.

3.1 Kinematic Model

The position and velocity of the center of rear wheel in the inertial coordinate frame are given by

$$\mathbf{r}_{O_1} = x_1\hat{\mathbf{i}} + y_1\hat{\mathbf{j}} \tag{1}$$

$$\mathbf{v}_{O_1} = \dot{x}_1\hat{\mathbf{i}} + \dot{y}_1\hat{\mathbf{j}}. \tag{2}$$

The velocity of the point P_1 on the wheel directly underneath the center and in contact with the ground is given by

$$\mathbf{v}_{P_1} = \mathbf{v}_{O_1} + \omega_1 \times \mathbf{r}_{O_1 P_1} - \dot{r}_1\hat{\mathbf{j}}. \tag{3}$$

where $\mathbf{r}_{O_1 P_1}$ is a vector from O_1 to P_1 and ω_1 is the angular velocity of the rear wheel. In this equation, $-\dot{r}_1\hat{\mathbf{j}}$ represents the velocity component of P_1 due to expansion of the rear wheel. From the kinematic description, $\omega_1 = -\dot{\theta}_1\hat{\mathbf{k}}$. On substituting these expressions in Eq. (3) and simplifying, we get

$$\mathbf{v}_{P_1} = (\dot{x}_1 - r_1\dot{\theta}_1)\hat{\mathbf{i}} + (\dot{y}_1 - \dot{r}_1)\hat{\mathbf{j}}. \tag{4}$$

Since the rear wheel rolls about P_1 without slipping, $\mathbf{v}_{P_1} = 0$. This gives the two rolling constraints for the rear wheels

$$\dot{x}_1 = r_1\dot{\theta}_1 \tag{5}$$

$$\dot{y}_1 = \dot{r}_1. \tag{6}$$

2

Using a similar procedure for the front wheel, we obtain

$$\dot{x}_2 = r_2 \dot{\theta}_2 \qquad (7)$$

$$\dot{y}_2 = \dot{r}_2. \qquad (8)$$

From the geometry of the vehicle,

$$sin(\alpha) = \frac{r_1 - r_2}{l}, \qquad (9)$$

$$cos(\alpha) = \frac{x_2 - x_1}{l}, \qquad (10)$$

where l is the length of the connecting rod between the wheels.

In summary, the vehicle is described by nine coordinates: x_1, y_1, r_1, θ_1, x_2, y_2, r_2, θ_2, and α. These nine variables are subject to four rate constraints given by Eqs. (5)-(8) and two configuration constraints of Eqs. (9) and (10).

3.2 Models for Planning

The above equations can be used to eliminate x_1, x_2, y_1, and y_2 and provide a description of motion in terms of r_1, r_2, θ_1, θ_2, α and their derivatives. On differentiating Eq. (9), we get

$$\dot{\alpha} = \frac{\dot{r}_1 - \dot{r}_2}{l cos(\alpha)}. \qquad (11)$$

On differentiating Eq. (10) and substituting Eqs. (5), (7), and (11), we get

$$\dot{\theta}_2 = -\frac{tan(\alpha)}{r_2}\dot{r}_1 + \frac{tan(\alpha)}{r_2}\dot{r}_2 + \frac{r_1}{r_2}\dot{\theta}_1. \qquad (12)$$

Eq. (12) is a non-integrable rate constraint equation while Eq. (11) is an integrable rate constraint equation. From the planning point of view, we can use one of the two alternate models: Model (A) Eq. (12) - a non-holonomic equation and Eq. (9) - a holonomic equation; Model (B) Eq. (12) - a non-holonomic equation and Eq. (11) - an integrable rate equation.

3.2.1 Model (A):

$$\begin{bmatrix} \dot{r}_1 \\ \dot{r}_2 \\ \dot{\theta}_1 \\ \dot{\theta}_2 \end{bmatrix} = \begin{bmatrix} 1 & 0 & 0 \\ 0 & 1 & 0 \\ 0 & 0 & 1 \\ \frac{-tan(\alpha)}{r_2} & \frac{tan(\alpha)}{r_2} & \frac{r_1}{r_2} \end{bmatrix} \begin{bmatrix} \dot{r}_1 \\ \dot{r}_2 \\ \dot{\theta}_1 \end{bmatrix} \qquad (13)$$

where $sin(\alpha) = \frac{r_1 - r_2}{l}$.

3.2.2 Model (B):

$$\begin{bmatrix} \dot{r}_1 \\ \dot{r}_2 \\ \dot{\theta}_1 \\ \dot{\theta}_2 \\ \dot{\alpha} \end{bmatrix} = \begin{bmatrix} 1 & 0 & 0 \\ 0 & 1 & 0 \\ 0 & 0 & 1 \\ \frac{-tan(\alpha)}{r_2} & \frac{tan(\alpha)}{r_2} & \frac{r_1}{r_2} \\ \frac{1}{lcos(\alpha)} & \frac{1}{lcos(\alpha)} & 0 \end{bmatrix} \begin{bmatrix} \dot{r}_1 \\ \dot{r}_2 \\ \dot{\theta}_1 \end{bmatrix} \qquad (14)$$

3.3 Dynamic Model

The Lagrangian formalism was used to develop a dynamic model for the mechanism. The following assumptions were made: (i) Each wheel consists of ten point masses, located at the intersection of a spoke and the circumference, (ii) the center of mass of the connecting rod between the two wheels is midway along the length and it has a moment of inertia.

The kinetic and potential energies for the rear wheel, front wheel, and connecting rod were computed. From the expressions of the kinetic and potential energy, the Lagrangian $\mathcal{L}(q, \dot{q})$ was developed, where $q = [r_1 \ r_2 \ \theta_1 \ \theta_2, \alpha]^T$. The dynamic model development was done in two stages. First, it was assumed that the vector q does not have any constraints on its elements and the following expressions were evaluated

$$\frac{d}{dt}\frac{\partial \mathcal{L}}{\partial \dot{q}_i} - \frac{\partial \mathcal{L}}{\partial q_i}, \quad i = 1, ...5. \qquad (15)$$

These expressions are then collected to form the following structured forms

$$A(q)\ddot{q} + b(q, \dot{q}) \qquad (16)$$

where $A(q)$ is a (5×5) matrix, $b(q, \dot{q})$ is a (5×1) vector. A vector of inputs F is formed where $F = (F_1, F_2, M_1, 0, 0)^T$. Here, F_1 is the radial force applied by the motors on the rear wheel, F_2 is the radial force applied by the motors on the front wheel, and M_1 is the driving moment applied by the actuator on the rear wheel.

In the second step, Eq. (14) is first written in the form

$$\dot{q} = C \dot{q}_g \qquad (17)$$

From [2], the equations of motion in the presence of the constraints are given by

$$C(q)^T[A(q)\ddot{q} + b(q, \dot{q})] = C(q)^T F \qquad (18)$$

On using the relation $\ddot{q} = C(q)\ddot{q}_g + \dot{C}(q)\dot{q}_g$, the above equation can be simplified to

$$C(q)^T A(q) C(q) \ddot{q}_g + C(q)^T (A(q)\dot{C}(q)\dot{q}_g + b(q, \dot{q}))$$
$$= C(q)^T F. \qquad (19)$$

This equation represents the *forward dynamic model* of the system. Given the trajectory $q_g(t)$, the required actuator forces/moments can be computed.

Similary, given the trajectory of actuator forces/moments, the trajectory of the vehicle can be computed as follows:

$$\ddot{q}_g = [C(q)^T A(q) C(q)]^{-1}[C(q)^T F$$
$$- C(q)^T (A(q)\dot{C}(q)\dot{q}_g + b(q, \dot{q}))] \qquad (20)$$

This equation represents the *inverse dynamic model* of the system. Given the trajectory $F(t)$, the trajectory of the vehicle can be computed. The differential algebraic equations (20) and (17) in the variables q and q_g constitute the dynamic equations of motion of the system.

3

4 Motion Planning

For motion planning, we use Model (A) developed in Section 3.2 given in Eq. (13). This model of the system is driftless and has control in an affine form. In classical literature, a driftless control system has the form

$$\dot{q} = g(q)u, \qquad (21)$$

where $q \in R^n$ are referred to as the states, $u \in R^m$ are the controls, and $g(q)$ are smooth vector fields in R^n. In our model, the three rates $u = \dot{q}_g = (\dot{r}_1, \dot{r}_2, \dot{\theta}_1)^T$ are the inputs to the system and the state space consists of $q = (r_1, r_2, \theta_1, \theta_2)^T$. The variable α is an internal variable of the system given by $sin(\alpha) = \frac{r_1 - r_2}{l}$.

4.1 Differential Flatness

Classes of dynamic systems, referred to as differentially flat systems, have the special property that Eq. (21) admits the following diffeomorphic representation over the state space [3]:

$$q = q(z, z^{(1)}, \ldots, z^{(p-1)}), \qquad (22)$$
$$u = u(z, z^{(1)}, \ldots, z^{(p)}), \qquad (23)$$

where $z \in R^m$ are suitably chosen output functions which are determined using results from linear and nonlinear systems theory. In the above equation, $p-1$ and p represent the highest derivatives of z in the expression for q and u, respectively. The integer p is a property of the system. Among others, flat systems include controllable linear systems as well as nonlinear systems linearizable by static and dynamic feedback.

For differentially flat systems, a trajectory in the space of outputs $z(t)$ and its derivatives is consistent with the dynamics if it satisfies the boundary conditions. The states $q(t)$ and inputs $u(t)$ can be computed from $z(t)$ according to Eqs. (22) and (23). Differentially flat systems have been studied in the context of trajectory generation ([3], [4]), optimal control ([5], [7]), and auxiliary constraints [6].

4.2 Driftless Systems

Some important results on linearization of driftless systems through static and dynamic feedback are summarized in [8]. Systems that exhibit these linearization properties fall in the class of differentially flat systems.

Since there are three inputs, we need to find three flat outputs $z = (z_1, z_2, z_3)$, such that all the system variables can be written as functions of z and their derivatives. The system is not static feedback linearizable since it is driftless. However, we can choose the following set of flat coordinates by inspection

$$z_1 = r_1 \qquad (24)$$
$$z_2 = r_2 \qquad (25)$$
$$z_3 = \frac{r_1}{r_2}\theta_1 - \theta_2 \qquad (26)$$

On differentiating Eq. (26), we get

$$\dot{z}_3 = (\frac{r_1}{r_2}\dot{\theta}_1 - \dot{\theta}_2) + \frac{\dot{r}_1}{r_2}\theta_1 - \frac{r_1\dot{r}_2}{r_2^2}\theta_1 \qquad (27)$$

Using Eq. (12), it can be simplified to

$$\dot{z}_3 = \frac{tan(\alpha)}{r_2}\dot{r}_1 - \frac{tan(\alpha)}{r_2}\dot{r}_2 + (\frac{\dot{r}_1}{r_2} - \frac{r_1\dot{r}_2}{r_2^2})\theta_1 \qquad (28)$$

Now, θ_1 can be solved using the above equation

$$\theta_1 = \frac{\dot{z}_3 - \frac{tan(\alpha)}{r_2}\dot{r}_1 + \frac{tan(\alpha)}{r_2}\dot{r}_2}{\frac{\dot{r}_1}{r_2} - \frac{r_1\dot{r}_2}{r_2^2}} \qquad (29)$$

where $tan(\alpha) = \frac{r_1 - r_2}{\sqrt{l^2 - (r_1 - r_2)^2}}$. Hence, θ_1 can be written in terms of the flat outputs and their derivatives

$$\theta_1 = \frac{\dot{z}_3 - \frac{tan(\alpha)}{z_2}\dot{z}_1 + \frac{tan(\alpha)}{z_2}\dot{z}_2}{\frac{\dot{z}_1}{z_2} - \frac{z_1\dot{z}_2}{z_2^2}} \qquad (30)$$

where $tan(\alpha) = \frac{z_1 - z_2}{\sqrt{l^2 - (z_1 - z_2)^2}}$. From Eqs. (24)-(26), we get

$$\theta_2 = \frac{z_1}{z_2}\theta_1 - z_3 \qquad (31)$$
$$r_1 = z_1 \qquad (32)$$
$$r_2 = z_2 \qquad (33)$$

On differentiating these expressions, the inputs $\dot{\theta}_1, \dot{r}_1, \dot{r}_2$ can also be expressed in terms of the flat outputs and their derivatives.

4.3 Trajectory Generation

The trajectory planning problem can be posed as finding a smooth trajectory of the variables $\theta_1(t)$, $\theta_2(t)$, $r_1(t)$, $r_2(t)$ between two given end-points over a time t_0 to t_f. The conditions of $\theta_1(t_0)$, $\theta_2(t_0)$, $r_1(t_0)$, $r_2(t_0)$ can be used in Eqs. (24)-(26) to compute $z_1(t_0)$, $z_2(t_0)$, and $z_3(t_0)$. Similarly, the conditions of $\theta_1(t_f)$, $\theta_2(t_f)$, $r_1(t_f)$, $r_2(t_f)$ can be used in Eqs. (24)-(26) to compute $z_1(t_f)$, $z_2(t_f)$, and $z_3(t_f)$.

These boundary conditions can be used to select a smooth trajectory for $z(t)$ between t_0 and t_f. Now, Eqs. (30)-(33) can be used to compute $\theta_1(t)$, $\theta_2(t)$, $r_1(t)$, $r_2(t)$ consistent with the dynamic equations (13). Note that the transformation is nonsingular as long as $z_2 \neq 0$ and $\dot{z}_1 z_2 - \dot{z}_2 z_1 \neq 0$. In the original coordinates, these translate to $r_2 \neq 0$ and $\dot{r}_1 r_2 - \dot{r}_2 r_1 \neq 0$. Since r_2 refers to the radius, it is never zero during the motion. The second condition implies that $\dot{r}_1 \neq \frac{\dot{r}_2 r_1}{r_2}$ anywhere during motion. This must be ensured through the choice of a proper trajectory.

A motion plan is developed using the following boundary conditions for the trajectory over 10 seconds of time: $r_1(0) = 0.3$, $r_2(0) = 0.3$, $\theta_1(0) = 0$, $\theta_2(0) = 0$; $\dot{r}_1(0) = 0.02$, $\dot{r}_2(0) = 0.01$, $\dot{\theta}_1(0) = 0$, $\dot{\theta}_2(0) = 0$;
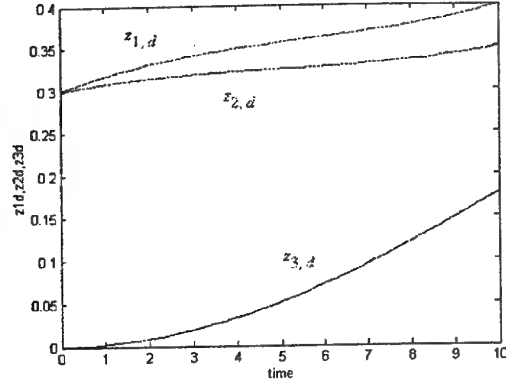
4

Figure 4: The computed trajectories of the three flat outputs z_{1d}, z_{2d}, z_{3d}.
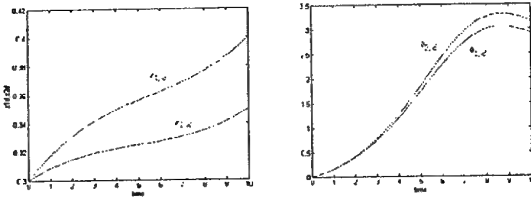

Figure 5: The computed trajectories of r_{1d}, r_{2d}, θ_{1d}, θ_{2d}.

$r_1(10) = 0.4$, $r_2(10) = 0.35$, $\theta_1(10) = 3$, $\theta_2(10) = 3.25$; $\dot{r}_1(10) = 0.015$, $\dot{r}_2(10) = 0.01$, $\dot{\theta}_1(10) = 0$, $\dot{\theta}_2(10) = 0$. All lengths are given in meters and all angles are in radians.

These boundary conditions when transformed to the space of flat variables give: $z_1(0) = 0.3$, $z_2(0) = 0.3$, $z_3(0) = 0$; $\dot{z}_1(0) = 0.02$, $\dot{z}_2(0) = 0.01$, $\dot{z}_3(0) = 0$; $z_1(10) = 0.4$, $z_2(10) = 0.35$, $z_3(10) = 0.17857$; $\dot{z}_1(10) = 0.015$, $\dot{z}_2(10) = 0.01$, and $\dot{z}_3(10) = 0.0306$. The flat output trajectories were chosen to be cubic polynomials in time using these boundary conditions and are shown in Fig. 4. On transforming these trajectories of the flat outputs, the state trajectories are shown in Fig. 5.

5 Feedback Control

From the model of the system, the inputs are related to the flat variables as follows:

$$u_1 = \dot{r}_1 = \dot{z}_1 \tag{34}$$

$$u_2 = \dot{r}_2 = \dot{z}_2 \tag{35}$$
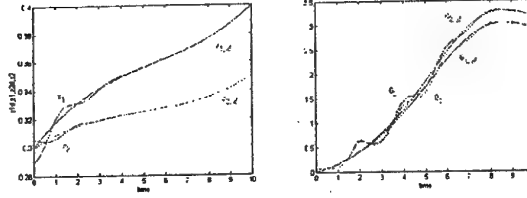
Figure 6: The feedback control performance about r_{1d}, r_{2d}, θ_{1d}, θ_{2d}.

$$u_3 = \dot{\theta}_1 = \frac{d}{dt}\left[\frac{\dot{z}_3 - \frac{tan(\alpha)}{z_2}\dot{z}_1 + \frac{tan(\alpha)}{z_2}\dot{z}_2}{\frac{\dot{z}_1}{z_2} - \frac{z_1 \dot{z}_2}{z_2^2}}\right] \tag{36}$$

$$= \gamma_1(z,\dot{z})\ddot{z}_1 + \gamma_2(z,\dot{z})\ddot{z}_2 + \gamma_3(z,\dot{z})\ddot{z}_3 + \gamma_4(z,\dot{z}) \tag{37}$$

where γ_i are functions of z and $\dot{z}$. In order to obtain a well defined relative degree with respect to each of the outputs, we need to perform a prolongation of the inputs in the model by defining $\zeta_1 = \dot{u}_1$ and $\zeta_2 = \dot{u}_2$ and

$$\ddot{z}_1 = \dot{\zeta}_1 = v_1 \tag{38}$$

$$\ddot{z}_2 = \dot{\zeta}_2 = v_2 \tag{39}$$

$$\ddot{z}_3 = \frac{1}{\gamma_3}(u_3 - \gamma_1\zeta_1 - \gamma_2\zeta_2 - \gamma_4) = v_3 \tag{40}$$

With this extension of the inputs, each output has a relative degree two as long as $\gamma_3(z,\dot{z}) \neq 0$. Now, the control law can be chosen to be of the form

$$v_i = \ddot{z}_{id} + k_{vi}(\dot{z}_{id} - \dot{z}_i) + k_{pi}(z_{id} - z_i), \quad i = 1,2,3 \tag{41}$$

where k_{vi} and k_{pi} are selected gains such that $z_i(t)$ asymptotically follows $z_{id}(t)$. With these choices, the input rates satisfy the following relationships:

$$\dot{u}_1 = \ddot{z}_{1d} + k_{v1}(\dot{z}_{1d} - \dot{r}_1) + k_{p1}(z_{1d} - r_1) \tag{42}$$

$$\dot{u}_2 = \ddot{z}_{2d} + k_{v2}(\dot{z}_{2d} - \dot{r}_2) + k_{p2}(z_{2d} - r_2) \tag{43}$$

$$u_3 = \gamma_1 \dot{u}_1 + \gamma_2 \dot{u}_2 + \gamma_4$$
$$+ \gamma_3[\ddot{z}_{3d} + k_{v3}(\dot{z}_{3d} - \dot{z}_3) + k_{p3}(z_{3d} - z_3)] \tag{44}$$

An example of an implementation of the feedback controller is shown in Fig. 6. The initial conditions at time $t = 0$ were chosen as $r_1 = 0.29$, $r_2 = 0.305$, $\theta_1 = 0$, $\theta_2 = 0$; $\dot{r}_1 = 0.02$, $\dot{r}_2 = 0.01$ so that the initial starting point is not on the given reference trajectory. The feedback gains were selected as $k_{v1} = 1.414$, $k_{p1} = 10$; $k_{v2} = 1.414$, $k_{p2} = 10$; $k_{v3} = 50$, $k_p3 = 100$. As shown in the plots, the trajectories follow closely the desired trajectory.

5

6 Conclusion

The paper described the design, modeling, trajectory planning, and control of a novel 4-wheel vehicle with expanding wheels. The first model assumes that the vehicle moves along a straight line on a falt floor and the contact point of the wheel with ground is directly underneath the center of the wheel and has no slip. The rolling constraints are nonholonomic, i.e., are non-integrable. The rate constraints were written in an input-affine drift-less control system. The structure of this drift-less control system allows to determine the differentially flat outputs of the system. Motion planning of the vehicle between two configurations is achieved through planning of these differentially flat outputs. These trajectories are then used to determine a feedback controller and simulated in MATLAB. The motions are currently being implemented on the physical hardware using a dSPACE control system.

Acknowledgments

References

[1] Agrawal, Sunil, K., Kumar, S., Yim, M, Suh, J., "Polyhedral Single Degree-of-freedom Expanding Structures", In Proceedings, *IEEE International Conference on Robotics and Automation*, 2001. (Expanded version to appear in *Jounal of Mechanical Design, Transactions of the ASME*, 2002.

[2] Kane, T. R. and Levinson, D. A., *Dynamics: Theory and Applications*, McGraw Hill Book Company, New York, 1985.

[3] Fliess, M., Levine, J., Martin, P., Rouchon, P., "Flatness and Defect of Nonlinear Systems: Introductory Theory and Examples", *International Journal of Control*, Vol. 61, No. 6, 1995, pp. 1327-1361.

[4] Nieuwstadt, M. J. and Murray, R. M., "Real Time Trajectory Generation for Differentially Flat Systems," *Int'l. J. Robust and Nonlinear Control*, Vol. 18, No. 11, 1998, pp. 995-1020.

[5] Agrawal, S. K., Faiz, N., "A New Efficient Method for Optimization of a Class of Nonlinear Systems Without Lagrange Multipliers", *Journal of Optimization Theory and Applications*, Vol. 97, No. 1, 1998, 11-28.

[6] Faiz, N. and Agrawal, S. K., Murray, R. M., "Trajectory Planning of Differentially Flat Systems with Dynamics and Inequalities", *AIAA Journal of Guidance, Control, and Dynamics*, Vol. 24, No. 2, 2001, 219-227.

[7] Veeraklaew, T. and Agrawal, S. K., "A New Computation Framework for Optimization of Higher-Order Dynamic Systems", *AIAA Journal of Guidance, Control, and Dynamics*, Vol. 24, No. 2, 2001, 228-236.

[8] Fossas, E., Franch, J., and Agrawal, S. K., "Linearization by Prolongations of Two-input Driftless Systems", In Proceedings, *IEEE Control Decision Conference*, 2000.

[9] Wagner, M. D., Apostolopoulos, D., Shillcutt, K., Shamah, B., Simmons, R., and Whittaker, W. L., "The Science Autonomy System of the Nomad Robot", In Proceedings, *IEEE International Conference on Robotics and Automation*, May, 2001, pp. 1742-1749.

6

Robotics and Autonomous Machines: Approaches to Dynamic Planning and Optimization

Sunil Kumar Agrawal, Ph.D.

Associate Professor
Department of Mechanical Engineering
University of Delaware, Newark, DE 19716

Problem Statement

- Develop *computationally efficient* algorithms for feasible and/or optimal planning of dynamic systems.

- State equations: $\dot{\bar{x}} = \bar{f}(\bar{x}) + \bar{g}(\bar{x})\bar{u}, \quad \bar{x} \in \Re^n, \quad \bar{u} \in \Re^m$
- Path and end constraints:
$$\bar{L}_1 \le \bar{u} \le \bar{L}_2, \quad \bar{p}(\bar{x}) \le 0, \quad \bar{c}(\bar{x},\bar{u}) \le 0, \quad \bar{x}(t_i) = \bar{x}_i$$
- Cost functional: $J = \int_{t_0}^{t_f} L(\bar{x},\bar{u},t)dt$

Motivation
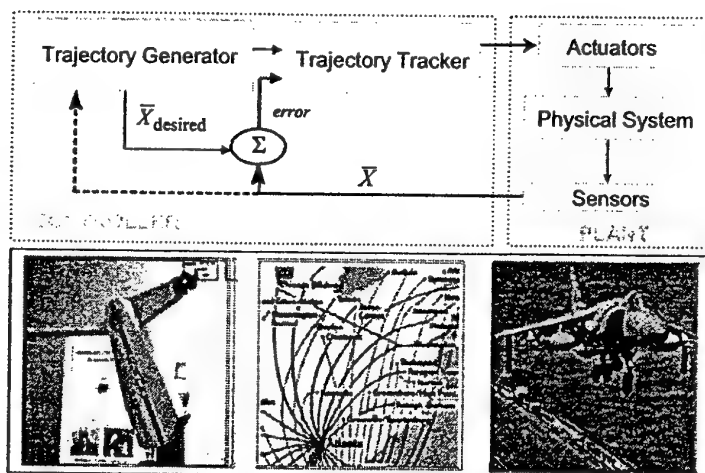
Differentially Flat or Higher-Order Systems

- Canonical transformation of state equations using linear and nonlinear systems theory

$$\boxed{\dot{\bar{x}} = f(\bar{x},u)} \quad \underset{y \in \mathfrak{R}^m}{\longleftrightarrow} \quad \boxed{\begin{array}{l} \bar{x} = \bar{x}(y,y^{(1)},\ldots,y^{(q)}) \\ u = u(y,y^{(1)},\ldots,y^{(q+1)}) \end{array}}$$

- Controllable linear time-invariant systems
- Classes of time-varying, time-periodic systems
- Feedback linearizable nonlinear systems
- Classes of nonholonomic systems
- Differentially flat systems

Higher-Order Systems: Trivial Examples
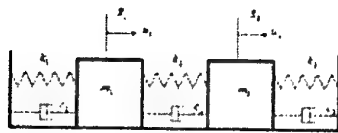
$$M\ddot{q} + D\dot{q} + Kq = u$$

$$\bullet \quad \begin{bmatrix} u \\ q \\ \dot{q} \end{bmatrix} = \begin{bmatrix} K & D & M \\ I & 0 & 0 \\ 0 & I & 0 \end{bmatrix} \begin{bmatrix} q \\ \dot{q} \\ \ddot{q} \end{bmatrix}$$

$$I\ddot{q}_1 + MgL \sin q_1 + k(q_1 - q_2) = 0$$
$$J\ddot{q}_2 - k(q_1 - q_2) = u$$

$$q_2 = q_1 + \frac{I}{k}\ddot{q}_1 + \frac{MgL}{k}\sin q_1$$
$$u = J\ddot{q}_2 - k(q_1 - q_2)$$

Non-trivial Flat Systems: Aircraft Dynamics

$$\dot{V} = -\frac{D}{m} - g \sin \vartheta$$
$$\dot{\alpha} = q - \dot{q} \sec\beta - (p \cos\alpha + r \sin\alpha) \tan\beta$$
$$\dot{\beta} = \dot{r} + p \sin\alpha - r \cos\alpha$$
$$col(\dot{\psi}, \dot{\vartheta}, \dot{\phi}) = M(\psi, \vartheta, \phi)\omega^\cdot$$
$$\dot{\omega} = J^{-1}\tilde{\omega} J\omega + J^{-1}T$$

$$\dot{p} = p \cos\alpha\cos\beta + (q - \dot{\alpha})\sin\beta + r \sin\alpha\cos\beta$$
$$\dot{q} = \frac{1}{mV}(L - mg \cos\vartheta\cos\phi)$$
$$\dot{r} = \frac{1}{mV}(-S + mg \cos\vartheta\sin\phi) \qquad \text{[Isidori 95]}$$

$$col(D,L,S) = G(V,\alpha,\beta) + F(V,\alpha,\beta)P$$
$$T = B(V,\alpha,\beta) + A(V,\alpha,\beta)\delta$$

For a typical Aircraft, the flat outputs are x, y, z, ϕ

$$V = V(\dot{x}, \dot{y}, \dot{z})$$
$$\psi = \psi(\dot{x}, \dot{y}, \dot{z})$$
$$\vartheta = \vartheta(\dot{x}, \dot{y}, \dot{z})$$
$$\alpha = \alpha(\dot{x}, \ddot{x}, \dot{y}, \ddot{y}, \dot{z}, \ddot{z}, \phi)$$
$$\beta = \beta(\dot{x}, \ddot{x}, \dot{y}, \ddot{y}, \dot{z}, \ddot{z}, \phi) \qquad \text{[Martin 96]}$$
$$P = P(\dot{x}, \ddot{x}, \dot{y}, \ddot{y}, \dot{z}, \ddot{z}, \phi)$$
$$\omega = \omega(\dot{x}, \ddot{x}, \dddot{x}, \dot{y}, \ddot{y}, \dddot{y}, \dot{z}, \ddot{z}, \dddot{z}, \phi, \dot{\phi})$$
$$\delta = \delta(\dot{x}, \ddot{x}, \dddot{x}, x^{(4)}, \dot{y}, \ddot{y}, \dddot{y}, y^{(4)}, \dot{z}, \ddot{z}, \dddot{z}, z^{(4)}, \phi, \dot{\phi}, \ddot{\phi})$$
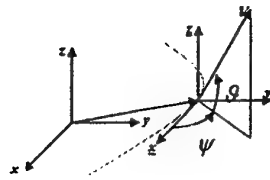
$$V = \sqrt{\dot{x}^2 + \dot{y}^2 + \dot{z}^2}$$
$$\psi = \arctan\left(\frac{\dot{y}}{\dot{x}}\right)$$
$$\vartheta = \arctan\left(\frac{\dot{z}}{\sqrt{\dot{x}^2 + \dot{y}^2}}\right)$$

ϕ not determined by trajectory

Feasible Trajectories without Inequalities

$$\dot{\bar{x}} = \bar{f}(\bar{x}) + \bar{g}(\bar{x})\bar{u}$$
$$\bar{x}_0 \xrightarrow{t} \bar{x}_f$$
$$t \in [t_0, t_f]$$
$$\bar{x} \in \Re^n, \bar{u} \in \Re^m$$

$[\bar{y} ... \bar{y}^q] = \Phi(\bar{x}, \bar{u})$

$[\bar{x}, \bar{u}] = \Phi^{-1}(\bar{y} ... \bar{y}^q)$

$$[\bar{y}_0 ... \bar{y}_0^p] \xrightarrow{t} [\bar{y}_f ... \bar{y}_f^p]$$
$$t \in [t_0, t_f]$$
(Algebraic Problem)
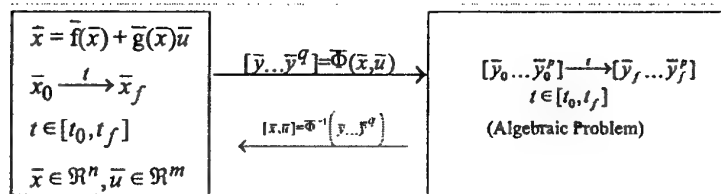
Example

$$I\ddot{q}_1 + MgL \sin q_1 + k(q_1 - q_2) = 0$$
$$J\ddot{q}_2 - k(q_1 - q_2) = u$$
$$q_2 = q_1 + \frac{I}{k}\ddot{q}_1 + \frac{MgL}{k}\sin q_1$$
$$u = J\ddot{q}_2 - k(q_1 - q_2)$$

$$q_1\big|_{t=0} = 0$$
$$q_1\big|_{t=1} = 1$$
$$q_2\big|_{t=0} = 0 \rightarrow \ddot{q}_1\big|_{t=0} = 0$$

$$q_1 = t$$
$$q_2 = t + \frac{MgL}{k}\sin t$$
$$u = MgL \sin t - \frac{JMgL}{k}\sin t$$

Optimal Trajectories: Feedback Linear Systems

$$\dot{\bar{x}} = \bar{f}(\bar{x}) + \bar{g}(\bar{x})\, u$$
$$\bar{x} \in \mathrm{R}^n, \quad \bar{u} \in \mathrm{R}^m$$
$$J = \int_{t_0}^{t_f} L(\bar{x}, \bar{u})dt$$

$y = T(x)$
$v = \alpha(x) + \beta(x)u$

$$\dot{\bar{y}} = A\,\bar{y} + B\,\bar{v}$$
$$\bar{y} \in \mathrm{R}^n, \quad \bar{v} \in \mathrm{R}^m$$
$$J = \int_{t_0}^{t_f} L(y_1, \dot{y}_1, \ldots, \overset{p}{y}_1)dt$$
Direct/Indirect Solution
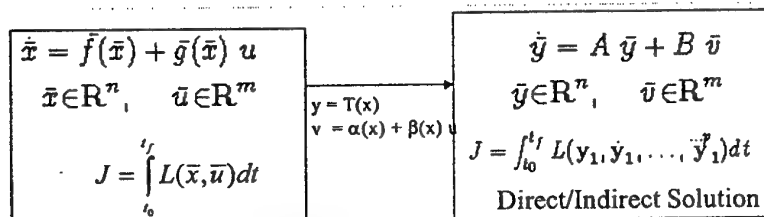
$$\delta J = \int_{t_0}^{t_f} h^T \left[\frac{\partial L}{\partial z} - \frac{d}{dt}\frac{\partial L}{\partial \dot{y}_1} + \frac{d^2}{dt^2}\frac{\partial L}{\partial \ddot{y}_1} + \ldots + (-1)^p \frac{d^p}{dt^p}\frac{\partial L}{\partial \overset{p}{y}_1} \right]dt$$

$$+ [h^T(\ldots) + \dot{h}^T(\ldots) + \ldots + \overset{p-1}{h}^T(\ldots)]_{t_0}^{t_f}$$

$$\overset{2p}{y}_1 = g\left(y_1, \dot{y}_1, \ldots, \overset{2p-1}{y}_1\right) \quad + \text{BC}$$

9

Example: Flexible Joint

$$I\ddot{q}_1 + MgL\sin(q_1) + k(q_1 - q_2) = 0$$
$$J\ddot{q}_2 - k(q_1 - q_2) = u$$

$$
\begin{aligned}
y_1 &= q_1 \\
y_2 &= q_2 \\
y_3 &= y_4 \\
y_4 &= v \\
y(t_0) &= y_0 \qquad y(t_f) = y_f
\end{aligned}
$$

$$\frac{\partial L}{\partial y_1} - \frac{d}{dt}\frac{\partial L}{\partial \dot{y}_1} + \frac{d^2}{dt^2}\frac{\partial L}{\partial \ddot{y}_1} - \frac{d^3}{dt^3}\frac{\partial L}{\partial \dddot{y}_1} + \frac{d^4}{dt^4}\frac{\partial L}{\partial \ddddot{y}_1} = 0$$

$$\overset{8}{\ddot{y}} = f(y_1, \dot{y}_1, \ldots, \overset{7}{\ddot{y}_1})$$

$$y_1(0), \dot{y}_1(0), \ddot{y}_1(0), \overset{3}{\dddot{y}_1}(0)$$
$$y_1(f), \dot{y}_1(f), \ddot{y}_1(f), \overset{3}{\dddot{y}_1}(f)$$
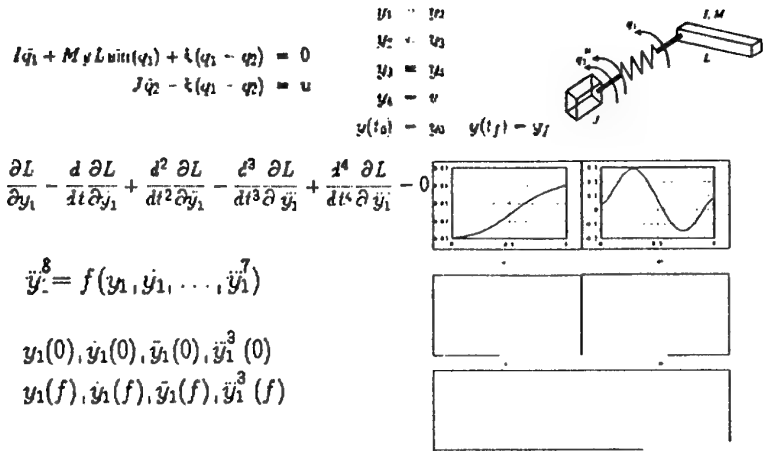
Experiment: Free-floating Robot
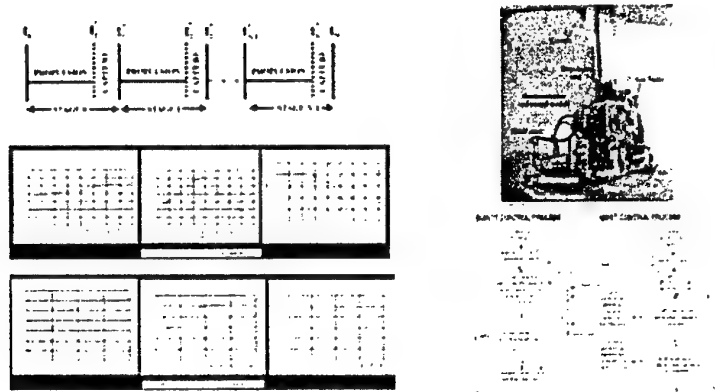
Feasible Planning: Inequalities

$$
\begin{aligned}
\bar{x} &= \bar{f}(\bar{x}) + \bar{g}(\bar{x})\bar{u} \\
\bar{x}_0 &\xrightarrow{t} \bar{x}_f \\
t &\in [t_0, t_f] \\
\bar{x} &\in \Re^n, \bar{u} \in \Re^m \\
c(\bar{x}, \bar{u}) &\le 0
\end{aligned}
$$

$$[\bar{y} \ldots \bar{y}^q] = \bar{\Phi}(\bar{x}, \bar{u})$$

$$[\bar{x}, \bar{u}] = \bar{\Phi}^{-1}(\bar{y} \ldots \bar{y}^q)$$

$$
\begin{aligned}
[\bar{y}_0 \ldots \bar{y}_0^p] &\xrightarrow{t} [\bar{y}_f \ldots \bar{y}_f^p] \\
t &\in [t_0, t_f] \\
c(\bar{y}, \dot{\bar{y}}, \ldots, \overset{p}{\bar{y}}) &\le 0
\end{aligned}
$$
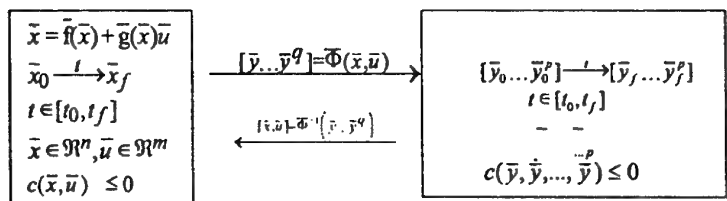
Polytopic Approximation

Semi-infinite Optimization
NPSOL
MATLAB

10

Experiment: Predator-Prey

$$x_2 = y \qquad x_1 = \frac{m_2}{k_2} y + \frac{c}{k_2} \dot{y} + y$$

$$-.03 \le x_2 \le .03 \quad -.03 \le x_1 \le .03 \quad u_{min} \le u \le u_{max}$$

$$C[y \;\; \dot{y} \;\; \ddot{y}]^T + \bar{d} \le 0$$

$$y(t) = \phi_0(t) + b_1\phi_1(t) + b_2\phi_2(t)$$

$$K = \left\{ E(t_i)\begin{bmatrix} b_1 \\ b_2 \end{bmatrix} + \bar{f}(t_i) \le 0, \quad t_i \in [0, t_1, \ldots t_f] \right\}$$

Optimal Planning: Pontryagin's Extensions

$z \in \mathcal{R}^n, z \in \mathcal{R}^m$ First-Order Form   Higher Order Form

$y, v \in \mathcal{R}^m$

	First-Order Form	Higher-Order Form
Dynamic Eqs.	$\dot{x} = f(x) + g(x)u$	$\overset{p}{y} = f(y, \dot{y}, \ldots \overset{p-1}{y}, v)$
Cost Functional	$J = \int_{t_0}^{t_f} L(x, u, t)dt$	$J = \int_{t_0}^{t_f} L(y, y, \ldots \overset{p}{y}, t)dt$
Constraints	$c(x, u, t) \le 0$	$c(y, y \ldots \overset{p}{y}, t) \le 0$

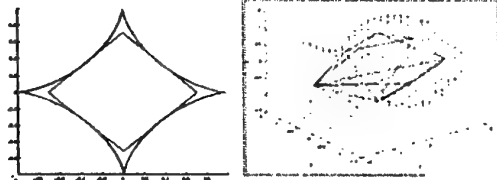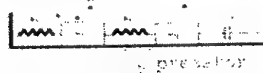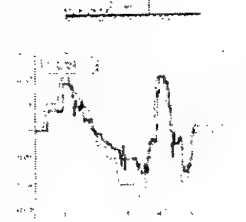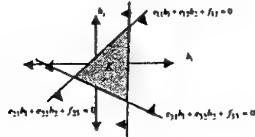|	First-Order Form $x \in \mathcal{R}^n, u \in \mathcal{R}^m$	Higher-Order Form $z \in \mathcal{R}^m, u \in \mathcal{R}^m$ $x(t)^T = (x^T \; \dot{x}^T \ldots \overset{p-1}{x}^T)^T$
Dynamic Eqs	$\dot{x} = f(x, u, t)$	$\overset{p}{x} = f(x, \dot{x}, \ldots \overset{p-1}{x}, u, t)$
Cost Function	$J = h(x_f, t_f) + \int_{t_0}^{t_f} L(x, u, t)dt$	$J = h(x_f, t_f) + \int_{t_0}^{t_f} L(x, \dot{x}, \ldots \overset{p-1}{x}, u, t)dt$
Constraints	$c(x, u, t) \le 0$	$c(x, \dot{x}, \ldots \overset{p-1}{x}, u, t) \le 0$
Hamiltonian	$\mathcal{H}(x, u, t) = L + \lambda^T f + \mu^T c$	$\mathcal{H}(x, u, t) = L + \lambda^T f + \mu^T c$
Minimum Pple	$\mathcal{H}(x, u^*, t) = \min \mathcal{H}(x, u, t)$	$\mathcal{H}(x, u^*, t) = \min \mathcal{H}(x, u, t)$
Costate Eqs	$\dot{\lambda} = -\mathcal{H}_x$	$(-1)^p \overset{p}{\lambda} = \mathcal{H}_x - \frac{d}{dt}\mathcal{H}_{\dot{x}} + \ldots + (-1)^{p-1}\frac{d^{p-1}}{dt^{p-1}}\mathcal{H}_{\overset{p-1}{x}}$

Higher-Order Toolboxes: Direct & Indirect

- Parameterized solution of higher-order variable and inputs
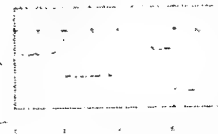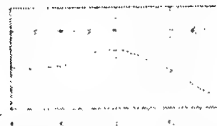
# of conditions must be satisfied (N-interval)	Higher-Order (p>1)	First-Order (n' = np)
1. Continuity & Boundary	$2np(N+1)$	$2n'(N+1) \ldots$(same)
2. State/costate equations with 2 collocation point in each interval	Direct....................... $2nN$ Indirect....................... $4nN$	Direct....................... $2n'N$ Indirect....................... $4n'N$
3. Constraints	$2rN$	$2rN \ldots$(same)

- Use NPSOL to solve NLP problem
- **Features:** Direct/Indirect, First-order/Higher-order, General cost, Boundary constraints, Automatic gradient computation, First integral of the solution, Matlab Mex-file, Graphical environment

New Toolbox: Computational Comparisons
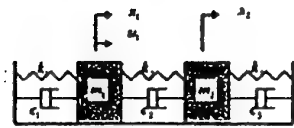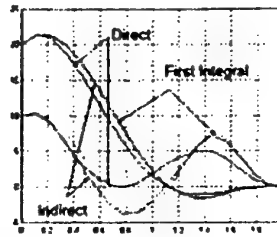
Systems	CPU run-time (Second)
1 Direct First-order (I)	20 66
2 Direct Second-order (II)	7 800
3 Direct Fourth-order (III)	2 91
4 Indirect First-order (I)	99 74
5 Indirect Second-order (II)	22 35
6 Indirect Fourth-order (III)	15 57

New Toolbox: Computational Comparisons
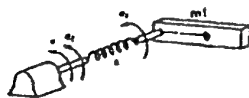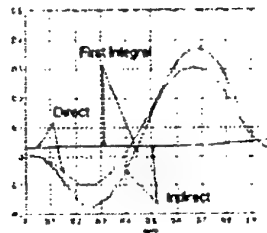
Systems	CPU run-time (Second)
1 Direct First-order (I)	10 00
2 Direct Second-order (II)	4 700
3 Direct Fourth-order (III)	2 850
4 Indirect First-order (I)	434 6
5 Indirect Second-order (II)	137 5
6 Indirect Fourth-order (III)	55 62
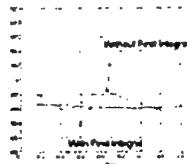
Optimal Planning of a Group of Flat Systems

$$\min \int_{t_0}^{t_f} \bar{L}(\bar{x}_1, \bar{x}_2, \ldots, \bar{x}_N, u_1, u_2, \ldots, u_N, t)$$

s.t.

$\dot{\bar{x}}_i = f_i(\bar{x}_i, u_i), \ i = 1, \ldots, N$ — System dynamic Eqs.

$\bar{g}(x_1, x_2, \ldots, x_N, t) \leq 0, \bar{g} \in \Re^{n_g}$ — Configuration constraints

$\bar{c}(\bar{x}_1, \bar{x}_2, \ldots, \bar{x}_N, u_1, u_2, \ldots, u_N, t) \leq 0, \bar{c} \in \Re^{n_c}$

  — Path and actuator const.

• Search for N(n+m) functions, Nn state Eqs. + inequalities

12

Planning of Groups: Formation Constraints and Flatness

If each unit is differentially flat and inequality constraints exhibit a specific structure

$$\gamma(x_1, x_2, \ldots, x_N, t) = 0 \begin{cases} x_2 = h_2(x_1, t) \\ x_3 = h_3(x_1, x_2, t) \\ \vdots \\ x_N = h_3(x_1, x_2, \ldots, x_{N-1}, t) \end{cases} \Rightarrow \bar{g}(x_1, x_2, \ldots, x_N, t) \leq 0$$

Entire system is differentially flat because the trajectory $x_1(t)$ of the first unit completely determines all remaining trajectories.

We plan the trajectory of the leader.
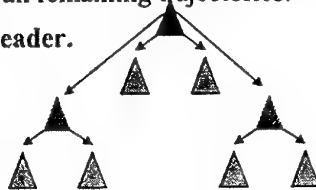
Example: Differential drive mobile robots

Kinematic equations:
$$\begin{aligned} \dot{x}_i &= u_{1i} \cos(\theta_i) \\ \dot{y}_i &= u_{1i} \sin(\theta_i) \\ \dot{\theta}_i &= u_{2i} \end{aligned}$$

x_i and y_i are the flat variables for each robot. Given $x_i(t)$ and $y_i(t)$, the remaining states and inputs are determined using

$$\begin{aligned} \theta_i &= \arctan\left(\frac{\dot{y}_i(t)}{\dot{x}_i(t)}\right) \\ u_{1i} &= \dot{x}_i \cos(\theta_i) + \dot{y}_i \sin(\theta_i) \\ u_{2i} &= \frac{d}{dt}(\theta_i) \end{aligned}$$

Laboratory Exp: MPC-like Strategy
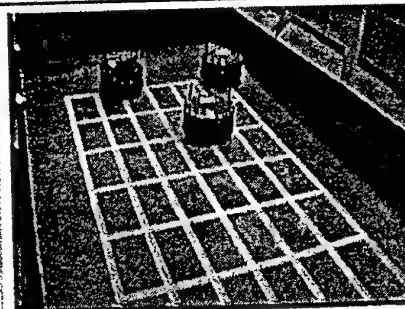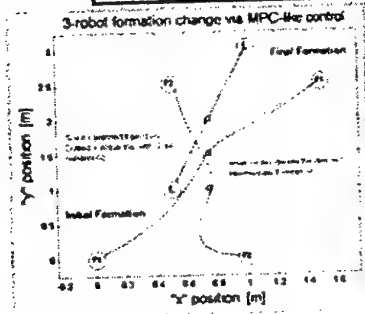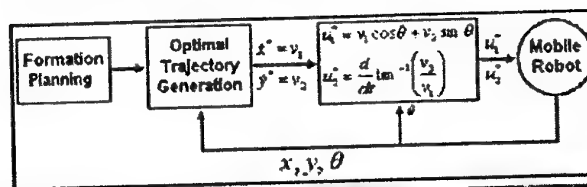
Cable Systems: PDEs and δ-flatness

- Cable continuum models are PDEs in x and t
- Input-output models are delay-differential Eqs.
- δ-flatness is a special structure of the DDEs.
- Compute inputs that modify flexural behavior
  - residual motion suppression in elevators

$$\frac{\partial^2 w_1(x,t)}{\partial x^2} = \frac{1}{c^2}\frac{\partial^2 w_1(x,t)}{\partial t^2}, \forall x \in (0, L_1)$$

$$\frac{\partial^2 w_2(y,t)}{\partial y^2} = \frac{1}{c^2}\frac{\partial^2 w_2(y,t)}{\partial t^2}, \forall y \in (0, L_2) \quad + \text{BC}$$

$$\frac{2H}{c}[\dot{w}_1(L_1,t) + \dot{w}_1(L_1,t - 2(\tau_1 + \tau_2))]$$
$$+ M[\ddot{w}_1(L_1,t) - \ddot{w}_1(L_1,t - 2\tau_2) + \ddot{w}_1(L_1,t - 2\tau_1) - \ddot{w}_1(L_1,t - 2(\tau_1 + \tau_2))]$$
$$+ B[\dot{w}_1(L_1,t) - \dot{w}_1(L_1,t - 2\tau_2) + \dot{w}_1(L_1,t - 2\tau_1) - \dot{w}(L_1,t - 2(\tau_1 + \tau_2))]$$
$$= 2[u_1(t - (\tau_1 + 2\tau_2)) - u_1(t - \tau_1)]$$
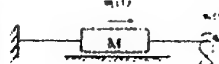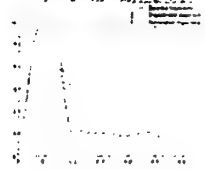
Conclusions

- Higher-Order approach is computationally effective for classes of dynamic systems

- Potential theoretical and Software extensions, Special purpose toolboxes for vehicles, robotics, others...

- Flatness and coupling of dynamic units in groups makes the computational problem more tractable.

- Trajectory plans that satisfy the system dynamics are better executable compared to geometric plans.

IMPACT OF RIGID AND FLEXIBLE MULTIBODY SYSTEMS: DEFORMATION DESCRIPTION AND CONTACT MODELS

J.A.C. AMBRÓSIO
IDMEC/Instituto Superior Técnico
Av. Rovisco Pais, 1049-001 Lisboa, Portugal
e-mail: jorge@dem.ist.utl.pt

1. Introduction

The multibody dynamics methodologies present the necessary characteristics to model systems that experience contact and impact conditions. The study of the biomechanics of impact is an example of an area where the multibody biomechanical models have dominated the numerical procedures. The design of vehicles for crashworthiness has also relied for long in conceptual models, which are in fact multibody models. Other type of systems, such as roller chain drives, gear drives or mechanisms with joint clearances, also require the description of the contact and impact between the system components and, eventually, the deformation of those elements. In all applications of multibody dynamics formulations that involve contact and impact it is required that proper contact models are used, the numerical integration procedures can accommodate the sudden change of the system conditions and the deformations of the system components are represented such a way that the model deformation patterns can be reproduced by the model.

The design requirements of advanced mechanical and structural systems and the real-time simulation of complex systems exploit the ease of use of the powerful computational resources available today to create virtual prototyping environments. These simulation facilities play a fundamental role in the study of systems that undergo large rigid body motion while their components experience material or geometric nonlinear deformations. The standard methodologies are unable to deal with systems that undergo material nonlinear deformations and consequently are not useful for applications involving structural impact of multibody systems. To overcome these limitations, Nikravesh and Sung [1] suggested a rigid body description of the multibody system with the nonlinear deformations lumped in force elements acting the kinematic joints and referred to as plastic hinges. This technique, further developed by Ambrósio and Pereira [2] and by Dias and Pereira [3], is applicable to systems for which the pattern of deformation can be assumed beforehand.

Using reference frames fixed to planar flexible bodies, Song and Haug [4] suggest a finite element based methodology, which yields coupled gross rigid body motion and small elastic deformations. The idea behind Song and Haug's approach is further developed and generalized by Shabana and Wehage [5,6] that use substructuring and the mode component synthesis to reduce the number of generalized coordinates required to represent the flexible components. Yoo and Haug [7] account for the contribution of the truncated modes by introducing static correction modes.

The community studying space dynamics has been dealing with the dynamics of flexible bodies undergoing large rigid body motion. The orbiting space structural systems are characterized by the use of very flexible lightweight components. The need to characterize dynamically and control such systems, in particular, motivated valuable investigations on flexible multibody dynamic [8,9]. In the framework of the spinning spacecrafts modeling, Kane, Ryan and Banerjee [10] showed that though most of the flexible multibody methods, at the time, could capture the inertia coupling between the elastodynamics of the system components and their large motion but they would still produce incorrect results. Actually, the floating reference frame methods used in flexible multibody dynamics have the ability to lower the geometric nonlinearities of the flexible bodies, but they do not eliminate them because the moderate rotation assumption about the floating reference frame is still required [11]. Recognizing the problem posed and using some of the approaches well in line with those of the finite element community Cardona and Geradin proposed formulations for the nonlinear flexible bodies using either a geometrically exact model [12] or through substructuring [13]. Defining it as an absolute nodal coordinate formulation, Shabana [14] used finite rotations nodal coordinates enabling the capture of the geometric nonlinear deformations. Another approach taken by Ambrósio and Nikravesh [15] to model geometrically nonlinear flexible bodies is to relax the need for the structures to exhibit small moderate rotations about the floating frame by using an incremental finite element approach within the flexible body description. The approach is further extended to handle material nonlinearities of flexible multibody systems also [16].

Applications of rigid and flexible multibody systems to impact scenarios require an efficient description of the contact conditions [17,18]. Some of the characteristics required from these contact models, in a multibody dynamics framework, concern their contribution to the stable integration of the equations of motion, the description of the geometry and properties of the surfaces in contact and the correct representation energy dissipation due the local and global deformation effects not modeled by the flexible bodies. The continuous

15

contact force model, proposed by Lankarani [19], fulfills the required characteristics to represent both nodal and rigid body contact. An alternative model, using the addition and deletion of kinematic constraints, is proposed for the nodal contact of the nonlinear finite elements representing the flexible components. In both cases of rigid and flexible body contact the dynamic friction forces are modeled.

The multibody formulations, able to describe material nonlinear deformations of the system components are reviewed here. Also, two methodologies able to describe efficiently contact in multibody systems are discussed in this work. Finally, the methodologies discussed are used in several application cases that involve vehicle and biomechanics impact.

2. Equations of Motion For Multibody Systems

The multibody system is a collection of rigid and flexible bodies joined together by kinematic joints and force elements, as shown in Fig. 1. For the ith body in the system q_i denotes a vector of coordinates which contains the Cartesian translation coordinates r_i and a set of rotational coordinates p_i. A vector of velocities for a rigid body i is defined as v_i, which contains the translation velocities $\dot{r}_i$ and the angular velocities ω_i. The vector of accelerations for the body is denoted by $\dot{v}_i$ and it is the time derivative of v_i. For a multibody system with nb bodies, the vectors of coordinates, velocities, and accelerations are q, v and $\dot{v}$ which contain the elements of q_i, v_i and $\dot{v}_i$, respectively, for i=1, ...,nb.
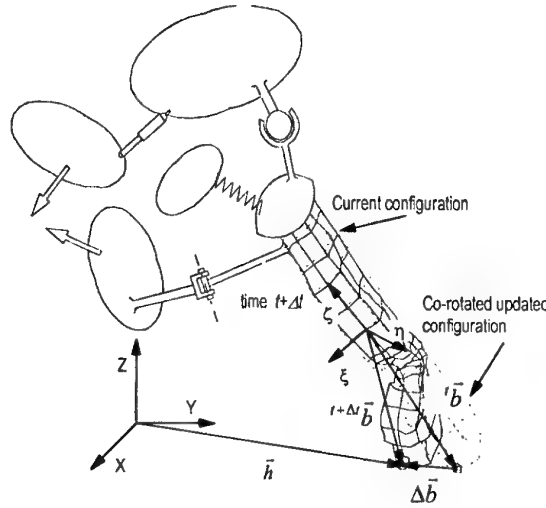
Figure 1. Generic multibody system in an impact fictitious scenario

The kinematic joints between rigid bodies are described by mr kinematic constraints

$$\Phi(q) = 0 \tag{1}$$

The time derivatives of the constraints result in the velocity and acceleration equations.

$$\dot{\Phi} = Dv = 0 \tag{2}$$

$$\ddot{\Phi} = \dot{D}v + D\dot{v} = 0 \tag{3}$$

where D is the Jacobian matrix of the constraints. The constraint equations are included in the equations of motion using the Lagrange multiplier technique [20]

$$M\dot{v} - D^T\lambda = g \tag{4}$$

where M is the inertia matrix, λ is the vector of Lagrange multipliers, and $g = g(q, v)$ has the gyroscopic terms and forces and moments acting on the rigid and flexible bodies.

The solution of equation (4) together with equation (3) constitutes the set of differential-algebraic equations that represent the motion of the multibody system. These are written in a matrix form as

$$\begin{bmatrix} M & D^T \\ D & 0 \end{bmatrix} \begin{bmatrix} \dot{v} \\ \lambda \end{bmatrix} = \begin{bmatrix} g \\ -\dot{D}v \end{bmatrix} \tag{5}$$

There is a wide range of multibody systems applications, involving impact, that can use models made solely of rigid bodies but that still have a representation of deformations, using the plastic hinge concept for instance

16

[1]. However, many applications of multibody systems that require the description of the system deformation. The use of flexible multibody models that include the description of the large deformations of the system components by nonlinear finite elements is necessary for these applications. However, before a methodology describing the distributed flexibility of multibody systems is presented the use of the plastic hinge concept in the context of multibody systems models to impact is briefly described here.

2.1. PLASTIC HINGES FOR MULTIBODY NONLINEAR DEFORMATIONS

In many impact situations, the individual structural members are overloaded, principally in bending, giving rise to plastic deformations in highly localized regions, called plastic hinges. These deformations, presented in Fig. 2, develop at points where maximum bending moments occur, load application points, joints or locally weak areas [21] and, therefore, for most practical situations, their location is predicted well in advance. Multibody models obtained with this method are relatively simple. This methodology is known in the automotive, naval and aerospace industries as conceptual modeling [1,22,23].
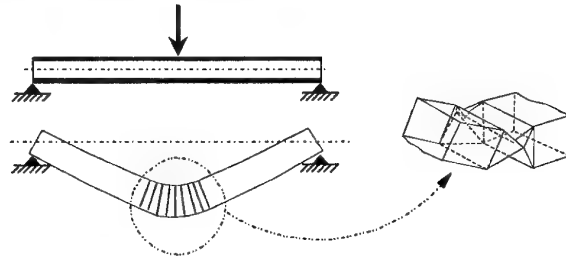
Figure 2. Localized deformations on a beam and a plastic hinge

The plastic hinge concept has been developed by using generalized spring elements to represent constitutive characteristics of localized plastic deformation of beams and kinematic joints [2], as illustrated in Fig. 3. The characteristics of the spring-damper that describe the properties of the plastic hinge are obtained by experimental component testing, finite element nonlinear analysis or simplified analytical methods. For a flexural plastic hinge the spring stiffness is expressed as a function of the change of the relative angle between two adjacent bodies connected by the plastic hinge, as shown in Fig. 4.
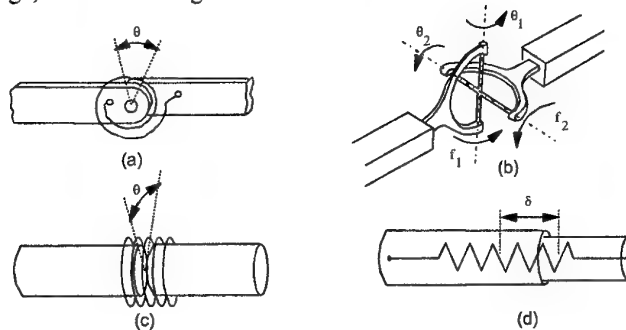
Figure 3. :Plastic hinge models for different loading conditions: a) one axis bending b) two axis bending; c) torsion; d) axial loading

For a bending plastic hinge the revolute joint axis must be perpendicular to the neutral axis of the beam and to the plastic hinge bending plane. The relative angle between the adjacent bodies measured in the bending plane is:

$$\theta_{ij} = \theta_i - \theta_j - \theta_{ij}^0 \tag{6}$$

where θ_{ij}^0 is the initial relative angle between the adjacent bodies.
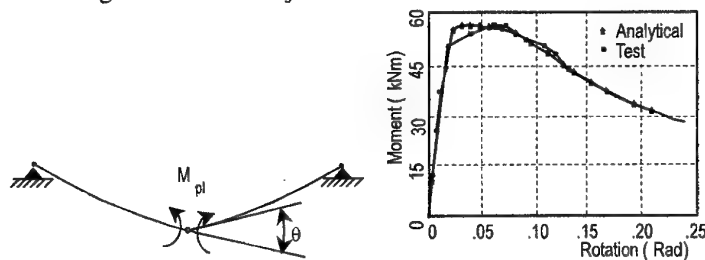
Figure 4. Plastic hinge bending moment and its constitutive relationship

17

The typical torque-angle constitutive relationship, as in Fig. 4, is found based on a kinematic folding model [24] for the case of a steel tubular cross section. This model is modified accounting for elastic-plastic material properties including strain hardening and strain rate sensitivity of some materials. A dynamic correction factor is used to account for the strain rate sensitivity [25].

$$P_d / P_s = 1 + 0.07 \ V_0^{0.82} \tag{7}$$

Here P_d and P_s are the dynamic and static forces, respectively, and V_0 is the relative velocity between the adjacent bodies. The coefficients appearing in Eq. (7) are dependent on the type of cross section and material.

3. Flexible Multibody Systems

Though the use of crushable elements or plastic hinges can be a valuable approach they require that the pattern of deformation of the structural component is known in advance. In complex cases, eventually involving multiple impacts, it is not possible to predict the loading of the vehicle structural components. Therefore, the use of a nonlinear finite element description is irreplaceable [26].

3.1. EQUATIONS OF MOTION FOR A SINGLE FLEXIBLE BODY

The motion of a flexible body, depicted by Fig. 5, is characterized by a continuous change of its shape and by large displacements and rotations, associated to the gross rigid body motion. Let XYZ denote the inertial reference frame and $\xi\eta\zeta$ a body fixed coordinate frame. Let the principle of the virtual works be used to express the equilibrium of the flexible body in the current configuration $t+\Delta t$ and an updated Lagrangean formulation be used to obtain the equations of motion of the flexible body [26].

Let the finite element method be used to represent the equations of motion of the flexible body. The finite elements used in the discretization of the flexible body are assembled, leading to the body equations of motion. In order to improve the numerical efficiency of the solution of the equations obtained, a lumped mass formulation is used and the nodal accelerations $\ddot{\mathbf{u}}'$, measured with respect to the body fixed frame, are substituted by the nodal accelerations relative to the inertial frame $\ddot{\mathbf{q}}'_f$. Furthermore, it is assumed that the flexible body has a rigid and a flexible part and that the body fixed coordinate frame is attached to the center of mass of the rigid part, as shown in Fig. 6. The flexible and rigid parts are attached by the boundary nodes ψ. The procedure is described in Ambrósio and
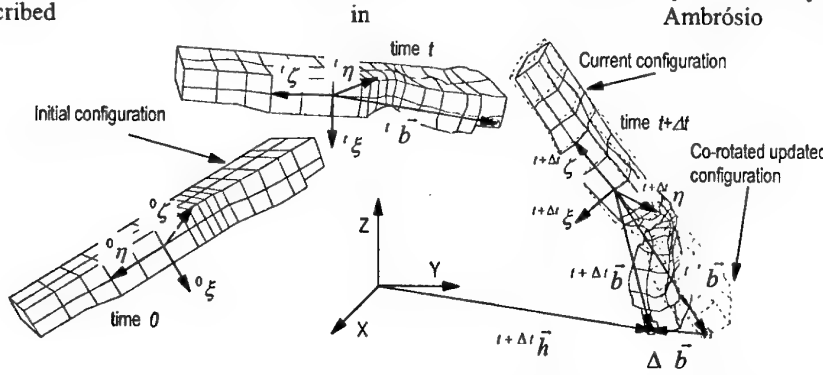
Figure 5. General motion of a flexible body

Nikravesh [26]. The resulting equations of motion for the flexible body are written as

$$\begin{bmatrix} m\mathbf{I} + \bar{\mathbf{A}}\underline{\mathbf{M}}^\bullet\bar{\mathbf{A}}^T & -\bar{\mathbf{A}}\underline{\mathbf{M}}^\bullet\mathbf{S} & \mathbf{0} \\ -\left(\bar{\mathbf{A}}\underline{\mathbf{M}}^\bullet\mathbf{S}\right)^T & \mathbf{J}' + \mathbf{S}^T\underline{\mathbf{M}}^\bullet\mathbf{S} & \mathbf{0} \\ \mathbf{0} & \mathbf{0} & \mathbf{M}_{ff} \end{bmatrix} \begin{bmatrix} \ddot{\mathbf{r}} \\ \dot{\boldsymbol{\omega}}' \\ \ddot{\mathbf{q}}'_f \end{bmatrix} = \begin{bmatrix} \mathbf{f}_r + \bar{\mathbf{A}}\mathbf{C}'_\delta \\ \mathbf{n}' - \tilde{\boldsymbol{\omega}}'\mathbf{J}'\boldsymbol{\omega}' - \mathbf{S}^T\mathbf{C}'_\delta - \bar{\mathbf{I}}^T\mathbf{C}'_\theta \\ \mathbf{g}'_f - \mathbf{f} - \left(\mathbf{K}_L + \mathbf{K}_{NL}\right)\mathbf{u}' \end{bmatrix} \tag{8}$$

where $\ddot{\mathbf{r}}$ and $\dot{\boldsymbol{\omega}}'$ are respectively the translational and angular accelerations of the body fixed reference frame, $\mathbf{J}'$ is the inertia tensor, expressed in body fixed coordinates, $\mathbf{f}_r$ is the vector of the external forces applied on the body and $\mathbf{n}'$ is the a vector with the force transport and external moments. Vector $\mathbf{u}'$ denotes the displacements increments from a previous configuration to the current configuration, measured in body fixed coordinates. The right-hand side of Eq. (8) contains, the vector generalized forces applied on the deformable body $\mathbf{g}$, matrices $\mathbf{K}_L$ and $\mathbf{K}_{NL}$, which are the linear and nonlinear stiffness matrices respectively, and $\mathbf{f}$ denotes the vector of equivalent nodal forces due to the state of stress. The reference to the linearity of the stiffness matrices $\mathbf{K}_L$ and $\mathbf{K}_{NL}$ is related to their relation with the displacements.

18
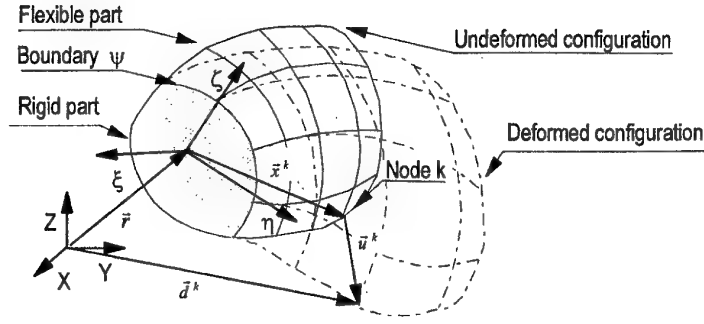
Figure 6. Flexible body with a rigid part

In Eq. (8) $\underline{\mathbf{M}}^{*}$ is a diagonal mass matrix containing the mass of the boundary nodes, and

$$\overline{\mathbf{A}}^{T} = \begin{bmatrix} \mathbf{A} & \mathbf{A} \cdots \mathbf{A} \end{bmatrix}^{T}; \quad \mathbf{S} = \left[\left(\overline{\mathbf{x}}_{1}' + \tilde{\delta}_{1}'\right)^{T} \left(\overline{\mathbf{x}}_{2}' + \tilde{\delta}_{2}'\right)^{T} \cdots \left(\overline{\mathbf{x}}_{n}' + \tilde{\delta}_{n}'\right)^{T} \right]^{T}; \quad \overline{\mathbf{I}} = \begin{bmatrix} \mathbf{I} \mathbf{I} \cdots \mathbf{I} \end{bmatrix}^{T}$$

Here $\mathbf{A}$ is the transformation matrix from the body fixed to global coordinate coordinates and $\mathbf{x}_k$ denotes the position of node k. Vectors $\mathbf{C}_{\delta}'$ and $\mathbf{C}_{\theta}'$ are the reaction force and moment of the flexible part of the body over the rigid part respectively, given by

$$\mathbf{C}_{\delta}' = \mathbf{g}_{\underline{\delta}}' - \mathbf{F}_{\underline{\delta}} - \left(\mathbf{K}_L + \mathbf{K}_{NL}\right)_{\underline{\delta}\delta} \delta' - \left(\mathbf{K}_L + \mathbf{K}_{NL}\right)_{\underline{\delta}\theta} \theta' \qquad (9)$$

$$\mathbf{C}_{\delta}' = \mathbf{g}_{\underline{\theta}}' - \mathbf{F}_{\underline{\theta}} - \left(\mathbf{K}_L + \mathbf{K}_{NL}\right)_{\underline{\theta}\delta} \delta' - \left(\mathbf{K}_L + \mathbf{K}_{NL}\right)_{\underline{\theta}\theta} \theta' \qquad (10)$$

In these equations, the subscripts δ' and θ' refer to the partition of the vectors and matrices with respect to the translation and rotational nodal degrees of freedom. The underlined subscripts are referred to nodal displacements of the nodes fixed to the rigid part.

4. Contact Models

The description of any crash phenomena is strongly dependent on the contact/impact model used to describe the interaction between the system components. These contact models must not only be formulated in a form compatible with the multibody description used but also allow for the representation of the local deformations, friction forces, energy dissipation and still contribute for the stability of the numerical methods involved.

4.1. CONTACT DETECTION

Let the flexible body approach a surface during the motion of the multibody system, as represented in Fig. 7. Without lack of generality, let the impacting surface be described by a mesh of triangle patches. In particular, let the triangular patch, where node k of the flexible body will impact, be defined by points i, j and l. The normal to the outside surface of the contact patch is $\vec{n} = \vec{r}_{ij} \times \vec{r}_{jl}$.

Let the position of the structural node k with respect to point i of the surface be

$$\mathbf{r}_{ik} = \mathbf{r}_k - \mathbf{r}_i \qquad (11)$$

This vector is decomposed in its tangential component, which locates point k^* in the patch surface, and a normal component, given respectively by

$$\mathbf{r}_{ik}^t = \mathbf{r}_{ik} - \left(\mathbf{r}_{ik}^T \mathbf{n}\right)\mathbf{n} \qquad (12)$$

$$\mathbf{r}_{ik}^n = \left(\mathbf{r}_{ik}^T \mathbf{n}\right)\mathbf{n} \qquad (13)$$

A necessary condition for contact is that node k penetrates the surface of the patch, i.e.

$$\mathbf{r}_{ik}^T \mathbf{n} \leq 0 \qquad (14)$$

In order to ensure that a node does not penetrate the surface through its 'interior' face a thickness e must be associated to the patch. The thickness penetration condition is

$$-\mathbf{r}_{ik}^T \mathbf{n} \leq e \qquad (15)$$

19
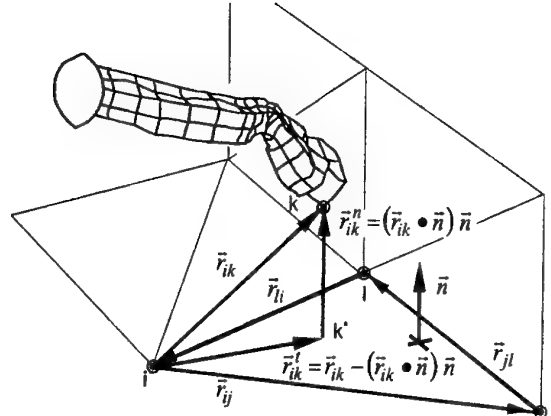
Figure 7. Contact detection between a finite element node and a surface

The condition described by equation (15) prevents that penetration is detected when the flexible body is far away, behind the contact surface. The remaining necessary conditions for contact results from the need for the node to be inside of the triangular patch, which are

$$\left(\tilde{\mathbf{r}}_{ik}^{t}\mathbf{r}_{ij}\right)^{T}\mathbf{n} \geq 0 \quad ; \quad \left(\tilde{\mathbf{r}}_{ik}^{t}\mathbf{r}_{jl}\right)^{T}\mathbf{n} \geq 0 \quad \text{and} \quad \left(\tilde{\mathbf{r}}_{ik}^{t}\mathbf{r}_{ki}\right)^{T}\mathbf{n} \geq 0 \tag{16}$$

Equations (14) through (16) are necessary conditions for contact. However, depending on the contact force model actually used, they may not be sufficient.

The contact detection algorithm is applicable to rigid body contact by using a rigid body point P instead of node k in equation (11). The global position of point P is given by $\mathbf{r}_{i}^{P} = \mathbf{r}_{i} + \mathbf{A}_{i}\mathbf{s}_{i}^{P'}$, where $\mathbf{s}_{i}^{P'}$ denotes the point location in body i frame.

4.2. CONTINUOUS FORCE MODEL

A model for the contact force must consider the material and geometric properties of the surfaces, contribute to a stable integration and account for some level of energy dissipation. Based on a Hertzian description of the contact forces between two solids, Lankarani and Nikravesh [19] propose a continuous force contact model that accounts for energy dissipation during impact.

Let the contact force between two bodies or a system component and an external object be a function of the pseudo-penetration δ and pseudo-velocity of penetration $\dot{\delta}$

$$\mathbf{f}_{s,i} = \left(K\delta^{n} + D\dot{\delta}\right)\mathbf{u} \tag{17}$$

where K is the equivalent stiffness, D is a damping coefficient and $\mathbf{u}$ is a unit vector normal to the impacting surfaces. The hysteresis dissipation is introduced in equation (17) by $D\dot{\delta}$, being the damping coefficient written as

$$D = \frac{3K\left(1-e^{2}\right)}{4\dot{\delta}^{(-)}}\delta^{n} \tag{18}$$

This coefficient is a function of the impact velocity $\dot{\delta}^{(-)}$, stiffness of the contacting surfaces and restitution coefficient e. The generalized stiffness coefficient K depends on the geometry material properties of the surfaces in contact. For the contact between a sphere and a flat surface the stiffness is [27]

$$K = 0.424\sqrt{r}\left(\frac{1-v_{i}^{2}}{\pi E_{i}} + \frac{1-v_{j}^{2}}{\pi E_{j}}\right)^{-1} \tag{19}$$

where v_{l} and E_{l} are the Poisson's ratio and the Young's modulus associated to each surface and r is the radius of the impacting sphere.

The nonlinear contact force is obtained by substituting equation (18) into equation (17)

$$\mathbf{f}_{s,i} = K \, \delta^{n}\left[1 + \frac{3\left(1-e^{2}\right)}{4}\frac{\dot{\delta}}{\dot{\delta}^{(-)}}\right]\mathbf{u} \tag{20}$$

This equation is valid for impact conditions, in which the contacting velocities are lower than the propagation

20

speed of elastic waves, i.e., $\dot{\delta}^{(-)} \leq 10^{-5}\sqrt{E/\rho}$.

4.3. FRICTION FORCES

The contact forces between the node and the surface include friction forces modeled using Coulomb friction. The dynamic friction forces in the presence of sliding are given by

$$\mathbf{f}^{friction} = -\mu_d f_d \left(\left|\mathbf{f}_k^n\right|/\left|\dot{\mathbf{q}}_k\right|\right)\dot{\mathbf{q}}_k \tag{21}$$

where μ_d is the dynamic friction coefficient, and $\dot{\mathbf{q}}_k$ is the velocity of node k. The dynamic correction coefficient f_d is expressed as

$$f_d = \begin{cases} 0 & \text{if} & |\dot{\mathbf{q}}_k| \leq v_0 \\ \left(|\dot{\mathbf{q}}_k| - v_0\right)/\left(v_1 - v_0\right) & \text{if} & v_0 \leq |\dot{\mathbf{q}}_k| \leq v_1 \\ 1 & \text{if} & |\dot{\mathbf{q}}_k| \geq v_1 \end{cases} \tag{22}$$

The dynamic correction factor prevents that the friction force changes direction for almost null values of the nodal tangential velocity, which is perceived by the integration algorithm as a dynamic response with high frequency contents, forcing it to reduce the time step size.

The friction model represented by equation (21) does not account for the adherence between the node and the contact surface. The interested reader is referred to the work of Wu, Yang and Haug [28] where stiction and sliding in multibody dynamics is discussed.

4.4. CONTACT MODELS USING UNILATERAL CONSTRAINTS

If contact between a node and a surface is detected, a kinematic constraint is imposed. Assuming fully plastic nodal contact, the normal components of the node k velocity and acceleration, with respect to the surface, are null during contact. Therefore the global nodal velocity and acceleration of node k, in the event of contact, become

$$\ddot{\mathbf{q}}_k = \ddot{\mathbf{q}}_k^{(-)} - \left(\ddot{\mathbf{q}}_k^{(-)T}\mathbf{n}\right)\mathbf{n} \tag{23}$$

$$\dot{\mathbf{q}}_k = \dot{\mathbf{q}}_k^{(-)} - \left(\dot{\mathbf{q}}_k^{(-)T}\mathbf{n}\right)\mathbf{n} \tag{24}$$

where $\dot{\mathbf{q}}_k^{(-)}$ and $\ddot{\mathbf{q}}_k^{(-)}$ represent the nodal velocity and acceleration immediately before impact.

The kinematic constraint implied by equations (23) and (24) is removed when the normal reaction force between the node and the surface becomes opposite to the surface normal. Representing by $\mathbf{f}_k$ the resultant of forces applied over node k, except for the surface reaction forces but including the internal structural forces due to the flexible body stiffness, the kinematic constraint over node k is removed when

$$\mathbf{f}_k^n = -\mathbf{f}_k^T \ \mathbf{n} > 0 \tag{25}$$

This model is not suitable to be used with rigid body contact. The sudden change of the rigid body velocity and acceleration would imply that the velocity and acceleration equations resulting from the kinematic constraints would not be fulfilled. Consequently constraint violations would develop throughout the integration of the state variables and the analysis would fail. The friction forces can still be included when using this contact model. However, as the normal contact reaction forces $\mathbf{f}_k^n$ are calculated using the Lagrange multipliers, the friction forces would be only approximate forces.

4.5. EXAMPLE OF IMPACT OF AN ELASTIC BEAM

The contact force models are exemplified with the oblique impact of a hyperelastic beam against a rigid wall. The impact scenario, proposed by Orden and Goicolea [29], is described in Fig 8. The beam, with a mass of 20 kg, length of 1 m and a circular cross-section, is made of a material with an elastic modulus of $E=10^8$ Pa, Poisson's ration of $v = 0.27$ and a mass density of $\rho = 7850$ kg/m^3. For this geometry and material properties the equivalent stiffness coefficient used in equation (20) is $K=1.2 \ 10^8$ kg/m$^{2/3}$.

The motion of the impacting beam is shown in Fig. 9 together with that of a rigid bar with similar inertia. In Fig. 10, the contact forces developed during nodal impact are presented. The motion predicted for the beam model using 10 elements is similar to that presented by Orden and Goicolea [29] for a model made of 20 elements and using an energy-momentum formulation to describe contact.

21
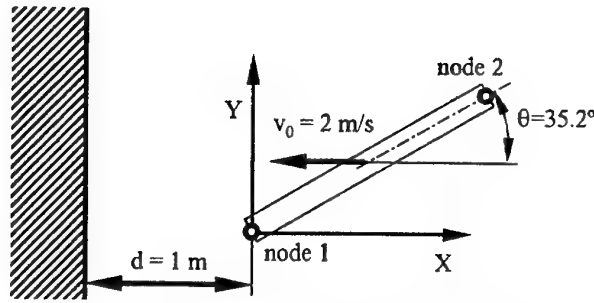
Figure 8. Impact scenario for an oblique elastic beam

A integration algorithm with variable time-step is used to integrate the equations of motion. The size of the integration time-step is controlled, during contact, by the time of travel of the elastic wave across one element, which is T_e=4.4 10^{-4} s for 20 elements [29]. Outside of contact, the integration time-step is controlled by the system response, generally associated to the flexible body higher frequencies. Table 1 shows the average time step taken by the algorithm in the various phases of the system motion.

Table 1. Average time-step of the integration algorithm

Type of contact model	Beam model	Avg. time-step before contact	Avg. time-step during contact	Avg. time-step after contact
Continuous force	4 elements	0.60 10^{-3}	0.20 10^{-3}	0.55 10^{-3}
Continuous force	10 elements	0.24 10^{-3}	0.15 10^{-3}	0.20 10^{-3}
Continuous force	20 elements	0.43 10^{-4}	0.34 10^{-4}	0.40 10^{-4}
Kinematic constraint	4 elements	0.60 10^{-3}	0.20 10^{-4}	0.55 10^{-3}
Kinematic constraint	10 elements	0.24 10^{-3}	0.74 10^{-5}	0.20 10^{-3}
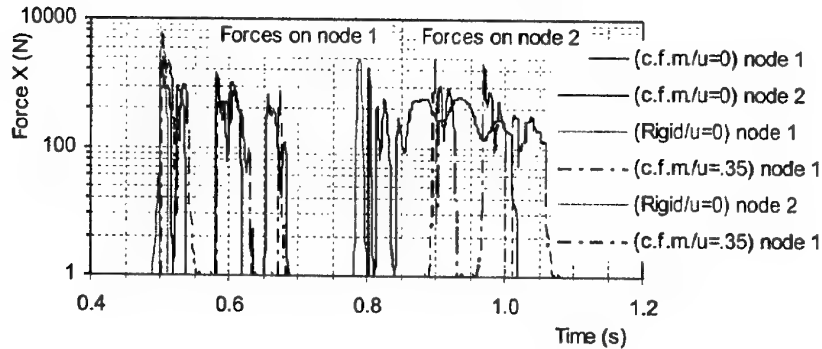
Figure 10. Forces developed between the (10 elements) beam end nodes and the rigid surface (c.f.m. – continuous force model; k.c. – kinematic constraint model)

Observing the contact forces, shown in Fig. 10, it is clear that the impact phenomena occurs with multiple contacts. Each of these contacts lasts 0.02 s, in average, which is similar to the contact duration of 0.018 s estimated by Orden and Goicolea [29] using the elastic wave travel time across the bar length.

5. Application To Train Impact

The application of the methodologies using only rigid multibody systems to train crashworthiness is exemplified by the study of a new anti-climber device for the interface between the cars of a train. This device, which ensures that train cars remain aligned during the crash, has been developed within the BRITE-EURAM project SAFETRAIN [30] and the analysis is described in detail by Milho, Ambrósio and Pereira in references [31,32].

22
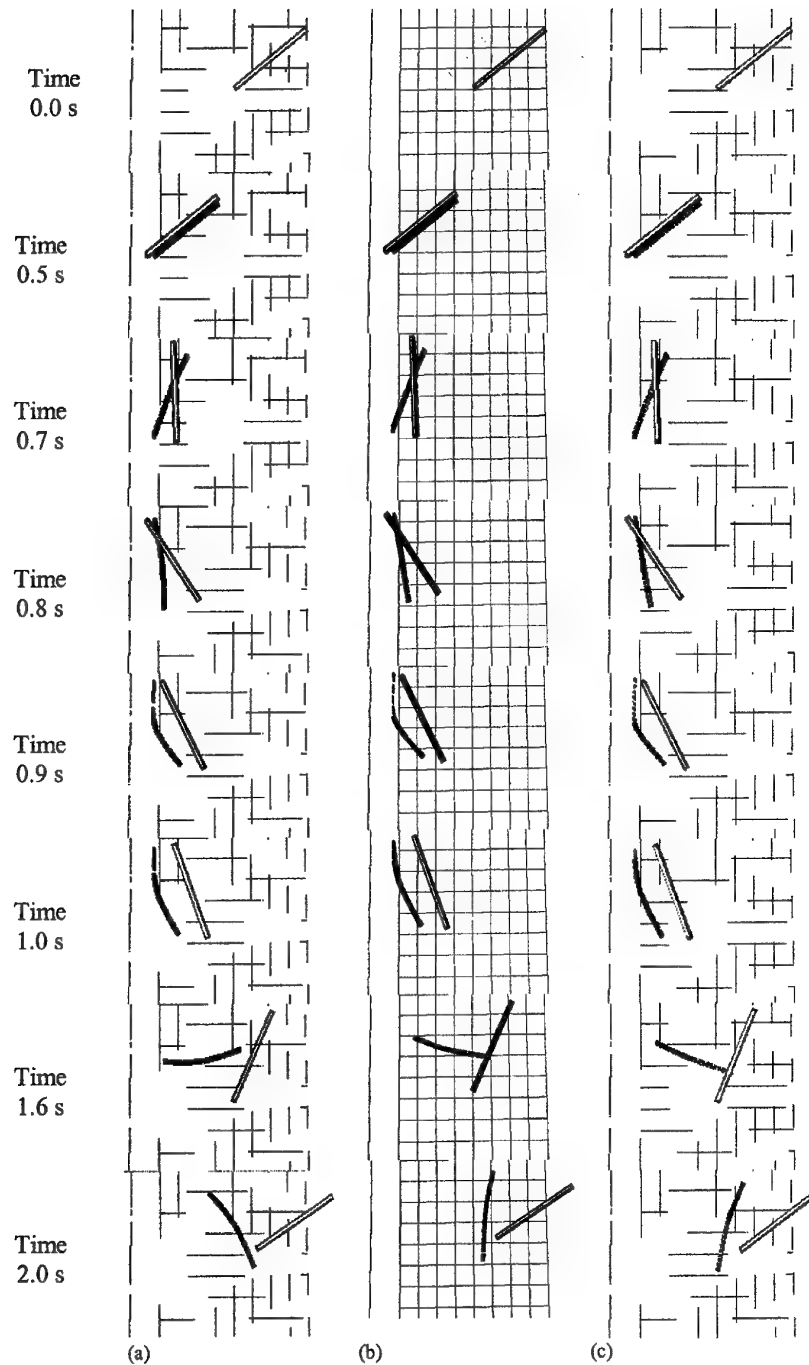
Figure 9. Frictionless impact of a hyperelastic beam in a rigid surface: (a) Beam model with 4 finite elements; (b) Model using 10 elements; (c) f.e.m. model with 20 elements

5.1. RAILWAY CRASHWORTHINESS

The methodology developed here is applied to the simulation of a train collision. Table 2 presents the arrangement of a train set with eight individual car-bodies and it includes the length and the mass of each one of them while in Fig. 11 the topology of each individual car is shown. Five rigid bodies, B_1 through B_5, which represent the passenger compartment, boggie chassis and deformable end extremities, are used in the car-body model. The inertia and mechanical properties of the system components are described in reference [31].

23

Table 2. Train set pattern

	HE	LE	LE	LE	LE	LE	LE	LE	HE
Length (m)	20	26	26	26	26	26	26	26	
Mass (10^3 Kg)	68	51	34	34	34	34	34	51	

The high-energy zones (HE) are located in the extremities of the train set in the frontal zone of the motor car-body and in the opposing back zone, in the last car-body. The HE are potential impact extremities between two train sets. The low-energy zones (LE) are located in the remaining extremities of the train car-bodies and correspond to regions of contact between cars of the same train set.
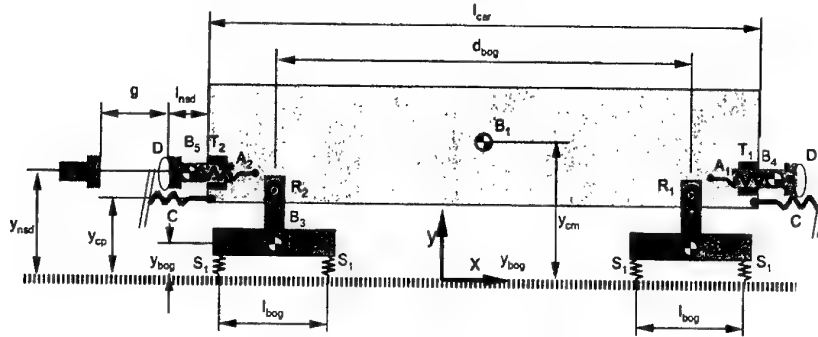
Figure 11. Car-body model for a single car

The objective is to identify, in the first design stage, the impact kinematics and the general forces developed during collision. In the second design stage the energy absorbing devices at the vehicle ends are defined, and the models simulated and validated.

The first simulation scenarios are characterized by a moving train, with velocities of 30, 40 and 55 km/h, which collides with another train that is parked with brakes applied. Of importance to the anti-climber design are the simulation results for the contact forces and the relative displacements between car-bodies extremities [31].

The vertical relative displacement between the points of the contact surfaces defining the anti-climber devices is described by the distance g measured along the contact surface, see Fig. 12. This displacement is calculated when contact between the end extremities of the car-bodies occurs. The vertical relative displacement in the interfaces between car-bodies obtained is illustrated in Fig 13.
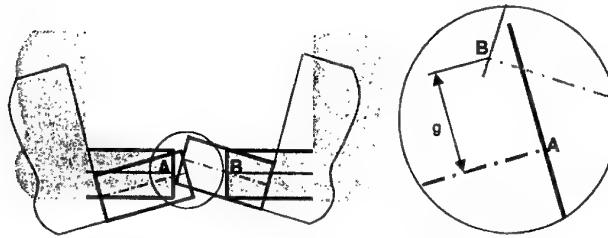
Figure 12. Anti-climber device contact geometry

The tangential force in the anti-climber device, illustrated in Fig. 14, is described as the tangential component of the contact force between the end extremities of the car-bodies. It is observed that the tangential force at the interfaces, tend to increase both in magnitude and frequency in the final stage of the train impact.

In a second design stage the conceptual railway vehicle model presented herein is simulated in a train crash scenario similar to that of an experimental test performed to validate a low-energy end design developed within the framework of Brite/Euram III project SAFETRAIN [30]. The experimental test consists in having a vehicle moving with a velocity of 54 Km/h toward a composition with two vehicles stopped on the railroad, as depicted in Fig. 15. The two stopped vehicles are equipped with the low-energy ends and connected by a coupler device. Vehicle C is also equipped with a high-energy device in the colliding end. The vehicles were instrumented in order to measure accelerations, forces transmitted in the buffers and coupler and relative displacements between system components.

The force time history for the buffers of wagon A is displayed in Fig. 16 for both the simulation and the experimental test. Note that the experimental test results are plotted for a single buffer while the expected force resulting from the simulation is shown for the cumulative effects of the two buffers of wagon A.

24
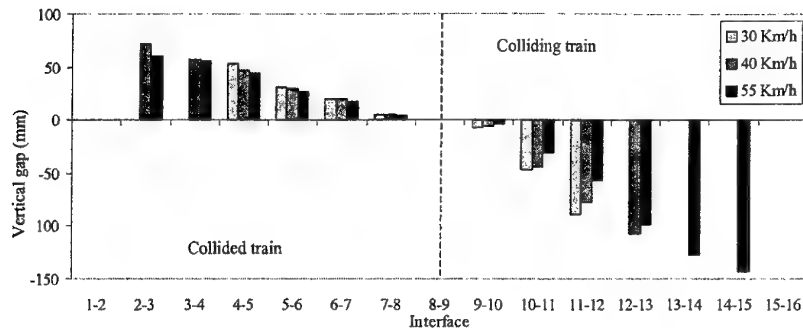
Figure 13. Vertical relative displacement between car-bodies in the interfaces
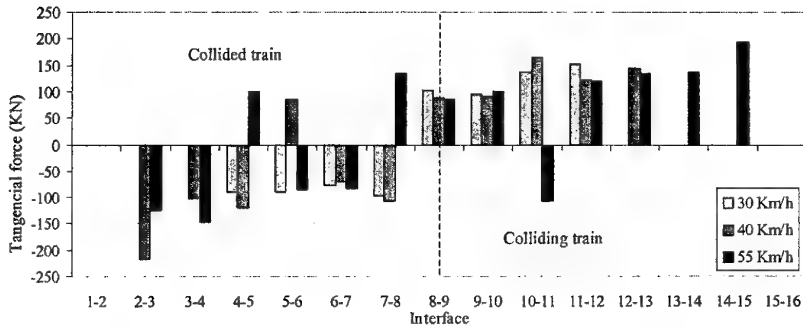
Figure 14. Maximum tangential force along the interfaces
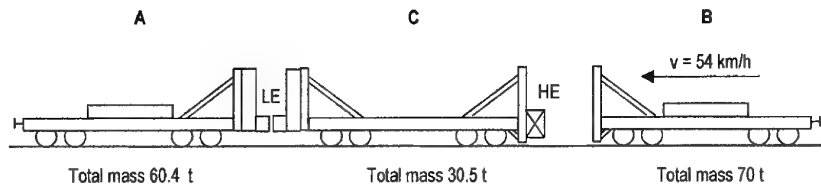
Figure 15. Collision scenario used in the numerical simulations and in the experimental test
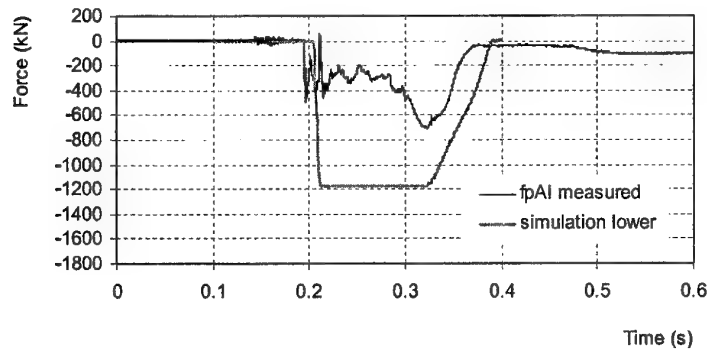
Figure 16. Force-time history of the buffers of wagon A (half of the force magnitude on the buffers is compared with the force measured in the left buffer of wagon A)

The force displacement history for the buffers of wagon A and wagon C are displayed in Fig. 17. There, it is observed that deformation predicted for the buffers of wagon C is a higher than that of wagon A. The buffer of wagon C is expected to be fully crushed.

25
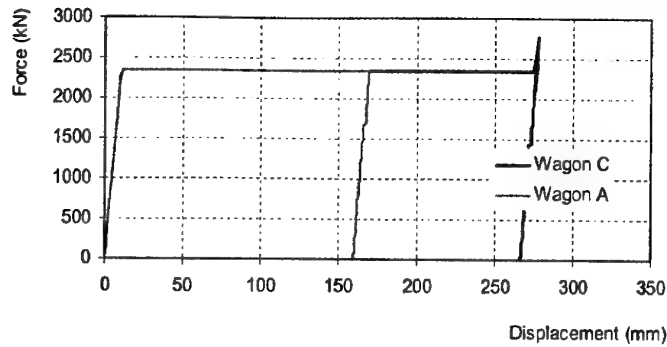
Figure 17. Forces experienced by the buffers of wagon A and C during the simulation

The velocities of the three cars during the simulation are plotted in Fig. 18. There it can be observed that the velocities predicted by the model are very similar to those observed in the experimental test. The contact between wagon A and C is predicted to happen with no initial vertical gap between the buffers, as shown in Fig. 19. However, as the buffers approach each other, the vertical gap between the wagons increases, reaching a maximum of 15 mm. The vertical forces, that the buffers have to support in order to prevent overriding, presented in Fig. 19, oscillate with a maximum peak of 15 ton.
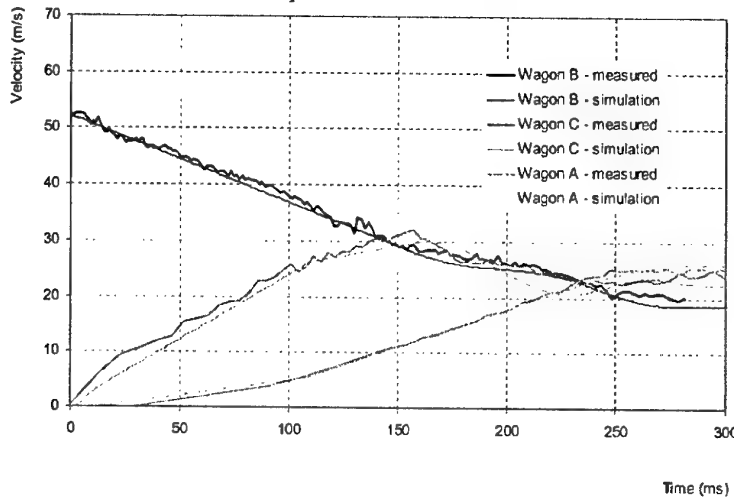
Figure 18. Time history for the wagons in the simulation and experimental test
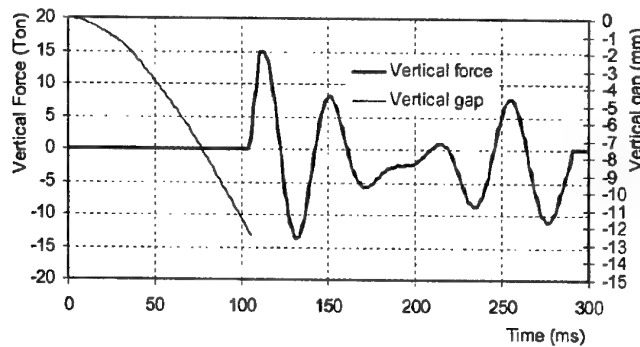
Figure 19. Time history of the gap and vertical contact forces in the buffers

The model presented for the preliminary design of the railway vehicle energy absorbing devices, is improved, based on the results obtained. The crushable structural elements mechanical characteristics are improved and the new force displacement curves implemented in the model. The procedure used is explained in detail in reference [32]

26

5.2. APPLICATION CASE : VEHICLE ROLLOVER WITH OCCUPANTS

The scenario in which the methodology described in this work is demonstrated is a rollover situation, depicted by Fig. 20, first proposed by Ambrósio, Nikravesh and Pereira [33]. This crash case is characterized by the existence of multiple impacts and by a complex interaction among the vehicle, occupants and ground that can hardly be represented by the more traditional approach of simulating the vehicle rollover first and then using the crash pulse as input for the occupants dynamic analysis. For more details on this application, the interested reader is referred to [34].

$\omega = 1.5$ rad/s

$V = 25$ m.p.h.

0.3 m
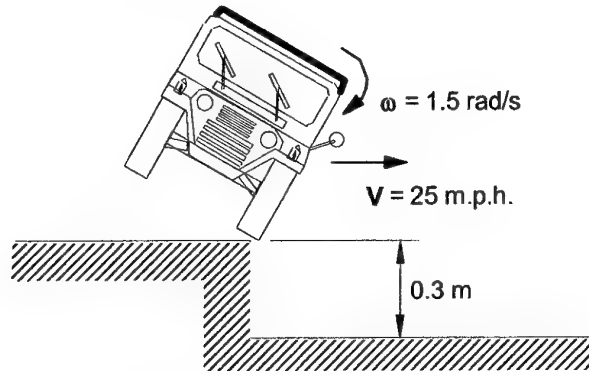
Figure 20. Rollover crash scenario.

5.2.1. Biomechanical Model For The Vehicle Occupants

For the representation of the vehicle occupants a suitable whole-body response biomechanical model is required. The biomechanical model, presented by Silva, Ambrósio and Pereira [35], includes 12 anatomic segments being the relative motion between adjacent bodies limited to be inside generalized cones of feasible motion. The model, pictured in Fig. 21, is general and accepts data for any individual.

(a)   (b)   (c)
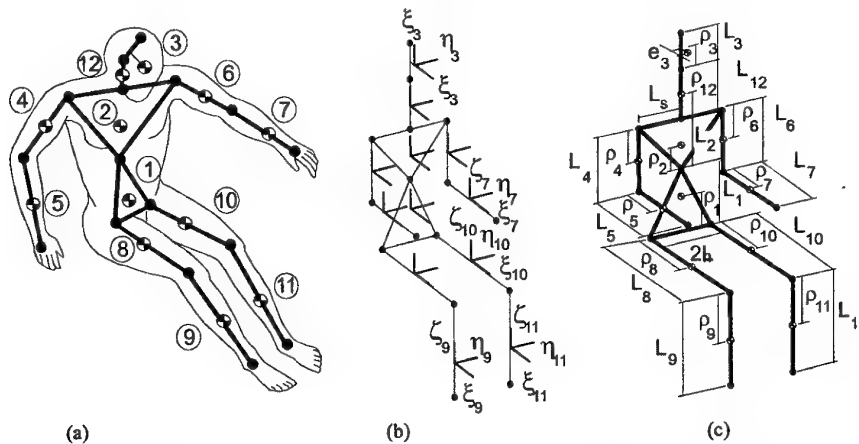
Figure 21. Three-dimensional biomechanical model for impact: (a) actual model; (b) local referential locations; (c) dimensions of the biomechanical segments.

In contact/impact simulations the relative kinematics of the head-neck and torso are important to the correct evaluation of the loads transmitted to the human body. Consequently, the head and neck are modeled as separate bodies and the torso is divided in two bodies. The hands and feet do not play a significant role in this type of problems and consequently are not modeled independently of the adjacent segments. In the biomechanical model no muscle activation is considered but the muscle passive behavior is represented by joint resistance torques. Physically unacceptable positions of the body segments are prevented by applying a set of penalty torques when adjacent segments of the biomechanical model reach the limit of their relative range of motion. The moment penalizing torque increases rapidly, from zero to a maximum value, when the two bodies interconnected by that joint, reach physically unacceptable positions. Details of this model can be found on reference [35].

A set of contact surfaces is also defined for the calculation of the external forces exerted on the model when the surfaces of the bodies contact other objects or different body segments. These surfaces are ellipsoids and cylinders with the form depicted by Fig. 22. When contact between components of the biomechanical model is

27

detected a contact force is applied in the point of contact and with a direction normal to the surface.
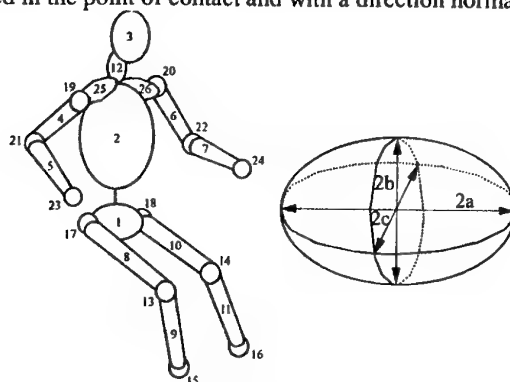
Figure 22. Representation of contact surfaces.

5.2.2. Evaluation Of The Initial Positions Of The Vehicle Occupants

The multibody dynamic analysis of the vehicle and occupant in a crash scenario requires that the initial positions and velocities of the system components are available. In order obtain these conditions for realistic occupant positions a process of recording the human body actual motion and to extract the position of its anatomical segments for every frame, designated by spatial reconstruction, is used here [36,37]. The most frequently used technique is photogrammetry, in which video cameras are used [37]. The laboratory apparatus of cameras is schematically represented in Fig. 23.
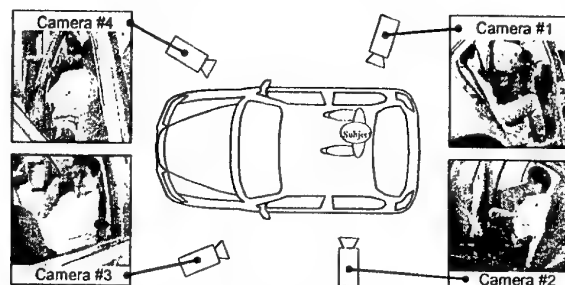
Figure 23. Vehicle and video cameras for the recording of the out-of-position occupants.

The images collected by a single camera are collections of two-dimensional information, resulting from the projection of a three-dimensional space into a two-dimensional one. Aziz and Karara [38], proposed a solution for the reconstruction process called Direct Linear Transformation. This method uses the two-dimensional information, collected by two or more cameras, to reconstruct the coordinates of the anatomical points.

The biomechanical model used in this work requires the reconstruction of the spatial position of the 23 anatomical points depicted in Fig. 24 for each frame of the analysis period. The spatial position and orientation of the anatomical segments of the biomechanical model are obtained from the spatial positions of these reconstructed points.

With the setup described in Fig. 23 a seated occupant is asked to adopt seated positions similar to those that would be used when riding car in different situations. Among those, which are videotaped and reconstructed, the positions presented in Fig. 24 are selected and used in the application of the methodology to a vehicle rollover.

5.2.3. Vehicle And Occupants Integrated Simulation

The vehicle rollover has been extensively analyzed with the purpose of studying the rollbar cage influence in the vehicle stability and its structural integrity. Here, the rollbar cage deformation is not included in the model though its deformations are implicitly described by the force contact model. Three 50%tile occupants, are also modeled and integrated with the vehicle. The two occupants in the front of the vehicle have shoulder and lap seat belts, described with the model proposed by Laananen, Bolusbasi and Coltman [39], while the occupant seated in the back of the vehicle has no seatbelt. The initial positions of the occupants correspond to a normally seated driver, a front passenger that is bent according to the position reconstructed and shown in Fig. 25, and a rear occupant with a 'relaxed' position, also reconstructed and presented in Fig. 25. The vehicle and occupants are simulated here in a rollover situation described in Fig. 26.

28
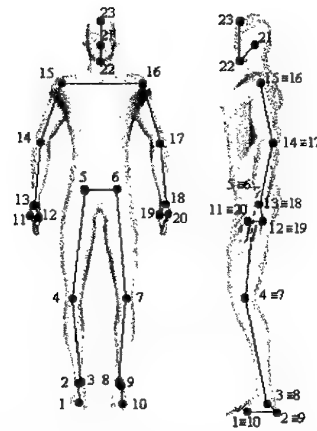
Figure 24. Set of 20 digitized points and kinematic structure.

(a)   (b)   (c)   (d)   (e)
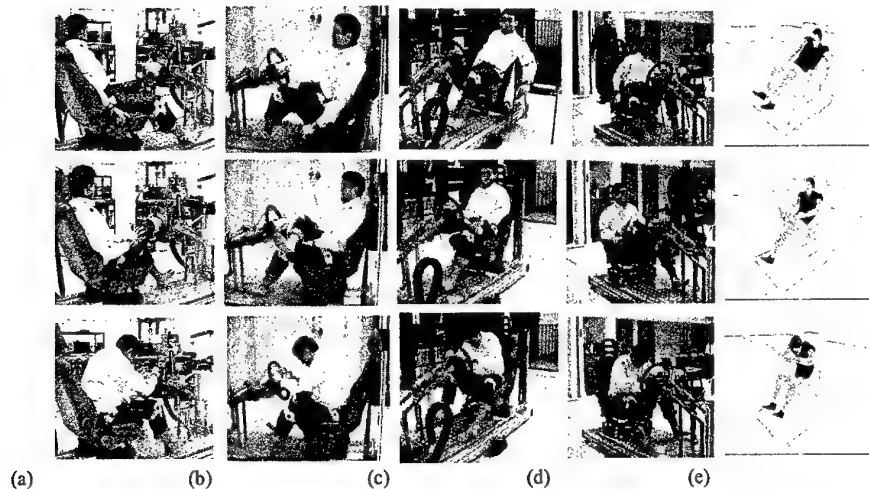
Figure 25. (a)-(d) Out-of-position occupants as viewed by the cameras and (e) spatial reconstructions.
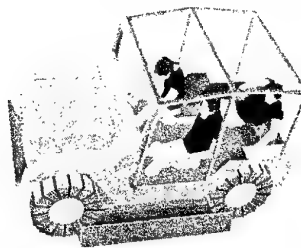
Figure 26. Initial position of the vehicle and occupants for the rollover

The results of this simulation are pictured in Fig. 27, where several frames of the animation of the vehicle rollover with occupants are presented. It is noticeable in this sequence that the vehicle first impacts the ground with its left tires. At this point the rear occupant is ejected. The rollover motion of the vehicle proceeds with an increasing angular velocity, mainly due to the ground - tire contact friction forces. The occupants in the front of the vehicle are hold in place by the seat belts. Upon continuing its roll motion, the vehicle impacts the ground with its rollbar cage, while the ejection of the rear occupant is complete. Bouncing from the inverted position the vehicle completes another half turn and impacts the ground with the tires again.

The Severity Index, plotted in Fig. 28, indicates a very high probability of fatal injuries for the occupants under the conditions simulated.

29

(b.01)   (b.02)   (b.03)   (b.04)   (b.05)

(b.06)   (b.07)   (b.08)   (b.09)   (b.10)
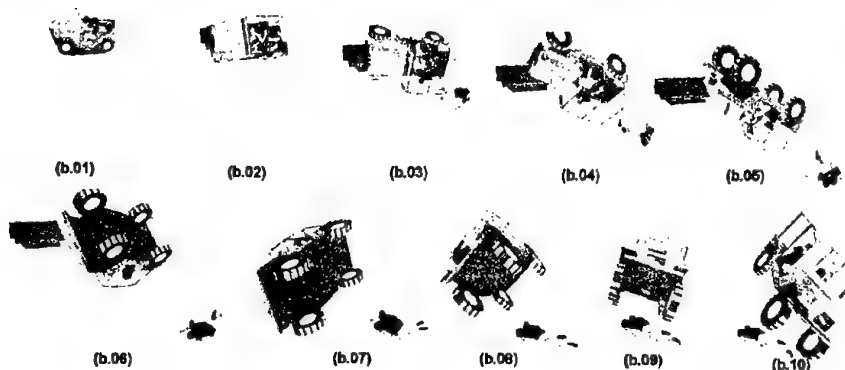
Figure 27. Front view of the rollover simulation of a vehicle with three occupants
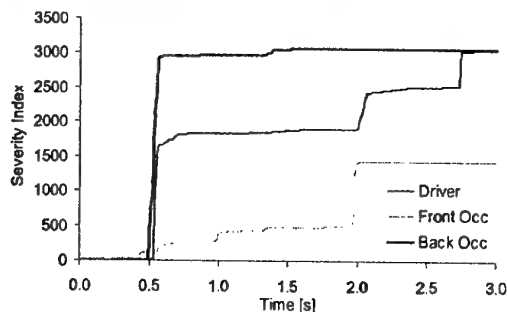
Figure 28. Severity Index for the vehicle occupants

Notice that the model has rigid seats, rigid interior trimming for the dashboard, side and floor panels, and that the ground is also considered to be rigid. It is expected that the head accelerations are somehow lower if some compliance is included in the seats and side panels of the vehicle interior.

5.3. SPORTS VEHICLE MULTIBODY MODEL

The formulation presented here is applied to a replica of the original Lancia Stratos, shown in Fig. 29, in different frontal and oblique collision scenarios. The multibody model, described by rigid bodies and spring-damper elements, includes the suspension elements, steering system and chassis. The front crash-box, modeled by nonlinear finite elements, is also included [40].
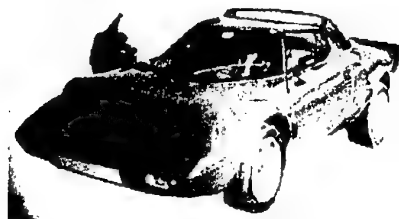
Figure 29. Prototype of the sports car

The multibody model of the vehicle is composed of 16 rigid bodies. The system components include the front double A-arm suspension system, the rear McPherson suspension system, wheels and chassis as depicted by Fig. 30. To model the tire interaction with the ground an analytical tire model with comprehensive slip is used [41].
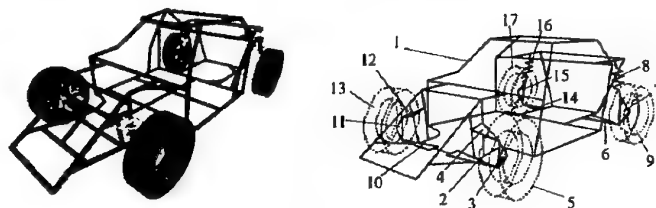
Figure 30. Multibody model of the sports vehicle

30

5.3.1. *Sports Car Crash-Box Model*

The sports car front crash box is depicted in Fig. 31. For the purpose of the frontal and oblique impacts at moderate velocities, the model for the chassis is considered rigid except for the front crash-box that is flexible.
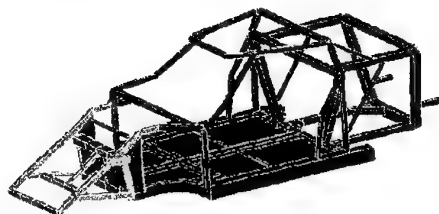
Figure 31. Model of sports car chassis with a nonlinear flexible front crash-box

The complete system has 15 degrees of freedom associated with the rigid bodies and 186 nodal degrees of freedom. This model is valid if plastic deformations are to occur in the parts of the vehicle modeled as flexible regions and no significant deformation takes place in the passenger compartment.

5.3.2. *Vehicle Frontal And Oblique Impact Simulations*

The sports vehicle with the front crash-box is analyzed for various impact scenarios, represented in Fig. 32, where the angle of impact and the topology of the road are different. For the crash scenarios the contact models are applied and the existence of friction forces is considered. The simulations are carried until the vehicle reaches a full stop.
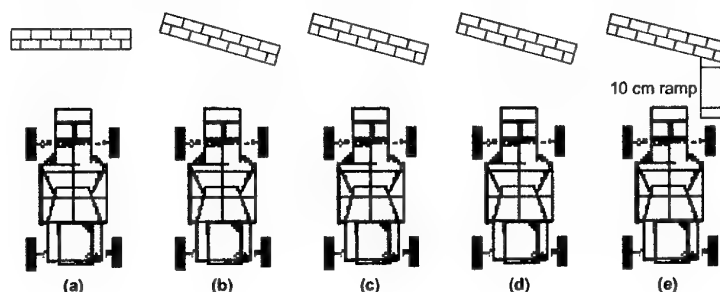
Figure 32. Impact with a) surface perpendicular to vehicle heading; b) 10° oblique surface, no friction; c) 20° oblique surface, no friction; d) 20° oblique surface, friction; e) Same as (d) but the vehicle goes over a 10 cm ramp.

The vehicle motion for different impact scenarios is presented in Fig. 33. For oblique contact with the obstacle there is a slight rotation of the vehicle during impact. This rotation is more visible in the case of frictionless impact. At the simulated impact speed the influence of the car suspension elements over the deformation mechanism is minimal. However, the suspension system plays an important role on the variation of the relative orientation between vehicle and obstacle before and after the crash.
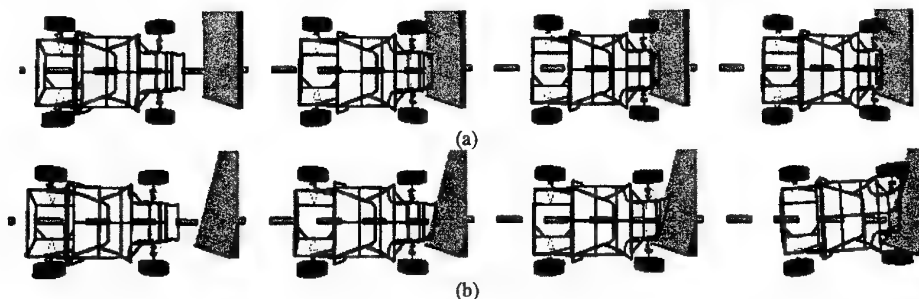
Figure 33. Motion of the vehicle for (a) Frontal impact; (b) 20° Oblique impact without contact friction

The efficiency of the crash-box to dissipate the kinetic energy of the vehicle decreases with the increase of the angle value between surface normal and vehicle heading. It is observed that for the frontal crash the front structure dissipates all kinetic energy. However, for oblique impacts with no surface friction, only part of that energy is absorbed by the crash-box. The vehicle motion is deflected, and would continue if no other component of the car entered in contact with the surface. In Fig. 34 the forces developed between vehicle and surface are

31

plotted.
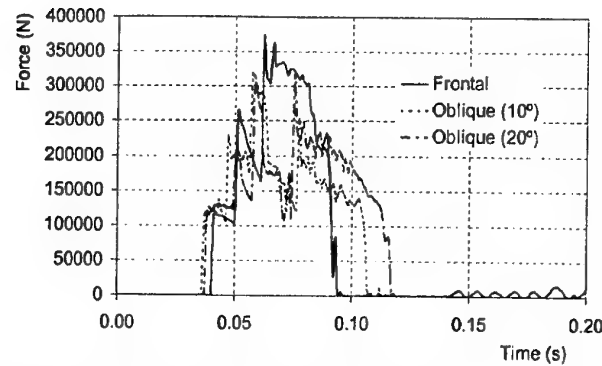
Figure 34. Forces developed between the front of the vehicle and impact surface

For the crash scenarios where friction is modeled, the deflection of the vehicle motion does not occur, enabling the structure to deform with a crushing mechanism similar to that of the frontal impact. Only a slight sideways translation of the vehicle is observed. This result clearly emphasizes the importance of a correct model for the friction forces developed during contact.

6. Conclusions

Deformation descriptions can be included in multibody system components for application in contact and impact situations. The deformations may be localized in a small region of the body, neighboring the point of contact, or they may occur in parts of the system away from contact. Therefore, the potential system deformation may be described by the contact model used, if these are localized at the contact point, or they may have to be included in the multibody formulation. Two representations of the system deformations have been proposed here.

The plastic hinge technique can be used when the deformation mechanisms are well known beforehand. Therefore, it is possible to model the structural components as a multibody sub-system having the kinematic joints located in the regions where the plastic hinges are expected. The second model reviewed uses nonlinear finite elements to represent the distributed deformations of the flexible body. This approach has the advantage of not requiring any particular knowledge of the deformation mechanisms beforehand but it is computationally more expensive.

The contact models used may also represent to a certain degree the structural deformations in the bodies in contact. A continuous force model has been described for both flexible and rigid multibody systems impact while a contact model based in unilateral constraints has been proposed for flexible multibody systems. It was shown that in the case of flexible multibody contact both models yield similar results, provided that the equivalent stiffness used for the continuous force model is based in the Hertzian elastic contact theory.

Through the application to vehicles and biomechanical impacts in diverse scenarios it was possible to appreciate the range of application of the different methodologies proposed and their combination.

7. References

1. Nikravesh, P., Chung, I. and Benedict, R. (1983) Plastic hinge approach to vehicle simulation using a plastic hinge technique, *J. Comp. Struct.* **16**, 385-400.
2. Ambrósio, J., Pereira, M. and Dias, J., (1996) Distributed and discrete nonlinear deformations on multibody systems, *Nonlinear Dynamics* **10**(4), 359-379.
3. Dias, J. and Pereira, M. (1997) Sensitivity analysis of rigid-flexible multibody systems, *Multibody System Dynamics* **1**(3), 303-322.
4. Song, J.O. and Haug, E.J. (1980) Dynamic analysis of planar flexible mechanisms, *Computer Methods in Applied Mechanics and Engineering*, **24**, 359-381.

32

5. Shabana, A.A. (1989) *Dynamics of Multibody Systems*, John Wiley & Sons, New York, New York.
6. Shabana A.A. and Wehage, R.A. (1989) A coordinate reduction technique for transient Analysis of spatial structures with large angular rotations, *Journal of Structural Mechanics* **11**, 401-431.
7. Yoo W.S.and Haug E.J., (1986) Dynamics of flexible mechanical systems using vibration and static correction modes, *ASME J. of Mechanisms, Transmissions and Automation in Design*, **108**, 315-322.
8. Modi, V.J. Suleman A. and Ng, A.C. (1991) An approach to dynamics and control of orbiting flexible structures, *Int. J. Nume. Methods Engng.* **32**, 1727-1748.
9. Banerjee, A.K. and Nagarajan, S. (1996) Efficient simulation of large overall motion of nonlinearly elastic beams, in Proceedings of ESA International Workshop on Advanced Mathematical Methods in the Dynamics of Flexible Bodies, ESA, Noordwijk, The Netherlands, June 3-5, pp. 3-23.
10. Kane, T., Ryan, R. and Banerjee, A. (1987) Dynamics of a cantilever beam attached to a moving base, *AIAA J of Guidance, Control and Dynamics* **10**, 139-151.
11. Geradin, M. (1996) Advanced methods in flexible multibody dynamics: review of element formulations and reduction methods, in Proceedings of ESA International Workshop on Advanced Mathematical Methods in the Dynamics of Flexible Bodies, ESA, Noordwijk, The Netherlands, June 3-5, pp. 83-106.
12. Cardona, A. and Geradin, M. (1988) A beam finite element non linear theory with finite rotations, *Int. J. Nume Methods in Engng.* **26**, 2403-2438.
13. Geradin, M. and Cardona, A. (1991)A Modelling of superelements in mechanism analysis, *Int. J. Nume Methods in Engng.* **32**, 1565-1594.
14. Shabana, A. (1997) Definition of the slopes and the finite element absolute nodal coordinate formulation, *Multibody System Dynamics* **1**, 339-348.
15. Ambrósio, J. and Nikravesh, P. (1992) Elastic-plastic deformations in multibody dynamics, *Nonlinear Dynamics* **3**, 85-104.
16. Ambrósio, J. and Seabra Pereira, M. (1994) Flexibility in multibody dynamics with applications to crashworthiness, In: M. Pereira and J. Ambrósio (ed.), Computer Aided Analysis of Rigid and Flexible Multibody Systems. Kluwer, Netherlands, pp. 199-232.
17. Pfeiffer, F., Glocker, C. (1996) *Multibody Dynamics With Unilateral Constraints*, John Wiley and Sons, New York, New York.
18. Martins, J.A.C., Barbarin, S., Raous, M., Pinto da Costa, A. (1999) Dynamic stability of finite dimensional linearly elastic systems with unilateral contact and Coulomb friction, *Comp. Meth. Appl. Mech. Engng.*, **177** (3-4), 289-328.
19. Lankarani H. M. and Nikravesh P. E. (1994) Continuous Contact Force Models for Impact Analysis in Multibody Systems, *Nonlinear Dynamics*, **5**, 193-207.
20. Nikravesh P. E. (1988) *Computer Aided Analysis Of Mechanical Systems*, Englewood Cliffs, New Jersey, Prentice-Hall.
21. Murray, N. (1983) The static approach to plastic collapse and energy dissipation in some thin-walled steel structures, In N. Jones & T. Wierzbicki Eds., *Structural Crashworthiness*, Butterworths: London, England, pp. 44-65.
22. Kindervater, C. (1997) Aircraft and helicopter crashworthiness: design and simulation, In J. Ambrósio, M. Pereira and F. Silva eds, *Crashworthiness Of Transportation Systems: Structural Impact And Occupant Protection*. NATO ASI Series E. V 332, Kluwer Academic Publishers, Dordrecht, Netherlands, pp. 525-577.
23. Matolcsy, M. (1997) Crashworthiness of bus structures and rollover protection. In J. Ambrósio, M. Pereira and F. Silva eds, *Crashworthiness Of Transportation Systems: Structural Impact And Occupant Protection*, NATO ASI Series E. Vol. 332, Kluwer Academic Publishers: Dordrecht, Netherlands, pp. 321-360.
24. Kecman, D. (1983) Bending collapse of rectangular and square section tubes, *Int. J. of Mech. Sci*, **25**(9-10), 623-636.
25. Winmer, A. (1977) Einfluß der belastungsgeschwindigkeit auf das festigkeits- und verformungsverhalten am beispiel von kraftfarhzeugen, *ATZ*, **77**(10), 281-286.
26. Ambrósio, J.A.C. and Nikravesh, P. (1992) Elastic-plastic deformations in multibody dynamics, *Nonlinear Dynamics*, **3**, 85-104.
27. Lankarani, H., Ma, D. and Menon, R., (1995) Impact dynamics of multibody mechanical systems and application to crash responses of aircraft occupant/structure, In M. Pereira and J. Ambrósio eds., *Computer Aided Analysis Of Rigid And Flexible Mechanical Systems*, NATO ASI Series E. Vol. 268, Kluwer Academic Publishers: Dordrecht, Netherlands, pp. 239-265.
28. Wu, S., Yang, S. and Haug, E., (1984) *Dynamics of Mechanical Systems with Coulomb Friction, Stiction, Impact and Constraint Addition-Deletion*, Technical Report 84-19, Center for Computer Aided Design, University of Iowa, Iowa City, Iowa.
29. Orden, J.C.G. and Goicolea, J.M. (2000) Conserving properties in constrained dynamics of flexible multibody systems, *Multibody System Dynamics*, **4**, 221-240.
30. SAFETRAIN, (2001) *Dynamic Tests*, BRITE/EURAM Project BE-309, SAFETRAIN Technical Report T8.2-F, Deutsche Bann, Berlin, Germany.
31. Milho, J., Ambrósio, J., and Pereira, M. (2002) A multibody methodology for the design of anti-climber devices for train crashworthiness simulation, *International Journal of Crashworthiness*, **7**(1), 7-20.
32. Milho, J., Ambrósio, J. and Pereira, M. (2002) Validated multibody model for train crash analysis, In E. Chirwa ed., *Proceedings of ICRASH2002 International Crashworthiness Conference*, Melbourne, Australia, February 25-27.
33. Ambrósio, J.A.C., Nikravesh, P.E. and Pereira, M.S. (1990) Crashworthiness Analysis of a Truck, *Mathematical Computer Modelling*, **14**, 959-964.
34. Silva, M.P.T. and Ambrósio, J.A.C. (2002) Out-of-position vehicle occupants models in a multibody integrated simulation environment, In *Proceedings of the 2002 IRCOBI Conference on the Biomechanics of Impact*, Munich, Germany, September 18-20.
35. Silva, M., Ambrósio, J. and Pereira, M., (1997) Biomechanical Model with Joint Resistance for Impact Simulation, *Multibody System Dynamics*, **1**(1), 65-84.
36. Allard, P., Stokes, I. and Blanchi, J. (1995) *Three-Dimensional Analysis of Human Movement*, Human Kinetics, Urbana-Champagne, Illinois.
37. Nigg, B. and Herzog, W. (1999) *Biomechanics of the Musculo-skeletal System*, John Wiley & Sons, New York.
38. Addel-Aziz, Y. and Karara, H., (1971) Direct linear transformation from comparator coordinates into object space coordinates in close-range photogrammetry, *Proceedings of the Symposium on Close-range Photogrammetry*, Falls Church, Virginia, pp. 1-18.
39. Laananen, D.H., Bolukbasi, A.O. and Coltman, J.W. (1983) *Computer Simulation of an Aircraft Seat and Occupant in a Crash Environment: Volume 1*, Technical Report DOT/FAA/CT-82/33-I, US Department of Transportation, Federal Aviation Administration, Atlanta City, New Jersey.
40. Ambrósio, J.A.C. and Gonçalves, J.P.C. (2001) Vehicle crashworthiness design and analysis by means of nonlinear flexible multibody dynamics, *Int. J. of Vehicle Design*, **26**(4), 309-330.
41. Gim G. (1988) *Vehicle Dynamic Simulation With a Comprehensive Model for Pneumatic Tires*, Ph.D. Dissertation, University of Arizona, Tucson, Arizona.

SOLVING NONCONVEX PROBLEMS OF MULTI-BODY DYNAMICS WITH CONTACT AND SMALL FRICTION BY SEQUENTIAL CONVEX RELAXATION

Mihai Anitescu *
Department of Mathematics University of Pittsburgh,
Pittsburgh, PA 15260, U.S.A., email: anitescu@math.pitt.edu

Gary Hart
Department of Mathematics University of Pittsburgh,
Pittsburgh, PA 15260, U.S.A., email: gdhart@pitt.edu

Abstract

We present a velocity-impulse linear complementarity framework for time-stepping in multi-body dynamics with contact and friction. The scheme is always consistent unlike acceleration force setups which may fail for some configurations. We demonstrate that, for some simple configurations, the solution set of the linear complementarity problem is not convex, for arbitrarily small but nonzero friction coefficients. Nevertheless we show that, for sufficiently small but nonzero friction coefficients, a fixed point iteration that solves at each step a convex linear complementarity problem will retrieve the unique velocity solution of disassemblable configurations.

1.   Introduction

Recently, time-stepping methods have been developed in an impulse-velocity framework that avoid the inconsistencies (Painleve paradoxes) that may appear in the classical approach [2, 3, 15, 14]. These methods can be modified to accommodate the most common types of stiffness [1]. Although an important difficulty was overcome, there is still the issue of solving efficiently the linear complementarity problem.

We show that, for very simple configurations, the velocity-impulse solution set can be nonconvex for arbitrarily small but nonzero friction coefficients, which is almost always an indication of exponential complexity in the resolution of the problem. Nevertheless, we show that, for sufficiently small coefficients, the velocity solution is unique whenever the frictionless configuration can be disassembled. We show that, for small friction coefficients at the contacts, the unknown velocity is a fixed point of a certain contraction mapping. To evaluate the mapping, one needs to solve only convex linear complementarity subproblems

(which are the optimality relations for some convex quadratic program). Therefore the fixed point iteration can be set up reasonably efficiently.

Several other approaches exist in computational contact mechanics that have a fixed-point iteration flavor where convex subproblems are used to compute the values of the contraction mapping [7, 12, 13]. These approaches evaluate successively the normal force keeping the tangential force fixed and then the tangential force keeping the normal force fixed. These approaches rely fundamentally on the assumption that, if the normal force is specified, the tangential force can be uniquely computed. In the simple example of one rigid rectangle sitting flat and at rest on top of another larger rigid rectangle that is not true: there is an infinite set of tangential forces that satisfy all the model constraints.

2. The linear complementarity problem of the time-stepping scheme

Our approach covers several types of constraints. In the following q and v will constitute the position and, respectively, velocity vector of a system of several bodies. **Complementarity Notation** We denote by $a \geq 0 \perp b \geq 0$ complementary vectors with nonnegative entries that satisfy $a^T b = 0$.

2.1 Model Constraints

Joint Constraints Such constraints are described by equations $\Theta^{(i)}(q) = 0, i = 1, 2, \dots, m$. We denote by $\nu^{(i)}(q)$ the gradient of the corresponding function, or $\nu^{(i)}(q) = \nabla_q \Theta^{(i)}(q)$, $i = 1, 2, \dots, m$. The impulse exerted by a joint on the system is $c_\nu^{(i)} \nu^{(i)}(q)$ where $c_\nu^{(i)}$ is a scalar related to the Lagrange multiplier of classical constrained dynamics [10].

Noninterpenetration Constraints. The noninterpenetration constraints are $\Phi^{(j)}(q) \geq 0$, $j = 1, 2, \dots, p$, where the generalized distance functions $\Phi^{(j)}(q)$ can be assumed to be differentiable in most cases by considering appropriate geometric primitives [8]. When the contact j is active, $\Phi^{(j)}(q) = 0$, a compressive normal impulse $c_n^{(j)} \geq 0$ acts on the system. In generalized coordinates the impulse becomes $c_n^{(j)} n^{(j)}$ where $n^{(j)} = \nabla_q \Phi^{(j)}(q)$. The fact that an inactive contact cannot exert an impulse is quantified by $\Phi^{(j)}(q) \perp c_n^{(j)} = 0$, $j = 1, 2, \dots, p$.

Frictional Constraints are expressed via a discretization of the friction cone [14, 2, 1]. For a contact j, we take a collection of coplanar vectors $d_i(q)$, $i = 1, 2, \dots, m_C$ which span the plane tangent at the contact (though the plane may cease to be tangent to the the contact normal when mapped in generalized coordinates, [5]). We denote by $D(q) = [d_1(q), d_2(q), \dots, d_{m_C}(q)]$. A tangential impulse will be $\sum_{i=1}^{m_C} \beta_i d_i(q)$, where $\beta_i \geq 0$, $i = 1, 2, \dots, m_C$. If we denote by $\beta = (\beta_1, \beta_2, \dots, \beta_{m_C})^T$, the total tangential impulse becomes $D(q)\beta$. The friction model, which ensures maximum dissipation for given c_n and velocity v, as well as that the total contact force is inside the discretized cone, is [14, 2]

$$D(q)^T v + \lambda e \geq 0 \quad \perp \quad \beta \geq 0, \qquad \mu c_n - e^T \beta \geq 0 \quad \perp \quad \lambda \geq 0. \tag{2.1}$$

Here $e = (1, 1, \dots, 1)^T$ is of dimension m_C, and μ is the friction parameter.

Dynamical data of the simulation. We denote by $M(q)$ the, symmetric, positive definite, mass matrix of the system and by $k(t, q, v)$ the external force.

Contact indexing convention. All quantities described in this section associated with contact j are denoted by the superscript $^{(j)}$.

Norm convention. When we use a vector or matrix norm whose index is not specified, it is the 2 norm.

2.2   The linear complementarity problem

For use in a time-stepping scheme, we linearize the constraints to obtain $\nu^{(i)^T}(q)v = 0$ for joint constraints and $n^{(j)}(q)^T v \geq 0$ for active noninterpenetration constraints. The set of active indices is denoted by $\mathcal{A}$, and is updated at every step, possibly following a collision resolution [2].

Let h be time step. If, at some time $t^{(l)}$, the system is at position $q^{(l)}$ and velocity $v^{(l)}$, then we choose the new position to be $q^{(l+1)} = q^{(l)} + hv^{(l+1)}$, where $v^{(l+1)}$ is the solution of the following mixed linear complementarity problem that collects all the constraints introduced above [2, 3]

$$
\begin{bmatrix}
M^{(l)} & -\widetilde{\nu} & -\widetilde{n} & -\widetilde{D} & 0 \\
\widetilde{\nu}^T & 0 & 0 & 0 & 0 \\
\widetilde{n}^T & 0 & 0 & 0 & 0 \\
\widetilde{D}^T & 0 & 0 & 0 & \widetilde{E} \\
0 & 0 & \widetilde{\mu} & -\widetilde{E}^T & 0
\end{bmatrix}
\begin{bmatrix}
v^{(l+1)} \\
\widetilde{c}_\nu \\
\widetilde{c}_n \\
\widetilde{\beta} \\
\widetilde{\lambda}
\end{bmatrix}
+
\begin{bmatrix}
-Mv^{(l)} - hk^{(l)} \\
0 \\
0 \\
0 \\
0
\end{bmatrix}
=
\begin{bmatrix}
0 \\
0 \\
\widetilde{\rho} \\
\widetilde{\sigma} \\
\widetilde{\zeta}
\end{bmatrix}
\qquad (2.2)
$$

$$
\begin{bmatrix}
\widetilde{c}_n \\
\widetilde{\beta} \\
\widetilde{\lambda}
\end{bmatrix}^T
\begin{bmatrix}
\widetilde{\rho} \\
\widetilde{\sigma} \\
\widetilde{\zeta}
\end{bmatrix}
= 0, \qquad
\begin{bmatrix}
\widetilde{c}_n \\
\widetilde{\beta} \\
\widetilde{\lambda}
\end{bmatrix} \geq 0, \qquad
\begin{bmatrix}
\widetilde{\rho} \\
\widetilde{\sigma} \\
\widetilde{\zeta}
\end{bmatrix} \geq 0. \qquad (2.3)
$$

Here $\widetilde{\nu} = [\nu^{(1)}, \nu^{(2)}, \dots, \nu^{(m)}]$, $\widetilde{c}_\nu = [c_\nu^{(1)}, c_\nu^{(2)}, \dots, c_\nu^{(m)}]^T$, $\widetilde{n} = [n^{(j_1)}, n^{(j_1)}, \dots, n^{(j_s)}]$, $\widetilde{c}_n = [c_n^{(j_1)}, c_n^{(j_2)}, \dots, c_n^{(j_s)}]^T$, $\widetilde{\beta} = [\beta^{(j_1)T}, \beta^{(j_2)T}, \dots, \beta^{(j_s)T}]^T$, $\widetilde{D} = [D^{(j_1)}, D^{(j_2)}, \dots, D^{(j_s)}]$, $\widetilde{\lambda} = [\lambda^{(j_1)}, \lambda^{(j_2)}, \dots, \lambda^{(j_s)}]$, $\widetilde{\mu} = diag(\mu^{(j_1)}, \mu^{(j_2)}, \dots, \mu^{(j_s)})^T$, and $\widetilde{E} = diag(e^{(j_1)}, e^{(j_2)}, \dots, e^{(j_s)})$ are the lumped LCP data, and $\mathcal{A} = \{j_1, j_2, \dots, j_s\}$ are the active contact constraints. The vector inequalities in (2.3) are to be understood componentwise. To simplify the presentation we have eluded the dependence of the geometrical parameters on the data of the simulation. Also $M^{(l)}$ is the mass matrix, which we assume to be positive definite, at time (l) and $k^{(l)}$ represents the external force at time (l).

3.   An example of configuration with nonconvex solution set

If the friction coefficients are $\mu^{(j)} = 0$, $j \in \mathcal{A}$, then the mixed linear complementarity problem (2.2–2.3) has a convex solution set and can be solved in a time that is polynomial with respect to the problem size [4]. An important question is whether it can be guaranteed that the mixed linear complementarity problem (2.2–2.3) can be solved efficiently, preferably in polynomial time, at least for small friction coefficients.

Consider, however, the configuration in Figure 1, where a block of mass 1 sits on a table. Assume that the friction coefficient is μ and that the initial velocity is 0. The mixed linear complementarity problem (2.2–2.3) can then be written such that both the contact and the friction force act only at the corners of the body [5].

We denote by the superscripts (1) and (2) quantities connected to the left and right corners of the body with the table, $\beta_i^{(j)}$, $i = 1, 2$, $j = 1, 2$ the tangent impulses acting in direction i for contact (j). $c_n^{(j)}$, $j = 1, 2$ are the normal impulses, g is the gravitational

$\beta_1^{(1)}$ $\beta_2^{(1)}$ $\beta_1^{(2)}$ $\beta_2^{(2)}$

$c_n^{(1)}$ $c_n^{(2)}$
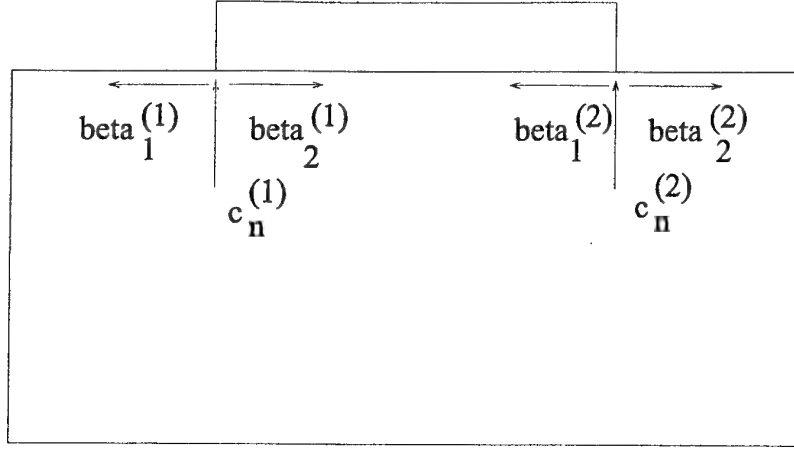
Figure 1.   Example of a nonconvex solution set.

acceleration and h is the time-step, v_x and v_y are the velocities of the body. Also $\lambda^{(j)}$, $j = 1, 2$ are the multipliers that complete the friction model (2.1). Here μ is the friction coefficient at both ends of the body.

All solutions must satisfy $v_x = v_y = 0$. Two solutions of (2.2–2.3) are

1 $c_n^{(1)} = c_n^{(2)} = \frac{hg}{2}$, $\beta_1^{(1)} = \beta_2^{(1)} = \beta_1^{(2)} = \beta_2^{(2)} = 0$, $\lambda^{(1)} = \lambda^{(2)} = 1$.

2 $c_n^{(1)} = c_n^{(2)} = \frac{hg}{2}$, $\beta_1^{(1)} = \beta_2^{(2)} = 0$, $\beta_1^{(2)} = \beta_2^{(1)} = \mu\frac{hg}{2}$, $\lambda^{(1)} = \lambda^{(2)} = 0$.

If we take the average of these solutions, we obtain $c_n^{(1)} = c_n^{(2)} = \frac{hg}{2}$, $\beta_1^{(1)} = \beta_2^{(2)} = 0$, $\beta_1^{(2)} = \beta_2^{(1)} = \mu\frac{hg}{4}$, $\lambda^{(1)} = \lambda^{(2)} = \frac{1}{2}$. It can be immediately verified that these choices, together with $v_x = v_y = 0$ *do not* satisfy (2.2–2.3), in particular the complementarity constraint

$$\beta_1^{(2)} \geq 0 \quad \perp \quad \lambda^{(2)} \geq 0.$$

which is clearly violated for our choice above when $\mu > 0$.

Therefore, even for simple cases and the smallest nonzero friction coefficients, the solution set of (2.2–2.3) will not be convex. Therefore the matrix of this linear complementarity problem cannot be P_*, which is the largest class of matrices for which polynomial time algorithms are known [4]. This raises an important difficulty in the path of efficiently finding solutions to the multibody dynamics problem with contact and friction, when a considerable number of contacts is active, even for the smallest friction coefficients. In the next section we will construct a fixed-point iteration that retrieves the velocity solution by solving positive semidefinite subproblems.

4.   A convex relaxation of (2.2–2.3)

In the following section, we will approximate the mixed linear complementarity problem (2.2–2.3) by the following mixed linear complementarity problem

$$
\begin{bmatrix}
M^{(l)} & -\tilde{\nu} & -\tilde{n} & -\tilde{D} & 0 \\
\tilde{\nu}^T & 0 & 0 & 0 & 0 \\
\tilde{n}^T & 0 & 0 & 0 & -\tilde{\mu} \\
\tilde{D}^T & 0 & 0 & 0 & \tilde{E} \\
0 & 0 & \tilde{\mu} & -\tilde{E}^T & 0
\end{bmatrix}
\begin{bmatrix}
v^{(l+1)} \\
\tilde{c}_\nu \\
\tilde{c}_n \\
\beta \\
\tilde{\lambda}
\end{bmatrix}
+
\begin{bmatrix}
-Mv^{(l)} - hk^{(l)} \\
0 \\
\Gamma \\
0 \\
0
\end{bmatrix}
=
\begin{bmatrix}
0 \\
0 \\
\tilde{\rho} \\
\sigma \\
\tilde{\zeta}
\end{bmatrix}
\qquad (4.4)
$$

$$
\begin{bmatrix}
\tilde{c}_n \\
\beta \\
\tilde{\lambda}
\end{bmatrix}^T
\begin{bmatrix}
\tilde{\rho} \\
\sigma \\
\tilde{\zeta}
\end{bmatrix} = 0,
\qquad
\begin{bmatrix}
\tilde{c}_n \\
\beta \\
\tilde{\lambda}
\end{bmatrix} \geq 0,
\qquad
\begin{bmatrix}
\tilde{\rho} \\
\sigma \\
\tilde{\zeta}
\end{bmatrix} \geq 0.
\qquad (4.5)
$$

Here Γ is a nonnegative vector that has as many components as active constraints (elements in $\mathcal{A}$). It is clear that the matrix of the linear complementarity problem, which we denote by M, is now positive semidefinite since $x^T M x \geq 0$, $\forall x$.

4.1 Fixed Point Iteration Algorithm

Based on the relaxation (4.4–4.5) we define the following fixed point iteration algorithm.

1 Set $\Gamma(0) = 0$, $\kappa = 0$, $\hat{v}^*(0) = 0$.

2 Solve the **convex** mixed linear complementarity problem (4.4-4.5) for $\Gamma = \Gamma(\kappa)$ and find the new velocity $\hat{v}^*(\kappa + 1) = v^*(\Gamma(\kappa))$.

3 Define $\hat{\lambda}(\kappa + 1)$, a component of the solution of (4.4-4.5) for $\Gamma = \Gamma(\kappa)$

$$
\hat{\lambda}^{(j)^*}(\kappa + 1) = \max_{i=1,2,\ldots,m_C^{(j)}} \left\{ d_i^{(j)^T} \hat{v}^*(\kappa + 1) \right\}, \quad j \in \mathcal{A}. \qquad (4.6)
$$

4 Define $\Gamma(\kappa + 1) = \tilde{\mu} \hat{\lambda}(\kappa + 1)$ (recall from the discussion following the definition of the mixed linear complementarity problem (2.2-2.3), $\tilde{\mu}$ is a diagonal matrix whose entries are the friction coefficients of the individual contacts). From the assumption that the tangential force description is symmetric we clearly have that $\Gamma(\kappa) \geq 0$, $\forall \kappa$.

5 Define $\kappa = \kappa + 1$ and return to step 2.

Our convergence result is based on a regularity assumption of the constraint geometry. We assume that the gradients of the equality constraints $\nu^{(i)}(q)$, $i = 1, 2, \ldots, m$ are linearly independent and that there exists $u^\# \neq 0$ such that

$$
\tilde{n}^T u^\# > 0, \quad \tilde{\nu}^T u^\# = 0.
$$

When this assumption holds the configuration can be disassembled [6]. This is also equivalent to the fact that the friction cone is pointed for sufficiently small friction coefficients.

This regularity assumption allows us to obtain the main result of our work. The proof is included in the extended version of the paper.

Theorem 1 *Under the constraint regularity assumption above there exists $\mu^\circ > 0$ such that, whenever $\|\tilde{\mu}\| \leq \mu^\circ$ the problem (2.2-2.3) has a unique velocity solution and the fixed-point algorithm above converges linearly to it.*

Acknowledgements

References

[1] Anitescu, M., and Potra, F.A., " A time-stepping method for stiff multibody dynamics with contact and friction", Reports on Computational Mathematics MCS-P884-0501, Mathematics and Computer Science Division, Argonne National Laboratory, 2001. To appear in *Computer Methods in Applied Mechanics and Engineering.*

[2] Anitescu, M., and Potra, F.A., "Formulating rigid multi-body-dynamics with contact and friction as solvable linear complementarity problems", *Nonlinear Dynamics* 14, 231–247, 1997.

[3] Anitescu, M., Stewart, D. and Potra,F. A., "Time-stepping for three-dimensional rigid body dynamics", *Comp. Methods Appl. Mech. Eng.* 177(3–4), 183–197, 1999.

[4] Anitescu, M., Lesaja, G. and Potra, F.A. Equivalence between different formulations of the linear complementarity problems, *Optimization Methods and Software* 7 (3-4), 265-290, 1997.

[5] Anitescu, M., Cremer, J., and Potra, F. A., "Formulating 3D contact dynamics problems", *Mechanics of Structures and Machines* 24(4), 405-437, 1996.

[6] Anitescu,M., Cremer,J.F. and Potra, F.A. "Properties of Complementarity Formulations for Contact Problems with Friction" in *Complementarity and Variational Problems: State of the Art*, Michael C. Ferris and Jong-Shi Pang, Editors, SIAM Publications, Philadelphia, 1997, pp. 12-21.

[7] Bisegna, P., Lebon, F. and Maceri, F. " D-PANA: a convergent block-relaxation solution method for the discretized dual formulation of the Signorini-Coulomb contact problem " *Comptes rendus de l'Academie des sciences - Serie I - Mathematique* 333(11), 1053-1058, 2001.

[8] Cremer, J., and Vanecek G., "Building simulations for virtual Environments", *Proceedings of the IFIP International Workshop on Virtual Environments*, October 1994, Coimbra, Portugal.

[9] Dirkse, S. P., and Ferris, M. C., "The PATH solver: a non-monotone stabilization scheme for mixed complementarity problems", *Optimization Methods and Software* 5, 123–156, 1995.

[10] Haug, E. J., *Computer Aided Kinematics and Dynamics of Mechanical Systems*, Allyn and Bacon, Boston, 1989.

[11] Munson, T. S., "Algorithms and Environments for Complementarity", Ph.D Thesis, Department of Computer Science, University of Wisconsin-Madison, 2000.

[12] Necas, J., Jarusek, J. and Haslinger, J: " On the solution of the Variational Inequality to the Signorini Problem with small Friction". *Bulletino U.M.I.* 17B, 796-811, 1980.

[13] Panagiotopoulos, P.D. *Hemivariational Inequalities.* Springer-Verlag, New York, 1993.

[14] Stewart, D. E., and Trinkle, J. C., "An implicit time-stepping scheme for rigid-body dynamics with inelastic collisions and Coulomb friction", *International Journal for Numerical Methods in Engineering* 39, 2673-2691, 1996.

[15] Stewart, D., "Rigid-body dynamics with friction and impact", *SIAM Review* 42 (1), 3–29, 2000.

CONTROL AND OPTIMIZATION OF SEMI-PASSIVELY ACTUATED MULTIBODY SYSTEMS*)

VIKTOR BERBYUK
Department of Machine and Vehicle Systems
Chalmers University of Technology, 412 96 Gothenburg, Sweden
viktor.berbyuk@me.chalmers.se

Abstract

The controlled multibody systems are under the consideration. At the lecture special emphasis is put on the study of underactuated and overactuated systems having different type of actuators (external powered drives, unpowered spring-damper like drives, etc.). Several questions are addressed about the role of inherent dynamics, and how much multibody system should be governed by external powered drives and how much by the system's inherent dynamics. The lecture consists of the following parts: introduction to the subject in question; mathematical statement of the optimal control problems that are suitable for modelling of controlled motion and optimization of semi-passively controlled multibody systems with different degrees of actuation; description of the methodology and the numerical algorithms for solution of control and optimization problems for semi-passively actuated multibody systems. The solutions of several optimal control problems for different kind of semi-passively actuated multibody systems are presented. Namely, the energy-optimal control of planar semi-passively controlled three-link manipulator robot, the energy-optimal control of closed-loop chain semi-passively actuated SCARA-like robot; optimization of the hydraulic and pneumatic drives of the multibody system modelled the human locomotor apparatus with above-knee prostheses, and others. Future perspectives in area of control and optimization problems of the semi-passively actuated multibody systems are discussed.

1. Introduction

Today our knowledge in mechanics, control engineering, electronics and computer sciences is actively integrated into a new interdisciplinary science – *mechatronics* [1]. One of the primary goals of mechatronics is to gain as many advantages as possible from the optimal interaction between the mechanical, control, electronic and computer subsystems. This requires more fundamental research on a number of topics of controlled multibody systems, e.g. parameter identification and optimal design, contact and impact problems, large deformation problems, control-structure interaction, etc., [2-3]. The research in above areas can help to improve performance characteristics of modern mechatronic products.

The most important and relevant characteristics of interaction between inherent dynamics and control of any mechanical system are its degree and type of actuation. Most technical systems, e.g. industrial robots, have been designed based on the commonsense rule of minimum complexity of the structure. The industrial robots have usually the same number of actuators as of the degrees of freedom of their mechanical subsystems, i.e. they belong to the class of fullyactuated mechanical systems. A lot of research has already been done in area of control and optimization of fullyactuated robotic systems that successfully supported industrial robotics. If multibody system (MBS) has less actuators than joints or more precisely if the dimension of the configuration space exceeds that of the control input space, the system is called *underactuated*. Examples of underactuated MBS are a car with n trailers having spring-damper-like joints, manipulator robots with failed actuators, free-flying space manipulators without jets or momentum wheels, manipulator robots with flexible links, legged robots with passive joints, etc. The general advantages of using underactuated mechanical systems reside in the fact that their weight is lower, and they consume less energy than their fullyactuated counterparts. For hyper-redundant robots or multi-legged mobile robots, where large kinematic redundancy is available for dexterity and specific task completion, underactuation allows a more compact design and simpler control schemes. The analysis of dynamics and control of underactuated MBS is significantly more complex than that for fullyactuated ones. A survey of papers in the above area has shown that the dynamics and control problems of underactuated mechanical systems have actively been studied for the last decade [4-7].

The next generation of robots must be autonomous and dexterous [8]. Dexterity implies the mechanical ability to carry out various kinds of tasks in various situations. Robots must have many sensors and more actuators than degrees of freedom, i.e. being the controlled mechanical system with sensing and actuation redundancies. To carry out optimally the complex tasks in various situations it can be desirable to change a number of actively controlled degrees of freedom of robotic system. It can easy be done, for instance, by locking or unlocking some of the actuators of robot during its performance of the specific subtask of a given complex task. From the point of view of control it means that robot can be considered as over, -fully, or underactuated

mechanical system during its performance of the complex task. Obviously, the type of actuators used can also be different depending on the task of robot [9-14].

The analysis of the literature and the above-mentioned fundamental aspects shows the importance of studying dynamics, control and optimization problems of MBS with different degrees of actuation and the robotic systems, in particular. This research is of a great challenge.

In the paper a controlled MBS of rigid bodies is under study. External controlling forces and moments can be applied directly to arbitrary points in the system. These controlling stimuli are generated by external (powered) drives. It is assumed that displacement and velocity dependent internal controlling forces and torques can also be applied to the system. These controlling stimuli are generated by internal (unpowered) drives, e.g. spring-damper actuators located between arbitrary points and described by linear and angular stiffness and damping parameters. MBS including both external (powered) and internal (unpowered) drives we shall term a semi-passively actuated MBS. In the paper we tackle optimization problems for MBS having unpowered actuators. The reasons of this study are as follows. To incorporate spring-damper actuators into the structure of MBS and to design optimally their parameters can give several advantages, e.g. to decrease a number of external drives and, as a consequence, to decrease the weight of moving links and the energy consumption of the system. It can give great advantages to use different passive compliance elements to control some degrees of freedom of manipulator robots and legged mechanisms for their performance of working tasks with periodic laws of motion [9-13]. We study a fundamental question about optimal interaction between the controlling stimuli generated by the external drives and the proportional-differential internal forces described by linear and angular stiffness and damping parameters. A range of questions is also addressed about the role of inherent dynamics in controlled motion, and how much MBS should be governed by the external drives and how much by the system's inherent dynamics. We are in particular investigating semi-passively actuated manipulator robots and bipedal walking mechanisms having spring-damper actuators.

In this paper we outline the results that will be presented during the lecture.

2. Statement of the problem

Consider a MBS the controlled motion of which can be described by the following equations:

$$x^{\bullet} = f(x, u, w(t, \xi)), \quad g(x, w(t, \xi)) = 0, \quad t \in [0, T] \tag{1}$$

Here $x = (x_1, x_2, ..., x_n)$ is a state vector, $u = (u_1, u_2, ..., u_m)$ is a vector of controlling stimuli (forces, torques) generated by the external (powered) drives of the MBS, $w = (w_1, w_2, ..., w_r)$ is a vector of the controlling stimuli of the internal (unpowered) drives of the MBS, and T is the duration of the controlled motion of MBS. Vector functions f and g are determined by the structures of the MBS and unpowered drives, respectively, ξ is a vector of design parameters of the unpowered drives.

Constraints and restrictions are imposed on the state vector $x(t)$, the controlling stimuli of the unpowered drives $w(t, \xi)$, and the external control laws $u(t)$ of the system. These restrictions can be written in the following way:

$$\{x(t)\} \in Q, \quad t \in [0, T] \tag{2}$$

$$w(t, \xi) \in W, \quad t \in [0, T] \tag{3}$$

$$u(t) \in U, \quad t \in [0, T] \tag{4}$$

In formulas (2) - (4), Q and U are given domains in the state and control spaces of the system, respectively; W is a set of addmissible controlling stimuli determined by the structure of the unpowered drives.

The differential equations (1) together with the restrictions (2)-(4) are called the mathematical model of the semi-passively actuated MBS. This model can be used for many applications, e.g. to solve the design problems of lower limb prostheses and to study control strategies for the stable motion of bipedal locomotion systems with compliance elements at the joints [6, 10], for computer simulation of the energy-optimal motion of closed-loop chain manipulator robots with unpowered drives [12], etc.

Assume that there exists a non-empty set of vector-functions $\{x(t), u(t), w(t, \xi), \; t \in [0, T]\}$ which satisfy the equations (1) and the constraints (2)-(4). The following optimal control problem can be formulated.

Problem A. Given a MBS the controlled motion of which is described by equations (1). It is required to determine the vector-function of unpowered drives $w_*(t, \xi)$, the motion of the system $x_*(t)$ and the external

controlling stimuli $u_*(t, x_*, w_*)$ which alltogether satisfy the equations (1), the restrictions (2)-(4), and which minimize the given objective functional $\Phi[u]$.

As a result of the solution of *Problem A* the optimal structure of MBS having both powered and unpowered drives is designed. The external controlling stimuli for the system are also found which minimize the given objective functional.

One of the primary goals for the incorporation of unpowered drives into the structure of MBS is an improvement of their control processes. It means that the validity of the following inequality is expected: $\Phi[u_*(t, x_*, w_*)] < \Phi[u_{0*}(t, x_{0*})]$, where $x_{0*}(t)$, $u_{0*}(t)$ are the optimal motion and the controlling stimuli of the MBS without the unpowered drives obtained under the restrictions (2), (4). In this sense the solution of *Problem A* could help to estimate the limiting possibility of improvement of the external control strategies for MBS due to incorporation into their structure different unpowered drives determined by the constraints (3).

3. Methodology

We have formulated the optimal control problem for the semi-passively actuated MBS. The key feature of the proposed mathematical statement of the problems is the direct utilization of the differential equations describing the inherent dynamics of internal unpowered drives together with all other constraints that are imposed on the state vector and the controlling stimuli of the system. It leads to the non-uniqueness of the solution of the direct and inverse dynamics problems and makes it possible to design optimal unpowered actuators for MBS.

In general case for MBS with many degrees-of-freedom powerful numerical algorithms are needed to solve *Problem A*. Futhermore, during the calculation of optimal control laws for MBS it is necessary to design at the same time the optimal structure of the unpowered drives taking into account the restriction (3). This can significantly increase the complexity of the computation.

The numerical method has been developed [6, 10, 12] for the solution of *Problem A* for MBS, which model semi-passively actuated manipulator robots and bipedal locomotion systems with unpowered drives at their joints. The method is based on a special procedure to convert the initial optimal control problem into a standard nonlinear programming problem. This is made by an approximation of the independent variable functions using a combination of polynomial and Fourier series and by the solution of semi-inverse dynamics problem. The key features of the method are its high numerical efficiency and the possibility to satisfy a lot of restrictions imposed on the phase coordinates of the system automatically and accurately. The efficiency of the developed method has been illustrated by solution of several problems, e.g. by computer simulations of the energy-optimal motion of closed-loop chain semi-passively actuated manipulator robot, the bipedal walking robot, by the solution of design problems of the energy-optimal above-knee prostheses with several types of unpowered knee mechanisms [6, 10, 12].

4. Optimal Passive Drives for Given Motion of MBS

Consider a MBS having n degrees-of-freedom. Let the equation of its controlled motion be as follows:

$$A(q)\ddot{q} + B(q, \dot{q}) = u(t), \qquad t \in [0, T] \tag{5}$$

Here $q = (q_1, q_2, ..., q_n)$ is a vector of the generelized coordinates, $u = (u_1, u_2, ..., u_m)$ is a vector of the controlling stimuli (forces, torques) generated by powered drives of the MBS, $w = (w_1, w_2, ..., w_m)$ is a vector of the controlling stimuli of the internal (unpowered) drives of MBS, $A(q)$, $B(q, \dot{q})$ are given matrices.

At the same time, assume that MBS has additional passive drives, namely non-linear visco-elastic spring-damper-like actuators in its structure. The mathematical model of the semi-passively actuated MBS can be written as follows:

$$A(q)\ddot{q} + B(q, \dot{q}) = u(t) + w(q, \dot{q}), \quad w(q, \dot{q}) + kf(q, \dot{q}) = 0, \qquad t \in [0, T] \tag{6}$$

where the function $f(q, \dot{q})$ determines the inherent dynamics of the passive drives under the restriction (3) and k is a "damper coefficient".

To estimate the quality of the control processes the following objective functional is exploied

$$\Phi[u(t)] = \int_0^T \|u(t)\|^2 dt, \quad \|u(t)\| = (u_1^2(t) + ... + u_n^2(t))^{1/2} \tag{7}$$

42

Let $\{q_0(t), \ u_0(t), \ t \in [0,T]\}$ be any pair of functions that satisfy equation (5).

It is assumed that the motion $\{q_0(t), \ t \in [0,T]\}$ can also be realised by the considered semi-passively actuated MBS. Using the equations (6), the external controlling stimuli that need for the motion are written as follows

$$u_{w0}(t) = u_0(t) + kf(q_0, \dot{q}_0), \text{ where } u_0(t) = A(q_0)\ddot{q}_0(t) + B(q_0, \dot{q}_0) \tag{8}$$

For the control law (8) the objective functional (7) will be equal to

$$\Phi[u_{w0}(t)] = \int_0^T \|u_0(t) + kf[q_0(t), \dot{q}_0(t)]\|^2 dt = \Phi[u_0(t)] + ak^2 + 2bk , \tag{9}$$

$$a = \int_0^T \|f(q_0, \dot{q}_0)\|^2 dt , \quad b = \int_0^T \langle u_0(t), f(q_0, \dot{q}_0) \rangle dt , \quad \langle u_0(t), f(q_0, \dot{q}_0) \rangle = (u_{01}f_1 + \dots + u_{0n}f_n) \tag{10}$$

It can be shown that the function $\Phi[u_{w0}(t)]$ has a global minimum with respect to the damper coefficient k. The value of this minimum is equal to $\Phi_{min} = \Phi[u_0(t)] - b^2 / a$ for the following optimal value of the damper coefficient $k_* = -b/a$.

The above mentioned makes it possible to conclude that for a MBS with n degrees-of-freedom and for any admissible motion $\{q_0(t), \ t \in [0,T]\}$ the energy-optimal non-linear visco-elastic spring-damper-like actuators are determined by the formulae $w_*(q_0, \dot{q}_0) + k_* f(q_0, \dot{q}_0) = 0, t \in [0,T]$.

As follows from above due to the incorporation of the optimal spring-damper-like actuators into the MBS structure the decrease in energy consumption is equal to

$$\Phi[u_0(t)] - \Phi_{min} = \left\{ \int_0^T \langle u_0(t), f(q_0, \dot{q}_0) \rangle dt \right\}^2 \bigg/ \int_0^T \|f(q_0, \dot{q}_0)\|^2 dt .$$

This value depends only on the given motion $\{q_0(t), \ t \in [0,T]\}$ and the function $f(q, \dot{q})$ determining the inherent dynamics of the passive drives.

Usually some restrictions are imposed on the external controlling stimuli $u(t)$. In this case the function $f(q, \dot{q})$ can not be choosen arbitrarily. Indeed, let us assume that the external controlling stimuli $u(t)$ are restricted by the constraint $\|u(t)\| \leq u_{max}, t \in [0,T]$ with given positive number u_{max}. Then the function $f(q, \dot{q})$ must satisfy not only the restriction (3) but also the inequality $\|u_0(t) - bf(q_0, \dot{q}_0)/a\| \leq u_{max}, \ t \in [0,T]$, where $u_0(t)$, a and b are determined by the expressions (8) and (10).

5. Optimization of Controlled Motion of Semi-Passively Actuated Manipulator Robots

Here we present several results of optimization of controlled motion of semi-passively actuated three-link manipulator robot (Figure 1) and closed-loop chain semi-passively actuated SCARA-like robot (Figure 2).

5.1. THREE-LINK MANIPULATOR ROBOTS

In the Figure 1 the sketch of semi-passive actuated three-link manipulator robot is shown. The robot can have powered drives U_i and unpowered (passive) drives P_i (spring-damper-like actuators) located at the joints. The torques of the unpowered drives are modelled by formulae

$$p_i = -k_i(\varphi_i - \varphi_{i0k}) - c_i \dot{\varphi}_i \quad i = 1,2,3 \tag{11}$$

where k_i are the stiffness coefficients, c_i are the damping coefficients, φ_{i0k} are the no-load angles of the torsional spring.

The controlled motion of the considered semi-passive actuated three-link manipulator robot is described by equations (6). For the robot in question several variants of the *Problem A* have been solved by using the

developing methodology. The functional (7) has been used to estimate energy consumption of the controlled motion of the robot. The set of pick-and-place operations of the robot are under the particular study. For comparison in the Figure 3-4 the polar paths of the end-effector of the robot are depicted that correspond to the solution of energy-optimal control problems obtained for fullyactuated robot without unpowered drives and for underactuated robot with powered drive located at the joints O and A and with unpowered spring-damper-like drive located at joint B, respectively.
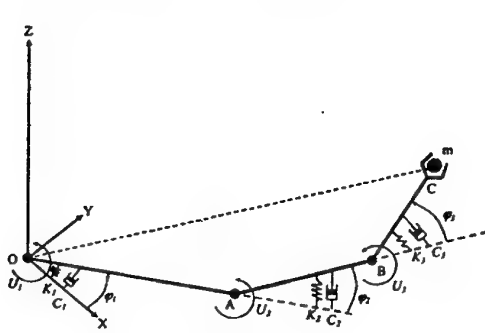
Figure 1.
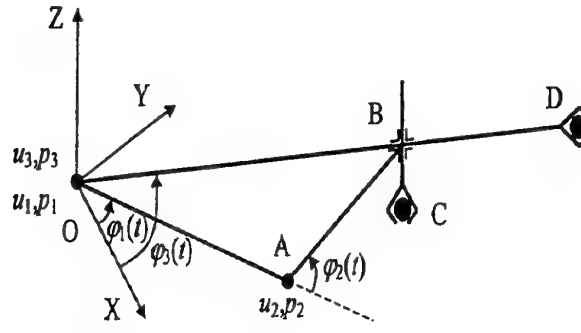
Figure 2.
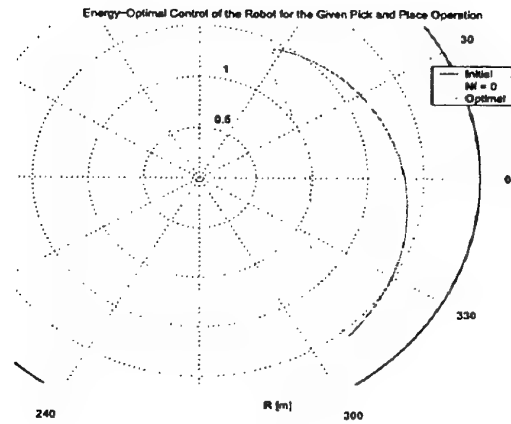
Figure 3.
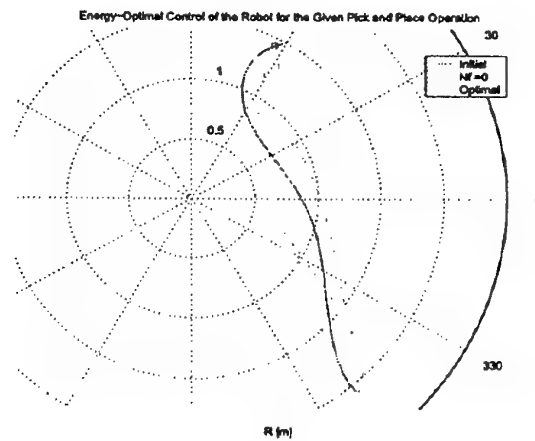
Figure 4.

44

5.2. SEMI-PASSIVELY ACTUATED SCARA-LIKE ROBOT

In the paper the optimal control problems of a new structure of manipulator robot (Figure 2) is under study. Proposed robotic system has the following new features in comparison with the well-known SCARA robot. In addition to powered drives it comprises several unpowered (passive) spring-damper-like drives. An additional link has also been incorporated into the structure that gives the possibility to obtain a semi-passively actuated closed-loop chain robot. Emphasis is put on a study of the interaction between the controlling stimuli of the powered drives and the torques exerted by the unpowered drives needed to provide the optimal motion of the robots with different degrees of actuation.

The robot depicted in Figure 2 comprises four links that are modeled by the rigid bodies OA, AB, OD and EC. There are one degree-of-freedom rotational joints at the points O and A, and translational joints at the point B. All joints are considered frictionless.

It is assumed that the robot's links OA, AB and OD move in the horizontal plane OXY under the action of the torques $u_1(t)$, $u_2(t)$ and $u_3(t)$ applied to the links OA, AB, and OD, respectively. Under the action of the force $F(t)$ the link EC moves along the direction of the axes OZ. The controlling stimuli $u_i(t)$, $i = 1, 2, 3$ and $F(t)$ are exerted by the powered drives of the robot. The robotic system also comprises spring-damper actuators at joints O and A. The torques exerted by these actuators p_1, p_2 and p_3 act on the links OA, AB and OD, respectively. They will be treated as the controlling stimuli of unpowered (passive) drives of the robot. Using ϕ_1, ϕ_2 and z as the generalized coordinates the equations of motion of the considered system can be derived by using the Lagrange formalism [12]. Here we study motions of the robot in the horizontal plane OXY only. The inherent dynamics of the passive drives of the robot can be modeled in different ways, e.g. by the differential constraints (11). The equations of the plane motion of the robot can be written as follows:

$$f_1(\phi_i,\dot\phi_i,\ddot\phi_i) = u_1 + p_1 + u_3 + p_3, \quad f_2(\phi_i,\dot\phi_i,\ddot\phi_i) = u_2 + p_2 + b(\phi_i)(u_3 + p_3) \tag{12}$$

The functions f_1 and f_2 are determined by means of the Lagrange operator [12].

The considered robot is an overactuated mechanical system. This makes it possible to optimize the controlling stimuli of powered drives for an arbitrary given motion of the robot.

Problem A.1. Assume that an arbitrary motion of the robot and control torques of unpowered drives are given, i.e. the functions $\phi_i(t), p_i(t)$ are specified. It is required to find the control stimuli $u = (u_1, u_2, u_3)$ which minimize the functional

$$E[u(t)] = \int_0^T (u_1^2(t) + u_2^2(t) + u_3^2(t))dt \tag{13}$$

subject to the differential constraints (12).

It can be shown that the solution of *Problem A.1.* is

$$u_3^*(t) = (g_1 + bg_2)/(2 + b^2), \quad u_1^*(t) = g_1 - u_3^*(t), \quad u_2^*(t) = g_2 - bu_3^*(t) \tag{14}$$

Here the functions g_1 and g_2 have the expressions:

$$g_1 = f_1 - p_1 - p_3, \quad g_2 = f_2 - p_2 - bp_3 \tag{15}$$

The obtained controlling stimuli (14) provide execution of an arbitrary given motion of the overactuated robot with minimal energy consumption E^*.

The simplest way to reduce the overactuation of the considered robot is to exclude one of the powered drives. For instance, assuming that

$$u_3(t) = 0, \quad t \in [0,T] \tag{16}$$

the unique solution for the functions $u_1(t)$, $u_2(t)$ can be obtained from the equations (12). In this case the functional (13) is

$$E^0 = \int_0^T (g_1^2(t) + g_2^2(t))dt \tag{17}$$

45

where the function $g_1(t)$, $g_2(t)$ are given by the formulas (15). Comparing the value E^0 with the value of the functional (13) for the obtained optimal controlling stimuli $u_i^*(t)$ it is easy to show the validity of the following expression

$$E^0 - E^* = \int_0^T (g_1(t) + bg_2(t))^2 / (2 + b^2) dt \qquad (18)$$

The formula (18) shows that the energy consumption needed to execute an arbitrary given motion by the considered overactuated robot with obtained optimal controlling stimuli (14), (15) is less than the energy consumption of the same robot but without powered drive acting on the link OD.

During the lecture other results of optimization of motion of closed-loop chain semi-passively actuated SCARA-like robot will be presented.

6. Optimization of Controlled Motion of Semi-Passively Actuated Bipedal Locomotion Systems

Here we will demonstrate the application of methodology of optimization of semi-passively actuated MBS to solve the design problems of lower limb prostheses.

There is an important difference between the dynamics of an intact limb and a prosthetic limb of an amputee. In the paper the mathematical modeling of a human gait of an amputee with the above-knee prosthesis is considered based on a supposition that the force moments at the knee and at the ankle joints of the prosthetic leg are passive ones. The values of these moments depend not only on the gait pattern, but also on the prosthesis construction.

The model of the amputee locomotor system (ALS) with above-knee prosthesis is depicted in Figure 5. It is assumed that the above-knee prosthesis comprises the linear-viscoelastic ankle mechanism and the hydraulic or the pneumatic knee mechanism.
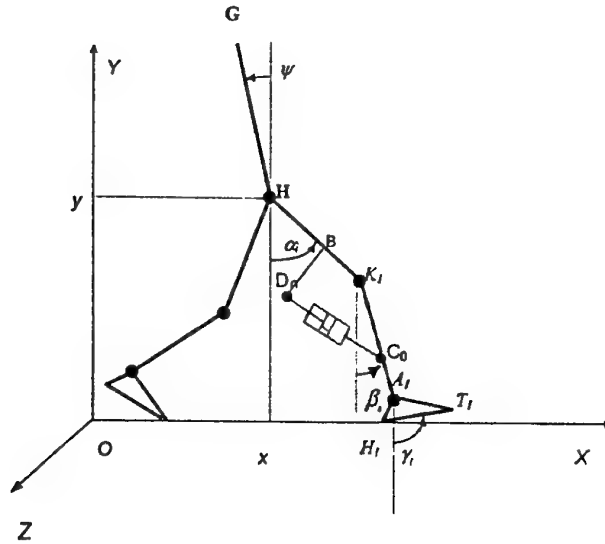
Figure 5.

During locomotion of ALS with the above-knee prosthesis the control torques

$$p_1(t) = C(\beta_1 - \gamma_1 + \pi/2) + K(\dot{\beta}_1 - \dot{\gamma}_1) + D, \qquad (19)$$

$$u_1(t) = (P_2 - P_1)S_p d_2 (d_1^2 + l_0^2)^{1/2} \sin(\alpha_1 - \beta_1 + \eta)/l_1$$

are generated at the ankle and at the knee joints of the prosthetic leg, respectively.

Here C, K are the torsion spring and the damping coefficients of the ankle mechanism; D is determined by the free angle of the spring and torsion spring coefficients; P_1, P_2 are the chamber pressures of the hydraulic or the pneumatic actuator that can be calculated by using the equations of dynamics of the knee mechanism of the prosthesis [15], S_p is the cylinder piston cross-area,

46

$$l_1 = (d_1^2 + d_2^2 + l_0^2 + 2d_2(d_1^2 + l_0^2)^{1/2} \cos(\alpha_1 - \beta_1 + \eta))^{1/2}, \quad \eta = a\tan(l_0/d_1), \quad (20)$$

$$d_1 = |BK_1|, \quad d_2 = |K_1C_0|, \quad l_0 = |BD_0|.$$

The controlled motions of ALS with above-knee prosthesis are described by the equations (6) and the formulae (19), (20).

The design problem of the above-knee prosthesis can be formulated as the optimal control problem with parameters (*Problem A*). The considered semi-passively actuated MBS that models ALS has the state vector $\left\{ x, \dot{x}, y, \dot{y}, \psi, \dot{\psi}, \alpha_i, \dot{\alpha}_i, \beta_i, \dot{\beta}_i, \gamma_i, \dot{\gamma}_i, i = 1,2 \right\}$, the vector of the powered drives controlling stimuli $u(t) = \left\{ q_1, q_2, u_2, p_2 \right\}$, and the vector of the constructive parameters of the unpowered drives $C_p = (C, K, D, d_1, d_2, l_0, S_p, S_0)$. The following functional

$$E_p = \frac{1}{2L} \int_0^T \left\{ \sum_{i=1}^2 |q_i(\dot{\psi} - \dot{\alpha}_i)| + |u_2(\dot{\alpha}_2 - \dot{\beta}_2)| + |p_2(\dot{\beta}_2 - \dot{\gamma}_2)| \right\} dt \quad (21)$$

is used during the solution of *Problem A*. The objective functional (21) estimates the energy expenditure per unit of distance traveling of ALS. The same approach as described in paragraph 3 has been used to solve the problem of design energy-optimal above-knee prostheses. Due to the dynamic constraints (19) the procedure of converting the *Problem A* into the standard nonlinear programming problem includes the solution of the semi-inverse dynamics problems for the mechanical system that models ALS with the above-knee prosthesis. It sufficiently increases the time consumption of the numerical algorithm for designing the energy-optimal above-knee prosthesis. The Problem A has been solved numerically for two types of the prostheses: the above-knee prosthesis with the hydraulic actuator at the knee, and the prosthesis with the pneumatic knee mechanism. Some kinematic and dynamic characteristics of the energy-optimal motion of ALS with optimal structure of the above-knee prosthesis obtained by the numerical solution of the Problem A for the gait with natural cadence are shown in Figures 6 - 9 (solid thin curves correspond to the prosthesis with the hydraulic actuator at the knee, dashed curves - to the prosthesis with the pneumatic knee mechanism). Knee angle ($\alpha_1 - \beta_1$) and hip angle ($\alpha_1 - \psi$) of the prosthetic leg are depicted in Figures 6-7, respectively, (in degrees). Hip torque of the prosthetic leg, ($q_1(t)/M$), and knee torque of the healthy leg, ($u_2(t)/M$) are presented in Figure 8-9, respectively, (in Nm/kg). For the comparison purposes in Figures 6-9 the domains of the values of the respective kinematic and dynamic characteristics obtained by the biomechanical experiments for a human normal gait [16, 17] are depicted by heavy solid curves.

Figure 6.

Figure 7.

<p style="text-align:center">%<i>of stride T</i></p>

<p style="text-align:center"><i>Figure 8.</i></p>

<p style="text-align:center">%<i>of stride T</i></p>
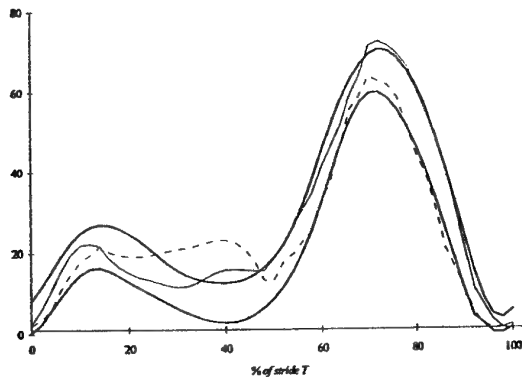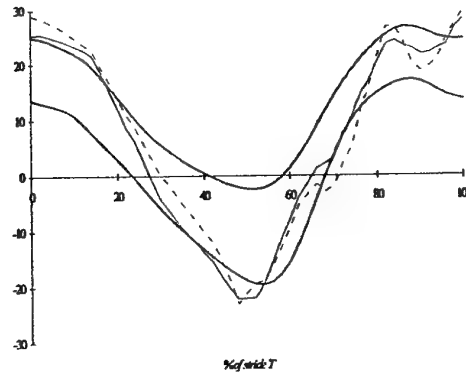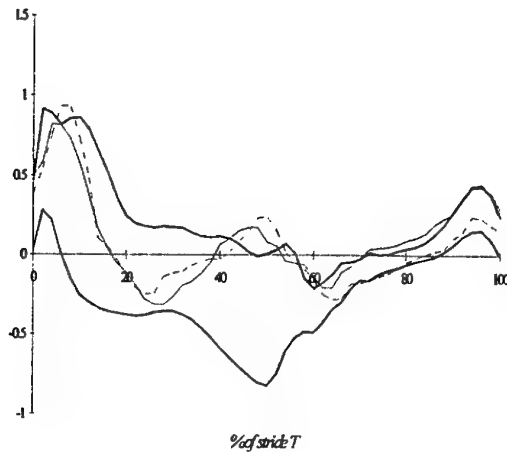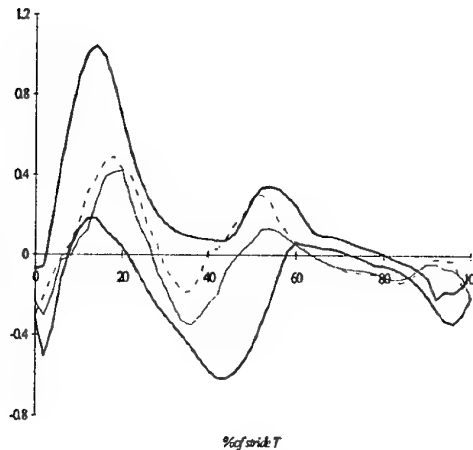
<p style="text-align:center"><i>Figure 9.</i></p>

The obtained kinematic and dynamic characteristics of the motion of ALS with optimal above-knee prosthesis structures are within reasonable proximity to the respective characteristics of a human normal gait [16, 17]. The analysis of a number of numerical simulations shows that the natural cadence of ALS gait gives a minimum to the energy expended per unit of distance traveled comparing to the amount of energy needed for the slow or fast gaits [10].

7. Conclusion

We have formulated the optimal control problem for the semi-passively actuated MBS (*Problem A*). The key feature of the proposed mathematical statement of the problems is the direct utilization of the differential equations describing the inherent dynamics of the passive actuators (internal unpowered drives) together with all other constraints that are imposed on the state vector and the controlling stimuli of the system. It leads to the non-uniqueness of the solution of the direct and inverse dynamics problems and makes it possible to design optimal passive actuators for MBS.

In the general case to solve *Problem A* for MBS with many degrees-of-freedom powerful numerical algorithms are needed. Futhermore, during the calculation of optimal control laws for MBS it is necessary to design at the same time the optimal structure of the passive drives taking into account the restriction (3). This can significantly increase the complexity of the computation.

Closed-form solution of *Problem A* has been obtained for arbitrary given motion of MBS having n degrees-of-freedom MBS and passive drives. The analysis of the obtained solutions shows that in several cases the incorporation of passive drives into the structure of MBS can decrease the energy consumption needed for the given motion of the system.

The numerical method has been developed for the solution of *Problem A* for MBS, which model several types of semi-passively actuated robotic and biorobotic systems. Efficiency of the proposed method is illustrated by computer simulations of the energy-optimal motion of closed-loop semi-passively controlled manipulator robot, the bipedal walking robot, the solution of design problems of the energy-optimal above-knee prostheses with several types of passively controlled knee mechanisms, etc. Analysis of the numerical results obtained has shown that during the optimal motion of the considered MBS there is a strong interaction between the gravity force, the external control torque exerted by the actively controlled drives and the internal torque exerted by the passive linear spring-damper actuators. Moreover, the incorporation of the optimal passive linear spring-damper actuators into the structure of the closed-loop robot leads to a significant reduction of the energy consumption of the robot for cyclic pick and place operations [12, 18]. The kinematic, dynamic, and energetic characteristics of controlled motion of MBS that model human locomotor system with above-knee prosthesis are strongly sensitive to the essential parameters of the passive actuators of the prosthesis. For a given individual and cadence of a gait there exist optimal values of the spring and damper parameters of the prosthesis's ankle and knee mechanisms. These parameters give minimum energy expended per unit of distance travelled [10].

Results obtained can help to design simpler control systems of manipulator robots and autonomous legged mechanisms having less weight and energy consumption. They will also be use to design energy efficient passively controlled mechanisms of the lower limb prostheses.

<p style="text-align:center">48</p>

8. Acknowledgements

9. References

1. Wikander, J., Torngren M., and Hanson M. (2001) The science and education of mechatronics engineering, *IEEE Robot Autom Mag* **8** (2), 20-26.
2. Schiehlen, W. (1997) Multibody System Dynamics: Roots and Perspectives. *J. Multibody System Dynamics* **1**, No 2, 149-188.
3. Shabana, A. A. (1997) Flexible multibody dynamics: Review of past and recent developments, *J. Multibody System Dynamics* **1**, No 2, 189-222.
4. De Luca, A., Mattone, R. and Oriolo, G. (1996) Control of underactuated mechanical systems: Application to the planar 2R robot, *Proceedings of the 35th Conference on Decision and Control,* Kobe, Japan, December 1996, 1455-1460.
5. Suzuki, T., Koinuma, M. and Nakamura, Y. (1996) Chaos and nonlinear control of nonholonomic free-joint manipulator, *Proceedings of the 1996 IEEE International Conference on Robotics and Automation,* 2668-2675.
6. Berbyuk, V. (1996) Multibody systems modeling and optimization problems of lower limb prostheses, in D. Bestle and W. Schiehlen (eds.), *IUTAM Symposium on Optimization of Mechanical Systems,* Kluwer Academic Publishers, pp.25-32.
7. Bullo, F. and Lynch, K. (2001) Kinematic controllability for decoupled trajectory planning in underactuated mechanical systems, *IEEE Transactions on Robotics and Automation,* **8**, (4), 402-412.
8. Nakamura, Y. (1991) *Advanced robotics: redundancy and optimization,* Addison-Wesley Publishing Company.
9. Berbyuk, V., Peterson, B. and Nishchenko, N. (1998) Linear viscoelastic actuator-based control system of a bipedal walking robot, in J. Adolfsson and J. Karlsen (eds.), *MECHATRONICS'98,* Elsevier Science Ltd., pp.379-384.
10. Berbyuk, V., (1999) Dynamic Simulation of Human Gait and Design Problems of Lower Limb Prostheses, *Biomechanics Seminar,* (ISSN 1100-2247), **12**, pp.1-20.
11. Berbyuk, V., Boström, A. and Peterson, B. (2000) Modelling an Design of Robotic Systems Having Spring-Damper Actuators, in *Proceedings of the 7th Mechatronics Forum International Conference,* 6-8 September 2000, Atlanta, Georgia, USA, (ISBN 0 08 043703 6), PERGAMON.
12. Lidberg, M. and Berbyuk, V. (2000) Modeling of Controlled Motion of Semi-Passively Actuated SCARA-Like Robot, in *Proceedings of the 7th Mechatronics Forum International Conference,* 6-8 September 2000, Atlanta, Georgia, USA, (ISBN 0 08 043703 6), PERGAMON.
13. Berbyuk, V. and Boström, A. (2001) Optimization Problems of Controlled Multibody Systems Having Spring-Damper Actuators, *International Applied Mechanics,* **37**, No. 7, pp.935-940.
14. Okada, M., Nakamura, Y. and Ban, S. (2001) Design of programmable passive compliance shoulder mechanism. In: *Proceedings of the IEEE International Conference on Robotics and Automation,* Seoul.
15. Berbyuk, V. and Nishchenko, N. (1998) Mathematical design of the energy-optimal above-knee prostheses, *Mathematical Methods and Physicomechanical Fields,* **41**, (4), 110-117.
16. Winter, D. (1991) *The Biomechanics and Motor Control of Human Gait,* University of Waterloo Press, Canada.
17. Berbyuk, V. and Lytwyn, B. (1998) The mathematical modeling of the human motions based on the optimization of the biodynamic system's controlled processes, *Mathematical Methods and Physicomechanical Fields,* **41**, (3), 153-161.
18. Lidberg M. and Berbyuk V. (2002) Energy-optimal control of semi-passively actuated SCARA-like robot, In: Peter Maisser and Peter Tenberge (eds.), *Proceedings of the First International Symposium on Mechatronics,* March 21-22, 2002, Chemnitz, Cermany, (ISBN 3-00-007504-6), pp.302-311.

Optimization of
Passive and Active Dynamic Systems

BTU

Prof. Dr.-Ing. habil. **Dieter Bestle**

Chair of Machine Dynamics
Brandenburg Technical University of Cottbus

Virtual Prototyping

Hardware-in-the-Loop Optimization

Parameter Identification
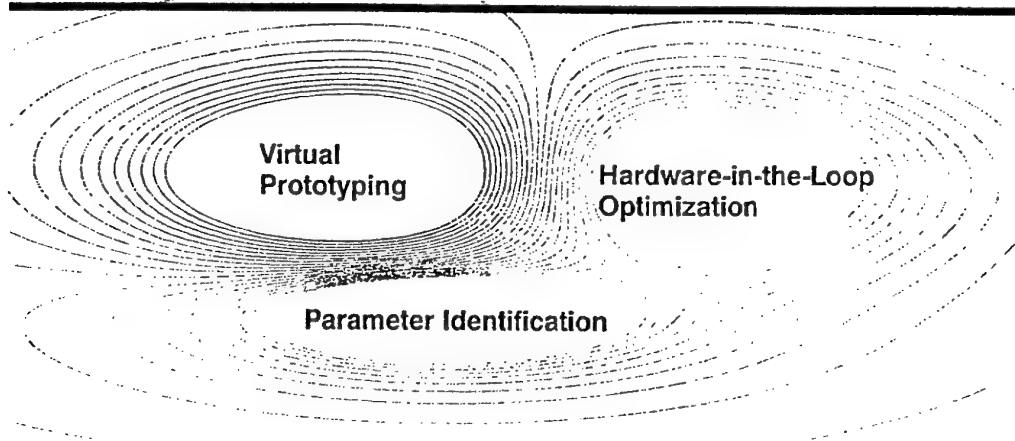
Virtual Prototyping: Integrated Modeling and Design Concept

modeling
dynamic system
mathematical model

criteria definition
design goals
performance criteria

parametrization
design flexibility
design variables

criteria evaluation

sensitivity analysis

multicriteria
optimization
strategy

optimization algorithm
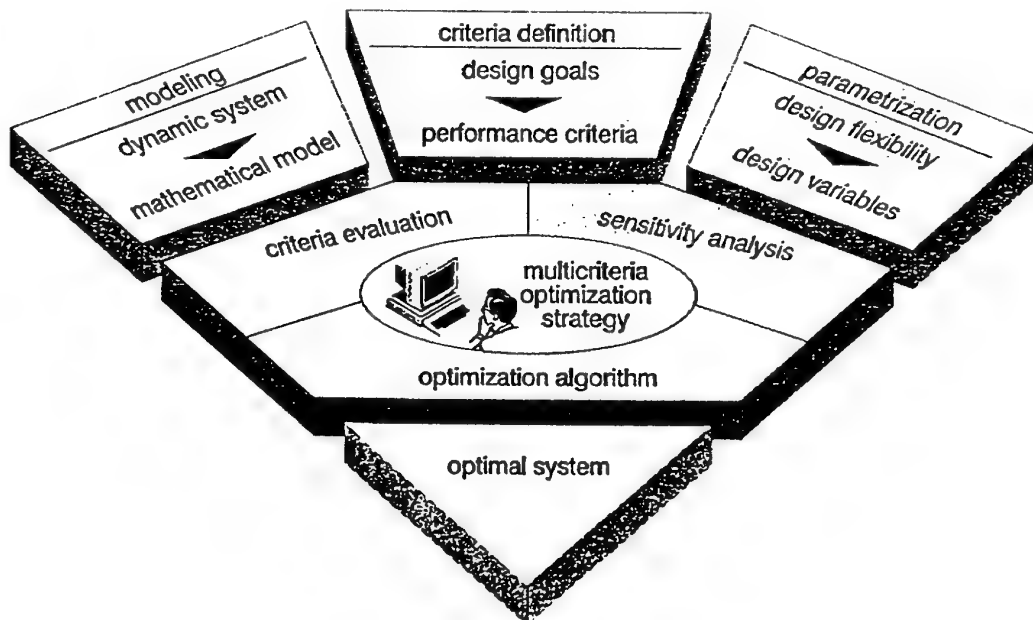
optimal system

Design Process

technical system

⬇ idealizations

mechanical model (MBS, FES)

⬇ principles of mechanics

mathematical model

⬇ design variables and design criteria

$$\text{e.g.} \quad M(t,y,p)\,\ddot{y} + k(t,y,\dot{y},p) = q(t,y,\dot{y},p)$$

multicriterion optimization problem

$$opt\, f(p), \quad NB: \; g(p) = 0$$
$$h(p) \leq 0$$

⬇ scalarization principles

nonlinear programming problem
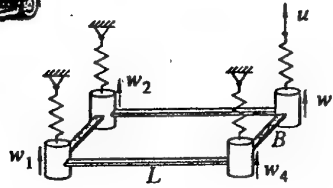
$$min\, f(p), \quad NB: \; g(p) = 0 \qquad \text{or} \qquad \min_{p} f(p)$$
$$h(p) \leq 0$$

⬇ optimization algorithms

constrained optimization problem

unconstrained optimization problem

optimal solution

Multicriterion Optimization vs. Nonlinear Programming

feasible design region: $\quad \mathcal{P} = \left\{ p \in I\!R^h \,\big|\, g(p)=0, \; h(p) \leq 0 \right\}$

single objective: $\quad \min_{p \in \mathcal{P}} f(p)$

multiple objectives: $\quad opt_{p \in \mathcal{P}} \begin{bmatrix} f_1(p) \\ f_2(p) \\ \vdots \end{bmatrix}$
$$\underbrace{\qquad\qquad}_{f(p)}$$

optimal

∇f_1

design space

$\nabla f_2 \qquad \nabla f_1$

design space

$\mathcal{F} = f(\mathcal{P})$

$f(p)$

Edgeworth-Pareto-optima

criterion space
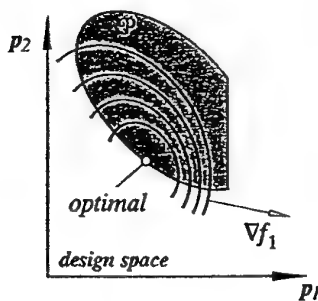
O total order
⇒ all designs comparable
O single optimal solution
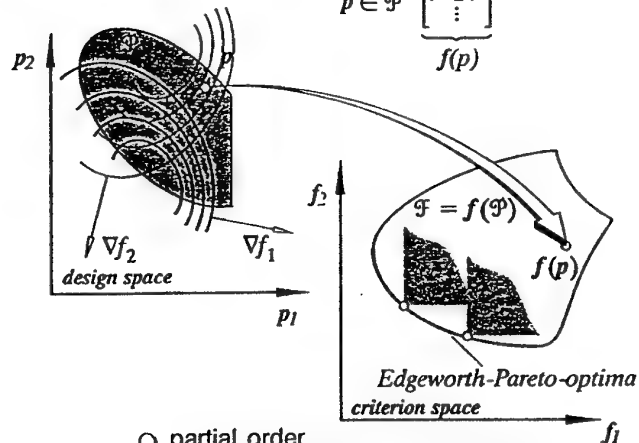
O partial order
⇒ not all designs comparable
O multiple optimal compromise solutions (Edgeworth-Pareto optima)

Case Study: Design of a Tuned Mass Damper

modal analysis of a frame structure

torsion → $a = \dfrac{(w_4 - w_3) - (w_1 - w_2)}{B}$
9.5 Hz

bending 17.3 Hz

short bending 32.8 Hz

inverse bending 28.0 Hz

inverse short bending 43.5 Hz
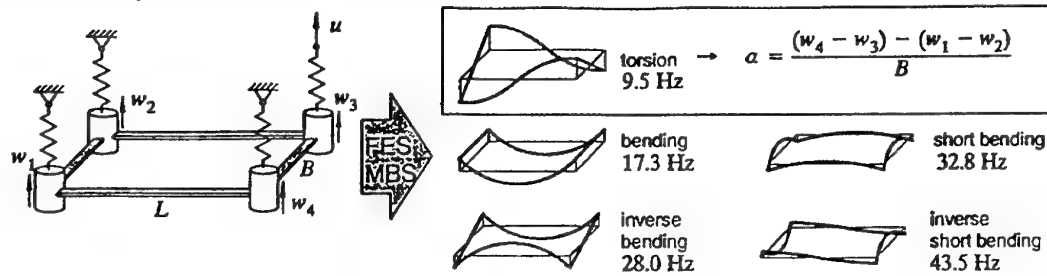
torsional response function for the frame with a passive tuned mass damper attached to it

frame without mass damper

10^1 [rad/m]

$D = 0$
$c = 567$ N/m
$c = 667$ N/m
$c = 767$ N/m
c

10^0

10^{-1}

10^{-2}

7 8 9 10 11 12
excitation frequency [Hz]

$c = 667$ N/m
$D = 0$
$D = 1.5\%$
$D = 3\%$
$D = 6\%$

$D = \dfrac{d}{2\sqrt{cm}}$

8 9 10 11 12
excitation frequency [Hz]

---
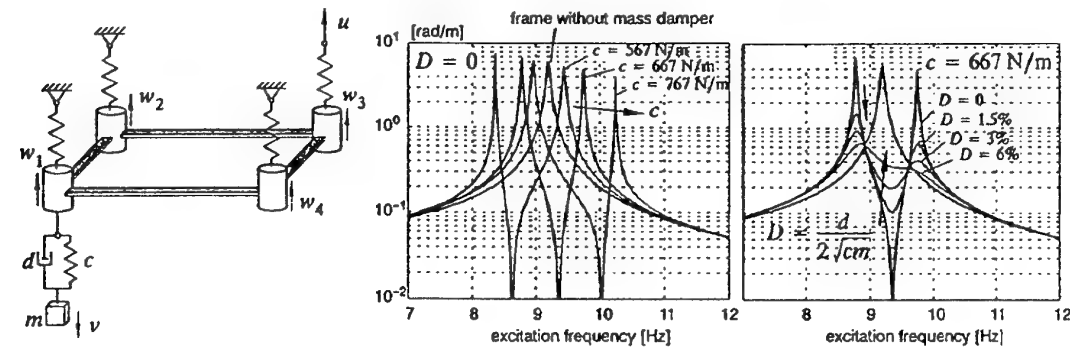
design of an active tuned mass damper for the frame

frame

$u(t)$

α

controlled actuator

v mass

control strategy: feed-back of angle α and angular velocity $\dot{\alpha}$

$$v_{tar} = - K \begin{bmatrix} \alpha \\ \dot{\alpha} \end{bmatrix} = - K_1 \alpha - K_2 \dot{\alpha}$$

ideal:

u → frame + mass → $a, \dot{a}$

$v = v_{tar}$ K

real:

actuator → frame + mass → accelerometers

v_{tar} K $a, \dot{a}$ filter $\ddot{w}_i$
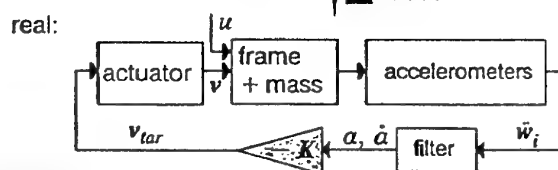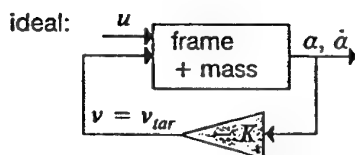
design variables: control gain $K = [K_a, K_{\dot{a}}]$

design criterion 1: $f_1 = \max_{\omega} |G(i\omega)|$ where $G(s) = \dfrac{\mathcal{L}\{a\}}{\mathcal{L}\{u\}} = \dfrac{A(s)}{U(s)}$ torsional vibration

design criterion 2: $f_2 = \max_{\omega} |G_T(i\omega)|$ where $G_T(s) = \dfrac{\mathcal{L}\{v\}}{\mathcal{L}\{u\}} = \dfrac{V(s)}{U(s)}$ mass amplitude

➡ multicriterion optimization problem $\underset{p}{\text{opt}} f(p)$ where $f = \begin{bmatrix} f_1 \\ f_2 \end{bmatrix}$, $p = [K_a, K_{\dot{a}}]^T$

simulation-based design optimization of active tuned mass damper

f_1　　f_2

$K_{\dot{\alpha}}$ [ms/rad]

∇f_2

∇f_1

5

4

3

2

1

K_α [m/rad]

design space

$f(p)$

mass amplitude [m/m]

5

4

3

2

1

torsion [rad/m]
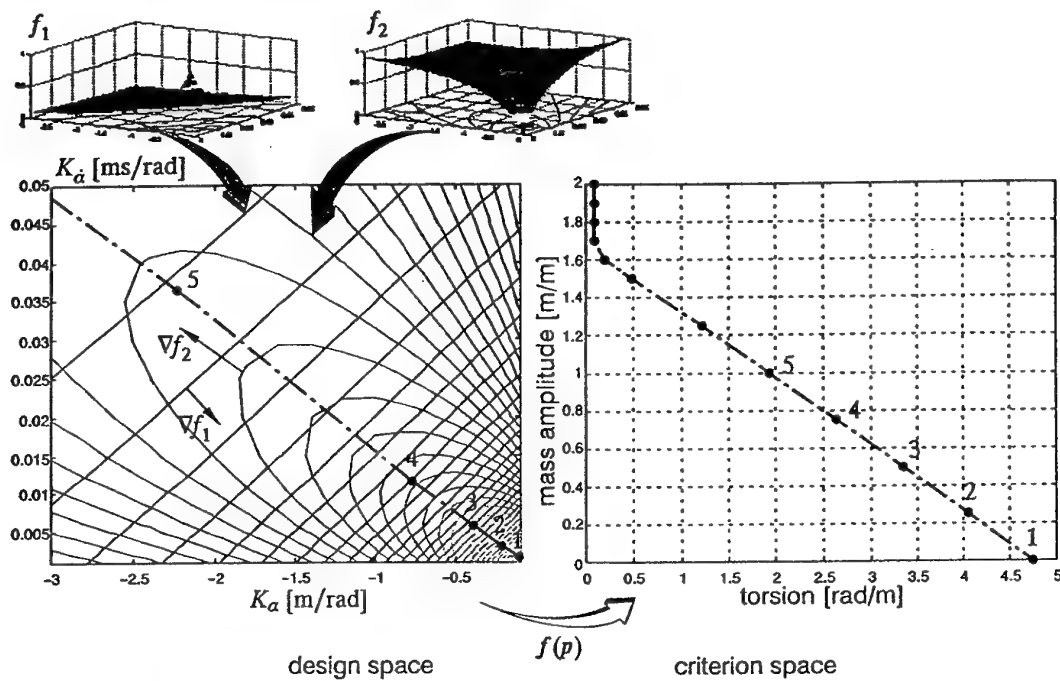
criterion space

Multicriterion Optimization Strategies

multicriterion optimization problem

reduction principle

scalar optimization problem

constraint 1

constraint 2

⋮

constraint m

○ scalarization

scalar utility function

○ hierarchization

1st level　　2nd level

○ combination

objective 1

objective 2

⋮

objective n

scalar optimization algorithm

53

○ scalarization

minimization of a scalar utility function $u(p)$ instead of the vector criterion $f(p)$:

$$\min_{p \in \mathcal{P}} u(p)$$

examples: ○ weighted criteria

$$u(p) := \sum_{i=1}^{n} w_i f_i(p) = w^T f(p), \quad w > 0, \quad \left[\sum_{i=1}^{n} w_i = 1\right]$$

geometrical interpretation
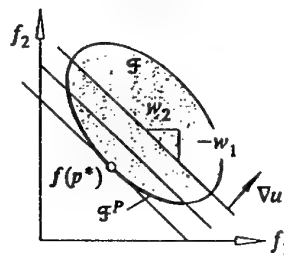
drawback:
not all EP-optimal designs computable
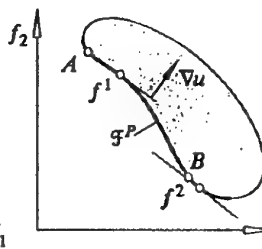
drawback:
highly nonlinear dependence of solution on weights w_i
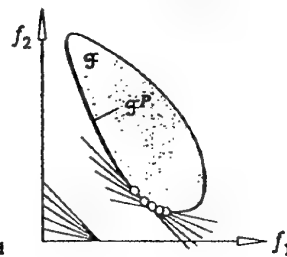
○ distance method

$$u(p) := \left[\sum_{i=1}^{n} |f_i(p) - f_i^0|^r\right]^{1/r}, \quad 1 \le r < \infty \qquad \text{absolute distance}$$

$$u(p) := \left[\sum_{i=1}^{n} \left|\frac{f_i(p) - f_i^0}{f_i^0}\right|^r\right]^{1/r}, \quad 1 \le r < \infty \qquad \text{relative distance}$$

where f^0: $f_i^0 = \min_{p \in \mathcal{P}} f_i(p)$, $i = 1(1)n$ (ideal solution)

$r = 1$

$r = 2$

$r \rightarrow \infty$
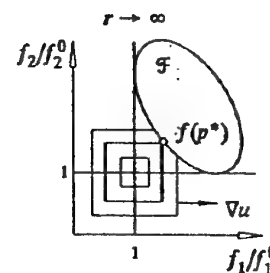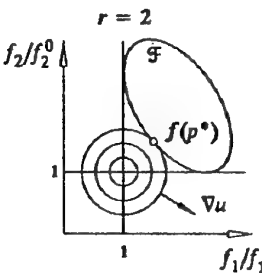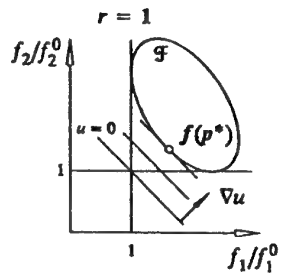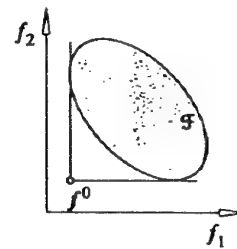
○ hierarchization

lexicographical order by level of importance $l_i \leftrightarrow f_i(p)$ (low number $\hat{=}$ high priority) and successive minimization of the objectives in the given sequence

example: ○ hierarchical optimization with user-defined tolerances $\varepsilon_i \geq 0$

$$
\begin{aligned}
&\text{for } j = 1,2,\dots : \\
&\quad \bar{f}_i = \min_{p \in \mathcal{P}^{j-1}} f_i(p) \quad \text{where} \quad i: l_i = j \\
&\quad \mathcal{P}^j := \{ p \in \mathcal{P}^{j-1} \mid f_i(p) \leq (1+\varepsilon_i)\bar{f}_i \} \\
&\quad \mathcal{P}^0 := \mathcal{P}
\end{aligned}
$$
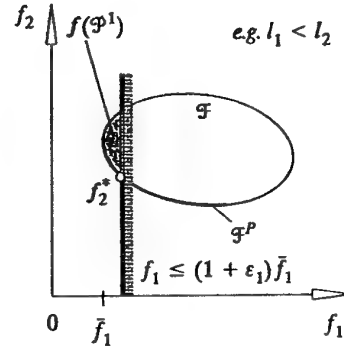
○ combination: scalarization + hierarchization

combination of equally important objectives to a scalar utility function, successive minimization of objectives on different importance levels

example: ○ goal programming with user-defined goals $\hat{f}_i$, priorities l_i and weights w_i, use as inequality constraints in successive optimization steps

$$
\begin{aligned}
&\text{for } j = 1,2,\dots : \\
&\quad u_j(p) := \sum_{i: l_i = j} w_i \left\langle f_i(p) - \hat{f}_i \right\rangle^1, \quad w > 0, \\
&\quad \bar{u}_j = \min_{p \in \mathcal{P}^{j-1}} u_j(p) \\
&\quad \mathcal{P}^j := \{ p \in \mathcal{P}^{j-1} \mid u_j(p) \leq \bar{u}_j \}, \\
&\quad \mathcal{P}^0 := \mathcal{P}
\end{aligned}
$$
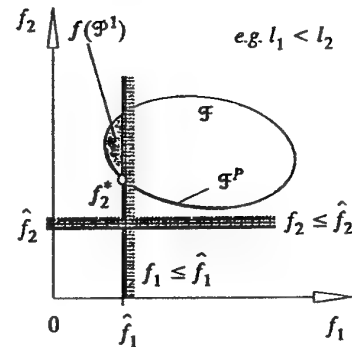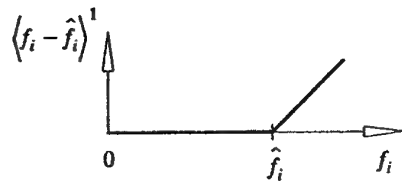
Hardware-in-the-Loop Optimization

offline optimization: optimization of the model

HiL-optimization: design optimization of the dynamic system
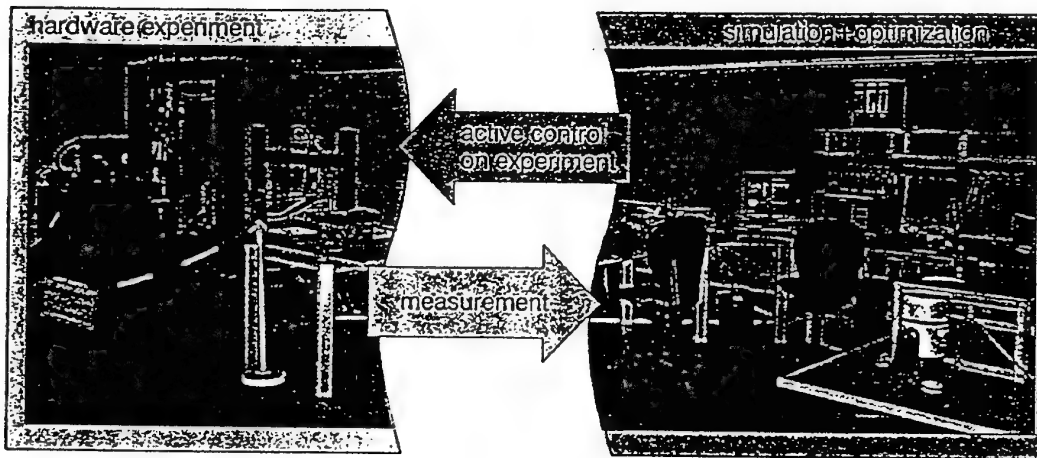
Case Study: HiL-Optimization of Active Tuned Mass Damper

rough criterion estimates
$\Rightarrow$ failure of conventional optimization algorithms

smoothed function and gradient estimates:

Taylor-series: $\psi(p^{(i)} + \Delta p) \approx \psi^{(i)} + \nabla\psi^{(i)T}\Delta p$

⬇ choice: $p_j := \left(p^{(i)} + \Delta p_j\right) \in \Omega^{(i)}, \quad j = 1(1)n \geq h + 1$

linear system
of equations

$$\begin{bmatrix}\psi(p_1)\\ \vdots \\ \psi(p_n)\end{bmatrix} = \begin{bmatrix} 1 & \left(p_1 - p^{(i)}\right)^T \\ \vdots & \vdots \\ 1 & \left(p_n - p^{(i)}\right)^T \end{bmatrix}\begin{bmatrix}\psi^{(i)}\\ \nabla\psi^{(i)}\end{bmatrix}$$

⎣ experiments ● ●

⬇

estimate $\psi^{(i)}, \ \nabla\psi^{(i)}$

⬇ SQP−algorithm

optimization
step   ◇ $\bar{p}^{(i+1)}$

⬇

safety against
instability   ◇ $p^{(i+1)} \in \Sigma^{(i)}$
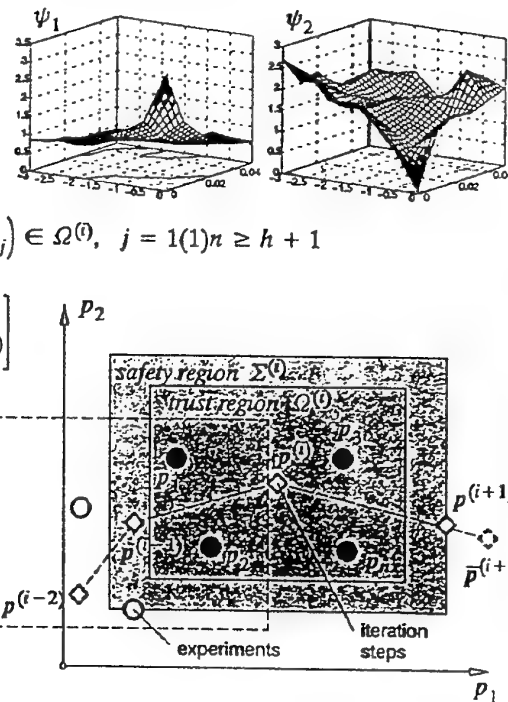
HiL-optimization based on a SQP-algorithm
(≤ 5 experiments/iteration step)

1) $\min\limits_{p} \psi_1(p)$

   where $\psi_2(p) < 1$, $p^{(0)} = 0$

2) $\min\limits_{p} \psi_1(p)$

   where $\psi_2(p) < 1.5$, $p^{(0)} = p_1^P$

$K_{\dot\alpha}$ [ms/rad]

iteration steps

K_α [m/rad]

transfer functions

torsion [rad/m]

without mass damper

$p^{(0)}$

p_1^P

p_2^P

frequency [Hz]

mass amplitude [m/m]

frequency [Hz]
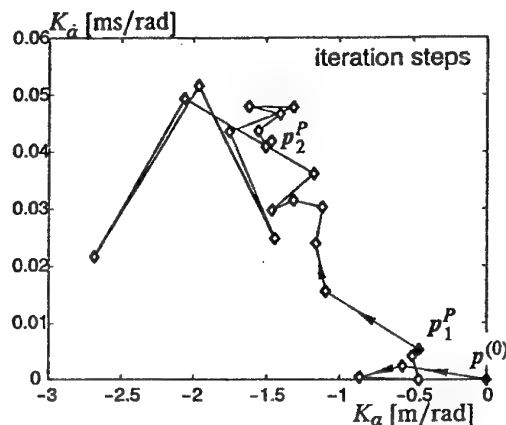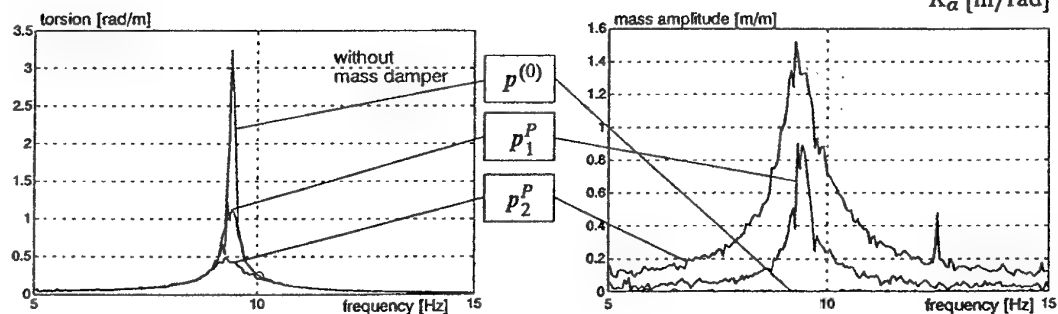
Parameter Identification by Multicriterion Optimization

modeling procedure and sources for differences between model and real system

technical system

⬇ simplification

mechanical model
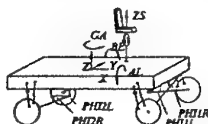
⬇ idealization

mathematical model

⬇ approximation

numerical problem

⬇ finite number precision

numerical solution
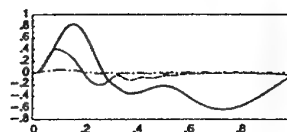
"minimize difference"

Case Study: Identification of a CNC-Machine

CNC / operator panel

controlled axis

amplifier

computer for
real-time simulation

simulation model

CNC — actual position
sensor signals (zero position, boundaries, etc.)
target speed

speed control | current control | voltage modulation | amplifier | synchronous motor

actual electr. current
actual rotational speed

electronics   mechanics
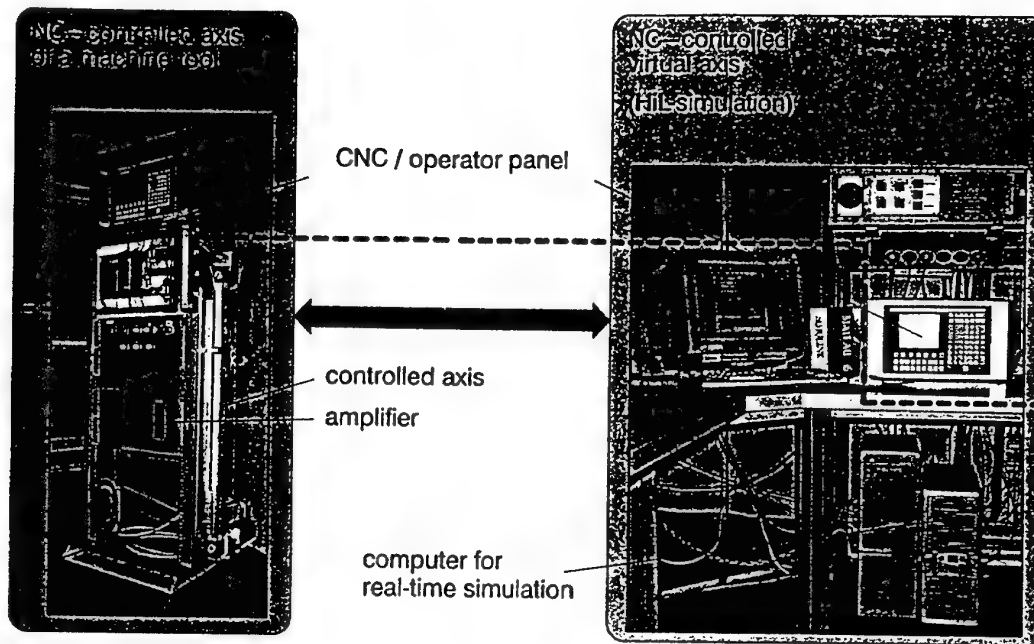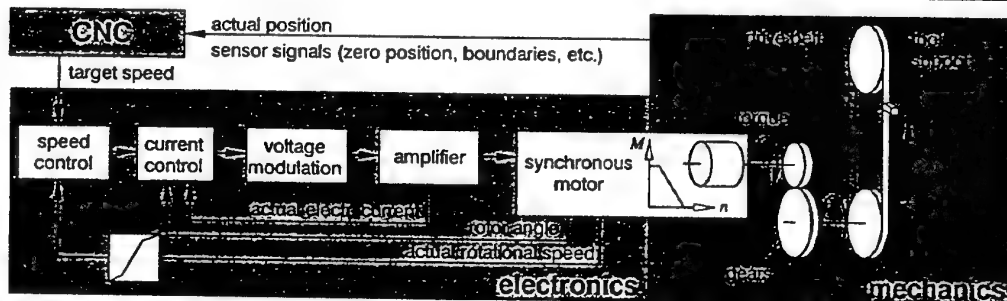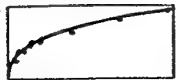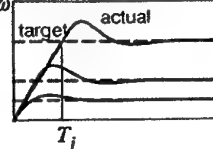
modeling
- topology identification of DOFs
- topology identification of controller
- topology identification of resistance

PI-control with limiter

speed control

partial model 2

motor + mechanical part
$$M_M = K_T i$$
$$I\dot{\omega} = M_M - M_R - M_L(t)$$

$$M_R = c_1 \omega^{c_2}$$

nonlinearity   gain   tachometer
1/1.09   1/39.7

overall model
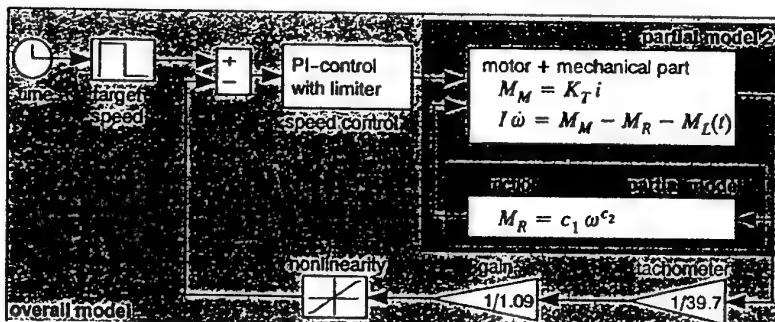
identification parameters

c_1 friction
c_2
I moment of inertia
(motor+gears
+tool support)
P control parameters
T_I
$\hat{i}$ limit for I–control

58

successive identification	design variables	experiment	optimization problem
partial model 1	friction c_1, c_2	stationary motion with different target speeds $M_M \sim i$	$\min \psi_1$ where $\psi_1 = \sum_j \left(M_j - c_1 \omega_j^{c_2} \right)^2$
partial model 2	moment of inertia I	step responses w.r.t. measured current signals for different target speeds	$\min \psi_2$ where $\psi_2 = \sum_j \left(T_{j,\,Mess} - T_{j,\,Sim} \right)^2$
overall model	control parameters P, T_I, $\hat{i}$, c_1, c_2, I	complete speeding-up and breaking maneuvers with different target speeds	$\min \psi_3 \quad \mid \psi_1 \le \bar{\psi}_1,\ \psi_2 \le \bar{\psi}_2$ where $\psi_3 = \sum_j \int_0^T \left(i_{Mess}(t) - i_{Sim}(t) \right)^2 dt$
	fine-tuning P, T_I, $\hat{i}$, c_1, c_2, I	complete speeding-up and breaking maneuvers with different target speeds	$\min \psi_4 \quad \mid \psi_1 \le \bar{\psi}_1,\ \psi_2 \le \bar{\psi}_2,\ \psi_3 \le \bar{\psi}_3$ where $\psi_4 = \sum_j \int_0^T w(t) \left(i_{Mess}(t) - i_{Sim}(t) \right)^2 dt$ $w(t) = e^{-\alpha\,(t-t_S)}$ $w(t) = \dfrac{1}{2\,\Delta t} \displaystyle\int_{t-\Delta t}^{t+\Delta t} \left| \dfrac{di}{dt}(\tau) \right| d\tau$

result

i_{tar} [A]

measurement
simulation

target speed 4134 rpm
target speed 2894 rpm
target speed 1654 rpm
target speed 827 rpm
target speed 413 rpm

t [s]
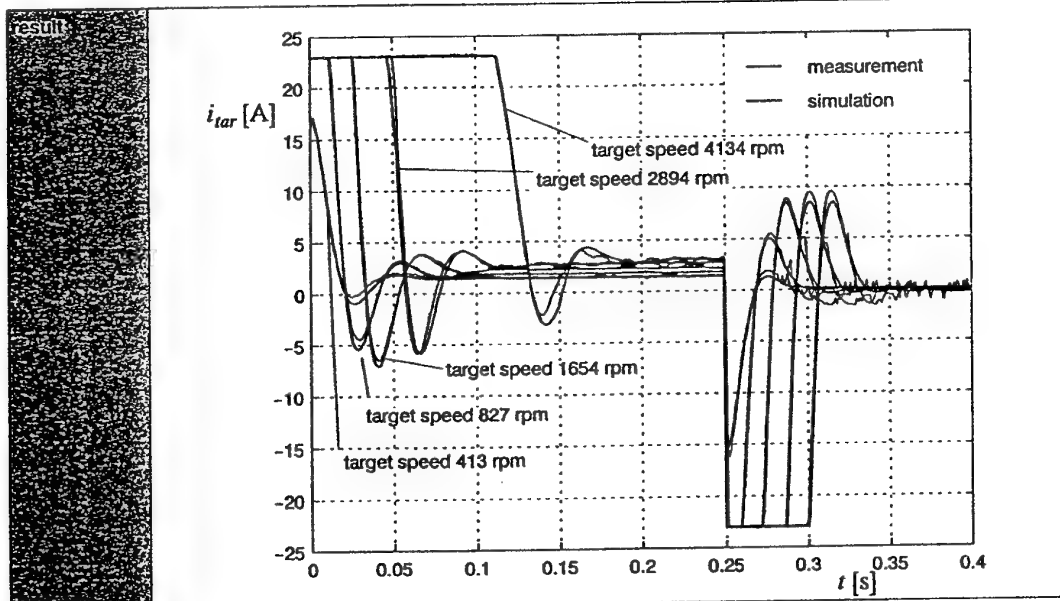
Geometrical Interpretation of Multibody Dynamics: Theory and Implementations

Wojciech BLAJER

Institute of Applied Mechanics, Technical University of Radom
ul. Krasickiego 54, PL-26-600 Radom, Poland; wblajer@poczta.onet.pl

1. Introduction

The purpose of this lecture is to associate multibody dynamics procedures with a geometrical picture involving the concepts of configuration manifolds, linear vector spaces, and projection techniques. An unconstrained system is assigned a free configuration manifold, and is regarded as a generalized particle on the manifold. The system dynamics is then considered in the local tangent space to the manifold at the system representation point. Imposed constraints on the system, the tangent space splits into the velocity restricted and the velocity admissible subspaces, and the configuration confines to the holonomic constraint manifold. Following these geometrical concepts, a uniform treatment of both holonomic and nonholonomic systems can be demonstrated [3,4,10,12,13], which gives an intuitive geometrical insight into the problems solved, and directly appeals to the geometry of constrained particle motion known from Newtonian dynamics. While exploiting the differential geometry formalism, the paper is written in standard matrix notation, well suited for computer implementations.

The projection method leads to compact schemes for obtaining different types of equations of motion and for the determination of constraint reactions [3,4]. Uniform projective formulations and geometrical interpretations of many classical methods of multibody dynamics can also be demonstrated [4,6,12]. The other useful implementations are schemes for elimination of constraint violations [5,17], improvements in the variable partitioning method [8,16] as well as some novel multibody codes such as augmented joint coordinate method [7] and an orthonormalization method [2].

2. Unconstrained system dynamics

Consider an n-degree-of-freedom autonomous system defined in generalized coordinates $\mathbf{p} = [p_1 \ \dots \ p_n]^T$ and velocities $\mathbf{v} = [v_1 \ \dots \ v_n]^T$ (generalized or quasi- velocities), which can be either a collection of unconstrained rigid bodies or a Lagrangian system defined in independent variables. The generic matrix form of the initial governing equations is [3,4,14,15]:

$$\dot{\mathbf{p}} = \mathbf{A}(\mathbf{p})\mathbf{v} \tag{1}$$

$$\mathbf{M}(\mathbf{p})\dot{\mathbf{v}} + \mathbf{d}(\mathbf{p},\mathbf{v}) = \mathbf{f}(\mathbf{p},\mathbf{v},t) \tag{2}$$

where $\mathbf{A}$ is the $n \times n$ transformation matrix, $\mathbf{M}$ is the $n \times n$ symmetric and positive definite generalized mass matrix, $\mathbf{d} = [d_1 \ \dots \ d_n]^T$ represents the centrifugal, Coriolis, and gyroscopic dynamic terms, $\mathbf{f} = [f_1 \ \dots \ f_n]^T$ are the applied forces related to $\mathbf{v}$, and t is the time.

The system can be viewed as a point on the n-dimensional configuration manifold $\mathcal{N}$ of the system. At each position $\mathbf{p} \in \mathcal{N}$, an n-dimensional tangent space to the manifold can
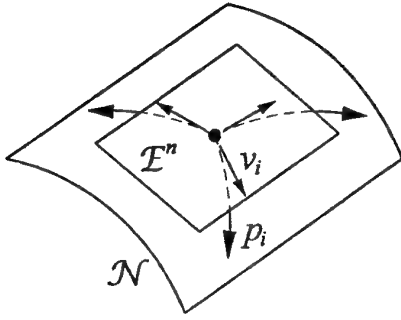
Fig. 1. The $\mathcal{N}$ and $\mathcal{E}^n$ spaces.

then be defined, whose positive-definite quadratic form is expressed by the system kinetic energy $2T = \mathbf{v}^T \mathbf{M} \mathbf{v}$. So endowed with the metric, $\mathcal{N}$ becomes a Riemannian manifold [3,4,10,12,13], and the said local tangent space at $\mathbf{p} \in \mathcal{N}$ is an Euclidean (linear vector) space $\mathcal{E}^n$ (Fig. 1). The generalized mass matrix $\mathbf{M}$ is thus the metric tensor matrix of a basis referred to $\mathbf{v}$, and the dynamic equation (2) can be viewed as a matrix representation of vector formula $\vec{b} = \vec{f}$, where $\mathbf{b} = \mathbf{M}\dot{\mathbf{v}} + \mathbf{d}$ and $\mathbf{f}$ are the generalized dynamic and applied forces, respectively. According to the geometrical interpretation, the kinetic energy T defined above can be seen as doubled dot product of the velocity vector $\vec{v}$ of the system, $2T = \vec{v} \circ \vec{v}$. Seemingly, the Appell's function can be defined as $2S = \vec{b} \circ \vec{b} = \mathbf{b}^T \mathbf{M} \mathbf{b} = (\dot{\mathbf{v}} + \mathbf{M}^{-1}\mathbf{d})^T \mathbf{M} (\dot{\mathbf{v}} + \mathbf{M}^{-1}\mathbf{d})$.

By changing the velocity components from $\mathbf{v}$ to $\mathbf{v}'$, a new basis of $\mathcal{E}^n$ is introduced, and the transformation formula is $\mathbf{v} = \mathbf{B}\mathbf{v}'$, where $\mathbf{B}$ is an $n \times n$ transformation matrix (for $\mathbf{v}' = \dot{\mathbf{p}}$, $\mathbf{B} = \mathbf{A}^{-1}$ as defined in (1)). By premultiplying (2) with $\mathbf{B}^T$, the dynamic equations are projected into the new basis [3,4], and by using $\mathbf{v} = \mathbf{B}\mathbf{v}'$ and $\dot{\mathbf{v}} = \mathbf{B}\dot{\mathbf{v}}' + \dot{\mathbf{B}}\mathbf{v}'$ they can then be expressed in the new velocity components,

$$\mathbf{B}^T[\mathbf{M}(\mathbf{B}\dot{\mathbf{v}}' + \dot{\mathbf{B}}\mathbf{v}') + \mathbf{d} = \mathbf{f}] \quad \Leftrightarrow \quad \mathbf{M}'(\mathbf{p})\dot{\mathbf{v}}' + \mathbf{d}'(\mathbf{p}, \mathbf{v}') = \mathbf{f}'(\mathbf{p}, \mathbf{v}', t) \tag{3}$$

where $\mathbf{M}' = \mathbf{B}^T \mathbf{M} \mathbf{B}$, $\mathbf{d}' = \mathbf{B}^T(\mathbf{M}\dot{\mathbf{B}}\mathbf{v}' + \mathbf{d})$ and $\mathbf{f}' = \mathbf{B}^T \mathbf{f}$ have the same meaning as in (2). This geometrically grounded projection technique constitutes a way for transformation of the governing equations between different sets of coordinates and velocity components. The method can be extended/generalized for constrained systems as well.

3. Geometry of constrained system dynamics

Let the system described in (1) and (2) be subjected to m_h holonomic and m_{nh} nonholonomic constraints, $m = m_h + m_{nh}$, all scleronomic for simplicity (for rheonomic constraints the reader is referred to e.g. [3,4]). The constraint equations, given implicitly, are:

$$\begin{cases} \Phi(\mathbf{p}) = 0 & \text{(4a)} \\ \mathbf{C}_{nh}(\mathbf{p})\mathbf{v} = 0 & \text{(4b)} \end{cases}$$

The holonomic constraints (4a) define a k-dimensional submanifold $\mathcal{K}$ in $\mathcal{N}$, $k = n - m_h$, and the constrained system configuration is confined to $\mathcal{K}$ on which k independent curvilinear coordinates $\mathbf{q} = [q_1 \ \dots \ q_k]^T$ can be defined. By differentiating with respect to time the holonomic constraints one obtains $\dot{\Phi} = \mathbf{C}_h(\mathbf{p})\mathbf{v} = 0$, where $\mathbf{C}_h = (\partial \Phi / \partial \mathbf{p})\mathbf{A}$. The uniform constraint equations at the velocity and acceleration levels are then

$$\Psi = \mathbf{C}(\mathbf{p})\mathbf{v} = 0 \tag{5}$$

$$\dot{\Psi} = \mathbf{C}(\mathbf{p})\dot{\mathbf{v}} - \xi(\mathbf{p}, \mathbf{v}) = 0 \tag{6}$$

where $\mathbf{C} = [\mathbf{C}_h^T \ \mathbf{C}_{nh}^T]^T$ is the $m \times n$ constraint matrix, and $\xi = -\dot{\mathbf{C}}\mathbf{v}$ is the m-vector of constraint induced accelerations (see Figure 2 for the geometrical interpretation).

The m constraint vectors, represented in $\mathbf{C}$ as rows, span an m-dimensional *constrained subspace* C^m in $\mathcal{E}^n$. According to (5) the projection of the system velocity $\vec{v}$ into C^m

61

vanishes (Fig. 2a), i.e. $\bar{v}$ is sunk in the *unconstrained subspace* $\mathcal{D}^r$, which complements C^m in $\mathcal{E}^n$, $\mathcal{D}^r \cup C^m = \mathcal{E}^n$ and $\mathcal{D}^r \cap C^m = 0$. For the considered case of systems with scleronomic constraints, C^m and $\mathcal{D}^r$ are then velocity restricted and velocity admissible subspaces, respectively. The subspace $\mathcal{D}^r$ can be defined by $r = n - m$ vectors represented as columns of an $n \times r$ matrix $\mathbf{D}$ which satisfies the condition

$$\mathbf{C}\mathbf{D} = 0 \qquad \Leftrightarrow \qquad \mathbf{D}^T\mathbf{C}^T = 0 \tag{7}$$

i.e. $\mathbf{D}$ is an orthogonal complement matrix to the constraint matrix $\mathbf{C}$ [3,4,12,15].
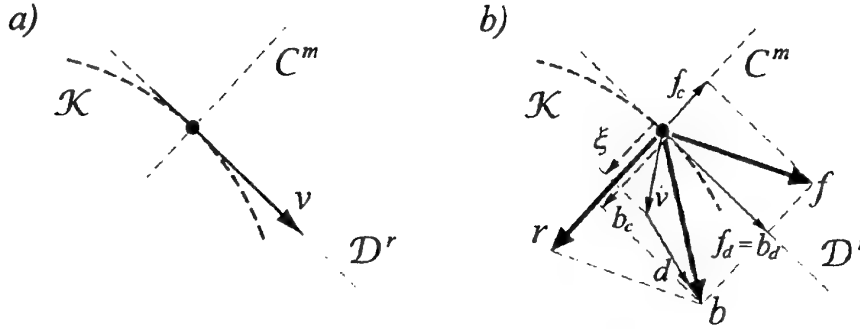
Fig. 2. The geometry of constrained system dynamics.

The reactions of *ideal* constraints are by assumption collinear with the constraint vectors, and are represented in C^m by m unknown Lagrange multipliers $\lambda = [\lambda_1 \ ... \ \lambda_m]^T$. The representation of the generalized constraint reaction force $\bar{r}$ in $\mathcal{E}^n$ is $\mathbf{r} = -\mathbf{C}^T\lambda$ [3,4,10,14,15], and the dynamic equations of the constrained system are

$$\mathbf{M}(\mathbf{p})\dot{\mathbf{v}} + \mathbf{d}(\mathbf{p},\mathbf{v}) = \mathbf{f}(\mathbf{p},\mathbf{v},t) - \mathbf{C}^T(\mathbf{p})\lambda \tag{8}$$

often referred to as Lagrange's equations of type one. The vector form of (8) is $\bar{b} = \bar{f} + \bar{r}$ (Fig. 2b). By assuming that the constraints (4) express the prohibited relative translations/rotations and the vanishing relative translational/rotational velocities in the joints, the components of λ are respective physical forces/torques.

The governing equations of the constrained system are the following $2n + m$ differential-algebraic equations (DAEs) in $2n$ differential variables $\mathbf{p}$ and $\mathbf{v}$, and m algebraic variables λ

$$\dot{\mathbf{p}} = \mathbf{A}\mathbf{v} \qquad\qquad\qquad \dot{\mathbf{p}} = \mathbf{A}(\mathbf{p})\mathbf{v} \tag{9a}$$

$$\begin{bmatrix} \mathbf{M} & \mathbf{C}^T \\ \mathbf{C} & 0 \end{bmatrix}\begin{bmatrix} \dot{\mathbf{v}} \\ \lambda \end{bmatrix} = \begin{bmatrix} \mathbf{f} - \mathbf{d} \\ \xi \end{bmatrix} \qquad \Leftrightarrow \qquad \mathbf{H}(\mathbf{p})\begin{bmatrix} \dot{\mathbf{v}} \\ \lambda \end{bmatrix} = \mathbf{h}(\mathbf{p},\mathbf{v},t) \tag{9b}$$

and the initial values of the state variables must satisfy the lower-order constraint equations (4a) and (5), $\Phi(\mathbf{p}_0) = 0$ and $\Psi(\mathbf{p}_0,\mathbf{v}_0) = 0$. Since the leading matrix $\mathbf{H}$ in (9b) is invertible if only $\det(\mathbf{C}\mathbf{M}^{-1}\mathbf{C}^T) \neq 0$ [4], standard ODE (ordinary differential equation) methods can be used to solve DAEs (9) for $\mathbf{p}(t)$ and $\mathbf{v}(t)$, and simultaneously $\lambda(t)$ can be determined using the current state variables.

4. Constraint-referred projection formulation

The formula (3) describes a projection of the dynamic equations (2) from a basis referred to $\mathbf{v}$ into a basis referred to $\mathbf{v}'$. In the case of a constrained system a similar projection of the dynamic constraint reaction-affected equations (8) can be performed with respect to the con-

62

strained and unconstrained directions, which is achieved by premultiplying (8) with $[\mathbf{D}^T \ (\mathbf{CM}^{-1})^T]^T$. The premultiplication stands for the projection of (8) from $\mathcal{E}^n$ (basis referred to v) into $\mathcal{D}^r$ and C^m, respectively, and yields:

$$\begin{bmatrix} \mathbf{D}^T \\ \mathbf{CM}^{-1} \end{bmatrix} (\mathbf{M}\dot{\mathbf{v}} + \mathbf{d} = \mathbf{f} - \mathbf{C}^T\lambda) \quad \begin{array}{l} \Rightarrow \quad \mathbf{D}^T\mathbf{M}\dot{\mathbf{v}} + \mathbf{D}^T\mathbf{d} = \mathbf{D}^T\mathbf{f} \quad\quad\quad\quad (10a) \\ \Rightarrow \quad \mathbf{C}\dot{\mathbf{v}} + \mathbf{CM}^{-1}\mathbf{d} = \mathbf{CM}^{-1}\mathbf{f} - \mathbf{CM}^{-1}\mathbf{C}^T\lambda \quad (10b) \end{array}$$

The geometric interpretation of (10a) and (10b) is $\vec{b}_d = \vec{f}_d$ and $\vec{b}_c = \vec{f}_c + \vec{r}$, respectively (Fig. 2b). Using the tangential projection (10a), $2n$ ODEs in p and v can be defined

$$\dot{\mathbf{p}} = \mathbf{A}\,\mathbf{v}$$
$$\begin{bmatrix} \mathbf{D}^T\mathbf{M} \\ \mathbf{C} \end{bmatrix} \dot{\mathbf{v}} = \begin{bmatrix} \mathbf{D}^T(\mathbf{f}-\mathbf{d}) \\ \xi \end{bmatrix} \quad \Leftrightarrow \quad \begin{array}{ll} \dot{\mathbf{p}} = \mathbf{A}(\mathbf{p})\,\mathbf{v} & (11a) \\ \mathbf{S}(\mathbf{p})\,\dot{\mathbf{v}} = \mathbf{s}(\mathbf{p},\mathbf{v},t) & (11b) \end{array}$$

The orthogonal projection provides then an algebraic equation for the determination of λ

$$\lambda(\mathbf{p},\mathbf{v},t) = (\mathbf{CM}^{-1}\mathbf{C}^T)^{-1}[\mathbf{CM}^{-1}(\mathbf{f}-\mathbf{d}) - \xi] \tag{12}$$

The dependent variable formulations (9) and (11) involve the second-order differential constraint equations (6). Thus, the exact realization of only these constraint equations is assured by assumption. The lower-order constraint equations (4a) and (5) may be violated by the numerical solutions $\widetilde{\mathbf{p}}(t)$ and $\widetilde{\mathbf{v}}(t)$ burdened with the numerical error of integration, $\widetilde{\Phi} = \Phi(\widetilde{\mathbf{p}}) \neq 0$ and $\widetilde{\Psi} = \Psi(\widetilde{\mathbf{p}},\widetilde{\mathbf{v}}) \neq 0$. The situation differs when independent state variables are used. Most of the independent variable formulations can conveniently be interpreted geometrically and assisted with the projection technique.

5. Geometrical/projective interpretations of some relevant independent variable formulations

5.1. Joint coordinate formulation for open-loop holonomic systems

Let us assume for a while that the system described in (1) and (2) is an open-loop (tree structure) holonomic system, and p and v are the absolute variables that describe the system position and velocity with respect to a global non-moving reference system. The constraints on the bodies due to the kinematical joints are then all holonomic, $m = m_h$ and $m_{nh} = 0$ in (4). By choosing $k = n - m_h$ independent coordinates $\mathbf{q} = [q_1 \ \dots \ q_k]^T$ to describe the relative configurations of the adjacent bodies, the holonomic constraint equations, given implicitly in (4a) by $\Phi(\mathbf{p}) = \mathbf{0}$, can also be expressed explicitly as

$$\mathbf{p} = \mathbf{g}(\mathbf{q}) \tag{13}$$

and by assumption the holonomic constraints are satisfied identically when substituting (13), $\Phi(\mathbf{g}(\mathbf{q})) \equiv \mathbf{0}$. By differentiating (13) with respect to time one receives:

$$\mathbf{v} = \mathbf{D}(\mathbf{q})\dot{\mathbf{q}} \tag{14}$$
$$\dot{\mathbf{v}} = \mathbf{D}(\mathbf{q})\ddot{\mathbf{q}} + \gamma(\mathbf{q},\dot{\mathbf{q}}) \tag{15}$$

where $\mathbf{D} = \mathbf{A}^{-1}(\partial\mathbf{g}/\partial\mathbf{q})$ and $\gamma = \dot{\mathbf{D}}\dot{\mathbf{q}}$ are of dimensions $n \times k$ and $n \times 1$, respectively. From substitution of (14) and (15) into (5) and (6) it follows that $\mathbf{D}$ defined above satisfies the conditions (7), i.e. it is an orthogonal complement matrix to $\mathbf{C}$ (now $\mathbf{C} = \mathbf{C}_h$), and then $\mathbf{C}\gamma = \xi$.

By applying the explicit forms (13) – (15) of holonomic constraints to the projective scheme described in Section 4, from the tangential projection (10a) one obtains

63

$$\mathbf{D}^T\mathbf{M}\,(\mathbf{D}\,\ddot{\mathbf{q}}+\gamma)+\mathbf{D}^T\mathbf{d}=\mathbf{D}^T\mathbf{f} \quad\Leftrightarrow\quad \overline{\mathbf{M}}(\mathbf{q})\ddot{\mathbf{q}}+\overline{\mathbf{d}}(\mathbf{q},\dot{\mathbf{q}})=\overline{\mathbf{f}}(\mathbf{q},\dot{\mathbf{q}},t) \tag{16}$$

where $\overline{\mathbf{M}}=\mathbf{D}^T\mathbf{M}\mathbf{D}$ is the $k\times k$ generalized mass matrix, $\overline{\mathbf{d}}=\mathbf{D}^T(\mathbf{M}\gamma+\mathbf{d})$ is the k vector that includes generalized centrifugal, Coriolis and gyroscopic terms, and $\overline{\mathbf{f}}=\mathbf{D}^T\mathbf{f}$ is the k vector of generalized applied forces, all related to $\mathbf{q}$. The same result can be obtained by using different methods, see e.g. [4,9-15]. The formula (12) for determination of constraint reactions can then be expressed symbolically as $\lambda(\mathbf{q},\dot{\mathbf{q}},t)$ or reformulated $(\mathbf{C}\gamma=\xi)$ to

$$\lambda(\mathbf{q},\dot{\mathbf{q}},t)=(\mathbf{C}\mathbf{M}^{-1}\mathbf{C}^T)^{-1}\mathbf{C}\,[\mathbf{M}^{-1}(\mathbf{f}-\mathbf{d})-\gamma] \tag{17}$$

The scheme as above can also be treated as a general code for holonomic systems for transforming the dynamic equations formulated in dependent variables $\mathbf{p}$ and $\mathbf{v}$ into a smaller set of equations in independent coordinates $\mathbf{q}$. However, the explicit form (13) of constraint equations at position level is not always attainable in practice (e.g. for closed-loop systems).

5.2. Velocity partitioning formulation

The approach is usually referenced to as *coordinate partitioning method* [16]. It is based on formulating the explicit constraint equations directly at the velocity and acceleration levels, in the form similar to (14) and (15). In a general sense of formulation of this paper it is thus rather a *velocity partitioning method* [4].

If $\text{rank}(\mathbf{C})=m=\max$, the implicit-form constraint equations (14) and (15) can always be resolved for some m dependent velocities/accelerations $\mathbf{w}/\dot{\mathbf{w}}$ in terms of the remaining r *independent* ones $\mathbf{u}/\dot{\mathbf{u}}$. The partition can be set symbolically as $\mathbf{v}=[\mathbf{u}^T\ \mathbf{w}^T]^T$, which yields appropriate factorization of the constraint matrix $\mathbf{C}=[\mathbf{U}\ \mathbf{W}]$, where $\mathbf{U}$ and $\mathbf{W}$ are the $m\times r$ and $m\times m$ matrices, respectively, and $\det(\mathbf{W})\neq 0$ is assumed. By applying the partition to (14) and (15), the explicit forms of the velocity and acceleration constraints can be obtained:

$$\mathbf{C}\mathbf{v}\equiv\mathbf{U}\mathbf{u}+\mathbf{W}\mathbf{w}=\mathbf{0}\quad\Rightarrow\quad \mathbf{v}=\begin{bmatrix}\mathbf{I}\\-\mathbf{W}^{-1}\mathbf{U}\end{bmatrix}\mathbf{u}\equiv\mathbf{D}(\mathbf{p})\mathbf{u} \tag{18}$$

$$\mathbf{C}\dot{\mathbf{v}}+\xi\equiv\mathbf{U}\dot{\mathbf{u}}+\mathbf{W}\dot{\mathbf{w}}+\xi=\mathbf{0}\quad\Rightarrow\quad \dot{\mathbf{v}}=\begin{bmatrix}\mathbf{I}\\-\mathbf{W}^{-1}\mathbf{U}\end{bmatrix}\dot{\mathbf{u}}+\begin{bmatrix}\mathbf{0}\\-\mathbf{W}^{-1}\xi\end{bmatrix}\equiv\mathbf{D}(\mathbf{q})\dot{\mathbf{u}}+\gamma(\mathbf{p},\mathbf{u}) \tag{19}$$

where $\mathbf{I}$ and $\mathbf{0}$ are the identity and null matrices of dimensions $r\times r$ and $r\times 1$, respectively. It is easy to check that the $n\times r$ matrix $\mathbf{D}$ is an orthogonal complement matrix to $\mathbf{C}$, $\mathbf{D}^T\mathbf{C}^T=\mathbf{0}$. The relations (18) and (19) stand thus for the explicit forms of the constraints at the velocity and acceleration levels, and correspond to (14) and (15). In order to avoid possible singularities when $\det(\mathbf{W})\to 0$, variant formulations for different coordinate partitions can be prepared in advance to change between them when necessary. A projective criterion for best (optimal) coordinate partitioning was proposed in [8].

With the use of (18) and (19) and the projection technique, the governing equations of a constrained system can be transformed to $n+r$ ODEs whose symbolic form is:

$$\dot{\mathbf{p}}=\overline{\mathbf{A}}(\mathbf{p})\mathbf{u} \tag{20a}$$

$$\overline{\mathbf{M}}(\mathbf{p})\dot{\mathbf{u}}+\overline{\mathbf{d}}(\mathbf{p},\mathbf{u})=\overline{\mathbf{f}}(\mathbf{p},\mathbf{u},t) \tag{20b}$$

where $\overline{\mathbf{A}}=\mathbf{A}\mathbf{D}$, and $\overline{\mathbf{M}}$, $\overline{\mathbf{d}}$ and $\overline{\mathbf{f}}$ are as defined in (16). The constraint reactions can then be obtained from either (12) or (17), which can both be represented symbolically as $\lambda(\mathbf{p},\mathbf{u},t)$. The velocity partitioning method provides one with a general and useful code for ODE formulations of closed-loop holonomic systems and nonholonomic systems [4,10,13].

5.3. The minimal-form formulation for closed-loop systems
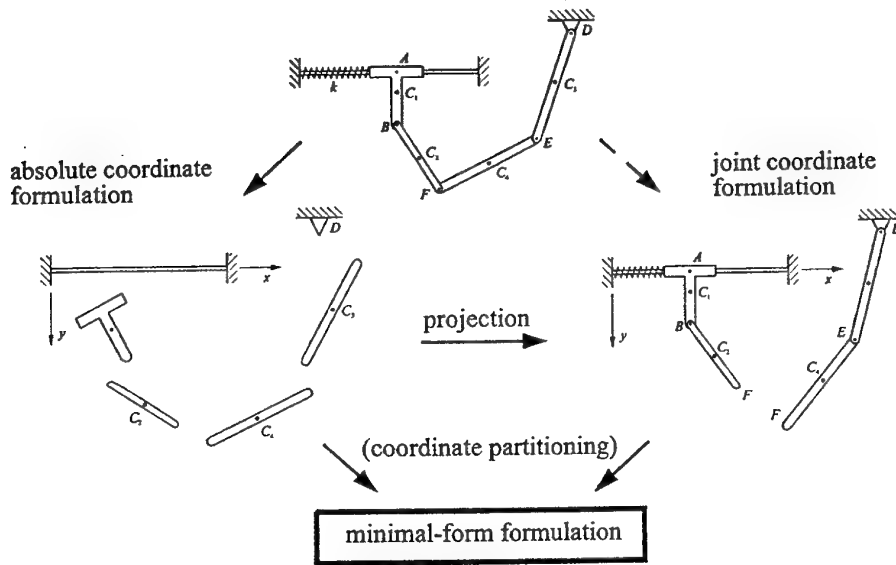
Fig. 3. Treatment of closed-loop systems.

A multibody system may contain one ore more closed kinematic loops. There are two basic treatments of such systems (Fig. 3): in absolute coordinates $\mathbf{p}$, when all the joints in the system are "opened", and in joint coordinates $\mathbf{q}$ of an equivalent open-loop system obtained after cutting each closed loop at one of the kinematic joints. Both $\mathbf{p}$ and $\mathbf{q}$ are dependent. In each case the arising initial governing equations are then DAEs, and can afterwards be transformed to ODEs by using the coordinate partitioning method.

The DAE and ODE formulations in $\mathbf{p}$ have already been described and are, respectively, $2n+m$ DAEs (9) and $n+r$ ODEs (20). The formulations in $\mathbf{q}$ require first to formulate the dynamic equations (16) for the equivalent open-loop system, $\overline{\mathbf{M}}(\mathbf{q})\ddot{\mathbf{q}} + \overline{\mathbf{d}}(\mathbf{q},\dot{\mathbf{q}}) = \overline{\mathbf{f}}(\mathbf{q},\dot{\mathbf{q}},t)$. Imposed the remaining $l = m - r$ closing constraints on the system, $\overline{\Phi}(\mathbf{q}) = 0$, the following $2k+l$ DAEs in $\mathbf{q}$, $\dot{\mathbf{q}} = \overline{\mathbf{v}}$ and $\overline{\lambda}$ arise, which correspond to (9):

$$\dot{\mathbf{q}} = \overline{\mathbf{v}} \qquad\qquad \dot{\mathbf{q}} = \overline{\mathbf{v}} \qquad\qquad (21a)$$

$$\begin{bmatrix} \overline{\mathbf{M}} & \overline{\mathbf{C}}^T \\ \overline{\mathbf{C}} & 0 \end{bmatrix} \begin{bmatrix} \dot{\overline{\mathbf{v}}} \\ \overline{\lambda} \end{bmatrix} = \begin{bmatrix} \overline{\mathbf{f}} - \overline{\mathbf{d}} \\ \overline{\xi} \end{bmatrix} \qquad \Leftrightarrow \qquad \overline{\mathbf{H}}(\mathbf{q}) \begin{bmatrix} \dot{\overline{\mathbf{v}}} \\ \overline{\lambda} \end{bmatrix} = \overline{\mathbf{h}}(\mathbf{q},\overline{\mathbf{v}},t) \qquad (21b)$$

where $\overline{\mathbf{C}} = \partial\overline{\Phi}/\partial\mathbf{q}$ is of dimension $l \times k$, $\overline{\xi} = -\dot{\overline{\mathbf{C}}}\dot{\mathbf{q}}$, and $\overline{\lambda} = [\overline{\lambda}_1 \ \dots \ \lambda_l]^T$ are the closing constraint reactions. The DAEs can then be solved for $\mathbf{q}(t)$, $\dot{\mathbf{q}}(t)$ and $\overline{\lambda}(t)$.

Using the coordinate partitioning method described in Section 5.2, used for $\overline{\Phi}(\mathbf{q}) = 0$ and $\dot{\mathbf{q}} = [\mathbf{u}^T \ \mathbf{w}^T]^T$, to produce $\dot{\mathbf{q}} = \overline{\mathbf{D}}(\mathbf{q})\mathbf{u}$ and $\ddot{\mathbf{q}} = \overline{\mathbf{D}}(\mathbf{q})\dot{\mathbf{u}} + \gamma(\mathbf{q},\mathbf{u})$ as described in (18) and (19), $k+r$ ODEs in $\mathbf{q}$ and $\mathbf{u}$ can be obtained,

$$\dot{\mathbf{q}} = \overline{\mathbf{D}}(\mathbf{q})\mathbf{u} \qquad\qquad (22a)$$

$$\overline{\overline{\mathbf{M}}}(\mathbf{q})\dot{\mathbf{u}} + \overline{\overline{\mathbf{d}}}(\mathbf{q},\mathbf{u}) = \overline{\overline{\mathbf{f}}}(\mathbf{q},\mathbf{u},t) \qquad\qquad (22b)$$

where $\overline{\overline{\mathbf{M}}} = \overline{\mathbf{D}}^T \overline{\mathbf{M}}\,\overline{\mathbf{D}}$, $\overline{\overline{\mathbf{d}}} = \overline{\mathbf{D}}^T(\overline{\mathbf{M}}\overline{\gamma} + \overline{\mathbf{d}})$, and $\overline{\overline{\mathbf{f}}} = \overline{\mathbf{D}}^T\overline{\mathbf{f}}$ The above ODEs can be considered as the minimal-form formulation for closed-loop systems.

65

5.4. Treatment of nonholonomic systems

In Section 3 a uniform treatment of holonomic and nonholonomic systems, respectively $m_{nh} = 0$ or $m_{nh} > 0$, is provided using dependent (possible absolute) variables $\mathbf{p}$ and $\mathbf{v}$. Using the projection method, the initial DAEs (9) can then be transformed to ODEs (20), and the transformation is based on the relations between the dependent and independent velocities and accelerations, $\mathbf{v} = \mathbf{D(p)u}$ and $\dot{\mathbf{v}} = \mathbf{D(p)}\dot{\mathbf{u}} + \mathbf{\gamma(p,u)}$. In general, these explicit forms of constraint equations, given implicitly in (5) and (6), can be determined by any method – by guess, inspection or, more usual, numerically [14,15], and the components of u may be either generalized velocities or quasi-velocities [3,4,10]. One effective techniques of the latter type is the velocity partitioning method described in Section 5.2, and another example can be a code based on Gram-Schmidt orthogonalization scheme described in [2].

In DAEs (9) and ODEs (20) the holonomic and nonholonomic constraints (4) are treated in a unified way, and the dependent coordinates $\mathbf{p}$ are used. The other possibility is first to "eliminate" the holonomic constraints (4a) and obtain the dynamic equations (16) in independent coordinates $\mathbf{q}$, followed the scheme provided in Section 5.1. The system described with these equations will then be subjected to only nonholonomic constraints (4b), expressed in the new variables by $\overline{\mathbf{C}}_{nh}(\mathbf{q})\,\dot{\mathbf{q}} = \mathbf{0}$. The followed governing DAEs are then as in (21), and further application of the projection method (and possibly the velocity partition scheme) will lead to the minimal-form ODEs (22) in the independent variables $\mathbf{q}$ and $\mathbf{u}$.

5.5. Gibbs'-Appell's equations

The Gibbs'-Appell's method provides one with another general approach to holonomic and nonholonomic systems [4,9]. According to the geometrical interpretation of Section 2, the Appell's function, after using $\mathbf{v} = \mathbf{D u}$ and $\dot{\mathbf{v}} = \mathbf{D}\dot{\mathbf{u}} + \mathbf{\gamma}$, can equivalently be written as

$$2S = (\dot{\mathbf{v}} + \mathbf{M}^{-1}\mathbf{d})^T \mathbf{M}\,(\dot{\mathbf{v}} + \mathbf{M}^{-1}\mathbf{d}) = (\mathbf{D}\dot{\mathbf{u}} + \mathbf{\gamma} + \mathbf{M}^{-1}\mathbf{d})^T \mathbf{M}\,(\mathbf{D}\dot{\mathbf{u}} + \mathbf{\gamma} + \mathbf{M}^{-1}\mathbf{d}) \qquad (23)$$

Applying S to Gibbs'-Appell's equations [9], which expressed respectively in $\mathbf{v}$ and $\mathbf{u}$ are:

$$\left(\frac{\partial S}{\partial \dot{\mathbf{v}}}\right)^T = \mathbf{f} \qquad \text{and} \qquad \left(\frac{\partial S}{\partial \dot{\mathbf{u}}}\right)^T = \bar{\mathbf{f}} \qquad (24)$$

where $\bar{\mathbf{f}} = \mathbf{D}^T\mathbf{f}$, and $(\partial S/\partial\dot{\mathbf{u}}) = \mathbf{D}^T(\partial S/\partial\dot{\mathbf{v}})$, one receives directly

$$\mathbf{M}\dot{\mathbf{v}} + \mathbf{d} = \mathbf{f} \qquad \text{and} \qquad \mathbf{D}^T\mathbf{M}(\mathbf{D}\dot{\mathbf{u}} + \mathbf{\gamma} + \mathbf{M}^{-1}\mathbf{d}) = \mathbf{D}^T\mathbf{f} \qquad (25)$$

which are equivalent to (2) and (20), respectively. The matrix setting of Gibbs'-Appell's is thus equivalent to the projective formulation.

5.6. Kane's method

Kane's formalism [11] can also been interpreted geometrically [12] as the projection of the initial dynamic equations (2) (Newton-Euler equations) into the unconstrained subspace. More specifically, the generalized active $\mathbf{K}$ and inertia $\mathbf{K}^{\bullet}$ forces, which constitute Kane's equations, can be interpreted, using the notation of this paper, as follows

$$\bar{\mathbf{f}}_d - \bar{\mathbf{b}}_d = \mathbf{0} \quad \Leftrightarrow \quad \mathbf{K} + \mathbf{K}^{\bullet} = \mathbf{0} \quad \Leftrightarrow \quad \mathbf{D}^T\mathbf{f} - \mathbf{D}^T\mathbf{M}[(\mathbf{D}\dot{\mathbf{u}} + \mathbf{\gamma}) + \mathbf{d}] = \mathbf{0} \qquad (26)$$

The *partial velocity matrix* used in Kane's method is thus the matrix $\mathbf{D}$ which relates the dependent velocities $\mathbf{v}$ and independent generalized speeds $\mathbf{u}$, $\mathbf{v} = \mathbf{D u}$. Kane's method entails then a methodology for setting up equations of motion in a practical way [11].

6. Other useful implementations

6.1. Geometric elimination of constraint violation
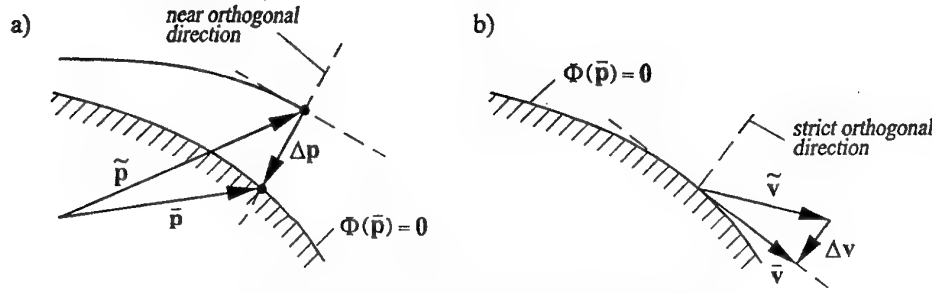
Fig. 4. The elimination of constraint violations.

For a system modeled in dependent state variables, when the governing equations involve constraint equations differentiated with respect to time, one consequence of numerical truncation errors is violation of the original constraint equations by the numerical solutions. The geometrical scheme developed in [5,17] lies in correcting the state variables so that to eliminate the constraint violations after each step of integrations (a sequence of steps). An important feature of the corrections is that they are performed in the constrained directions, and do not influence the system kinetic motion (Fig. 4). For a current numerical position $\tilde{p}$ and velocity $\tilde{v}$, $\tilde{\Phi} = \Phi(\tilde{p}) \neq 0$ and $\tilde{\Psi} = \Psi(\tilde{p}, \tilde{v}) \neq 0$ are measures along the constrained directions of the distance from $\tilde{p}$ to the virtual holonomic constraint manifold, and of projection of $\tilde{v}$ into these constrained directions. The appropriate state corrections are as follows [5]:

$$\Delta p = -A M^{-1} C^T (C M^{-1} C^T)^{-1} \begin{bmatrix} \tilde{\Phi} \\ 0 \end{bmatrix} \quad \text{and} \quad \Delta v = -M^{-1} C^T (C M^{-1} C^T)^{-1} \tilde{\Psi} \qquad (27)$$

where $\Delta p = \bar{p} - \tilde{p}$, $\Delta v = \bar{v} - \tilde{v}$, for $\bar{p}$ and $\bar{v}$ being the constraint consistent state variables, $\Phi(\bar{p}) = 0$ and $\Psi(\bar{p}, \bar{v}) = 0$. In computations the position correction should be performed first and may require few iterations. Then, the velocity correction can be done in one step.

6.2. Augmented joint coordinate method

The formulation of ODEs (16) involves only the explicit constraint equations (13) – (15). If the constraint reactions λ need to be determined according to (17), the constraint matrix C is required in addition, i.e. the implicit constraint equations (4) and (5) need to be introduced, and this means additional modeling effort. Another inconvenience of scheme (17) is that the $m \times m$ matrix $C M^{-1} C^T$ must be inverted, which may be a numerically inefficient task. The novel scheme developed in [7] is released from the inconveniences. In the approach, the explicit constraint equations are modified to

$$p = g(q, z) \quad \Rightarrow \quad \dot{p} = \left(\frac{\partial g}{\partial q} \right)\bigg|_{z=0} \dot{q} + \left(\frac{\partial g}{\partial z} \right)\bigg|_{z=0} \dot{z} \equiv D(q)\dot{q} + E(q)\dot{z} \qquad (28)$$

where both the *joint* and *open-constraint* coordinates, q and z, are involved to describe the admissible and prohibited relative motions in the joints. The explicit constraint equations (13) and (14) are then retrieved for $z = 0$ and $\dot{z} = 0$. In fact, the dependence on z in equations (28) is needed only to grasp the prohibited motion directions in the joints, represented as columns in the $n \times m$ matrix E. An important characteristic of matrix E is

67

$$CE = I \quad \Leftrightarrow \quad E^T C^T = I \qquad (29)$$

where I is the $m \times m$ identity matrix. In other words, E is a *pseudoinverse* of the rectangular matrix C (refer to [7] for more details). Using E, the new projection formula is

$$\begin{bmatrix} D^T \\ E^T \end{bmatrix} \left(M\dot{v} + d = f - C^T \lambda \right) \quad \begin{array}{l} \Rightarrow \quad D^T M (D\ddot{q} + \gamma) + D^T d = D^T f \qquad (30a) \\ \Rightarrow \quad E^T M (D\ddot{q} + \gamma) + E^T d = E^T f - \lambda \qquad (30b) \end{array}$$

The tangential projection (30a) leads to ODEs (16), and (30b) results then in

$$\lambda(q, \dot{q}, \ddot{q}, t) = E^T \left(f - M(D\ddot{q} + \gamma) \right) \qquad (31)$$

The constraint reactions λ are then obtained directly in a "resolved" form – no matrix inversion is required. The scheme does not require the implicit constraint equations (4) - (6). Instead, the explicit constraint equations (13) - (15) are slightly modified to the forms of (28).

6.3. Geometric interpretation of augmented Lagrangian formulation

A geometric interpretation of the augmented Lagrangian formulation [1] is presented in [6]. Instead of imposing constraints on a system in the traditional sense, large artificial masses μ resisting in the constrained directions are added, and the system motion is enforced to evolve primarily in the directions with smaller masses (in the unconstrained directions). Then, the residual motion in the constrained directions is removed by applying the constraint reactions to the system, estimated effectively in few iterations. The formulation is simple and
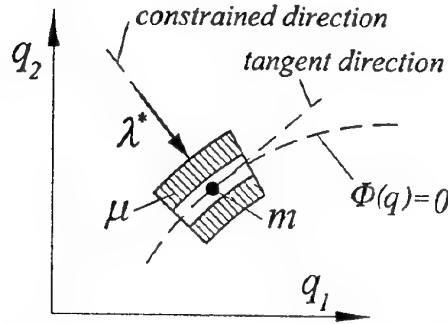
Fig. 5.. The geometric interpretation of the augmented Lagrangian formulation.

leads to computationally efficient numerical codes. Applications of the formulation to the analysis of constrained multibody systems with possible singular configurations, massless links and redundant constraints can are shown in [6].

6.4. Orthonormalization method

The final example of implementations stimulated by the geometrical interpretations of multibody systems in the orthonormalization method proposed in [2]. An effective scheme for converting the equations of motion expressed in terms of absolute variables, DAEs (9), into a convenient minimal-form set of equations in independent kinematical parameters is developed. Exploiting the fact that $\mathcal{E}^n$ is a metric space, the Gram-Schmidt orthogonalization scheme is adopted to generate a genuine orthonormal basis of $\mathcal{D}^r$, $C \xrightarrow{\text{orthonormalization}} \hat{D}$. Using the orthonormal basis defined by $\hat{D}$, the independent kinematic parameters $\hat{u}$ can be introduced, $v = \hat{D}\hat{u}$, and the dimensions of $\hat{u}$ is $[\sqrt{kg} \, m/s]$, just between the dimensions of momentums Mv and velocities v. A useful peculiarity of this approach is that in the minimal-form dynamic equations (20b) produced this way, $\hat{D}^T M \hat{D} = I$, i.e. the related mass matrix is the identity matrix (the dynamic equations are obtained directly in a "resolved" form). The method is especially efficient for $M = const$, it can thus be considered as an effective solver for absolute variable formulations.

7. Conclusion

The geometrical interpretation of multibody system dynamics can be both insightful and stimulative. Appealing directly to the geometry of particle dynamics known from Newtonian dynamics, it provides one with a precise and powerful investigation tool for handling constrained motion problems. The followed mathematical formulations resolve then themselves to compact matrix transformations suitable for computer implementations. Systems subject to holonomic and nonholonomic constraints can be treated, and the analysis can be performed in either generalized or quasi-velocities. Variant forms of equations of motions can be obtained, relevant to many other methods of classical mechanics. Finally, novel contributions and amendments in the theory of constrained systems can be stimulated.

References

[1] Bayo E., Ledesma R.: "Augmented Lagrangian and mass-orthogonal projection methods for constrained multibody dynamics", *Nonlinear Dynamics*, **9** (1996), 113-130.

[2] Blajer W.: "An orthonormal tangent space method for constrained multibody systems", *Computer Methods in Applied Mechanics and Engineering*, **121** (1995), 45-57.

[3] Blajer W.: "A geometric unification of constrained system dynamics", *Multibody System Dynamics*, **1** (1997), 3-21.

[4] Blajer W.: "A geometrical interpretation and uniform matrix formulation of multibody system dynamics", *ZAMM*, **81** (2001), 247-259.

[5] Blajer, W.: "Elimination of constraint violation and accuracy aspects in numerical simulation of multibody systems", *Multibody System Dynamics*, **7** (2002), 265-284.

[6] Blajer, W.: "Augmented Lagrangian formulation: geometrical interpretation and application to systems with singularities and redundancy", *Multibody System Dynamics*, (in press).

[7] Blajer, W., Schiehlen, W.: "Efficient determination of constraint reactions in multibody systems", *Multibody System Dynamics*, (submitted).

[8] Blajer W., Schiehlen W., Schirm W.: "A projective criterion to the coordinate partitioning method for multibody dynamics", *Archive of Applied Mechanics*, **64** (1994), 86-98.

[9] Desloge E.A.: "The Gibbs-Appell equations of motion", *American Journal of Physics*, **56** (1988), 841-846.

[10] Jungnickel U.: "Differential-algebraic equations in Riemannian spaces and applications to multibody system dynamics", *ZAMM*, **74** (1994), 409-415.

[11] Kane T.R., Levinson D.A.: *Dynamics: Theory and Applications*, McGraw-Hill, New York, 1985.

[12] Lesser M.: "A geometrical interpretation of Kane's equations", *Proceedings of the Royal Society in London*, **A436** (1992), 69-87.

[13] Maißer P.: "Analytical dynamics of multibody systems", *Computer Methods in Applied Mechanics and Engineering*, **91** (1991), 1391-1396.

[14] Nikravesh, P.E., *Computer-Aided Analysis of Mechanical Systems*, Prince-Hall, Englewood Cliffs, New Jersey, 1988.

[15] Schiehlen W.: "Multibody system dynamics: roots and perspectives", *Multibody System Dynamics*, **1** (1997), 149-188.

[16] Wehage R.A., Haug E.J.: "Generalized coordinate partitioning for dimension reduction in analysis of constrained dynamic systems", *Journal of Mechanical Design*, **104** (1982), 247-255.

[17] Yoon S., Howe R.M., Greenwood D.T.: "Geometric elimination of constraint violations in numerical simulation of Lagrangian equations", *Journal of Mechanical Design*, **116** (1994), 1058-1064.

Snake-like Locomotions of Multilink Systems

Felix L. Chernousko

Institute for Problems in Mechanics,
of the Russian Academy of Sciences,
pr. Vernadskogo 101-1, Moscow 119526, Russia,
email: chern@ipmnet.ru

Abstract

Motions of plane multilink mechanisms over a horizontal plane are investigated. The system under consideration is a multibody system consisting of rigid bodies connected by revolute joints with vertical axes. Control torques are created by actuators placed at the joints. Dry friction forces between the linkage and the horizontal plane act upon the system. It is shown that the system under consideration can perform lengthwise, sideways, and rotational motions in the horizontal plane so that it can reach any position and orientation in the plane. Control laws for various modes of periodic and wave-like motions are proposed for multilink mechanisms with different number of links: two, three, and many. The displacements and speed of motion are estimated. Optimal geometrical and mechanical parameters of linkages are determined. The results of computer simulation as well as experimental results confirm the obtained theoretical calculations.

Keywords: modelling, control, multibody system, biomechanics.

1 Introduction

Crawling motions of snakes, worms, and other limbless animals have always been of great interest for specialists in mechanics and biomechanics. Different aspects of snake-like motions are considered, for example, in [1–7]. Biomechanical studies show that snakes always try to use vertical or inclined objects (walls, stones, grass, and other obstacles) to exert forces having projections on the direction of motion and thus to compensate dry friction. Snake-like nonholonomic mechanism considered in [4] and other papers consists of many elements having wheels and connected by joints. By twisting, these mobile multilink robots achieve the similar result: the wheels exert on the surface horizontal forces perpendicular to the wheels and thus produce the desirable forces in the direction of motion.

In this paper, we consider simple plane multibody systems (linkages) without wheels which can move along the horizontal plane in the presence of dry friction between the linkage and the plane. Control torques are created by actuators

installed at the joints of the linkage. It is shown that the linkage can peform various motions along the plane. For a three-link system which is investigated in more detail, and for a two-link system the motion consists of slow and fast phases. For a linkage with more than four links, a slow wave-like motion is possible. Displacements and speed of the motions are estimated. The paper is based on the results obtained in [8–12].

2 Three-link mechanism

Consider a plane linkage $O_1C_1C_2O_2$ moving over a horizontal plane Oxy (Fig. 1). For the sake of simplicity, we assume that the links O_1C_1, C_1C_2, and C_2O_2 are rigid and massless bars, and the mass of the linkage is concentrated at its joints C_1 and C_2 which are equal point masses m_1, and at the end points O_1 and O_2 which are equal point masses m_0. Thus, the total mass of the linkage is $m = 2(m_1 + m_0)$. The length of the central link C_1C_2 is $2a$, and the lengths of the end links are equal to ℓ. Denote by x, y the coordinates of the middle of the control link, by θ the angle between this link and the x-axis, and by α_i the angles between the central link and the end links $O_iC_i, i = 1, 2$ (Fig. 1).
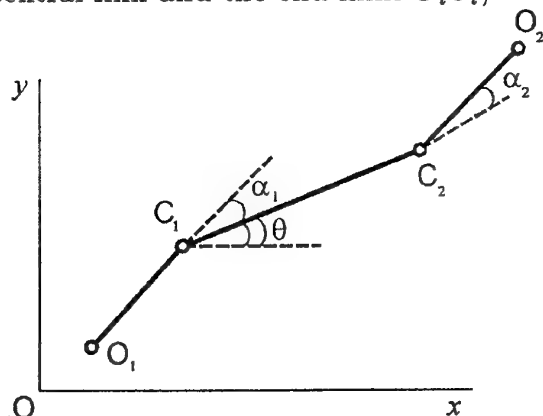
Fig. 1. Three-member linkage.   Fig. 2. Longitudinal motion.
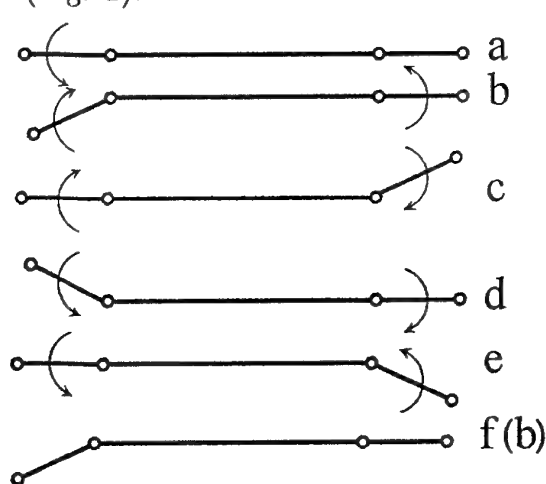
Suppose the dry friction acting between the masses $O_i, C_i, i = 1, 2$, and the horizontal plane obeys Coulomb's law. If a point mass m moves, the friction force is opposite to the point velocity and equal to its weight mg multiplied by the friction coefficient k. If the point mass is at rest, the friction does not exceed mgk, and its direction can be arbitrary. We assume that the friction coefficient

for the masses m_1 and m_0 is equal to k_1 and k_0, respectively. The control torques M_1 and M_2 are applied at the joints C_1 and C_2. Suppose that these torques can produce some prescribed time-history of angles $\alpha_i(t), i = 1, 2$.

We will construct the desired motions of the linkage as a combination of more simple motions which we call elementary [8]. All elementary motions begin and end at the states of rest of the linkage. In each elementary motion, the angles $\alpha_i(t), i = 1, 2$, change within the interval $(-\pi, \pi)$ between the prescribed initial value α_i^0 and terminal value α_i^1; the time-histories $\alpha_i(t)$ can be more or less arbitrary. If both angles $\alpha_i(t)$ take part in the elementary motion, then they rotate synchronously either in the same direction, or in opposite directions, so that $\dot{\alpha}_2(t) = \pm\dot{\alpha}_1(t)$.

Elementary motions are divided into slow and fast ones.

In slow motions, the angular velocities and accelerations of the end links are small enough, so that the central link does not move. Denote by ω_0 and ε_0 maximal values of the angular velocities and accelerations during the slow motions

$$\omega_0 = \max|\dot{\alpha}_i(t)|, \quad \varepsilon_0 = \max|\ddot{\alpha}_i(t)| \tag{2.1}$$

Here, the maxima are taken along the whole slow motion. They do not depend on $i = 1, 2$.

The sufficient condition which ensures that the central link stays at rest during the slow motion can be expressed as follows [10]

$$m_0\ell\{[\omega_0^4 + (\varepsilon_0 + gk_0\ell^{-1})^2]^{1/2} + (\varepsilon_0 + gk_0\ell^{-1})\ell a^{-1}\} \leq m_1 gk_1 \tag{2.2}$$

This condition holds in the case of one rotating end link and also in the case where both links rotate in the same direction. If the end links rotate in the opposite directions, this condition can be replaced by a weaker one [10]

$$m_0\ell[\omega_0^4 + (\varepsilon_0 + gk_0\ell^{-1})^2]^{1/2} \leq m_1 gk_1 \tag{2.3}$$

Note that condition (2.2) always holds for very slow motions, i.e., if ω_0 and ε_0 in (2.1) are sufficiently small, and $m_0 k_0(a + \ell) < m_1 k_1 a$. Similarly, condition (2.3) holds, if ω_0 and ε_0 are sufficiently small and $m_0 k_0 < m_1 k_1$.

In fast motions, the angular velocities and accelerations of the end links are sufficiently high, and the duration τ of this motion is much less than the duration T of the slow motion: $\tau \ll T$. The magnitudes of the control torques M_1 and M_2 during the fast motion are high compared to the torques produced by the friction

$$|M_i| \gg m^* g k^* \ell^*, \quad i = 1, 2$$
$$m^* = \max(m_1, m_0), \quad k^* = \max(k_1, k_0), \quad a^* = \max(a, \ell) \tag{2.4}$$

Hence, the friction can be neglected during the fast motion. Therefore, the center of mass of the linkage stays at rest, and its angular momentum is zero during the fast motion. Using these conservation laws, one can easily evaluate the terminal state of the linkage after the fast motion.

3   Construction of motions

Let at the initial state the linkage be at rest, with all its links parallel to the x-axis. We have $\theta = \alpha_1 = \alpha_2 = 0$ in this state (Fig. 2).

The *longitudinal* motion is implemented by means of the following stages (Fig. 2). In what follows, we denote slow and fast motions by capital S and F, respectively, indicating the initial and terminal values α^0 and α^1 of angles α_i in each elementary motion as follows $\alpha_i : \alpha_i^0 \to \alpha_i^1, \quad i = 1, 2$.

Using this notation, the longitudinal motion of a three-member linkage is described as follows (Fig. 2).

1. $S, \quad \alpha_1 : 0 \to \gamma, \quad \alpha_2(t) \equiv 0$.
2. $F, \quad \alpha_1 : \gamma \to 0, \quad \alpha_2 : 0 \to \gamma$.
3. $S, \quad \alpha_1 : 0 \to -\gamma, \quad \alpha_2 : \gamma \to 0$.
4. $F, \quad \alpha_1 : -\gamma \to 0, \quad \alpha_2 : 0 \to -\gamma$.
5. $S, \quad \alpha_1 : 0 \to \gamma, \quad \alpha_2 : -\gamma \to 0$.

Here, $\gamma \in (-\pi, \pi)$ is some fixed angle.

After stage 5, the configuration of the linkage becomes identical to its configuration after stage 1: $\alpha_1 = \gamma, \alpha_2 = 0$. The cycle of four elementary motions 2–5 can be repeated. To return the linkage to its original rectilinear configuration $\alpha_1 = \alpha_2 = 0$, it is sufficient to perform the slow motion: $S, \alpha_1 : \gamma \to 0, \quad \alpha_2 \equiv 0$.

During the slow motions, the central link stays at rest, whereas the center of mass of the linkage moves. During the fast motions, on the contrary, the center of mass stays at rest, while the central link moves. It is shown in [8] that the total displacement of the central link along the x-axis during the cycle of motions 2–5 is

$$\Delta x = 8 m_0 m^{-1} \ell \sin^2(\gamma/2), \quad m = 2(m_0 + m_1) \tag{3.1}$$

The total displacement of the middle of the central link along the y-axis and the total angle of rotation of this link during the same cycle are zero: $\Delta y = 0$,

$\Delta\theta = 0$. The average speed of the longitudinal motion is

$$v_1 = \Delta x (2T)^{-1}. \qquad (3.2)$$
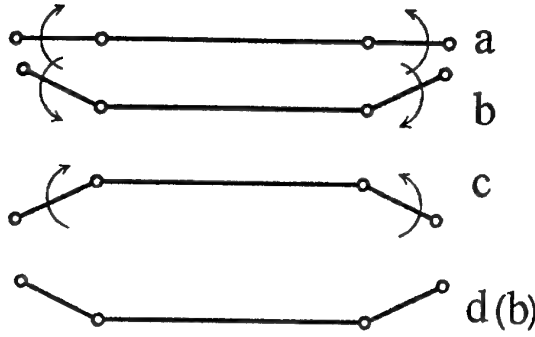
Fig. 3. Lateral motion.
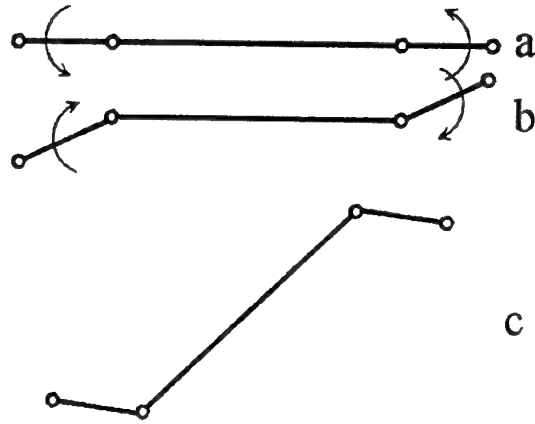
Fig. 4. Rotation.

Lateral motion can be performed as follows (Fig. 3).

1. S, $\quad \alpha_1 : 0 \to -\gamma$, $\quad \alpha_2 : 0 \to -\gamma$.
2. F, $\quad \alpha_1 : -\gamma \to \gamma$, $\quad \alpha_2 : \gamma \to -\gamma$.
3. S, $\quad \alpha_1 : \gamma \to -\gamma$, $\quad \alpha_2 : -\gamma \to \gamma$.

After stage 3, the configuration of the linkage is identical to its configuration after stage 1: $\alpha_1 = -\gamma$, $\alpha_2 = \gamma$. The cycle of motions 2, 3 can be repeated. To return to the original rectilinear configuration $\alpha_1 = \alpha_2 = 0$, it is sufficient to perform the motion: S, $\quad \alpha_1 : -\gamma \to 0$, $\quad \alpha_2 : \gamma \to 0$. During the cycle of motions 2, 3, the total displacement of the middle of the central link along the x-axis and the total rotation are zero: $\Delta x = 0$, $\quad \Delta\theta = 0$, whereas the total displacement along the y-axis and the average velocity along this axis are [8]

$$\Delta y = 4m_0 m^{-1} \ell \sin \gamma, \quad v_2 = \Delta y T^{-1} \qquad (3.3)$$

The rotation of the linkage can be performed as follows (Fig. 4).

1. S, $\quad \alpha_1 : 0 \to \gamma_1$, $\quad \alpha_2 : 0 \to \gamma_1$.
2. F, $\quad \alpha_1 : \gamma_1 \to \gamma_2$, $\quad \alpha_2 : \gamma_1 \to \gamma_2$.
3. S, $\quad \alpha_1 : \gamma_2 \to \gamma_1$, $\quad \alpha_2 : \gamma_2 \to \gamma_1$.

Here, γ_1 and γ_2 are angles from the interval $(-\pi, \pi)$. Motions 2, 3 can be repeated. To return the linkage to the initial rectilinear state $\alpha_1 = \alpha_2 = 0$, it is necessary to perform the motion: S, $\quad \alpha_1 : \gamma_1 \to 0$, $\quad \alpha_2 : \gamma_1 \to 0$. The

total displacement of the middle of the central link during the cycle 2, 3 is zero: $\Delta x = \Delta y = 0$, and the angle of rotation $\Delta \theta$ can be easily evaluated [8].

Combining the motions described above, the linkage can perform arbitrary displacement in the horizontal plane.

4 Two-member linkage

Consider now a system of two bodies connected by a joint O^* which can move along the horizontal plane Oxy. The masses of the bodies are denoted by m_1 and m_2, their centers of masses by C_1 and C_2, their moments of inertia about the axis O^* by J_1 and J_2, the distances O^*C_1 and O^*C_2 by a_1 and a_2, and the friction coefficients for these bodies by k_1 and k_2, respectively. The body with index 1 will be referred to as a body, whereas the body with index 2 will be called a tail (Fig. 5). The joint O^* is considered as a point mass m_0 with a friction coefficient k_0.

We again consider the motion of the linkage along the horizontal plane Oxy. The torque at the joint O^* is denoted by M. The coordinates of the joint O^* are denoted by x, y, the angle between O^*C_1 and Ox by θ, and the angle between C_2O^* and O^*C_1 by α_1 (Fig. 5).

Again, we introduce the notion of slow and fast motions. In the slow motions, the tail rotates slowly enough, so that the body stays at rest. In the fast motions, the friction can be neglected, so that the conservation of momentum and angular momentum holds.

Denote

$$\omega_0 = \max |\dot{\alpha}(t)|, \quad \varepsilon_0 = \max |\ddot{\alpha}(t)| \tag{4.1}$$

where the maxima are taken along the slow motion. Then the following two inequalities are a sufficient condition which ensures that the body stays at rest during the slow motions of the tail [11]

$$J_2\varepsilon_0 + m_2 g k_2 a_2 \leq m_1 g k_1 a_1$$

$$J_2\varepsilon_0 + m_2 g k_2 a_2 + m_2 a_1 a_2 [\omega_0^4 + (\varepsilon_0 + g k_2 a_2^{-1})^{1/2}] \leq m_0 g k_0 a_1 \tag{4.2}$$

These inequalities always hold for very slow motions, if ω_0 and ε_0 in (4.1) are sufficiently small and the following two inequalities are true

$$m_2 k_2 a_2 < m_1 k_1 a_1, \quad m_2 k_2 (a_1 + a_2) < m_0 k_0 a_1$$

The following sequence of elementary motions constitute the longitudinal motion of a two-member linkage (Fig. 6).

1. $S,\quad \alpha:0\to\beta.$

2. $F,\quad \alpha:\beta\to 0.$

3. $S,\quad \alpha:0\to -\beta.$

4. $F,\quad \alpha:-\beta\to 0.$

5. $S,\quad \alpha:0\to -\beta.$

6. $F,\quad \alpha:-\beta\to 0.$

7. $S,\quad \alpha:0\to\beta.$

8. $F,\quad \alpha:\beta\to 0$
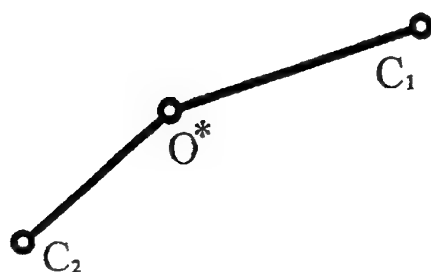
Fig. 5. Two-member linkage.
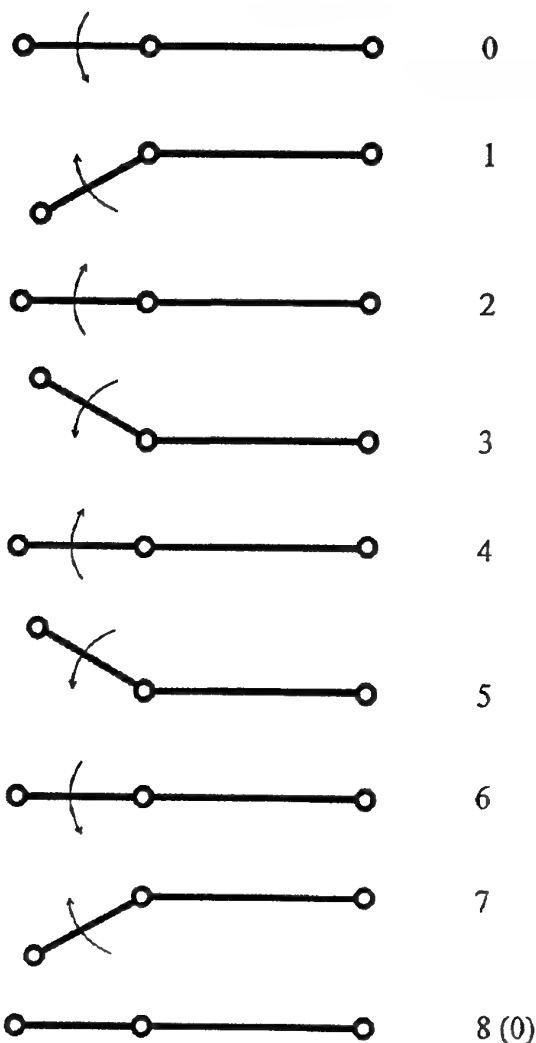
Fig. 6. Longitudinal motion of a two-member linkage.

Here, β is some fixed angle, $\beta \in (-\pi,\pi)$. As a result of this sequence of motions, the linkage moves along itself by the distance [11]

$$\Delta x = 8m^{-1}m_2 a_2 \sin\frac{\beta}{2}\cos\frac{\gamma}{2}\sin\frac{\beta-\gamma}{2} \qquad (4.3)$$

the total lateral motion and rotation being zero.

In (4.3), the following denotations are used

$$m = m_0 + m_1 + m_2, \quad \gamma = \frac{\beta}{2} + \frac{A_0}{A_1 A_2}\text{arctg}\left[\frac{A_1}{A_2}\text{tg}\left(\frac{\beta}{2}\right)\right]$$

$$A_0 = m(J_2 - J_1) + m_1^2 a_1^2 - m_2^2 a_2^2 \tag{4.4}$$

$$A_{1,2} = [m(J_1 + J_2) - (m_1 a_1 \pm m_2 a_2)^2]^{1/2}$$

The average speed of the longitudinal motion is $v_3 = \Delta x/(4T)$. It can be shown that, combining slow and fast motions, the two-member linkage can perform arbitrary displacements in the horizontal plane.

5   Multilink systems

Motions of multilink systems along a horizontal plane are investigated in [9]. For these systems, wave-like modes of motion are proposed in which only several (three or four) links move at each instant of time. Due to the wave travelling along the linkage, the multilink system can move as a whole in the longitudinal direction. These periodic motions do not include fast phases and can be carried out as slow quasi-static motions. The required torques created by the actuators are rather small: they do not exceed $2mgk\ell$, where m is a mass of the link, ℓ is its length, and k is the coefficient of friction. Note that for the fast motions considered above the required torque is much higher: $M \gg mgk\ell$, see (2.4). The slow wave-like motions can be performed by multilink systems having more than four links.

6   Example

Consider a three-link mechanism having the following parameters

$$a = \ell = 0.2m, \quad m_1 = 1.2kg, \quad m_0 = 0.4kg$$

$$m = 3.2kg, \quad k_1 = k_0 = 0.2, \quad g = 9.81m \cdot s^{-2}$$

Let the angular velocities in the slow motions obey the piecewise linear law

$$\omega_i(t) = \varepsilon_0 t, \quad t \in [0, T/2]; \quad \omega_i(t) = \dot\varepsilon_0(T - t), \quad t \in [T/2, T]$$

$$\omega_i(t) = |\dot\alpha_i(t)|, \quad i = 1, 2; \quad \omega_0 = \varepsilon_0 T/2, \quad |\Delta\alpha| = |\alpha_i^1 - \alpha_i^0| = \varepsilon_0 T^2/4$$

with $\varepsilon_0 = 4s^{-2}$. The maximal angle of rotation of the end links is $\gamma = 1\text{rad}$. Then for the logitudinal motion we have $|\Delta\alpha| = 1$, $T = 1s$, $\omega_0 = 2s^{-1}$, whereas for the lateral motion $|\Delta\alpha| = 2$, $T = 1.4s$, $\omega_0 = 2.8s^{-1}$. The conditions (2.2) and (2.3) for both motions are satisfied, and their velocities, according to (3.1)–(3.3),

are $v_1 = 0.023 m \cdot s^{-1}$, $v_2 = 0.034 m \cdot s^{-1}$. The required magnitude of control torques evaluated according to (2.4) is $6 \div 8 N \cdot m$.

7   Optimization

The average speed of motion of linkages depends on their geometrical and mechanical parameters such as lengths and masses of links, angles of rotation, coefficients of friction, etc. Parametric optimization of the average speed (see (3.2)) of the three-member and two-member linkages with respect to their parameters is performed in [12].

Let us note some properties of optimal solutions. The average speed grows with the increase of the angle of rotation of the links. Also, it grows with the coefficient of friction of the main body k_1, both for the three-member and two-member linkages. For the three-member linkage, the optimal length ℓ of the end links is greater than the half-length a of the central link: $\ell > a$. By contrast, the optimal length a_2 of the tail of the two-member linkage is smaller than the half-length of its body: $a_2 < a_1/2$. The gain in speed due to the optimization of lengths and masses is rather essential, up to 50% and more.

It is shown that the maximal longitudinal speed of the three-member linkage can be estimated by the formula

$$v_1 \sim 0.1(gak_1)^{1/2} \tag{7.1}$$

The maximal speed of the lateral motion is several times higher.

The maximal speed of the two-member linkage is approximately two times smaller than v_1 from (7.1). This difference can be easily explained by the fact that the three-member linkage is equipped with two actuators, whereas the two-member linkage has only one.

8   Conclusions

A plane linkage consisting of two, three, or more bodies can move over a rough horizontal surface in different directions using internal control torques created by the actuators placed at the joints. The vehicle has a very simple structure and can use, in fact, only one actuator. Different modes of motions are described, and sufficient conditions are derived which ensure the possibility of required motions. Estimates of displacements, average speed, and required control torques are given. Maximization of the average speed of linkages with respect to their geometrical

and mechanical parameters is performed. Computer simulation of the motion of linkages is carried out based on the numerical integration of complete sets of nonlinear differential equations of the linkages. Results of the simulation confirm theoretical considerations and estimates. Because of the simplicity of the structure of snake-like mechanisms, the proposed principle of motion can be useful for mobile robots, especially for small ones. First experiments performed at the Technical University of Munich by Prof. F.Pfeiffer, Mr. Gienger, and Mr. Mayr show that the snake-like motions described above can be implemented.

References

[1] Lavrentyev, M.A., Lavrentyev, M.M. (1962) On one principle for creating the thrust in motion. *Journal of Applied Mechanics and Technical Physics*, (4) 6–9.

[2] Gray, J. (1968) *Animal Locomotion*, Weidenfeld & Nicolson, London, UK.

[3] Dobrolyubov, A.J. (1987) *Running Waves of Deformation*, Nauka i Tekhnika, Minsk, USSR.

[4] Hirose, S. (1993) *Biologically Inspired Robots: Snake-like Locomotors and Manipulators*, Oxford University Press, Oxford, UK.

[5] Burdick, J.W., Radford, J. and Chirikjan, G.S. (1993) A 'sidewinding' locomotion gait for hyper-redundant robots, In *Proceedings of the IEEE International Conference on Robotics and Automation*, Atlanta, Georgia, USA, **3** 101–106.

[6] Ostrowski, J., Burdick, J. (1996) Gait kinematics for a serpentine robot, In *Proceedings of the IEEE International Conference on Robotics and Automation*, Minneapolis, Minnesota, USA, **2** 1294–1300.

[7] Bayraktaroglu, Z.Y., Blazevic, P. (2000) Snake-like locomotion with a minimal mechanism, In *Proceedings of the Third International Conference on Climbing and Walking Robots CLAWAR 2000*, M.Armada and P.Gonzalez de Santos, eds., Madrid, Spain, 201–207.

[8] Chernousko, F.L. (2000) The motion of a multilink system along a horizontal plane, *Journal of Applied Methematics and Mechanics*, **64** (1) 5–15.

[9] Chernousko, F.L. (2000) The wavelike motion of a multilink system on a horizontal plane, *Journal of Applied Mathematics and Mechanics*, **64** (4) 497–508.

[10] Chernousko, F.L. (2001) The motion of a three-link system along a plane, *Journal of Applied Mathematics and Mechanics*, **65** (1) 13–18.

[11] Chernousko, F.L. (2001) The controlled motion of a two-member linkage along a horizontal plane, *Journal of Applied Mathematics and Mechanics*, **65** (4) 578–591.

[12] Smyshlyaev, A.S., Chernousko, F.L. (2001) Optimization of the motion of multilink robots on a horizontal plane, *Journal of Computer and Systems Sciences International*, **40** (2) 340–348.

VIRTUAL RECONSTRUCTION OF IMPAIRED HUMAN HEARING

A. EIBER, H.-G. FREITAG and C. BREUNINGER
Institute B of Mechanics, University of Stuttgart,
Pfaffenwaldring 9, D-70550 Stuttgart, Germany
E-mail: ae@mechb.uni-stuttgart.de

1. Introduction

The hearing organ, a marvelous and highly developed part in the human body provides a very important sense in the daily life. In the middle ear there are pure mechanical mechanisms of sound transfer whereas in the inner ear a complex transduction from mechanical entities via chemical processes to electrical stimulation of hearing nerves take place. In case of hearing loss due to diseases or accidents a mechanical reconstruction is performed by inserting passive or active implants into the middle ear.

2. Aims and Motivation

Virtual scenarios of the complex hearing process for pathological situations are becoming an increased meaning in the clinical practice to diagnose and to reconstruct an impaired hearing successfully:

- The *audiologist* needs a deep insight into the dynamical behavior of the mechanical middle ear structures to give a correct diagnosis about a specific disease.
- For a successful reconstruction the *surgeon* must have a detailed knowledge about the frequency dependent spatial motion of the ossicular chain during sound transfer through the middle ear to assess the effects of surgical manipulations. For reconstructions he has to choose an appropriate implant and to insert it in a suitable manner.
- The *developer* of passive and actively driven implants has to regard the dynamics of the implant itself together with the dynamical behavior of the remaining middle ear structure in the design and the optimization process.

By virtue of simulation of the hearing process and animation of the spatial motion of the middle ear structures 'virtual hearing' can be carried out and demonstrated at the computer which serves as a common base for the work of audiologists, surgeons and developers of implants. This procedure needs appropriate models with different complexity and confident parameters to describe linear and nonlinear effects of sound transfer through the outer and middle ear.

3. Modeling of the Hearing Mechanism

To describe the dynamical behavior of the hearing organ mechanical and electrical models are used. With models based on electrical circuits only the global sound transfer is described between the scalar input pressure p and the scalar output of 'hearing', e.g. Zwislocki [1] and Shaw and Stinson [2]. These models were derived from electro-acoustical and electro-mechanical analogies based on very strong simplifications. Due to the simplifications and the non-physical description they are less meaningful and less flexible than mechanical models.

Finite element models of tympanic membrane and ossicles were published by Wada et al. [3], Beer et al. [4] and Prendergast et al. [5]. This approach leads to large systems with a huge number of parameters.

With three-dimensional multibody system models of the human ossicular chain presented in [6], the spatial motion of ossicles can be described. The methods of continuous systems, finite element systems and in particular multibody systems are used here to model the air in the outer ear canal, the tympanic membrane, the ossicles of the middle ear with its visco-elastic ligaments and the fluid of the inner ear. For the outer ear canal an air column in a rigid cylindrical tube is considered. Modeling the air column as a lumped mass system allow the description of the natural frequencies in the frequency range of the human hearing. The finite element approach is used to describe the membrane with its nonuniform thickness and bending stiffness in order to derive a lumped mass model which is coupled with the air column and the ossicular chain. The three ossicles are modeled as rigid bodies spatially suspended by the ligaments in the air-filled middle ear cavity. The ligaments are considered as massless spring/damper combinations [7]. In figure 1 the final multibody system model of the hearing mechanism is shown with the ear canal, the ear drum, the rigid bodies of the ossicles and the inner ear fluid. Using a multibody systems formalism [8], the equation of motion can be generated in a symbolical form

$$M\ddot{y} + k = q, \tag{1}$$

81
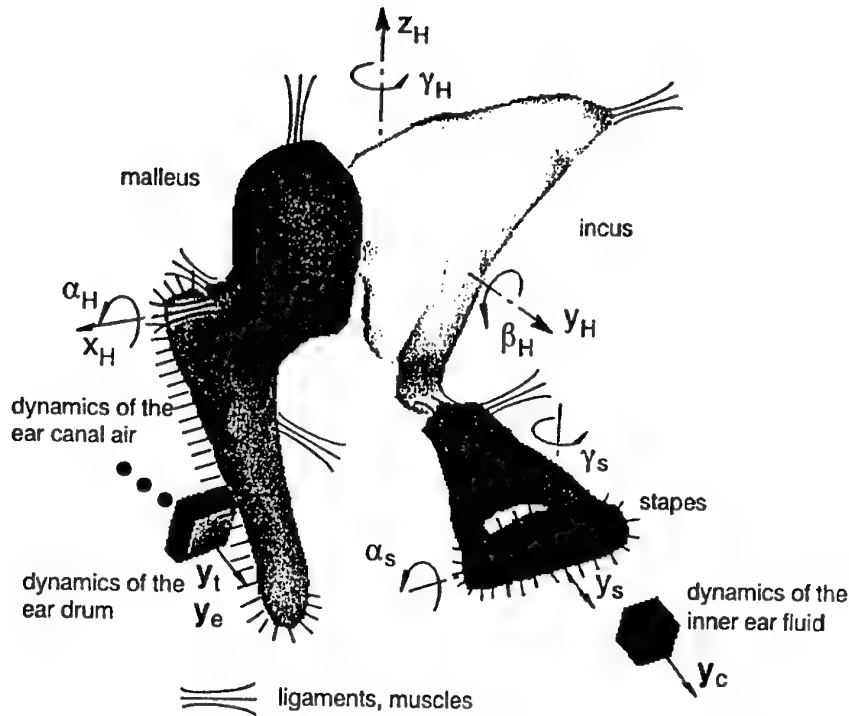
Figure 1. Mechanical model of the middle ear and its adjacent structures air of outer ear canal, ear drum, and fluid of inner ear. The ligaments and muscles are indicated as black lines. In particular the translations x_H, y_H and z_H and rotations α_H, β_H and γ_H of the incudo-malleal block, translation y_S and rotations α_S, and γ_S of the stapes are specified.

with the generalized coordinates $y \in I\!\!R^f$, the mass matrix M, the vector of generalized centrifugal, Coriolis and gyroscopic forces k and the vector of generalized applied forces q. The entire model of a normal ear has $f = 77$ degrees of freedom comprising the air in the ear canal, the tympanic membrane, the ossicles and parts of the inner ear.

For moderate sound pressure levels linear kinematics and linear constitutive equations can be assumed and the joint between malleus and incus is considered as fixed [3]. Then the equation (1) can be linearized to perform eigenvalue analysis. For high sound pressure levels and in particular for impulsive noise, a nonlinear behavior of the middle ear occur. This is due to a nonlinear kinematic as well as to nonlinear constitutive equations of the ligaments and the ear drum. Moreover the deflection of some elements in the middle ear like the annular ring is limited. Another source of nonlinear behavior are the active processes in the inner ear. For high force intensity the joint between malleus and incus is articulated for decoupling both ossicles like a mechanical safety clutch to prevent the hearing from overload.

82
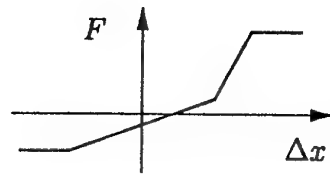
Figure 2. Asymmetric stiffness and limited transfer force of a ligament or coupling between implant and ossicle.

Distinct pathological situations like otosclerosis or partial malleus head fixation can be described with the established models by changing of specific parameters or the structure of the models.

Reconstructions of the middle ear structure are carried out to repair missing or disfunctional parts of the ossicular chain. *Passive* implants are used to replace ossicles in order to bridge a gap in the ossicular chain. Here the attachment points of implant and ossicles determine the kinematics of the reconstructed ear. The coupling conditions between ossicles and implant influence the dynamic of the spatial motion of the reconstructed ear. *Active* implants additionally can drive the middle ear in order to compensate hearing losses due to imperfect sound transfer of the middle ear or damaged inner ear [9]. They can act as force or displacement transducers imposing a translational or a rotational motion. Beside the attachment point and coupling conditions between implant and ossicle, the spatial orientation of the excitation is essential. A restricted coupling force and a distortion due to nonlinear coupling mechanisms may lead to unacceptable hearing results. On the base of the models of the natural ear, models of ears reconstructed with passive or active implants have also been established applying the multibody system approach.

Generally, the mechanism of coupling is highly nonlinear due to gaps or asymmetrical stiffness and damping behavior with respect to inward and outward movement. In particular the commonly used intermediate medium between prosthesis and ossicles like fascia show approximately a behavior with partially linear force/displacement relation as sketched in figure 2. In some cases the coupling between implant and ossicle is performed by pressing both parts against it. Then a so-called unilateral constraint is given which shows a highly nonlinear behavior. Such a asymmetric stiffness of the springs may lead to harmonic distortion in the sound transfer through the middle ear even in the case of moderate excitation. Using powerful active implants, the applied excitation may cause high coupling forces which exceed a physical limit and leading also to a distorted sound transfer. They may also cause feedback effects which inhibit the full compensation of a particular disease.
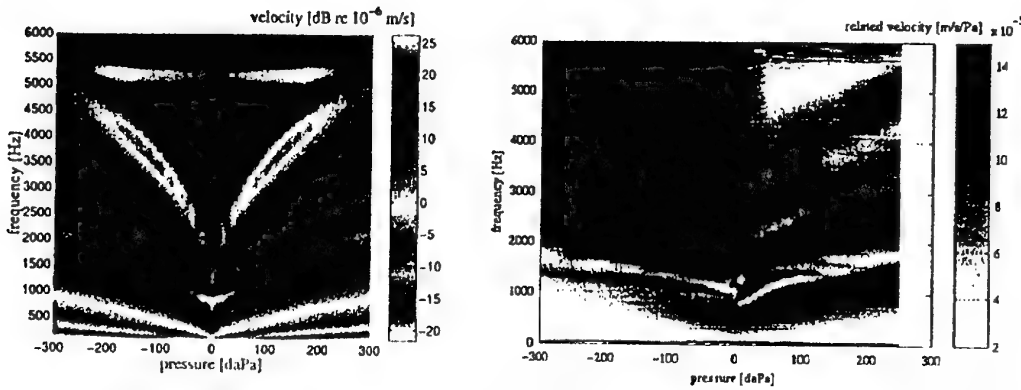
Figure 3. Spectrum of velocity of the umbo depending on static pressure p in ear canal for simulation (left) and measurement (right).

4. Measurements and Parameter Estimation

Measurements in the clinical practice and in the lab have been conducted to determine the dynamical behavior of the hearing organ and to derive the belonging parameters of the models. Due to the very small displacements and velocities and the low masses, non-contact measurement principles like laser Doppler vibrometry (LDV) have to be applied.

Especially nonlinear effects could be detected by using LDV and extended procedures of the multifrequency-tympanometry (MFT). In the classical tympanometry a varying static pressure in the ear canal but only a fixed excitation frequency is used to determine the acoustical properties of the middle ear. Applying modern measurement and data processing techniques of the MFT, the nonlinear mechanical properties of the middle ear structures become apparent. Taking the simulated velocity of the tip of malleus handle (umbo) and calculating the spectrum a contour plot results as shown in figure 3 left part. The corresponding plot resulting from measurement with LDV is shown on the right part of figure 3. These diagrams are called local multifrequency-tympanometry (LMFT) due to their similarity to those obtained from MFT [10]. The shift in the natural frequencies can be seen due to the nonlinear behavior of the ear drum and the middle ear ligaments. Comparing measurements of the MFT with simulations, the nonlinear behavior of the models could be approximated by power series. Based on virtual MFT diagrams the influence of particular pathologies like malleus head fixation or otosclerosis can be studied. The investigations for describing nonlinearities in the sound transfer and for parameter estimations are still ongoing.

84

5. Virtual Prototyping

Based on the results of the simulations and animations the surgeon is able to predict the effect of particular surgical incisions. For developers of implants virtual 'test series' can be carried out by including the models of existing implants or new prototypes in the entire model. This allows the improvement of passive and active implants with respect to specific conditions in the middle ear. This is very effective since particular parameters can be varied while remaining conditions are kept constant. Such virtual tests are helpful to shorten clinical trial series with living animals or human patients.

An optimization of hearing result is not only focused on the design of the implant itself but includes the dynamic behavior of the entire system with the particular way of inserting of the implant by the surgeon. One part of the parameters of the model are given by the specific anatomy. Another part can be chosen by the designer of implants and by the surgeon, they are denoted as design variables p. Some parameters q may vary due to operational conditions which cannot be influenced. Adjusting the design variables the sound transfer through the ear can be improved applying an optimization procedure. The goal is may be the best compensation of a particular disease or to get a good sound transfer in a particular frequency range associated with a low sensitivity against variations in the parameters q to get a sufficient robustness. For this, appropriate criteria of the kind

$$\psi_i = \psi_i(t, y, \dot{y}, \ddot{y}, p), \quad i = 1(1)n, \tag{2}$$

have to be formulated assessing the dynamical behavior of the system. These criteria have to be minimized applying an appropriate optimization algorithm [11].

To show the optimization of a passive implant, in figure 4 the frequency dependent response of the inward/outward motion of stapes for a normal ear and reconstructed ears are plotted. The sound transfer is strongly governed by the position of the points where the implant is attached to the ossicles and the coupling conditions which are set as design variables. The surgeon is able to choose the position of attachment as well as the coupling conditions by adjusting the statical preload between ossicle and implant. For the optimization two criteria have been formulated: To assess the loudness, the amplitude y_S of inward/outward motion of the stapes should be large in the whole frequency range. To assess the sound quality, the dependence on frequency should similar to the normal ear. Taking both criteria into account and applying a multi-criteria optimization a better performance is obtained as shown in figure 4.

For an optimal design and use of passive and active implants reliable models of the entire hearing organ are needed. They have to describe
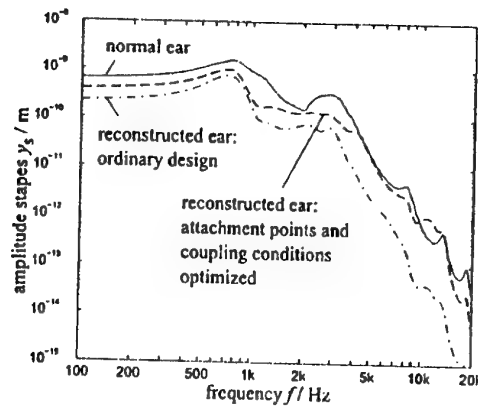
Figure 4. Comparison in the frequency response of normal ear and reconstructed ears.

the three-dimensional motion and nonlinear behavior of the mechanical structure.

References

1. J. Zwislocki. *Analysis of the middle ear function. Part I Input Impedance.* J Acoust Soc Am 1962; 34:1514-1523
2. E. A. G. Shaw, M. R. Stinson. *The Human External and Middle Ear: Models and Concepts.* In: E. De Boer, M. A. Viergever (eds): Mechanics of Hearing. Delft: University Press 1983, p. 3-10.
3. H. Wada, T. Metoki, T. Kobayashi. *Analysis of dynamic behaviour of human middle ear using a finite element model.* J Acoust Soc Am 1992; 24:319-327.
4. H.-J. Beer, M. Bornitz, H.-J. Hardtke, R. Schmid, G. Hofmann, U. Vogel, T. Zahnert, K.-B. Hüttenbrink. *Modelling of Components of the Human Middle Ear and Simulation of Their Dynamic Behaviour.* Audiol Neurootol 1999; 4:156-162.
5. P. J. Prendergast, P. Ferris, H. J. Rice, A. W. Blayney. *Vibro-Acoustic Modelling of the Outer and Middle Ear Using the Finite-Element Method.* Audiol Neurootol 1999; 4:185-191.
6. A. Eiber, W. Schirm. *Mechanics of Hearing -Dynamics of the Middle Ear-.* Proc. 2nd Polish-German Workshop March 1991 Paderborn. R. Bogacz, J. Lückel, K. Popp (eds) Warsaw: IPPT, Polish Academy of Sciences, 1991.
7. A. Eiber; H.-G. Freitag; C. Burkhard; W. Hemmert; M. Massen; H.-P. Zenner. Dynamics of Middle Ear Prostheses - Simulations and Measurements. *Audiol Neurootol* 1999;4:178-184.
8. W. Schiehlen, (ed.). *Advanced Multibody Systems Dynamics.* Dordrecht: Kluwer, 1993.
9. J.-I. Suzuki (ed.). *Middle Ear Implant: Implantable Hearing Aids.* Basel: Karger, 1988.
10. Eiber, A; Freitag, H.-G.; Hocke, T.: On the Relationship between Multifrequency Tympanometry Patterns and the Dynamic Behavior of the Middle Ear. In: Rosowski, J.; Merchant, S. (eds.), The function and Mechanics of Normal, Diseased and Reconstructed Ears. The Hague: Kugler, 2000.
11. D. Bestle. *Analyse und Optimierung von Mehrkörpersystemen.* Berlin: Springer, 1994.

86

VIRTUAL PROVING GROUND SIMULATION FOR HIGHWAY SAFETY RESEARCH AND VEHICLE DESIGN

Edward J. Haug
L. D. Chen
Yiannis Papelis
Dario Solis

Industry/University Cooperative Research Center for
Virtual Proving Ground Simulation

The University of Iowa
Iowa City, Iowa USA

Abstract

Fundamentally new ground vehicle virtual proving ground capabilities, made possible by the National Advanced Driving Simulator whose development has recently been completed by the US Department of Transportation and The University of Iowa, are presented. Highway safety research and vehicle and equipment design applications using revolutionary new virtual proving grounds are reviewed and capabilities of the simulator are summarized. Technological developments enabling these new capabilities are presented, including high fidelity real-time dynamic simulation techniques, computer image generation enhancements, precision motion control capabilities, and virtual environment modeling tools.

1. Introduction

Aircraft flight simulators have evolved to a high level of maturity during the six decades since E.A. Link invented his initial flight training simulator (Link, 1930). While flight simulators are most commonly viewed as training tools, significant use is made of advanced flight simulators in the process of aircraft development.

NASA Vertical Motion Base Flight Simulator The most advanced flight simulator shown in the left of Fig. 1 is the Vertical Motion Simulator (VMS) operated by NASA, at its Ames facility in California. This simulator has an ideal motion envelope for flight; namely travels of 60 feet vertical, 40 feet lateral, and 6 feet longitudinal. The frequency response of this flight simulator, however, is far lower than is required for ground vehicle simulation.

Daimler-Chrysler Driving Simulator The previous most advanced ground vehicle simulator shown in the right of Fig. 1 is operated by Daimler-Chrysler in Berlin, Germany (Drostol, Panik, 1985; Kading, Hoffmeyer, 1995). The motion system consists of a six-degree-of-freedom hexapod, but with somewhat lower frequency response characteristics than are ideal for ground vehicle virtual prototyping. This hexapod is mounted on a single-degree-of-freedom lateral track that moves 20 feet, providing one-dimensional braking or lane change acceleration cues, but not both simultaneously.
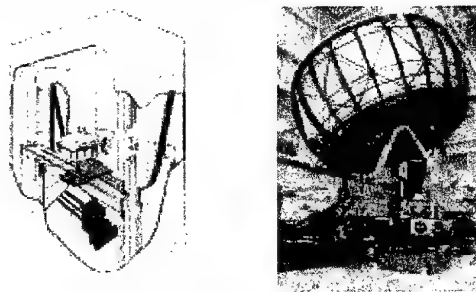
Figure 1 NASA Vertical Motion Flight Simulator and
Daimler-Chrysler Driving Simulator

Army Military Vehicle Simulators The US Army Tank-automotive and Armaments Command (TACOM) operates a family of military vehicle simulators in Warren, Michigan, with motion capabilities appropriate for harsh off-road military vehicle applications. The Turret Motion Base Simulator shown in the left of Fig. 2, supports hardware-in-the-loop simulation with a payload of 25 tons. Both this simulator and the new Ride Motion Simulator shown in the right of Fig. 2 have high frequency and acceleration capabilities that are beyond the capability of any other known ground vehicle simulator.

Figure 2 Army Military Vehicle Simulators

National Advanced Driving Simulator The National Advanced Driving Simulator (NADS) shown in the left of Fig. 3, with a view over the shoulder of the driver in the right of Fig. 3, is by far the most advanced ground vehicle driving simulator ever created. It embodies advanced technologies described in Section 2 and creates a driving environment that is within the threshold of human perception for most cues. It thus creates a fundamentally new experimental facility for driver-vehicle interaction research, supporting both highway safety and vehicle system engineering applications.

Figure 3 National Advanced Driving Simulator

The purpose of this paper is to outline (1) fundamentally new human-centered research that is enabled by the NADS and (2) technological developments that have enabled development and implementation of the NADS, the most advanced ground vehicle driving simulator ever developed. To set the stage for presentation of enabling technologies, experimental capabilities of the NADS are illustrated through description of typical experiments being carried out with the simulator.

2. The National Advanced Driving Simulator

The National Highway Traffic Safety Administration of the US Department of Transportation and The University of Iowa have created the NADS to enable research that will enhance US highway safety and vehicle system design (Haug, et. al, 1990; 1995; 1998). The Department of Transportation invested approximately $69 million in development of the NADS system, and The University of Iowa provided $11 million in software and a building to house the NADS. Development of the simulator system was completed in early 2002, and the NADS is now operational on The University of Iowa's Oakdale campus. It is being used for both highway safety research and vehicle system engineering.

The goal of the NADS project is to achieve fundamental improvements in highway safety, transportation efficiency, and effectiveness of US vehicle and equipment manufacturers. Specific objectives of the project include conduct of research using the NADS simulator that will (1) lead to safer highways, significantly reducing the number of crashes on US highways that currently lead annually to approximately 42,000 lives lost and a cost of $230 billion and (2) enhance vehicle and equipment product development effectiveness for an industrial sector that accounts for 11 percent of US Gross Domestic Product.

In a related development, the US National Science Foundation awarded a multi-university Industry/University Cooperative Research Center (I/UCRC) for Virtual Proving Ground Simulation to the Universities of Iowa and Texas-Austin in 1997. The goal of the Center during its first five years of operation was to create a virtual proving ground capability for the NADS, in order to support advanced vehicle engineering. The initial proving ground capability now operating with the NADS was created during the period 1987-2001. In early 2002, the National Science Foundation awarded the Center a second five-year grant to build upon and advance the proving grounds, carrying out advanced vehicle system engineering research with industrial and government sponsors. The universities are cooperating with the National Science Foundation, the Department of Defense, and industry to develop advanced virtual proving grounds and associated simulation research programs using the NADS that will lead to fundamental advances in vehicle and equipment product

development effectiveness. Strong support for this research has been obtained from the agricultural, construction, and off-road military vehicle and equipment manufacturing sectors.

The purpose of this section is to provide a concrete definition of the NADS system, including simulation environments that are available to researchers, and to place NADS capabilities in context with existing ground vehicle driving simulators. The NADS, as it currently exists on the University of Iowa campus, is shown in the left of Fig. 3. The NADS contains nine advanced technology modules that interact with the driver to create a highly realistic simulated driving environment, as follows.

Visual System A revolutionary new Evans & Sutherland Harmony visual system provides the driver with a highly realistic 360-degree field of view, similar to the environment shown in the right of Fig. 3, including rear view mirror images. The visual system database includes a full range of current and new highway traffic control devices (signs and signals), three-dimensional objects that vehicles encounter (animals, potholes, concrete joints, pillars), high-density multiple-lane traffic interacting with the driver's vehicle, common intersection types, and roadway weather environments.

Motion System The motion system shown in the left of Fig. 3 provides the largest translational motion envelope ever developed for a driving simulator (64 feet square). It also provides 360-degree horizontal yaw, as well as pitch, roll, and high-frequency cues that duplicate vehicle motion cues to the driver, over the full range of driving maneuvers.

Control Feel System Control feel systems for steering, brakes, clutch, transmission, and throttle provide the driver with a realistic feel of the road and vehicle response to driver inputs, over the full vehicle maneuvering and operating range. The control feel system is capable of representing control characteristics such as power steering, existing and experimental drivetrains, anti-lock braking systems, and headway control systems.

Audio System The audio system provides realistic three-dimensional sound sources that are coordinated with other sensory systems. The audio database includes sounds emanating from current and new design highway surfaces, contact with three-dimensional objects that vehicles encounter (potholes, concrete/tar joints, etc.), high-density multiple-lane traffic, and vehicle operation (engine, brake, wind noise, and weather effects).

Vehicle Dynamics High fidelity vehicle dynamics software provided by The University of Iowa accurately represents vehicle motions and control feel conditions in response to driver control actions, road surface conditions, and aerodynamic disturbances. Vehicle dynamics models of the scope shown in the left of Fig. 4 simulate light passenger cars and trucks, heavy trucks and buses, and off-road wheeled and tracked vehicles. The models encompass normal driving conditions and extreme maneuvers encountered during crash avoidance situations, including spinout and incipient rollover. More detail is provided in Section 4.

Scenario Authoring The NADS scenario control and authoring module developed by The University of Iowa simulates, in real time, traffic elements such as passenger cars, motorcycles, trucks, buses, rail-based vehicles and pedestrians, each with autonomous, reactive behaviors (see illustration on right of Fig. 4). Specialized runtime agents simulate operation of traffic control devices, weather effects including wind and fog, and ambient traffic around the simulator driver. A suite of Windows NT-hosted graphical tools allows rapid development of scenes and scenarios, without explicit programming, for use by experimenters to develop and test scenarios before proceeding to the NADS facility.
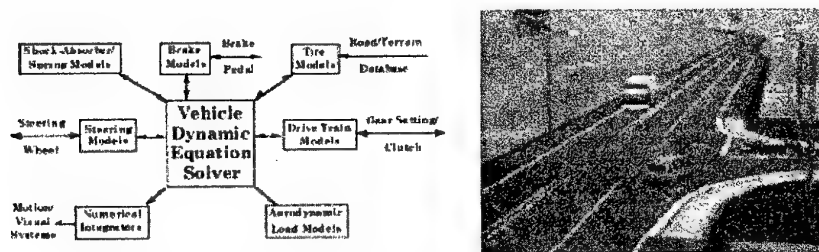
Figure 4 Real-Time Vehicle Dynamics and Scenario Authoring Software

Vehicle Cab System Vehicle cabs in which the driver functions consist of actual vehicle cabs, configured to fit within the visual dome on the motion system. Four cabs were initially delivered with the NADS system, including cabs for a Chevrolet Malibu, Ford Taurus, Jeep Cherokee, and class-8 Freightliner truck. The cabs have a full range of standard, optional, and new design vehicle instrumentation interfaces. Cabs allow rapid interchangeability, in order to meet an unprecedented high experimental efficiency during NADS operation.

Computer System A system of dozens of computers control all aspects of NADS operations. Databases defining vehicle characteristics, the visual driving environment, audio characteristics of the environment, and

89

roadway characteristics that influence performance of the vehicle are highly integrated, to enable the researcher to create and supervise controlled experiments.

Simulation Development Module A NADS-like simulator, called the simulation development module for off-line development of experiments and virtual environments, contains all the basic elements of the NADS except motion. This very capable unit operates separately from the motion-based NADS simulator, thus enabling experimenters to cost-effectively preview scenarios and drive through scenes to assure themselves that the experiment is well structured before carrying out experiments on the full NADS system.

3. Nads-Based Virtual Proving Ground Experiments

Since its initiation of operation in early 2002, three sets of experiments have been carried out to initiate highway safety and virtual proving ground engineering applications. The first set of experiments involved verification of simulator performance in highway safety crash avoidance limit maneuvers; i.e., spin-out and related vehicle maneuvers in the NADS shown in Fig. 5 that represent extreme limits of vehicle performance with interaction of the driver. Qualitatively excellent results have been obtained, correlating well with quantitative measures of performance of the vehicle. These results provide the foundation for a current set of highway safety experiments being carried out by The University of Iowa for the U.S. National Highway Traffic Safety Administration.
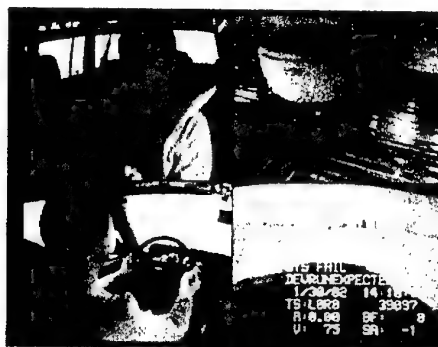
Figure 5 Highway Safety Crash Avoidance Limit Maneuvers

The initial virtual proving ground experiment involved linking the NADS shown in the right of Fig. 6 with the Army Ride Motion Simulator shown in the left of Fig. 6, to demonstrate the feasibility of high fidelity engineering simulator interaction, coupled with computer-aided engineering design change analysis and verification with the driver in the loop. Army and NADS test drivers operated high fidelity simulated vehicles on a simulated Army proving ground, including the capability to see each other's vehicle and interact. In addition to achieving excellent network-based interaction of engineering fidelity simulations, design characteristics of the vehicle functioning in the Ride Motion Simulator were modified in a CAE environment as the simulations occurred, to evaluate the driver's interaction with nominal and modified vehicle designs. Results indicate the feasibility of (1) interactive simulation of vehicle designs with the driver in the loop, and (2) greatly reducing the time required for vehicle system development.

Figure 6 Interactive Simulation with Engineering Fidelity RMS and NADS

A second virtual proving ground experiment that was carried out in early April, 2002, focused on validation of a NADS-based agricultural virtual proving ground. This project, carried out with Deere & Co., involved a John Deere tractor, shown in the upper left of Fig. 7, with the NADS simulator cab shown below the tractor. The tractor and a proving ground were modeled at an engineering level of fidelity, and experiments were carried out on the actual proving ground shown in the center of Fig. 7. The model created of the tractor was exercised, with

90

the operator in the loop, on the simulated proving ground in the NADS, as shown in the right of Fig. 7. Initial qualitative and quantitative performance analysis indicates that an adequate level of correlation exists between the actual and virtual proving ground to form the basis for equipment design and evaluation using the virtual proving ground.

Figure 7 Validation of NADS-Based Agricultural Proving Ground Simulation

4. Technologies Enabling Vehicle Virtual Proving Grounds

Technologies that enable design-level-of-fidelity virtual proving grounds are summarized in this section. They include computational methods for high fidelity dynamics and tire-road surface/terrain interaction, synthetic environment modeling for on- and off-road simulation, and managing databases and synthetic environment modeling tools.

High Fidelity Dynamics

Even though the human can respond cognitively only to cues in a frequency range up to 2-5 Hz, transient events lead to the requirement that actuators and controllers with which the driver interacts must accurately predict transient dynamic effects at high frequency. For example, large transient forces that can arise in operation on rutted roads require high frequency compensation in the steering system, in order to avoid serious problems with the driver's ability to control the vehicle. Such control systems often respond with transients involving frequencies up to 100 Hz.

Similarly, anti-lock brake and active suspension systems experience response of the wheel assembly up to 20 g, leading to transient effects requiring controller compensation in excess of 80 Hz. Even though hydraulic pulse rates in anti-lock brakes are typically below 7 Hz, the reaction times of controllers and actuators are typically below 20 milliseconds. Since such components interact to first order with wheel spin, which contains stiff transients, one millisecond or less numerical integration step size is required in simulation with explicit numerical integrators to predict anti-lock brake subsystem performance that influences the driver's ability to control the vehicle. This translates to a frequency content above 80 Hz. Similarly active suspension performance in the presence of potholes and short wavelength roadway undulations such as rumble strips requires that frequencies of 50 Hz or more be accounted for in designing the control system to maintain vehicle control by the driver.

Automated Highway System concepts of the future place an even greater demand on high simulation fidelity for support of device design to interact effectively with the driver. The automotive design industry will accept a driving simulator for use in subsystem design on a virtual proving ground only if extremely high fidelity, equivalent to a frequency response up to 100 Hz, is accounted for in subsystem simulations.

Real-Time Modeling And Simulation Methods Innovative vehicle design technologies based on advanced control algorithms are commonly used in modern vehicles to achieve optimum power transfer from mechanical and electromechanical powertrains through the wheels to the road. The interaction between the tires and the road is governed by multiple sources of high frequency excitation coming from roughness of the road profile, tire flexible modes of vibration, and powertrain actuator response. In order to resolve this high frequency content, high fidelity dynamic algorithms, coupled with modern and efficient numerical integration techniques (Haug, Deyo, 1991), are necessary to guarantee the stability of the numerical solution used to predict motion cues for the driver within the simulator environment. In emerging vehicle subsystems such as hybrid-electric powertrains, the vehicle system engineer will be required to conduct human factors and engineering based studies on the interaction of such subsystems with the driver. These systems are very demanding in terms of the numerical approach used to accurately predict their transient performance.

For the foregoing reasons, advanced dynamics formulations and implicit and multirate numerical integration techniques have been developed and tested for use in the NADS. Advanced numerical methods presented in a Special Session of the 1998 ASME Design Automation Conference (Serban, Haug, 1998; Solis, Schwarz, 1998)

91

provide some of the capability required for simulating modern high frequency vehicle subsystems for design in a virtual proving ground.

In order to determine what vehicle modeling and simulation features are normally used by vehicle manufacturers during analysis and design, NADS and LMS International held a two-day workshop October 25 and 26, 2001. During this workshop, it was found that the on-road vehicle developer community was calling for better representation and integration of flexible bodies into the vehicle models, and for higher fidelity bushings, shock absorbers, and tire component models. Some of the manufacturers do not even consider vehicle models without bushings for their dynamic evaluations. For this reason, a task to develop numerical techniques to efficiently deal with bushings in vehicle simulation was started. Implicit integrators with exact Jacobian matrices for bushing elements were formulated and are currently being implemented to address the real-time simulation of vehicle models containing bushings. Body flexibility, normally left for nonreal-time simulation analysis, is being included into current simulation codes at NADS to allow for body compliance that affects vehicle performance and its interaction with the driver.

Tire-Road/Soil Interface To meet virtual proving ground goals of simulating both on- and off-road vehicles at a design level of fidelity, a capability that includes not only driving vehicles over hard rigid soils but also over soft deformable soils must be provided. One of the key core technology developments required to achieve this capability is significantly enhanced tire/soil interaction modeling. This technology requires development in three main thrusts; (1) flexible tire-hard soil interaction, (2) rigid tire-deformable soil interaction, and (3) flexible tire-deformable soil interaction. Focusing the technology development in this fashion helps identify critical elements during vehicle simulation over highways and compact rural roads, mild off-road applications, and severe soft terrain off-road applications.

Within thrust (1), kinematic tire information calculated by the multibody dynamics module is coupled with terrain profile information to compute forces generated at the tire-road interface. Longitudinal and lateral forces at the tire-road interface are computed based on the slip developed in the respective directions. Normal forces are computed using geometrical information that is given in terms of position and velocity of the wheel hub and shape of the terrain profile under each wheel, and combining it with stiffness and damping of the tire. The approach in this thrust is the most commonly used for both on and off-road vehicle simulation, due to the large percentage of applications for which the rigid terrain assumption is applicable. Also, it involves the tire but not the soil, which is more difficult to represent. The complexity of the models under this thrust is a function of the amount of compliance and vibration modes in the tire. Its compliance is due to the amount of deformation and the existence of vibration modes depends on the size and type of tire.

Figure 8 shows three contact models for thrust (1). Single point contact queries the terrain at the point directly below the wheel attachment point. The intersection between the tire profile and the terrain determines the tire deformation length that is used to compute the normal force. This approach is widely used for on-road flat surfaces but is not recommended for off-road applications.
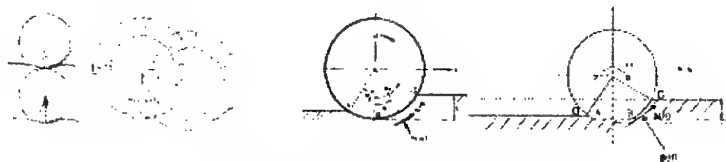
Figure 8 Wheel/Tire-Soil Contact Models

The distributed contact model, queries the terrain in multiple points under the wheel attachment point to determine the shape of the contact. An averaging technique is then used to calculate the effective contact force between the tire and the terrain. The number of segments in the model is chosen based on the roughness and spatial frequency of the terrain.

The 2D model shown in the left of Fig. 8 is based on a finite element representation using beam elements for both radial and tangential members. This model allows for a distributed stiffness parameter representation of the tire that can be used to improve the single-parameter model used in the two previous models. It also includes tire inertial effects, which are critical for many applications.

Thrust (2) concentrates on applications for which tire deformation is small compared to soil deformation. Analytical soil mechanics equations are used to compute tire forces due to deformation. This is made known by the simple shape of the undeformed tire, which greatly simplifies the calculation. The right of Fig. 8 shows a schematic of a rigid-wheel on deformable terrain. Variations of this approach include the addition of a tire deformation section of known geometry. This known shape still allows for the integration of the normal

92

pressure exerted by the soil on the tire using analytical expressions and provides a correction for tire deformation that extends the applicability of this approach to relatively harder soils or tires with lower pressures.

Finally, thrust (3) addresses the more general problem of deformable tire and soil. A general nonlinear finite element approach is applied to solve for forces generated within the tire-soil interface and the resulting terrain profile deformation, as shown in the left of Fig. 9. The on-going activity to develop a better predicting capability for off-road vehicle simulation is targeting the soil formulations needed in the finite element representation for different soil types. This high-fidelity model is being used to improve the understanding of the traction phenomena and to develop better real-time models. This thrust also supports determining the trafficability of off-road vehicles over a given terrain.
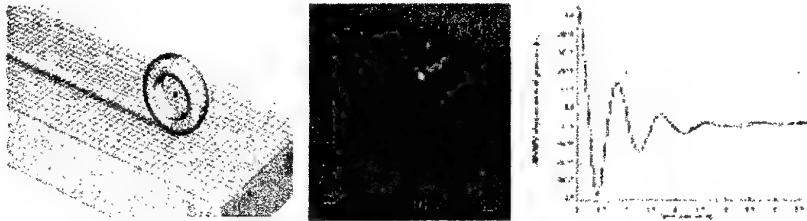
Figure 9 Flexible Tire-Soil Model and Integrated High-Fidelity Simulation Environment

Vehicle System/Subsystem Simulation For Design Due to the increasing complexity of vehicle and component design, as well as the nature of technologies that are being integrated into modern vehicles, the traditional design approach that depends on building and testing many physical prototypes is not a cost effective approach for vehicle product development. The simulation-based-design approach has varying degrees of implementation that range from modeling and simulating components, such as antilock brakes and headway control devices, to modeling, simulating, and integrating an entire vehicle system. Depending on system complexity and size, this integrated environment requires a large amount of computational resources to produce a solution in a timely manner. Complete vehicle systems are now being used to reduce the number of physical tests in the design optimization process. In off-road applications, recent developments in tire-soil modeling and simulation coupled with integrated vehicle simulation environments have enabled a higher degree of dynamic predictability for complete vehicle systems. This new capability is being used with good results on rigid surfaces but further development is necessary to incorporate the soil compliance more effectively. The right side of Fig. 9 shows a settling run of a High Mobility Multipurpose Wheeled Vehicle model simulated in DADS, integrated with four high-fidelity tires modeled using the ABAQUS software.

Synthetic Environments

The creation of realistic synthetic driving environments poses many challenges (Cremer, Kearney, Papelis, 1996). In particular, driving simulation requires scene databases of large geographic regions with properly modeled roads, high-fidelity terrain, natural foliage, and appropriate cultural features. Because of the nearness of surroundings, synthetic driving environments must be modeled at a much higher resolution than flight terrain databases. Synthetic environments must also support the creation and execution of scenarios involving vehicular and pedestrian traffic that meet experimenter requirements (Cremer, et al., 1994). The NADS synthetic driving environment comprises multiple correlated databases, each providing data about the same synthetic environment, but in views that are specialized to the interrogating subsystem. Specialized views are provided to support image generation, autonomous traffic elements, audio cue generation, vibration special effects, and tire-road interface.

On- and off-road applications have differing database requirements. For example, road surfaces are typically hard, allowing use of static database structures for roadway networks. In contrast, off-road terrain must be able to support real-time terrain updates corresponding to tire rut generation and other ground-vehicle interactions. Furthermore, road surfaces are typically much smoother and more well defined than off-road terrain. This results in the use of different representations for on- and off-road surfaces. On-road modeling is well developed, building directly on substantial experience gained with a previous generation of simulator. Accurate real-time modeling of dynamic off-road synthetic environments is less well developed. The following briefly summarizes the features of NADS on- and off-road synthetic environments being created.

On-Road Synthetic Environment The most complex view of the NADS synthetic environment database is the Virtual Roadway Environment Database (VRED), which contains information about the logical and physical layout of roadways and can manage real-time interrogation of static and dynamic objects. Logical roadway information encompasses enough detail to support navigation and conforming to traffic rules. It includes the number, direction, and type of lanes, including standard, automated highway systems, and high-occupancy

93

vehicles; the nature of lane separators; shoulder information; road markers; and a complete intersection model that supports an arbitrary number of incident roads.

The physical roadway representation incorporates a hybrid model that uses three-dimensional splines with two-dimensional continuity for the roadway surfaces and a uniform grid of elevation and material posts used for intersections, special effects, and other non-standard roadway terrain. Any number of disjoint elevation grid maps can be included in a synthetic environment, and they can overlap the splinar representation. Road holes, seams, or other localized perturbations can be modeled using overlapping terrain. The splinar representation utilizes two independent splines, one for the longitudinal roadway axis and one for the lateral axis. The lateral spline can change at any point along the longitudinal axis, allowing modeling of arbitrary variations in road geometry. To support real-time interrogation of the terrain elevation by the tire module, VRED uses specialized data structures that utilize two-dimensional hashing algorithms to quickly access the spline or grid parameters.

Off-Road Synthetic Environment The terrain database component of the NADS synthetic environment provides a high-resolution representation of ground surface characteristics, including elevation, surface type, roughness, and friction, for both on-road and off-road applications. Off-road applications involving driving over extended regions of soft soil present severe modeling challenges. First, the drivable area that must be represented at high resolution generally becomes greater when vehicles are permitted to leave the confines of well-defined road paths. Second, off-road applications involving agricultural, construction, and military vehicles often involve dynamic interaction of wheels and soft soil, thus making it necessary to support real-time update of the terrain database, as determined by the tire-soil interaction subsystem. Third, some applications include significant interactions between the ground and parts of the vehicle other than the tires, such as when rocks or bumps impact the vehicle undercarriage. Thus, off-road synthetic environments must support detection and characterization of geometric contact between vehicles and the ground and other objects.

These requirements make real-time modeling of off-road environments a considerable challenge. It is not feasible, for visual display purposes, to represent the entire database at the highest required resolution. Researchers are developing dynamic terrain modeling techniques based on variable resolution meshes that may be updated in real time as terrain updates are computed. The techniques being developed require tight integration of the terrain and visual databases, in order to achieve real-time display of terrain updates at appropriate fidelity.

Management Of The Synthetic Environment An arbitrary number of static and dynamic objects are managed in real time within the synthetic simulator environment (see the right side of Fig. 4). Static objects that are used to model traffic signs, poles, vegetation, structures, or any other necessary obstruction can be associated with a particular location on a road, or on off-road terrain. Dynamic objects represent participants that can move freely. VRED is responsible for storing the state of moving objects and providing, in real time, information about their location with respect to a specialized network coordinate system. For on-road applications, this coordinate system utilizes the road, lane, and parameterized distance along a road as the three coordinates for locating objects in space. Autonomous object behaviors use this coordinate system, because it is much simpler (and computationally cheaper) to compare the relative position of vehicles along a roadway by using the parameterized distance, as opposed to using vector-based methods. For off-road applications, the situation is more complex and remains to be investigated.

Authoring Synthetic Environments The creation of synthetic on-road driving environments containing road networks that are consistent with civil engineering standards is a difficult process that requirs substantial effort by scene database specialists. Researchers are developing tools to support rapid construction, modification, refinement, and debugging of scene databases.

5. Conclusions

High-fidelity real-time simulation capabilities and emerging ground vehicle driving simulators outlined in this paper provide the foundation for vehicle subsystem and system virtual proving grounds, at a design level of fidelity. Together with the virtual proving ground simulation capability enabled very recently by the National Advanced Driving Simulator for real-time interaction of the vehicle and driver, a revolutionary new environment is now available for designing and testing vehicle subsystems and components. Realistic load histories obtained from vehicle system virtual proving ground simulations can now be used to design and test component hardware in the laboratory. This new capability serves two purposes; (1) it improves component design and testing by generating realistic duty cycle information early in the design cycle, and (2) it provides hardware measurements to validate on-line models to improve overall simulation accuracy and realism.

References

Cremer, J., Kearney, J., and Papelis, Y., 1996, "Driving Simulation: Challenges for VR Technology", IEEE Computer Graphics and Applications, pp. 16-20.

Cremer, J. Kearney, J., Papelis, Y., and Romano, R., 1994, "The Software Architecture for Scenario Control in the Iowa Driving Simulator", Proceedings of the 4th Computer Generated Forces and Behavioral Representation Conference, pp. 373-381.

Drostol, J., and Panik, F., 1985, "The Daimler-Benz Driving Simulator-a Tool for Vehicle Development", SAE Paper No. 850334.

Grant, P., Freeman, J. S., Vail, R., and Huck, F., 1998, "Preparation of a Virtual Proving Ground for Construction Equipment Simulation", ASME Design Automation Conference, Special Session on Virtual Proving Ground Simulation.

Haug, E.J., et. al,1990, Feasibility Study and Conceptual Design of a National Advanced Driving Simulator, Report DOT-HS-807586, National Highway Traffic Safety Administration, Washington, DC.

Haug, E.J., Choi, K.K., Kuhl, J.K., and Wargo, J.D., 1995, "Virtual Prototyping Simulation for Design of Mechanical Systems," Journal of Mechanical Design, Vol. 117, pp. 63-70.

Haug, E. J., Cremer, J., Papelis, Y., Solis, D., and Ranganathan, R., 1998, "Virtual Proving Ground Simulation for Vehicle Design", ASME Design Automation Conference, Special Session on Virtual Proving Ground Simulation.

Haug, E.J., and Deyo, R.C. (eds.), 1991, Real-Time Integration Methods for Mechanical System Simulation, Springer-Verlag, Heidelberg.

Kading, W., and Hoffmeyer, F., 1995, "The Advanced Daimler-Benz Driving Simulator", SAE Paper No. 950175.

Link, E.A., 1930, " Combination Training Device for Student Aviators and Student Entertainment Apparatus", US Patent Specification 127,82.

Serban, R., and Haug, E. J., 1998, "Globally Independent Coordinates for Real-Time Vehicle System Simulation", ASME Design Automation Conference, Special Session on Virtual Proving Ground Simulation.

Solis, D., and Schwarz, C., 1998, " Multi-Rate Integration in Hybrid-Electric Vehicle Virtual Proving Grounds", ASME Design Automation Conference, Special Session on Virtual Proving Ground Simulation.

THE DEVELOPMENT OF A REAL-TIME MULTIBODY VEHICLE DYNAMICS AND CONTROL MODEL FOR A LOW COST VIRTUAL REALITY VEHICLE SIMULATOR: AN APPLICATION TO ADAPTIVE CRUISE CONTROL

SUNG-SOO KIM, MOONCHEOL WON, B. SOHN, K. SONG, S. JUNG
Department of Mechatronics Engineering, Chungnam National University
220 Kung-Dong, Yusong-Ku, Daejeon, 305-764, Korea

Abstract

In this paper, a real-time multibody vehicle dynamics and control model has been developed for a PC based low cost virtual reality vehicle simulator in the application to ACC (Adaptive Cruise Control). The model consists of a scenario module for preceding vehicle motions, a control module including an ACC logic based on sliding mode control, and a throttle/brake switching logic, and a real-time multibody vehicle dynamics module based on the subsystem synthesis method. For a virtual environment implementation, a graphic modeling tool, 3D Studio Max, and a real-time rendering tool OpenGVS are used. To verify the effectiveness of the developed model, typical ACC simulations such as cut-out, cut-in, stop-and-go have been carried out.

1. Introduction

The concept of the ACC system is shown in Fig. 1. ACC system controls the throttle valve and the brake master cylinder to maintain a desired space between the preceding vehicle and the ACC vehicle. To evaluate performance of the ACC system and driver's response to the intelligent vehicles, a vehicle simulator with a virtual reality feature can be a very effective tool. For such a vehicle simulator, a real-time vehicle dynamics and control model is essential.

The purpose of this paper is to propose a real-time integrated vehicle dynamics and control model for a virtual reality vehicle simulator, especially in the application to ACC simulations.
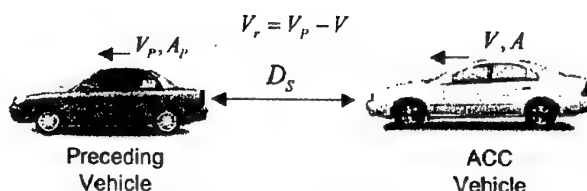
Figure 1. ACC Concept

2. Real-time Multibody Vehicle Dynamics and Control Model

The computational model for real-time vehicle dynamics and control consists of three modules, i.e., a preceding vehicle movement scenario module, a control module that includes

96

the ACC logic and the throttle and brake switching logic, and a real-time multibody vehicle dynamics module. The preceding vehicle movement scenario module generates the preceding vehicle motion for the control module. With the preceding vehicle motion and the ACC vehicle states from the vehicle dynamics module, the control module computes required throttle angles and brake angles for the real-time vehicle dynamics module.

2.1. REAL-TIME MULTIBODY VEHICLE DYNAMICS MODEL

The vehicle model used in this paper is HMMWV (High Mobility Multipurpose Wheeled Vehicle) [1]. HMMWV model consists of 4 independent SLA (Short-Long Arm) suspension subsystems, a power-train subsystem, STI tire subsystem [2], a rack and pinion steering subsystem, a brake subsystem, and a real-time multibody vehicle dynamics equation generator that is based on the subsystem synthesis method [3]. To use the subsystem synthesis method, the vehicle model is decomposed into 4 suspension subsystems and a chassis as shown in Fig. 2. For each suspension subsystem, the closed loop subsystem equations of motion can be obtained using the recursive formulation in multibody dynamics.

$$\begin{bmatrix} \mathbf{M}_{qq} & \mathbf{\Phi}_{\bar{q}}^T \\ \mathbf{\Phi}_{\bar{q}} & \mathbf{0} \end{bmatrix} \begin{bmatrix} \ddot{\mathbf{q}} \\ \lambda \end{bmatrix} = \begin{bmatrix} \mathbf{P}_q \\ \gamma \end{bmatrix} - \begin{bmatrix} \mathbf{M}_{yq}^T \\ \mathbf{0} \end{bmatrix} \dot{\mathbf{Y}}_0 \tag{1}$$

For the chassis, 6x6 matrix form of equations of motion can be expressed as follows;

$$(\hat{\mathbf{M}}_0 + \sum_{i=1}^{4} \breve{\mathbf{M}}_i) \dot{\hat{\mathbf{Y}}}_0 = (\hat{\mathbf{Q}}_0 + \sum_{i=1}^{4} \breve{\mathbf{P}}_i) \tag{2}$$

where $\breve{\mathbf{M}}_i$ and $\breve{\mathbf{P}}_i$ (i=1~4) are the effective inertia matrix and the effective force vector of each subsystem, respectively [3]. In the subsystem synthesis method, 6x6 matrix form of chassis equations of motion, as shown in Eq. 2, is first solved. Then, for each suspension subsystem, equations shown in Eq. 1 are solved for suspension acceleration. Since several small size equations of motion are solved instead of solving large size equations, the subsystem synthesis method provides computational efficiency.

2.2. ACC CONTROL MODEL

Fig. 3 shows the computational flow in the control module. Sliding mode control is used to design a spacing controller for ACC [4]. According to relative distance between the preceding vehicle and the ACC vehicle, the required engine or brake torque is calculated. Using throttle and brake switching logic, either throttle or brake control is determined [5]. In the throttle control, inverse torque map is used to compute the desired throttle pedal angle. In the brake control, necessary torque and the corresponding desired brake pedal angle are computed. These pedal angles are the inputs of real-time multibody vehicle dynamics model. In this control model, the headway time control strategy is utilized to design the desired relative distance. The head way time is defined as the time that the ACC vehicle collides with the preceding vehicle, when the preceding vehicle stops immediately. According to the headway time strategy, the desired vehicle spacing, x_{r_des} is obtained from

$$x_{r\_des} = v_f \cdot t_h \tag{3}$$

where v_f is the following ACC vehicle speed, and t_h is headway time. The desired acceleration is also obtained as [4];

$$a_{f\_des} = \frac{v_r - \lambda\, Sat(\frac{s}{\Phi})}{t_h}$$ (4)

where v_r is the relative velocity, λ is a positive gain, $Sat(.)$ is the saturation function, s is the sliding surface defined as $s = x_{r\_des} - x_r$, and Φ is the boundary layer thickness. The saturation function is used to have better riding quality by preventing wild throttle movement. In order to prohibit jerking motion of the ACC vehicle, the desired acceleration a_{f_des} is bounded between $1 m/s^2$ and $-2.5 m/s^2$.
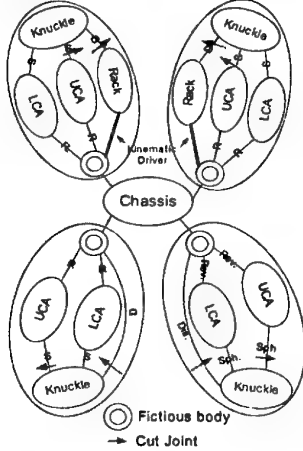
Figure 2. Topology of vehicle model with subsystems
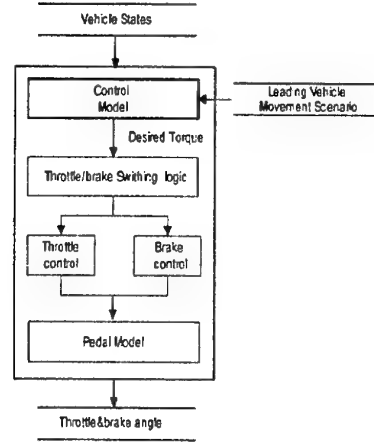
Figure 3. Control module flow chart

The desired engine torque corresponding to the desired acceleration in Eq. 4 can be obtained using simplified vehicle equations of motion and the simple engine model [4].

$$T_{eng\_des} = [J_{eff} \cdot (\frac{v_{f\_des}}{H_r \cdot r_{drive} \cdot r_{gear}}) + H_r \cdot r_{drive} \cdot r_{gear}(F_a + F_r)] / r_{tq}$$ (5)

where H_r is the tire radius, r_{drive} is final drive gear ratio, r_{gear} is current gear ratio, r_{tq} is the torque ratio in the torque converter, J_{eff} is the effective total inertia from the engine, F_r is rolling resistance and F_a is aerodynamic drag.

After obtaining the desired engine torque, throttle and brake switching logic is applied to determine whether engine braking or active braking is necessary. If the amount of the desired torque is smaller than that of the torque generated from engine brake, then active braking is applied. Once engine braking or active braking is determined, the desired throttle angle, α_{des}, is obtained from the inverse engine performance map.

$$\alpha_{des} = T^{-1}_{eng}(\omega, T_{eng\_des})$$ (6)

For active braking, the necessary brake torque is computed in Eq. 7 and the brake pedal angle can be obtained from the linear relationship between the braking torque and pedal angles.

$$T_{b\_des} = \frac{T_{net} - T_{net\_des}}{r_{drive} \cdot r_{gear}}$$ (7)

where T_{b_des} is the necessary braking torque, T_{net_des} is the desired torque to maintain desired relative distance and T_{net} is the engine brake torque that is generated with zero throttle angle in the current engine speed.

3. A Low Cost Virtual Reality Vehicle Simulator

A PC based low cost virtual reality vehicle simulator is shown in Fig. 4. The simulator consists of two PCs (one for real-time vehicle dynamics and control, and the other for real-time graphic rendering), a visualization system such as a beam projector, and a vehicle cockpit. Two PCs are networked using TCP/IP. Every 40mili-seconds, vehicle states are transferred to the graphic PC to generate 25 frame/s display rate.

To generate virtual reality environment, a graphic modeler 3D Studio Max, a real-time rendering scene generator OpenGVS have been employed. Fig. 5 shows the virtual environment for ACC simulations.

Figure 4. A low cost vehicle simulator

Figure 5. Virtual reality graphic scene

4. ACC Simulations

In order to verify the developed multibody vehicle dynamics and control model, typical simulations for the ACC vehicle have been carried out; i.e., stop-and-go, cut-in, and cut-out simulations. Fig. 6 shows the results of stop-and-go simulations. In this simulation, the preceding vehicle makes a complete stop and then restarts. The first figure of Fig. 6 shows that the ACC vehicle properly follows the preceding vehicle. The second figure of Fig. 6 shows the acceleration and brake pedal angles. It shows that the switching logic in ACC is properly working.
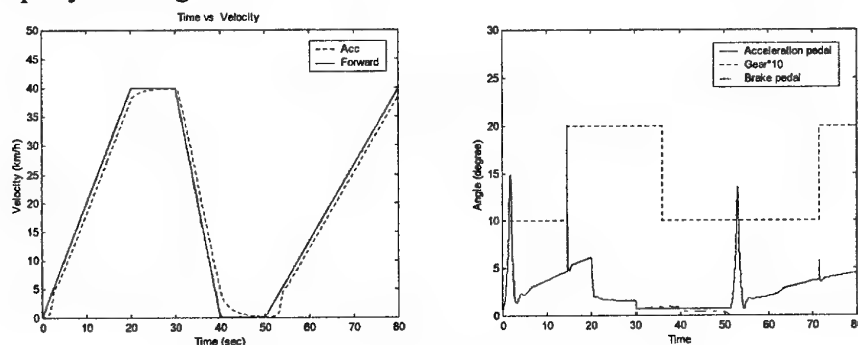
Figure 6. Stop-and-go Simulation

Cut-out simulations have been also carried out as shown in Fig. 7. In the cut-out situation, two preceding vehicles run ahead of the ACC vehicle. The second vehicle (V2), which is just in front of the ACC vehicle, changes lane. Thus, the ACC vehicle suddenly has to follow the first vehicle (V1). In this case, the ACC vehicle experiences sudden changes in the relative position and the relative velocity between the ACC and the preceding vehicles. The first figure of Fig. 7 shows the velocities of the preceding vehicles and the ACC vehicle.

99

After the lane change occurs, the ACC vehicle accelerates itself to and then keeps the constant velocity that is larger than that of the preceding vehicle (V1) to maintain the desired distance. The second figure of Fig. 7 shows the relative distance between the preceding and the ACC vehicles. The ACC vehicle gradually recovers the desired distances.
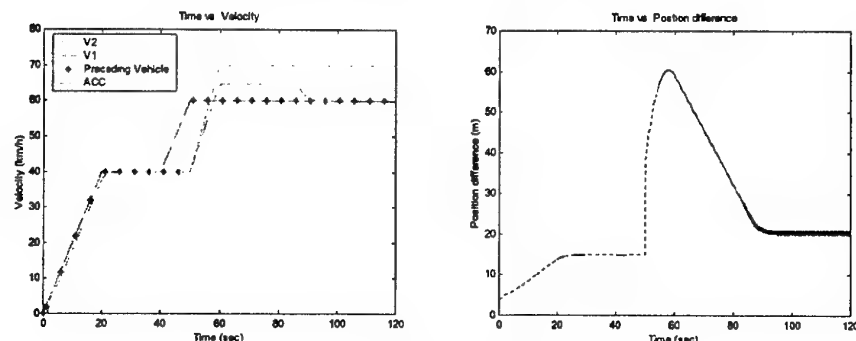
Figure 7. Cut-out simulation

Cut-in simulations have been also carried out. In this situation, during the ACC vehicle follows the preceding vehicle with constant speed, the other vehicle with the same speed in the next lane abruptly cuts in between the preceding and the ACC vehicles. The first figure of Fig. 8 shows the velocities of the ACC vehicle. After cut-in occurs, the ACC vehicle slows down a little bit. The second figure of Fig. 8 shows the relative distance between the preceding and the ACC vehicles. Due to cut-in at 50 sec., the relative distance is suddenly reduced. According to the headway time strategy, relative distance is increased back to the original distance within 10 seconds.
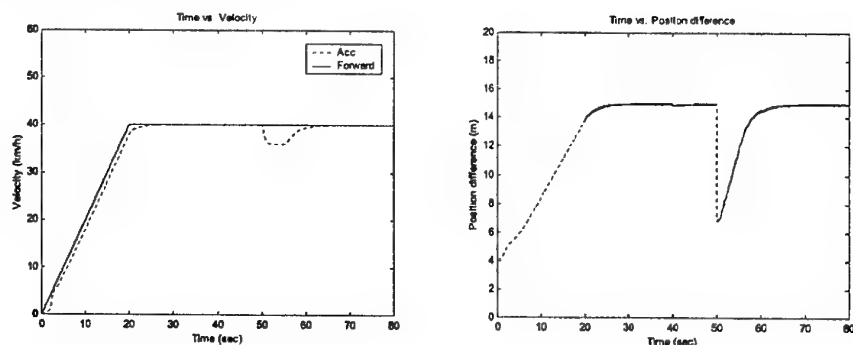
Figure 8. Cut-in simulation

To see the real-time capability of the developed model, CPU time has been measured in Pentium IV 1.6 Ghz CPU with RAM 256 Mb. For 120 second overall simulation time, 5.23 seconds computational CPU time has been measured. For numerical integration, Adams Bashforth 3rd order formula is used with 8 ms integration step size. This proves the developed model indeed has a real-time simulation capability.

100

5. Conclusions

A real-time multibody vehicle dynamics and control model has been developed for a low cost virtual reality ACC vehicle simulator. Subsystem synthesis method is employed to generate efficient multibody vehicle equations of motion. The sliding mode control and throttle/brake switching logic are used for the ACC. Several simulations such as stop-and-go, cut-in, and cut-out, show that the developed model is suitable for ACC simulations. The CPU time measure proves the real-time capability of the proposed model.

6. References

1. Aardema J. (1989) Failure analysis of the Lower Rear Ball Jiont on the High-Mobility Multipurpose Wheeled Vehicle (HMMWV), *Technical report 13337*, RDE center, U.S. Army.
2. Allen R. Wade, Raymond E. Magdaleno, Theodore J. Rosenthal, (1995) Tire Modeling for Vehicle Dynamic Simulation, *SAE Paper No. 950312*,
3. Kim, Sung-Soo. (2002) A subsystem Synthesis Method for Efficient Vehicle Multibody Dynamics. *Multibody System Dynamics*, **7(2)**, 189-207.
4. Won M., Kim S-S., Kang B.B., and Jung H.J. (2001) Test Bed for Vehicle Longitudinal Control Using Chassis Dynamometer and Virtual Reality: An Application to Adaptive Cruise Control, *KSME International Journal*, **15(9)**, 1248-1256.
5. Lee S., Hong J., and Yi K. (2001) A Modeling and Control of Intelligent Cruise Control Systems", *Transactions of the Korean Society of Mechanical Engineers A*, **25(2)**, 286-288.

Dynamics and Stability of Spaghetti and Reverse Spaghetti Problems Coupled with Fluid Force

Nobuyuki KOBAYASHI ; Professor, E-mail; kobanobu@me.aoyama.ac.jp
Masahiro WATANABE ; Associate Professor, E-mail; watanabe@me.aoyama.ac.jp
Takamune IRIE and Keisuke KOZONO ;   Graduate Student,
Department of Mechanical Engineering, Aoyama Gakuin University,
6-16-1 *Chitosedai, Setagaya-ku, Tokyo,* 157-8572, *Japan*

ABSTRACT

The dynamic behavior of a flexible beam that is pulled into and drawn out of a gap in an elastic wall with a constant velocity is studied using a mechanical model and experiments. We focus particularly on the effects of the guide in front of the inlet of the gap and the fluid force on these behaviors. Our simulation model is verified to simulate well the behavior of beam when the guide is provided in front of the inlet. In the case of the drawing out the beam, we found out that the fluid force works to be the beam destabilized, and the divergence type instability phenomena is caused in the beam due to the fluid force when the driving velocity is high and the density of the fluid is also high through numerical simulations.

1. INTRODUCTION

We all know that if we rapidly snuck a spaghetti noodle into our mouth, the end tip of it comes to vibrate in amplitude more heavily as the length of free end becomes shorter. This phenomenon is called the *Spaghetti Problem* [1]. A similar phenomenon is observed in mechanical systems when a flexible beam or plate is pulled axially into a gap in a wall with a large driving velocity, as displayed by several industrial machines; e.g., machines that coil thin steel plate, the space satellite dynamics related to extend its antenna [2], and flexible extensile robot arms [3].

When it is drawn axially out from a gap in a wall, the divergence type instability due to the fluid force, namely, the *Reverse Spaghetti Problem* is observed; e.g., apparatus that ejects paper sheets such as high speed printing and copy machines [4,5].

A great interest in vibration and instability mechanism has aroused to not only industrial but also scientific problem. Analyses of such systems have been carried out with models as employing boundary conditions and a vibrating body of time-independent length. Stylianou and Tabarrok have done the analysis using a time varying shape function [6]. Vu-Quoc and Li presented the analysis using Lagrangian formulation and

Galerkin method for accounting the large deformation and overall motion [7].

However, the mechanism by which the lateral vibration increases rapidly with large deflection and a large driving velocity has not been examined sufficiently. Moreover, fluid force interaction due to the motion of the axially moving body also has not been considered in these studies, though this effect come to significant in actual machine operating with a large driving velocity in air and fluid environment.

One of present authors hypothesized that the elasticity of the inlet of the wall gap has a significant effect on the behavior in the *Spaghetti Problem*, and of these presented two kinds of modeling methodologies for this problem [8]. One of these models is based on a developed finite element formulation and the other is based on the finite segment method. We demonstrated that these models provide a good description of the *Spaghetti Problem* from the results of numerical simulations and experiments [9].

This paper presents two topics. One is the effect of a tapered guide in front of the inlet of the wall gap on the *Spaghetti Problem*. We developed our finite-segment-based *Spaghetti* model in the case that the tapered guide is provided in front of the inlet of the wall gap. Effects of the taper angle and the pulling velocity on the spaghetti behavior are discussed with experimental and numerical investigations. The other is the effect of the fluid force on the *Reverse Spaghetti Problem*. We introduce the fluid force that is derived from the complex velocity potential flow on our model. Especially, stability and the divergence type instability phenomena are discussed.

2. MODELING OF SPAGHETTI
2.1 Mechanical model

Figure 1 describes the mechanical model of the *Spaghetti Problem* with the tapered guides that is evolved out of the model by the authors [8]. A flexible beam of length L and thickness t is divided into nb rigid bodies, which are connected by hinged joints. Rotational springs denoted k_ϕ which represent the bending stiffness of the

102

beam, are located at the joints. The reaction forces from the elastic wall gap and the tapered guide are modeled with hard springs and dampers. The flexible beam is pulled into or drawn out from the elastic wall gap with a certain velocity V.

We fix the origin of the global coordinate system O-XY at the inlet of the gap and the origin of the body coordinate system o_i-$x_i y_i$ of the i-th body at the center of gravity of the body. The length, mass and moment of inertia of the i-th body are $2l_i$, m_i and J_i, respectively. We choose generalized coordinate $\mathbf{q}$ to represent the center of gravity and the attitude of all bodies:

$$\mathbf{q} = \{x_1\, y_1\, \phi_1\, x_2\, y_2\, \phi_2 \cdots \cdots x_i\, y_i\, \phi_i \cdots \cdots x_{nb}\, y_{nb}\, \phi_{nb}\} \cdots (1).$$

2.2 Reaction from wall gap and tapered guide

In the case that there is a finite clearance between the beam and the elastic wall gap as shown Fig1, the beam is pulled into the gap while undergoing reaction force and friction force exerted by the elastic wall at the time that the beam contacts the wall. We define the clearance C_p between the beam and the side of the wall gap as the sum of the upper clearance c_u and lower clearance c_l.

At the time that the beam is pulled into the gap with elastic deformation, the attitude of body i of the beam at the inlet of the gap is illustrated in Fig.2 (a).

The body i experiences reaction forces exerted by the side of the elastic wall gap when the body contacts them. We define two kinds of reaction forces, $\mathbf{F}_1$ and $\mathbf{F}_2$, representing the spring force and damper force. $\mathbf{F}_1$ is the reaction force exerted by the side of the wall gap that is determined by k_1 and c_1. The direction of $\mathbf{F}_1$ always coincides the global Y-axis. $\mathbf{F}_2$ is the reaction force exerted by the inlet of the wall gap, and is determined by k_2 and c_2. The direction of $\mathbf{F}_2$ varies as the attitude of body i changes.

As the X component of elastic deformation at the contact point of gap, ΔX_1, is very small in the case that the stiffness of the wall is sufficiently large, the X and Y directional components of the deformation of the upper side of the gap are given as

$$\left.\begin{array}{l}\Delta X_1 = 0 \\ \Delta Y_1 = (y_i + l\sin\phi_i) - c_u \quad if\ \Delta Y_1 \le 0,\ \Delta Y_1 = 0\end{array}\right\} \cdots (2).$$

The X and Y directional components of elastic deformation at the upper inlet of the gap can be obtained from the geometrical relationship between the body and the upper inlet as

$$\left.\begin{array}{l}\Delta X_2 = (y_d - c_u)\sin 2\phi_i / 2 \\ \Delta Y_2 = (y_d - c_u)(\cos 2\phi_i + 1)/2\end{array}\right\} \quad for\ y_d \ge c_u \quad \cdots (3)$$

$$\Delta X_2 = \Delta Y_2 = 0 \qquad for\ y_d < c_u \qquad \cdots (4)$$

where, y_d is the Y coordinate at the intersection of the Y axis and the x_i axis attached to body i:

$$y_d = y_i - x_i \tan\phi_i \qquad \cdots (5).$$

The body i experiences reaction forces by the guide
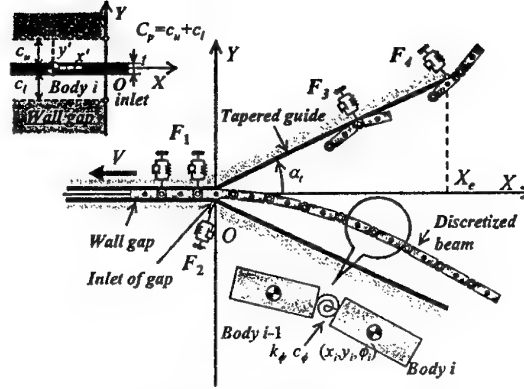
Fig.1 Mechanical model with guide
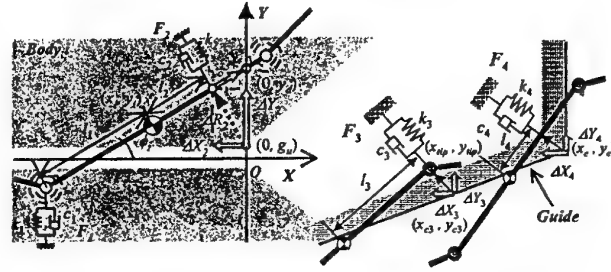
(a) Reaction force exerted   (b) Reaction force exerted
    by elastic wall   by tapered guide

Fig.2 Kinematical configuration between beam and wall

at the time that the beam contacts it of the X directional length x_e and the taper angle α_t, as illustrated in Fig.2 (b). We define two reaction forces, $\mathbf{F}_3$ and $\mathbf{F}_4$, representing the spring force and damper force. $\mathbf{F}_3$ is the reaction force exerted by the side of the tapered guide that is determined by k_3 and c_3. $\mathbf{F}_4$ is that exerted by the edge of the tapered guide. It is determined by k_4 and c_4.

The X and Y components of elastic deformation at the upper guide can be obtained from the geometrical relationship between the body and the upper inlet as

$$\left.\begin{array}{l}\Delta X_3 = (y_{c3} - y_i)\sin\phi_i \cos\phi_i - (x_{c3} - x_i)\sin^2\phi_i \\ \Delta Y_3 = -(y_{c3} - y_i)\cos^2\phi + (x_{c3} - x_i)\sin\phi_i \cos\phi_i\end{array}\right\} \cdots (6)$$

where, x_{c3} and y_{c3} are X and Y coordinate of the contact point of the guide, x_{tip} and y_{tip} are those of the right hand side end of the body contacted with the guide. The relations of them are determined as

$$\left.\begin{array}{l}x_{c3} = \dfrac{x_{tip} + y_{tip}\tan\phi_i}{1 + \tan\alpha_t\,\tan\phi_i} \\[3mm] y_{c3} = \dfrac{\left(x_{tip} + y_{tip}\tan\phi_i\right)\tan\alpha_t + c_u}{1 + \tan\alpha_t\,\tan\phi_i}\end{array}\right\} \quad \cdots (7).$$

The elastic deformation at the edge of the tapered guide, ΔX_4 and ΔY_4 are given by substituting the coordinate of the edge (x_e, y_e) into (x_{c3}, y_{c3}) of Eq. (6).

103

Those of the lower side of the gap are obtained by simply substituting c_l for c_v in previous equations..

The components of the reaction forces F_1, F_2, F_3 and F_4 exerted by the elastic wall and guide are obtained as

$$\left.\begin{aligned} F_{mx} &= -k_m \Delta X_m - c_m \Delta \dot{X}_m \\ F_{my} &= -k_m \Delta Y_m - c_m \Delta \dot{Y}_m \end{aligned}\right\} \quad \cdots (8)$$

where $m = 1$ to 4 correspond to F_1 to F_4, respectively.

The generalized force $^mQ_{in}$ which is derived from the reaction force and its moment exerted by the elastic wall and guide, can be obtained as

$$\begin{aligned} ^mQ_{in} &= \left\{ ^mQ_{ix} \quad ^mQ_{iy} \quad ^mQ_{i\phi} \right\}^T \\ &= \left\{ F_{mx} \quad F_{my} \quad l_m \left(F_{my} \cos\phi_i - F_{mx} \sin\phi_i \right) \right\}^T \end{aligned} \quad \cdots (9)$$

The quantities k_m and c_m represent spring constants and damping coefficients of the elastic wall and guide, respectively. l_m is the distance from the origin of the body coordinates to the line of action of the reaction force, and is obtained from geometrical relations as

$$\left.\begin{aligned} l_1 &= l_3 = l, \\ l_2 &= -l + \left(l \cos\phi_i - x_i \right), \\ l_4 &= \left(y_e - y_i \right)\sin\phi_i + \left(x_e - x_i \right)\cos\phi_i \end{aligned}\right\} \quad \cdots (10)$$

The friction force $^mQ_{ic}$ between the beam and the wall and guide is given with friction coefficient μ as

$$^mQ_{ic} = \left\{ -\mu\, ^mQ_{iy} \quad \mu\, ^mQ_{ix} \quad 0 \right\}^T \quad \cdots (11)$$

From Eqs.(9) and (11), the generalized force associated with the contact force ^mQ_i can be written as

$$^mQ_i = {}^mQ_{in} + {}^mQ_{ic} \quad \cdots (12)$$

The generalized force Q^a_i which work on body i are the gravitational force, the rotational spring and damper force due to the bending stiffness of the beam.

$$\begin{aligned} Q^a_i = \Big\{ 0 \quad &- m_i g \quad -k_{\phi_i}\left(\phi_i - \phi_{i-1}\right) - k_{\phi_{i+1}}\left(\phi_i - \phi_{i+1}\right) \\ &- c_{\phi_i}\left(\dot\phi_i - \dot\phi_{i-1}\right) - c_{\phi_{i+1}}\left(\dot\phi_i - \dot\phi_{i+1}\right) \Big\}^T \end{aligned} \quad \cdots (13)$$

2.3 Fluid force on bodies

We derive the fluid force acting on the bodies from the discrete vortex method and Blasius Theorem, which is a kind of the numerical method for the complex velocity potential flow. We thought this method is adequate for estimating the fluid force in the case that the boundary layer is sufficiently small.

Figure 3 illustrates vortexes and reference points we put on the discretized beam. Small circles indicate vortexes and large circles indicate reference points that is placed the midpoint of adjoined vortexes. We put nc vortexes with regular intervals on the each discritized beam then total number of vortexes on the beam is $nc^*nb+1 = nv+1$. We also define $\Gamma_{bv(j)}$;($j=1, ..., nv+1$) as the circulation of the vortex located at $z_{bv(j)}$.

The induced velocity of the flow at the k-th reference point $z_r(k)$ on the body surface u_{rk} ;($k = 1, ..., nv$) is
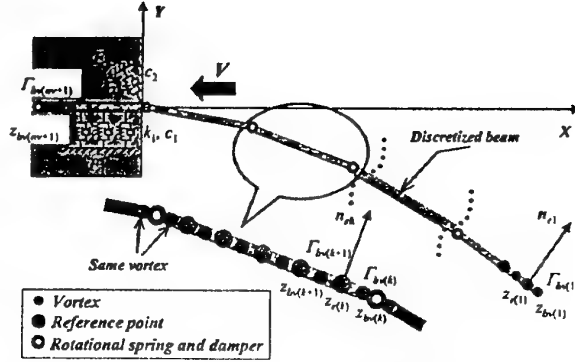
Fig.3 Discrete vortex model

given by combination of the steady velocity U and the fluid velocity associated with circulations of vortexes as,

$$\bar{u}_{rk} = \bar{U} - \frac{i}{2\pi} \sum_{j=1}^{nv+1} \frac{\Gamma_{bv(j)}}{z_{r(k)} - z_{bv(j)}} \quad \cdots (14)$$

As the fluid flows along the body surface, the normal component of u_{rk} relative to the body surface must be coincident with the moving velocity of the body for inviscid flow. This gives the following boundary condition for the k-th reference point as,

$$\mathrm{Re}\!\left[\bar{u}_{rk} \cdot n_{rk}\right] = \mathrm{Re}\!\left[\bar{V}_{rk} \cdot n_{rk}\right] \quad \cdots (15)$$

where $\bar{V}_{rk}$ is the moving velocity of the body. The unit normal vector on the k-th reference point the beam surface n_{rk} is given as

$$\bar{n}_{rk} = -\left(z_{bv(k+1)} - z_{bv(k)} \right)i \quad \cdots (16)$$

Substituting Eqs. (14) and (16) into Eq.(15), we obtain the following relation

$$\sum_{j=1}^{nv+1} a_{k,j}\Gamma_{bv(j)} = b_k \quad \cdots (17),$$

where

$$\left.\begin{aligned} a_{k,j} &= \mathrm{Re}\!\left[\frac{1}{2\pi} \frac{z_{bv(k+1)} - z_{bv(k)}}{z_{r(k)} - z_{bv(j)}} \right], \\ b_k &= \mathrm{Im}\!\left[\left(\bar{U} - \bar{V}_{rk}\right)\!\left(z_{bv(k+1)} - z_{bv(k)}\right)\right] \end{aligned}\right\} \quad \cdots (18)$$

The circulation at the end of the beam $\Gamma_{bv(nv+1)}$ is set as zero by Kutta condition. From these relations, we obtain the strength of circulations of all referenced points by solving the following equation

$$\begin{bmatrix} a_{1,1} & \cdots & \cdots & a_{1,nv+1} \\ \vdots & & & \vdots \\ a_{nv,1} & \cdots & \cdots & a_{nv,nv+1} \\ 0 & \cdots & 0 & 1 \end{bmatrix} \begin{bmatrix} \Gamma_{bv(1)} \\ \vdots \\ \Gamma_{bv(n)} \\ \Gamma_{bv(nv+1)} \end{bmatrix} = \begin{bmatrix} b_1 \\ \vdots \\ b_{nv} \\ b_{nv+1} \end{bmatrix} \quad \cdots (19)$$

The complex velocity potential $f(z)$ corresponding to Eq.(14) is derived as

$$f(z) = \bar{U}z - \frac{i}{2\pi}\sum_{j=1}^{nv+1}\Gamma_{bv(j)}\log(z - z_{bv(j)}) \quad \cdots (20)$$

Substituting Eq.(20) into Blasius Theorem, we obtain

104

the fluid force exerted on the body as the Kutta-Joukowski lift force,

$$F_{fx} - iF_{fy} = \frac{1}{2} i\rho \oint_c \left(\frac{df(z)}{dz} \right)^2 dz = i\rho \overline{U} \sum_{j=1}^{nv+1} \Gamma_{bv(j)} \quad \cdots (21).$$

The fluid force acting on the i-th discritized beam, namely body i, is easily given from Eq.(21) as

$$F_{fx(i)} - iF_{fy(i)} = i\rho \overline{U} \sum_{j=i^n(nv-1)+1}^{i^n nv} \Gamma_{bv(j)} \quad \cdots (22).$$

To avoid D'Alembert's paradox, we introduce the drag D as the X-directional resistance force with the form

$$D = C_D A \frac{\rho U^2}{2} \quad \cdots (23),$$

where C_D and A are the drag coefficient and A is the projected frontal area of the beam.

The generalized fluid force Q_i^f acting on body i is given as

$$Q_i^f = \begin{bmatrix} \cos\phi_i & -\sin\phi_i \\ \sin\phi & \cos\phi_i \end{bmatrix} \begin{Bmatrix} F_{fx(i)} \\ F_{fy(i)} \end{Bmatrix} + \begin{Bmatrix} D \\ 0 \end{Bmatrix} \quad \cdots (24).$$

2.4 Equation of motion

The constraint equation of the beam is written as

$$\Phi = \left\{ \Phi^{K^T} \; \Phi^D \right\}^T \quad \cdots (25),$$

where Φ^K is the kinematic constraint equation for the hinge between bodies i-1 and i, and Φ^D is the driving constraint equation for the left-end body

$$\Phi^D = (x_1 - l) + \int V dt = 0 \quad \cdots (16).$$

The equation of motion with constraint is obtained by introducing Lagrange multiplier λ [e.g. 10,11] as

$$\begin{bmatrix} M & \Phi_q^T \\ \Phi_q & 0 \end{bmatrix} \begin{Bmatrix} \ddot{q} \\ \lambda \end{Bmatrix} = \begin{Bmatrix} Q \\ \gamma \end{Bmatrix} \quad \cdots (27),$$

where M and Φ_q are mass matrix and Jacobian matrix.

When the contact force and fluid force work on body i, the response simulation must be carried out by adding not only Q_i^a but also ^mQ_i and Q_i^f to Q_i in Eq.(27).

$$Q_i = Q_i^a + {}^mQ_i + Q_i^f \quad \cdots (28).$$

3. EXPERIMENT OF SPAGHETTI
3.1 Experimental setup

Figure 4 shows the experimental setup that we developed for investigating the *Spaghetti Problem*. The FRP thin beam is regarded as the *Spaghetti* 'specimen'. One end of the FRP thin beam is clamped at the circumference point of the driving wheel. The FRP beam is also supported horizontally by the constraint block, which is made of Teflon. The wheel has 400mm diameter and is driven by the AC servomotor. The FRP thin beam is pulled into the gap at the inlet of the constraint block with velocity V. A couple of tapered guides are provided in front of the inlet of the constraint block.
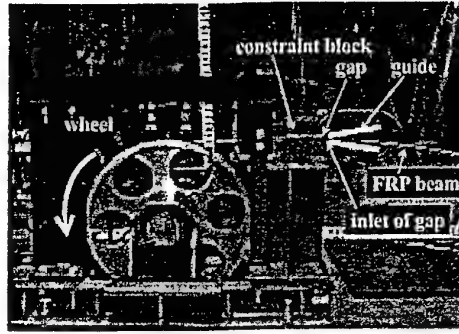
Fig.4 Experimental setup
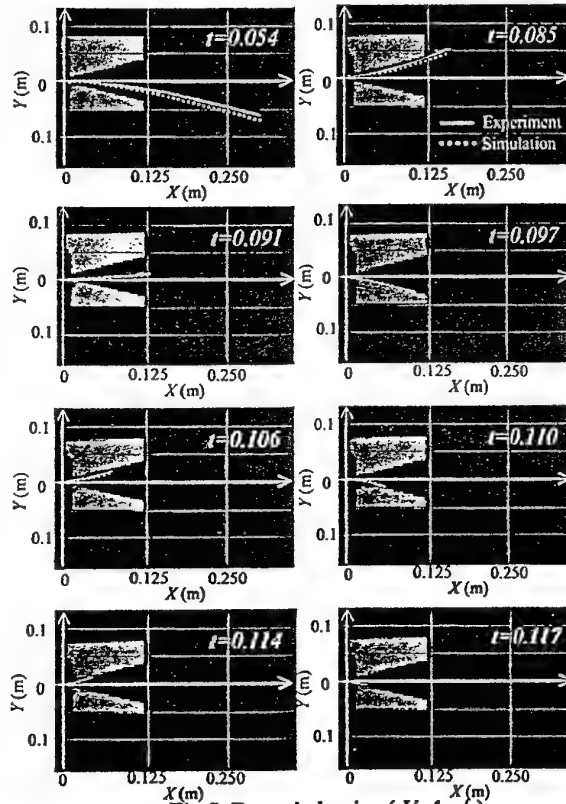
Fig.5 Beam behavior (V=4m/s)

The length, width and thickness of FRP beam are 500mm, 30mm and 1.6mm. Its density, Young's modulus and damping ratio of it are $1.4\times10^3 kg/m^3$, $7.5\times10^9 N/m^2$ and 0.043. The pulling velocity V, the tapered guide angle α_t and clearance size C_p are regarded as parameters. We set V=1.0, 2.0, 3.0 and 4.0m/s, α_t=10, 15, 30 and 60deg., C_p=0.1, 0.8 and 1.6mm. In each experiment, the wheel was controlled to have a constant angular velocity within 0.05second.

The lateral displacement of the FRP beam is measured by the laser beam position sensor located

105

20mm in front of the inlet of the gap. The deformed shape of the FRP beam is also recorded with a high-speed video camera of 1000 frames/s.

3.2 Experimental and simulation results

Experimental results for the time evolution at the deformation of the FRP beam with the tapered guide are compared with simulation results in Fig. 5. These snap-shots were recorded by a high-speed video camera for a system with $V = 4.0$ m/s, $\alpha_t =15$deg. and $C_p =0.1$mm. It is found that at first the intermediate point of the beam contact the upper guide and the beam end bends upward, then the most of the beam surface contacts the upper and lower guides as it is pulled into the guide.

In the numerical simulations, we divided the FRP beam into 48 elements. It was found that this number is large enough to obtain the sufficiently precise value of static deformation with the finite segment method used in this simulation. We set the spring constant k_ϕ and the damping coefficient c_ϕ between each body as 65.1Nm /rad. and 5.67×10^{-5}Nm·s/rad.. We also set the spring constants and the damping coefficients of the gap as $k_1= 3.0 \times10^6$ Nm/rad., $k_2= 6.0 \times10^6$Nm/rad., $c_1=1.53\times10^{-4}$Nm ·s/rad. and $c_1=1.53\times10^{-4}$Nm·s/rad..

From this result, we find that good agreement between the numerical and experimental results for both frequency and deformed shape. This indicates that the model can simulate the *Spaghetti Problem* quite well.

4. SPAGHETTI IN FLUID
4.1 Simulation parameters

We conducted numerical simulations to examine the effect of fluid force on the *Spaghetti* and *Reverse Spaghetti Problems* in cases for pulling into and drawing out from the wall gap with the beam of three kind of material, namely, FRP, Aluminum alloy and steel as shown in Table 1.

We choose fluid density ρ, pulling or drawing velocity V and beam material as parameters. We set fluid density ρ as 0.0, 1.2, 1000 kg/m^3 representing in the vacuum, in the air and in the water. We also set the driving velocity V as 1, 2, 3, 4 and 5 m/s.

We put five discrete vortexes on each rigid body ($nc=5$), because it is sufficient number to simulate the fluid force that is obtained by the well-known theoretical ones on the plate. We set the steady velocity of flow U as

Table1 Beam properties

Material	FRP	Al. alloy	Steel
Length (mm)		500	
Thickness (mm)		1.6	
Density (x10^{3}kg/m^3)	1.40	2.86	7.85
Mass of Beam (kg)	1.12	2.29	6.28
Young's Modulus (GPa)	7.80	99.0	206
Bending Rigidity (Nm^2)	2.66	33.8	70.3

zero, that is, the relative flow velocity to bodies is equal to the driving velocity. We omit the gravity force in the case of *Reverse Spaghetti Problems*, because the gravity force makes it difficult to judge the divergence type instability from the deformation of the beam ·

In the case of *Reverse Spaghetti Problems*, we apply the impulse type disturbance at the free end of the beam tip for Y-direction when a quarter length of beam is drawn out from the inlet of the wall. Such a disturbance is very important to judge the stability or instability of the system.

4.2 Simulation results

Figure 6 shows the time history of lateral displacement at the free tip of the steel beam for five kinds of the driving velocity in the case of the density of the fluid $\rho=1000$kg/m^3. In the case of $V=1$m/s, the displacement of the steel beam decreases with the damped free vibration after the disturbance is applied, and it is stable. In the case of $V=2$m/s, the displacement of it decreases more quickly. In the case of $V=3$m/s, the displacement of it decreases like an over damping motion and a small residual displacement is observed. In the cases of $V=4$ and 5m/s, the displacements of it increase monotonously, namely, it is the divergence type instability. Then the divergence type instability is getting to arise between 2 and 3m/s. In the cases of the aluminum alloy and FRP beam, the divergence type instability is caused about 2m/s, and is caused lower than 1m/s, respectively. These results indicate followings: fluid force suppress the displacement of the beam as the damping force in the low driving velocity, and it works the exciting force in the high driving velocity, the bending stiffness of the beam gives significant affect on the stability.

Figure 7 shows the effect of the fluid density on the response of lateral displacements at the free tip of the steel beam in the case of $V=4$m/s. In the case of $\rho=0.0$kg/m^3 and $\rho=1.2$kg/m^3, free vibration is caused after the disturbance is applied and an imperceptible difference is observed between amplitudes of the beam. In the case of $\rho=1000$kg/m^3, the displacement increases monotonously. This result indicates that the effect of the fluid force is more effective as the fluid density is increase and the fluid force by high-density fluid works so as to unstable the system.

Figure 8 shows the effect of beam material on the response of lateral displacement in the case of fluid of $\rho=1000$kg/m^3 and $V=3$m/s. The lateral displacement of the steel beam holds about 0mm, while lateral displacements of the aluminum alloy and FRP beams increases with time. These results indicate that the rigidity of the beam is higher, the displacement is smaller.

From these simulation results, the fluid force is clarified to play an important role at the *Reverse*

106

Spaghetti Problem in our simulation condition. Because the lift force generated by circulations works to diverge the system in the *Reverse Spaghetti Problem*. Then its magnitude increases in proportion to the square of driving velocity.
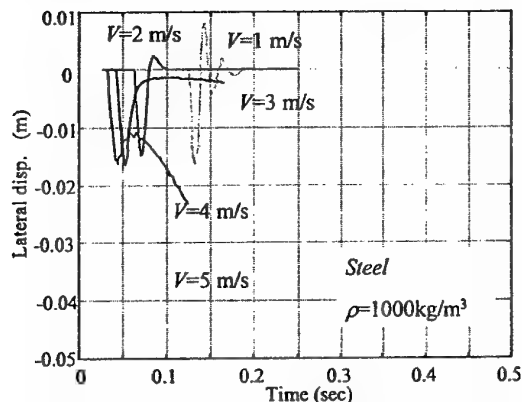
Fig.6 Driving velocity effect on beam displacement
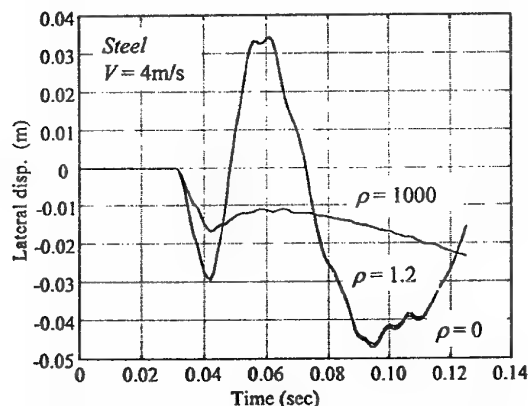
Fig.7 Fluid density effect on beam displacement
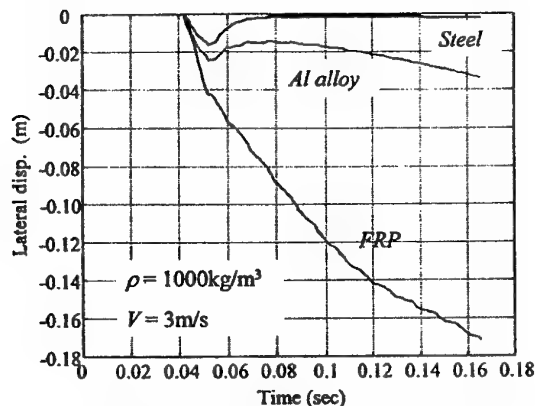
Fig.8 Fluid force effect on beam material

5. CONCLUSION

We have presented a mechanical model based on a finite segment method to simulate the *Spaghetti Problem* and the *Reverse Spaghetti Problem*. It is found that our model is capable of accurately simulating the dynamic behavior of the *Spaghetti Problem*: The vibration of the free beam tip becomes larger as the beam is pulled into the gap. Next, we introduced the fluid-elastic interaction force by employing the discrete vortex method for the *Spaghetti Problem* and the *Reverse Spaghetti Problem*.

Then, numerical simulations and experiments with the FRP beam demonstrated that the vibration amplitude of the beam rapidly increases as the clearance in the gap becomes smaller or the pulling velocity becomes larger. In addition, the accuracy of our model for the *Spaghetti Problem* was examined by comparing the results of numerical simulations and experiments.

Finally, numerical simulation results clarified that the fluid force works to lead the system unstable in the *Reverse Spaghetti Problem* with the higher driving velocity, the higher fluid density and the lower bending rigidity beam, while it works the damping force with the lower driving velocity, the low fluid density and the higher bending rigidity beam.

REFERENCES

[1] Carrier. G. F. (1979) The Spaghetti Problem, *American Mathematical Monthly*, 56, pp669-672

[2] Tabarrok B., Leech C. M. and Kim Y. I. (1974) On the Dynamics of an Axially Moving Beam, *J. Franklin of Institute*. 297, pp.201-220.

[3] Yuh J. and Young T. (1991) Dynamic Modeling of an Axially Moving Beam in Rotation: Simulation and Experiment, Trans. ASME *J. Dynamics Systems and Measurement*, 113, pp34-40.

[4] Mansfield L. and Simmond J. G. (1987) The Reverse Spaghetti Problem: Drooping Motion of an Elastica Issuing from a Horizontal Guide, Trans. ASME *J. Applyed Mechanics*, 54, pp.147-150

[5] Stolte,J. and Benson, R.C. (1992) Dynamic Deflection of Paper Emerging from a Channel, *J.Vibration and Acoustics* 114, pp187-193

[6] Stylianou M. and Tabarrok B. (1994) Finite Element Analysis of an Axially Moving Beam, Part-1: Time Integration, *J.Sound Vibration*, 178, pp433-453.

[7] Vu-Quoc L. and Li S. (1995) Dynamics of sliding geometrically-exact beams: large angle maneuver and parametric resonance, *Computer methods in applied mechanics and engineering*, 120, pp.65-118.

[8] Sugiyama, H. and Kobayashi, N. (1998) Analysis on Dynamic Behavior of Spaghetti Problem, *Proc. 4th Int. Conf. MOVIC*, Vol.1, pp311-316

[9] Komaki, Y., Kobayashi, N. and Watanabe, M. (2001) Experimental and Analytical Investigation on Spaghetti Problem, *18th Biennial Conf. on Mechanical Vibration and Noise*, ASME, DETC2001/VIB-21356, pp1-7

[10] Haug,E.J. (1989) *Computer Aided Kinematics and Dynamics of Mechanical Systems*, Allyn and Bacon.

[11] Shabana A. A. (1994) *Computational Dynamics*, John Wiley & Sons.

107

Multibody System Dynamics in Ocean Engineering
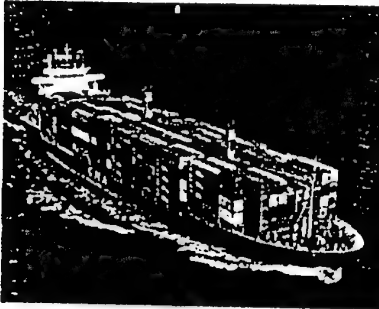
Edwin Kreuzer and
Katrin Ellermann
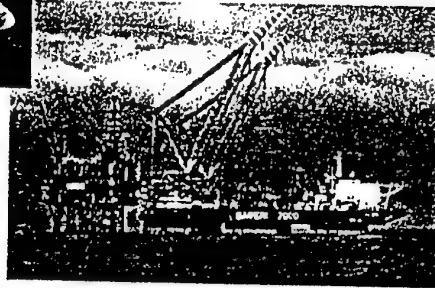
TUHH
Technische Universität Hamburg-Harburg

NATO ASI on Virtual Nonlinear Multibody Systems
Prague, June 29, 2002

Mechanical Systems in Ocean Engineering

Underwater-Robots

Floating Cranes

Chains and
Mooring Systems

Ships

Platforms

TUHH
Technische Universität Hamburg-Harburg

108
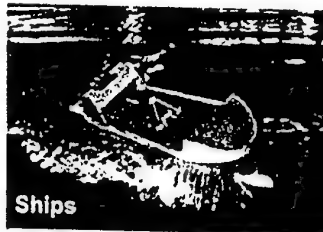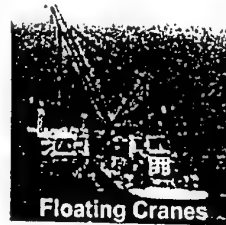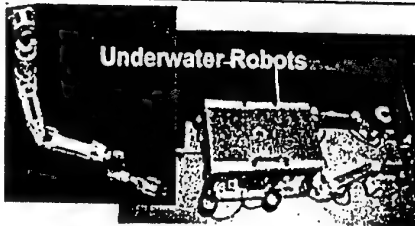
Modeling

Demands:

Modeling of all six rigid body degrees of freedom

Nonlinear hydrostatics

Hydrodynamics for large motions
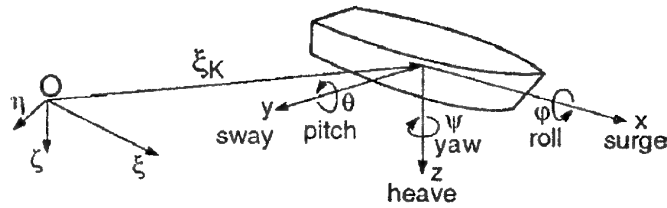
$$M\ddot{y} + k(y,\dot{y}) = q(y,\dot{y},t)$$

Computer Programs for Hydrodynamics

Calculation of

Froude-Krylov forces   Diffraction forces

Radiation forces   Hydrostatic forces

Strip methods
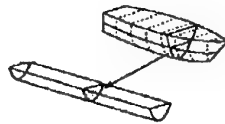
$\Rightarrow$ **SIMBEL**

Panel methods

$\Rightarrow$ **SPLASH**

influence of forward velocity

Forces

$$M\ddot{y} + k(y,\dot{y}) = q(y,\dot{y},t)$$

nonlinear kinematics k
nonlinear applied forces q

hydrostatics   undisturbed incoming wave   diffraction   radiation

---
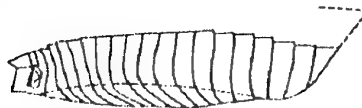
The Flow Problem

Flow:

$$\Delta\Phi = \Phi_{xx} + \Phi_{yy} + \Phi_{zz} = 0$$

$$\Phi_t + \tfrac{1}{2}(\nabla\Phi \cdot \nabla\Phi) - gz + \frac{p}{\rho} = \frac{p_0}{\rho}$$

Boundary conditions

$$n \cdot \dot{u} = \frac{\partial\Phi}{\partial n}$$

$$\nabla\Phi \cdot \nabla\zeta + \frac{\partial\zeta}{\partial t} = \Phi_z$$

$$\Phi_t + \tfrac{1}{2}(\nabla\Phi \cdot \nabla\Phi) - gz = 0$$

Solution in SIMBEL:
sources
on the boundaries
of the strip

• linearization

for a number of
sections,
heelings,
draughts

$\Rightarrow$ hydrodynamics as a planar problem

110

Radiation and Diffraction Forces

Frequency dependent forces: $\quad q(\omega) = -A(\omega)\cdot\omega + B(\omega)\cdot i\omega$

for harmonic excitation with frequency ω

Approximation of frequency dependent forces using rational polynomials

$$\left(\sum_{k=0}^{K} R_k \cdot (i\omega)^k\right)^{-1}\left(\sum_{k=0}^{K} Q_k \cdot (i\omega)^k\right) \approx A(\omega) + \frac{i}{\omega}B(\omega)$$

Transformation into time domain for each strip $\dot{s}_1 = s_2 + Q_0\dot{u}_x - R_1 q' + U\frac{\partial s_1}{\partial x}$

$\Rightarrow$ additional state variables for each strip

During integration:

switching between polynomial coefficients

depending on draught and heeling

$$\dot{s}_2 = -R_0 q' + U\frac{\partial s_2}{\partial x}$$

$$q' = s_1 + Q_1\dot{u}_x + Q_2\ddot{u}_x - U\frac{\partial Q_2\dot{u}_x}{\partial x}$$
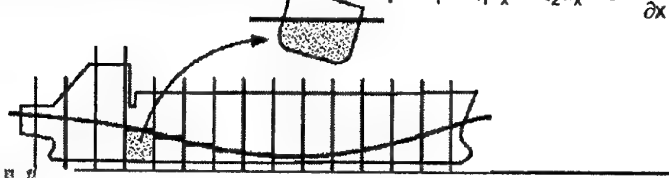
TUHH
Technische Universität Hamburg-Harburg

Simulation Parameters

Container ship:

$\Rightarrow$ length 169m   24 sections

$\Rightarrow$ width 28m   8   heelings

$\Rightarrow$ heigth 16m   43 draughts

Parameters:

- wave heights $\zeta_w = 2m - 10m$

- wave frequency $\omega = 0.5\ rad/s,...$

- heading angle $\mu = 0°, 30°$

- forward velocity $v = 11 m/s$

- draught $T = 9.32m$
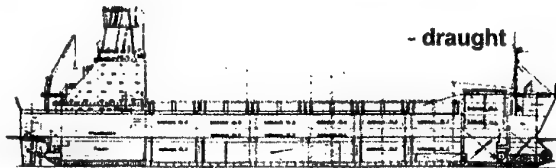
Simulation for regular seaways

TUHH
Technische Universität Hamburg-Harburg
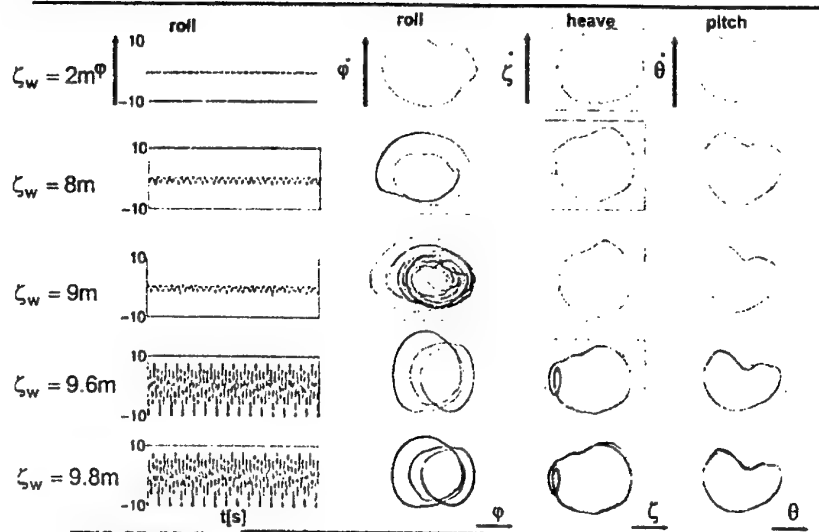
Simulation: μ=0°, ω=0.5rad/s

Animation

$\mu = 0°$

$H = 9.6m$

$T = 12.6s$

$v = 11m/s$
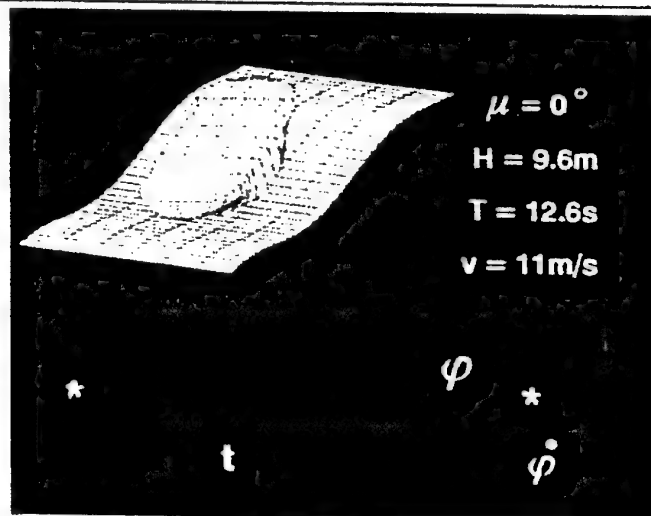
Compact Structures

Total Potential	Incoming harmonic wave	Potential of diffracted wave
$\Phi = \Phi_0 + \Phi_7 + \sum\limits_{j=1}^{6} \Phi_j$	$\Phi_0(\omega)$	$\Phi_7(\omega)$

$\zeta(t) = \zeta_0 \cos(kx - \omega t + \varepsilon)$

Body motion potential

$$\sum_{j=1}^{6} \Phi_j = \sum_{j=1}^{6} \dot{s}_j \varphi_j$$

added mass

$$a = a\,(\omega \to \infty)$$

frequency ω [rad/s]

added damping

frequency ω [rad/s]

wave excitation

frequency ω [rad/s]
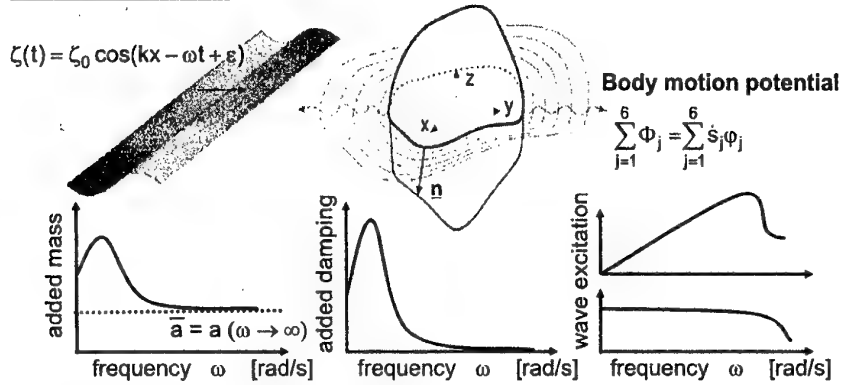
Time Domain Formulation

Assumption: the motion of the floating crane is (nearly) harmonic

$$(M + A(\omega))\,\ddot{y} + B(\omega)\,\dot{y} + k(y,\dot{y}) = q(y,\dot{y})$$

Time domain formulation (Cummins) ➔ **Impulse response functions**

$$\sum_{j=1}^{6} \left\{ (m_{ij} + \overline{a}_{ij})\ddot{x}_j + \int_{-\infty}^{t} K_{ij}(t-\tau)\dot{x}_j(\tau)\,d\tau + k_{ij} \right\} = q_i$$

with

$$K_{ij}(\tau) = \frac{2}{\pi} \int_0^{\infty} b_{ij}(\omega)\cos(\omega\tau)\,d\omega$$

K_{ij}

10^5

0

-10^5

0 25

t

113
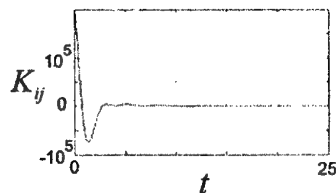
Mooring Systems

Single Point Mooring (SPM)

Nylon rope

Steel chain
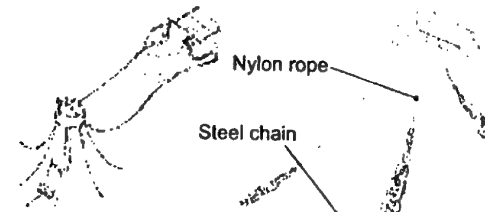
Spread Mooring System (SMS)
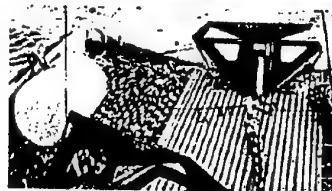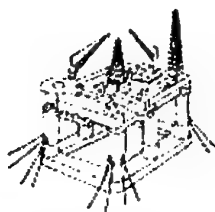
Typical components of a mooring line

TUHH
Technische Universität Hamburg-Harburg

Relative Size *k*

Compact floating structure

$k > 0.2$

heave (z)

yaw (θ_z)

roll (θ_x)

sway (y)

pitch (θ_y)

surge (x)

Transparent mooring line

$0 < k \leq 0.2$

$\rightarrow$ Relative size $\quad k = \dfrac{\text{Diameter}}{\text{Wavelength}} = \dfrac{D}{L}$
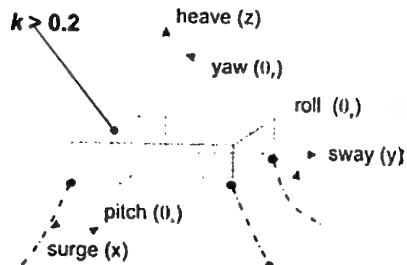
Hydrodynamic Analysis of the *compact* structure using the sink-source method

Transparent mooring line modeled using MORISON's equation

$dF_n(\ddot{x}, \dot{x}, x, t)$

TUHH
Technische Universität Hamburg-Harburg

114
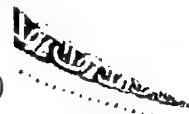
Transparent Structures

Modified formulation by MORISON et al.

Transparent member:

$$dF_n = \rho \frac{\pi D^2}{4} ds \frac{\partial v_n}{\partial t} + C_a \rho \frac{\pi D^2}{4} ds \frac{\partial u_m}{\partial t} + C_d \frac{\rho}{2} Dds|u_m|u_m$$

- Normalized acceleration of the fluid

$$\frac{\partial v_n}{\partial t} = e_t \times (\frac{\partial v}{t} \times e_t)$$

- Relativ normalized acceleration between fluid and structure

$$\frac{\partial u_m}{\partial t} = e_t \times (\frac{\partial u_r}{t} \times e_t)$$

- Normalized relativ velocity between fluid and structure

$$u_m = e_t \times (u_r \times e_t)$$

with

$$u_k = (u_T + \omega \times r_s)$$

$$u_r = v - u_k$$

GCS
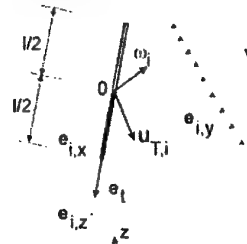
TUHH
Technische Universität Hamburg-Harburg

Short Term Statistics

- Random sea state is represented by its energy density spectrum $S(\omega)$ derived by statistical properties, e.g., parameters for sea condition (significant wave height H_s, characteristic wave period T_0)

- The random wave train and its corresponding forces are computed using the superposition principle of waves

$$\zeta_a(t) = \sum_{n=1}^{N} \sqrt{2S(\omega_n)\Delta\omega_n} \cos(-\omega_n t + \varepsilon(\omega_n))$$

$$F_i^{(1)}(t) = \sum_{n=1}^{N} F_i(\omega)\sqrt{2S(\omega_n)\Delta\omega_n} \cos(-\omega_n t + \varepsilon(\omega_n))$$

- Second order drift forces are

$$F_i^{(2)}(t) = \frac{\int_0^\infty F_i^{(2)}(\omega)S(\omega)d\omega}{\int_0^\infty S(\omega)d\omega} A^2(t)$$
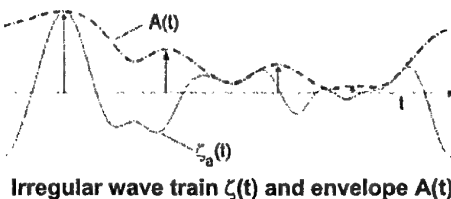
Irregular wave train $\zeta(t)$ and envelope $A(t)$

TUHH
Technische Universität Hamburg-Harburg

Line Generation (1)

Mooring line as a spatial problem
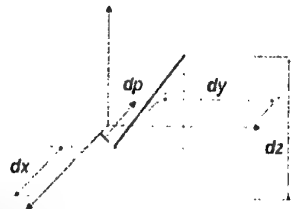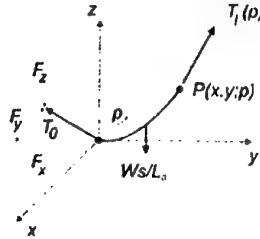
- **Forces**

$$T_0 = \sqrt{F_x^2 + F_y^2 + F_z^2}$$

$$T_l = \sqrt{F_x^2 + F_y^2 + (F_z + w \cdot s_l)^2}$$

- **Geometrical Compatibility**

$$\left(\frac{dx}{dp}\right)^2 + \left(\frac{dy}{dp}\right)^2 + \left(\frac{dz}{dp}\right)^2 = 1$$

- **Equilibrium**

$$\sum F_x = 0 \quad : \quad T_l \frac{dx}{dp} = F_x$$

$$\sum F_y = 0 \quad : \quad T_l \frac{dy}{dp} = F_y$$

$$\sum F_z = 0 \quad : \quad T_l \frac{dz}{dp} = F_z + \frac{Ws}{L_0}$$

TUHH
Technische Universität Hamburg-Harburg

Line Generation (2)

Introducing HOOKE's law

$$T_l = EA\varepsilon \quad \text{with} \quad \varepsilon = \left(\frac{dp}{ds} - 1\right)$$

Ansatz to solve the differential equations

with $\tilde{x} = x[p(s)]$ follows

$$\frac{d\tilde{x}}{ds} = x'(p) \cdot p'(s) = \frac{dx}{dp} \cdot \frac{dp}{ds} \qquad \ldots$$

Integration yields a nonlinear system of equations

$$x_l = f(F_x, F_y, F_z) = \frac{F_x L_0}{EA} + \frac{F_x L_0}{W} \ln\left(\frac{F_z + W + \sqrt{F_x^2 + F_y^2 + (F_z + W)^2}}{F_z + \sqrt{F_x^2 + F_y^2 + F_z^2}}\right)$$

$$y_l = g(F_x, F_y, F_z) = \ldots$$

$$z_l = h(F_x, F_y, F_z) = \ldots$$

TUHH
Technische Universität Hamburg-Harburg

116

Line Generation (3)

- Solution by means of a damped Newton-Raphson method using the boundary conditions
- Design parameters subsystem: dx, dy (geometry), w, E, A (material)
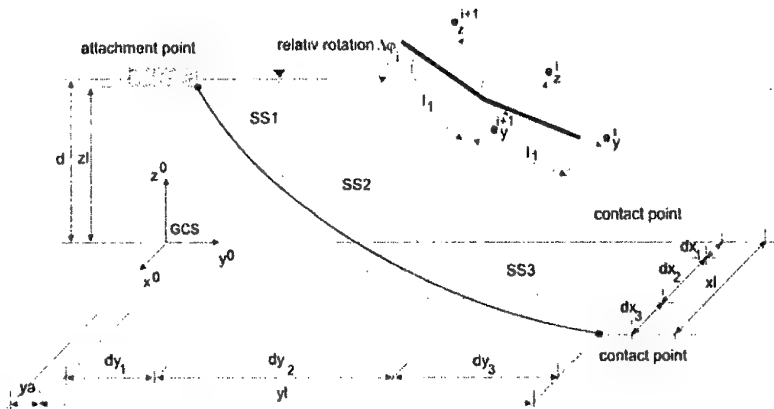
TUHH
Technische Universität Hamburg-Harburg

Description of Body Positions

- Structure of mass matrix describing the body position with generalized coordinates

a) starting from an endpoint   b) starting near the center of the system
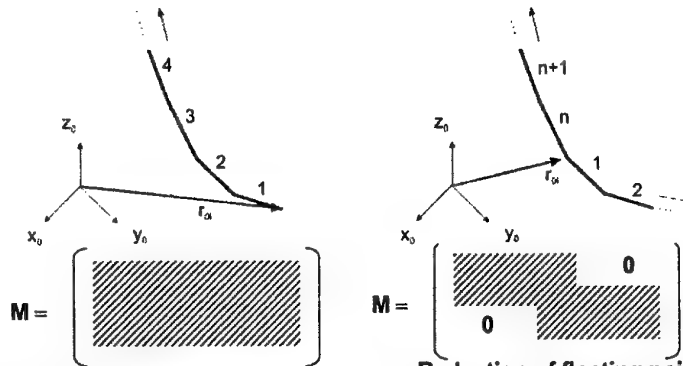
$\Rightarrow$ Reduction of floating point operations for each time step

TUHH
Technische Universität Hamburg-Harburg

117

Equations of Motion

Calculation and simulation using the multibody system method with program package UNIVERSAL MECHANISM by POGORELOV

→ Position and rotation of each body in generalized coordinates

$$r_i^m = r_i(y_m, t)$$

$$S_i^m = S_i(y_m, t)$$

→ Generation of the equations of motion of each subsystem using a direct NEWTON-EULER algorithm

$$M_m(y_m, t)\ddot{y}_m + k_m(\dot{y}_m, y_m, t) = Q_m(\dot{y}_m, y_m, t)$$

→ Considering possible constraints within a subsystems, e.g. fixed contact point on the sea bed

$$g_m(y_m, t) = 0, \quad G_m(y_m, t) = \frac{\partial g_m(y_m, t)}{\partial y_m^T}$$

→ Representation in the EULER-LAGRANGE form

$$M_m(y_m, t)\ddot{y}_m + k_m(\dot{y}_m, y_m, t) = Q_m(\dot{y}_m, y_m, t) + G_m^T(y_m, t)\lambda_m$$

$$g_m(y_m, t) = 0$$

TUHH
Technische Universität Hamburg-Harburg

Spread Mooring System
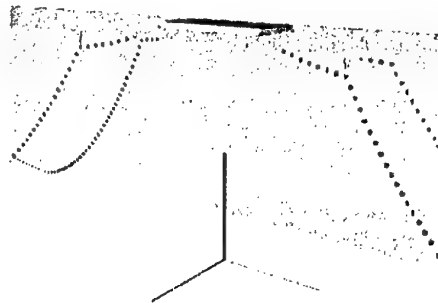
' Configuration of the system
→ (568+6) degrees of freedom
→ 45 subsystems

TUHH
Technische Universität Hamburg-Harburg

Crane Vessels

Crane barge
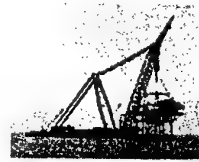
Crane ship

Semi-submersible

TUHH
Technische Universität Hamburg-Harburg

Aims

* **Prediction of stability for specific operating conditions**

* **Determination of critical operating ranges**

* **Comparability with experimental data**

* **Augmentation of operating range**

TUHH
Technische Universität Hamburg-Harburg

Procedure

Mathematical model of crane vessel

Numerical investigation

simulation
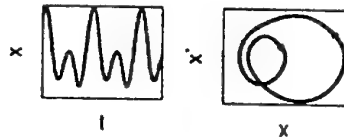
bifurcation analysis

Analytical investigation

adaptation of model

analytical solution

$$y = f(\lambda_1, \lambda_2, \lambda_3, ...)$$

Verification and Technical Use

Mathematical investigation	Experiment
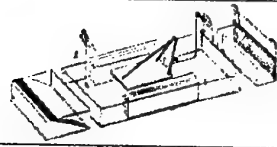
Technical use of the results

Instructions for use

Guidelines for construction, development, and operation

→ Increasing safety

→ Growing operating ranges

Mathematical Model

- **Multibody system**

- **Nonlinear mooring**

- **Periodic forcing of waves**

- **Linear hydrodynamics**
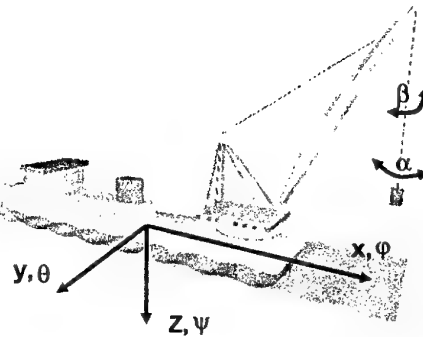
Mathematical Model

$$M(y)\ddot{y} + k(y,\dot{y}) = q(y,\dot{y})$$

- inertia, masses, added masses
- gyroscopic and Coriolis forces
- external forces

nonlinearities

- kinematic coupling
- mooring system

$$F(x) = -c_1 x - c_2 x|x| - c_3 x^3$$

121
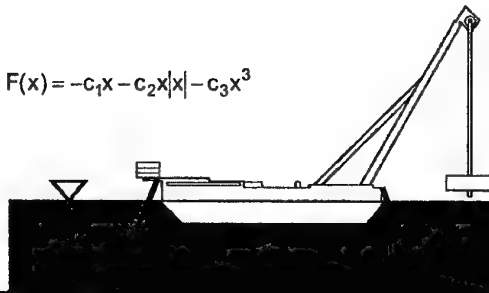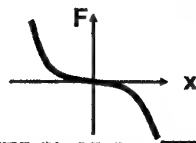
Numerical Bifurcation Analysis

Ordinary differential equation

$\downarrow$

Discretization of periodic orbits

$\downarrow$

Tracing of periodic solutions

$\downarrow$

Bifurcation diagram, path following (Predictor-corrector scheme, stepsize control)

$\dot{\mathbf{x}} = \mathbf{f}(\mathbf{x}, \lambda)$

$\mathbf{P}^l(\mathbf{x}, \lambda) - \mathbf{x} = 0$

$[\mathbf{x}_n, \lambda_n] \to [\mathbf{x}_{n+1}, \lambda_{n+1}]$
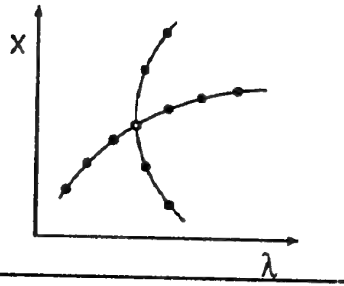
TUHH
Technische Universität Hamburg-Harburg

Numerical Results
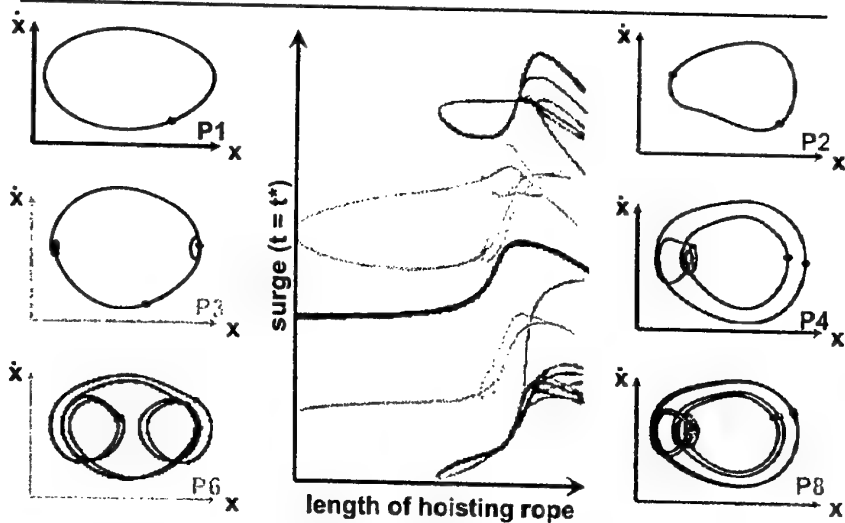
TUHH
Technische Universität Hamburg-Harburg

Example: Results of Path Following

operating conditions:

$a = 0.5\,m$

$c_1 = 33{,}4\,kN/m$

$c_2 = 2{,}9\,kN/m^2$

$c_3 = 45{,}5\,kN/m^3$

$l = 25\,m$

surge x $(t = t^*)$ [m]

frequency ω [rad/s]
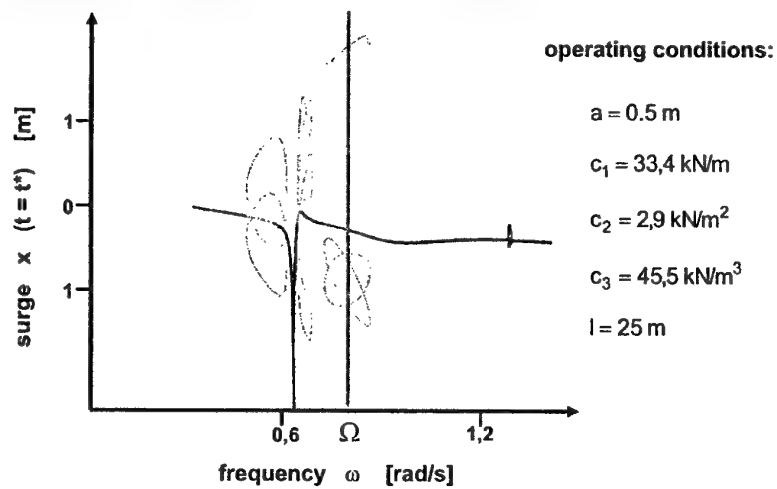
Simulation

P1 - Motion

$a = 0.5\,m$

$\Omega = 0{,}8\,rad/s$
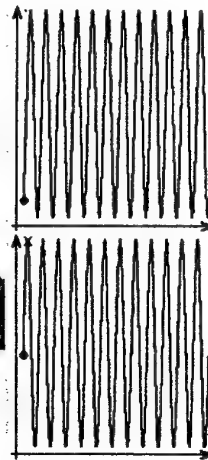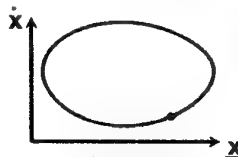
$l = 25\,m$

$c_1 = 33{,}4\,kN/m$

$c_2 = 2{,}9\,kN/m^2$

$c_3 = 45{,}5\,kN/m^3$

Simulation

P3 - Motion

$a = 0.5\,m$

$\Omega = 0,8\,rad/s$

$l = 25\,m$

$c_1 = 33,4\,kN/m$

$c_2 = 2,9\,kN/m^2$

$c_3 = 45,5\,kN/m^3$
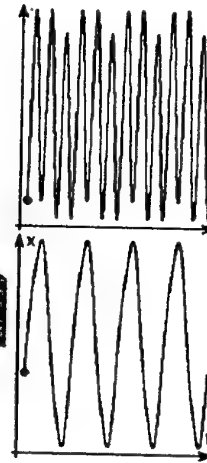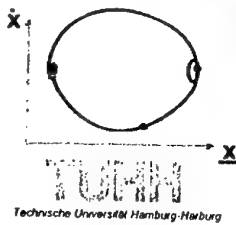
Method of Multiple Scales

Idea:

- Time is expressed by a sequence of independent time scales

$$T_n = \varepsilon^n t \qquad 0 < \varepsilon \ll 1 \qquad n = 0,1,2$$

- Ansatz-function

$$y(\varepsilon,t) \sim \sum_{m=0}^{n-1} \varepsilon^m y_m(T_0, T_1, \ldots)$$

→ Assumption: weak nonlinearity

→ Investigation of:

- primary resonances
- subharmonical resonances
- internal and combinational resonances

$\omega_i \approx \Omega$

$2\omega_i \approx \Omega$
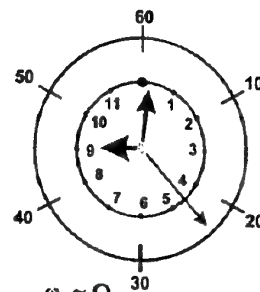
$\omega_i \approx 2\omega_j, \quad \omega_i + \omega_j = \Omega$

Method of Multiple Scales

- Re-ordering of linear and nonlinear terms

$$M\ddot{y} + Ky = \bar{F}(\Omega t, y, \dot{y}, \ddot{y})$$

> excitation, damping, nonlinear terms

- Approximation of nonlinear terms by polynomials

$$\sin(\theta) = \theta - \tfrac{1}{6}\theta^3 + O(\theta^4), \qquad \cos(\theta) = 1 - \tfrac{1}{2}\theta^2 + O(\theta^4)$$

- Modal analysis

$$y = \Phi q$$

$$\ddot{q} + \Omega_0^2 q = F(\Omega t, q, \dot{q}, \ddot{q})$$

Example: Results of Path Following

Operating conditions:

$a = 0.5\,m$

$c_1 = 33{,}4\ kN/m$

$c_2 = 2{,}9\ kN/m^2$

$c_3 = 45{,}5\ kN/m^3$

$l = 25\ m$

125
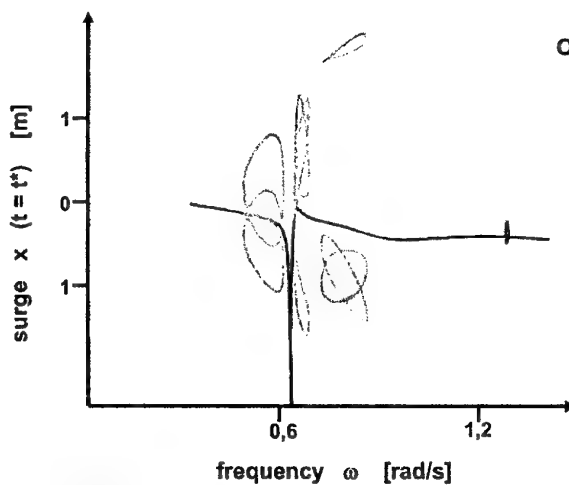
Path Following: Maxima
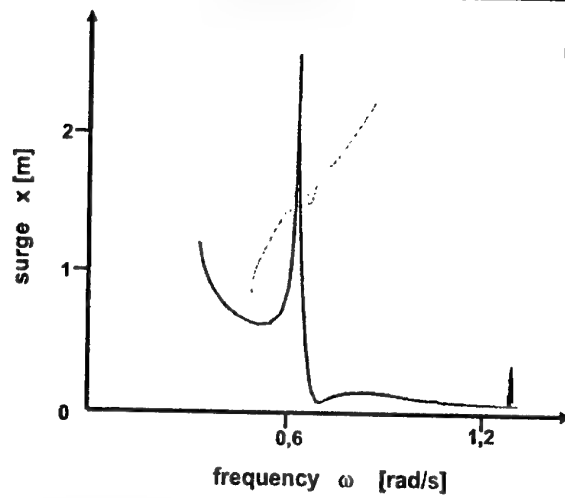
Operating conditions:

$a = 0.5\,\mathrm{m}$

$c_1 = 33{,}4\,\mathrm{kN/m}$

$c_2 = 2{,}9\,\mathrm{kN/m^2}$

$c_3 = 45{,}5\,\mathrm{kN/m^3}$

$l = 25\,\mathrm{m}$

surge x [m]

frequency ω [rad/s]

0,6 1,2

Method of Multiple Scales: Results

Results of the
path following

surge x [m]

frequency ω [rad/s]

surge x [m]

frequency ω [rad/s]

0,6 1,2

126
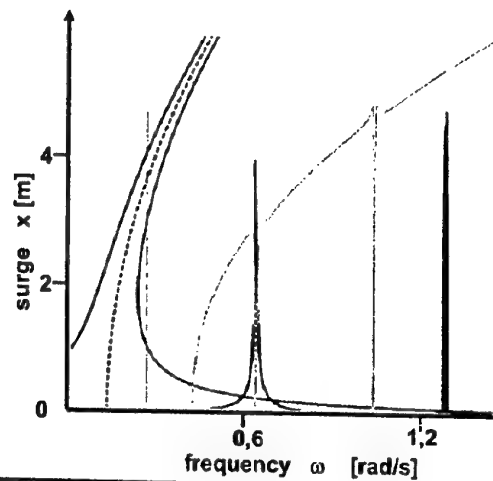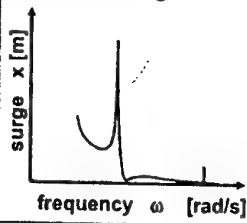
Experimental Setup (TUB)
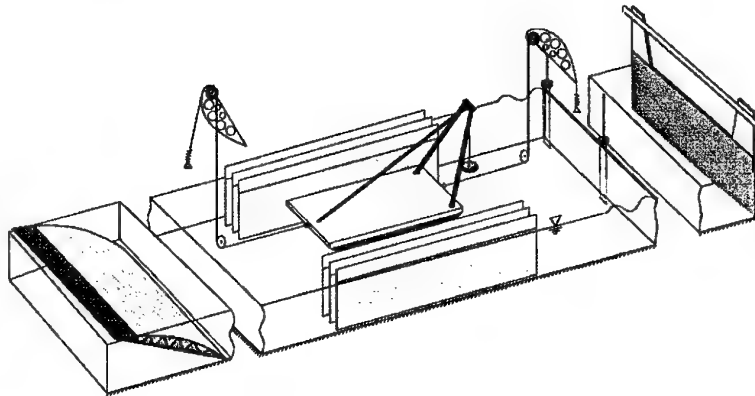
TUHH
Technische Universität Hamburg-Harburg

Experimental Mooring System

Significant nonlinearities in mooring line forces of crane vessels

→ **realization difficult in experiment**
→ **development of spring mechanism**

Polynomial approximation of mooring line forces

$$F(x) = -c_1 x - c_2 x|x| - c_3 x^3$$

→ $F(\beta(x))$

→ geometry of the cams
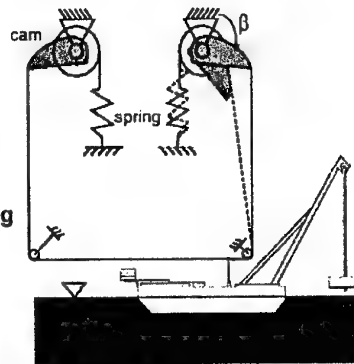
TUHH
Technische Universität Hamburg-Harburg

Experimental Results (TUHH)

Bifurcation diagram
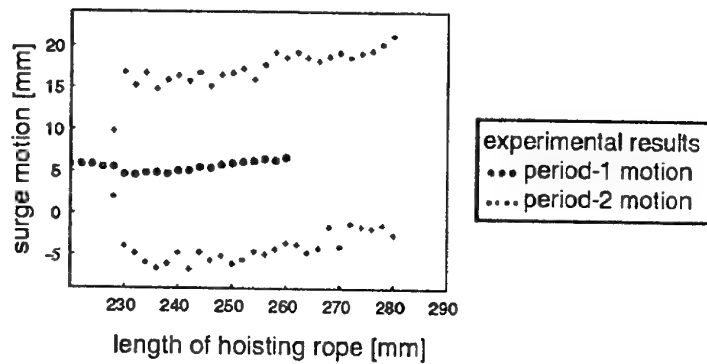
Dynamics of Crane Ship – P2-Solution
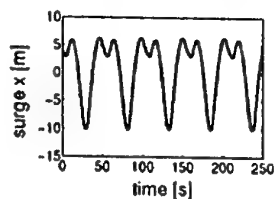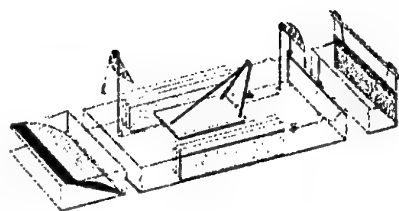
Experiment (TUB)   Simulation
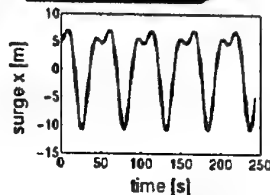
$A = 2.25m$, $\omega = 0.23\frac{rad}{s}$, $l = 49.5m$, $c_1 = 669.8\frac{kN}{m}$, $c_2 = -37.5\frac{kN}{m^2}$, $c_3 = 8\frac{kN}{m^3}$

Dynamics of Crane Barge – P3-Solution

Experiment (TUB)   **Simulation**
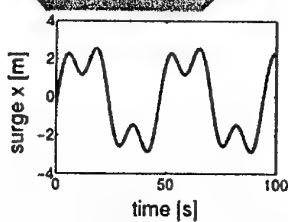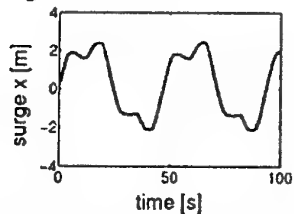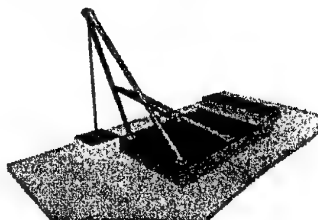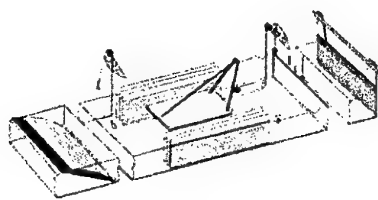
$A = 0.75m$, $\omega = 0.4 \frac{rad}{s}$, $l = 25m$, $c_1 = 21.0 \frac{kN}{m}$, $c_2 = 9.4 \frac{kN}{m^2}$, $c_3 = 0.014 \frac{kN}{m^3}$

TUHH
Technische Universität Hamburg-Harburg

A VIRTUAL MULTIBODY AND FINITE ELEMENT ANALYSIS ENVIRONMENT IN THE FIELD OF AEROSPACE CRASHWORTHINESS

H. M. LANKARANI, G. OLIVARES and H. NAGARAJAN

National Institute for Aviation Research, Wichita State University, Wichita, KS 67260-0093, USA

Abstract – Computer-aided analysis tools typically used in the studies of the aircraft crashworthiness are discussed. A methodology is presented for the entire design cycle from airframe to the cabin, seat, restraint and egress system. The methodology incorporates a combination of multibody modeling and non-linear finite element analysis of the airframe, seat and the occupant as well as component testing in early design stages, and sled and/or full-scale testing in later stages of design evaluations. A Virtual Reality (VR) system is utilized for effective system visualization and to better understand the interaction between the various subsystems. Examples of the use of this methodology for some of the current crash safety issues are presented.

1. INTRODUCTION

A theory is often a general statement of principle abstracted from observation and a model is a representation of a theory that can be used for prediction. To be useful, a model must be realistic and yet simple to understand and easy to manipulate. These are conflicting requirements, for realistic models are seldom simple and simple models are seldom realistic. Often, the scope of a model is defined by what is considered relevant. Features or behavior that are pertinent must be included in the model and those that are not can be ignored. Modeling here refers to the process of analysis and synthesis to arrive at a suitable mathematical description that encompasses the relevant dynamic characteristics of the component, preferably in terms of parameters that can be easily determined in practice (component testing). The procedure for developing a model is often an iterative one. The cycle begins with identifying the purpose of the model and its constraints, as well as the kinds of simplifying assumptions or omissions that can be made, determining the means of obtaining parameters and insight into the discipline are essential to making appropriate simplifying assumptions. Whereas oversimplification and omissions may lead to unacceptable loss of accuracy, a model that it's too detailed can be cumbersome to use.

Modeling and simulation are especially beneficial to solve aerospace crashworthiness applications, where the actual system does not exist or is too expensive, time consuming or hazardous to conduct, or when experimenting with an actual system can cause unacceptable disruptions. Changing the values of parameters, or exploring a new concept or operating strategy, can often be done more quickly in a simulation that by conducting a series of experimental studies on the actual system. The design of aircraft for improvement of its crashworthiness requires the knowledge and integration of several items. These items include the specifications and standards, human tolerance, injury criteria, energy absorption concepts in airframe design, seat legs, seat pan, seat cushion, restraint systems, surrounding structures, fire safety, economic and ergonomic considerations.

The development of current aircraft crash dynamics standards dates back to the 1970's during which the product liability grew for small aircraft [1]. To address the crashworthiness characteristics of the transport category aircraft, small general aviation aircraft, and rotorcraft, Federal Aviation Administration (FAA) and National Aeronautics and Space Administration (NASA) initiated a wide range of research and development programs. These programs represented a concentrated effort to analyze the aircraft behavior and the occupant characteristics through interrelated studies of accident data, dynamic analyses of crash events, full-scale aircraft impact tests, and aircraft seat tests. A panel named GASP (General Aviation Safety Panel) was also formed in 1978 to make recommendations on crashworthiness requirements. They considered survivable accidents for which the floor remained intact. The results of these studies formed the basis for the development of crashworthiness design standards for civil aircraft [2]. These requirements are defined in the *Federal Aviation Regulations* (FARs) Parts 23, 25, and 27 for general aviation aircraft, transport aircraft, and rotorcraft respectively [3-5]. These regulations were first proposed in 1982 and they became effective in 1988. In general, the FARs contains two distinct dynamic test conditions. Test-1 conditions, illustrated and described in Figure 1, require a seat inclination of 60 degrees in pitch and a mean velocity change of no less than 30 ft/sec (20 mph = 9 m/s), and is intended to evaluate the means provided to reduce the spinal loading and related injuries produced by the combined vertical/horizontal load environment typically generated by an aircraft crash event. Test-2 conditions, illustrated and described in Figure 1,

require the inclination of the seat on the track by 10 degrees in yaw direction and a mean velocity change of no less than 42 ft/sec (29 mph = 13 m/s) in the longitudinal direction. To account for a reasonable floor warpage level that may occur during a crash, one of the seat tracks is misaligned by 10 degrees in pitch and the other one by 10 degrees in roll. The Test-2 conditions are intended to provide an assessment of the seat structural performance and the occupant restraint system. The deceleration pulses in both tests are triangular shaped.

DYNAMIC TEST REQUIREMENTS	PART 23	PART 25	PART 27
TEST 1			
Test Velocity - ft/sec	31 (9.5 m/sec)	35 (10.7 m/sec)	30 (9.2 m/sec)
Seat Pitch Angle - Degrees	60	60	60
Seat Yaw Angle - Degrees	0	0	0
Peak Deceleration - G's	19/15	14	30
Time To Peak - sec	0.05/0.06	.08	0.031
Floor Deformation - Degrees	None	None	10 Pitch/10 Roll
TEST 2			
Test Velocity - ft/sec	42 (12.8 m/sec)	44 (13.4 m/sec)	42 (12.8 m/sec)
Seat Pitch Angle - Degrees	0	0	0
Seat Yaw Angle - Degrees	±10	±10	±10
Peak Deceleration - G's	26/21	16	18.4
Time To Peak - sec	0.05/0.06	0.09	0.071
Floor Deformation - Degrees	10 Pitch/10 Roll	10 Pitch/10 Roll	10 Pitch/10 Roll
COMPLIANCE CRITERIA			
HIC	1000	1000	1000
Lumbar Load - lb	1500 (6675 N)	1500 (6675 N)	1500 (6675 N)
Strap Loads - lb	1750/2000 (7785 N/8900 N)	1750/2000 (7785 N/8900 N)	1750/2000 (7785 N/8900 N)
Femur Load - lb	N/A	2250	N/A

† passenger ‡ pilot

Figure 1 - Dynamic test requirements.

The pass/fail criteria are based on the data collected from accidents and the recommendation of the GASP on the frequency of major fatal injuries to specific body regions in aircraft accidents. The injury and pass/fail criteria in the FARs include the following:

a. Maximum compressive load measured between the pelvis and the lumbar spine (of the Part 572 Subpart B Hybrid II ATD, per FARs) must not exceed 1500 pounds (6675 N).

b. Loads in the individual straps must not exceed 1750 pounds (7785 N) for pilot and 2000 pounds (8,900 N) for passengers.

c. The compressive load in the femur of Hybrid II ATD (Anthropomorphic Test Dummy) must not exceed 2250 pounds (10,000 N). This requirement is only for transport category (Part 25) aircraft.

d. The Head Injury Criteria (HIC), evaluation for the Hybrid II ATD must not exceed 1000 [6].

$$HIC = \left[(t_2 - t_1) \left\{ \frac{1}{(t_2 - t_1)} \int_{t_1}^{t_2} a(t) dt \right\}^{2.5} \right]_{max}$$

In contrast with the automotive industry, in the aerospace industry numerical simulation methods are primarily used at the very end of the product development process. Often they are applied to confirm the reliability of an already existing design, or sometimes for further design improvements by means of optimization methods. Numerical simulation methods are much more efficient when used at an early stage of the product development process. In this way, the number of hardware tests can be reduced since a profound knowledge of the model already exists. The intend on this paper is to give an overview of the different simulation techniques (multibody and finite element method approach) that could be implemented at the early design stages of the airframe, interior, and evacuation systems. Crashworthiness problems are best addressed in a systems approach utilizing combinations of CAE tools, component tests, sled and/or full-scale tests.

2. COMPUTE AIDED ENGINEERING TOOLS FOR SEAT, OCCUPANT AND AIRFRAME MODELING

To improve aircraft crash safety, conditions critical to an occupant's survival during a crash must be known. A large number of possible aircraft crash environments exist, and the impact sled testing may neither be possible nor feasible for some configurations. Cost and time are also other burdens of testing procedures. Furthermore, prior to testing, multiple simulations (analysis) must be conducted to better define the experimental testing program. Rigorous analytical techniques are necessary for design of crashworthy aircraft airframes, seats, occupant surroundings, and restraint systems. Validated analytical models also reduce the necessity of fabrication of design

131

modifications. Some of the non-linear finite element analysis codes used for modeling and analysis of aircraft seats and interiors (structures) are LS-DYNA, MSC/DYTRAN, MARC and PAM-CRASH. Analysis codes that model the dynamic response of a human or ATD during a crash are known as gross motion simulators. These models are comprised basically of kinematically connected body segments with joint stiffness and contact forces between penetrating segments or segments in contact with the surrounding. Some of the existing body gross motion simulators include: ROS, CAL2D, HSRI, MVMA2D, SIMULA, PROMETHEUS, CAL3D, UCIN, SOM-LA/TA, ATB, and MADYMO [12]. Currently, the codes mostly used for reconstruction of aircraft crash scenarios are SOM-LA/TA, ATB, and MADYMO. More advanced ATD and human finite element models are also available these days for detailed assessment of the injury potential to different body regions. A systems approach, shown in Figure 2, is used for seat design problems utilizing nonlinear finite element tools with experimental component tests to validate the models, and iterative analysis for the final seat design. Each element in the load path, namely, the seat legs, pan, and cushion, is analyzed individually as well as its function in the entire seat model.
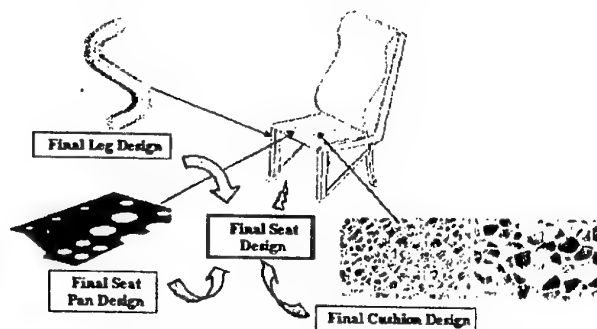
Figure 2. Systems approach in designing an aircraft seat.

The survivability of the occupant in the event of an aircraft accident primarily depends on a number of key features like maintaining a survivable volume around the occupant, which is the passenger compartment, having effective restraints features to properly restraint the occupant within the survivable volume, limiting the occupant loads by having energy absorbing structures and seats to have effective evacuation systems in place for the mitigating of post-crash hazards. A methodology, shown in Figure 3, is used for the development of safety systems in an aircraft utilizing finite element tools, multibody modeling techniques and virtual reality tools for the safe egress of the occupant from an aircraft in the event of a crash. The methodology uses the responses from the aircraft response with the impact surface, obtained from finite element modeling of the impact, being applied to the occupants and designing effective systems for the safety of the occupant during the event using multibody modeling tools and the modeling the egress of the occupant from the aircraft using virtual reality tools.
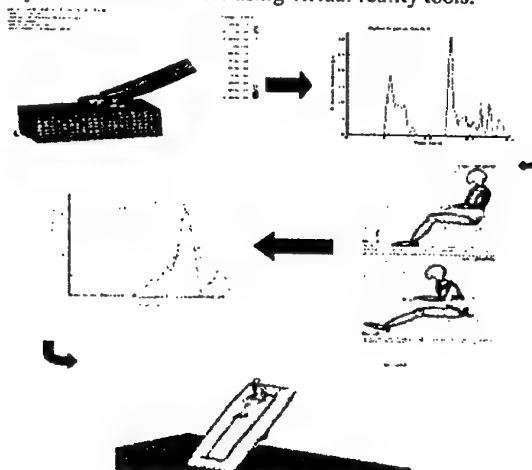
Figure 3. Virtual development cycle for aerospace safety systems.

3. AIRFRAME CRASHWORTHINESS DESIGN

Crash-resistant features and design methodologies, such as Aircraft Crash Survival Design Guide [1] are based on hard surface impacts. Accident data, however, indicates that only 18% of potentially survivable civilian crashes occur on hard, prepared surfaces [2]. The statistics are even lower for the army at 7% and the Navy at zero percent [3]. In contrast, 51% of civilian and 83% of Navy crashes occur on water and soft soil. The crash-resistant subsystems designed for rigid surface impacts, such as landing gears or sub floors, are not as effective in soft soil and water since the structure undergoes different loading conditions. Hard surface impacts introduce distributed loads into the stiffest structural members, such as keel beams and frames.

Nowadays, there is no reliable procedure for predicting the interaction processes that will occur between soil or water and an aircraft. While the in-flight behavior of the aircraft can be predicted with an optimum degree of precision, the same cannot be said for the phenomenological behavior that takes place at impact. This is due primarily to the lack of knowledge and to the complexity of the soil behavior to allow a reliable prediction of reactive forces against various geometries of the impact when subjected to a dynamic loading situation. The functional relationships and behavioral characteristics of soil and water are much more complex than for other common engineering materials, thus making generalized behavior conditions extremely difficult to determine with reliable accuracy.

3.1 ANALYSIS OF AND AIRCRAFT DROP TEST ON SOFT SOIL

A soil model developed in LS DYNA [10] is validated against experimental results. Figure 4 shows a model of the instrumented cone used in the experimental setup, wherein the cone was dropped from a predefined height on to the soft soil and the depth of indentation was measured, and the also the model developed in LS DYNA.
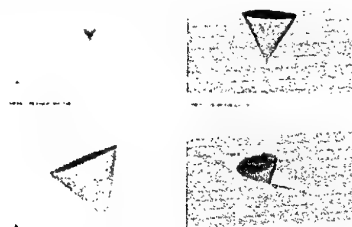
Figure 4. Modeling a cone impact on soft soil.

Four identical four-place, high wings, single-engine airplane specimens with nominal masses of 1043 kg were crashed at the Langley Impact Dynamics Research Facility [8] under controlled free-flight test conditions. These tests were conducted with nominal velocities of 25 m/sec along the flight path at various flight-path angles, ground-contact pitch angles, and roll angles. Three of the airplane specimens were crashed on a concrete surface; one was crashed on soil. Each airplane had a gross mass of 1043 kg and the pilot, copilot were represented by anthropomorphic dummies. The airplane specimen, suspended by two swing cables attached to the top of the gantry, is drawn back and above the impact surface by a pullback cable to a height of about 49m as shown in figure 5.
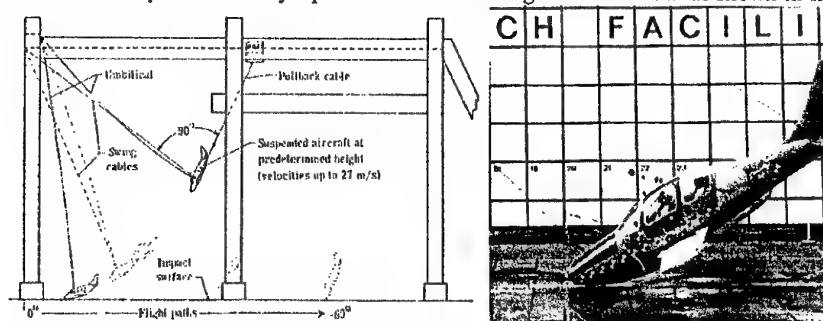
Figure 5. Full-scale crash impact test facility [8]

133

The airplane contacted the soil impact surface on the nose gear with the velocity of 25.3 m/sec along a flight path angle of –32 degrees and at a roll angle of –1.5 degrees. Prior to the tests the engines were completely removed from the fuselage. The accelerations measured on the floor of the aircraft were nominally 20 to 25g's. The aircraft was modeled using the finite element method. The model is meshed using 4 node quadrilateral shell elements. The model had the same mass of 1043 kg as in the actual test. Figure 6 illustrates the crash simulation of the airplane during a negative pitch (node down) crash starting at the initial ground contact. The airplane contacted the soil impact surface with a velocity of 25.3 m/sec along a flight path angle of –32 degrees. The nose began to buckle immediately after initial ground contact followed by the fuselage at 0.09 sec into the impact. The aft section of the fuselage failed at 0.16 sec. The airplane model began to plough into the soil creating a crater in the soil model throwing out the deleted nodes. The acceleration profile in the Z-direction had two spikes, the first one is when the nose just touches the soil, and the second one is due to the fuselage impact on the soft soil. The first one reached a maximum of 18g while the second one had reached 30g. The acceleration data was obtained at the center of mass of the aircraft model unlike in the drop test where it was measured at different locations on the cabin floor. Overall, the simulation had a reasonable representation of the actual airplane crash test.
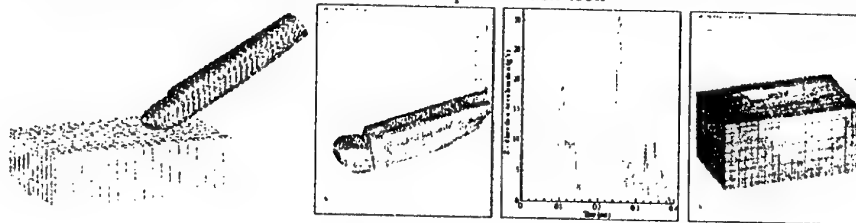
Figure 6. Aircraft impact on soft soil.

The acceleration profiles from this test are used as input for the occupant simulation using multibody tools, to obtain the occupant responses during the impact. Aircraft systems like seats and restraints are suitably designed to reduce the injuries to the occupant.

3.1 HELICOPTER IMPACT ON WATER

A water model developed in LSDYNA is validated against experimental results conducted by dropping a ball into a beaker of water. Figure 7shows the process of validation of the water model using the experimental results and finite element model.
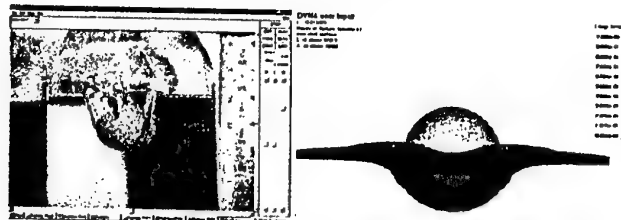
Figure 7. Validation of water model.

Simula Technologies at U.S Army Yuma Proving Ground utilizing a surplus Bell Helicopter UH-1H "Huey" airframe conducted a vertical dynamic test. The test helicopter had been striped of nearly all components such as engine/transmission, tail boom, landing gear, etc., leaving the bare hull. The test weight was 2260 lbs. The test was purely a vertical drop of approximately 9 ft. measured from the lowest point of the helicopter belly to the water surface. This provided a calculated impact velocity of approximately 24 ft/sec. Fresh water was utilized with, no surface waves. The water depth at the impact point was approximately 90 inches. The peak pressure reading at the various sensors ranged from a low of 2.3 psig to a maximum of 18.4 psig. The peak accelerometer readings ranged from a minimum of 27.9g to a maximum of 69g.

The dimensions of the air and water models used in the eulerian simulation of ball impact on water were scaled up to accommodate the helicopter model, shown in Figure 8. The element formulation of the model is the same. The mesh

134

density and the total number of the solid elements remain the same. Helicopter is lagrangian solid here modeled with Belytschko-Tsay shell elements and air/water stays as the eulerian fluid. The boundary conditions also are similar to the eulerian ball impact simulation.

Figure 8. Deformed helicopter showing the stress distribution and the acceleration profile of impact.

The water depth at the impact point was 90 inches. The impact attitude was pure flat (no pitch or roll). The helicopter sustained major structural damage from the water impact. Figure 9. shows stressed state of helicopter at initial touchdown. The stresses increase till the time the whole body comes in initial contact with the water surface. Subsequently, the stresses drop as the helicopter sinks down with a constant velocity. The peak value of acceleration is around 77'g' and a second peak of 23'g'comes a little later. Then slowly the acceleration drops down to zero when the helicopter is sinking down with a constant velocity. There's another acceleration peak of about 3-4'g' when the wings impact the water surface. Since, the velocity has already reduced to a minimal value after the initial impact, the value of the deceleration because of the wing impact is meager

4. CAE AND VR TOOLS FOR CABIN INTERIOR MODELING AND VISUALIZATION

Both the multibody and the finite element method offer their specific advantages and disadvantages for cabin interior crashworthiness design applications. The multibody approach is particularly attractive due to its capability of simulating in very efficient way complex kinematical connections, while the finite element method offers the capability of describing (local) structural deformations and stress distribution. The following example application will give an overview on how the coupling of these two methods in conjunction with component testing is applied throughout the system development cycle.

4.1 FRONT-ROW OCCUPANT ENVIRONMENT DEVELOPMENT CYCLE
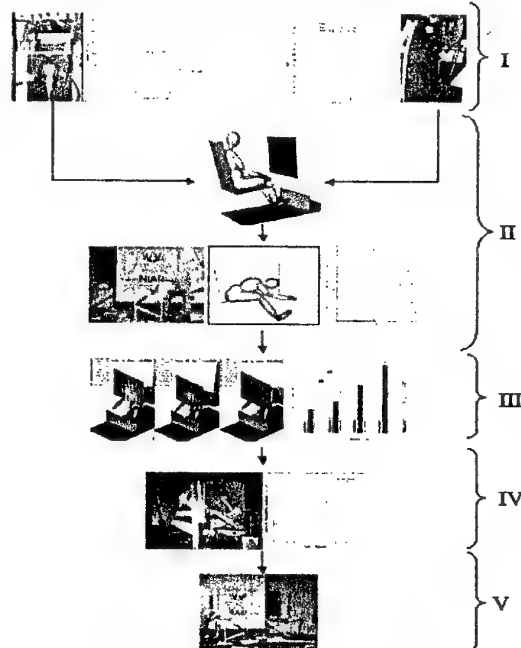
Figure 9. CAE/Testing Development Cycle.

135

Airline seat manufacturers have experienced some difficulty in satisfying the Head Injury Criteria (HIC) contained in the FAR 25.562 [1] 16 g dynamic seat test requirements for so-called "front-row seats" that are located behind a bulkhead or cabin class divider. Traditionally sled testing has been used to develop aircraft interiors. Due to the high cost, test set up time, and complexity of developing the system by using sled testing, a Multibody/FEA approach combined with component and sled testing is presented. In this project the front-row seat environment had to be defined. Initially three different lap belt (nylon, polyester 8%, and polyester 19%), three bulkhead (Aluminum, Standard Nomex Honeycomb, and Modified Nomex Honeycomb) materials were available; and six possible seat setback configurations (28, 30, 33, 35, 38, and 40 inches) to choose from. If we were to develop this system the traditional way (sled testing) we would have to test 54 different configurations, and since usually two sled tests are conducted per configuration we would have a total of 108 sled tests. A program like this could take up to three months of sled testing, and hundreds of thousands of dollars in components. In order to avoid the high cost and the long development cycle CAE and VR tools in conjunction with component and sled testing can reduce the development cycle to a month of simulation work, including 6 sled tests for model validation, 4 component tests, and 2 final system certification tests.

a) *PHASE I AND II:* COMPONENT TEST, MODEL DEFINITION AND VALIDATION

A Multibody/FEA model of the seat/ATD/bulkhead test configuration is shown in Figure 8. The rigid seat was represented as two planes that are fixed in space. One plane represents the seat pan while the other represents the seat back. The contact forces between these planes and the appropriate anthropomorphic test dummy (ATD) body segments were defined in terms of the appropriate loading and unloading curves obtained through component testing.
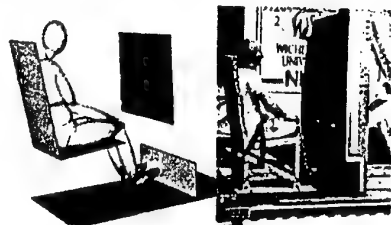
Figure 10. Multibody/fea model and sled test setup.

The 50th percentile Hybrid II ATD multibody model was placed in the seat. A two-point restraint system was modeled using belt properties that were representative of the system used in the sled tests. The anchor points of the belt were located at the intersection of the seat pan and seat back as shown in Figure 8. The floor was also modeled by means of a rigid plane. An additional rigid plane was placed in front of the legs just below the bulkhead. The bulkhead was modeled using 180 quadrilateral shell elements representing a 30 x 24 in. (76.2 x 60.9 cm) bulkhead surface. An elasto-plastic material model was used to define the behavior of the bulkhead materials. The stress-strain curve used in the model were acquired from a series of tensile tests of using an MTS servo-hydraulic test stand and linear impactor load/deflection tests since this data was not available in literature. Prior to conducting the parameter studies the models were validated with sled test data for the three different bulkhead configurations. As shown on figure 11 there is good correlation between the models and the sled tests.

	Sled	Model
HIC	1394	1399
Δt	11	13.7

	Sled	Model
HIC	882	889
Δt	31	33
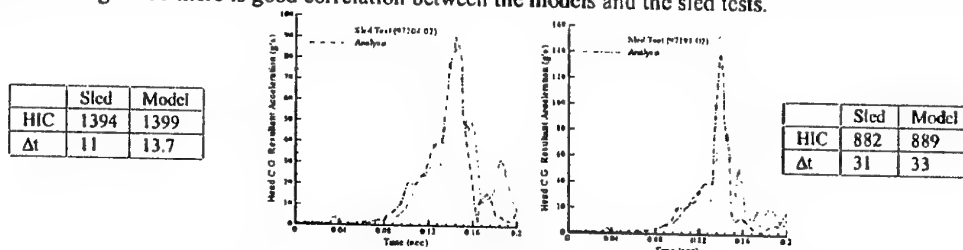
Figure 11. Comparison Head Acceleration Profile Sled and MADYMO Production Bulkhead.

b) *PHASE III:* PARAMETER STUDY

The purpose of this parameter study was to observe the injury criteria and kinematics of the ATD under various seat setback conditions (28, 30, 33, 35, 38, and 40 inches), various lap belt (nylon, polyester 8%, and polyester 19%),

136

and bulkhead material configurations (aluminum panel, standard Nomex honeycomb, and modified Nomex honeycomb). These three factors were identified as the most important parameters influencing the magnitude of the HIC values. This is due to the fact that these are the parameters that dictate the head impact angle, head impact velocity, head impact acceleration, and the translation of the lower torso. From the parameter study we concluded that the lower the head impact angle, the higher the peak acceleration and HIC values become. The stiffness of the lap belt material and the seat setback distance are the parameters that dictate the magnitude of the Head Impact Angle. Belts with higher stiffness allow less movement of the lower torso. When we have the same setback distance and different lap belt materials we can observe that the stiffer lap belt material the larger the Head Impact Angle becomes, this is due to the fact that a stiffer belt allows less forward lower torso displacement prior to ATD/Bulkhead impact hence allowing more rotation of the upper torso prior to impact. From the sled test analysis and the computer models we can observe that the longer the seat setback distance the more critical the rearward translation of the torso after initial head impact becomes. This movement of the lower torso during impact becomes more critical for longer seat setback distances as well as when softer materials are used to the bulkhead structure construction.
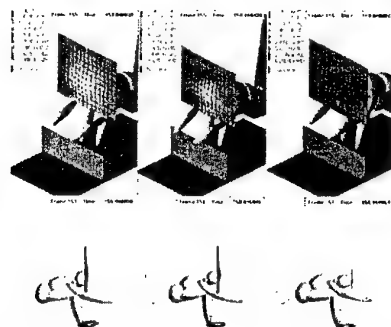
Figure 12. Deformation of the panels during impact for different seat setback configurations.

From the parameter study it was observed that the configuration that meets all the design requirements (biomechanical performance, cost, legroom, and component availability) as well as FAR 25 requirements was the aluminum bulkhead with a seat setback distance of 35 (0.89meters) inches as shown in the table bellow.

c) *PHASE IV AND V:* COMPONENT TEST AND CERTIFICATION SLED TEST OF THE FINAL DESIGN

Due to the high cost, test set up time, and complexity of a sled test, NIAR's Enhanced Head Injury Criteria Component Tester was used to validate the final design prior to conducting the final certification tests. This component tester is an inverted pendulum type impactor. It consists of an accelerator, pendulum arm, support arm, ATD head/neck assembly, signal processing electronics, and a computerized control and data acquisition system. As shown on table 1 the component test confirms the results obtained from the simulation design, consequently we concluded that the system was ready to proceed with phase V, the sled test certification process.

Table 1. Final System Configuration.

Parameter	Sled	Component	Simulation
Bulkhead Material	AL 2024 -O	AL 2024-O	AL 2024 -O
Seat Setback Distance – in	35	35	35
Head Impact Velocity –ft/s	45.08	44	44
Head Impact Angle – deg	38°	38°	42°
Head C.G. Peak Acceleration – g	143	143	140
HIC	694	685	634
HIC Window (Δt) – ms	23.7	21.4	22.8
Average Head Acceleration –g	61	63	60

The results from the sled test certification process confirm the results of both the component and the simulation model see table 3 and figure 13. By using this Multibody/FEA technique in conjunction with component testing and

137

minimal sled testing we were able not only of selecting the proper system configuration to meet the system requirements, but also through simulation we gained a better understanding on the ATD (by using 3D Virtual Reality visualization of the system) responses to the different input parameters.
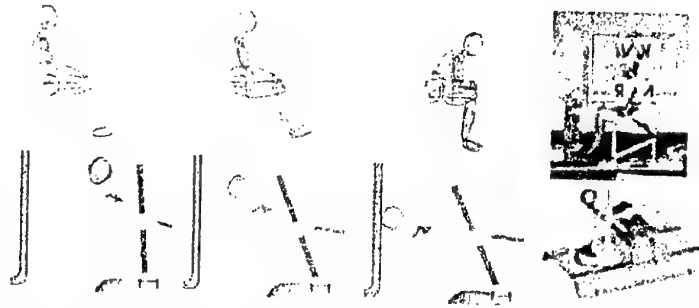
Figure 13. Final configuration resultant head c.g. Acceleration time history for sled and NIAR component test.

5. APPLICATION OF CAE AND VR TOOLS FOR VIRTUAL TESTING OF EVACUATION SYSTEMS

Throughout the more than 40 years since the birth of this industry, governmental requirements have continuously increased and placed stricter regulations on the design of evacuation systems. As aircraft became larger and carried more people, the systems became more sophisticated and complex. Demand for improvements such as increased safety, greater evacuee throughput, decreased inflation time and weight reductions are constantly forcing the industry forward [11]. This specific CAE and VR application shows how we could analyze the performance of the evacuation system under different ambient conditions (0 C, 23 C, and 44 C). Due to the size of an evacuation system a test like this would be very difficult and expensive to perform in a temperature chamber, but using FEA techniques to describe the evacuation system, and a multibody model of the ATD we can easily evaluate the performance of the system. A model of the evacuation system was created using MADYMO. The slide model consists of 9800 triangular elements. A typical evacuation system inflator mass flow rate was defined to inflate the slide. Appropriate contacts were defined between the multibody ATD and the evacuation system surfaces.

Figure 14. ATD Biomechanical Response.
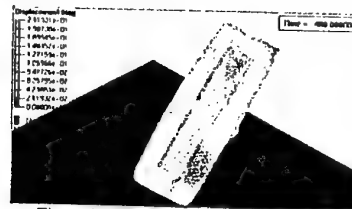
Figure 15. Evacuation System Response.

The biomechanical response of the ATD under these different ambient conditions is shown on Figure 14, as we can observe for both the cold and hot ambient conditions the head acceleration is greater than for nominal ambient conditions. For the cold ambient condition case this is due to the reduction in the internal pressure and total volume of the bag due to the effect of lower temperatures (see Figure 15), this makes the impact with the ground more severe. On the other hand for the hot load case, the increase in pressure and slide volume make the slide stiffer hence increasing the sliding velocity of the ATD, and increasing the rebound of the head at the end of the slide.

6. VIRTUAL REALITY CENTER

In order to gain a better understanding of the evacuation system performance the NIAR's Virtual Reality facilities were used. This VR facility allows the user to visualize the results of the simulation in a screen 7 ft high and 15 ft wide (see figure 16). Virtual Reality offers a way for engineers to visualize, manipulate and interact with computers and extremely complex data. VR improves visualization of the system by allowing the user to co-exist in the same space as the system model therefore gaining a better appreciation of the system geometry and performance. VR also improves interaction with design in terms of more intuitive model manipulation and functional experimentation, the designer can effectively interact with the product model directly rather than using the conventional 2-D mouse and

138

cursor. Another advantage of particular importance is the sense of scale, which can only be conveyed by immersing the designer in the "design". The simulation technique showed on this section could be easily implemented to conduct 'virtually' all the required product testing to ensure it's optimum functionality prior to building a physical model. The data generated by the multibody simulation of the various crash event provides a myriad amount of data which needs to be effectively understood. The virtual reality environment provides a suitable platform for the effective viewing of these data and also in understanding their significance.
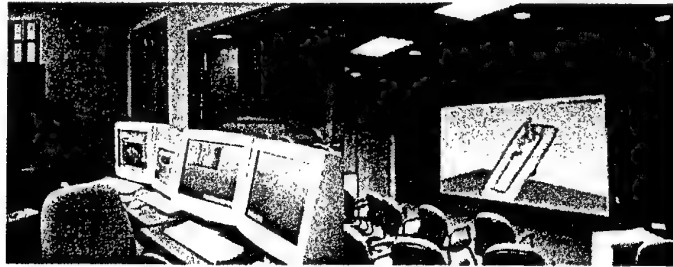
Figure 16. Virtual reality control room and visualization of the evacuation simulation model at the NIAR.

7. CONCLUSIONS

This paper presents examples of the use of a systems approach methodology to some of the current aircraft crashworthiness problems. It makes use of appropriate injury criteria, component performance tests, full-scale sled tests, and the presented some of the latest CAE and VR tools. The modeling of the aircraft impact/accident is accomplished by using finite element analysis and multibody dynamic simulation tools as well as projections onto a virtual reality environment. The importance of CAE tools in aircraft crashworthiness problems is demonstrated via examples. This provides much insight into the nature of the seat, occupant, and airframe responses individually and collectively. The main purpose of utilizing this methodology is the anticipation that due to myriad amount of data that is generated by the finite element and multibody simulation CAE and VR tools need to be effectively utilized for analysis during the design phase.

8. REFERENCES

1. J W Olcott, The development of dynamic performance standards for federal aviation aircraft seats, *Business and Commercial Aviation,* 1995.

2. R F Chandler, Crash injury protection in civil aviation, in A M Nahum and J W Melvin (eds.), *Accidental Injury Biomechanics and Prevention*, Springer-Verlag, New York, 151-185, 1993.

3. *Title 14 U.S. code of Federal Regulations, Part 23*, Amendment 23-39, Section 23.562, published in the Federal Register of August 14, 1988, effective date of September 14, 1988.

4. *Title 14 U.S. code of Federal Regulations, Part 25*, Amendment 25-64, Section 25.562, published in the Federal Register of May 17, 1988, effective date of June 16, 1988.

5. *Title 14 U.S. code of Federal Regulations, Part 27*, Amendment 27-25, Section 27.562, published in the Federal Register of November 13, 1989, effective date of December 13, 1989.

6. SAE, AS8049, *Performance standards for seats in civil rotorcraft and transport airplanes*, Aerospace Standards, 1990.

7. E S Gurdjian, H R Lissner, F R Latimer, B F Haddad, and J E Webster, Quantitative determination of acceleration and intercranial pressure in experimental head injury, *Neurology* 3, 417-423, 1953.

8. E S Gurdjian, V L Roberts, L M Thomas, Tolerance curves of acceleration and intercranial pressure and protective index in experimental head injury, *J. of Trauma* 6, 600, 1964.

9. Department of Transportation Occupant crash protection - Head Injury Criterion, *NHTSA Docket Number 69-7*, Notice 19, S6.2 of FMVSS 208, March 1971.

10. J S Soltis, J W Nissley, 'The development of dynamic performance standards for civil aircraft seats', *Aircraft interiors/ flammability, maintenance, refurbishment and impact requirements conference*, Wichita, April 1990.

11. M M Sadeghi, 'Evolution and design of vehicle structures for crash protection - A system approach', Crashworthiness of transportation systems: structural impact and occupant protection, *Proceeding of the NATO advanced study institute*, Volume II, July 1996.

12. TNO. *MADYMO Theoretical manual, Version 5.3*, TNO, Delft, Netherlands, 1998.

GRAPH-THEORETIC MODELLING OF MULTIBODY SYSTEMS

J.J. MCPHEE
University of Waterloo
Systems Design Engineering
Waterloo, Ontario, Canada N2L 3G1

1. Introduction

The most recent developments in applying linear graph theory to multibody system dynamics are presented, with particular emphasis on the symbolic generation of simple, compact equations that are well-suited for real-time simulation.

An overview of the modelling of flexible multibody systems is presented in the next section, taking advantage of the unique features of linear graph theory and symbolic computer programming. Graph theory is then used to generate equations in terms of user-selected coordinates that are well-suited to a given problem, and to exploit special topologies such as that found in parallel robotic manipulators. Graph theory also facilitates the modelling of multibody and mechatronic systems using subsystem models; this is particularly useful for virtual reality (VR) applications when sections of a model are changing while others remain constant.

2. Symbolic Modelling of Flexible Multibody Systems

Consider the two-link robotic manipulator shown in Figure 1, along with its linear graph representation. Nodes in the graph represent body-fixed reference frames, while edges represent kinematic or dynamic transformations associated with physical components. Edges m_1 and m_2 represent the two bodies, which may be rigid or flexible. Newton's Laws require that the edges originate at an inertial frame (node) and terminate at a body-fixed frame (node) — usually at the center of mass for a rigid body, and at one end of a flexible beam element. For clarity, the physical components are superimposed on the linear graph with dotted lines.

Edges h_7 and h_8 are the two revolute joints connecting the bodies; the "arm elements" $r_3 - r_5$ represent transformations from the body frame to the joint frames. These transformations are functions of the body rotation and, for flexible bodies, the elastic deflections. Edge r_6 is included for the purpose of tracking the
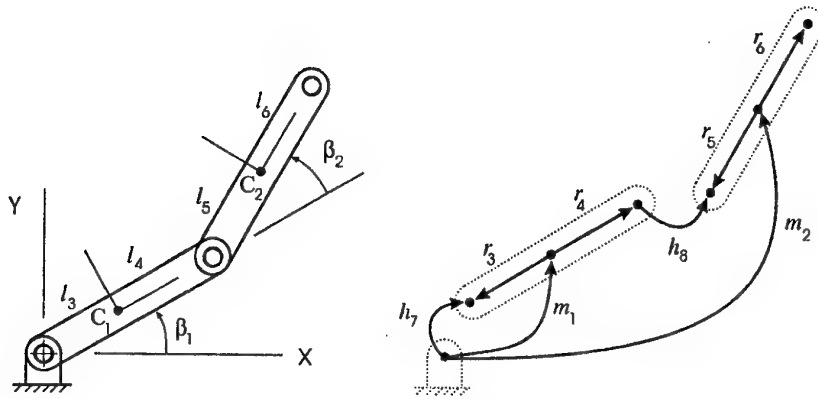
Figure 1. Two-link robot manipulator and linear graph

position and orientation of the tip of the manipulator. Additional physical effects, e.g. motor torques and weights, are easily added to the system graph.

Associated with each edge are through (force, torque) and across (translation, rotation) variables that satisfy the fundamental cutset and circuit equations [1]. For mechanical systems, the cutset equations provide dynamic equilibrium equations for any combination of components, while the circuit equations provide closure conditions around any loop.

If a tree is selected for the graph, then the circuit equations can be used to express all kinematic variables as linear combinations of the coordinates associated with the tree edges ("branches") [2]. For dependent branch coordinates, which is always the case for systems with closed kinematic chains, the kinematic constraint equations are generated by *projecting the circuit equations for cotree joints onto the reaction space for that joint.* For holonomic constraints, one obtains m nonlinear algebraic equations in terms of the n branch coordinates $\mathbf{q}$:

$$\Phi(\mathbf{q}, t) = 0 \qquad (1)$$

where $n - m = f$, the degrees of freedom (DOF) of the system.

Once the kinematic equations are obtained, the dynamic equations can be systematically generated by *projecting the cutset equations for branch components onto the motion space for that component* [2]:

$$\mathbf{M}\ddot{\mathbf{q}} + \Phi_{\mathbf{q}}^{T}\lambda = \mathbf{F} \qquad (2)$$

where $\mathbf{M}$ is the mass matrix, $\Phi_{\mathbf{q}}$ is the Jacobian of the constraint equations, the Lagrange multipliers λ correspond to reactions in cotree joints, and $\mathbf{F}$ contains external forces and quadratic velocity terms.

141

Alternatively, the principle of virtual work may be employed, especially when flexible bodies are included in the system model [3], to obtain the dynamic equations (2). Symbolic programming was found to be particularly useful in implementing this latter formulation [4]. Multiplications by 0 and 1 are eliminated, and trigonometric simplifications are automated. The final kinematic and dynamic equations can be visually examined for physical insight, or exported as optimized C or Fortran code for subsequent simulation. We have used the Maple symbolic programming language to develop our DynaFlex software[1] for modelling flexible multibody systems.

Symbolically, one can also partition the first variation of the constraint equations into f independent coordinates q_i and m dependent coordinates q_d:

$$\Phi_{q_d}\delta q_d + \Phi_{q_i}\delta q_i = 0 \tag{3}$$

where $\Phi_{q_i} = \partial\Phi/\partial q_i$ and $\Phi_{q_d} = \partial\Phi/\partial q_d$ is non-singular as long as the given physical constraints are not redundant. One can then solve these linear equations (3) for the transformation from dependent to independent variations:

$$\delta q_d = -\Phi_{q_d}^{-1}\Phi_{q_i}\delta q_i = J\,\delta q_i \tag{4}$$

By summing the contributions of all working components to the system virtual work δW, and using the above transformation, one obtains:

$$\delta W = Q^T\delta q = Q^T\left[\begin{array}{c} J \\ 1 \end{array}\right]\delta q_i = Q_i^T\delta q_i = 0 \tag{5}$$

where Q_i are the generalized forces associated with δq_i. Since these variations are independent, each generalized force can be set to zero to obtain one dynamic equation per degree of freedom, from which the constraint reactions λ are eliminated. In matrix form,

$$\widetilde{M}\ddot{q} = \widetilde{F}(q, \dot{q}, t) \tag{6}$$

where $\widetilde{M}$ is an unsymmetric $f \times n$ mass matrix. In a later section, this form of the dynamic equations will be used to advantage in inverse dynamic analyses.

3. Coordinate Selection

By selecting a spanning tree for the graph, the branch coordinates q that appear in the kinematic and dynamic equations are defined. This is an important feature of a graph-theoretic approach, since most other multibody formulations are restricted to a pre-defined set of coordinates, usually absolute [5] or joint [6].

Using graph theory, one can generate equations in absolute coordinates (select all bodies into the tree), joint coordinates (select joints into the tree), or some

[1]http://real.uwaterloo.ca/~dynaflex

142

combination of the two. One can even select two different trees — one to generate rotational equations and one to generate translational equations. By doing this, one can reduce the total number of equations to be solved, and reduce their complexity at the same time [2]. By selecting coordinates that are best suited to the problem at hand, one obtains equations that are very well-suited to real-time simulation in either a virtual reality environment or an operator-in-the-loop simulation.

By defining and selecting "virtual joints" into the tree [7], it is even possible to generate equations in "indirect coordinates" corresponding to bodies that are not necessarily adjacent [8]. Consider the open-loop multibody system taken from [8], and its corresponding linear graph in Figure 2.
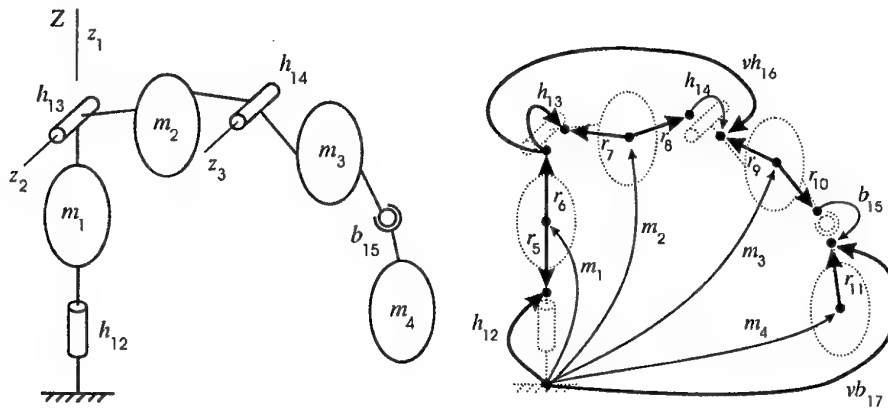
Figure 2. Open-loop multibody system and linear graph

Once again, bodies are represented by edges $m_1 - m_4$, body-fixed transformations by arm elements $r_5 - r_{11}$, revolute joints by edges $h_{12} - h_{14}$, and the spherical joint by b_{15}. In addition, two virtual joints are added: a virtual revolute joint vh_{16} representing the rotation of m_3 relative to m_1, and a virtual spherical joint vb_{17} to represent the rotation of m_4 relative to the ground. Fayet and Pfister [8] have shown that the corresponding indirect coordinates result in equations that are simpler in form than the more traditional joint coordinate equations. This is due to the fact that joint axes z_2 and z_3 are parallel, and absolute angular coordinates are preferred over relative angular coordinates [9]. With a graph-theoretic approach, one can generate the motion equations in indirect coordinates by simply selecting vh_{16} and vb_{17} into the tree in place of h_{14} and b_{15}.

Applying this approach to a serial manipulator comprised of bodies $m_1 - m_3$, the dynamic equations (2) were generated in terms of the joint coordinates $\mathbf{q}_\beta = [\beta_{12}, \beta_{13}, \beta_{14}]^T$ and the indirect coordinates $\mathbf{q_i} = [\beta_{12}, \beta_{13}, \beta_{16}]^T$. Both sets of coordinates are independent for this serial manipulator, so there are no kinematic

143

constraint equations and no constraint reactions λ appearing in the dynamic equations. However, some of the entries in these equations will differ for the two sets of coordinates, e.g. the second diagonal entry in the two mass matrices:

$$\mathbf{M}_\beta(2,2) = I_{2z} + m_2 l_7^2 + I_{3z} + m_3[l_{78}^2 + 2l_{78}l_9 \cos\beta_{14} + l_9^2]$$
$$\mathbf{M}_i(2,2) = I_{2z} + m_2 l_7^2 + m_3 l_{78}^2$$

The use of indirect coordinates results in a simplification of the mass matrix, for which the diagonal entries correspond to moments of inertia of "compound augmented bodies" [8]. Table 1 provides the number of additions, multiplications, and function calls needed to evaluate the two mass matrices.

TABLE 1. Number of operations

	Adds.	Mults.	Functs.
$\mathbf{M}_\beta$:	27	53	12
$\mathbf{M}_i$:	20	43	11

4. Application to Parallel Manipulators

For multibody systems with special topologies, such as the parallel manipulators shown in Figure 3 that have legs of identical configuration, linear graph theory can be used to exploit this topology during the equation generation process. In comparison with serial robots, parallel manipulators have very good performance in terms of rigidity, accuracy and dynamic characteristics, but they are more difficult to model. Merlet [11] writes that one school of thought recommends that dynamic models should not be used because modelling errors are too numerous. Despite this, and the fact that dynamic equations can be generated automatically, many authors [12, 13] are still performing manual derivations for parallel manipulators.

Symbolic solutions for the inverse dynamics are especially useful for real-time control of parallel manipulators and other multibody systems [10]. Given that parallel manipulators are frequently used as input devices for real-time simulations, or as platforms for flight simulators, the automatic generation of inverse dynamic solutions facilitates the development of virtual reality environments.

To show how this can be effected using graph theory and symbolic computing, consider the 3-DOF planar parallel manipulator [14] shown in Figure 3. The three revolute joints connecting the end effector 7 to links 4, 5, and 6 are placed in the cotree of the linear graph representation; the corresponding joint coordinates are thereby eliminated from all equations. From the projected circuit equations for these three joints, one obtains the $m = 6$ nonlinear kinematic constraint equations:

$$\Phi(\mathbf{q}, t) = \Phi(\theta_1, \theta_2, \theta_3, \theta_4, \theta_5, \theta_6, x_7, y_7, \theta_7, t) = 0 \qquad (7)$$

144
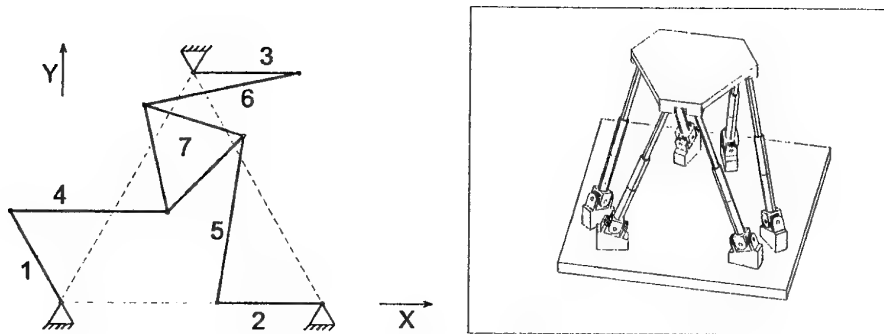
Figure 3. Planar 3-DOF and spatial 6-DOF parallel manipulators

where θ_i, $i = 1 \ldots 6$, is the coordinate for the revolute joint on the proximal side of link i, while x_7, y_7, and θ_7 represent the motion of the end effector 7. Each of these coordinates correspond to a joint in the spanning tree of the graph, including a "virtual joint" between the ground and the end effector.

These constraint equations can be used to obtain the transformation (4) from dependent variations to independent variations which, when combined with our symbolic virtual work routines, allows the dynamic equations to be written in the embedded form given by equation (6). In an inverse dynamic problem for which $\mathbf{q}(t)$ is known, equation (6) can be solved for the f actuator loads. Note that the actuator loads will always appear linearly in $\widetilde{\mathbf{F}}$. Furthermore, by choosing the actuated joint variables as the independent coordinates $\mathbf{q}_i$, the actuator loads will be decoupled in equation (6), i.e. exactly one actuator load appears explicitly in each equation. Hence, no matrix inversion is needed, unlike the approach in [12].

The direct application of Maple algorithms to the solution of the linear equations (3) for the dependent variations will be called the *direct symbolical* approach. Due to memory limitations associated with symbolic programming, this approach will fail when the number of loop closure equations is large, which is the case for the 6-DOF Gough-Stewart platform shown in Figure 3. In this situation, one can still obtain the dynamic equations (6) by using a *pseudo-variable* approach to solve equation (3) in a way that exploits the special topology [10].

To accomplish this, the set of coordinates are further partitioned as $\mathbf{q} = (\mathbf{q_i}, \mathbf{q_e}, \mathbf{q_{dd}})$, where $\mathbf{q_i}$ are the independent variables (associated with the actuators), $\mathbf{q_e}$ are the end effector variables, and $\mathbf{q_{dd}}$ are the variables associated with the unactuated joints. The so-called pseudo-independent variables are defined as $\mathbf{q_{pi}} = \mathbf{q_e}$, and the pseudo-dependent variables $\mathbf{q_{pd}} = (\mathbf{q_i}, \mathbf{q_{dd}})$. This re-partitioning of the joint coordinates leads to a largely decoupled linear system of equations (3); this is the essential feature of the pseudo-variable approach.

To demonstrate, consider selecting the actuated joint angles θ_1, θ_2, and θ_3 as

145

independent coordinates q_i for the planar 3-DOF manipulator. The partial derivatives (Jacobian matrices) of the loop closure equations (7) with respect to the dependent and pseudo-dependent variables have the structures:

$$
\Phi_{q_d} = \begin{bmatrix}
* & & & * & & * \\
* & & & & * & * \\
& * & & * & & * \\
& * & & & * & * \\
& & * & * & & * \\
& & * & & * & *
\end{bmatrix} \quad , \quad
\Phi_{q_{pd}} = \begin{bmatrix}
* & * & & & & \\
* & * & & & & \\
& & * & * & & \\
& & * & * & & \\
& & & & * & * \\
& & & & * & *
\end{bmatrix} \tag{8}
$$

where an asterisk $*$ indicates a non-zero entry. One can clearly see the decoupling that is present in the Jacobian matrix $\Phi_{q_{pd}}$ for the pseudo-dependent variables. Once the pseudo-dependent variations are obtained, it is a simple matter [10] to recover the pseudo-independent variations and the symbolic transformation (4).

In addition to the direct symbolical and pseudo-variable approaches, three others have been implemented for comparison. In an *implicit symbolical* approach, the actuator loads are expressed in terms of the entries of the transformation matrix J, which are calculated and saved symbolically. In a combined symbolic/numeric approach, the actuator loads are again expressed in terms of the entries in J, which are obtained numerically by solving f linear systems $\Phi_{q_d} j_k = -\varphi_k, k = 1 \ldots f$, where j_k and φ_k are the k-th column of the matrices J and Φ_{q_i}, respectively. In another combined approach, the actuator loads are expressed in terms of $\Phi_{q_d}^{-1}$, which is also obtained using numerical methods during the evaluation process.

Symbolic expressions for the torques actuating the 3-DOF parallel manipulator are identical to those derived by hand in [14]. The explicit expressions are too lengthy to be displayed here[2].

TABLE 2. Computational efficiency for one inverse dynamic analysis (333-MHz Pentium II)

Approach	Flops	CPU [ms]
direct symbolic	967	6.0
pseudo-variable	871	6.1
implicit symbolic	879	7.6
symbolic/numeric (dummy J)	923	15.4
symbolic/numeric (dummy $\Phi_{q_d}^{-1}$)	1235	19.8

The CPU time and number of flops required for one inverse dynamic evaluation of the three driving torques are shown in Table 2. The kinematic solution,

---

[2] Available upon request, for both the 3-DOF manipulator and the Gough-Stewart platform.

performed prior to the dynamic analysis, is not counted. It can be seen that the direct symbolic and pseudo-variable approaches are equivalent regarding the CPU time, while the implicit symbolic approach requires about 25% more CPU time. The combined symbolic/numeric approaches require more than twice the CPU time compared to the symbolic approaches.

We can draw the conclusion that, for problems of this complexity, the symbolic approaches are preferred because they are faster than the numerical approaches. Furthermore, they do not need matrix manipulation capabilities — this is advantageous in microprocessor-based control applications. Similar conclusions have been drawn for the 6-DOF Gough-Stewart platform and, more recently, for spatial parallel manipulators with less than 6-DOF.

5. Efficient Modelling via Subsystems

The modelling of multibody systems is greatly facilitated by the use of subsystem models. Models of entire sub-assemblies can be created and stored (symbolically) for future use. For systems with a repetitive structure, this can be very helpful. In a time-varying topological situation, e.g. a virtual reality application in which the user is adding or removing parts to their model, the system equations can be reformulated quickly by focusing attention only on the modified subsystems.
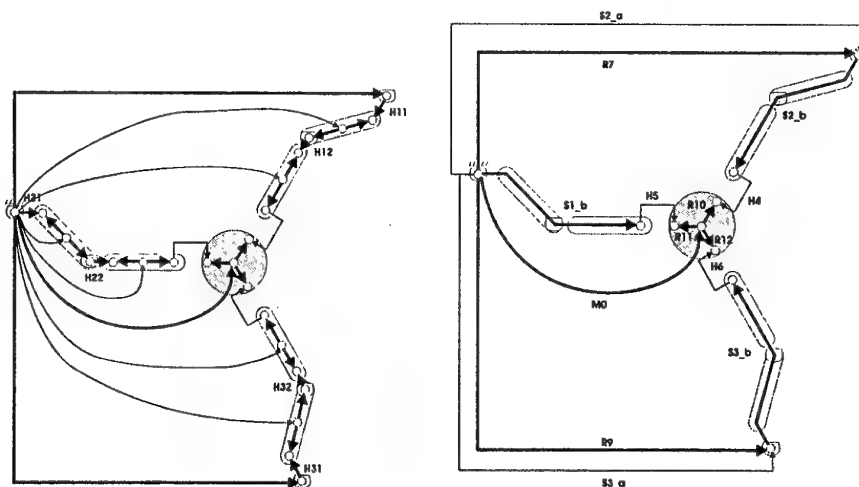
Figure 4. Linear graphs of parallel manipulator: conventional and subsystem models

Subsystem models are particularly well-suited for the topologies that are typical of parallel manipulators. Each leg can be modelled as a subsystem that is kinematically decoupled from the other leg subsystems. This allows the equations

147

for kinematics and inverse dynamics to be generated and solved in parallel, either symbolically or numerically on a parallel computing platform. Graph theory is naturally suited to the modelling of systems via subsystem models. Although the subsystem modelling of electrical circuits was achieved decades ago using graph theory, it has only recently been extended to the nonlinear kinematics and dynamics of multibody systems.

To demonstrate, consider the 3-DOF parallel manipulator again. Shown in Figure 4 is a conventional graph for the system, and a second graph comprised of subsystems S_{1b}, S_{2b}, and S_{3b} — one for each leg. These subsystems were developed by starting with a single link plus revolute joint, which were combined into a low-level subsystem. Two of these were then combined to form the 2-link subsystems S_{1b}, S_{2b}, and S_{3b}. The constitutive equations for these subsystems are systematically obtained using graph-theoretic generalizations of the well-known Norton and Thevenin theorems from electrical network theory.

6. Extension to Mechatronic Systems

Graph-theoretic modelling is not restricted to mechanical systems; it has long been applied to electrical, pneumatic, and hydraulic systems, and is easily adapted to the modelling of electro-mechanical multibody systems [15].
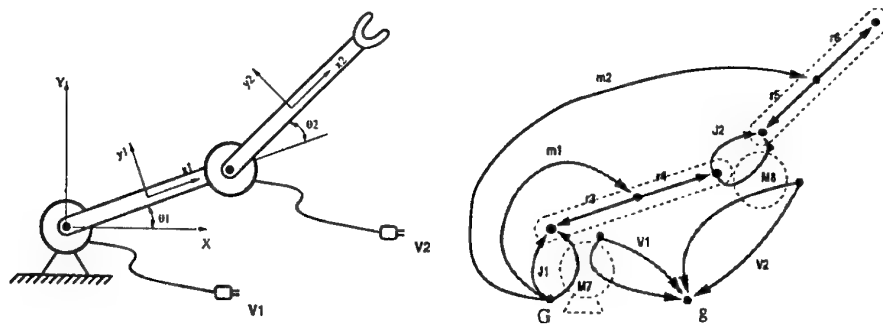
Figure 5. DC motor-driven robot manipulator and linear graph

To demonstrate, consider the two-link manipulator shown in Figure 5 with its linear graph representation. The joint angles θ_1 and θ_2 are controlled by two DC motors which are powered by voltage sources V_1 and V_2. The linear graph of the system contains the standard mechanical components, the two voltage sources, and the two motors M_7 and M_8. Note that the graph consists of two parts, one for the mechanical domain and one for the electrical domain, and that the motors have edges in each domain. This is true for any transducer element that converts energy between different domains.

It was relatively easy to extend our graph-theoretic symbolic algorithms to the modelling of electro-mechanical multibody systems. For the two-link manipulator, one obtains four differential equations, two for each of the two domains, in terms of θ_1, θ_2, and the two motor currents. These system equations can be used for find inverse solutions for the motor currents required to drive a particular trajectory, or as the basis of a forward dynamic simulation that tests out different controller strategies [15].

7. Conclusions

When combined with symbolic programming, linear graph theory provides a very efficient approach to modelling the kinematics and dynamics of flexible multibody systems. By selecting a spanning tree for a graph representation, one can define a set of coordinates that is well-suited to the problem at hand, including absolute, joint, or indirect coordinates. The special topologies of parallel manipulators can be exploited, especially if a subsystem modelling approach is adopted. Graph theory is equally applicable to electro-mechanical multibody systems.

References

1. Koenig, H.E., Tokad, Y., and Kesavan, H.K. (1967) *Analysis of Discrete Physical Systems*, McGraw-Hill, New York.
2. McPhee, J. (1998) Automatic generation of motion equations for planar mechanical systems using the new set of 'branch coordinates', *Mechanism and Machine Theory* 33, 805-823.
3. Shi, P., and McPhee, J. (2000) Dynamics of flexible multibody systems using virtual work and linear graph theory, *Multibody System Dynamics* 4, 355-381.
4. Shi, P. and McPhee, J. (2002) Symbolic programming of a graph-theoretic approach to flexible multibody dynamics, *Mechanics of Structures and Machines* 30, 123-154.
5. Haug, E.J. (1989) *Computer-Aided Kinematics and Dynamics of Mechanical Systems*, Allyn and Bacon, Boston.
6. Wittenburg, J. (1977) *Dynamics of Systems of Rigid Bodies*, B.G. Teubner, Stuttgart.
7. McPhee, J. (2001) A unified formulation of multibody kinematic equations in terms of absolute, joint, and indirect coordinates", *Proceedings* of the ASME Design Engineering Technical Conference, Pittsburgh U.S.A.
8. Fayet, M., and Pfister, F. (1994) Analysis of multibody systems with indirect coordinates and global inertia tensors, *European Journal of Mechanics, A/Solids* 13, 431-457.
9. Huston, R.L., Liu, Y.S, and Liu, C. (1994) Use of absolute coordinates in computational multibody dynamics, *Computers and Structures* 52, 17-25.
10. Geike, T. and McPhee, J. (2001) Inverse dynamic analysis of parallel manipulators with full mobility, *Mechanism and Machine Theory*, under review.
11. Merlet, J. (2000) *Parallel Robots*, Kluwer Academic Publishers, Dordrecht.
12. Tsai, L.-W. (2000) Solving the inverse dynamics of a Stewart-Gough manipulator by the principle of virtual work, *Journal of Mechanical Design* 122, 3-9.
13. Wang, J. and Gosselin, C. (1998) New approach for the dynamic analysis of parallel manipulators, *Multibody System Dynamics* 2, 317-334.
14. Ma, O. and Angeles, J. (1989) Direct kinematics and dynamics of a planar 3-DOF parallel manipulator, *Advances in Design Automation - 1989*, 3, 313-320.
15. Scherrer, M. and McPhee, J. (2002) Dynamic modelling of electromechanical multibody systems, *Multibody System Dynamics*, in press.

STABILIZATION METHODS FOR THE INTEGRATION OF DAE IN THE PRESENCE OF REDUNDANT CONSTRAINTS

MARIA AUGUSTA NETO[1] AND JORGE AMBRÓSIO[2]
2FCTUC, Universidade de Coimbra, Coimbra, Portugal
e-mail: augusta.neto@dem.uc.pt
2IDMEC/IST, Av. Rovisco Pais, 1049-001 Lisboa, Portugal
e-mail: jorge@dem.ist.utl.pt

1   Introduction

In the simulation of multibody systems it is necessary to devise efficient and versatile formulations for the problem in order to achieve computational efficiency and accuracy in the solution of the problem. The choice of the coordinates has a direct influence in the structure of the equations of the motion that describe the multibody model and it can be another reason for a method to be more efficient and accurate than another [1]. Cartesian coordinates based formulations lead to sets of differential-algebraic equations, which require proper numerical methods to ensure the stability and accuracy of the solution [2]. The work now presented is developed in the framework of Cartesian coordinates.

The numerical solution of the differential equations of motion is an approximation of the exact solution in which the accuracy depends on the quality of the initial guess for the positions and velocities, ability to recover from the perturbations introduced by the solution process, aptitude to deal with redundant constraints, capability to handle singular positions for the multibody system and eventually the existence of intermittent and unilateral constraints. The set of differential algebraic equations of motion does not use explicitly the position and velocity equations associated to the kinematic constraints. Therefore, small errors in the state variables of the system due to the integration process or to their initial guess by the user cannot be corrected in the course of the solution of the dynamic problem. The strategies generally used to overcome this problem are the coordinate partition method [3], the Baumgarte stabilization method [4] or the augmented Lagrangian formulation [5].

In general spatial models it is very often impossible to avoid the use of redundant constrains that lead to Jacobian matrices with linear dependent rows. Consequently, the system of equations formed by the equations of motion and the constraint acceleration equations has a left-hand-side matrix which is singular or that becomes ill-conditioned [6]. The application of formulations that use generalized inverses of the system nonsquare matrix, that result from the existence of redundant constraints or of the row-deficiency, have been proposed in multibody dynamics in recent years [6,7,8,9]. Among these, the Singular Value Decomposition is suitable to solve singular, overconstrained or undetermined problems. Kim and Vanderploeg [8] use QR decomposition for the same purpose. Based on the work by Udwadia and Kalaba [10] a formulation using the K-U formulation has been proposed by Arabyan and Wu [6]. The advantage of this formulation is that the redundant constraints are handled in the solution of the system equations of motion and the problems that involve singular configurations and intermittent constraints, associated with changing the number of degrees-of-freedom, are managed. However, as the proposed methodology does not include the constraint and velocity equations it does provides any solution for the constraint violation problem. Therefore, some technique that minimizes or eliminates such constraint violation errors is still required.

This paper presents a discussion on the use of the different methodologies to handle the constraint violation correction or stabilization and the existence of redundant constraints. Among these methods the use of the K-U formulations for multibody systems with holonomic constrains is emphasized. Different forms of calculating this pseudo-inverse based on Singular Value Decomposition, QR decomposition and Gram-Schmidt orthogonalization are presented.

2   Dynamic Analysis of Multibody Systems

A multibody system is a collection of rigid and flexible bodies joined together by kinematic joints and force elements as depicted in Fig. 1. For the ith body of the system $\mathbf{q}_i$ denotes a vector containing the translational coordinates $\mathbf{r}_i$ and a set of rotational coordinates $\mathbf{p}_i$. A vector of velocities for a rigid body i is defined as $\dot{\mathbf{q}}_i$ contains a 3-vector of translational velocities $\dot{\mathbf{r}}_i$ and a 3-vector with the rotationl coordinates velocities $\dot{\mathbf{p}}_i$. Another body velocity vector defined as $\dot{\mathbf{q}}_i^*$ includes the angular velocities $\boldsymbol{\omega}_i$ instead of the rotational coordinates velocities. When Euler parameters are used as rotational coordinates the relation between their velocities and the angular velocities is given by $2\dot{\mathbf{p}} = \mathbf{L}^T\boldsymbol{\omega}'$. The vector of accelerations for the body is denoted by $\ddot{\mathbf{q}}_i$, the time derivative of $\dot{\mathbf{q}}_i$. For a multibody system containing nb bodies, the vectors of coordinates, velocities, and accelerations are $\mathbf{q}$, $\dot{\mathbf{q}}$ and $\ddot{\mathbf{q}}$ that contain the elements of $\mathbf{q}_i$, $\dot{\mathbf{q}}_i$ and $\ddot{\mathbf{q}}_i$, respectively, for

150

$i=1,...,nb$. The system velocity and acceleration vectors, using angular velocities and accelerations instead of the Euler parameters velocities and accelerations are denoted by $\dot{\mathbf{q}}^*$ and $\ddot{\mathbf{q}}^*$ respectively.
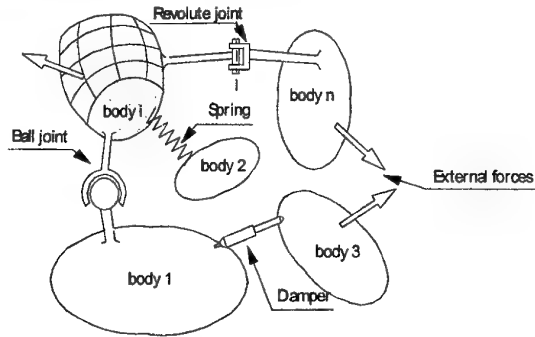
Figure 1. Schematic representation of a multibody system

The constraint equations describing the relative motion between contiguous bodies arise from the kinematic joints. The kinematic constraints are described by mr independent equations as

$$\Phi(\mathbf{q},t) = \mathbf{0} \tag{1}$$
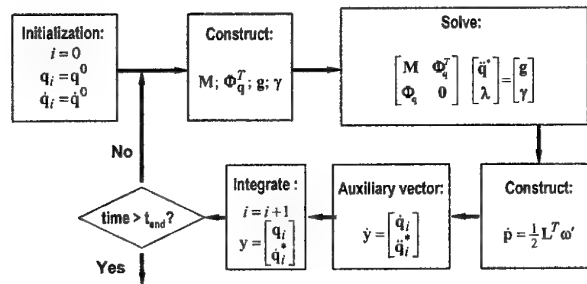
Figure 2. Solution procedure for the dynamic analysis of multibody systems

The first and second derivatives of the constraints yield the kinematic velocity and acceleration equations, respectively

$$\dot{\Phi}(\mathbf{q},t) = 0 \quad \equiv \quad \Phi_{\mathbf{q}}\,\dot{\mathbf{q}}^* = \mathbf{v} \tag{2}$$

$$\ddot{\Phi}(\mathbf{q},\dot{\mathbf{q}},t) = 0 \quad \equiv \quad \Phi_{\mathbf{q}}\,\ddot{\mathbf{q}}^* = \gamma \tag{3}$$

where $\Phi_{\mathbf{q}}$ is the Jacobian matrix of the constraints. The equations of motion for the system of rigid bodies are written [14]

$$\mathbf{M}\ddot{\mathbf{q}}^* + \Phi_{\mathbf{q}}^T\lambda = \mathbf{g} \tag{4}$$

where $\mathbf{M}$ is the inertia matrix, λ is a vector of unknown Lagrange multipliers, and $\mathbf{g}=\mathbf{g}(\mathbf{q},\dot{\mathbf{q}})$ contains the forces, moments and gyroscopic terms.

Equations (3) and (4) form a system of differential-algebraic equations that must be solved together to obtain the accelerations and Lagrange multipliers. This system is

$$\begin{bmatrix} \mathbf{M} & \Phi_{\mathbf{q}}^T \\ \Phi_{\mathbf{q}} & \mathbf{0} \end{bmatrix}\begin{bmatrix} \ddot{\mathbf{q}}^* \\ \lambda \end{bmatrix} = \begin{bmatrix} \mathbf{g} \\ \gamma \end{bmatrix} \tag{5}$$

The standard numerical solution of these equations proceeds as illustrated in Fig. 2. No special provision is made to correct for the constraint velocity and positions violations. Moreover, it is assumed that the matrix is not singular or ill-conditioned.

2.1 STANDARD SOLUTION OF THE SYSTEM EQUATIONS OF MOTION

The system equations (5) can be solved by applying any method suitable for the solution of linear algebraic equations. The existence of null elements in the main diagonal of the matrix and the possibility of ill-conditioned matrices suggest that methods using partial or full pivoting are preferred. None of these

151

formulations help with the presence of redundant constraints. The direct solution of equation (5) is hereafter designated by the Lagrange Multiplier Method 1 (LM1).

2.2 DIRECT INVERSION OF THE SYSTEM MATRIX

The left-hand-side matrix of the system equations (5) can be inverted analytically. Equation (4) is rearranged to put the acceleration vector in evidence in the left-hand-side and the result is substituted in equation (3), which is also rearranged to give:

$$\lambda = (\Phi_q M^{-1} \Phi_q^T)^{-1} \Phi_q M^{-1} g - (\Phi_q M^{-1} \Phi_q^T)^{-1} \gamma \tag{6}$$

In these equations it is assumed that the multibody model does not include any body with null mass or inertia so that the inverse of the mass matrix M exists. The substitution of equation (6) in equation (4) provides the expression for the system accelerations written as

$$\ddot{q}^* = \left[M^{-1} - M^{-1} \Phi_q^T (\Phi_q M^{-1} \Phi_q^T)^{-1} \Phi_q M^{-1} \right] g + M^{-1} \Phi_q^T (\Phi_q M^{-1} \Phi_q^T)^{-1} \gamma \tag{7}$$

Equations (6) and (7) are now rearranged in a compact form and written as

$$\begin{bmatrix} \ddot{q}^* \\ \lambda \end{bmatrix} = \begin{bmatrix} \left[M^{-1} - M^{-1} \Phi_q^T (\Phi_q M^{-1} \Phi_q^T)^{-1} \Phi_q M^{-1} \right] & M^{-1} \Phi_q^T (\Phi_q M^{-1} \Phi_q^T)^{-1} \\ (\Phi_q M^{-1} \Phi_q^T)^{-1} \Phi_q M^{-1} & -(\Phi_q M^{-1} \Phi_q^T)^{-1} \end{bmatrix} \begin{bmatrix} g \\ \gamma \end{bmatrix} \tag{8}$$

The matrix in the right-hand side of equation (8) is the inverse of the system matrix that appears in equation (5). The solution process enunciated by equation (8) is referred to as the Lagrange Multiplier Method 2 (LM2).

3 Solution Methods To Deal With Constrains Violations

The initial conditions and the integration of the velocities and accelerations of the multibody system introduce some errors in the new positions and velocities obtained. This is due to the finite precision of the numerical methodologies and to the constraint and velocity equations not appearing anywhere in the solution procedure outlined in Fig. 2. Therefore, methods able to eliminate errors in the constraint or velocity equations or, at least, keep such errors under control must be implemented.

3.1 BAUMGARTE STABILIZATION METHOD

The second-order equations, such as equation (3) are unstable. Small perturbations, such as the numerical errors introduced by the integration process, cannot be corrected naturally and they only tend to be amplified. The solution is to introduce feedback terms that penalize the system response with any violation on the constraint or velocity equations [4]. Therefore, the right-hand side of equation (3) is modified,

$$\Phi_q \ddot{q}^* = \gamma - 2\alpha \dot{\Phi} - \beta^2 \Phi \tag{9}$$

where α and β are positive constants that weight the violations of the velocity and constraint equations respectively. These constants, for a multibody system made of rigid bodies, are values in the range of 1-10, being α, $\beta = 5$ a value often used [1].

The use of the Baumgarte stabilization method is done by using equation (9) instead of equation (3) during the system of equations solution process. It should be noted that the method does not correct the constraint violations but simply keeps them under control.

3.2 COORDINATE PARTITIONING METHOD

Based on the original work by Wehage and Haug [3], the coordinate partition method eliminates completely the errors of the velocities and positions that would otherwise accumulate during the integration process. This method requires that the sets of independent and dependent coordinates are first identified. Then, only the independent accelerations and velocities are integrated and the dependent quantities are calculated using partitions of the velocity and constraint equations.

3.2.1 Automatic Selection of the Independent Coordinates

The definition of the dependent and independents coordinates can be automatic by using a matrix factorization technique, such as the Gaussian elimination with full pivoting. For a multibody system with m constrains and n coordinates the Jacobian is an $m \times n$ matrix and the order of the columns of the matrix

152

corresponds to the order of elements of vector $\mathbf{q}$. Consider a $m \times n$ matrix $\mathbf{A}$ for which the factorization results in the following form

$$\mathbf{A} \rightarrow \begin{array}{cc} m-k & n-(m-k) \\ \begin{bmatrix} \mathbf{B} & \mathbf{R} \\ \mathbf{S} & \mathbf{D} \end{bmatrix} & \begin{array}{l} \}m-k \\ \}k \end{array} \end{array} \qquad (10)$$

where it is found that there are k redundant rows in the matrix and m-k dependent constraints. As a result of the full pivoting procedure used the k redundant constraints end in the factorized matrix bottom rows. The sub matrix $\mathbf{B}$ is a $(m$-$k)\times(m$-$k)$ non-singular matrix associated to the dependent coordinates, and $\mathbf{R}$ is the sub matrix $(m$-$k)\times(n$-m+$k)$ associated to the independent coordinates.

In what follows let it be assumed that $\mathbf{A}$ represents the Jacobian matrix $\mathbf{\Phi_q}$. Without loss of generality, let it be assumed in what follows that there are no redundant constraints in the multibody model, or that these have been identified and eliminated. In this case the Jacobian matrix can be partitioned into

$$\mathbf{\Phi_q} = \begin{bmatrix} \mathbf{\Phi_u} & \mathbf{\Phi_v} \end{bmatrix} \qquad (11)$$

that has the same form of the sub-matrix $[\mathbf{B} \ \mathbf{R}]$ of equation (10). Equation (11) implies the partition of the coordinate vector into vectors of dependent and independent coordinates, denoted by $\mathbf{u}$ and $\mathbf{v}$ respectively. This coordinate partition also implies the partition of the velocity and acceleration vectors given as $\dot{\mathbf{q}} = [\dot{\mathbf{u}}^T \ \dot{\mathbf{v}}^T]$ and $\ddot{\mathbf{q}} = [\ddot{\mathbf{u}}^T \ \ddot{\mathbf{v}}^T]$ respectively.

3.2.2 Evaluation of the Dependent Coordinates and Velocities

Let it be assumed that the vector of system accelerations is calculated through the use of equation (5) or (8). The integration vector $\dot{\mathbf{y}}$, appearing in Fig. 2, only includes the independent coordinates and it is written as

$$\dot{\mathbf{y}} = \begin{bmatrix} \dot{\mathbf{v}}^T & \ddot{\mathbf{v}}^T \end{bmatrix}^T \qquad (12)$$

which after integration results in vector $\mathbf{y} = \begin{bmatrix} \mathbf{v}^T & \dot{\mathbf{v}}^T \end{bmatrix}^T$.

The dependent velocities and positions are calculated using the velocity and constraint equations respectively. To evaluate the dependent velocities let equation (2) be partitioned

$$\mathbf{\Phi_u} \dot{\mathbf{u}} + \mathbf{\Phi_v} \dot{\mathbf{v}} = \mathbf{v} \qquad (13)$$

The dependent velocities $\dot{\mathbf{u}}$ are evaluated by solving the system of equations

$$\mathbf{\Phi_u} \dot{\mathbf{u}} = -\mathbf{\Phi_v} \dot{\mathbf{v}} + \mathbf{v} \qquad (14)$$

The dependent positions are obtained through the solution of the constraint equations given the independent coordinates, this is,

$$\mathbf{\Phi}(\mathbf{u}, \mathbf{v}, t) = \mathbf{0} \qquad (15)$$

The Newton-Raphson method is used for the solution of equation (15) to obtain the dependent positions $\mathbf{u}$. To achieve convergence some reliable estimates must be provided for these coordinates. A good estimative for $\mathbf{u}^i$ at time t^i, to start the iterative solution procedure, is evaluated using the information from the previous time t^{i-1} as [1]

$$\mathbf{u}^i = \mathbf{u}^{i-1} + h\dot{\mathbf{u}}^{i-1} + 0.5h^2\ddot{\mathbf{u}}^{i-1} \qquad (16)$$

where h is the integration time step from t^i to t^{i-1}.

3.3 AUGMENTED LAGRANGIAN FORMULATION

The Augmented Lagrangean formulation is a methodology that penalizes the constraint violations, very much in the same form as the Baumgarte stabilization method [4]. However, this is an iterative procedure that presents a great number of advantages relative to other methods because it involves the solution of a smaller set of equations, it handles redundant constraints and it can still deliver accurate results in the vicinity of singular configurations. The Augmented Lagrangian formulation consists in solving the system equations of motion, represented by equation (5), by an iterative process. Let index i denote the ith iteration. The evaluation of the system accelerations in a given time step starts as:

$$\mathbf{M}\ddot{\mathbf{q}}_i^* = \mathbf{g} \qquad (i = 0) \qquad (17)$$

The iterative process to evaluate the system accelerations proceeds with the evaluation of

153

$$\bar{\mathbf{M}}\ddot{\mathbf{q}}_{i+1}^{\bullet} = \bar{\mathbf{g}} \tag{18}$$

where the generalized mass matrix $\bar{\mathbf{M}}$ and load vector $\bar{\mathbf{g}}$ are given by

$$\begin{aligned}\bar{\mathbf{M}} &= \mathbf{M} + \mathbf{\Phi}_q^T \alpha \mathbf{\Phi}_q \\ \bar{\mathbf{g}} &= \mathbf{M}\ddot{\mathbf{q}}_i^{\bullet} + \mathbf{\Phi}_q^T \alpha (\gamma_i - 2\omega\mu\mathbf{\Phi}_q\dot{\mathbf{q}}_i^{\bullet} - \omega^2\mathbf{\Phi}_i)\end{aligned} \tag{19}$$

In equation (19) the mass matrix $\mathbf{M}$, the Jacobian matrix $\mathbf{\Phi}_q$ and the right-hand side of the acceleration equations γ are the same as those used in equation (5). The penalty terms α, μ and ω ensure not only that the constraint violations feedback are accounted for during the solution of the system equations. The iterative process continues until

$$\left\| \ddot{\mathbf{q}}_{i+1}^{\bullet} - \ddot{\mathbf{q}}_i^{\bullet} \right\| \le \varepsilon \tag{20}$$

The Augmented Lagrangian formulation involves the solution of a system of equations with a size equal to the number of coordinates of the multibody system. The mass matrix $\mathbf{M}$ is generally positive semi-definite but the leading matrix of equation (18) $\mathbf{M} + \mathbf{\Phi}_q^T \alpha \mathbf{\Phi}_q$ is always positive definite [5]. Even when the system is close to a singular position or when in presence of redundant constraints the system of equations can still be solved.

4 Methods to Deal With Redundant Constraints

In many practical situations the multibody systems models include redundant constraints. In some multibody systems it also happens that some constraints are either intermittent or they vanish. Several improved formulations, using the Moore-Penrose generalized inverse, that are suitable for these kind of multibody systems, are revised here.

4.1 THE MOORE-PENROSE GENERALIZED INVERSE

Let the accelerations of the unconstrained multibody system be $\ddot{\mathbf{q}}_{unc}^{\bullet} = \mathbf{M}^{-1}\mathbf{g}$, where it is assumed again that all bodies of the system have non-null masses and inertias. Equation (7) can now be rearranged as

$$\ddot{\mathbf{q}}^{\bullet} = \ddot{\mathbf{q}}_{unc}^{\bullet} + \mathbf{M}^{-1}\mathbf{\Phi}_q^T(\mathbf{\Phi}_q\mathbf{M}^{-1}\mathbf{\Phi}_q^T)^{-1}\left(\gamma - \mathbf{\Phi}_q\ddot{\mathbf{q}}_{unc}^{\bullet}\right) \tag{21}$$

Let the inverse of the mass matrix be written as $\mathbf{M}^{-1} = \mathbf{M}^{-\frac{1}{2}}\mathbf{M}^{-\frac{1}{2}}$. Equation (21) becomes

$$\ddot{\mathbf{q}}^{\bullet} = \ddot{\mathbf{q}}_{unc}^{\bullet} + \mathbf{M}^{-1/2}\left(\mathbf{M}^{-1/2}\mathbf{\Phi}_q^T\right)(\mathbf{\Phi}_q\mathbf{M}^{-1/2}\mathbf{M}^{-1/2}\mathbf{\Phi}_q^T)^{-1}\left(\gamma - \mathbf{\Phi}_q\ddot{\mathbf{q}}_{unc}^{\bullet}\right) \tag{22}$$

An auxiliary variable $\mathbf{D} = \mathbf{\Phi}_q\mathbf{M}^{-1/2}$ is defined that upon substitution in equation (22) leads to

$$\ddot{\mathbf{q}}^{\bullet} = \ddot{\mathbf{q}}_{unc}^{\bullet} + \mathbf{M}^{-1/2}\mathbf{D}^T(\mathbf{D}\mathbf{D}^T)^{-1}\left(\gamma - \mathbf{\Phi}_q\ddot{\mathbf{q}}_{unc}^{\bullet}\right) \tag{23}$$

The Moore-Penrose generalized inverse of $\mathbf{D}$, denoted by $\mathbf{D}^+$ has the properties [6]

$$\begin{aligned}\mathbf{D}\mathbf{D}^+\mathbf{D} &= \mathbf{D} \\ \mathbf{D}^+\mathbf{D}\mathbf{D}^+ &= \mathbf{D}^+\end{aligned} \tag{24}$$

being $\mathbf{D}^+\mathbf{D}$ and $\mathbf{D}\mathbf{D}^+$ both symmetric matrices. Consequently

$$\mathbf{D}^T(\mathbf{D}\mathbf{D}^T)^{-1} = \mathbf{D}^T\left(\mathbf{D}^+\right)^T\mathbf{D}^+ = \left(\mathbf{D}^+\mathbf{D}\right)^T\mathbf{D}^+ = \mathbf{D}^+\mathbf{D}\mathbf{D}^+ = \mathbf{D}^+ \tag{25}$$

The result expressed by equation (25) is substituted in equation (23) leading to

$$\ddot{\mathbf{q}}^{\bullet} = \ddot{\mathbf{q}}_{unc}^{\bullet} + \mathbf{M}^{-1/2}\mathbf{D}^+\left(\gamma - \mathbf{\Phi}_q\ddot{\mathbf{q}}_{unc}^{\bullet}\right) \tag{26}$$

The solution of equation (16), hereafter designated by MPI, always exists because the Moore-Penrose pseudo-inverse exists even when the inverse of the leading matrix of equation (5) does not exist. This means that in the presence of redundant constraints or in the presence of constraints that vanish instantaneously, such as the unilateral constraints, the pseudo-inverse matrix $\mathbf{D}^+$ still exists.

154

4.2 COMPUTATION OF THE GENERALIZED INVERSE

4.2.1 *Single Value Decomposition*

The calculation of the system accelerations using equation (26) assumes that the pseudo-inverse matrix $\mathbf{D}^+$ can be calculated. Let $\mathbf{D}$ be a M×N nonsquare matrix. Its singular value decomposition (SVD) leads to

$$\mathbf{D} = \mathbf{U} \ \mathbf{S} \ \mathbf{V}^T \qquad (27)$$

where $\mathbf{U}$ and $\mathbf{V}$ are M×M and N×N square orthogonal matrices respectively. The nonsquare matrix $\mathbf{S}$ has nonzero elements only on its diagonal and, therefore, the calculation of its pseudo-inverse $\mathbf{S}^+$ is trivial [11]. The pseudo-inverse of $\mathbf{D}$ is

$$\mathbf{D}^+ = \mathbf{V} \ \mathbf{S}^+ \mathbf{U}^T \qquad (28)$$

where the relations $\mathbf{U}^T = \mathbf{U}^{-1}$ and $\mathbf{V}^T = \mathbf{V}^{-1}$, valid for orthogonal matrices, have been used.

4.2.2 *Gram-Schmidt Orthogonalization*

The Gram-Schmidt orthogonalization process (G-S) can be used to compute the pseudo-inverse matrix $\mathbf{D}^+$. With this method matrix $\mathbf{D}$ is decomposed in [11]

$$\mathbf{D} = \mathbf{Q} \ \mathbf{R} \qquad (29)$$

where $\mathbf{Q}$ is a M×N matrix whose columns are orthogonal to each other, i.e., $\mathbf{Q}^T \mathbf{Q} = \mathbf{I}$, and $\mathbf{R}$ is a N×N upper triangular matrix. The computation of the pseudo-inverse is then obtained as

$$\mathbf{D}^+ = \mathbf{R}^{-1}\mathbf{Q}^T \qquad (30)$$

The use of the Gram-Schmidt orthogonalization requires that the columns of matrix $\mathbf{D}$ are all independent.

5 Application Examples

The virtues and shortcomings of the different methods proposed are presented with their application to several simple mechanical systems, both in kinematic and dynamic analysis.

5.1 KINEMATIC ANALYSIS OF A PLANAR FOUR BAR LINKAGE

Typically the solution of a kinematic analysis consists in first solving equation (1) using the Newton-Raphson method and after solving the linear systems of equations (2) and (3). To use equation (26) for the kinematic analysis the system mass matrix becomes the identity matrix and the forces in the system are eliminated. The result is

$$\ddot{\mathbf{q}} = \mathbf{D}^+ \gamma \qquad (31)$$

The vector of accelerations is integrated together with the velocities to obtain new velocities and positions, using the sequence depicted by Fig. 2. This procedure, by itself, does not ensure that the constraint equations are fulfilled. Therefore, the use of a methodology that stabilizes the constraint violations is still required.

Consider the planar four-bar linkage, shown in Fig. 3, with a = b = 0.5 m where the bar 2 has a constant angular velocity, $\omega_n = 124.8$ rad/s. Though the motion of the four-bar linkage is planar, the system model made with two revolute joints, in points A and D, and two universal joints, in points B and C, is three dimensional.

The 6 bodies that make the system model account for 24 coordinates while the revolute and universal joints the ground body and the driving constrains account for 25 constraints. The model has 2 redundant constraints. The existence of the redundant constraint can be eliminated with the substitution of the universal joints by a spherical joint. Two initial positions for the initial orientation of body 2 are considered: body 2 aligned with X, i.e., $\theta_2 = n\pi$; $\theta_2 = \pi/4$ .and $\theta_2 = \pi/2$. The system is simulated using alternatively LM2, ALF and MPI methods to calculate the accelerations. The pseudo-inverse is calculated by using the singular value decomposition or the Gram-Schmidt orthogonalization methods. The Baumgarte stabilization and the coordinate partitioning methods are also used when equations (7) and (26) are applied when the system required that the constraint violations are kept under control. The comparison of the results using the different methodologies, and their combinations, is presented in Table 1.

155
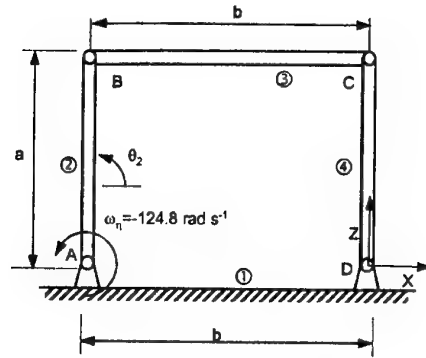
Figure 3. Parallel four-bar linkage

The results presented in table 1 shows that method LM2 fails due to the presence of redundant constraints and it presents numerical difficulties when singular positions appear. Method MPI leads to the correct solution of the system accelerations but the use of constraint stabilization or coordinate partition methods is required in order to ensure that the system constraint equations are fulfilled. Figure 4 shows the constraint violation for GS and SVD technique without the coordinate partitioning method and in the Fig. 5 the same type of results are presented when the coordinate partitioning is used.

TABLE 1. Comparison of the outcome in the use of different methods in the four-bar linkage

Methods	Initial position		
	$\theta_2 = n\pi$	$\theta_2 = \pi/4$	$\theta_2 = \pi/2$
LM2	Fail (M.S.)	Diverge(t=0,044s)	Diverge(t=0,063s)
LM2+Baumg. Stab.	Fail (M.S.)	Diverge(t=0,044s)	Fail (M.S.,t=0,03)
LM2+Coord. Part.	Fail (M.S.)	Converge	Fail (M.S.,t=0,27)
ALF	Const.Viol.(12)	Const.Viol.(9)	Const.Viol.(9)
MPI(SDV)	Diverge(t=0s)	Diverge(t=0,044s)	Diverge(t=0,03s)
MPI(SDV)+ Baumg. Stab.	Diverge(t=0s)	Diverge(t=0,044s)	Diverge(t=0,063s)
MPI(SDV)+Coord. Part.	Diverge(t=0s)	Converge	Converge
MPI(G-S)	Diverge(t=0s)	Diverge(t=0,044s)	Diverge(t=0,03s)
MPI(G-S)+ Baumg. Stab.	Diverge(t=0s)	Diverge(t=0,044s)	Diverge(t=0,063s)
MPI(G-S)+Coord. Part.	Diverge(t=0s)	Converge	Converge
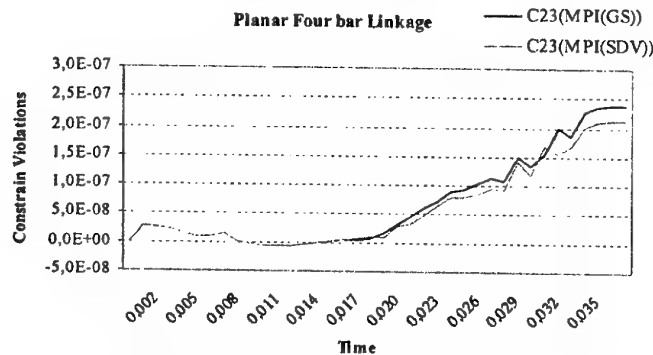
Figure 4. Violation constrains number 23 without the coordinate partitioning

5.2   DYNAMIC ANALYSIS OF A PLANAR SLIDER CRANK

A planar slider-crank, shown in Fig. 6, for which some singular configurations are achieved during the dynamic analysis is presented here. The mechanism is driven by an applied moment of 100 Nm. A first model has the linkages 2 and 3 with the same size, i.e., a=b=0.308 m, reaches singular configurations, while the second model considers these linkages with different lengths, more specifically a=0.304 m and b=0.405 m. Both models are built by including revolute, spherical joint, translation joints and a ground body, which corresponds to 24 coordinates and 24 kinematic constraints, being 1 constraint redundant.
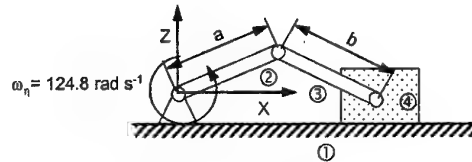
Figure 6. Planar Slider-Crank

The simulation of the mechanism when the coordinate partitioning method is used diverges when the singular positions are reached. The formulation using the pseudo-inverse is calculated, either by G-S or SVD factorization, provides results. As shown in Fig. 7, the dynamic response diverges, as the mechanism motion follows two different branches.
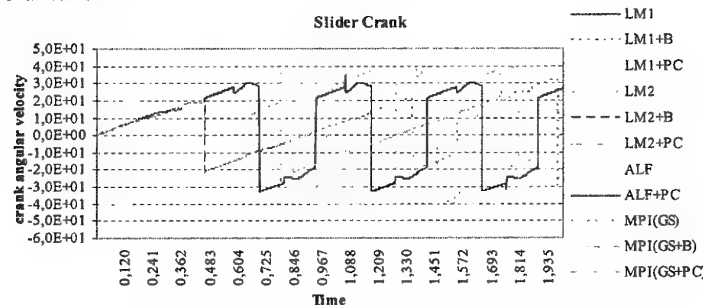
Figure 7. Crank angular velocity and the Singular Positions

To verify that the branching of the slider crank motion is due to the singular position reached, a new slider crank model with a connecting rod different from the crank is modeled. In this case the dimensions of the crank and connecting rod are a = 0.304 m and b = 0.4048 m. As observed in Fig. 12 only with LM1 and GS formulations provide similar results, when no coordinate partitioning is used. The LM2 fails because the matrix is Singular and the ALF formulation fails because the violation constrains is to0olarge.
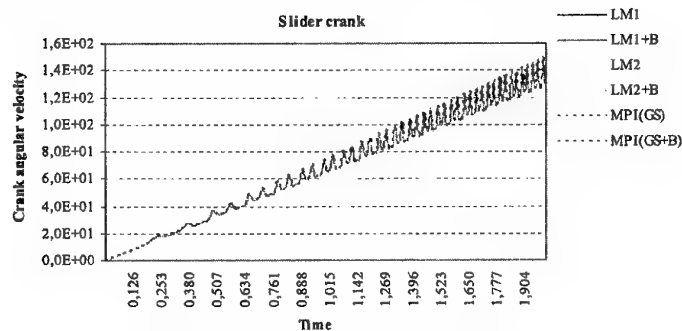
Figure 8. Crank angular velocity without singular positions

When the coordinate partitioning is used in the analysis of the multibody model, the numerical results, presented in Fig. 9 , are slightly different in this case as the constraint violations are prevented.
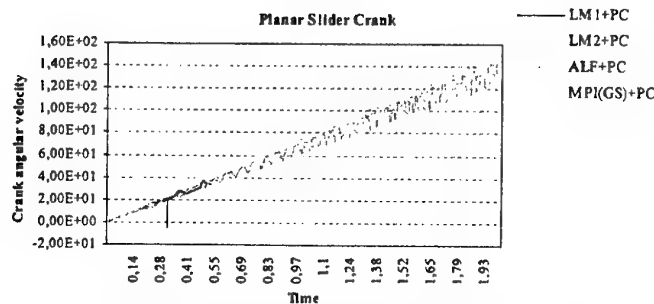
Figure 9. Crank angular velocity with coordinate partitioning

6   Conclusions

General formulations for the dynamic and kinematic analysis rigid mechanical systems have been reviewed here. First, the violation of the constraint and velocity equations, that arise from the integration of the differential-algebraic equations, associated to the multibody models described by Cartesian coordinates, can be handled by using constraint stabilization methodologies, such as the Baumgarte stabilization method or the augmented Lagangian formulation, or by using the coordinate partitioning method. It was shown that the use of the coordinate partition method requires that a set of independent coordinates is set beforehand. The factorization procedures that use on full pivoting not only provide the necessary tools for the coordinate partitioning but also identify the redundant constraints of the model. Therefore, in the process of using the coordinate partitioning method the elimination of the redundant constraints comes for free. Second, the existence of redundant constraints or singular configurations for the multibody system can be handled by applying a procedure that makes use of the Moore-Penrose pseudo-inverse. This pseudo-inverse can be calculated using a singular value decomposition or by applying the Gram-Schmidt orthogonalization procedure.

By using several simple spatial multibody systems the relative efficiency and suitability of the different methods, and of their combination, was tested. For all proposed applications it was observed that the control of the constraint violation is fundamental for long running times. It was also observed that the elimination of the redundant kinematic constraints, after they are identified by using the factorization procedure, is more efficient than the use of the pseudo-inverse methodologies. However, in the case of singular positions of intermittent constraints the use of the Moore-Penrose pseudo-inverse is fundamental.

7   Acknowledgements

8   References

1. Nikravesh, P.E., (1988) *Computer-Aided Analysis of Mechanical Systems*, Prentice Hall, Englewood Cliffs, New Jersey.
2. Petzold, L., Serban, R., Li, S., Raha, S. and Cao, Y., (2001) Sensitivity Analysis and Design Optimization of Differential-Algebraic Equation Systems, *Computational Aspects of Nonlinear Structural Systems with Large Rigid Body Motion*, (J. Ambrósio, M. Kleiber Eds.), IOS Press, Amsterdam, The Netherlands.
3. Wehage, R. and Haug, E., (1982) Generalized Coordinate Partitioning of Dimension Reduction in Analysis of Constrained Dynamic Systems, *ASME Journal of Mechanical Design*, **104**, 247-255.
4. Baumgarte, J., (1972) Stabilization of Constraints and Integrals of Motion, *Concept. Methods Appl. Mech. Eng.*, **1**, 1-66.
5. Jalon, J. de and Bayo, E., (1993) *Kinematic and dynamic simulation of multibody systems*, Springer-Verlag, Heidelberg, Germany.
6. Arabyan, A. and Wu, F., (1998) An Improved Formulation for Constrained Mechanical Systems, *Multibody Systems Dynamics*, **2**(1), 49-69.
7. Kim, S.S., Vanderploeg, M.J., (1986) QR Decomposition for State Space Representation of Constrained Mechanical Dynamical Systems, *ASME Journal of Mechanisms, Transmissions, and Automation in Design*, **108**, 183-188.
8. Singh, R.P. and Likins, P.W., (1985) Singular Value Decomposition for Constrained Dynamical Systems, *Journal of Applied Mechanics*, **52**, 943-948.
9. Meijaard, J.P., (1993) Applications of the Single Value Decomposition in Dynamics, *Computer Methods in Applied Mechanics and Engineering*, **103**, 161-173.
10. Udwadia, F.E. and Kalaba, R.E., (1996) *Analytical Dynamics: A New Approach*, Cambridge University Press, Cambridge, United Kingdom.
11. Pina, H.L.G., (1995)*Métodos Numéricos*, (*Numerical Methods*), McGraw-Hill, Lisboa, Portugal.

158

MODEL REDUCTION TECHNIQUES IN FLEXIBLE MULTIBODY DYNAMICS

PARVIZ E. NIKRAVESH
Department of Aerospace and Mechanical Engineering
University of Arizona, Tucson, AZ 85721 U.S.A.
pen@spock.ame.arizona.edu

In most applications of multibody analysis, it is desirable to reduce the number of equations of motion in order to improve the computational efficiency. This becomes even more important when the model contains deformable bodies. Therefore it would be desirable to reduce the number of the deformable body degrees-of-freedom without too much loss in the accuracy of the results. In this manuscript we present the equations of motion for a simple but general rigid-flexible multibody system in a semi-abstract form in order to keep our focus on reduction techniques. Several model reduction techniques are reviewed and the advantages and disadvantages of each process are briefly discussed.

1. Introduction

One interesting issue in multibody dynamics is computational efficiency and real-time simulation. This issue becomes even more serious when a multibody model contains deformable bodies. Although a deformable body may only represent small linear deflections, the overall multibody equations must be treated as a nonlinear system. Due to this particular issue, it is highly desirable to reduce the number of degrees-of-freedom.

In the past two decades researchers have proposed a variety of model reduction techniques. Each technique is based on certain assumptions; consequently, approximation error is introduced into the model. Therefore, it is important to understand the differences among these methods and apply them where appropriate. In this manuscript we review several model reduction methods and discuss their differences.

It is assumed that the reader has some familiarity with the equations of motion for a deformable body. These equations have been stated without proof. In order to concentrate on concepts and not to be distracted by the complex form of equations, we assume that a node in a finite-element model exhibits only translational degrees-of-freedom. Elimination of the rotational degrees-of-freedom does not make the discussion any less general. The rotational degrees-of-freedom can be added to these formulations if necessary.

Due to page limitation, no literature review has been provided. Most of the topics discussed in this manuscript could be referenced to more than one source, but in order to save space the list of references has been kept to a minimum.

2. Notation

In this manuscript the matrix notation is used in order to keep our attention on concepts without any loss of details. The reader should find the notation to be effective in multibody formulation of equations of motion. The following nomenclature is used:

Right superscripts:
  b boundary node
  d deleted (truncated) mode
  k kept mode
  m master (kept) node
  s slave (deleted) node
  u unconstrained (free) node
Right subscripts:
  c constrained
  f free-free (unconstrained)
  G Guyan
  r index of a rigid body
Left superscripts:
  '   (prime) components are described in the body-fixed frame
Over-scores:
  ~   (tilde) transforms a 3-vector to a skew-symmetric matrix
  ^   (hat) stacks vertically 3-vectors or 3×3 skew-symmetric matrices
  —   (bar) repeats a 3×3 matrix to form a diagonal or block-diagonal matrix

The right superscripts and subscripts are self-explanatory. The left superscript "prime" is of great importance—it indicates that an entity is described in terms of its body-fixed components. Therefore, an entity without a "prime" left superscript refers to the global components. Assume that $\mathbf{I}$ is a 3×3 identity matrix, $\tilde{\mathbf{b}}^i$ is a 3×3 skew-symmetric matrix for $i=1, ..., n$, and $\mathbf{A}$ is a 3×3 rotational transformation matrix. The over-scores "^" and "-" are used as:

$$\hat{\mathbf{I}} = \begin{bmatrix} \mathbf{I} \\ \vdots \\ \mathbf{I} \end{bmatrix}, \quad \hat{\tilde{\mathbf{b}}} = \begin{bmatrix} \tilde{\mathbf{b}}^1 \\ \vdots \\ \tilde{\mathbf{b}}^n \end{bmatrix}, \quad \bar{\mathbf{I}} = \begin{bmatrix} \mathbf{I} & & \\ & \ddots & \\ & & \mathbf{I} \end{bmatrix}, \quad \bar{\mathbf{A}} = \begin{bmatrix} \mathbf{A} & & \\ & \ddots & \\ & & \mathbf{A} \end{bmatrix}$$

3. Equations of Motion for A Deformable Body

In this section we state the equations of motion for a deformable body first without considering on how a reference frame is attached to the body. The equations of motion are initially stated for a structure without any rigid-body motion. Then, the structure is allowed to deform and undergo rigid-body translation and rotation. Finally, the so-called mean-axis conditions are used to attach a reference frame to the moving deformable body.

3.1. EQUATIONS OF MOTION IN NODAL COORDINATES

Assume that a deformable body is described by n_{nodes} nodes. The positions of the nodes are defined with respect to a non-moving body-fixed $\xi - \eta - \zeta$ frame as shown in Fig. 1. The mass and stiffness matrices, $'\mathbf{M}$ and $'\mathbf{K}$, are $n_{dof} \times n_{dof}$ each where $n_{dof} = 3 \times n_{nodes}$. The equations of motion for this body are written as

$$'\mathbf{M}\,'\ddot{\delta} = '\mathbf{f} - '\mathbf{K}\,'\delta \qquad (3.1)$$

where $'\mathbf{f}$ and $'\delta$ are each n_{dof} arrays containing external forces and nodal translational deflections respectively. We are reminded that the left superscript "prime" indicates that a vector, an array, or a matrix is described in terms of its components in the $\xi - \eta - \zeta$ frame.

160

It should be noted that the stiffness matrix $'\mathbf{K}$ has a rank deficiency of six since we have not yet imposed any boundary conditions.
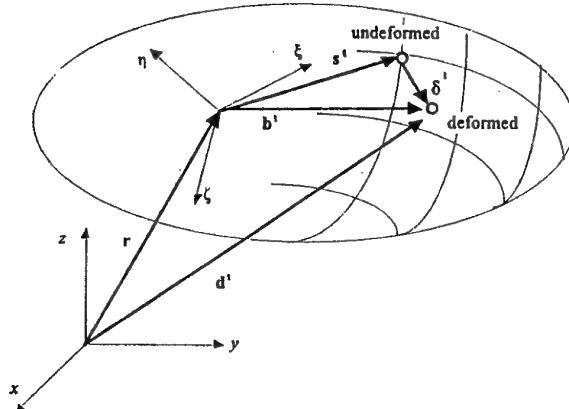
Figure 1. A deformable body and its body-fixed and global reference frames.

We introduce another nonmoving coordinate frame, x-y-z, that does not coincide with $\xi - \eta - \zeta$. A 3×3 rotational transformation matrix, $\mathbf{A}$, between the two non-moving frames is defined. Components of any vector in the $\xi - \eta - \zeta$ frame can be transformed to the x-y-z frame; e.g., $\delta^i = \mathbf{A}\,'\delta^i$. Using the block-diagonal matrix $\overline{\mathbf{A}}$, and the transformations $'\delta = \overline{\mathbf{A}}^T \delta$ and $'\ddot{\delta} = \overline{\mathbf{A}}^T \ddot{\delta}$, Eq. 3.1 is expressed in terms of the x-y-z components of its entities as

$$\mathbf{M}\ddot{\delta} = \mathbf{f} - \mathbf{K}\delta \tag{3.2}$$

where,

$$\mathbf{M} = \overline{\mathbf{A}}\,'\mathbf{M}\,\overline{\mathbf{A}}^T \quad (3.3.a), \qquad \mathbf{K} = \overline{\mathbf{A}}\,'\mathbf{K}\,\overline{\mathbf{A}}^T \quad (3.3.b), \qquad \mathbf{f} = \overline{\mathbf{A}}\,'\mathbf{f} \quad (3.3.c)$$

Most mass matrices have the characteristics to yield $\mathbf{M} = '\mathbf{M}$, but in general this may not be the case[1]. Equations 3.1 or 3.2 are valid only if there is no rigid body motion; i.e., the nodal accelerations are only due to structural deformation.

Now we allow the flexible body and its $\xi - \eta - \zeta$ frame to move with respect to the x-y-z frame. For a flexible body with n_{nodes} nodes, as shown in Fig. 1, we can write n_{dof} equations in n_{dof} accelerations as

$$\mathbf{M}\ddot{\mathbf{d}} = \mathbf{f} - \mathbf{K}\delta \tag{3.4}$$

The array of accelerations, $\ddot{\mathbf{d}}$, contains the absolute nodal accelerations described with respect to the x-y-z frame. Hence, the external and structural forces are also expressed in terms of their components in the same frame. The mass matrices and the force arrays in Eqs. 3.2 and 3.4 are the same. The only difference is in the acceleration arrays.

The absolute position of a typical node i, as shown in Fig. 1, is expressed as:

$$\mathbf{d}^i = \mathbf{r} + \mathbf{b}^i = \mathbf{r} + \mathbf{s}^i + \delta^i \tag{3.5}$$

The absolute velocity and acceleration of the node are expressed as:

$$\dot{\mathbf{d}}^i = \dot{\mathbf{r}} - \tilde{\mathbf{b}}^i \omega + \dot{\delta}^i \tag{3.6}$$

$$\ddot{\mathbf{d}}^i = \ddot{\mathbf{r}} - \tilde{\mathbf{b}}^i \dot{\omega} + \ddot{\delta}^i + \mathbf{w}^i \tag{3.7}$$

---

[1] For most lumped and consistent mass matrices with only translational nodal degrees-of-freedom, $\mathbf{M} = '\mathbf{M}$. In certain cases, for example when the mass matrix is condensed through Guyan reduction, $\mathbf{M} \neq '\mathbf{M}$.

161

where ω and $\dot{\omega}$ are the angular velocity and acceleration of the body-fixed frame, and

$$\mathbf{w}' = \tilde{\omega}\tilde{\omega}\mathbf{b}' + 2\tilde{\omega}\dot{\delta}' \tag{3.8}$$

The position, velocity, and acceleration of all the nodes are written in stack form as:

$$\mathbf{d} = \hat{\mathbf{I}}\mathbf{r} + \mathbf{b} \tag{3.9}$$

$$\dot{\mathbf{d}} = \hat{\mathbf{I}}\dot{\mathbf{r}} - \hat{\tilde{\mathbf{b}}}\omega + \dot{\delta} = \begin{bmatrix} \hat{\mathbf{I}} & -\hat{\tilde{\mathbf{b}}} & \bar{\mathbf{I}} \end{bmatrix} \begin{Bmatrix} \dot{\mathbf{r}} \\ \omega \\ \dot{\delta} \end{Bmatrix} \tag{3.10}$$

$$\ddot{\mathbf{d}} = \hat{\mathbf{I}}\ddot{\mathbf{r}} - \hat{\tilde{\mathbf{b}}}\dot{\omega} + \ddot{\delta} + \mathbf{w} = \begin{bmatrix} \hat{\mathbf{I}} & -\hat{\tilde{\mathbf{b}}} & \bar{\mathbf{I}} \end{bmatrix} \begin{Bmatrix} \ddot{\mathbf{r}} \\ \dot{\omega} \\ \ddot{\delta} \end{Bmatrix} + \bar{\tilde{\omega}}\bar{\tilde{\omega}}\mathbf{b} + 2\bar{\tilde{\omega}}\dot{\delta} \tag{3.11}$$

We substitute Eq. 3.11 into Eq. 3.4 to get

$$\mathbf{M}\begin{bmatrix} \hat{\mathbf{I}} & -\hat{\tilde{\mathbf{b}}} & \bar{\mathbf{I}} \end{bmatrix} \begin{Bmatrix} \ddot{\mathbf{r}} \\ \dot{\omega} \\ \ddot{\delta} \end{Bmatrix} = \mathbf{f} - \mathbf{Mw} - \mathbf{K}\delta \tag{3.12}$$

Equation 3.12 represents n_{dof} equations in $n_{dof} + 6$ accelerations. Assuming that the external, structural, and velocity dependent forces are known, Eq. 3.12 cannot be solved for the accelerations since there are more unknowns than the equations.

Equation 3.12 can also be written in a different form if we pre-multiply it by the transpose of the coefficient matrix of Eq. 3.10. This new form is

$$\begin{bmatrix} m\mathbf{I} & -\hat{\mathbf{I}}^T\mathbf{M}\hat{\tilde{\mathbf{b}}} & \hat{\mathbf{I}}^T\mathbf{M} \\ -\hat{\tilde{\mathbf{b}}}^T\mathbf{M}\hat{\mathbf{I}} & \mathbf{J} & -\hat{\tilde{\mathbf{b}}}^T\mathbf{M} \\ \mathbf{M}\hat{\mathbf{I}} & -\mathbf{M}\hat{\tilde{\mathbf{b}}} & \mathbf{M} \end{bmatrix} \begin{Bmatrix} \ddot{\mathbf{r}} \\ \dot{\omega} \\ \ddot{\delta} \end{Bmatrix} = \begin{Bmatrix} \hat{\mathbf{I}}^T(\mathbf{f} - \mathbf{Mw}) \\ -\hat{\tilde{\mathbf{b}}}^T(\mathbf{f} - \mathbf{Mw}) \\ \mathbf{f} - \mathbf{Mw} - \mathbf{K}\delta \end{Bmatrix} \tag{3.13}$$

where,

$$\hat{\mathbf{I}}^T\mathbf{M}\hat{\mathbf{I}} = m\mathbf{I} \quad (\hat{\mathbf{I}}^{T\,'}\mathbf{M}\hat{\mathbf{I}} = m\mathbf{I}) \quad (3.14.a), \qquad \hat{\tilde{\mathbf{b}}}^T\mathbf{M}\hat{\tilde{\mathbf{b}}} = \mathbf{J} \quad (\hat{\tilde{\mathbf{b}}}^{T\,'}\mathbf{M}\,'\hat{\tilde{\mathbf{b}}} = \,'\mathbf{J}) \quad (3.14.b)$$

$$\hat{\mathbf{I}}^T\mathbf{K}\delta = 0 \quad (\hat{\mathbf{I}}^{T\,'}\mathbf{K}\,'\delta = 0) \quad (3.14.c), \qquad \hat{\tilde{\mathbf{b}}}^T\mathbf{K}\delta = 0 \quad (\hat{\tilde{\mathbf{b}}}^{T\,'}\mathbf{K}\,'\delta = 0) \quad (3.14.d)$$

In Eqs. 3.14.a and 3.14.b, m and $\mathbf{J}$ represent the total mass and the instantaneous rotational inertia matrix of the body. In Eq. 3.13 we have also used the two identities given in Eqs. 3.14.c and 3.14.d. These identities state that the sum of internal structural forces and moments is equal to zero.

Equation 3.13 can also be transformed to other forms. For example, we can express the nodal deformation array with respect to the body-fixed frame:

$$\begin{bmatrix} m\mathbf{I} & -\hat{\mathbf{I}}^T\mathbf{M}\hat{\tilde{\mathbf{b}}} & \hat{\mathbf{I}}^T\mathbf{M}\bar{\mathbf{A}} \\ -\hat{\tilde{\mathbf{b}}}^T\mathbf{M}\hat{\mathbf{I}} & \mathbf{J} & -\hat{\tilde{\mathbf{b}}}^T\mathbf{M}\bar{\mathbf{A}} \\ \bar{\mathbf{A}}^T\mathbf{M}\hat{\mathbf{I}} & -\bar{\mathbf{A}}^T\mathbf{M}\hat{\tilde{\mathbf{b}}} & \,'\mathbf{M} \end{bmatrix} \begin{Bmatrix} \ddot{\mathbf{r}} \\ \dot{\omega} \\ \,'\ddot{\delta} \end{Bmatrix} = \begin{Bmatrix} \hat{\mathbf{I}}^T(\mathbf{f} - \mathbf{Mw}) \\ -\hat{\tilde{\mathbf{b}}}^T(\mathbf{f} - \mathbf{Mw}) \\ \,'\mathbf{f} - \,'\mathbf{M}\,'\mathbf{w} - \,'\mathbf{K}\,'\delta \end{Bmatrix} \tag{3.15}$$

Equations 3.12, 3.13, and 3.15 are different representations of Eq. 3.4. Although so far we have not discussed how to attach a reference frame to the body, let us assume that the modal deflections are known; therefore, the array of forces at the right-hand side of these equations can be determined. Equation 3.4 contains n_{dof} equations that can be solved to determine n_{dof} unknown accelerations. Equation 3.12 contains n_{dof} equations in $n_{dof} +$

6 unknown accelerations and therefore they cannot be solved for the accelerations. Equation 3.13 or 3.15 each contains $n_{dof} + 6$ equations in $n_{dof} + 6$ unknown accelerations. However, since in each set of equations there are six redundant equations, they cannot be solved for the accelerations either.

3.1.1. *Boundary and Unconstrained Nodes*

In a multibody system, a flexible body is often connected to other rigid or flexible bodies. The connections are through kinematic joints, springs, dampers, or other elements. For this purpose we split the nodes of a flexible body into two sets as shown in Fig. 2: the *boundary* nodes having superscript "*b*", and the *unconstrained* nodes with superscript "*u*". The boundary nodes will be used to connect the deformable body to other bodies, and the unconstrained nodes remain free. Based on this categorization, all entities associated with a flexible body will be split into subsets, for example:

$$\mathbf{K} = \begin{bmatrix} \mathbf{K}^{bb} & \mathbf{K}^{bu} \\ \mathbf{K}^{ub} & \mathbf{K}^{uu} \end{bmatrix} = \begin{bmatrix} \mathbf{K}^{b,} \\ \mathbf{K}^{u,} \end{bmatrix} = \begin{bmatrix} \mathbf{K}^{,b} & \mathbf{K}^{,u} \end{bmatrix}, \quad \mathbf{M} = \begin{bmatrix} \mathbf{M}^{bb} & \mathbf{M}^{bu} \\ \mathbf{M}^{ub} & \mathbf{M}^{uu} \end{bmatrix} = \begin{bmatrix} \mathbf{M}^{b,} \\ \mathbf{M}^{u,} \end{bmatrix} = \begin{bmatrix} \mathbf{M}^{,b} & \mathbf{M}^{,u} \end{bmatrix} \quad (3.16)$$
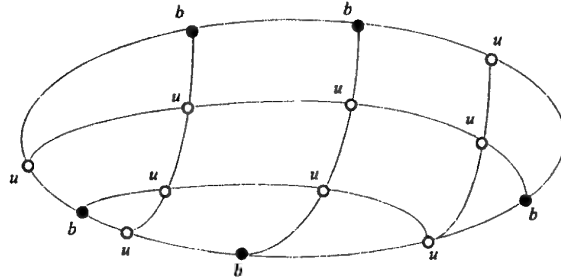
Figure 2. Boundary and unconstrained nodes.

3.2. BODY-FIXED FRAME

In order to attach a body-fixed frame to a deformable body, we need to define six conditions. With these conditions, the number of nodal deflection degrees-of-freedom becomes $n_{dof} = 3 \times n_{nodes} - 6$; i.e., the rigid-body degrees-of-freedom are removed. The common procedure in finite element method is to introduce boundary conditions to set six of the nodal deflections to zero. Another procedure defines six so-called *mean-axis* conditions [1].

The mean-axis conditions are defined at the velocity level as[2]

$$\hat{\mathbf{I}}^T \mathbf{M} \dot{\boldsymbol{\delta}} = 0 \qquad (\hat{\mathbf{I}}^{T'} \mathbf{M} \dot{\boldsymbol{\delta}} = 0) \qquad (3.17)$$

---

[2] The mean-axis conditions can be obtained from the minimization of the deformation kinetic energy. The kinetic energy associated with the deformation is expressed as:

$$T = \tfrac{1}{2} \dot{\boldsymbol{\delta}}^T \mathbf{M} \dot{\boldsymbol{\delta}} = \tfrac{1}{2} (\dot{\mathbf{d}} - \hat{\mathbf{I}} \dot{\mathbf{r}} + \hat{\tilde{\mathbf{b}}} \boldsymbol{\omega})^T \mathbf{M} (\dot{\mathbf{d}} - \hat{\mathbf{I}} \dot{\mathbf{r}} + \hat{\tilde{\mathbf{b}}} \boldsymbol{\omega})$$

The partial derivatives of the kinetic energy with respect to the translational and angular velocities of the body-fixed frame are:

$$T_{\dot{\mathbf{r}}} = -(\dot{\mathbf{d}} - \hat{\mathbf{I}} \dot{\mathbf{r}} + \hat{\tilde{\mathbf{b}}} \boldsymbol{\omega})^T \mathbf{M} \hat{\mathbf{I}} = -\dot{\boldsymbol{\delta}}^T \mathbf{M} \hat{\mathbf{I}}$$

$$T_{\boldsymbol{\omega}} = \tfrac{1}{2} (\dot{\mathbf{d}} - \hat{\mathbf{I}} \dot{\mathbf{r}} + \hat{\tilde{\mathbf{b}}} \boldsymbol{\omega})^T \mathbf{M} \tilde{\mathbf{b}} = \dot{\boldsymbol{\delta}}^T \mathbf{M} \tilde{\mathbf{b}}$$

The minimum kinetic energy is achieved if these derivatives are set to zero.

163

$$\hat{\tilde{b}}^T M \dot{\delta} = 0 \qquad ('\hat{\tilde{b}}^{T} \, 'M \, '\dot{\delta} = 0) \tag{3.18}$$

The time derivative of these equations yields

$$\hat{I}^T M \ddot{\delta} = 0 \qquad (\hat{I}^{T} \, 'M \, '\ddot{\delta} = 0) \tag{3.19}$$

$$\hat{\tilde{b}}^T M \ddot{\delta} = -\tilde{\dot{\delta}}^T M \dot{\delta} \qquad ('\hat{\tilde{b}}^{T} \, 'M \, '\ddot{\delta} = -'\tilde{\dot{\delta}}^{T} \, 'M \, '\dot{\delta}) \tag{3.20.a}$$

The right-hand side of Eq. 3.20.a could be zero depending on the characteristics of the mass matrix. Therefore, the simpler form of Eq. 3.20.a is

$$\hat{\tilde{b}}^T M \ddot{\delta} = 0 \qquad ('\hat{\tilde{b}}^{T} \, 'M \, '\ddot{\delta} = 0) \tag{3.20.b}$$

Other identities can be derived based on Eqs. 3.17 and 3.18. For example, the integral of Eq. 3.17; i.e., $\hat{I}^T M \delta = 0$, yields

$$\hat{I}^T M \tilde{b} = \hat{\tilde{b}}^T M \hat{I} = 0 \qquad (\hat{I}^{T} \, 'M \, '\tilde{b} = '\hat{\tilde{b}}^{T} \, 'M \, \hat{I} = 0) \tag{3.21}$$

This is known as the first-moment equation. It states that the origin of the reference frame stays at the instantaneous mass center of the body.

Substituting Eqs. 3.19, 3.20.a, and 3.21 into Eq. 3.13 yields

$$\begin{bmatrix} mI & 0 & 0 \\ 0 & J & 0 \\ M\hat{I} & -M\hat{\tilde{b}} & M \end{bmatrix} \begin{Bmatrix} \ddot{r} \\ \dot{\omega} \\ \ddot{\delta} \end{Bmatrix} = \begin{Bmatrix} \hat{I}^T(f - Mw) \\ -\hat{\tilde{b}}^T(f - Mw) + \tilde{\dot{\delta}}^T M \dot{\delta} \\ f - K\delta - Mw \end{Bmatrix} \tag{3.22.a}$$

The coefficient matrix in Eq. 3.22.a is non-singular. Therefore, if all of the forces are known, the equations can be solved for the accelerations. If we use Eq. 3.20.b in the above process instead of Eq. 3.20.a, Eq. 3.22.a finds the following form:

$$\begin{bmatrix} mI & 0 & 0 \\ 0 & J & 0 \\ M\hat{I} & -M\hat{\tilde{b}} & M \end{bmatrix} \begin{Bmatrix} \ddot{r} \\ \dot{\omega} \\ \ddot{\delta} \end{Bmatrix} = \begin{Bmatrix} \hat{I}^T(f - Mw) \\ -\hat{\tilde{b}}^T(f - Mw) \\ f - K\delta - Mw \end{Bmatrix} \tag{3.22.b}$$

In this manuscript we use Eq. 3.22.b instead of Eq. 3.22.a. This means that we make the assumption that the mass matrix has the required characteristics such that Eq. 3.20.b is valid. Furthermore, depending on the characteristics of the mass matrix, some other terms on the right-hand side of Eq. 3.22.a could further be simplified.

Equations 3.19 and 3.20.b could be incorporated into Eq. 3.22.b (or Eq. 3.13) using the Lagrange multiplier technique to obtain

$$\begin{bmatrix} mI & 0 & 0 & 0 & 0 \\ 0 & J & 0 & 0 & 0 \\ M\hat{I} & -M\hat{\tilde{b}} & M & M\hat{I} & M\hat{\tilde{b}} \\ 0 & 0 & \hat{I}^T M & 0 & 0 \\ 0 & 0 & \hat{\tilde{b}}^T M & 0 & 0 \end{bmatrix} \begin{Bmatrix} \ddot{r} \\ \dot{\omega} \\ \ddot{\delta} \\ \lambda_t \\ \lambda_r \end{Bmatrix} = \begin{Bmatrix} \hat{I}^T(f - Mw) \\ -\hat{\tilde{b}}^T(f - Mw) \\ f - K\delta - Mw \\ 0 \\ 0 \end{Bmatrix} \tag{3.23}$$

where λ_t and λ_r contain six Lagrange multipliers. In Eq. 3.23 the mean-axis conditions at the acceleration level are explicitly present and therefore they are definitely enforced. In Eq. 3.22.b these conditions are not explicitly present, therefore, when we solve Eq. 4.10.b for the accelerations, the result may not exactly satisfy Eqs. 3.19 and 3.20.b. Although the amount of error could be extremely small, in the process of integration of the equations of motion this error may accumulate and may cause numerical instability.

4. Nodal and Modal Transformations

The number of nodes, and consequently the number of degrees-of-freedom associated with a deformable body, may be too large for any realistic simulation. Therefore, various processes have been developed to reduce the number of degrees-of-freedom. The reduction process may be performed either in the nodal or in the modal space.

4.1. STATIC CONDENSATION

In the so-called static or Guyan condensation, it is assumed that some of the nodes of a finite element model are kept and the rest are deleted [2]. For this purpose, we use superscripts m and s for the *master* (kept) and *slave* (deleted) nodes[3]. The structural equations of motion, Eq. 3.1, are re-written as

$$\begin{bmatrix} {}^{\cdot}\mathbf{M}^{mm} & {}^{\cdot}\mathbf{M}^{ms} \\ {}^{\cdot}\mathbf{M}^{sm} & {}^{\cdot}\mathbf{M}^{ss} \end{bmatrix} \begin{Bmatrix} {}^{\cdot}\ddot{\delta}^m \\ {}^{\cdot}\ddot{\delta}^s \end{Bmatrix} + \begin{bmatrix} {}^{\cdot}\mathbf{K}^{mm} & {}^{\cdot}\mathbf{K}^{ms} \\ {}^{\cdot}\mathbf{K}^{sm} & {}^{\cdot}\mathbf{K}^{ss} \end{bmatrix} \begin{Bmatrix} {}^{\cdot}\delta^m \\ {}^{\cdot}\delta^s \end{Bmatrix} = \begin{Bmatrix} {}^{\cdot}\mathbf{f}^m \\ {}^{\cdot}\mathbf{f}^s \end{Bmatrix} \tag{4.1}$$

We now assume that the inertia of the entire structure is allocated to the master nodes and no external forces are applied to the slave nodes; i.e.,

$$\begin{bmatrix} {}^{\cdot}\mathbf{M}_G & 0 \\ 0 & 0 \end{bmatrix} \begin{Bmatrix} {}^{\cdot}\ddot{\delta}^m \\ {}^{\cdot}\ddot{\delta}^s \end{Bmatrix} + \begin{bmatrix} {}^{\cdot}\mathbf{K}^{mm} & {}^{\cdot}\mathbf{K}^{ms} \\ {}^{\cdot}\mathbf{K}^{sm} & {}^{\cdot}\mathbf{K}^{ss} \end{bmatrix} \begin{Bmatrix} {}^{\cdot}\delta^m \\ {}^{\cdot}\delta^s \end{Bmatrix} = \begin{Bmatrix} {}^{\cdot}\mathbf{f}^m \\ 0 \end{Bmatrix} \tag{4.2}$$

where ${}^{\cdot}\mathbf{M}_G$ is the mass matrix associated with the master nodes containing the entire structural inertia. This matrix will be determined as a function of the original sub-matrices. The second row of the equations of motion yields:

$$ {}^{\cdot}\mathbf{K}^{sm}\,{}^{\cdot}\delta^m + {}^{\cdot}\mathbf{K}^{ss}\,{}^{\cdot}\delta^s = 0 $$

From this equation we get

$$ {}^{\cdot}\delta^s = {}^{\cdot}\mathbf{G}\,{}^{\cdot}\delta^m \tag{4.3}$$

where

$$ {}^{\cdot}\mathbf{G} = -{}^{\cdot}\mathbf{K}^{ss-1}\,{}^{\cdot}\mathbf{K}^{sm} \tag{4.4}$$

is known as the static condensation matrix. This matrix can be used to determine the reduced mass and stiffness matrices as:

$$ {}^{\cdot}\mathbf{M}_G = {}^{\cdot}\mathbf{M}^{mm} + {}^{\cdot}\mathbf{M}^{ms}\,{}^{\cdot}\mathbf{G} + {}^{\cdot}\mathbf{G}^T\,{}^{\cdot}\mathbf{M}^{sm} + {}^{\cdot}\mathbf{G}^T\,{}^{\cdot}\mathbf{M}^{ss}\,\mathbf{G} \tag{4.5}$$

$$ {}^{\cdot}\mathbf{K}_G = {}^{\cdot}\mathbf{K}^{mm} - {}^{\cdot}\mathbf{K}^{ms}\,{}^{\cdot}\mathbf{K}^{ss-1}\,{}^{\cdot}\mathbf{K}^{sm} \tag{4.6}$$

Matrices ${}^{\cdot}\mathbf{M}_G$ and ${}^{\cdot}\mathbf{K}_G$ can now be used in any of the equations of motion instead of ${}^{\cdot}\mathbf{M}$ and ${}^{\cdot}\mathbf{K}$.

4.2. MODAL MATRICES

In the following sub-sections we use modal data for different mass and stiffness matrices. In general, it is assumed that the matrix of mode shapes, ${}^{\cdot}\Psi$, provides the following transformation between the modal and nodal coordinates:

$$ {}^{\cdot}\delta = {}^{\cdot}\Psi\,\mathbf{z} \tag{4.7}$$

If we define another modal matrix as

$$ \Psi = \overline{\mathbf{A}}\,{}^{\cdot}\Psi \tag{4.8}$$

---

[3] The *boundary* nodes are a sub-set of the *master* nodes. The *slave* nodes contain some or all of the *unconstrained* nodes.

165

then we have another form of the transformation equation as

$$\delta = \Psi \, z \tag{4.9}$$

Equation 4.8 is also applicable to matrix $\dot{G}$ in Eq 4.3.

4.2.1. *Free-Free Modes*

The matrices of the mode shapes and modal frequencies obtained from $\dot{M}$ and $\dot{K}$ are:

$$\left[\hat{I} \quad -\hat{\dot{s}} \quad \dot{\Psi}_f\right], \quad diag(0, \ 0, \ \Lambda_f) \tag{4.10}$$

In the matrix of mode shapes, $\hat{I}$ and $-\hat{\dot{s}}$ represent the translational and rotational rigid body mode shapes (each is an $n_{dof} \times 3$ matrix), and $\dot{\Psi}_f$ which is an $n_{dof} \times (n_{dof} - 6)$ matrix represents the deformation mode shapes. The diagonal matrix of eigenvalues contains six zero eigenvalues associated with the rigid body modes and the natural frequencies Λ_f. Note that the subscript *"f"* emphasizes that these entities correspond to a *free-free* structure.

The modal-to-nodal transformation equation is written as

$$\dot{\delta} = \dot{\Psi}_f \, z \tag{4.11}$$

The modal stiffness and mass matrices are

$$M_f = \dot{\Psi}_f^{\ T} M \dot{\Psi}_f, \quad K_f = \dot{\Psi}_f^{\ T} K \dot{\Psi}_f \tag{4.12}$$

Considering the partitioning of the nodes based on the boundary and unconstrained nodes, Eq. 4.11 becomes

$$\begin{Bmatrix} \dot{\delta}^b \\ \dot{\delta}^u \end{Bmatrix} = \begin{bmatrix} \Psi_f^b \\ \Psi_f^u \end{bmatrix} z \tag{4.13}$$

4.2.2. *Constrained Modes*

Assume that the boundary nodes are constrained not to have any deflections; i.e., $\dot{\delta}^b = \ddot{\delta}^b = 0$. In this case sub-matrices $\dot{M}^{uu}$ and $\dot{K}^{uu}$ are used to obtain modal matrices $\dot{\Psi}_c$ and Λ_c. If the boundary nodes eliminate at least six degrees-of-freedom, there will be no zero eigenvalues in Λ_c. The subscript *"c"* emphasizes that these entities correspond to a *constrained* structure. The transformation equation is

$$\dot{\delta}^u = \dot{\Psi}_c \, z \tag{4.14}$$

The modal stiffness and mass matrices are obtained as

$$M_c = \dot{\Psi}_c^{\ T} \dot{M}^{uu} \dot{\Psi}_c, \quad K_c = \dot{\Psi}_c^{\ T} \dot{K}^{uu} \dot{\Psi}_c \tag{4.15}$$

4.2.3. *Constrained Modes and Static Condensation*

We can assume that the deflections of the unconstrained (free) nodes are expressed in terms of the deflection of the boundary nodes and the constrained modal matrix $\dot{\Psi}_c$ as

$$\dot{\delta}^u = E \, \dot{\delta}^b + \dot{\Psi}_c \, z$$

where E is a coefficient matrix to be determined. For the complete set of deflections this equation is written as

$$\begin{Bmatrix} \dot{\delta}^b \\ \dot{\delta}^u \end{Bmatrix} = \begin{bmatrix} I & 0 \\ E & \Psi_c \end{bmatrix} \begin{Bmatrix} \dot{\delta}^b \\ z \end{Bmatrix} \tag{4.16}$$

Using the coefficient matrix, the stiffness matrix is transformed to modal space as

166

$$\begin{bmatrix} I & E^T \\ 0 & '\Psi_c^T \end{bmatrix} \begin{bmatrix} 'K^{bb} & 'K^{bu} \\ 'K^{ub} & 'K^{uu} \end{bmatrix} \begin{bmatrix} I & 0 \\ E & \Psi_c \end{bmatrix} \Rightarrow \begin{bmatrix} 'K^{bb} + 'K^{bu}E + E^T('K^{ub} + 'K^{uu}E) & ('K^{bu} + E^{T'}K^{uu})'\Psi_c \\ \Psi_c^{T}('K^{ub} + 'K^{uu}E) & \Psi_c^{T'}K^{uu}'\Psi_c \end{bmatrix} \quad (4.17)$$

In order to uncouple the revised stiffness matrix between the boundary and the unconstrained nodes, we set

$$E = -'K^{uu^{-1}} \, 'K^{ub} = 'G \quad (4.18)$$

This matrix is identical to the static condensation matrix in Guyan reduction as stated in Eq. 4.4. Here, the master and slave nodes are replaced by the boundary and unconstrained nodes. Then, Eq. 4.16 becomes [3, 4]

$$\begin{Bmatrix} '\delta^b \\ '\delta^u \end{Bmatrix} = \begin{bmatrix} I & 0 \\ 'G & '\Psi_c \end{bmatrix} \begin{Bmatrix} '\delta^b \\ z \end{Bmatrix} \quad (4.19)$$

Now Eq. 4.17 is written as

$$\begin{bmatrix} I & 'G^T \\ 0 & \Psi_c^T \end{bmatrix} \begin{bmatrix} 'K^{bb} & 'K^{bu} \\ 'K^{ub} & 'K^{uu} \end{bmatrix} \begin{bmatrix} I & 0 \\ 'G & \Psi_c \end{bmatrix} \Rightarrow \begin{bmatrix} 'K_G & 0 \\ 0 & K_c \end{bmatrix} \quad (4.20)$$

Similarly, for the mass matrix we get

$$\begin{bmatrix} I & 'G^T \\ 0 & \Psi_c^T \end{bmatrix} \begin{bmatrix} 'M^{bb} & 'M^{bu} \\ 'M^{ub} & 'M^{uu} \end{bmatrix} \begin{bmatrix} I & 0 \\ 'G & \Psi_c \end{bmatrix} \Rightarrow \begin{bmatrix} 'M_G & M_{Gc}^T \\ M_{Gc} & M_c \end{bmatrix} \quad (4.21)$$

where $M_{Gc} \equiv '\Psi_c^T('M^{ub} + 'M^{uu'}G)$.

4.2.4. *Constrained Modes and Modal Condensation*

In Section 6 the equations of motion will be truncated to obtain smaller sets of equations. When this process is performed in modal space, the mode shapes and corresponding entities are split into the kept and deleted sets. The process discussed in this sub-section will be applicable to the condensation techniques used in Section 6.

Assume that the equations of motion for a structure, Eq. 3.1, are transformed to modal space using the constrained transformations; i.e., Eqs. 4.14 and 4.15. Furthermore, we split the modal coordinates into the kept and deleted modes to get

$$\begin{bmatrix} 'M^{bb} & 'M^{bu}\Psi_c^k & 'M^{bu}\Psi_c^d \\ \Psi_c^{kT'}M^{ub} & M_c^k & 0 \\ \Psi_d^{kT'}M^{ub} & 0 & M_c^d \end{bmatrix} \begin{Bmatrix} '\ddot{\delta}^b \\ \ddot{z}^k \\ \ddot{z}^d \end{Bmatrix} + \begin{bmatrix} 'K^{bb} & 'K^{bu}\Psi_c^k & 'K^{bu}\Psi_c^d \\ \Psi_c^{kT'}K^{ub} & K_c^k & 0 \\ \Psi_d^{kT'}K^{ub} & 0 & K_c^d \end{bmatrix} \begin{Bmatrix} \delta^m \\ z^k \\ z^d \end{Bmatrix} = \begin{Bmatrix} f^m \\ \Psi_c^{kT'}f^u \\ \Psi_c^{dT'}f^u \end{Bmatrix} \quad (4.22)$$

In a process similar to that of the static condensation, we assume that the inertia associated with the deleted modes are allocated to the boundary nodes; and furthermore, there are no forces associated with the deleted modes [5]. With this assumption, the third row of Eq. 4.22 yields

$$z^d = \Theta \, '\delta^b \quad (4.23)$$

where

$$\Theta = -K^{d^{-1}} \, '\Psi_c^{dT} \, 'K^{ub} \quad (4.24)$$

Note that Θ transforms a set of nodal coordinates to modal coordinates.

5. Equations of Motion for A Rigid-Flexible Multibody System

A multibody system may contain both flexible and rigid bodies. The Newton-Euler equations for a typical free rigid body are written as

$$\begin{bmatrix} \mathbf{M}_r & 0 \\ 0 & \mathbf{J}_r \end{bmatrix} \begin{Bmatrix} \ddot{\mathbf{r}}_r \\ \dot{\boldsymbol{\omega}}_r \end{Bmatrix} = \begin{Bmatrix} \mathbf{f}_r \\ \mathbf{n}_r \end{Bmatrix} \tag{5.1}$$

where $\mathbf{M}_r = m_r\mathbf{I}$ is the mass of the body, $\mathbf{J}_r$ is the rotational inertia matrix, and $\mathbf{f}_r$ is the external force vector acting on the body. The term $\mathbf{n}_r = \mathbf{n} + \tilde{\mathbf{s}}_r^P \mathbf{f}_r - \tilde{\boldsymbol{\omega}}_r \mathbf{J}_r \boldsymbol{\omega}_r$ is the sum of applied moments, $\mathbf{n}$, the moment of the force $\mathbf{f}_r$, and the gyroscopic moment. It is assumed that the origin of the body-fixed frame is at the mass center. The Euler equations are normally written in terms of the body-fixed components, however, in order to be consistent with our flexible body formulations, we have expressed the equations in terms of the global components.
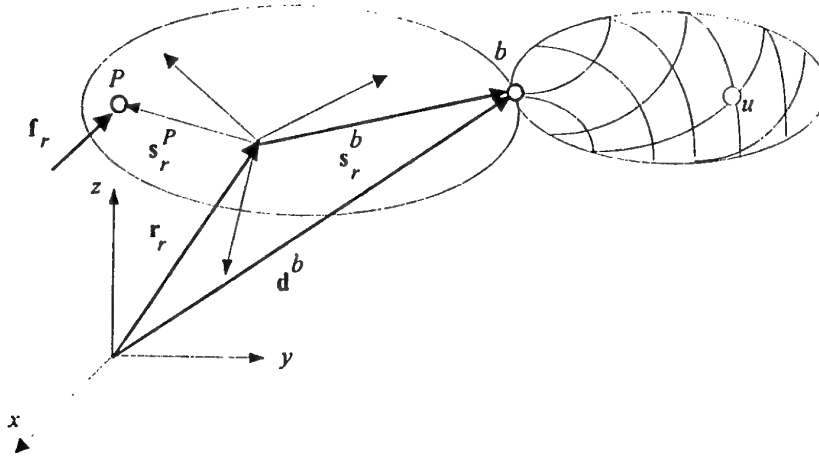
Figure 3. A simple rigid-flexible multibody system.

In order to discuss different formulations for a rigid-flexible multibody system, without any loss of generality, we concentrate on a simple multibody system containing only one rigid and one flexible body. We further assume that the connection between the two bodies, as shown in Fig. 3, is at point b representing one spherical joint.

The kinematic constraint equations at a typical spherical joint is

$$\mathbf{r}_r + \mathbf{s}_r^b - \mathbf{d}^b = 0 \tag{5.2}$$

The velocity and acceleration constraints are:

$$\dot{\mathbf{r}}_r - \tilde{\mathbf{s}}_r^b \boldsymbol{\omega}_r - \dot{\mathbf{d}}^b = 0 \tag{5.3}$$

$$\ddot{\mathbf{r}}_r - \tilde{\mathbf{s}}_r^b \dot{\boldsymbol{\omega}}_r - \ddot{\mathbf{d}}^b + \tilde{\boldsymbol{\omega}}_r \tilde{\boldsymbol{\omega}}_r \mathbf{s}_r^b = 0 \tag{5.4}$$

Using Eq. 3.7, Eq. 5.4 can also be expressed as

$$\ddot{\mathbf{r}}_r - \tilde{\mathbf{s}}_r^b \dot{\boldsymbol{\omega}}_r - \ddot{\mathbf{r}} + \tilde{\mathbf{b}}^b \dot{\boldsymbol{\omega}} - \ddot{\boldsymbol{\delta}}^b = \boldsymbol{\gamma}^b \tag{5.5}$$

where

$$\boldsymbol{\gamma}^b = -\tilde{\boldsymbol{\omega}}_r \tilde{\boldsymbol{\omega}}_r \mathbf{s}_r^b + \mathbf{w}^b \tag{5.6}$$

If there are several spherical joints between the bodies, Eq. 5.4 or 5.5 is repeated for every constrained node.

5.1. ABSOLUTE NODAL MOTION

With the aid of Lagrange multiplier technique [6], we append Eqs. 5.1, 3.4, and 5.4 to form the equations of motion for the multibody system as

168

$$\begin{bmatrix} \mathbf{M}_r & 0 & 0 & 0 & \mathbf{I} \\ 0 & \mathbf{J}_r & 0 & 0 & -\tilde{\mathbf{s}}_r^{bT} \\ \hline 0 & 0 & \mathbf{M}^{bb} & \mathbf{M}^{bu} & -\mathbf{I} \\ 0 & 0 & \mathbf{M}^{ub} & \mathbf{M}^{uu} & 0 \\ \hline \mathbf{I} & -\tilde{\mathbf{s}}_r^b & -\mathbf{I} & 0 & 0 \end{bmatrix} \begin{Bmatrix} \ddot{\mathbf{r}}_r \\ \dot{\boldsymbol{\omega}}_r \\ \hline \ddot{\mathbf{d}}^b \\ \ddot{\mathbf{d}}^u \\ \hline \lambda \end{Bmatrix} = \begin{Bmatrix} \mathbf{f}_r \\ \mathbf{n}_r \\ \hline \mathbf{f}^b - \mathbf{K}^{b}\boldsymbol{\delta} \\ \mathbf{f}^u - \mathbf{K}^u\boldsymbol{\delta} \\ \hline -\tilde{\boldsymbol{\omega}}_r\tilde{\boldsymbol{\omega}}_r\mathbf{s}_r^b \end{Bmatrix} \tag{5.7}$$

5.2. NODAL DEFLECTIONS

We now transform Eq. 5.7 to a different form where, instead of the absolute accelerations, accelerations associated with nodal deformation are used. For this purpose we use Eqs. 3.22.b, 5.1 and 5.5 to get

$$\begin{bmatrix} \mathbf{M}_r & 0 & 0 & 0 & 0 & 0 & \mathbf{I} \\ 0 & \mathbf{J}_r & 0 & 0 & 0 & 0 & -\tilde{\mathbf{s}}_r^{bT} \\ \hline 0 & 0 & m\mathbf{I} & 0 & 0 & 0 & -\mathbf{I} \\ 0 & 0 & 0 & \mathbf{J} & 0 & 0 & \tilde{\mathbf{b}}^{bT} \\ 0 & 0 & \mathbf{M}^{b}\hat{\mathbf{I}} & -\mathbf{M}^{b}\hat{\tilde{\mathbf{b}}} & \mathbf{M}^{bb} & \mathbf{M}^{bu} & -\mathbf{I} \\ 0 & 0 & \mathbf{M}^{u}\hat{\mathbf{I}} & -\mathbf{M}^{u}\hat{\tilde{\mathbf{b}}} & \mathbf{M}^{ub} & \mathbf{M}^{uu} & 0 \\ \hline \hat{\mathbf{I}} & -\tilde{\mathbf{s}}_r^b & -\mathbf{I} & \tilde{\mathbf{b}}^b & -\mathbf{I} & 0 & 0 \end{bmatrix} \begin{Bmatrix} \ddot{\mathbf{r}}_r \\ \dot{\boldsymbol{\omega}}_r \\ \hline \ddot{\mathbf{r}} \\ \dot{\boldsymbol{\omega}} \\ \ddot{\boldsymbol{\delta}}^b \\ \ddot{\boldsymbol{\delta}}^u \\ \hline \lambda \end{Bmatrix} = \begin{Bmatrix} \mathbf{f}_r \\ \mathbf{n}_r \\ \hline \mathbf{f}_o \\ \mathbf{n}_o \\ \mathbf{f}_t^b \\ \mathbf{f}_t^u \\ \hline \boldsymbol{\gamma}^b \end{Bmatrix} \tag{5.8}$$

where $\mathbf{f}_o = \hat{\mathbf{I}}^T(\mathbf{f}-\mathbf{M}\mathbf{w})$, $\mathbf{n}_o = -\hat{\tilde{\mathbf{b}}}^T(\mathbf{f}-\mathbf{M}\mathbf{w})$, and $\mathbf{f}_t^j \equiv \mathbf{f}^j - \mathbf{M}^{j}\mathbf{w} - \mathbf{K}^{j}\boldsymbol{\delta}; j = b, u$.

5.3. FREE-FREE MODES

We can transform Eq. 5.8 to modal coordinates using the free-free modal data. Using Eqs. 4.11-4.13, we get

$$\begin{bmatrix} \mathbf{M}_r & 0 & 0 & 0 & 0 & \mathbf{I} \\ 0 & \mathbf{J}_r & 0 & 0 & 0 & -\tilde{\mathbf{s}}_r^{bT} \\ \hline 0 & 0 & m\mathbf{I} & 0 & 0 & -\mathbf{I} \\ 0 & 0 & 0 & \mathbf{J} & 0 & \tilde{\mathbf{b}}^{bT} \\ 0 & 0 & \boldsymbol{\Psi}_f^T\mathbf{M}\hat{\mathbf{I}} & -\boldsymbol{\Psi}_f^T\mathbf{M}\hat{\tilde{\mathbf{b}}} & \mathbf{M}_f & -\boldsymbol{\Psi}_f^T \\ \hline \mathbf{I} & -\tilde{\mathbf{s}}_r^b & -\mathbf{I} & \tilde{\mathbf{b}}^b & -\boldsymbol{\Psi}_f & 0 \end{bmatrix} \begin{Bmatrix} \ddot{\mathbf{r}}_r \\ \dot{\boldsymbol{\omega}}_r \\ \hline \ddot{\mathbf{r}} \\ \dot{\boldsymbol{\omega}} \\ \ddot{\mathbf{z}} \\ \hline \lambda \end{Bmatrix} = \begin{Bmatrix} \mathbf{f}_r \\ \mathbf{n}_r \\ \hline \mathbf{f}_o \\ \mathbf{n}_o \\ f_f \\ \hline \boldsymbol{\gamma}^b \end{Bmatrix} \tag{5.9}$$

where $f_f \equiv \boldsymbol{\Psi}_f^T(\mathbf{f}-\mathbf{M}\mathbf{w}) - K_f\mathbf{z}$.

5.4. CONSTRAINED MODES

Equation 5.8 can also be transformed to modal coordinates using the constrained modal data from Eqs. 4.14 and 4.15:

$$
\begin{bmatrix}
\mathbf{M}_r & 0 & 0 & 0 & 0 & 0 & \mathbf{I} \\
0 & \mathbf{J}_r & 0 & 0 & 0 & 0 & -\tilde{\mathbf{s}}_r^{b\,T} \\
\hline
0 & 0 & m\mathbf{I} & 0 & 0 & 0 & -\mathbf{I} \\
0 & 0 & 0 & \mathbf{J} & 0 & 0 & \tilde{\mathbf{b}}^{b\,T} \\
0 & 0 & \mathbf{M}_1\hat{\mathbf{I}} & -\mathbf{M}_1\hat{\tilde{\mathbf{b}}} & {}'\mathbf{M}^{bb} & \mathbf{M}_3^{T} & -\mathbf{A}^{T} \\
0 & 0 & \mathbf{M}_2\hat{\mathbf{I}} & -\mathbf{M}_2\hat{\tilde{\mathbf{b}}} & \mathbf{M}_3 & M_c & 0 \\
\hline
\mathbf{I} & -\tilde{\mathbf{s}}_r^{b} & -\mathbf{I} & \tilde{\mathbf{b}}^{b} & -\mathbf{A} & 0 & 0
\end{bmatrix}
\begin{Bmatrix}
\ddot{\mathbf{r}}_r \\ \dot{\boldsymbol{\omega}}_r \\ \ddot{\mathbf{r}} \\ \dot{\boldsymbol{\omega}} \\ {}'\ddot{\delta}^{b} \\ \ddot{\mathbf{z}} \\ \boldsymbol{\lambda}
\end{Bmatrix}
=
\begin{Bmatrix}
\mathbf{f}_r \\ \mathbf{n}_r \\ \mathbf{f}_o \\ \mathbf{n}_o \\ {}'\mathbf{f}_l^{b} \\ f_c \\ \boldsymbol{\gamma}^{b}
\end{Bmatrix}
\tag{5.10}
$$

where $\mathbf{M}_1 \equiv \overline{\mathbf{A}}^{T}\mathbf{M}^{b\cdot}$, $\mathbf{M}_2 \equiv \boldsymbol{\Psi}_c^{T}\mathbf{M}^{u\cdot}$, $\mathbf{M}_3 \equiv {}'\boldsymbol{\Psi}_c^{T}\mathbf{M}^{ub}$, $f_c \equiv \boldsymbol{\Psi}_c^{T}({}'\mathbf{f}^{u} - {}'\mathbf{M}^{u\cdot}\,\mathbf{w} - {}'\mathbf{K}^{ub\prime}\boldsymbol{\delta}^{b}) - K_c\mathbf{z}$.

5.5. CONSTRAINED MODES AND STATIC CONDENSATION

Equations 4.19-4.21 transform Eq. 5.8 to the following form:

$$
\begin{bmatrix}
\mathbf{M}_r & 0 & 0 & 0 & 0 & 0 & \mathbf{I} \\
0 & \mathbf{J}_r & 0 & 0 & 0 & 0 & -\tilde{\mathbf{s}}_r^{b\,T} \\
\hline
0 & 0 & m\mathbf{I} & 0 & 0 & 0 & -\mathbf{I} \\
0 & 0 & 0 & \mathbf{J} & 0 & 0 & \tilde{\mathbf{b}}^{b\,T} \\
0 & 0 & \mathbf{M}_1\hat{\mathbf{I}} & -\mathbf{M}_1\hat{\tilde{\mathbf{b}}} & {}'\mathbf{M}_G & \mathbf{M}_{Gc}^{T} & -\mathbf{A}^{T} \\
0 & 0 & \mathbf{M}_2\hat{\mathbf{I}} & -\mathbf{M}_2\hat{\tilde{\mathbf{b}}} & \mathbf{M}_{Gc} & M_c & 0 \\
\hline
\mathbf{I} & -\tilde{\mathbf{s}}_r^{b} & -\mathbf{I} & \tilde{\mathbf{b}}^{b} & -\mathbf{A} & 0 & 0
\end{bmatrix}
\begin{Bmatrix}
\ddot{\mathbf{r}}_r \\ \dot{\boldsymbol{\omega}}_r \\ \ddot{\mathbf{r}} \\ \dot{\boldsymbol{\omega}} \\ {}'\ddot{\delta}^{b} \\ \ddot{\mathbf{z}} \\ \boldsymbol{\lambda}
\end{Bmatrix}
=
\begin{Bmatrix}
\mathbf{f}_r \\ \mathbf{n}_r \\ \mathbf{f}_o \\ \mathbf{n}_o \\ {}'\mathbf{f}_l^{b} \\ f_c \\ \boldsymbol{\gamma}^{b}
\end{Bmatrix}
\tag{5.11}
$$

where $\mathbf{M}_1 \equiv \overline{\mathbf{A}}^{T}\mathbf{M}^{b\cdot} + \mathbf{G}^{T}\mathbf{M}^{u\cdot}$, $\mathbf{M}_2 \equiv \boldsymbol{\Psi}_c^{T}\mathbf{M}^{u\cdot}$, ${}'\mathbf{f}_l^{b} \equiv {}'\mathbf{f}^{b} - {}'\mathbf{M}^{b\cdot}\,\mathbf{w} + \mathbf{G}^{T}({}'\mathbf{f}^{u} - {}'\mathbf{M}^{u\cdot}\,\mathbf{w}) - {}'\mathbf{K}_G\boldsymbol{\delta}^{b}$
and $f_c \equiv \boldsymbol{\Psi}_c^{T}({}'\mathbf{f}^{u} - {}'\mathbf{M}^{u\cdot}\,\mathbf{w}) - K_c\mathbf{z}$.

At any instant in time if the coordinates and deflections, velocities, and external and structural forces are known, Eqs. 5.7, 5.8, 5.9, 5.10, or 5.11 could be solved to determine the accelerations and Lagrange multipliers.

6. Model Reduction

So far we have derived the equations of motion for a multibody system in a variety of forms. For reducing these equations into smaller sets with fewer degrees-of-freedom, we need to eliminate some of the equations associated with the deformable body. In order to reduce the amount of error associated with any elimination, we must minimize the amount of coupling between the kept and eliminated equations. An inspection of the equations of motion reveals the following: If the mass matrix of the deformable body is diagonal, many of the terms in the equations of motion, including the coupling terms in the mass matrix, vanish. Even if the mass matrix is not diagonal but the elements around the boundary nodes are small, then the coupling terms $\mathbf{M}^{bu}$ and $\mathbf{M}^{ub}$ could be neglected. This process uncouples the two sets of equations in the mass matrix.

6.1. NODAL COORDINATES

In order to reduce the number of equations in the nodal coordinate space, the static condensation process of Section 4.1 can be applied to Eq. 5.8. With this process, some or all of the unconstrained nodes are removed, and a set of condensed mass and stiffness

matrices are obtained. It should be noted that with these condensed matrices, some of the simplifications in the equations of motion may no longer be valid. For example, we may need to use Eq. 3.20.a instead of 3.20.b.

6.2. MODAL COORDINATES

The modal equations of motion for a single deformable body can be truncated to a smaller set since the modal matrices are uncoupled between the kept and deleted modes. However, when the deformable body is part of a multibody system, the reduction process is not as straight forward. As it will be seen in the following sub-sections, the modal matrices are split into a kept set (superscript k) and a deleted set (superscript d). The idea is to eliminate the modal accelerations $\ddot{z}^d$ and its corresponding equations from the equations of motion. Due to the size of the following equations of motion, only those portions associated with the modal coordinates that are important in this process are shown.

6.2.1. *Free-Free Modes*

Equation 5.9 is split into the kept and deleted parts as

$$
\left[\begin{array}{ccc|c}
\cdots & M_f^k & 0 & -\Psi_f^{k\mathrm{T}} \\
\cdots & 0 & M_f^d & -\Psi_f^{d\mathrm{T}} \\
\hline
\cdots & -\Psi_f^k & -\Psi_f^d & 0
\end{array}\right]
\left\{\begin{array}{c}
\vdots \\
\ddot{z}^k \\
\ddot{z}^d \\
\hline
\lambda
\end{array}\right\}
=
\left\{\begin{array}{c}
\vdots \\
f_f^k \\
f_f^d \\
\hline
\gamma^b
\end{array}\right\}
\tag{6.1}
$$

where $f_f^j \equiv \Psi_f^{j\mathrm{T}}(f - M w) - K_f^j z$; $j = k,\ d$. If we eliminate $\ddot{z}^d$ and the corresponding equation, we observe that the term $-\Psi_f^d \ddot{z}^d$ in the acceleration constraints is also eliminated. This elimination causes the constraints to be violated and to cause erroneous results.

6.2.2. *Constrained Modes*

Equation 5.10 is re-written in the following form for the reduction process:

$$
\left[\begin{array}{cccc|c}
\cdots & M^{bb} & M_3^{k\mathrm{T}} & M_3^{d\mathrm{T}} & -A^\mathrm{T} \\
\cdots & M_3^k & M_c^k & 0 & 0 \\
\cdots & M_3^d & 0 & M_c^d & 0 \\
\hline
\cdots & -A & 0 & 0 & 0
\end{array}\right]
\left\{\begin{array}{c}
\vdots \\
\ddot{\delta}^b \\
\ddot{z}^k \\
\ddot{z}^d \\
\hline
\lambda
\end{array}\right\}
=
\left\{\begin{array}{c}
\vdots \\
f_t^b \\
f_c^k \\
f_c^d \\
\hline
\gamma^b
\end{array}\right\}
\tag{6.2}
$$

where $f_c^j \equiv \Psi_c^{j\mathrm{T}}(f^u - M^{u,} w - K^{ub} \delta^b) - K_c^j z$; $j = k,\ d$. If we eliminate $\ddot{z}^d$ and the corresponding equation, we observe that unlike Eq. 6.1, we do not eliminate anything from the constraint equation. Therefore there will be no violation in the constraints due to this process. However, the term $M_3^{d\mathrm{T}} \ddot{z}^d$ gets eliminated from the equation associated with the boundary node. This process can produce enough error to make the results unacceptable.

6.2.3. *Constrained Modes and Static Condensation*

For the reduction process, Eq. 5.11 is re-written as

$$
\left[\begin{array}{ccc|c}
\cdots & {}^{\prime}\mathbf{M}_G & \mathbf{M}_{Gc}^{k\,\mathrm{T}} & \mathbf{M}_{Gc}^{d\,\mathrm{T}} & -\mathbf{A}^{\mathrm{T}} \\
\cdots & \mathbf{M}_{Gc}^{k} & M_c^{k} & 0 & 0 \\
\cdots & \mathbf{M}_{Gc}^{d} & 0 & M_c^{d} & 0 \\
\hline
\cdots & -\mathbf{A} & 0 & 0 & 0
\end{array}\right]
\left\{\begin{array}{c}
\vdots \\
{}^{\prime}\ddot{\delta}^{b} \\
\ddot{z}^{k} \\
\ddot{z}^{d} \\
\hline
\lambda
\end{array}\right\}
=
\left\{\begin{array}{c}
\vdots \\
{}^{\prime}\mathbf{f}_t^{b} \\
f_c^{k} \\
f_c^{d} \\
\hline
\gamma^{b}
\end{array}\right\}
\tag{6.3}
$$

where $\mathbf{M}_{Gc}^{j} \equiv {}^{\prime}\Psi_c^{j\,\mathrm{T}}({}^{\prime}\mathbf{M}^{ub} + {}^{\prime}\mathbf{M}^{uu\,\prime}\mathbf{G})$ and $f_c^{j} \equiv {}^{\prime}\Psi_c^{j\,\mathrm{T}}(\mathbf{f}^{u} - {}^{\prime}\mathbf{M}^{u\prime}\mathbf{w}) - K_c^{j}z$; $j = k, d$. Eliminating $\ddot{z}^{d}$ from this equation does not effect the constraint equation. However, we do eliminate the term $\mathbf{M}_{Gc}^{d\,\mathrm{T}}\ddot{z}^{d}$ from the equation associated with the boundary node. The amount of error associated with this elimination is much smaller (almost negligible) compared to the elimination of $\mathbf{M}_3^{d\,\mathrm{T}}\ddot{z}^{d}$ from Eq. 6.2. This difference is due to the fact that in Eq. 6.2, δ^u is purely dependent on the modal coordinates. However, in Eq. 6.3, δ^u is a function of both δ^b and the modal coordinates (refer to Eq 4.19). Therefore, the truncation some of the modes from Eq. 6.3 is not as severe as it is in Eq. 6.2.

6.2.4. *Constrained Modes and Modal Condensation*

The transformation matrix of Eq. 4.23 can be substituted into Eq. 6.2 in order to express the deleted modes in terms of the boundary nodal deflections. Then the equations of motion associated with the boundary nodes are pre-multiplied by Θ^{T}, and the equations associated with the deleted modes are removed to obtain

$$
\left[\begin{array}{cccc|c}
\cdots & \mathbf{M}_{m1}\hat{\mathbf{I}} & -\mathbf{M}_{m1}\hat{\tilde{\mathbf{b}}} & \mathbf{M}_4 & \mathbf{M}_{m3}^{k\,\mathrm{T}} & -\Theta^{\mathrm{T}}\mathbf{A}^{\mathrm{T}} \\
\cdots & \mathbf{M}_2^{k}\hat{\mathbf{I}} & -\mathbf{M}_2^{k}\hat{\tilde{\mathbf{b}}} & \mathbf{M}_3^{k} & M_c^{k} & 0 \\
\hline
\cdots & -\mathbf{I} & \tilde{\mathbf{b}}^{b} & -\mathbf{A} & 0 & 0
\end{array}\right]
\left\{\begin{array}{c}
\vdots \\
{}^{\prime}\ddot{\delta}^{b} \\
\ddot{z}^{k} \\
\hline
\lambda
\end{array}\right\}
=
\left\{\begin{array}{c}
\vdots \\
\Theta^{\mathrm{T}}\,{}^{\prime}\mathbf{f}_t^{b} \\
f_c^{k} \\
\hline
\gamma^{b}
\end{array}\right\}
\tag{6.4}
$$

where $\mathbf{M}_{m1} \equiv \Theta^{\mathrm{T}}\mathbf{M}_1$, $\mathbf{M}_4 \equiv \Theta^{\mathrm{T}}(\mathbf{M}^{bb} + \mathbf{M}_3^{d\,\mathrm{T}}\Theta)$, and $\mathbf{M}_{m3}^{k} \equiv \mathbf{M}_3^{k}\Theta$. Simulation with Eq. 6.4 provides the same results as those obtained from the truncated Eq. 6.3. The process that led us to Eq. 6.4 has restored some of the information associated with the deleted modes into the equations of motion. This is analogous to the restoration of information in Eq. 6.3 through the Guyan matrix. The main difference is that in Eq. 6.4 the information is restored in the modal space, whereas in Eq. 6.3 it is done in the nodal space.

7. Summary

The equations of motion for a simple rigid-flexible multibody system have been presented in this manuscript in a semi-abstract form. Nodal rotational degrees-of-freedom have been excluded in order to simplify the appearance of the equations. Mean-axis conditions have been used to attach a reference frame to the deformable body. Several model reduction techniques in nodal and modal spaces have been reviewed.

The model reduction in nodal space is very simple to implement. However, the mass and stiffness matrices that are obtained from a static condensation may cause numerical instability. It is recommended that, if possible, smaller matrices to be obtained directly from a courser finite element mesh rather than through a static condensation process.

Model reduction in modal space, either from a free-free or a constrained structure, without any compensation terms (such as in Eqs. 6.1 or 6.2) is not recommended. These

processes yield either severe constraint violation with inaccurate results, or no violation and still unacceptable results. In contrast, when compensation terms are incorporated in the condensation process (such as in Eqs. 6.3 and 6.4), not only there will be no constraint violation, also reasonably accurate results should be expected. The accuracy of the results, however, is proportional to the degree of mode truncation. Several variations of these compensation terms can be found in published literature.

8. References

1. Agrawal, O.P. and Shabana, A.A. (1986) Application of Deformable-Body Mean Axis to Flexible Multibody System Dynamics, *Computer methods in Applied Mechanics and Engineering* **56**, 217-245.

2. Guyan, R.J. (1965) Reduction of Stiffness and Mass Matrices, *AIAA Journal*, Vol. **3**, No. 2, 380.

3. Hurty, W.C. (1965) Dynamic Analysis of Structural Systems Using Component Modes, *AIAA Journal*, Vol. **3**, No. 4, 678-685.

4. Craig, R.Jr.R. and Bampton, M.C.C. (1968) Coupling of Substructures for Dynamic Analyses, *AIAA Journal*, Vol. **6**, No. 7, 1313-1319.

5. Nikravesh, P.E. (1998) Model reduction with mode condensation, Unpublished class notes, University of Arizona.

6. Nikravesh, P.E. (1988) *Computer-Aided Analysis of Mechanical Systems*, Prentice-Hall.

NUMERICAL SIMULATION OF FLEXIBLE MULTIBODY SYSTEMS BY USING A VIRTUAL RIGID BODY MODEL

M. PASCAL, T. GAGARINA, Laboratoire CEMIF SC,
Université d'Evry Val d'Essonne, 91020, EVRY,FRANCE

1.Introduction

In the past decade, interest in multibody system dynamics has grown, leading to several computer codes [1] available for the generation of the motion equations. If in the beginning, only multibody systems with rigid components [2] were considered, weight minimization and large accelerations in many technical problems lead to an increasing tendancy for elastic vibrations. In recent years, many works [3] deal with the dynamical simulation of these systems in which each flexible component undergoes large rigid body motion but small elastic deformations. It results that the motion equations of the whole system involve ordinary differential equations coupled with partial differential equations. Approximated methods are used in which the displacement field of each flexible component is discretized by a Rayleigh-Ritz method leading to a new system with a finite number of degrees of freedom.
The aims of this work is to show that it is possible to use any existing rigid body codes for the dynamical simulation of elastic multibody systems provided that these codes are based on variational methods like Lagrange's equations or direct applications of d'Alembert principle. A first attempt for this possibility was made in [4] for planar interconnected flexible beams. In the present work, three dimensional interconnected flexible bodies are considered and the method used to identify the approximated model of the flexible multibody system with a fictitious rigid multibody system is rather different from the idea used in [4]. An example is shown, using the symbolic dynamical code AUTOLEV [5] devoted to rigid body simulation.

2. Problem Formulation

Let us consider a multibody system composed of several rigid or flexible bodies connected by p hinges. Each flexible component undergoes large rigid body motion coupled with small structural deformations.

174

Let us consider one flexible component (S) of the system and its fixed reference configuration (S_0) at $t = 0$. The assumption of large displacement and small strains lead to the standard method in which an intermediate configuration $(\widetilde{S})$ of the body is introduced : $(\widetilde{S})$ is deduced from the reference configuration (S_0) by means of a rigid transformation. For each material point M, we define the displacement field $\vec{u} = \overrightarrow{M'M}$ where M' is rigidly connected to $(\widetilde{S})$. The position of M with respect to an inertial reference frame $(O_0, \vec{x}_0, \vec{y}_0, \vec{z}_0)$ is given by :

$$\vec{r} = \vec{c} + \vec{x} + \vec{u} \qquad \vec{c}(t) = \overrightarrow{O_0 O}; \quad \vec{x} = \overrightarrow{OM'}; \quad \vec{u} = \vec{u}(\vec{x}, t)$$

O is the origin of a « floating reference frame » [6] $(O; \vec{x}, \vec{y}, \vec{z})$ rigidly connected to $(\widetilde{S}), \vec{\omega}$ is the angular velocity vector of the floating reference frame.

The kinetic energy of the flexible body (S) can be written as :

$$T = 1/2 \left[m \dot{\vec{c}}^2 + \vec{\omega}.\vec{\vec{J}}_0 \vec{\omega} + \int_S \dot{\vec{u}}^2 \, dm + 2 \dot{\vec{c}}.\int_S \dot{\vec{u}} \, dm \right.$$

$$\left. + 2 \vec{\omega}.\int_S (\vec{x} + \vec{u}) \wedge \dot{\vec{u}} \, dm + 2 \dot{\vec{c}}.\vec{\omega} \wedge \int_S (\vec{x} + \vec{u}) dm \right]$$

(1)

where $\vec{\vec{J}}_0 = \int_S \left[(\vec{x} + \vec{u})^2 \vec{\vec{E}} - (\vec{x} + \vec{u}) \otimes (\vec{x} + \vec{u}) \right] dm$ is the inertia tensor in point O of the body (S) in its deformed configuration. The displacement field $\vec{u}$ is approximated by a finite number of mode shapes :

$$\begin{cases} \vec{u} = \underline{\vec{N}}(\vec{x}) \underline{q}(t) \\ \underline{\vec{N}} = [\vec{N}_1, ..., \vec{N}_n] \quad \underline{q} = {}^t[q_1, ..., q_n] \end{cases}$$

(2)

It results for the kinetic energy the following approximated expression :

$$T = \frac{1}{2} \left[m \dot{\vec{c}}^2 + \vec{\omega}.\vec{\vec{J}}_0 \vec{\omega} + {}^t \dot{\underline{q}} \underline{\underline{M}} \dot{\underline{q}} + 2 \dot{\vec{c}}.\underline{\vec{\alpha}} \dot{\underline{q}} \right.$$

$$\left. + 2 \vec{\omega}.\underline{\vec{G}} \dot{\underline{q}} + 2 \dot{\vec{c}}.(\vec{\omega} \wedge m \vec{x}_0) + 2 \dot{\vec{c}}.\vec{\omega} \wedge \underline{\vec{\alpha}} \underline{q} + 2 \vec{\omega}. {}^t (\underline{\vec{H}} \underline{q}) \underline{q} \right]$$

(3)

with the following notations :

$$\begin{cases} \vec{J}_0 = \vec{I}_0 + {}^t\underline{q}\,\vec{\beta} + {}^t\vec{\beta}\,\underline{q} + {}^t\underline{q}\,\vec{\gamma}\,\underline{q} \\[2mm] \vec{\beta} = \int\limits_S \left[\left({}^t\underline{N}.\vec{x} \right)\vec{E} - {}^t\underline{N}\otimes\vec{x} \right]dm \\[2mm] \vec{\gamma} = \int\limits_S \left[\left({}^t\underline{N}.\underline{N} \right)\vec{E} - {}^t\underline{N}\otimes\underline{N} \right]dm \\[2mm] \vec{\underline{G}} = \int\limits_S \vec{x}\wedge\underline{N}\,dm \end{cases}$$

$$\begin{cases} \vec{\underline{H}} = \int\limits_S {}^t\underline{N}\wedge\underline{N}\,dm \\[2mm] \underline{M} = \int\limits_S {}^t\underline{N}.\underline{N}\,dm \\[2mm] \vec{\underline{\alpha}} = \int\limits_S \underline{N}\,dm \\[2mm] \vec{I}_0 = \int\limits_S \left(\vec{x}^2\,\vec{E} - \vec{x}\otimes\vec{x} \right)dm \\[2mm] m\,\vec{x}_0 = \int\limits_S \vec{x}\,dm \end{cases} \qquad (4)$$

Let us assume that the body is subjected to body forces $\vec{f}$ and surface forces $\vec{F}$ applied on the boundary ∂S of the body. For a virtual velocity field defined by

$$\vec{V}^*(M) = \dot{\vec{c}}^* + \vec{\omega}^*\wedge\left(\vec{x}+\vec{u}\right) + \dot{\vec{u}}^*$$

we obtain the corresponding virtual power of the applied forces :

$$\Im_1^* = \int\limits_S \vec{f}.\vec{V}^*(M)\,dv + \int\limits_{\partial S} \vec{F}.\vec{V}^*(M)\,d\sigma$$

Using the approximated value (2) of the displacement field, the following expression of $\Im_1^*$ is obtained :

$$\Im_1^* = \vec{R}.\dot{\vec{c}}^* + \left(\vec{M}_0 + \underline{B}\,\underline{q}\right)\vec{\omega}^* + \underline{D}\,\dot{\underline{q}}^* \qquad (5)$$

176

where

$$
\begin{cases}
\underline{\vec{R}} = \int_S \vec{f}\, dv + \int_{\partial S} \vec{F}\, d\sigma & ; & \vec{M}_0 = \int_S \vec{x} \wedge \vec{f}\, dv + \int_{\partial S} \vec{x} \wedge \vec{F}\, d\sigma \\[2mm]
\underline{D} = \int_S \vec{f}.\underline{\vec{N}}\, dv + \int_{\partial S} \vec{F}.\underline{\vec{N}}\, d\sigma & ; & \underline{\vec{B}} = \int_S \underline{\vec{N}} \wedge \vec{f}\, dv + \int_{\partial S} \underline{\vec{N}} \wedge \vec{F}\, d\sigma
\end{cases}
\tag{6}
$$

Assuming linear constitutive laws, the elastic potential energy is approximated by $V_e = 1/2\ ^t\underline{q}\,\underline{K}\,\underline{q}$, where $\underline{K} = \left(K_{ij}\right)$ is the n x n constant stiffness matrix.

3. Rigid body model

The rigid body model $\left(\Sigma_R\right)$ is composed of a rigid body $\left(S_R\right)$ rigidly connected to the floating reference frame $\left(O; \vec{x}, \vec{y}, \vec{z}\right)$ and a total number of 3n materials points M_i of mass m_i defined by $\overrightarrow{OM_i} = \overrightarrow{X_i} + \overrightarrow{\underline{A}_i}\,\underline{q}$ (i = 1,2,...,3n). In this formula, $\vec{X}_i$ is a vector fixed with respect to the floating reference frame while $\underline{\vec{A}}_i$ is a 1 x n matrix of whose the columns are vectors fixed with respect to the same reference frame. The absolute velocity of the material point M_i is given by $\vec{V}\left(M_i\right) = \dot{\vec{c}} + \vec{\omega} \wedge \overrightarrow{OM_i} + \underline{\vec{A}}_i\,\underline{\dot{q}}$

It results for the system $\left(\Sigma_R\right)$ the following expression of the kinetic energy

$$
\begin{cases}
2\widetilde{T} = \left(m_0 + \displaystyle\sum_{i=1}^{3n} m_i\right)\dot{\vec{c}}^2 + \vec{\omega}.\left(\widetilde{K}_0 + \displaystyle\sum_{i=1}^{3n} \widetilde{J}_i\right)\vec{\omega} + 2\dot{\vec{c}}.\left(\vec{\omega} \wedge m_0\,\vec{y}_0\right) + \\[4mm]
\displaystyle\sum_{i=1}^{3n}\left(\underline{\vec{A}}_i\,\underline{\dot{q}}\right)\left(\underline{\vec{A}}_i\,\underline{\dot{q}}\right) \\[4mm]
+ 2\dot{\vec{c}}.\vec{\omega} \wedge \displaystyle\sum_{i=1}^{3n}\left(\vec{X}_i + \underline{\vec{A}}_i\,\underline{\dot{q}}\right) + 2\dot{\vec{c}}.\displaystyle\sum_{i=1}^{3n}\underline{\vec{A}}_i\,\underline{\dot{q}} + 2\,\vec{\omega}.\displaystyle\sum_{i=1}^{3n}\left[\left(\vec{X}_i + \underline{\vec{A}}_i\,\underline{\dot{q}}\right) \wedge \underline{\vec{A}}_i\,\underline{\dot{q}}\right]
\end{cases}
\tag{7}
$$

where m_0 and $\widetilde{K}_0$ are the mass and the inertia tensor in point O of the rigid body $\left(S_R\right)$ and $m_0\,\vec{y}_0 = \int_{S_R} \vec{x}\, dm$ defines the position of the center of mass of (S_R) with respect to point O.
At last

$$
\widetilde{J}_i = m_i\left[\left(\vec{X}_i + \underline{\vec{A}}_i\underline{q}\right)^2 \vec{E} - \left(\vec{X}_i + \underline{\vec{A}}_i\underline{q}\right)^2 \otimes \left(\vec{X}_i + \underline{\vec{A}}_i\underline{q}\right)\right] \qquad (i = 1,2,...3n)
\tag{8}
$$

By identification of the kinetic energy of $\left(\Sigma_R\right)$ with the expression (3) of the kinetic energy of the flexible component (S), we obtain the following equations :

177

$$\int_S \underline{\vec{N}}\, dm = \sum_{i=1}^{3n} m_i\, \underline{\vec{A}}_i \qquad (9)$$

$$\int_S \underline{\vec{N}} \otimes \vec{x}\, dm = \sum_{i=1}^{3n} m_i\, \underline{\vec{A}}_i \otimes \vec{X}_i \qquad (10)$$

$$\int_S {}^t \underline{\vec{N}} \otimes \underline{\vec{N}}\, dm = \sum_{i=1}^{3n} m_i\, {}^t\underline{\vec{A}}_i \otimes \underline{\vec{A}}_i \qquad (11)$$

In order to make the identification for the applied and elastic forces of the real system, let us assume that for the rigid body model, the applied forces on the part (S_R) is composed of a resultant force $\vec{\phi}$ and a resultant torque $\vec{\Gamma}_O$ applied in point O while each point M_i is submitted the force:

$$\vec{F}_i = \lambda_i\, \vec{X}_i - \underline{\vec{A}}_i\, \underline{q}, \; (\lambda_1,...,\lambda_n) \text{ are constants}$$

The virtual power of the applied forces for the rigid body model (Σ_R) is given by

$$\Im_2{}^* = \dot{\vec{c}}{}^* \cdot \left(\vec{\phi} + \sum_{i=1}^{3n} \vec{F}_i \right) + \vec{\omega}^* \cdot \left(\vec{\Gamma}_0 + \sum_{i=1}^{3n} \overrightarrow{OM_i} \wedge \vec{F}_i \right) +$$

$$\sum_{i=1}^{3n} \left(\lambda_i\, \vec{X}_i - \underline{\vec{A}}_i\, \underline{q} \right) \underline{\vec{A}}_i\, \underline{\dot{q}}{}^*$$

By identification with the virtual power of the applied and elastic forces of the real system :

$$\Im_2{}^* = \Im_1{}^* - {}^t\underline{q}\, \underline{K}\, \underline{\dot{q}}{}^*$$

we obtain the following relations :

$$\vec{R} = \vec{\phi} + \sum_{i=1}^{3n} \vec{F}_i = \vec{\phi} + \sum_{i=1}^{3n} \left(\lambda_i\, \vec{X}_i - \underline{\vec{A}}_i\, \underline{q} \right) \qquad (12)$$

$$\vec{M}_0 + \underline{\vec{B}}\, \underline{q} = \vec{\Gamma}_0 + \sum_{i=1}^{3n} \overrightarrow{OM_i} \wedge \vec{F}_i = \vec{\Gamma}_0 + \sum_{i=1}^{3n} \left(\underline{\vec{A}}_i\, \underline{q} \wedge (\lambda_i + 1)\vec{X}_i \right) \qquad (13)$$

$$\underline{D} = \sum_{i=1}^{3n} \lambda_i\, \vec{X}_i \cdot \underline{\vec{A}}_i \qquad (14)$$

$$\underline{K} = \sum_{i=1}^{3n} {}^t\underline{\vec{A}}_i \cdot \underline{\vec{A}}_i \qquad (15)$$

The two first equations (12) and (13) define the resultant force $\vec{\phi}$ and the resultant torque $\vec{\Gamma}_0$ applied on (S_R) when $\lambda_i, \vec{X}_i, \underline{\vec{A}}_i$ are known.

We conclude that to obtain a rigid body model of the flexible component we have to solve with respect to the unknown quantities $\left(m_i, \underline{\vec{A}}_i, \vec{X}_i, \lambda_i\right)$ the equations (9), (10), (11), (14) and (15).
The total number of unknown variables is

$$X = 3n + 9n^2 + 9n + 3n = 9n^2 + 15n.$$

The total number of equations to be fullfilled is :

$$E = 3n + 9n + 3n\frac{(3n+1)}{2} + n + n\frac{(n+1)}{2} = 5n^2 + 15n$$

It results that the number of unknown variables being greater than the number of equations, founding a rigid body model is always possible and there are several solutions.

4. Conclusions

In this paper, we have shown that it is possible to use any dynamical codes devoted to rigid multibody systems in which the motion equations are obtained from d'Alembert principle for the simulation of flexible multibody systems in which the flexible components are discretized by a Rayleigh-Ritz procedure. Three dimensional elastic components are considered and not only elastic beams as in [4]. The method is based on the identification of the kinetic energy, potential energy and virtual work of the applied forces for the real system and a fictitious rigid multibody system. The main interest of this result is the possibility of using symbolic dynamical codes mainly available for rigid multibody systems for the dynamical simulation of flexible multibody systems Several simulations tests are done using the symbolic code AUTOLEV showing the efficiency of the method.

5. References

1. SCHIEHLEN, W. (1990) *Multibody Systems Handbook*, Springer-Verlag, Berlin.
2. WITTENBURG, J. (1977) *Dynamics of Systems of Rigid Bodies*, Teubner, Stuttgart.
3. SHABANA, A.A. (1989) *Dynamics of Multibody Systems*, Wiley, Chichester.
4. BOTZ, M. and HAGEDORN, P. (1990) Multiple Body Systems with Flexible Members, *Nonlinear Dynamics*. **1**, 433-447.
5. SCHAECHTER, D.B. and LEVINSON, D.A., KANE,T.R. (1988) *Autolev User's Manual*. On Line Dynamics, Inc. Sunnyvale.
6. PASCAL, M. (1995) Nonlinear Effects in Transient Dynamic Analysis of Flexible Multibody Systems, Proceedings of the 1995 ASME Design Eng. Techn. Conf., Boston, Massachussets, Sept. 17-20, **3**, part A, 75-86.

A NOVEL ROLLER-CHAIN DRIVE MODEL
USING MULTIBODY DYNAMICS ANALYSIS TOOLS

SINE L. PEDERSEN AND JOHN M. HANSEN
Department of Mechanical Engineering, Solid Mechanics
Technical University of Denmark,
Nils Koppels Allé, Bygn. 404, DK-2800 Kgs. Lyngby, Denmark
e-mail: slp@mek.dtu.dk and jmh@mek.dtu.dk

JORGE A.C. AMBRÓSIO
IDMEC / Instituto Superior Técnico
Av.Rovisco Pais, 1049-001 Lisboa, Portugal
e-mail: jorge@dem.ist.utl.pt

1 Introduction

A novel methodology for the analysis of roller chain drives is developed and implemented in a computer code in order to study the dynamics of a roller-chain drive, which includes the chain flexibility, its transversal and longitudinal vibrations and meshing contact/impact models. The main components of the roller chain drives include fixed or moving sprockets and the chain made of rollers and links, which are modeled as rigid bodies, mass particles and springs–damper assemblies respectively. The models proposed represent effectively the polygonal effect, always present in this type of drives, and therefore, all vibrational dynamics associated to it.

Two contact/impact methods are proposed to describe the contact between the rollers of the chain and the teeth of the sprockets. These formulations are based on the use of unilateral constraints and a continuous force method, respectively. In the unilateral constraint method the kinematic constraints are introduced in the system anytime a contact between the rollers and the sprockets is detected. The condition for the constraint addition is based on the relative distance between the roller center and the sprocket center, i.e. a constraint is added when such distance is less than the pitch radius. The unilateral kinematic constraint is removed when the constraint reaction force associated with it is pulling it away from the sprocket. In order to improve the numerical efficiency of the methodology only the first and last roller seated on each sprocket and the two free rollers nearest to the sprocket are checked for capture or release.

In the continuous force method the contact is represented by forces applied on each seated roller and in the respective sprocket teeth, which are functions of the pseudo penetrations between roller and sprocket, impacting velocities and a restitution coefficient. In this method the geometry of the tooth profile is represented in order to allow for a correct representation of the tangential forces.

The two methods are demonstrated through examples of application to roller-chain drives that include sprockets with different sizes. Finally the proposed methodology is applied to the simulation and analysis of the roller-chain drive of a large marine diesel engine. Moreover, the application model includes a chain tightener and off-center sprockets, used in second-order compensators to cancel the vibrations induced by the main engine.

2 Roller-Chain Models With Unilateral Constraints

A typical roller-chain drive in a marine diesel engine is composed of one chain that wraps around two or more sprockets. The roller-chain is somewhat similar to a bicycle chain in the way it looks. For the purpose of the study presented here, the mass of the chain, is assumed to be lumped at the roller locations. Translational springs and dampers with constant stiffness and damping coefficients model the links. In this model the rotational inertia of the rollers about their center of gravity is neglected.

The tooth flexibility of the sprocket is neglected in this model, i.e. the sprocket is considered to be a rigid body. The roller-chain wraps around the sprocket forcing the rollers to seat between the teeth at a distance from the center of the sprocket equal to the radius of the pitch circle. In this study it is assumed that during engagement the chain pitch equals the sprocket pitch. Effects like chain wear and the pitch elongation during engagement are neglected.
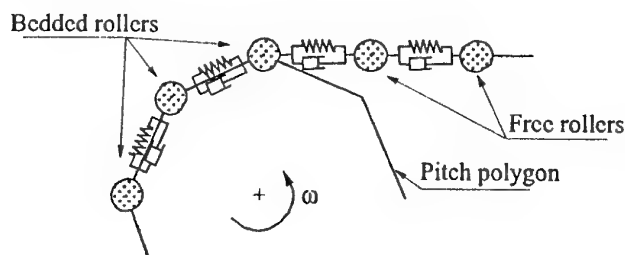
Figure 1. Numerical representation of the roller engagement with the sprocket

2.1. EQUATIONS OF MOTION FOR THE ROLLER-CHAIN DRIVE

The rollers that are not seated in the sprockets constitute a particle system free in space. Their equations of motion are

$$m_r \mathbf{I} \ \ddot{\mathbf{q}}_r = \mathbf{f}_r \tag{1}$$

where $\mathbf{I}$ is the unit matrix, m_r is the mass of the links and $\ddot{\mathbf{q}}_r$ is the translational accelerations of the rollers. The right hand side $\mathbf{f}_r$ is the vector with the forces acting on the individual chain links due to the links flexibility.

For a sprocket having an external applied force $\mathbf{f}_s$ the equations of motions are given in equation (2). The external forces are made up from the forces with which the chain affect the sprocket and from optional directly applied forces.

$$\mathbf{M}_S \ \ddot{\mathbf{q}}_S = \mathbf{f}_S \tag{2}$$

181

where the matrix $\mathbf{M}_s$ contains the mass and polar moment of inertia of the sprocket, the vector $\ddot{\mathbf{q}}_s$ contains the acceleration of the sprocket in the x- and y-direction and the angular acceleration, thus rotational inertia for the sprocket is taken into account.

In the constraint method the rollers that are seated on the sprockets are treated as constrained bodies. For the bedded rollers on a sprocket, constraint equations that force the rollers to be seated on the pitch circle at the bottom of the tooth profile are defined. Differentiating these equations twice with respect to time, and using the Lagrange multiplier technique [3], leads to a set of equations of motion for sprocket number s and for the rollers in contact with it is written as

$$
\begin{bmatrix}
\mathbf{M}_S & 0 & \mathbf{S}^T \\
0 & m_r\mathbf{I} & \mathbf{I} \\
\mathbf{S} & \mathbf{I} & 0
\end{bmatrix}
\begin{Bmatrix}
\ddot{\mathbf{q}}_S \\
\ddot{\mathbf{q}}_r \\
\lambda
\end{Bmatrix}
= -
\begin{Bmatrix}
\mathbf{g}_S \\
\mathbf{f}_r \\
\gamma_S
\end{Bmatrix}
\tag{3}
$$

where λ is the vector Lagrange multipliers, γ_s is the right hand side from the acceleration of the constraint equations and the matrix [S I] is the Jacobian matrix. One of the attractive features of this formulation is that the forces developed during the engagement process of the rollers in the sprockets are always available.

A roller is captured onto a sprocket if the distance between the center of the roller and the center of the sprocket is less than the radius of the pitch circle. A roller can leave a sprocket and become part of the "free" chain segment again if the reaction force between the sprocket and the roller changes from a pushing force to a pulling force. For further details see [1].
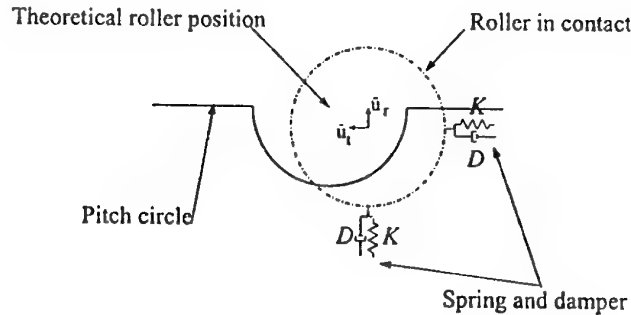
Figure 2. The indentation contact between a roller and a sprocket

2 Force Model of The Roller-Sprocket Engagement

An alternative procedure to describe the capture of the roller by a sprocket is to use a non-linear force contact model that takes into account the impact that occurs during engagement. Based on the Hertzian contact theory several models have been proposed which take into account the energy dissipation due to heat, noise, vibrations or localized deformations. Lankarani and Nikravesh [2] proposed an impact-contact model that besides providing an accurate description of the physical phenomena is numerically stable, leading to an efficient computer implementation. The contact model proposed

182

here to describe the roller-sprocket engagement is based on the model by Lankarani and Nikravesh and it takes into account the specificity of the roller-chain dynamics.

2.1. THE CONTACT-IMPACT FORCE MODEL

For a roller-chain drive, with equal chain and sprocket pitch, the capture of a roller by the sprocket is instantaneous, i.e., the roller will seat at the low part of the tooth profile, without rolling into it from some neighboring position. This is seldom the case in a normal chain-roller drive due to the wear of the chain or because the links are not rigid and elongate as a result of the dynamic loading. In the numerical model now presented for the contact a pseudo-penetration of a roller in a tooth profile is determined and in turn gives raise to contact forces that tend to balance the remaining forces over the bedded roller.

All the rollers are 'free' in this model and the contact forces are added to the right hand side of equations (1) and (2). Let the contact force between the roller i and the sprocket s be a function of the pseudo penetration and pseudo velocity of penetration given by [2]

$$f_{s,i} = \left(K\,\delta_r^n + D\,\dot{\delta}_r \right)\mathbf{u}_r + \left(K\,\delta_t^n + D\,\dot{\delta}_t \right)\mathbf{u}_t\,, \text{ with } D = \frac{3K\left(1-e^2\right)}{4\dot{\delta}^{(-)}}\delta^n \qquad (4)$$

where D is a damping coefficient and K is a generalized stiffness coefficient that depends on the geometry of the surfaces in contact and their material properties and the exponent n is set to 1.5 for metallic surfaces, see figure (2). The components of the pseudo penetration δ in the radial and tangential direction are respectively $\delta_r = \mathbf{u}_r^T\delta$ and $\delta_t = \mathbf{u}_t^T\delta$, where $\mathbf{u}_r$ and $\mathbf{u}_t$ are unit vectors in the radial and tangential directions respectively that pass by the theoretical position of the roller center in its bedded position. The pseudo penetration velocity components are $\dot{\delta}_r$ and $\dot{\delta}_t$. The damping coefficient D introduces the hysteresis form of the energy dissipation, which depends on the restitution coefficient (e=1 for a fully elastic contact and e=0 for a fully plastic contact), on the relative approach velocity between the roller and sprocket, on the generalized stiffness coefficient and on the exponent n.

If the position of the actual roller center is between the pitch and the outer diameter of the sprocket there is a potential for pseudo-penetration in the tooth. The contact with the tooth profile is modeled as in equation (4) and it is assumed sufficient to consider the profile of the tooth to be approximately linear. For further details see [1].

3 Model of Chain tighteners in the force model

While the engine is running the roller chain wears and consequently extends. Therefore, the chain has to be tightened frequently as it gradually extends, in order to keep its functionality. To this purpose one of the driven sprockets is located in a chain tightener system. This sprocket center can move from its initial position and then tighten the chain. To avoid the manual tightenings of the chain automatic chain tighteners have been introduced on some engines. This has caused undesirable vibration patterns of the chain and chain tightener that were not immediately explainable.

183

The sprocket that is in the chain tightener translates and its movement depends on the movement of the other elements in the chain tightener system. The chain tightener system has been included in the force model. This is done by introducing kinematic constraints between the sprocket and the other bodies (e.g. weight-arm) in the tightener system and for the chain tightener with a hydraulic damper this is modeled as a spring-damper.

The constraint equations are set up for the chain tightener system including revolute joint constraint and translational joint constraints [3]. These constraint equations are differentiated twice with respect to time, and using the Lagrange multiplier technique as in equation (3) the total set of equations for the sprocket in the chain tightener system is written as

$$
\begin{bmatrix} \mathbf{M}_S & 0 & \mathbf{J}_S^T \\ 0 & \mathbf{M}_B & \mathbf{J}_B \\ \mathbf{J}_S & \mathbf{J}_B & 0 \end{bmatrix} \begin{Bmatrix} \ddot{\mathbf{q}}_S \\ \ddot{\mathbf{q}}_B \\ \lambda \end{Bmatrix} = - \begin{Bmatrix} \mathbf{g}_S \\ \mathbf{f}_B \\ \gamma_t \end{Bmatrix}
$$

(5)

where $\mathbf{M}_B$ is the mass and inertia of the other bodies in the chain tightener system, $\ddot{\mathbf{q}}_B$ is the accelerations of the bodies, $\mathbf{f}_B$ is the forces on the bodies, γ_t is the right hand side from the acceleration of the constraint equations and $[\mathbf{J}_S\ \mathbf{J}_B]$ is the Jacobian matrix.

4 Application to A Roller-Chain Drive

The total methodology is applied to the simulation of a two-stroke diesel marine engine roller-chain drive. The drive is standard in the engines that have between 4 and 12 cylinders for a power range of 1760 to 7800 KW. The roller-chain drive, composed of four sprockets and a chain made of 122 links, transmits the motion of the crankshaft to the camshaft. Each link of the chain, with a pitch of 0.0889 m and a mass of 3.01 Kg, is modeled as a flexible element with a stiffness of 640 MN/m, according to the experimental data obtained from the manufacturer.
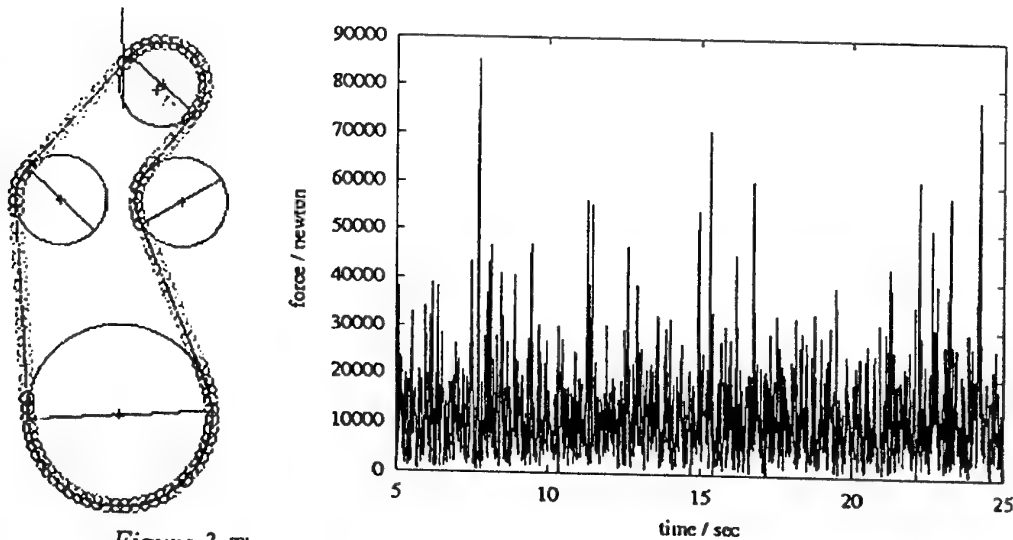
Figure 3. The computer model and The link forces between consecutive links.

The top sprocket, in figure 3, is connected to a weight-arm, which in turn is connected with a hydraulic damper. These elements together form the chain tightener system. The sprocket is connected to the weight-arm with a revolute joint and the weight-arm is connected to the ground through a revolute joint and a spring-damper.

The methodology proposed here is implemented in a computer code and applied to the roller-chain drive described. The model is simulated during a time period of 25 second being accelerated from rest to a constant angular velocity during 2 seconds. The results of the simulations are summarized by the force on a reference link shown in figure (3).

5 Conclusions

New formulations for the simulation of the dynamics of roller-chain drives are described in this work. With these methods it is possible to perform a dynamic simulation of the roller-chain/sprocket system, including the polygonal effect, which appears when the individual chain links engages and disengages the sprockets, the roller impact at engagement, the flexibility of the links and the coupling between axial and transverse vibrations. Moreover, the formulation allows for the introduction off-center sprockets in the roller-chain drives, which are sources of extra excitations on the drive.

The application to the roller-chain drive to a large marine engine demonstrates the level of modeling that is possible to achieve with the purposed formulation. The variation of the link forces exemplifies the type of results necessary for the design of the roller-chain drives in terms of fatigue and wear.

The constraint method does, however, not include clearance between pin and bushing, the rotational inertia of the link elements, tooth flexibility, and the actual shape of the teeth. The continuous force method allows the modeling of the referred effects by tuning up the coefficients of contact law. The results show a very high sensitivity of the results on the chain stiffness, actually suggesting that a more in-depth investigation of the material behavior of the chain and sprocket is required. Further results of the application of both methodologies described are necessary in order to compare their relative merits and their sensitivity to the initial data set of the roller-chain drive.

Acknowledgements

References

1   Ambrósio, J.A., Hansen, J.M and Pedersen, S.L., A Contact Model for the Roller and Sprocket Engagement in Roller-Chain Drives, *2nd European Conference on Computational Mechanics Solids, Structures and Coupled Problems in Engineering*, Institute of Computer Methods in Civil Engineering, Cracow University of Technology, Cracow, Poland, 492-493 (+ 16 p. on CD) (2001)

2   H.M. Lankarani, P.E. Nikravesh, Continuous Contact Force Models for Impact Analysis in Multibody Systems, *Nonlinear Dynamics*, 5, 193-207 (1994).

3   Nikravesh, P.E., *Computer-Aided Analysis of Mechanical Systems*, Prentice-Hall, Englewood-Cliffs, New Jersey (1988)

OPTIMIZATION OF RIGID-FLEXIBLE MULTIBODY SYSTEMS WITH APPLICATION TO VEHICLE DYNAMICS AND CRASHWORTHINESS

M. S. Pereira and J. P. Dias
IDMEC - Instituto de Mecânica - Polo IST
Instituto Superior Técnico.
Lisbon, Portugal.

Abstract

The optimal design of vehicle structures is usually carried out using finite elements programs. However, the design tools for multibody systems can be an alternative to the finite elements tools, especially in the first stages of the project and when crashworthiness and dynamics requirements are to be included.
In this paper a framework for the dynamics, sensitivity analysis and optimization of multibody systems are presented.
The formulation for the dynamic analysis is based in a moving frame approach to describe the kinematics of the deformable bodies where the large rigid motion is described using Cartesian coordinates and the flexibility is introduced using the finite element method.
Analytic sensitivities obtained by the direct differentiation method and finite differences sensitivities are used in the optimization process. The optimization process includes constrained, multicriteria and multiload optimization methodologies.
The framework for the design of rigid-flexible multibody systems is applied to a group of applications, including the design of train structures in crashworthiness, design of automotive chassis using dynamic loads and other mechanisms related with vehicles.

1. Introduction

The design of vehicle structures is usually carried out using finite elements programs. In order to optimize parameters or characteristics of the vehicle for crashworthiness, finite elements programs, such as LS-DYNA or PAM-CRASH, leads to several drawbacks: the time necessary to develop the models is large and in general these programs do not include optimization procedures.
In the first stages of the design project, when the detailed characteristics of the structure are not yet known, simplified models that allows simulation and optimization can be used with success. Alternative design tools based on multibody dynamics formulations can be used. The design of vehicle structures for crashworthiness and the elastic design of vehicle chassis under dynamic loads are two of these scenarios.
Different design tools can be created in order to achieve different design goals, during the product development. Train crashworthiness is one of the industrial applications where this design framework can be applied. Uni-dimensional rigid models can be used for the analysis of the energy distribution along the train during a collision, as also to evaluate overall deformations, forces and accelerations. The 1D design models can be used to optimize the

characteristics of the energy absorption devices. Two-dimensional models (rigid or flexible) can be used to analyze the structural behavior of the end-underframe of the train cars or the overlapping phenomena and to the optimal design of the structural elements. Three-dimensional models can be used for detailed analysis and design of the structures and to study the entire car shells as also to design the structural elements. In all these models optimal design plays an important role, so the sensitivity analysis and the optimization of multibody systems are important topics in the development of these tools.

Optimal design is currently a topic of intensive research in the field of multibody systems [1]. During the last two decades the multibody dynamics formulations have been developed, being now several commercial codes for the analysis of such systems. However there is still a lack in the development of optimal design tools especially for flexible systems.

In this work, formulations and methodologies for the analysis and optimal design of flexible multibody systems are presented within the framework of multibody dynamics, sensitivity analysis and optimization. This framework is presented in figure *1*.
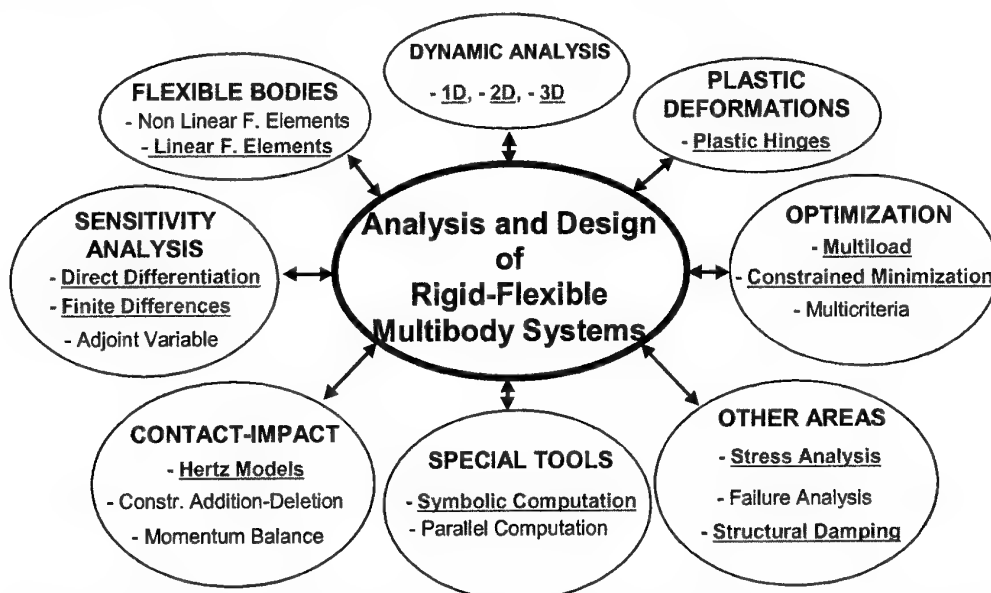
Figure 1. Framework for the optimal design of rigid-flexible multibody systems

Multibody dynamics formulations are developed using a moving frame approach to describe the kinematics of the deformable bodies. The large rigid motion is described using Cartesian coordinates and the flexibility is introduced using the finite element method. To reduce the number of elastic degrees of freedom, the component mode synthesis is used. The mean axis condition method is applied to the reference conditions to reduce the dynamic coupling between rigid and flexible coordinates.

For the optimization procedure the multibody dynamics code is linked with general optimization algorithms included in the package DOT/DOC. The optimization procedure requires the sensitivities of the objective function and design constraints. For this purpose, numerical sensitivities using the finite difference method and analytic sensitivities from the direct differentiation method are used.

The framework for the design of rigid-flexible multibody systems is applied to a group of applications, including the design of train structures in crashworthiness, design of automotive chassis using dynamic loads and other mechanisms related with vehicles.

187

2. Dynamic Analysis

The equations of motion for a rigid-flexible multibody system, written in terms of modal coordinates, are briefly written as [2]

$$\begin{bmatrix} \overline{\mathbf{M}}_{rr} & \overline{\mathbf{M}}_{rf} & \overline{\mathbf{\Phi}}_{\mathbf{q}_r}^{\mathrm{T}} \\ \overline{\mathbf{M}}_{fr} & \overline{\mathbf{M}}_{ff} & \overline{\mathbf{\Phi}}_{\mathbf{p}_f}^{\mathrm{T}} \\ \overline{\mathbf{\Phi}}_{\mathbf{q}_r} & \overline{\mathbf{\Phi}}_{\mathbf{p}_f} & 0 \end{bmatrix} \begin{Bmatrix} \ddot{\mathbf{q}}_r \\ \ddot{\mathbf{p}}_f \\ \lambda \end{Bmatrix} = \begin{Bmatrix} \overline{\mathbf{f}}_r + \overline{\mathbf{g}}_r \\ \overline{\mathbf{f}}_f + \overline{\mathbf{g}}_f - \overline{\mathbf{K}}_{ff}\mathbf{p}_f - \overline{\mathbf{C}}_{ff}\dot{\mathbf{p}}_f \\ \overline{\gamma} \end{Bmatrix} \qquad (1)$$

Where $\mathbf{M}_{rr}$ contains the rigid body inertia $\mathbf{M}_{ff}$ is the standard finite element mass matrix, $\mathbf{M}_{rf}$ is the inertia coupling between rigid and flexible coordinates, λ is the Lagrange multiplier vector, $\mathbf{f}_r$ and $\mathbf{f}_f$ are the generalized external forces, $\mathbf{g}_r$ and $\mathbf{g}_f$ are the quadratic forces including gyroscopic, Coriolis forces and other terms associated with kinetic energy. The coupling between elastic deformation and rigid body motion is represented by the term $\mathbf{K}_{ff}\mathbf{q}_f$ in the right-hand side of equation. $\mathbf{C}_{ff}$ is the damping matrix and $\mathbf{\Phi}_{\mathbf{q}_r}^{\mathrm{T}}, \mathbf{\Phi}_{\mathbf{q}_f}^{\mathrm{T}}$ are the Jacobian terms associated to the rigid and flexible coordinates respectively. Equation (1) with the initial conditions

$$\left\{ \mathbf{q}_r(t^0) = \mathbf{q}_r^0 \ , \ \mathbf{p}_f(t^0) = \mathbf{p}_f^0 \ , \dot{\mathbf{q}}_r(t^0) = \dot{\mathbf{q}}_r^0 \ , \ \dot{\mathbf{p}}_f(t^0) = \dot{\mathbf{p}}_f^0 \right\} \qquad (2)$$

can be integrated in time to obtain all the state variables of the system, i. e. positions, velocities, accelerations and Lagrange multipliers.

The dynamic analysis tools developed include several features necessary to solve specific problems specially related with crashworthiness such as, local plastic hinges models, dynamic stress analysis and Hertz contact-impact models.

3. Sensitivity Analysis

The analytic sensitivity equations, obtained using the direct differentiation method are here summarily presented in the modal form. The sensitivity equations can be written in a compact form matrix form identical to the equations of motion, as [2]

$$\begin{bmatrix} \overline{\mathbf{M}}_{rr} & \overline{\mathbf{M}}_{rf} & \overline{\mathbf{\Phi}}_{\mathbf{q}_r}^{\mathrm{T}} \\ \overline{\mathbf{M}}_{fr} & \overline{\mathbf{M}}_{ff} & \overline{\mathbf{\Phi}}_{\mathbf{p}_f}^{\mathrm{T}} \\ \overline{\mathbf{\Phi}}_{\mathbf{q}_r} & \overline{\mathbf{\Phi}}_{\mathbf{p}_f} & 0 \end{bmatrix} \begin{bmatrix} \ddot{\mathbf{q}}_{r_b} \\ \ddot{\mathbf{p}}_{f_b} \\ \lambda_b \end{bmatrix} = \begin{bmatrix} \overline{\mathbf{R}} \\ \overline{\mathbf{F}} \\ \overline{\gamma}_b \end{bmatrix} \qquad (3)$$

Equation (3) can be integrated in time provided the initial conditions

$$\left\{ \mathbf{q}_{r_b}(t^0) = \mathbf{q}_b^0, \ \mathbf{p}_{f_b}(t^0) = \mathbf{p}_{f_b}^0, \ \dot{\mathbf{q}}_{r_b}(t^0) = \dot{\mathbf{q}}_b^0, \ \dot{\mathbf{p}}_{f_b}(t^0) = \dot{\mathbf{p}}_{f_b}^0 \right\} \qquad (4)$$

The modal sensitivities are then transformed to nodal or physical sensitivities. Either an updated-mode approach, where a Nelson's scheme is used to evaluate the derivatives of the vibration modes, or a fixed-modes approach, where the derivatives of vibration modes are neglected, are considered.

Different types of design variables related to flexible elements such as area of the sections, Young Modulus, moment of inertia, and design variables involving element actuators and kinematic constraints may be considered.

The calculation of the terms in the right-hand side of sensitivity equations (3) represents the major computational effort. The symbolic computation program MAPLE is used to obtain these terms for a given set of design variables. For the differentiation of the finite element matrices, an exact method is used once the analytical expressions for the mass, stiffness and other matrices involving the flexible terms, are given in closed form for specific finite elements.

As in the case of rigid body sensitivities, the left-hand side of the dynamic and sensitivity equations is the same. Both equations are integrated simultaneously in time.

4. Examples

In this section, three application examples of the framework for the analysis and design of rigid-flexible multibody systems are presented. These examples correspond to the application of the increasing complexity design tools. 1D tools for train collisions, 2D tools for mechanisms and structures with planar motion such as end-underframes of trains and 3D tools for vehicle dynamics.

4.1. SIMULATION OF TRAIN COLLISIONS WITH 1D MODELS

This example represents the kind of simulation tasks carried out in the European Project Safetrain [3], where collisions between train sets representative of the European railway have been simulated. Figure 2 illustrates a front-front collision between two equal trains composed by 3 cars. One of the trains travels at 55 km/h and collides with the other train stopped and braked on the line. This speed covers 90% of all the real train collisions in this collision scenario (front-front). In figure 3 an example of the results obtained from the simulation is presented. The simulation results include displacements, velocities, sustained accelerations, energy distribution along the train and dissipated energy on each energy absorption device.
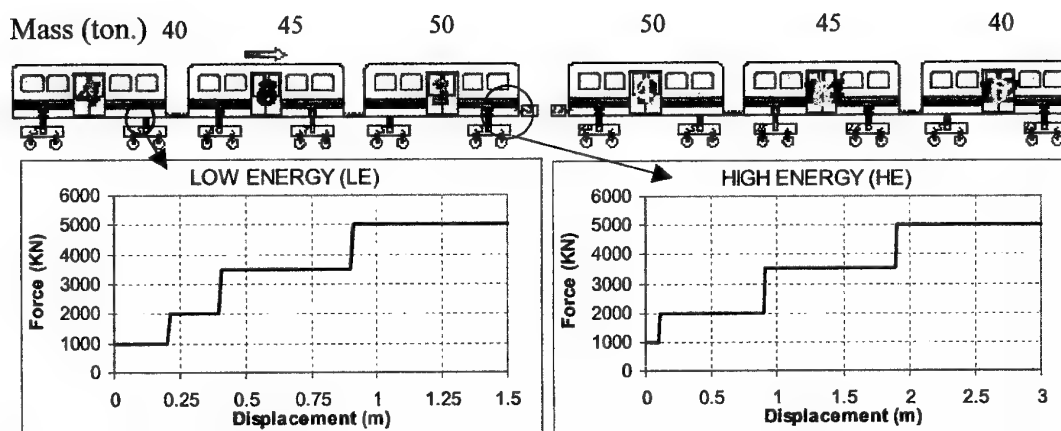
Figure 2. Characteristics and data of the front-front collision between two 3-car trains

From the analysis of figure 3, it can be observed that sustained accelerations levels are below 5 G that is the value usually accepted as the limit allowed. In fact the accelerations are one of the most important parameters to be considered into the project, because they are directly related with vehicle occupant injuries.

189
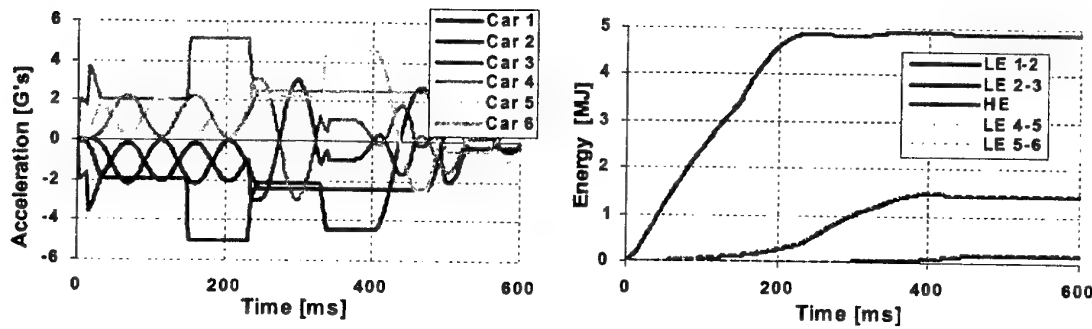
Figure 3. Accelerations and energy absorbed for the front-front collision between two 3-car trains

4.2. OPTIMIZATION OF THE ENERGY ABSORPTION DEVICES

The characteristics of energy absorption devices located in the front of the cars, establishes the overall behavior of the trains and consequently the occupants safety. The characteristics of these devices represented in the models by force-displacement curves, as shown in figure 2, can be optimized in order to increase the safety of the vehicles.

In this example, a 5-car train is considered. Preliminary studies have shown that the safety increases when the amount of energy absorbed in the front of the trains increases. Another important aspect is that, to increase the energy absorption between cars, more space is needed for deformation, but the space available between cars is limited by functional reasons, and less space required for deformation allows more space for the passenger compartment. That's why the design function as been chosen as the minimization of the energy absorbed between cars (LE-Low energy interfaces). This design function will cause an energy absorption transfer from the LE interfaces to the HE Interfaces, so a design constraint should be specified for the energy absorbed in fronts (HE-High Energy Interfaces).

The design variables are related with the characteristics of the energy absorption devices, more specifically with the force levels of the energy absorption devices.

In this example the energy absorption devices are optimized for the front-front collision scenario at 55 km/h. The optimization problem is summarized in table I.

TABLE I. Optimization problem of the energy absorption devices in a train

Design Function	$\min \sum_{i=1}^{n_{Le}} LE_i$
Design Constraints	- $acc_i < 5g$ $i=1, ..., n_{cars}$ - $LE_i < 1$ MJ $i = 1, ..., n_{LE}$; $HE_i < 10$ MJ $i = 1, ..., n_{HE}$ - $Def_i < x_1$ $i = 1, ..., n_{Le} + n_{He}$; $L_{xe_i} > L_{xe_{i-1}} + 500KN$
Design Variables	$\left[\{ L_{Le1}, L_{Le2}, L_{Le3} \}; \{ L_{He1}, L_{He2}, L_{He3} \} \right]$

With: n_{cars} Total number of cars; n_{LE} - Number of Low-Energy Interfaces (LE); n_{HE} - Number of High-Energy Interfaces (HE); LE_i - Energy Absorbed in Low Energy interface i; acc_i - Maximal acceleration level in car i; Def_i - Maximal allowed deformation in interface i; $L_{LE1}, L_{LE2}, L_{LE3}$ - Low-Energy plastic limits; $L_{HE1}, L_{HE2}, L_{HE3}$ - High energy plastic limits.

190

The optimization problem has 6 design variables and 36 design constraints. This constrained minimization problem is solved using a quadratic programming algorithm. The initial and optimal plastic levels are presented in table II. The design function that corresponds to the energy absorbed in the Low-Energy interfaces has been reduced; from 8.88 MJ to 7.03 MJ that represents a decrease of 22%.

TABLE II. Optimization results of the energy absorption devices in a train

		Low Energy Devices			High Energy Devices		
Force Level ID		L_{LE1}	L_{LE2}	L_{LE3}	H_{HE1}	H_{HE2}	H_{HE3}
Force	Initial	1000	2000	3500	1000	2000	3000
	Optimal	1022	2245	3234	1343	2126	2929
Displacement	Both	100	800	1000	200	200	500

Reductions in the sustained acceleration peaks are obtained. These reductions that correspond to an increase of the passive safety of the vehicle are due to higher deformations in the front of the trains. In fact, due to the design function selected, an energy absorption transfer from the interfaces between cars to the front of the train has occurred.

From the optimal specifications for the energy absorption devices obtained, and verified the safety of the train in others collision scenarios, the devices can be then designed, using more detailed simulation tools such as finite element programs. The requirement for the detailed models is that the crashworthiness behavior of the designed structure and energy absorption devices must averagely satisfy the force levels specified.

4.3. MULTI-LOAD DESIGN FOR CRASHWORTHINESS OF A TRAIN WAGON

In this example a multi-load optimization procedure is applied to the design of the end-underframe of a train. The objective function corresponds to the minimization of the accelerations levels at the structure for a typical impact velocity (30 km/h) against a rigid wall. Service loads (5 km/h) are included as design constraints. The optimization problem is indicated in table III and in the optimization results in table IV.

In figure 4 the train carshell and multibody model are shown schematically. The end underframe is modeled with 13 rigid bodies and 10 flexible bodies, connected by 26 plastic hinges.

For the initial design, all the constraints are satisfied which means that the structure for the low speed simulation can allow higher levels of deformation. During the optimization process the acceleration levels, for the 30 km/h simulation are reduced with the increase in deformation levels for the low velocity simulation (5 Km/h). At the optimal design all the design constraints are satisfied so no plastic deformation occurs. This is achieved, reducing the sections of the beams.

191
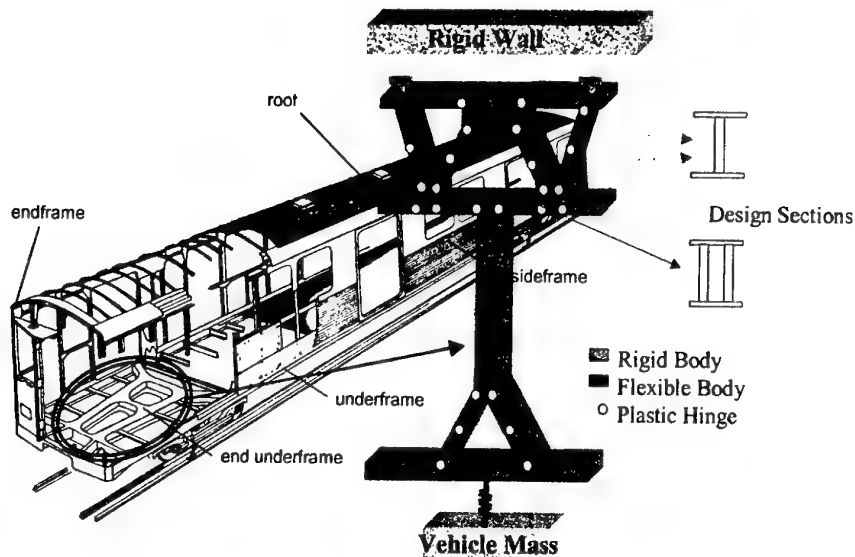
Figure 4. Train Carshell and model of the end underframe.

TABLE III. End-underframe optimization problem

Design Function	$VCSI = \dfrac{1}{T} \int \ddot{a}^2 \, dt \Big|_{V = 30 \text{ km / h}}$
Design Constraints	$M_{p_i} < M_{max_i} \ \big|_{V = 5 \text{ km / h}}$ (i=1, .., 7)
Design variables	Width of the I beams (figure 4)

TABLE IV. End-underframe optimization results

		Initial	Optimal
Design Function		20.2	13.6
Design variables	b_1 (mm)	120	97.36
	b_2 (mm)	100	75.3
	b_3 (mm)	150	130.38
Critical Design Constraint		4.71×10^{-1}	-9.06×10^{-3}

4.4. DESIGN OF A 3D VEHICLE CHASSIS UNDER DYNAMIC LOADS

The design of a vehicle chassis under the action of dynamic loads, using the 3D tools, is herein presented. The vehicle model comprises four wheels connected to the flexible chassis by a simplified suspension system. A simplified unidirectional tire model is used in the simulation. For the optimization of the chassis, two bump conditions are considered in order to induce dynamic bending and torsion. The mass of the chassis is chosen as the design function to be minimized. Concerning the design variables, the chassis is divided in three different zones, identified in figure 5, for each one a design variable is considered, corresponding to the thickness of the hollow circular section beams of the chassis.

b₁ rendered: $\cdots\cdots$ b₁ $\cdots$ b₂ ——— b₃
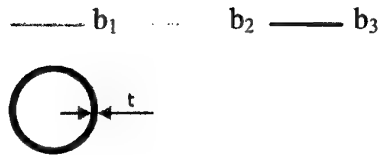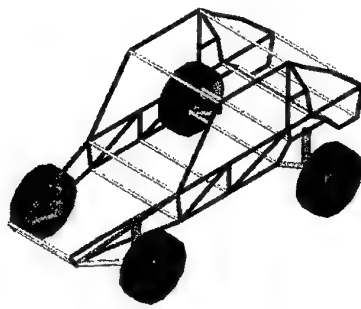
MODEL
- 4 wheels
- Flexible chassis: 51 nodes,
91 beam elements; 306 DOF

Figure 5. 3D Model of the vehicle chassis

The optimal design problem of the vehicle chassis is presented in table V. The results are presented in table VI.

TABLE V. Optimal design problem of the Vehicle Chassis

Design Function	Total Mass of the Vehicle
Design Constraints	$\sigma_i \leq \sigma_{adm}$ i=1,..,2*N_{LC}*N_{ele}*N_{cc}
Number of load cases (N_{LC})	2
Number of elements (N_{ele})	91
Maximal admissible stress σ_{adm} (Mpa)	200
Number of critical stress constraints per element (N_{cc})	2
Total number of design constraints	364
Design Variables	$b^k = t^k$
Number of design variables	3
Initial design vector ($\mathbf{b}^I$) (mm)	$\{5 \quad 5 \quad 5\}$
Lower limits vector ($\mathbf{b}^L$) (mm)	$\{0.5 \quad 0.5 \quad 0.5\}$
Upper limits vector ($\mathbf{b}^U$) (mm)	$\{50 \quad 50 \quad 50\}$

TABLE VI. Optimization results of the Vehicle Chassis

		Initial	Optimal
Objective Function (Mass)		262.1	63.4
Design Variables	b_1 (mm)	5.0	3.49
	b_2 (mm)	5.0	1.33
	b_3 (mm)	5.0	0.97
Critical Design Constraint		-0.567	0.0

For the initial design, the section of the beams of the chassis are clearly oversized, being the value of the maximum stress in the chassis (86 Mpa) considerably below the allowable maximum stress (200 MPa). The optimization process drives to a global reduction of the thickness of the beam sections, with the consequent decrease of the weight of the chassis and the increase of the stresses. For the optimal design, it is observed that the largest thickness of the beam sections corresponds to the frontal zone (variable b_1) and the zone of smaller thickness is the lateral panels. For the optimal design, two of the design constraints are active and the remaining ones are verified. The active design constraints correspond to the traversal beams of the roof in the zone of the passenger's compartment. These active design constraints occur for the torsion ride, which shows that in this case the critical loads correspond to torsion conditions.

5. Conclusions

General design methodologies for rigid-flexible multibody systems have been presented. These methodologies that are based on rigid-flexible multibody dynamics formulations have been linked with general optimization algorithms and include numerical and analytical sensitivities.

The methodologies presented have been applied to the design for vehicle crashworthiness. 1D model have been used to simulate collisions between trains, where overall deformations, accelerations, forces and absorbed energies are obtained. 1D design tools have been applied to the specification of the energy absorption devices. These methodologies have been applied and validated with a range of commercial trains and collision scenarios. 2D models, where the plastic deformations are modeled using plastic hinges, have been used to simulate end-underframes of trains under impact. Multiload design concepts that allow simulating impacts at different velocities have been used in the design process, and applied to the design of an end underframe of a train, allowing reducing the acceleration levels in the structure without any plastic deformation for the service loads. Analytic sensitivities based on the direct differentiation method have proved its efficiency for this kind of time-consuming problems. 1D and 2D models provide computationally efficient and sufficiently accurate tools, which are to be used in earlier design stages.

Finally these design methodologies have been applied for the design of a 3D vehicle chassis under dynamic solicitations. When compared with the classical structural design techniques that use only static load conditions, the methodology proposed allows the design of the vehicle chassis under dynamic loads, which result from transposition of obstacles or vehicle trajectories.

6. References

1. Bestle, D. and Schiehlen, W., Editors, (1996), *IUTAM Symposium on Optimization of Mechanical Systems*, Kluwer Academic Publishers, Dordrecht.
2. Dias, J. P. and Pereira, M. S., (1997), Sensitivity Analysis of Rigid Flexible Multibody Systems, *Multibody System Dynamics*, **1**, 303-322.
3. http://europa.eu.int/comm/research/growth/gcc/projects/safe-train.html

DEVELOPMENT OF A ROLLER COASTER MODEL

João Pombo* and Jorge Ambrósio**
IDMEC/IST, Av. Rovisco Pais, 1049-001 Lisboa, Portugal
Tel. +351 218417680; Fax +351 218417915
* e-mail: jpombo@dem.ist.utl.pt ; ** e-mail: jorge@dem.ist.utl.pt

ABSTRACT

The dynamic analysis of a roller coaster, or any other type of rail-guided vehicle, requires that a suitable description of the track, for the multibody model, is available. In this communication the development and implementation of an appropriate methodology for the accurate description of a roller coaster track spatial geometry, in the framework of multibody dynamics, is presented. Depending on the specific application the track geometry can be described by different types of parametric curves. In this work, three types of track geometric descriptions, using cubic splines, Akima splines and shape preserving splines, are discussed. The track description adopted uses Frenet frames, which provide the appropriate track referential at every point. For the complete characterization of the track, the cant angle, defined here as the roll of the osculating plane about the longitudinal tangent vector, is also considered. Taking into account that most of the rail geometry is time invariant, a pre-processor is used to define the nominal geometry of a roller coaster track based on the interpolation of a discrete number of points given by the user. In order to achieve computational efficiency, the pre-processor generates, in a tabular manner and as a function of the rail length, all the track position data and other general quantities required for the multibody code. At every time step, the program interpolates linearly the railway database in order to form a track kinematic constraint that enforces the vehicle model to have its wheelsets constrained to move along the track with a prescribed angular orientation with respect to the railway Frenet frames. The advantages and drawbacks of this formulation are discussed emphasizing the influence of the type of parametric curves used to construct the database that describe the track geometry. The discussion is supported through the application of the formulation to a roller coaster model with complex rail geometry.

1   Introduction

The dynamic analysis of railway [1–3], roller coaster [4] or any other type of rail-guided vehicles requires an accurate description of the track geometry. The track is composed of two rails defined in a plane that sits in a spatial curve, defined hereafter as the reference path. The basic ingredient to define the track is, therefore, the geometry of the reference path. Typically, the track irregularities can be modeled by adding to the track perfect geometry small perturbations that are either measured experimentally or generated numerically. The objective of this work is to present a description of the spatial geometric features of the tracks, and its computational implementation, in a form suitable to the multibody methodology adopted for the modeling of railway systems. The introduction of the track irregularities is not considered in this work.

Depending on the specific application, the reference path of the track geometry can be described by a number of types of parametric curves [5]. For railway and light track vehicles the description of the nominal geometry of the track is generally done by putting together straight and circular track segments, interconnected by transition segments that ensure the continuity of the first and second derivatives of the railway in the transition points [1,6]. For other applications, parametric curves that interpolate a given number of control points are commonly used to define the track geometry. In any case, the complete characterization of the tracks also requires the definition of the cant angle variation along the reference path. For flat tracks, the cant angle in a given point of the reference path is measured in the plane perpendicular to the reference path, between a line that seats on both rails and the horizontal plane. For tracks with a full spatial geometry, a new definition of this angle is introduced. It is proposed that the osculating plane [5] of the reference track plays the role of the horizontal plane of the flat track in measuring the cant angle.

In this work three types of track geometric descriptions are discussed in the framework of the multibody models for railway dynamics analysis, i.e., cubic splines [10,11], Akima splines [16,20] and shape preserving splines [20]. The application of cubic splines to interpolate a set of control points describing the track geometry leads to undesired oscillations in the track model [12]. Other methodologies using Akima splines or shape preserving splines are alternative interpolation techniques for the parameterization of the reference path geometry that minimize the undesired oscillations of the interpolated curve.

The reference path parameterization with analytical segments, which use straight, circular and transition curves, does not introduce unwanted oscillations on the track geometry. However, this description is rather complex to model railways with large slopes or with vertical curves. Some of the commercial codes, that adopt this description, impose that the tracks are basically horizontal in order to avoid difficulties [7–9]. Therefore, the

track description with analytical segments cannot be used to parameterize fully spatial geometries like the ones used on roller coasters.

Regardless of the form in which the reference path geometry is described, a suitable kinematic constraint must be defined in order to enforce, not only that a particular point of given body of the multibody systems follows the reference path, but also that the body orientation does not change with respect to a Frenet-frame [5] associated to the curve. The methodology proposed here for the general spatial curve joint can use any descriptive form for the reference path. The position, the Frenet-frame vectors and their derivatives, which are used in the definition of the kinematic constraint, are pre-processed and included in a table as function of the curve length. Therefore, during the dynamic analysis the quantities involved in the general spatial curve joint are obtained by linear interpolation of the tabulated values. The spatial curve constraint is implemented in the general purpose multibody computer program "*DAP-3D*" [13].

2   Analytic Properties of Parametric Curves

The definition of the general spatial curve kinematic constraint requires a rather elaborate geometric description of the parametric curves used to describe the track geometry. In this section only the analytic properties that are important for the definition of the kinematic constraint are presented. Additional information can be obtained in [5,17,18].

2.1   PARAMETRIC CURVES

A parametric curve is a point-bounded collection of points that have Cartesian coordinates given by continuous, one-parameter, single-valued mathematical functions [5]. Considering u as the parametric variable, the coordinates of any point on a parametric curve are treated as the components of the vector $g(u)$ given by:

$$\mathbf{g} \equiv \mathbf{g}(u) = \left\{ \begin{array}{ccc} x(u) & y(u) & z(u) \end{array} \right\}^T \tag{1}$$

2.2   FRENET FRAMES AND THE OSCULATING PLANE

In order to define the spatial curve kinematic constraint it is necessary to obtain the local properties of the curve, depicted in Figure 1, at every point. A set of three orthogonal vectors $\mathbf{t}$, $\mathbf{n}$ and $\mathbf{b}$, representing a moving frame known as Frenet frame [5,17,18], needs to be defined.
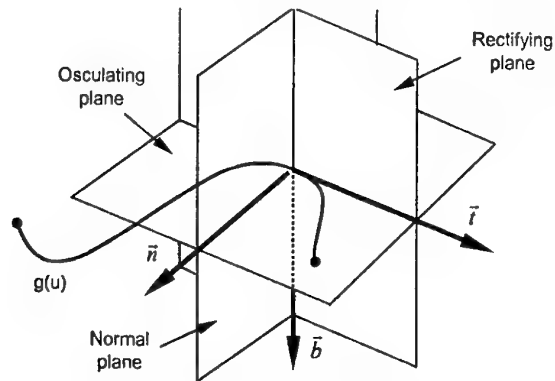
Figure 1 – The Frenet frame associated to the curve point

The osculating plane, at a given point P on a curve, is defined as the plane of closest contact to the curve in the neighborhood of P. This geometric property can be used to define the cant angle. Therefore, it is proposed here that, for tracks with a full spatial geometry, the cant angle is measured with respect to the osculating plane.

2.3   UNIT TANGENT, NORMAL AND BINORMAL VECTORS

On a parametric curve, the tangent vector at point P is denoted by $\mathbf{g}^u$, which is obtained by differentiating the point position $\mathbf{g}(u)$ with respect to the parametric variable. Considering that when u appears as a superscript, it indicates differentiation with respect to u, the unit tangent vector to the curve at point $\mathbf{g}(u)$ is given by [5]:

$$\mathbf{t} = \frac{\mathbf{g}^u}{\left\| \mathbf{g}^u \right\|} \tag{2}$$

196

The principal normal vector at point $\mathbf{g}(u)$ is normal to the curve and must lie in the plane normal to the unit tangent vector. Among the many possible normal vectors, the principal unit normal vector, $\mathbf{n}$, points towards the spatial center of curvature of the curve and is given by [5]:

$$k = \mathbf{g}^{uu} - \frac{\mathbf{g}^{uu^T}\mathbf{g}^u}{\left\|\mathbf{g}^u\right\|^2}\mathbf{g}^u \quad ; \quad \mathbf{n} = \frac{\mathbf{k}}{\left\|\mathbf{k}\right\|}$$

(3)

where $\mathbf{g}^{uu}$ is the second derivative of $\mathbf{g}(u)$ with respect to the parameter u. For the definition of the Frenet frame associated to a reference path, another vector normal to the curve must be defined. Using the principal tangent and normal vectors, given by equations (2) and (3), the third vector, denominated by binormal vector, is defined as [5]:

$$\mathbf{b} = \tilde{\mathbf{t}}\,\mathbf{n}$$

(4)

2.4   ARC LENGTH

The arc length is a global characteristic of the curve that does not vary from point to point. The length of a parametric curve $\mathbf{g}(u)$ is given by [5]:

$$L = \int_{u_1}^{u_2}\sqrt{\mathbf{g}^{u^T}\mathbf{g}^u}\,du$$

(5)

3   General Spatial Curve Kinematic Constraints

In this section, the formulation of the general spatial curve kinematic constraints are presented and the developed methodology is implemented in the computer program *DAP-3D* [13]. These constraints are the basis of track definition for rail-guided vehicles enforcing that, not only the railway path is followed, but also the spatial orientation of the wheelset is prescribed, according to the railway characteristics defined by the moving Frenet frame.

3.1   PRESCRIBED MOTION CONSTRAINT

The objective here is to define the constraint equations that enforce a certain point, of a given rigid body, to follow a reference path [19]. Consider a point R, located on a rigid body i, that has to follow a specified path, as depicted in Figure 2. The path is defined by a parametric curve $\mathbf{g}(L)$, which is controlled by a global parameter L that represents the length traveled by the point along the curve until the current location of point R. The kinematic constraint is written as:

$$\Phi^{(pmc,3)} = \mathbf{0} \quad \equiv \quad \mathbf{r}_i^R - \mathbf{g}(L) = \mathbf{0}$$

(6)

where $\mathbf{r}_i^R = \mathbf{r}_i + \mathbf{A}_i\,\mathbf{s}_i^{R'}$ are the coordinates of point R with respect to the global coordinate system, $\mathbf{r}_i$ is the vector that defines the location of the body-fixed coordinate system, $\mathbf{A}_i$ is the transformation matrix from the

body-fixed coordinates to the global frame and $\mathbf{s}_i^{R'}$ are the coordinates of point R with respect to the body-fixed frame. The vector $\mathbf{g}(L)=\{x(L),\ y(L),\ z(L)\}^T$ represents the Cartesian coordinates of the curve where point R is constrained to move and L is the curve parametric variable. The velocity and acceleration equations, associated to these kinematic constraints, are obtained as the first and second time derivatives of equation (6). The complete formulation can be found in [22].

197

Figure 2 – Prescribed motion constraint
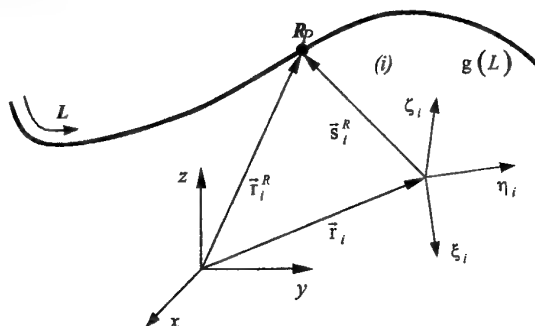
3.2 LOCAL FRAMES ALIGNMENT CONSTRAINT

The second part of the spatial curve kinematic constraints ensure that the spatial orientation of a body remains unchanged with respect to the moving Frenet frame, as represented in Figure 3. Consider a rigid body i where $(\mathbf{u}_\xi, \mathbf{u}_\eta, \mathbf{u}_\zeta)_i$ are the unit vectors associated to the body-fixed coordinate system. Consider also that the Frenet frame, of the curve $\mathbf{g}(L)$, is defined by the unit vectors $(\mathbf{t}, \mathbf{n}, \mathbf{b})_L$. Assume that, at the initial time of analysis, the relative orientation between the body vectors $(\mathbf{u}_\xi, \mathbf{u}_\eta, \mathbf{u}_\zeta)_i$ and the curve local frame $(\mathbf{t}, \mathbf{n}, \mathbf{b})_L$ are such that the following equations hold

$$\Phi^{(lfac,3)} = 0 \quad \equiv \quad \begin{Bmatrix} \mathbf{n}^T \cdot \mathbf{u}_\xi \\ \mathbf{b}^T \cdot \mathbf{u}_\xi \\ \mathbf{n}^T \cdot \mathbf{u}_\zeta \end{Bmatrix} - \begin{Bmatrix} a \\ b \\ c \end{Bmatrix} = 0 \tag{7}$$
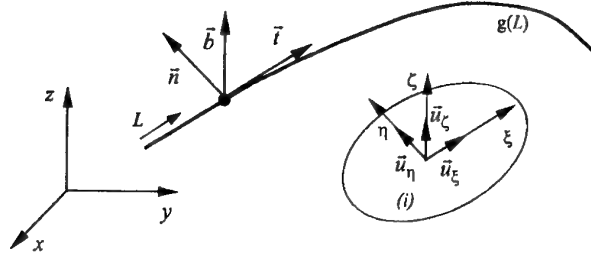
Figure 3 Local frame alignment constraint

With the purpose of having a more compact notation, consider the transformation matrix from the body i fixed coordinates to the global coordinate system and let the following unit vectors be defined as:

$$\mathbf{A}_i = \begin{bmatrix} \mathbf{u}_\xi & \mathbf{u}_\eta & \mathbf{u}_\zeta \end{bmatrix}_i \quad ; \quad \mathbf{u}_1 = \{1 \quad 0 \quad 0\}^T \quad ; \quad \mathbf{u}_2 = \{0 \quad 1 \quad 0\}^T \quad ; \quad \mathbf{u}_3 = \{0 \quad 0 \quad 1\}^T \tag{8}$$

Hence, the equation (7) can be re-written as

$$\Phi^{(lfac,3)} = 0 \quad \equiv \quad \begin{Bmatrix} \mathbf{n}^T \, \mathbf{A}_i \, \mathbf{u}_1 \\ \mathbf{b}^T \, \mathbf{A}_i \, \mathbf{u}_1 \\ \mathbf{n}^T \, \mathbf{A}_i \, \mathbf{u}_3 \end{Bmatrix} - \begin{Bmatrix} a \\ b \\ c \end{Bmatrix} = 0 \tag{9}$$

The velocity and acceleration equations, associated to these kinematic constraints, are obtained as the first and second time derivatives of equation (9). The complete formulation can be found in [22].

4 Pre-Processor for Railway Geometric Description

For multibody analysis, the track models must be defined in the form of parameterized curves. Here, three different parametric track descriptions, using cubic splines, Akima splines and shape preserving splines, are presented. A pre-processor program uses these parametric descriptions in order to define the nominal geometry of a railway using a discrete number of points, which are organized in a database as function of the curve length parameter.

4.1 CURVE FOR THE REFERENCE PATH BY CUBIC SPLINES INTERPOLATION

The reference path curve can be described using cubic spline curves that interpolate a set of control points given by the user, and ensure the continuity of their first and second derivatives. A parametric cubic curve is defined as [10]:

$$\mathbf{g}(u) = \mathbf{a}_3 \, u^3 + \mathbf{a}_2 \, u^2 + \mathbf{a}_1 \, u + \mathbf{a}_0 \tag{10}$$

where $\mathbf{g}(u)$ are the coordinates of a point on the curve, u is the parametric variable and $\mathbf{a}_i$ are the unknown algebraic coefficients. Let a set of points $\mathbf{g}_i$, representing the reference path, be defined by their coordinates $(x,y,z)_i$. When the cubic spline segments are used to represent the interpolation curve, the algebraic coefficients $\mathbf{a}_i$

are written explicitly in terms of the boundary conditions. In this sense, the equations of the cubic splines segments are given by [10]

$$\mathbf{g}\left(u\right) = \begin{bmatrix} u^3 & u^2 & u & 1 \end{bmatrix} \begin{bmatrix} 2 & -2 & 1 & 1 \\ -3 & 3 & -2 & -1 \\ 0 & 0 & 1 & 0 \\ 1 & 0 & 0 & 0 \end{bmatrix} \begin{Bmatrix} \mathbf{g}(0) \\ \mathbf{g}(1) \\ \mathbf{g}'(0) \\ \mathbf{g}'(1) \end{Bmatrix} \tag{11}$$

where the spline local parameter $u \in [0,1]$ and $\mathbf{g}(0)$ and $\mathbf{g}(1)$ represent the coordinates of the end points of each segment. The spline derivatives, $\mathbf{g}'(0)$ and $\mathbf{g}'(1)$, at the end points are calculated in order to ensure C^2 continuity between spline segments and, for this case, it is assumed that natural splines are used [10,11,16].

In order for the cubic spline to be used in the spatial curve kinematic constraint, its geometric characteristics must be expressed as function of the reference path length L, measured from its origin, and not as a function of the spline parametric variable u. The relation between L and u is given by

$$L\left(u\right) = \sum_{n=1}^{k-1} L_n^0 + L_k^{actual}\left(u\right) \tag{12}$$

where k is the number of the spline segment where the point is located, L_i^0 is the length of the ith spline segment and $L^{actual}(u)$ represents the length of the actual spline segment from its origin to the actual location of the point [22].

In order to implement the spatial curve kinematic constraint in the computer code it is necessary to find the value of the cubic spline parametric variable u that corresponds to a prescribed segment length L. It is clear from equations (12) and (5) that the relation between these two parameters is not linear. Consider the parametric variable, u^R, corresponding to a point R, located on the kth cubic spline segment, and to which it is associated a curve length L_k^R, measured from the kth segment origin. In this case, the parameter u is obtained from the parameter L using [22]

$$\int_0^{u^R} \sqrt{\mathbf{g}^{u^T}\mathbf{g}^u}\, du \; - \; L_k^R = 0 \tag{13}$$

This non-linear equation is solved using the Newton-Raphson method [11,13].

4.2   CURVE FOR THE REFERENCE PATH BY AKIMA SPLINES INTERPOLATION

The reference path parameterization with Akima cubic splines has the objective of minimizing the undesired wiggles of the curves observed on the cubic spline interpolation [16]. This formulation is implemented in the pre-processor using the FORTRAN subroutines as implemented in the IMSL math library [20]. The pre-processor uses the routine *DCSAKM* [20], from IMSL library, to compute three Akima cubic splines that interpolate the sets of data points (u_i, x_i), (u_i, y_i) and (u_i, z_i), where x_i, y_i and z_i are the Cartesian coordinates of the N control points to interpolate. The parametric curve obtained consists of three piecewise cubic polynomials [16,20] written as

$$\mathbf{g}\left(u\right) = \begin{Bmatrix} x(u) \\ y(u) \\ z(u) \end{Bmatrix} = \begin{Bmatrix} c_{1i}^x + c_{2i}^x\left(u - \overline{u}_i\right) + \dfrac{c_{3i}^x}{2}\left(u - \overline{u}_i\right)^2 + \dfrac{c_{4i}^x}{6}\left(u - \overline{u}_i\right)^3 \\ c_{1i}^y + c_{2i}^y\left(u - \overline{u}_i\right) + \dfrac{c_{3i}^y}{2}\left(u - \overline{u}_i\right)^2 + \dfrac{c_{4i}^y}{6}\left(u - \overline{u}_i\right)^3 \\ c_{1i}^z + c_{2i}^z\left(u - \overline{u}_i\right) + \dfrac{c_{3i}^z}{2}\left(u - \overline{u}_i\right)^2 + \dfrac{c_{4i}^z}{6}\left(u - \overline{u}_i\right)^3 \end{Bmatrix} \; ; \quad \begin{array}{c} \overline{u}_i \le u < \overline{u}_{i+1} \\ i = 1, \ldots, N-1 \end{array} \tag{14}$$

where $\mathbf{g}(u)$ is a point on the curve, u is the parametric variable, c_{ji}^x, c_{ji}^y and c_{ji}^z are the local polynomial coefficients that must be calculated, and $\overline{u}_i$ are the breakpoints of the Akima cubic splines, which are assumed to be strictly increasing.

The advantage of the Akima splines parameterization is that no unwanted oscillations are introduced by the interpolation algorithm in geometric description of the track. Nevertheless, this interpolation scheme only ensures C^1 continuity between spline segments. Therefore, the continuity of the reference path curvature is not ensured, which may conflict with some of the properties required for railway geometries [6].

199

4.3 CURVE FOR THE REFERENCE PATH BY SHAPE PRESERVING SPLINES INTERPOLATION

The shape preserving cubic splines are spline functions that preserve the concavity of the interpolation data [16,20,21]. This interpolation scheme is implemented in the pre-processor using the Fortran subroutines implemented in the IMSL math library [20]. The pre-processor uses the routine *DCSCON* [20], from IMSL library, to compute the shape preserving cubic splines that interpolate the sets of data points (u_i, x_i), (u_i, y_i) and (u_i, z_i), where x_i, y_i and z_i are the Cartesian coordinates of the control points, $u_i = 1, \dots, N$ is the parametric variable of the cubic curve corresponding to each control point, and N is the number of control points to interpolate. The parametric curve obtained consists of three piecewise cubic polynomials [20], written as

$$\mathbf{g}(u) = \begin{Bmatrix} x(u) \\ y(u) \\ z(u) \end{Bmatrix} = \begin{Bmatrix} c_{1i}^x + c_{2i}^x\left(u-\bar{u}_i^x\right) + \dfrac{c_{3i}^x}{2}\left(u-\bar{u}_i^x\right)^2 + \dfrac{c_{4i}^x}{6}\left(u-\bar{u}_i^x\right)^3 \\ c_{1j}^y + c_{2j}^y\left(u-\bar{u}_j^y\right) + \dfrac{c_{3j}^y}{2}\left(u-\bar{u}_j^y\right)^2 + \dfrac{c_{4j}^y}{6}\left(u-\bar{u}_j^y\right)^3 \\ c_{1k}^z + c_{2k}^z\left(u-\bar{u}_k^z\right) + \dfrac{c_{3k}^z}{2}\left(u-\bar{u}_k^z\right)^2 + \dfrac{c_{4k}^z}{6}\left(u-\bar{u}_k^z\right)^3 \end{Bmatrix} \; ; \; \begin{cases} \bar{u}_i^x \leq u < \bar{u}_{i+1}^x \; ; i=1,\dots,N_x-1 \\ \bar{u}_j^y \leq u < \bar{u}_{j+1}^y \; ; j=1,\dots,N_y-1 \\ \bar{u}_k^z \leq u < \bar{u}_{k+1}^z \; ; k=1,\dots,N_z-1 \end{cases} \quad (15)$$

where $\mathbf{g}(u)$ is a vector with the coordinates of a point on the curve, u is the parametric variable, c_{mi}^x, c_{mj}^y and c_{mk}^z are the local polynomial coefficients that must be calculated. $\bar{u}_i^x$, $\bar{u}_j^y$ and $\bar{u}_k^z$ are respectively the N_x, N_y, and N_z breakpoints for $x(u)$, $y(u)$ and $z(u)$ of the shape preserving cubic splines, which are assumed to be strictly increasing.

The advantage of the shape preserving splines parameterization is that it is consistent with the concavity of the data, which is rather useful when it is important to preserve the convex and concave regions implied by the control points. This interpolation scheme also ensures C^2 continuity between spline segments, i.e., it guarantees that the parameterized curve has a continuous curvature.

4.4 INTRODUCTION OF A PRESCRIBED CANT ANGLE IN THE KINEMATIC CONSTRAINT

In horizontal curves the outer rail is usually raised in order to reduce the effects of the centrifugal acceleration on vehicles [3]. In this sense, the railway cant has to be taken into account by the pre-processor when creating the railway databases. The cant angle is defined here as the angle between vector $\mathbf{n}$ and the osculating plane, being measured in the normal plane, as described in Figure 4.
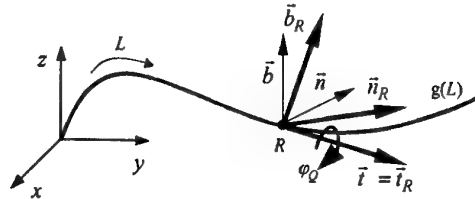
Figure 4 – Cant angle contribution to the track model

Let the track cant angle, on a point R of the parametric curve $\mathbf{g}(L)$, be designated by φ_R. Assume that the reference path Frenet frame is defined by its principal unit vectors $(\mathbf{t},\mathbf{n},\mathbf{b})_L$. Thus, due to the track cant, the parametric curve reference frame rotates about the $\mathbf{t}$ axis by an angle φ_R, as shown in Figure 4. Therefore, it is necessary to calculate the new components of the principal unit vectors $(\mathbf{t}_R,\mathbf{n}_R,\mathbf{b}_R)_L$ of the curve moving frame after the cant angle rotation. According to [22], the new components are expressed as:

$$\begin{aligned} \mathbf{t}_R &= \mathbf{t} \\ \mathbf{n}_R &= \mathbf{n}\ cos\left(\varphi_R\right) + \mathbf{b}\ sin\left(\varphi_R\right) \\ \mathbf{b}_R &= -\mathbf{n}\ sin\left(\varphi_R\right) + \mathbf{b}\ cos\left(\varphi_R\right) \end{aligned} \quad (16)$$

With this formulation, the user must set the cant angle for the beginning and for the end of every track segment. The values of the cant angle are linearly interpolated between the segment end points, regardless of the parametric description of the curve. With the complete information available, the pre-processor program uses equation (16) to calculate the geometric parameters that define the reference path geometry.

4.5   TRACK INFORMATION INCLUDED IN RAILWAY DATABASE

The direct use, in the spatial curve constraints, of the equations obtained by any of the parametric descriptions presented, is neither practical nor efficient from the computational point of view. As the kinematic constraints is to be used in the framework of a dynamic analysis program, the solution of the nonlinear equations (13) and the sets of equations (11), (14), (15) and (16) and so forth at every time step would be an heavy burden on the code. An alternative implementation of these equations is the construction of a lookup table where all quantities appearing in the definition of the kinematic constraints are tabulated as function of the global length parameter.

After selecting any of the parametric descriptions of the spatial curve presented, the length parameter step ΔL adopted for the database construction has to be chosen. Then, the pre-processor program automatically constructs the lookup table with all parameters necessary to define the geometric characteristics of the reference path, taking into account the track cant variation. These geometric parameters are organized in columns as function of the length parameter L of the track. Then, the multibody code interpolates linearly the table in order to obtain all required quantities to set the constraints. Figure 5 presents the structure of the railway database obtained with the pre-processor.

L	x	y	z	$\dfrac{dx}{dL}$	$\dfrac{dy}{dL}$	$\dfrac{dz}{dL}$	$\dfrac{d^2x}{dL^2}$	$\dfrac{d^2y}{dL^2}$	$\dfrac{d^2z}{dL^2}$	t_x	......	$\dfrac{d^2b_y}{dL^2}$	$\dfrac{d^2b_z}{dL^2}$
0	...	...	...	...	...	...	...	...	...	...	......	...	...
0.05	...	...	...	...	...	...	...	...	...	...	......	...	...
0.10	...	...	...	...	...	...	...	...	...	...	......	...	...
.....	...	...	...	...	...	...	...	...	...	...	......	...	...

Figure 5 – Structure of reference path geometric information table

5   Application Example

The discussion of the methodology proposed for the general spatial curve constraint is carried here based on an application example. It concerns the application to a three-dimensional track model with the geometry illustrated in Figure 6, which is analogous to the ones used on roller coasters design [4].

Three alternative roller coaster models are built using cubic, Akima and shape preserving splines. The track models are first pre-processed and the relevant geometric information is included in the railway databases. The roller coaster model is assembled considering, for the horizontal curve $G–I$, transition curves with lengths of 60 m each. The cant angle for this circular curve is –1.014 rad (-58.1°) and it varies linearly in the transition segments.
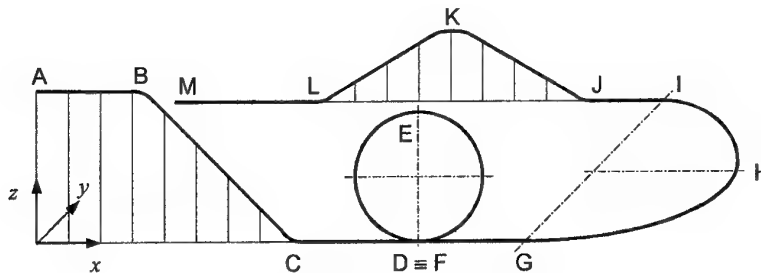
Figure 6 – Roller coaster geometry

In Figure 7, a graphic that represents the z Cartesian coordinate of the roller coaster model built using cubic, Akima and shape preserving splines, is presented. This graphic is drawn as function of the track length L, in the neighborhood of point B, from Figure 6, and for a control point increment of 1 m. As it can be seen, the curve parameterized with cubic splines leads to oscillations in the transition between the straight segment and the circular segment. The other two parameterization schemes do not exhibit oscillations, and preserve the shape of the data.

As the emphasis of this work is the track model and not the vehicle model itself, only a single rigid body, representing a roller coaster vehicle, is considered for the dynamic analysis performed here. Figure 8 represents a view of the roller coaster vehicle at the entrance of the looping, i.e., at point D in Figure 6. This result was obtained during dynamic analysis, using Akima splines for track description, and correspond to a constraint violation of 2.9×10^{-1}. The violation occurs in the second constraint of equation (9), i.e., the perpendicularity between the unit vector $\mathbf{u}_\xi$, associated to the axis of the body-fixed coordinate system and the binormal vector $\mathbf{b}$ of the Frenet frame associated to the reference path curve. Moreover, when comparing the maximum constraint

201

violations obtained during dynamic analyses, using the different track descriptions, it is observed that the reference path curves parameterized with Akima splines produce maximum constraint violations proportional to 10^{-1} while for the other interpolation schemes the constraint violations are proportional to 10^{-2}. This can be explained by the fact that the track curve, described by Akima splines, only has C^{I} continuity, not ensuring the continuity of the curvature. Once the results obtained using Akima splines for track parameterization are not satisfactory, this interpolation method is not considered hereafter.
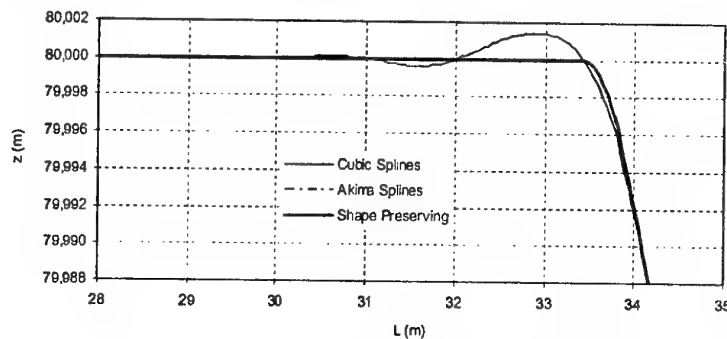
Figure 7 – z Cartesian coordinate of the roller coaster model
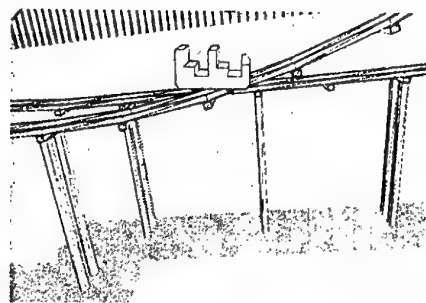
Figure 8 – View of the roller coaster vehicle at the looping entrance using Akima splines for track description

The roller coaster vehicle accelerations in the z direction, for the track models obtained with cubic and shape preserving splines, are presented in Figure 9. As it can be seen, there is a good agreement between the results obtained with the two forms of parameterization. The large peaks of acceleration observed are direct results of the sudden change of the vertical curvature between parts of the track with different geometric characteristics. These sudden changes reflect the fact that no vertical transition curves are used in this roller coaster design. The smaller perturbations observed in the results, result from the oscillations interpolation processes and, therefore, do not have a physical meaning.
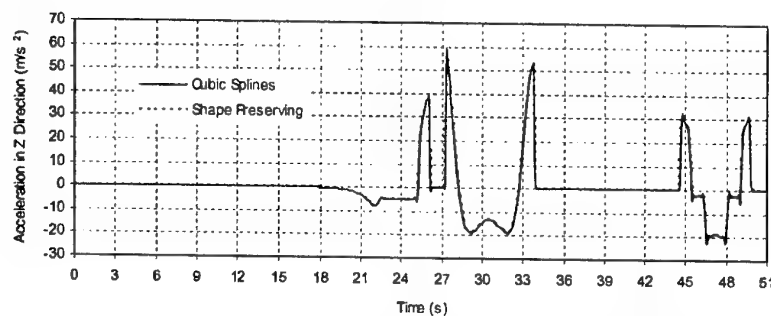
Figure 9 – Acceleration of the roller coaster vehicle in z direction for distances between control points of 1 m

6 Conclusions and Future Developments

A kinematic constraint representing a general spatial curve joint has been developed here and its computational implementation has been presented. The strategy adopted for the computer implementation of the joint starts by having the spatial curve expressed in a parametric form. A moving reference frame is defined in the curve with its axis defined in the intersections of the normal, osculating and rectifying planes. The introduction of the cant angle and of its variation along the curve has also been implemented. The reference

202

plane used in the spatial curve to define the cant angle is the osculating plane, which is the horizontal plane in case of a flat curve. A transformation in the parameterization is proposed to replace the actual parameter by another that uses the arc length of the curve. Recognizing the fact that the transformation equations are nonlinear and that it is not efficient to calculate the curve vectors and their derivatives during the dynamic analysis a pre-processor to generate all geometric properties of the curve is implemented. The result is a database where all quantities involved in the constraint are tabulated as function of the arc length traveled by the constrained point of a system body in the curve. This methodology has the advantage of making the time required for the dynamic simulation of the rail-guided vehicle completely independent of the track complexity and of the type of parametric curve used. Any descriptive form of parametric curves is dealt with in the pre-processor while the dynamic analysis program only has to proceed with linear interpolations of the railway table. By ensuring that the arc-length step is small enough the linear interpolation procedure does not introduce any significant error in the geometric description of the curve.

The track parameterization with cubic splines or with shape preserving splines can be used to describe the track geometry of fully three-dimensional roller coasters. The major drawback of the cubic splines formulation is that it leads to undesired oscillations in the track model, which can be perceived as track irregularities during dynamic analysis. The use of shape preserving splines leads to the best representation of the railway reference path. Track parameterization with Akima cubic splines is also presented and it is shown that it leads to high constraint violations in the transitions between parts of the track with different geometric characteristics. These violations are big enough to originate results that are not consistent track regularity required, i.e., with the need for C^2 continuity. Other parametric descriptions of the general spatial curve, such as splines with tension, can be implemented in the pre-processor program as alternative techniques for railway parameterization.

The general spatial curve kinematic joint, now described, serves as the basis for the construction of the railway as it provides a moving frame, associated to the curve where the osculating plane is defined and with respect to which the cant angle is defined. The actual geometry of the tracks can now be described with respect to this moving frame providing one of the basic ingredients for the use of the multibody code in the context of railway dynamics.

8   References

[1]   Dukkipati, R.V., Amyot, J.R., *Computer-Aided Simulation in Railway Dynamics*, Marcel Dekker Inc., New York, New York, 1988.
[2]   Garg, V.K., Dukkipati, R.V., *Dynamics of railway vehicle systems*, Academic Press, Toronto, Canada, 1984.
[3]   Andersson, E., Berg, M., Stichel, S., *Rail vehicle dynamics, fundamentals and guidelines*, Royal Institute of Technology (KTH), Stockholm, Sweden, 1998.
[4]   Wayne, T., *Roller Coaster Physics – An Educational Guide to Roller Coaster Design and Analysis for Teachers and Students*, Charlottesville, Virginia, 1998.
[5]   Mortenson, M.E., *Geometric Modeling*, John Wiley & Sons, New York, New York, 1985.
[6]   Pinto, A.R.V., *Bases Técnicas dos Traçados do Metroplitano de Lisboa*, (*Track Geometry Technical Bases of Lisbon Underground Company*), Revista da Ordem dos Engenheiros, Portugal, 1978.
[7]   MDI - Mechanical Dynamics, *ADAMS/Rail 9.1 – Technical Manual*, Ann Arbor, Michigan, 1995.
[8]   MDI - Mechanical Dynamics, *ADAMS/Rail 9.1.1 ADtranz Milestone I – Release Notes*, Ann Arbor, Michigan, 1999.
[9]   MDI - Mechanical Dynamics, *ADAMS/View 9.0 – Training Documentation*, Ann Arbor, Michigan, 1998.
[10] Anand, V., *Computer Graphics and Geometric Modeling for Engineering*, John Wiley and Sons, New York, New York, 1994.
[11] Pina, H.L.G., *Métodos Numéricos*, (*Numerical Methods*), McGraw-Hill, Lisboa, Portugal, 1995.
[12] Ambrósio, J., *Trainset kinematic: A Planar Analysis Program for the Study of the Gangway Insertion Points*, Technical Report IDMEC/CPM/97/005, Institute of Mechanical Engineering, Instituto Superior Técnico, Lisbon, Portugal, 1997.
[13] Nikravesh, P.E., *Computer-Aided Analysis of Mechanical Systems*, Prentice Hall, Englewood Cliffs, New Jersey, 1988.
[14] Ambrósio, J., *Implementation of Typical Track Geometries*, Technical Report PEDIP Nº 25/00379, Institute of Mechanical Engineering, Instituto Superior Técnico, Lisbon, Portugal, 2000.
[15] Jalon, J. de, Bayo, E., *Kinematic and dynamic simulation of multibody systems*, Springer-Verlag, Heidelberg, Germany, 1993.
[16] De Boor, C., *A Practical Guide to Splines*, Springer-Verlag, New York, New York, 1978.
[17] Yamaguchi, F., *Curves and Surfaces in Computer Aided Geometric Design*, Springer-Verlag, Heidelberg, Germany, 1988.
[18] Farin, G., *Curves and Surfaces for Computer Aided Geometric Design – A Practical Guide*, Academic Press, Boston, Massachusetts, 1990.
[19] Farid, M., Amirouche, L., *Computational Methods in Multibody Dynamics*, Prentice Hall, Englewood Cliffs, New Jersey, 1992.
[20] Visual Numerics, Inc., *IMSL Fortran 90 Math Library 4.0 - Fortran Subroutines for Mathematical Applications*, Huston, Texas, 1997.
[21] Vore, R.A. de, Lorentz, G.G., *Constructive Approximation*, Springer-Verlag, Heidelberg, Germany, 1993.
[22] Pombo, J., Ambrósio, J., General Rail Track Joint for the Dynamic Analysis of Rail Guided Vehicles, Proceeding of the Euromech Colloquium No. 427 on Computational Techniques and Applications in Nonlinear Dynamics of Structures and Multibody Systems, Cachan, France, September 24-27, 2001

203

Virtual Assembly in Multibody Dynamics

W. Schiehlen, C. Scholz

Institute B of Mechanics, University of Stuttgart
Pfaffenwaldring 9, 70550 Stuttgart, Germany

Abstract:
Simulation of complex engineering systems requires modelling and computation of components from different engineering fields, e.g. multibody dynamics, control and electronics. Each component can be modelled and computed with its domain-specific tool. But nondomain-specific components of the system can not be sufficiently treated by these tools resulting in unsatisfying simulations. It has been shown that approaches for simulator coupling open a systematic and accurate way to combine simulation tools and get satisfying results. Therefore, the global system has to be decomposed into subsystems due to the different engineering disciplines using engineering intuition to treat it efficiently by a team of engineers. With the iterative simulator coupling method stabilizing the modular simulation the computation of the global system is realized by a time discrete linker and scheduler which combines the inputs and outputs of the corresponding subsystems and establishes communication between them. In this approach the communication between the coupled simulation tools is executed at fixed time steps. However, if the coupled modules are characterized by large differences in their eigendynamic, an increase of the numerical efficiency by an automatic communication step size control can be achieved. Therefore, two methods of step size control, Richardson extrapolation and embedded formula, are discussed. It is important that the communication step size control does not interfere with the coupled simulation tools because of the subsystems black-box description within the modular simulation. It will be shown that such an automatic communication step size control allows to minimize the quantity of communications between the coupled subsystems as well as to use well-known integration methods for each independent module. Accordingly, a better efficiency and quality by a faster computation can be expected if the dynamic characteristics of the subsystems show large differences.

1 Introduction

The dynamic analysis of complex engineering systems requires the modelling of components from different engineering fields. The modular decomposition of the global system is based on engineering intuition of corresponding engineering disciplines. Once the interfaces of the subsystems have been defined these subsystems can be modeled independently from each other. The exchange and modification of a subsystem is also independent from any other component as well as different and independent software tools can be used for every engineering discipline.

The overall simulation is achieved by coupling of all subsystems in order to obtain the global system behaviour. For mechatronic systems the coupling of subsystems may be realized on three different levels of model description as illustrated in Figure 1.
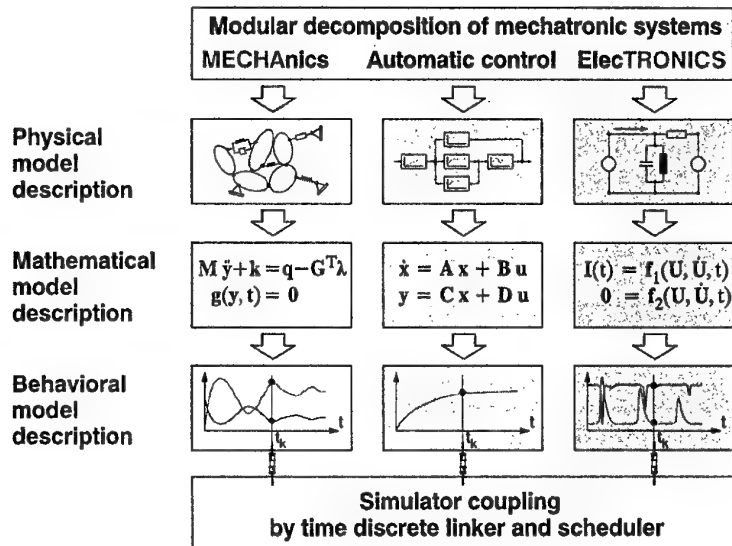
Figure 1: Modular decomposition and simulation of mechatronic systems

In the physical model description a system is represented by a physical model, e.g. in case of multibody systems there are rigid bodies, massless joints and coupling force elements. The mathematical model description is a representation of a system by mathematical equations which can be derived from the physical model description, e.g. the equations of motion of a multibody system. The simulation results of the mathematical model description are considered as the behavioral model description, e.g. the trajectories of position and velocity of the bodies.

Coupling of models in the behavioral model description is referred to as simulator coupling or modular simulation. The simulation of the global system is realized by a time discrete linker and scheduler which combines the inputs and outputs of the corresponding subsystems and establishes communication between the subsystems to discrete time instants. Therefore, it is possible to use different software packages for each subsystem and then to link the solvers together.

2 Modular modelling

For a modular simulation the global system has to be decomposed into subsystems which are described in a block representation. The subsystems are characterized by the blocks' input vector u and output vector y. It is assumed that the ouputs have no feedback to the inputs within one block. This description can be used for the dynamical analysis

without knowledge of the internal structure. A representation by the well known "black-box" is used which allows access to the system only by means of the input and output terminals, see Figure 2.
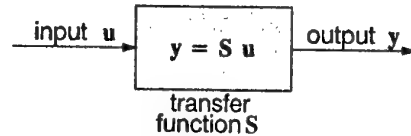
Figure 2: Black box for modular modelling

Then, the global system consists of different subsystems with interconnections between the corresponding blocks, see Figure 3.
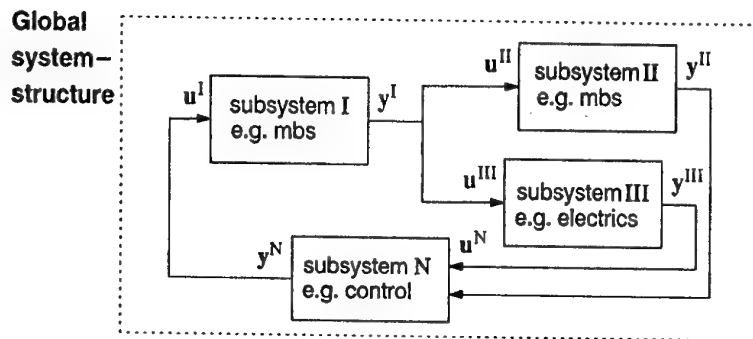
Figure 3: Global system structure

On this basis systems are classified into feed-through, which means that input changes result in output changes without time delay by internal dynamics, and no feed-through systems. If any interconnections result in a closed loop of feed-through subsystems, then an algebraic loop does exist which does not allow explicit determination of all inputs. In this case an additional numerical solution of these algebraic loops is necessary.

3 Simulator coupling

There are two options for the simulation of systems given in the previously mentioned modular description. On one hand simulation tools which are based on this description, often referred to as block simulators, can be used, such as ACSL [6] or SIMULINK [5]. On the other hand it is possible to couple different simulation tools. The advantage of block simulators is the use of standard numerical integration methods with additional solution of algebraic loops if required. With a sufficiently exact solution of algebraic loops, the properties of numerical integration methods remain unchanged. The disadvantages are the requirements to supply all subsystems in one simulation tool and to use the same

numerical method for all subsystems. Coupling of simulation tools allows subsystems to be simulated by different programs avoiding the mentioned disadvantages of block simulators. But additional numerical problems may arise due to the coupling with standard solvers for each subsystem.

Simulator coupling requires that integration of each subsystem is carried out with extrapolation of the inputs, followed by the evaluation of the output equations of all subsystems. For an arbitrary number of simulators, each subsystem i can be represented by an integration and output equation written as

$$x_{k+1}^i = \Phi^i(u_k^i), \tag{1}$$
$$y_{k+1}^i = g^i(x_{k+1}^i, u_k^i), \qquad i = 1(1)N. \tag{2}$$

It is known, see Kübler [3], that zero-stability for an non-iterative simulator coupling is only guaranteed if algebraic loops do not exist between the subsystems. Otherwise, instability of the modular simulation may occur. For such a simulator coupling a method to obtain zero-stability is required. In the general case of systems with algebraic loops non-iterative solutions are not qualified.

With an iterative simulator coupling the integration of each subsystem is carried out according to the non-iterative simulator coupling with extrapolation of the inputs, followed by the coupled solution of the output equations of all subsystems. For an arbitrary number of simulators, each subsystem i can be written as

$$x_{k+1}^i = \Phi^i(u_k^i), \tag{3}$$
$$y_{k+1}^i = g^i(x_{k+1}^i, u_{k+1}^i), \qquad i = 1(1)N. \tag{4}$$

In contrast to the non-iterative approach no extrapolation is needed for the input vector u_{k+1}^i which is now found by iteration. The inputs of the output equation can be recursively eliminated, leading to a system of nonlinear algebraic equations for the outputs of the global system

$$y_{k+1} = \Psi(y_{k+1}) \tag{5}$$

which has to be solved by an iterative method for each global time step. In Figure 4 the iterative simulator coupling is illustrated for $N = 2$ subsystems.

As an iterative method the Gauss-Jacobi and Gauss-Seidel method can be used but they do not guarantee local convergence. Newton's method is locally convergent, however, the Jacobian is not available generally in coupled simulation. Consequently, a quasi-Newton method has to be applied which uses an approximation to the Jacobian. One of the most reliable quasi-Newton method's is Broyden's method, see Broyden [1], which uses a secant approximation to the Jacobian and is also locally convergent.

With the iterative method a stable modular simulation can be successfully executed. An investigation of the dynamics of a vehicle convoy with the coupled tools SIMULINK
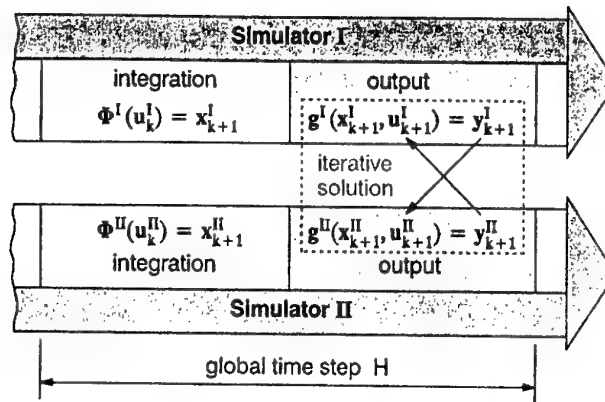
Figure 4: Iterative simulator coupling

[5], SIMPACK [2] and NEWEUL [4] showed a stable simulation result which was verified by experiments with two passenger cars, see KÜBLER [3].

4 Communication step size control

For an efficient computation of systems changing strongly their dynamic behaviour during the numerical solution there are integration methods with automatic step size control available. Therefore, nearly all simulation tools consist of such integration methods. Executing a simulator coupling it is possible to use the integration methods of each coupled tool but there is also a need to control the global time step for the communication between the subsystems.

For a communication step size control two different error estimation methods based on the classical step size control are regarded. The Richardson-extrapolation estimates an error by the difference of two solutions computed by the same integration method but with different step sizes. The error estimation based on the embedded formula uses the difference of two solutions computed by two integration methods with different integration order but the same step size.

In order to generate a communication step size control based on the embedded formula each subsystem i has to execute a global time step from t_k to t_{k+H} by two integration methods Φ and Ω of different order, see Figure 5.

At the end of this time step the difference of the new input values serves for the error estimation written as

$$err_{mr} = \| \ \hat{u}(t_k + H, \Phi) - \bar{u}(t_k + H, \Omega) \ \| \ . \tag{6}$$

For the communication step size control based on the embedded formula the subsystems need additional information, an access to the system only by means of the input

208
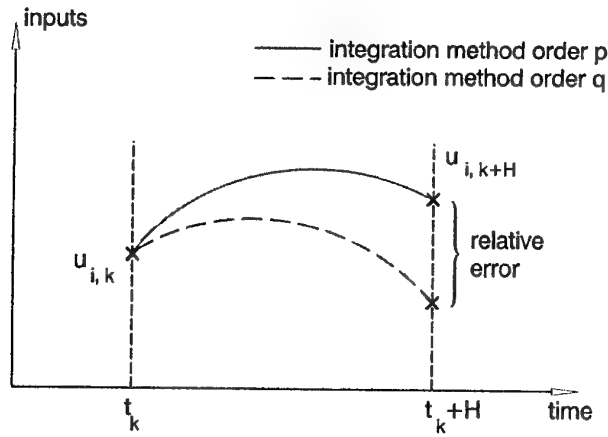
Figure 5: Embedded Formula

and output terminals can not be guaranteed. Accordingly, the defined requirements for a simulator coupling can not be met.

For a communication step size control based on the Richardson-extrapolation each subsystem i has to execute a global time step from t_k to t_{k+H} by one integration method with two different step sizes, see Figure 6.
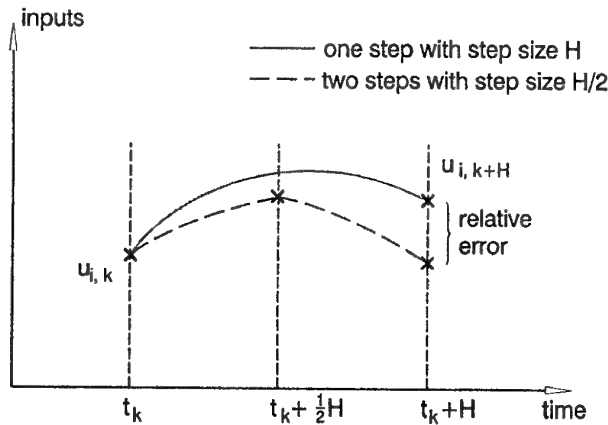
Figure 6: Richardson-Extrapolation

At the end of this time step the difference of the new input values serves for the error estimation leading to

$$err_{mr} = \| \, \boldsymbol{u}_H(t_k + H) - \boldsymbol{u}_{2\text{x}H/2}(t_k + H) \, \| \, . \tag{7}$$

In contrast to the embedded formula, the requirement not to interfere with the coupled tools is met. In Figure 7 the iterative simulator coupling with added communication step size control based on the Richardson-extrapolation is illustrated for $N = 2$ subsystems.
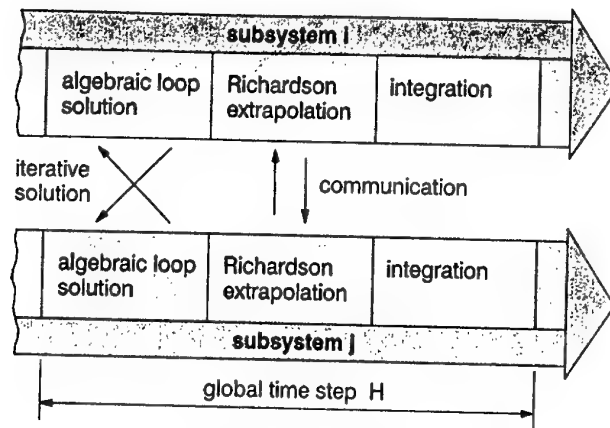
Figure 7: Simulator coupling procedure

5   Test example

The considered model of a vehicle suspension on a flexible track is illustrated in Figure 8. The model consists of a wheel mass which is connected by a spring-damper-combination to the vehicle body and by a second spring to the track mass connected by a third spring to the ground. This global system is decomposed into two subsystems. The first subsystem consists of the spring-damper-combination c_1, d_1, the wheel mass m_1 and the second spring c_2. The second subsystem consists of the track mass m_2 and the third spring c_s. Both subsystems are connected via a node point. The node motions as well as the force acting on the node are exchanged by the corresponding inputs and outputs of each subsystem, see Figure 8.

The simulation experiment setup with the given parameters illustrates Figure 9. With the given parameters the two eigenfrequencies of the system follow as $f_{eig,1} \approx 20Hz$ and $f_{eig,2} \approx 1.6kHz$. With this large difference in the two frequency values the coupled modules are characterized by large differences in their eigendynamic properties. Both subsystems are modelled with the tool NEWEUL [4] which generates the equations of motion. For the simulation the tool NEWMOS [7] was applied. Both subsystems use the Runge-Kutta integration method of 4. order with a local step size $h = 10^{-5}$ and the inputs are extrapolated by a method of 3. order. The error barriers for the control of the global time step are chosen as 10^{-3} for the relative and absolute error.

Comparing computations with and without communication step size control the difference of the computation time can be determined. The simulation time with variable global step size is about $t_{sim} \approx 8s$ while the computation time with fixed global step size $H = h$ requires about $t_{sim} \approx 29s$. Changing the parameters resulting in a model with similar eigenfrequencies a reduction of computation time has not been observed. Accordingly an increase of efficiency can be expected in particular for subsystems described by large differences in their eigendynamics.
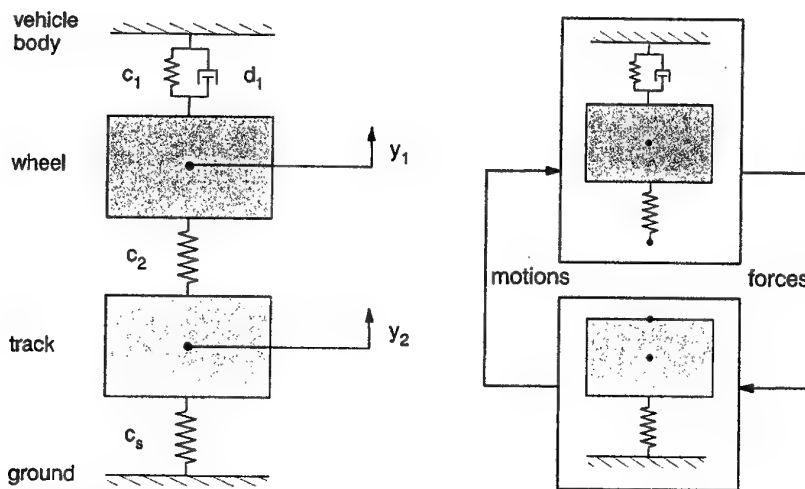
Figure 8: Model setup and decomposition

Regarding the properties of the communication step size control the global time step depends on the inputs of each module. For example, the size of the global time step depends mainly on the exchanged force acting on the node and less on the motion of the node. Figure 10 illustrates the behaviour of the spring force and the corresponding global time step.

The global time step adapts to large values in case of small force value changes. Vice versa having large changes of the force value small global time steps have to be used. Knowing the same behaviour from integration step size control the functionality of the communication step size control is approved by plausibility.

6 Summary

A block representation of mechatronic systems is presented in order to decompose a global system into subsystems. Then, the subsystems are coupled by interconnecting their inputs and outputs. Based on that a modular simulation can be executed.

The dynamical analysis of the global system is realized by a time discrete linker and scheduler which combines the inputs and outputs of the corresponding subsystems and establishes communication between them. This modular simulation is stabilized by the iterative simulator coupling method. An increase of the numerical efficiency by an automatic communication step size control can be achieved. Therefore, two methods of step size control are discussed, and one of them is recommended for engineering applications.

The method proposed for modular modeling and simulation is applied for a vehicle supension on a flexible track. The advantages of the communication step size control are clearly described by this example. Thus, a communication step size control is recom-

Parameters

$$m_1 = 1.0e02 \quad \text{kg}$$
$$c_1 = 2.0e04 \quad \text{N/m}$$
$$d_1 = 1.0e03 \quad \text{Ns/m}$$
$$c_2 = 1.5e06 \quad \text{N/m}$$
$$m_2 = 1.0e02 \quad \text{kg}$$
$$c_s = 1.0e10 \quad \text{N/m}$$
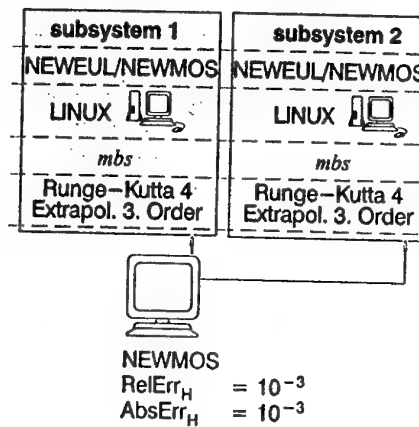
Figure 9: Simulation parameters and setup

mended for all kind of mechatronic systems.

Bibliography

[1] **Broyden, C.G.**: Solving Nonlinear Simultaneous Equations. Mathematics of Computation, Vol. 19, 1965, pp. 577–593.

[2] **INTEC GmbH**: SIMPACK User's Manual. Wessling, 1998.

[3] **Kübler, R.**: Modulare Modellierung und Simulation mechatronischer Systeme. Fortschritt-Berichte VDI, Reihe 20, Nr. 327. Düsseldorf: VDI Verlag, 2000.

[4] **Leister, G.**: Programmsystem NEWEUL'92. Stuttgart: Universität, Institut B für Mechanik, Anleitung AN-32, 1993.

[5] **The Mathworks Inc.**: SIMULINK User's Manual. 1996.

[6] **Mitchell & Gauthier Assoc.**: ACSL Newsletter, Concord, 1985.

[7] **Rükgauer, A.**: Modulare Simulation mechatronischer Systeme mit Anwendung in der Fahrzeugdynamik. VDI-Fortschrittberichte, Reihe 20, Nr. 248. Düsseldorf: VDI Verlag, 1997.
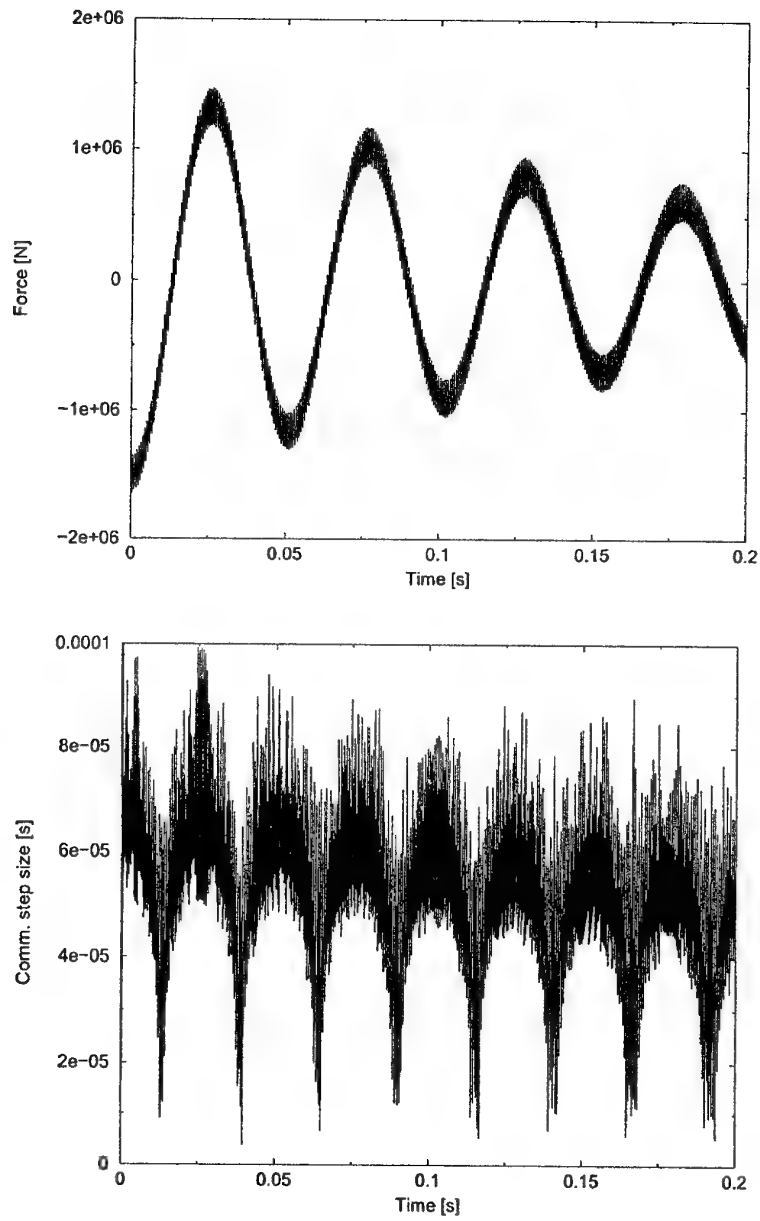
Figure 10: Simulation results

Simulation of Railway Vehicles:
Necessities and Applications

Schupp Gunter (gunter.schupp@dlr.de)
Institute of Aeroelasticity, German Aerospace Center, Germany

1. Introduction

Virtual prototyping, comprising computational simulation and computational design, represents an efficient way to reduce costs and time of development for new vehicles simultaneously. To reach this goal in the field of railway vehicles, an efficient modelling and simulation of complex wheel–rail systems performing arbitrary manoeuvres under arbitrary conditions is necessary. The growing and often contradictory demands for a reduction of travel times, lower energy consumption, low–noise and environment–friendly railway traffic etc., require for unconventional solutions in modern and future railways designs far away from the traditional wheelset. Examples for already applied or potential future design principles are independently suspended wheels, driven, steered or slip controlled. Mechatronic components for the application of car body tilting techniques and/or active/semi–active suspension elements to increase ride comfort may help further. Accordingly, a modern simulation tool must enable the engineer to examine and to design the more traditional as well as those modern design principles.

The paper relates to the multibody system simulation software SIMPACK with the main focus being on the simulation of wheel–rail systems; thereby the mentioned demands for a modern simulation tool will be emphasized. Besides a short overview over multibody simulation and the wheel–rail functionality two challenging applications are presented.

2. Modelling of Railway Vehicles

The *multibody system* (MBS) approach is a powerful and widely used method for the description and examination of the system dynamics of mechanical systems and particularly of vehicle systems. To avoid the time consuming and error–prone task of compiling the mathematical model as system of equations by hand, different professional software packages built upon this approach are commercially available. They provide the engineer not only with software tools for the model set up but usually also allow to apply a wide range of different numerical algorithms for an extensive analysis of the automatically generated system equations in a way optimized on the specific modelling and on the simulation task. As indicated in figure 1, the simulation of railway vehicles requires the simulation software to provide additionally some wheel–rail specific functionalities like the guidance along arbitrary tracks or the modelling of the complicated interaction between wheel and rail. An overview over simulation software within the scope of vehicle dynamics is given in [4], whereas [2] is dedicated to wheel–rail systems only. The following software specific descriptions are based on the simulation package SIMPACK, [7].

For analyzing the dynamic behaviour of railway vehicles running on arbitrary tracks under arbitrary manoeuvres, usually the vehicle (and the maybe necessary environment) is abstracted basically as a multibody system which is encircled eventually by appropriate software tools of the CAE–family (CAE – Computer Aided Engineering) to reproduce specific phenomena.

214
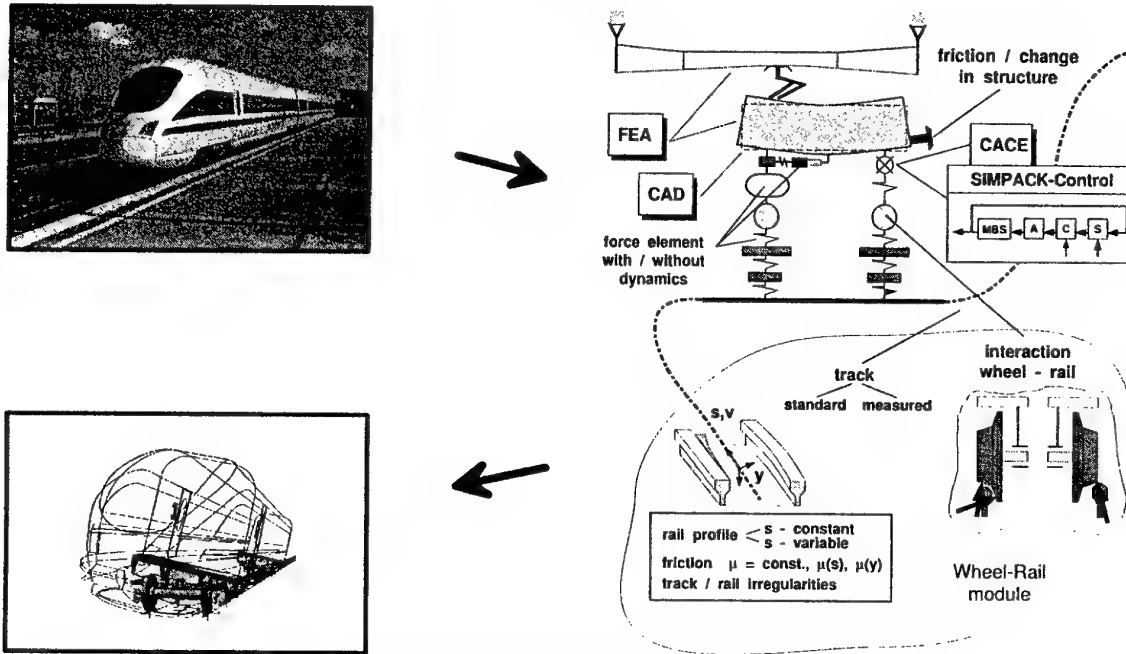
Figure 1. Algorithmic software elements typically applied within simulation models for the analysis of the running behaviour of railway vehicles and basing on an MBS approach (Photograph: C. Splittgerber, Internet: http://mercurio.iet.unipi.it).

Modelling primary (wheelset – bogie) and secondary (bogie – car body) suspensions of railway vehicles, the complete spectrum of linear and nonlinear force elements might come into operation. Typical examples of force elements to be modelled are leaf and flexi–coil springs, air–springs and damper elements with rubber bearings.

Two cars usually interact via buffers and/or a draw–gear, [6]. Buffers sometimes are in contact, sometimes they are not; if they are, friction between spherical surfaces including stick–slip effects has to be taken into account.

An interface to Finite–Element–software (FEA) allows the efficient modelling of flexible bodies within the MBS – a modelling task becoming more and more important with regard to the growing trend to lightweight structures, see e.g. [8]. With respect to the other way round, a dynamic stress analysis with the FEA–software might be based on the dynamic forces and accelerations following from a time–integration of the system equations, [1].

More and more actively controlled elements like actuators or tilting technique are implemented in vehicles to increase for example ride comfort or safety. To incorporate active/semi–active elements into the simulation models in a mechatronic sense, either internal controller design tools or interfaces to CACE–software like MATLAB–Simulink can be applied, [9].

To integrate physical and graphical CAD–data, and thus extending the graphical abilities of simulation and concurrently making MBS–setup very much easier, faster and more secure, an interface to CAD–software exists. Vice versa MBS–simulation might be used to support the design process within CAD–software itself by dynamic and kinematic analysis.

One characteristic feature of railway vehicles is the guidance of the vehicle along arbitrary tracks. Additionally, irregularities from those ideal tracks have to be considered usually. In both cases, the modelling possibilities should include standard models to be defined easily as well as the definition of realistic tracks/perturbations by measured data.

A vehicle crossing a switch is a simulation task, where the usual assumption of a non–varying profile of the rail's cross–sections is not sufficient to reproduce motions and most notably the

215
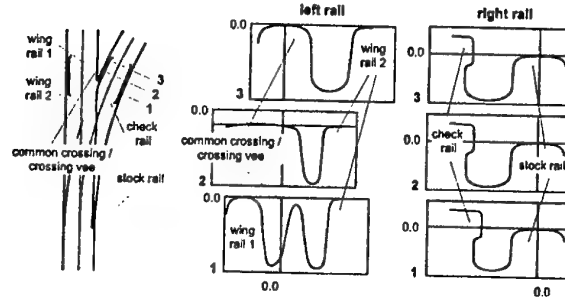
Figure 2. Switch defined by rail profiles, varying along the track: Top view and selected cross sections in the vicinity of the common crossing.

interacting forces in the wheel–rail interface satisfactorily. Hence it should be possible to define rail profiles varying along the track, [5]. Figure 2 presents the geometry of a typical switch by top view and some different cross-sections of the rails in the vicinity of the crossing vee (1), and at the end of the switch (2, 3).

3. Modelling the Wheel–Rail Interface

The distinctive feature of railway vehicles and their simulation is the contact between steel wheel and steel rail. For modelling vehicles with the traditional wheelset and vehicles with singly suspended wheels, a general wheel–rail contact module describing basically the contact between one wheel and the rail is a prerequisite. In the sequel, a wheel–rail functionality based on this idea will be pointed out; a more detailed description is given in [5] and [7].

3.1. System equations

Interpreting the interaction between wheel and rail as rigid, i.e. as *kinematic constraint*, the equations of motion of the wheel–rail system could be formulated in the position coordinates $\mathbf{p}(t)$ and the velocity coordinates $\mathbf{v}(t)$ as Lagrange equations of the first kind, yielding a *differential–algebraic* system (DAE)

$$\dot{\mathbf{p}} = \mathbf{v} \tag{1}$$

$$\mathbf{M}(\mathbf{p}, t)\,\dot{\mathbf{v}} = \mathbf{f}(\mathbf{p}, \mathbf{v}, \boldsymbol{\lambda}, t) - \mathbf{G}^T(\mathbf{p}, t)\,\boldsymbol{\lambda} \tag{2}$$

$$\mathbf{0} = \mathbf{g}(\mathbf{p}, t) . \tag{3}$$

Herein, the algebraic constraints (3) describing the contact conditions are coupled to the dynamic equations (2) by the Lagrangian multipliers $\boldsymbol{\lambda}(t)$. The constraint forces $-\mathbf{G}^T(\mathbf{p}, t)\,\boldsymbol{\lambda}$ with $\mathbf{G}(\mathbf{p}) := \partial \mathbf{g}(\mathbf{p})/\partial \mathbf{p}$ guarantee the kinematic constraints to be always fulfilled. The force vector $\mathbf{f}(\mathbf{p}, \mathbf{v}, \boldsymbol{\lambda}, t)$ comprises all applied forces (including coriolis forces etc.), thus encompassing the friction forces between wheel and rail which depend directly on the constraint forces $\boldsymbol{\lambda}(t)$, too. The symmetric mass matrix is denoted $\mathbf{M}(\mathbf{p})$.

3.2. The quasi-elastic contact model

Due to rotational symmetry, the position of a wheel as a rigid body with respect to the rail might be described uniquely by the five coordinates $\mathbf{q}(\mathbf{p}, t) = (x, y, z, \varphi, \psi)^T$, see figure 3, left. Introducing the distance function $d(s, \mathbf{q})$, that measures the distance of two corresponding points on the wheel's and the rail's profile cross sections in the normal z-direction, the geometry

216
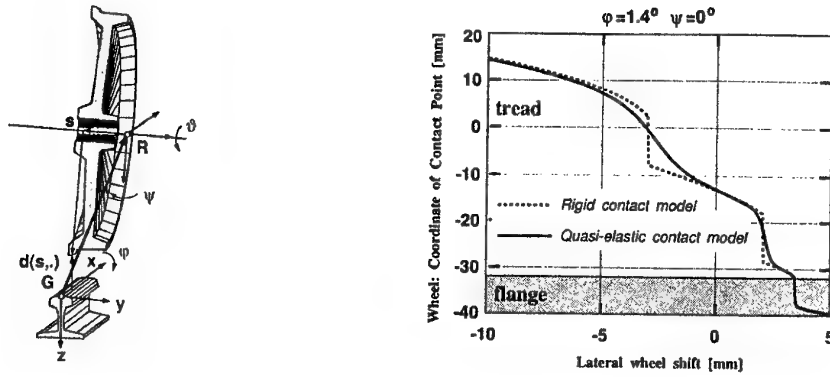
Figure 3. *Left*: Relative coordinates of a wheel with respect to the rail. *Right*: Lateral location $\bar{s}$ of the point of contact on the wheel in dependency of the relative lateral shift between wheel and rail (profiles: UIC60/S1002).

problem can be reduced to a one–dimensional one. This leads to the classical contact condition

$$g(\mathbf{q}) \ = \ \max_s d(s, \mathbf{q}) \ = \ 0 \ . \tag{4}$$

Since the relative position vector $\mathbf{q}$ as well as the contact coordinate s depends on the MBS coordinates $\mathbf{p}$, this contact condition defines the kinematic constraint in equation (3). Thus, the point of contact follows from the necessary condition $\partial d(s, \mathbf{q})/\partial s = 0$.

The crucial point for the simulation of wheel–rail systems is the differentiability of equation (4). For so–called 'wear profiles[1]' the location of the contact point is discontinuous with respect to $\mathbf{q}$, see figure 3. Hence, the usual smoothness assumptions of the integration algorithm are violated by this constraint. To overcome this difficulty, a new numerical analysis was developed in [5]. Here, the elastic deformation of the wheel–rail interface is taken into account on the whole contact patch qualitatively. Such a *quasi–elastic* contact model avoids unrealistic step changes of the contact point location which are known from classical rigid contact models.

The contact condition (4) is replaced by

$$g(\mathbf{q}) \ = \ \varepsilon \ln \left(\int_{s_{\min}}^{s_{\max}} \exp(\frac{1}{\varepsilon} d(s, \mathbf{q})) \, ds \ / \int_{s_{\min}}^{s_{\max}} ds \right) \ = \ 0, \tag{5}$$

with a small positive parameter ε. With the weighting function $w(s, \mathbf{q}) := \exp(d(s, \mathbf{q})/\varepsilon)$ the straightforward generalization of defining the contact point where the contact forces act, leads then to the formula of the weighted mean value of the contact coordinate s,

$$\bar{s} \ = \ \int_{s_{\min}}^{s_{\max}} s \cdot w(s, \mathbf{q}) \, ds \ / \int_{s_{\min}}^{s_{\max}} w(s, \mathbf{q}) \, ds \ . \tag{6}$$

The success of this quasi–elastic contact model is verified on the right hand side of figure 3, showing the smoothed wheel contact coordinate $\bar{s}$ versus the relative lateral wheel–shift y in comparison to the steep gradients in the vicinity of the jumps of the rigid contact model.

Further, the computation time of the dynamic simulation might be reduced drastically by the approximation of contact parameters with three–dimensional tensor–product splines. For that purpose, the spline coefficients of the contact point location, the constraint and the frictional parameters are computed during model setup in a *pre–processing* step and stored on table files. Then, during simulations, only these tables have to be evaluated.

---

[1] Wear profiles represent the long time evaluation of the shape of wheel and rail surfaces due to wear caused by the process of rolling contact.
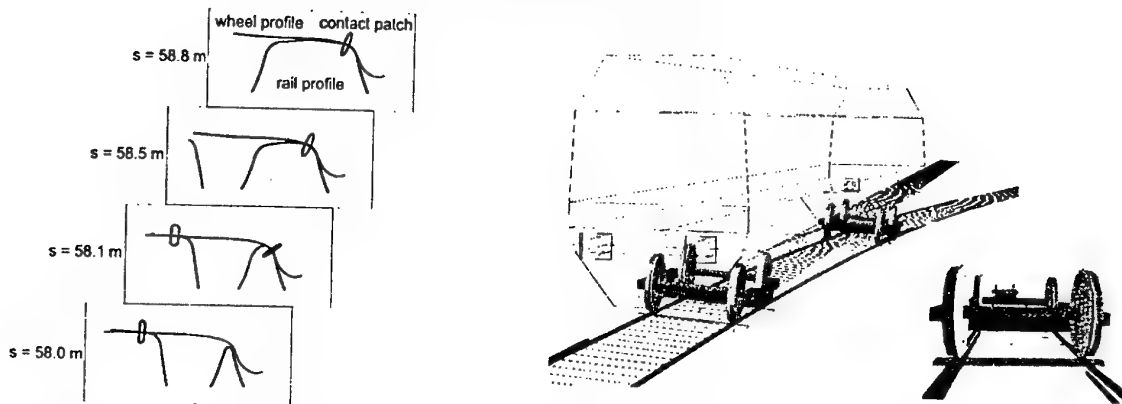
Figure 4. Passenger car running through a switch. *Left:* Contact patches between left wheel and running rail in the vicinity of the crossing vee. *Right:* Snap-shot of simulation model with leading bogie entering the common crossing and the inner wheels being guided by the check rail (large – back view, small – front view).

The contact forces are subdivided into normal forces and tangential friction (slip) forces. Formulating the algebraic constraint condition (3) appropriately, the normal force follows directly from the generalized constraint forces $-\mathbf{G}^T \boldsymbol{\lambda}$ of the equations of motion (1)–(3). The calculation of the tangential creep forces is based on Hertzian contact properties and usually performed by the code FASTSIM which applies Kalkers simplified theory of rolling contact, [3].

4. Exemplary Simulation Task

Multibody simulation has gained a wide field of application not only within research but also within industry. As an application, the simulation of a *passenger car running through a switch* has been chosen, following [5, 6]. In the lecture, simulations of a bogie with tilting technique and an active suspension system will be described additionally.

The simulation of a railway vehicle running through a switch as shown in figure 4 requires a couple of rather unusual features. Firstly, the profile cross sections of the rails vary along the track, see figure 2. Secondly, multiple points of contact have to be expected, primarily when the contact point on the left wheel changes from the wing rail to the crossing vee, see figure 4. Thirdly, during this transition, the wheel may lift-off from the rail, a structural change handled by switching from the rigid to an elastic contact model. Throughout this situation, the wheelset is guided by the contact of the back of the right wheel with the check rail; hence, fourthly, an additional contact element between the back of wheels and check/wing rails is necessary. Exemplary simulation results are presented in figure 5.

5. Conclusions

A generally applicable simulation tool was presented with the main focus on the analysis and design of arbitrary wheel–rail systems. Due to the described wheel–rail module, the potential modelling range comprises the classical rigid wheelset and singly suspended wheels as well. Interfaces to established CAD–, FEA– and CACE–software facilitate to meet simulation tasks arising from the growing application of rather new design principles further – and sometimes only their extensive application allows to fulfil them at all. A simulation study of a passenger car running through a switch as a highly complicated exemplary application demonstrates the efficiency and applicability of the MBS–software as well as of the incorporated wheel–rail module.

218
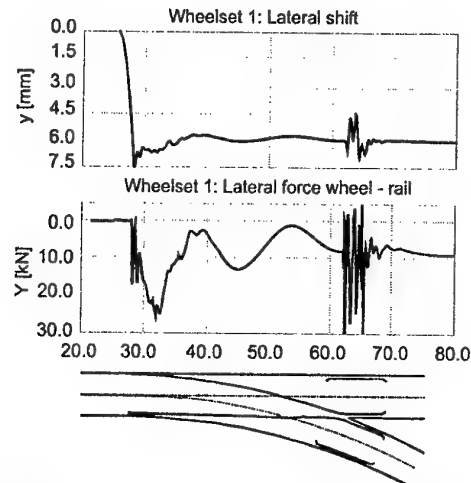
Figure 5. Passenger car running through a switch with velocity $v = 60\,\mathrm{km/h}$. Results of simulation, leading wheelset: Lateral shift with respect to track centre line and lateral force of wheelset towards track.

In the lecture, as second example the design of a modern passenger car bogie including tilting technique and an active suspensions system will be described.

References

1. Dietz, S.: 1999, *Vibration and Fatigue Analysis of Vehicle Systems Using Component Modes*, Fortschritts-berichte VDI Reihe 12 (Verkehrstechnik/Fahrzeugtechnik), Nr. 401. Düsseldorf: VDI Verlag.
2. Iwnicki, S. (ed.): 1999, *The Manchester Benchmarks for Rail Vehicle Simulation*, Vol. 31 of *Supplement to Vehicle System Dynamics*. Lisse: Swets & Zeitlinger.
3. Kalker, J. J.: 1990, *Three–Dimensional Elastic Bodies in Rolling Contact*. Kluwer Academic Publishers, Dorndrecht, Boston, London.
4. Kortüm, W. and R. S. Sharp (eds.): 1993, *Multibody Computer Codes in Vehicle System Dynamics*, Vol. 22 of *Supplement to Vehicle Sytem Dynamics*. Amsterdam: Swets & Zeitlinger.
5. Netter, H.: 1998, *Rad–Schiene–Systeme in differential–algebraischer Darstellung*, Fortschrittsberichte VDI Reihe 12 (Verkehrstechnik/Fahrzeugtechnik) Nr. 352. Düsseldorf: VDI Verlag.
6. Netter, H., G. Schupp, W. Rulka, and K. Schroeder: 1997, 'New Aspects of Contact Modelling and Validation within Multibody System Simulation of Railway Vehicles'. In: *The Dynamics of Vehicles on Roads and Tracks*, 15th *IAVSD-Symposium, Budapest, Hungary, 1997.*
7. Rulka, W.: 1998, 'Effiziente Simulation der Dynamik mechatronischer Systeme für industrielle Anwendun-gen'. Ph.D. thesis, Technical University of Vienna, Faculty of Mechanical Engineering. (Also: Internal Report IB 532–01–06, DLR – Deutsches Zentrum für Luft– und Raumfahrt Oberpfaffenhofen, Abteilung Fahrzeug–Systemdynamik, D–82230 Wessling).
8. Stribersky, A., F. Moser, and W. Rulka: 2000, 'Structural Dynamics of Rail Vehicle Systems: A Virtual Systems Approach'. In: *5th International Conference on Computational Structures Technology, Leuven, Belgium.*
9. Stribersky, A., S. Steidl, H. Müller, and B. Rath: 1995, 'On Dynamic Analyses of Rail Vehicles with Electron-ically Controlled Suspensions'. In: *The Dynamics of Vehicles on Roads and Tracks*, 14th *IAVSD-Symposium, Ann Arbor, 1995.* pp. 614–628.

Address for Offprints:
German Aerospace Center
Institute of Aeroelasticity
Vehicle System Dynamics
P.O.Box 1116
D – 82230 Wessling
Germany

HOW TO LINEARIZE YOUR NON-HOLONOMIC MULTIBODY SYSTEM

A. L. SCHWAB AND J. P. MEIJAARD

Laboratory for Engineering Mechanics
Delft University of Technology
Mekelweg 2
NL-2628 CD Delft
The Netherlands
E-mail: a.l.schwab@wbmt.tudelft.nl

Abstract. In this paper it is shown how non-holonomic constraints can be included in the formulation of the dynamic equations of flexible multibody systems. The equations are given in state space form with the degrees of freedom, their derivatives and the kinematic coordinates as state variables, which circumvents the use of Lagrangian multipliers. With these independent state variables for the system the derivation of the linearized equations of motion is straightforward. The incorporation of the method in a finite element based program for flexible multibody systems is discussed. The method is illustrated by a stability analysis of the nominal steady motion of a swivel wheel.

1. Introduction

The motion of mechanical systems having rolling contact, as occur in road vehicles and track-guided vehicles, can be investigated in an approximate way by a mechanical model having non-holonomic constraints. These constraints express the conditions of vanishing slips at the contact points. Whereas the dynamics of mechanical systems with ideal holonomic constraints was almost completed by the publication of Lagrange's monumental *Méchanique analitique* [1], Hertz [2] was the first to describe and name systems with non-holonomic constraints. Although the principle of minimal action fails for these systems, the principle of virtual power and the principle of D'Alembert can be applied. In their excellent book [3] Neĭmark and Fufaev treat the kinematics and dynamics of non-holonomic mechanical systems in great detail. They illustrate the presented theory with worked-out examples and give an elaborate reference list with 513 items.

The study of small vibrations and stability of conservative non-holonomic systems near equilibrium states has lead to some controversy in the past. Whittaker in his *Analytical Dynamics* [4, Section 90] concluded that for such cases "the difference between holonomic and non-holonomic systems is unimportant" and that the vibration motion of a given non-holonomic system with n independent coordinates and m non-holonomic constraints is the same as that of a certain holonomic system with $n - m$ degrees of freedom. Bottema [5] showed that this was incorrect, and pointed out that the characteristic determinant of such a non-holonomic system is asymmetric and that the corresponding characteristic equation possesses as many vanishing roots as there are non-holonomic constraints. However, besides a manifold of equilibrium states, some non-holonomic systems also possess a manifold of steady motion. Due to these motions some vanishing roots may get non-zero values.

220

In this paper we pesent a procedure for including non-holonomic constraints in the formulation of the dynamical equations of flexible multibody systems. These equations are given for a set of minimal coordinates rather than with the aid of Lagrangian multipliers. The configuration is described by the degrees of freedom and the generalized kinematic coordinates, as many as there are non-holonomic constraints. The velocities of the system are described by the time derivatives of the degrees of freedom. The dynamical equations in a state space form comprise the equations of motion and the kinematic differential equations, which give the time derivatives of the configuration coordinates.

The derivation of the linearized equations from the dynamical equations is rather straightforward. The linearized equations can be used to analyse, among other things, the stability of a nominal steady motion, as will be shown in an example.

2. Dynamics of Non-Holonomic Flexible Multibody Systems

2.1. FINITE ELEMENT MODELLING

Multibody systems with deformable bodies may well be modelled by finite elements. The distinguishing point in the finite element approach as it has been developed in Delft and implemented in the program SPACAR [6] is the specification of independent deformation modes of the finite elements, the so-called generalized deformations or generalized strains. These are the algebraic analogue to the continuous field description of deformations. Rigid body motions are displacements for which the generalized strains are zero. If the specification of the generalized strains remains valid for arbitrary large translations and rotations, rigid multibody systems such as mechanisms and machines can be analysed by setting all generalized strains to zero. These strain equations are now the constraint equations which express rigidity. Deformable bodies are handled by allowing non-zero strains and specifying constitutive equations for the generalized stresses, which are the duals of the generalized strains.

Instead of imposing constraint equations for the interconnection of bodies, which is a widespread approach in multibody system dynamics formalisms, permanent contact of elements is achieved by letting them have nodal points in common. With the help of a rather limited number of element types it is possible to model a wide class of systems. Typical types of elements are beam, truss and hinge elements, while more specialized elements can be used to model joint connections and transmissions of motion.

2.2. HOLONOMIC AND NON-HOLONOMIC CONSTRAINTS

In a finite element description of a multibody system the configuration is described by a number of nodal points with coordinates $\mathbf{x}$ and a number of elements with generalized deformations or generalized strains ε. The nodal coordinates can be absolute coordinates of the position or parameters that describe the orientation of the nodes, such as Euler parameters. The generalized deformations depend on the nodal coordinates and can be expressed as

$$\varepsilon = \mathbf{D}(\mathbf{x}). \tag{1}$$

Usually holonomic constraints are imposed on some generalized deformations and nodal coordinates. For instance, the conditions for rigidity of element e are $\varepsilon^e = \mathbf{D}^e(\mathbf{x}^e) = \mathbf{0}$. If the holonomic constraints are consistent, the coordinates can locally be expressed as functions of the generalized coordinates $\mathbf{q}$ by means of a transfer function $\mathbf{F}$ as

$$\mathbf{x} = \mathbf{F}(\mathbf{q}, t). \tag{2}$$

The prescribed motions, or rheonomic constraints, which are known explicit functions of time, are represented here by the time t. The generalized coordinates can be chosen from components of the nodal coordinate vector $\mathbf{x}$ and the generalized deformation vector ε. Generally the transfer function cannot be calculated explicitly, but has to be determined by solving the constraint

221

equations numerically in an iterative way. Partial derivatives are calculated by means of implicit differentiation.

The non-holonomic constraints, as may arise from elements having idealized rolling contact, can be expressed in terms of slips that are zero [9]. Such a slip is usually defined as some relative velocity between the two bodies in the contact area, and is therefore linear in the velocities. For instance, if element e has non-slipping contacts, it has to satisfy the constraints $\mathbf{s}^e = \mathbf{V}^e(\mathbf{x}^e)\dot{\mathbf{x}}^e = \mathbf{0}$. Assembly of all conditions of zero slip for the system results in the non-holonomic constraints

$$\mathbf{s} = \mathbf{V}(\mathbf{x})\dot{\mathbf{x}} = \mathbf{0}. \tag{3}$$

Owing to these constraints, the generalized velocities $\dot{\mathbf{q}}$ are now dependent. This dependency is expressed by a splitting of the generalized coordinates $\mathbf{q}$ into the degrees of freedom $\mathbf{q}^d$ and the generalized kinematic coordinates $\mathbf{q}^k$. The velocities of the system can now be expressed in terms of the first-order transfer function $\mathbf{H}$ times the velocities of the degrees of freedom and a term representing the prescribed motion, as in

$$\dot{\mathbf{x}} = \mathbf{H}(\mathbf{q},t)\dot{\mathbf{q}}^d + \mathbf{v}(\mathbf{q},t). \tag{4}$$

The expressions for the first-order transfer function and the prescribed motion terms are found by differentation of (2) and splitting of terms as in

$$\dot{\mathbf{x}} = \mathbf{F}_{,\mathbf{q}^d}\dot{\mathbf{q}}^d + \mathbf{F}_{,\mathbf{q}^k}\dot{\mathbf{q}}^k + \mathbf{F}_{,t}, \tag{5}$$

where partial derivatives are denoted by a subscript comma followed by the variable. Substitution in the non-holonomic constraints (3) results in

$$\mathbf{V}[\mathbf{F}_{,\mathbf{q}^d}\dot{\mathbf{q}}^d + \mathbf{F}_{,\mathbf{q}^k}\dot{\mathbf{q}}^k + \mathbf{F}_{,t}] = \mathbf{0}. \tag{6}$$

From these equations, as many as there are kinematic coordinates $\mathbf{q}^k$, the velocities $\dot{\mathbf{q}}^k$ can be solved as

$$\dot{\mathbf{q}}^k = -(\mathbf{V}\mathbf{F}_{,\mathbf{q}^k})^{-1}[\mathbf{V}\mathbf{F}_{,\mathbf{q}^d}\dot{\mathbf{q}}^d + \mathbf{V}\mathbf{F}_{,t}]. \tag{7}$$

Substitution of this result in (5) and comparing terms with (4) results in the first-order transfer function

$$\mathbf{H} = [\mathbf{I} - \mathbf{F}_{,\mathbf{q}^k}(\mathbf{V}\mathbf{F}_{,\mathbf{q}^k})^{-1}\mathbf{V}]\mathbf{F}_{,\mathbf{q}^d}, \tag{8}$$

and the velocities $\mathbf{v}$, representing the prescribed motion, as

$$\mathbf{v} = [\mathbf{I} - \mathbf{F}_{,\mathbf{q}^k}(\mathbf{V}\mathbf{F}_{,\mathbf{q}^k})^{-1}\mathbf{V}]\mathbf{F}_{,t}. \tag{9}$$

In both expressions we identify the use of the inverse of the Jacobian of the non-holonomic constraints with respect to the generalized kinematic coordinates

$$\mathbf{V}\mathbf{F}_{,\mathbf{q}^k}. \tag{10}$$

If this Jacobian is singular, we have to choose another set of generalized kinematic coordinates and consequently another set of degrees of freedom to describe the system uniquely. Having taken into account all constraints we can define the state of the system at a time t as

$$(\dot{\mathbf{q}}^d, \mathbf{q}^d, \mathbf{q}^k). \tag{11}$$

Next we will derive the dynamical equations of the system, or, in other words, the time derivative of the state of the system.

2.3. EQUATIONS OF MOTION

The derivative of the first part of the state vector, $\dot{\mathbf{q}}^d$, with respect to time follows from the equations of motion of the system. The equations of motion for the constraint multibody system

222

will be derived from the principle of virtual power and the principle of D'Alembert. This method can be traced back to Lagrange who by his monumental *Méchanique analitique* [1] became the founder of the study of motion of systems of bodies. The inclusion of non-holonomic constraints was not foreseen by Lagrange. Hertz [2] was the first to describe and this type of constraints.

First for each node and element in the system, we determine a mass matrix $\mathbf{M}^e$ and a force vector $\mathbf{f}^e$, which give a contribution to the virtual power of

$$\delta\dot{\mathbf{x}}^{eT}(\mathbf{f}^e - \mathbf{M}^e\ddot{\mathbf{x}}^e) \tag{12}$$

The virtual power equation of the system is obtained by assembling the contribution of all elements and nodes in a global mass matrix $\mathbf{M}$ and a global force vector $\mathbf{f}$, which results in

$$\delta\dot{\mathbf{x}}^T[\mathbf{f}(\dot{\mathbf{x}}, \mathbf{x}, t) - \mathbf{M}(\mathbf{x})\ddot{\mathbf{x}}] = 0. \tag{13}$$

Here, $\delta\dot{\mathbf{x}}$ are kinematically admissible virtual velocities, which satisfy all instantaneous kinematic constraints. They follow directly from (4) as

$$\delta\dot{\mathbf{x}} = \mathbf{H}\delta\dot{\mathbf{q}}^d. \tag{14}$$

The coordinate accelerations are obtained by differentation of the velocities (4), resulting in

$$\ddot{\mathbf{x}} = \mathbf{H}(\mathbf{q}, t)\ddot{\mathbf{q}}^d + \mathbf{g}(\dot{\mathbf{q}}, \mathbf{q}, t), \tag{15}$$

where we have collected all convective and prescribed accelerations in the $\mathbf{g}$ terms. These accelerations, which depend only on the state of the system, are given by

$$\mathbf{g} = \mathbf{H}_{,\mathbf{q}}\dot{\mathbf{q}}^d\dot{\mathbf{q}} + \mathbf{H}_{,t}\dot{\mathbf{q}}^d + \mathbf{v}_{,\mathbf{q}}\dot{\mathbf{q}} + \mathbf{v}_{,t}. \tag{16}$$

Substitution of the acceleration (15) in the virtual power equation (13) yields the reduced equations of motion

$$\bar{\mathbf{M}}(\mathbf{q}^d, \mathbf{q}^k, t)\ddot{\mathbf{q}}^d = \bar{\mathbf{f}}(\dot{\mathbf{q}}^d, \mathbf{q}^d, \mathbf{q}^k, t), \tag{17}$$

with the reduced global mass matrix,

$$\bar{\mathbf{M}} = \mathbf{H}^T\mathbf{M}\mathbf{H}, \tag{18}$$

and the reduced global force vector,

$$\bar{\mathbf{f}} = \mathbf{H}^T[\mathbf{f} - \mathbf{M}\mathbf{g}]. \tag{19}$$

The time derivative of the second part of the state vector, $\mathbf{q}^d$, is obviously the first part of the state vector itself. The time derivative of the generalized kinematic coordinates, $\mathbf{q}^k$, as found in (7), can in general be expressed as

$$\dot{\mathbf{q}}^k = \mathbf{A}(\mathbf{q}, t)\dot{\mathbf{q}}^d + \mathbf{b}(\mathbf{q}, t), \tag{20}$$

where the matrix $\mathbf{A}$ and the velocity vector $\mathbf{b}$, which represents the velocities of the rheonomic constraints, are given by

$$\mathbf{A} = -(\mathbf{V}\mathbf{F}_{,\mathbf{q}^k})^{-1}\mathbf{V}\mathbf{F}_{,\mathbf{q}^d}, \quad \text{and} \quad \mathbf{b} = -(\mathbf{V}\mathbf{F}_{,\mathbf{q}^k})^{-1}\mathbf{V}\mathbf{F}_{,t}. \tag{21}$$

Note in both expressions the presence of the inverse of the Jacobian (10).

We summarize by writing down the time derivative of the state vector or the state equations as

$$\frac{\mathrm{d}}{\mathrm{d}t}\begin{bmatrix} \dot{\mathbf{q}}^d \\ \mathbf{q}^d \\ \mathbf{q}^k \end{bmatrix} = \begin{bmatrix} \bar{\mathbf{M}}^{-1}\bar{\mathbf{f}} \\ \dot{\mathbf{q}}^d \\ \mathbf{A}\dot{\mathbf{q}}^d + \mathbf{b} \end{bmatrix} \tag{22}$$

223

2.4. LINEARIZED EQUATIONS OF MOTION

To describe the small vibrations or motions with respect to a nominal steady motion we have to linearize the dynamical equations (22). For the description of the small motions we will use the dynamic degrees of freedom $\mathbf{q}^d$. The linearization is done in the nominal reference state which is characterized by $(\dot{\mathbf{q}}^d, \mathbf{q}^d, \mathbf{q}^k) = (\mathbf{0}, \mathbf{0}, \mathbf{q}_0^k)$, where $\mathbf{q}_0^k$ stands for the kinematic coordinates in the reference state. Linearization of the first part of the state equations (22), the reduced equations of motion (17), results in

$$\bar{\mathbf{M}}\Delta\ddot{\mathbf{q}}^d + \bar{\mathbf{C}}\Delta\dot{\mathbf{q}}^d + \bar{\mathbf{K}}^d\Delta\mathbf{q}^d + \bar{\mathbf{K}}^k\Delta\mathbf{q}^k = -\mathbf{f}^d, \tag{23}$$

where the prefix Δ denotes a small increment. $\bar{\mathbf{M}}$ is the reduced mass matrix as in (18), $\bar{\mathbf{C}}$ is the velocity sensitivity matrix which contains terms resulting from damping and gyroscopic effects, $\bar{\mathbf{K}}^d$ and $\bar{\mathbf{K}}^k$ are the total stiffness matrices. The forcing, $-\mathbf{f}^d$, on right-hand side of the equations results from the nominal steady motion solution. In order to maintain the prescribed values for the dynamic degrees of freedom and the kinematic coordinates during this motion, usually additional forces have to be introduced in the right-hand side of the reduced equations of motion (17). The sum of the reduced forces has to be zero, as in

$$\mathbf{H}^T[\mathbf{f} - \mathbf{M}\mathbf{g}] + \mathbf{f}^d = \mathbf{0}, \tag{24}$$

from which the forces $\mathbf{f}^d$ are found.

The matrices of the linearized equations are determined in the following way. First for all elements and nodes the contribution to the global stiffness matrix $\mathbf{K}$ and the global velocity matrix $\mathbf{C}$ are determined as

$$\mathbf{C}^e = -(\mathbf{f}^e)_{,\dot{\mathbf{x}}^e} \quad \text{and} \quad \mathbf{K}^e = (\mathbf{M}^e\ddot{\mathbf{x}}^e - \mathbf{f}^e)_{,\mathbf{x}^e}. \tag{25}$$

These global matrices having been determined, the matrices in the linearized equations are given by

$$\bar{\mathbf{C}} = \mathbf{H}^T\mathbf{C}\mathbf{H} + \mathbf{H}^T\mathbf{M}\mathbf{g}_{,\dot{\mathbf{q}}^d},$$
$$\bar{\mathbf{K}} = [\bar{\mathbf{K}}^d\ \bar{\mathbf{K}}^k] = \mathbf{H}^T\mathbf{K}\mathbf{F}_{,\mathbf{q}} + \mathbf{H}_{,\mathbf{q}}^T[\mathbf{M}\ddot{\mathbf{x}} - \mathbf{f}] + \mathbf{H}^T[\mathbf{M}\mathbf{g}_{,\mathbf{q}} + \mathbf{C}\mathbf{v}_{,\mathbf{q}}]. \tag{26}$$

Note that all matrices are generally a function of time due to the non-linear steady motion. Linearization of the second part of equation (22) is trivial. The last part, the linearization of the rate of the generalized kinematic coordinates is derived from (20) as

$$\Delta\dot{\mathbf{q}}^k = \mathbf{A}(\mathbf{q}, t)\Delta\dot{\mathbf{q}}^d + \mathbf{B}^d(\mathbf{q}, t)\Delta\mathbf{q}^d + \mathbf{B}^k(\mathbf{q}, t)\Delta\mathbf{q}^k. \tag{27}$$

The **B**-matrices express the sensitivity of the generalized kinematic velocities with respect to the generalized coordinates, and are given by

$$\mathbf{B}^d(\mathbf{q}, t) = \mathbf{b}_{,\mathbf{q}^d} \quad \text{and} \quad \mathbf{B}^k(\mathbf{q}, t) = \mathbf{b}_{,\mathbf{q}^k} \tag{28}$$

We conclude by summarizing the linearization of the state equations in matrix vector form as

$$\begin{bmatrix} \bar{\mathbf{M}} & \mathbf{0} & \mathbf{0} \\ \mathbf{0} & \mathbf{I} & \mathbf{0} \\ \mathbf{0} & \mathbf{0} & \mathbf{I} \end{bmatrix} \begin{bmatrix} \Delta\ddot{\mathbf{q}}^d \\ \Delta\dot{\mathbf{q}}^d \\ \Delta\dot{\mathbf{q}}^k \end{bmatrix} + \begin{bmatrix} \bar{\mathbf{C}} & \bar{\mathbf{K}}^d & \bar{\mathbf{K}}^k \\ -\mathbf{I} & \mathbf{0} & \mathbf{0} \\ -\mathbf{A} & -\mathbf{B}^d & -\mathbf{B}^k \end{bmatrix} \begin{bmatrix} \Delta\dot{\mathbf{q}}^d \\ \Delta\mathbf{q}^d \\ \Delta\mathbf{q}^k \end{bmatrix} = \begin{bmatrix} -\bar{\mathbf{f}}^d \\ \mathbf{0} \\ \mathbf{0} \end{bmatrix}. \tag{29}$$

The stability of a system in steady motion can be investigated by the homogeneous linearized state equation from (29). Under the usual assumption of an exponential motion with respect to time for the small variations $(\Delta\dot{\mathbf{q}}^d, \Delta\mathbf{q}^d, \Delta\mathbf{q}^k)^T$ we end up with a characteristic equation for the unknown exponents. The stability of an equilibrium state, the case of zero steady motion as investigated by Bottema [5], corresponds to vanishing **B**-matrices and consequently results in vanishing roots, as many as there are kinematic coordinates or non-holonomic constraints.

224

3. Example: Swivel Wheel Shimmy

To illustrate the general method for the derivation of the state equations of a non-holonomic system and their linearization we shall revisit the shimmy problem of an aircraft landing gear as treated by Den Hartog [7]. He simplified the problem in order to show the principal mechanism responsible for the shimmy phenomenon. The mass and stiffness of the airplane are assumed large with respect to those of the swivel landing wheel, so that the attachment point of the swivel axis to the airplane may be assumed to move forward at a constant speed. The tire is assumed to be rigid and the inertia along the axis of rotation of the wheel is not taken into account. Then
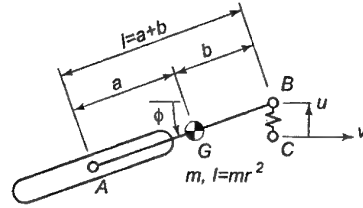
Figure 1. Swivel wheel

in Figure 1, which is a plan view of the shimmying wheel seen from above, point C is the point where the wheel strut is built into the airplane. Point B is the bottom point of the strut; normally B is right under C, but while shimmying the strut is assumed to flex sideways through distance u at a stiffness k. The wheel is behind B with angle ϕ, the shimmy angle, which is zero for normal ideal operation. A is the centre of the wheel, and G is the centre of gravity of the combined landing gear. The finite element model consists of a wheel element [9] attached in point A to a rigid beam. The wheel has zero lateral slip which is the non-holonomic condition in the system. The beam is connected in point B to a cylindrical bearing element. The bearing is rigid in the longitudinal and flexible in the lateral and rotational direction and the generalized deformations are denoted by u and ϕ. The lateral stiffness is k while the rotational stiffness is assumed to be zero. The bearing is moved forward with a constant speed of v. The generalized coordinates of the system are given by $\mathbf{q} = (u, \phi)$. The zero lateral slip condition on the wheel reduces the coordinates to the degree of freedom $\mathbf{q}^d = (u)$ and the kinematic coordinate $\mathbf{q}^k = (\phi)$. The steady state undeformed motion is characterized by $(\dot{u}, u, \phi) = (0, 0, 0)$. With the variations $\Delta\dot{\mathbf{q}}^d = \Delta\dot{u}$, $\Delta\mathbf{q}^d = \Delta u$ and $\Delta\mathbf{q}^k = \Delta\phi$, the coefficients of the linearized state derivatives according to (29) are

$$
\begin{aligned}
\bar{\mathbf{M}} &= m(\frac{a^2 + r^2}{l^2}), \\
\bar{\mathbf{C}} &= m(\frac{ab - r^2}{l^2})\frac{v}{l}, & \mathbf{A} &= \frac{1}{l}, \\
\bar{\mathbf{K}}^d &= k, & \mathbf{B}^d &= 0, \\
\bar{\mathbf{K}}^k &= -m(\frac{ab - r^2}{l^2})\frac{v^2}{l}, & \mathbf{B}^k &= -\frac{v}{l}, \\
\bar{\mathbf{f}} &= 0.
\end{aligned}
\tag{30}
$$

These coefficients are usually numerically calculated by the program but we present them here in an analytical form so we can compare them with the approach as presented by Den Hartog [7]. His ad hoc analysis leads to an eigenvalue problem. The systematically derived linearized state derivatives (30) lead to the same eigenvalue problem and consequently to the same prediction of unstable shimmy behaviour.

To investigate the shimmy motion we start with the usual assumption of an exponential motion for the small variations $\Delta\mathbf{q}$ of the form $\Delta\mathbf{q}_0 \exp(\lambda t)$. The characteristic equation of the eigenvalue problem from (29) with the coefficients from (30) is

$$
\lambda^3 + (1 + \mu)\omega\lambda^2 + \omega_n^2\lambda + \omega\omega_n^2 = 0,
\tag{31}
$$

225

with the mass distribution factor $\mu = (ab - r^2)/(a^2 + r^2)$, the driving frequency $\omega = v/l$ and the natural frequency $\omega_n = \sqrt{kl^2/(m(a^2 + r^2))}$. A neccessary and sufficient condition for asymptotic stability is given by the requirement that all roots of (31) have negative real parts. Application of Hurwitz's theorem on the characteristic equation (31) yields

$$\omega > 0 \quad \text{and} \quad \mu > 0. \tag{32}$$

In other words, the motion is stable if the driving speed v is positive and the centre of mass is positioned such that $a(l - a) > r^2$. The latter corresponds to a region of $\pm\sqrt{(l/2)^2 - r^2}$ around the midpoint $a = l/2$. For the critical case, where $a(l - a) = r^2$, there is one real eigenvalue $\lambda_1 = -\omega$ describing the non-oscillating decaying motion and a pair of conjugated imaginary values $\lambda_{2,3} = \pm\omega_n i$ which describe the undamped oscillatory solution. This critical case corresponds to a mass distribution where point B is the centre of percussion or in other words, the lateral contact force in A has no influence on the lateral spring force in B.

Eigenmode for $a/l=0.3$, $\lambda=0\pm\omega_0 i$.
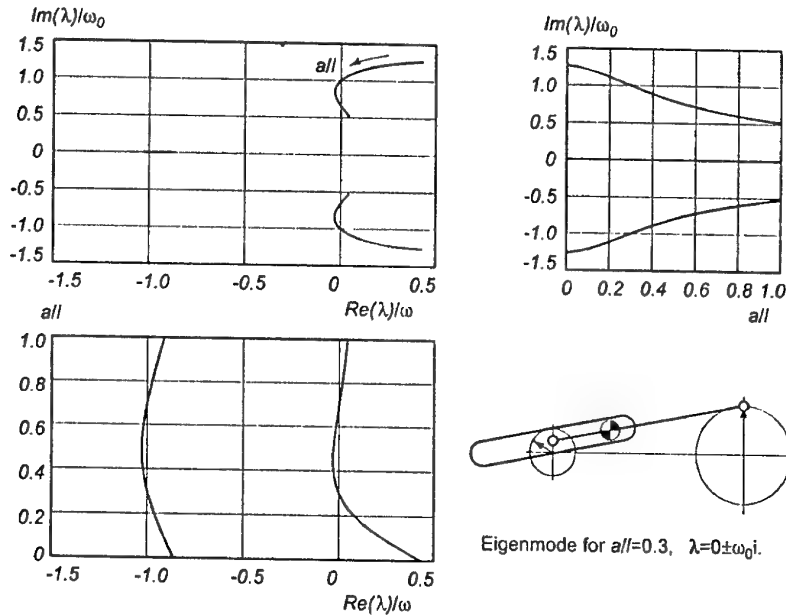
Figure 2. Root loci of the eigenvalues λ for the swivel wheel with moment of inertia $I = 0.21ml^2$ in the centre of mass position range of $0 \le a/l \le 1$ and eigenmode for the undamped oscillatory case $a/l = 0.3$, with driving frequency $\omega = v/l$ and undamped eigenfrequency $\omega_0 = \sqrt{k/(0.3m)}$.

The general solution for the eigenvalues can be found by solving the characteristic equation (31). However, the general solution of a cubic equation leads to lengthy expressions and give little insight in the nature of the solution. To illustrate the behaviour of the system at the non-critical cases, consider a swivel wheel with mass moment of inertia $I = 0.21ml^2$. The motion is stable if the centre of mass position a is between $0.3l$ and $0.7l$. The root loci for this example in range of $0 \le a/l \le 1$ are shown in Figure 2 together with the eigenmode for the undamped oscillatory case $a/l = 0.3$. The lateral displacement of the attachment point B, u, and the lateral displacement of the centre of the wheel A, denoted by w, are illustrated in the figure by the vertical projection of the rotating arrows. Note that the lateral displacements are not in phase. The phase angle, ψ, and the amplitude ratio, $\Delta w_0/\Delta u_0$, are for given eigenvalue $\lambda = \gamma_0 + \omega_0 i$ uniquely determined by the kinematic rate equation (27) and read

$$\tan\psi = -\frac{\omega_0}{\omega + \gamma_0} \quad \text{and} \quad \frac{\Delta w_0}{\Delta u_0} = \frac{\omega}{\sqrt{(\omega + \gamma_0)^2 + \omega_0^2}}. \tag{33}$$

226

The wheel centre and the attachment point are always out of phase, even in the undamped oscillatory case where $\gamma_0 = 0$.

4. Conclusion

A procedure has been described for formulating the dynamical equations of non-holonomic mechanical systems as well as their linearized equations. The procedure can be applied to systems with flexible bodies with the same ease as to systems with rigid bodies. Advantages of the procedure are the use of a set of minimal independent state variables, which avoid the use of differential-algebraic equations, and the analytic linearization, which is more accurate than numerical differentiation. The linearized equations can be used to analyse small vibrations superimposed on a rigid body motion, as is described in [8] for holonomic systems.

It is planned to apply the procedure for more general forms of rolling contact than a sharp edged disk on a surface [9], for instance the contact as occurs between wheels and rails in railway vehicles.

References

1. Lagrange, J. L., *Analytical Mechanics*, Kluwer, Dordrecht, 1997. (Original French first edition "Méchanique analitique," Desaint, Paris, 1788) (Translated from the French second edition "Mécanique analytique," Courcier, Paris, 1811, by A. Boissonnade and V. N. Vagliente)
2. Hertz, H., *Die Prinzipien der Mechanik in neuem Zusammenhange dargestellt*, Johann Ambrosius Barth, Leipzig, 1894.
3. Neĭmark, Ju. I., and Fufaev, N. A., *Dynamics of Nonholonomic Systems*, (Translated from the Russian edition, Nauka, Moscow, 1967), A.M.S., Providence RI, 1972.
4. Whittaker, E. T., *A Treatise on the Analytical Dynamics of Particles and Rigid Bodies*, fourth edition, Cambridge University Press, Cambridge, UK, 1937.
5. Bottema, O., "On the small vibration of non-holonomic systems," *Proceedings Koninklijke Nederlandse Akademie van Wetenschappen* **52**, 1949, pp. 848–850.
6. Jonker, J. B., and Meijaard, J. P., "SPACAR–Computer program for dynamic analysis of flexible spatial mechanisms and manipulators," in *Multibody Systems Handbook*, W. Schiehlen (ed.), Springer-Verlag, Berlin, 1990, pp. 123–143.
7. Den Hartog, J. P., *Mechanical Vibrations*, 4th ed., McGraw-Hill, New York and London, 1956.
8. Schwab, A. L., and Meijaard, J. P., "Small vibrations superimposed on a prescribed rigid body motion," *Multibody System Dynamics*, 2002, in press.
9. Schwab, A. L., and Meijaard, J. P., "Dynamics of flexible multibody systems having rolling contact: Application of the wheel element to the dynamics of road vehicles," *Vehicle System Dynamics Supplement* **33**, 1999, pp. 338–349.

NON-LINEAR DYNAMICS OF MULTIBODY SYSTEMS WITH GENERALIZED AND NON-GENERALIZED COORDINATES

Ahmed A. Shabana
Department of Mechanical Engineering
University of Illinois at Chicago
842 West Taylor Street
Chicago, Illinois 60607-7022, U.S.A.

ABSTRACT For efficient dynamic simulation of mechanical and aerospace systems, the use of different sets of coordinate types may be necessary. The components of multibody systems can be rigid, flexible or very flexible and can be subject to contact forces. Examples of challenging problems encountered when multibody systems are considered are crashworthiness, problems of cables used in rescue operations and heavy load handling, leaf spring system design, tire deformations, large deformation of high-speed rotors, stability problems, and contact problems. Most large displacement problems in structural mechanics are being solved using incremental solution procedures. On the other hand, general purpose flexible multibody computer tools and methodologies in existence today are not, in general, capable of systematically and efficiently solving applications that include, in addition to rigid bodies and bodies that undergo small deformations, bodies that experience very large deformations. The objective of this paper is to discuss the development of new computational algorithms, based on non-incremental solution procedures, for the efficient simulation of multibody systems with flexible components. These new algorithms that do not require special measures to satisfy the principles of work and energy and lead to optimum sparse matrix structure can be used as the basis for developing a new generation of flexible multibody computer programs. The proposed non-incremental algorithms integrate three different formulations and three different sets of generalized coordinates for modeling rigid bodies, flexible bodies with small deformations, and very flexible bodies that undergo large deformations. The implementation of a general contact model in multibody algorithms is also presented as an example of mechanical systems with non-generalized coordinates. The kinematic equations that describe the contact between two surfaces of two bodies in the multibody system are formulated in terms of the system-generalized coordinates and the *non-generalized surface parameters*. Each contact surface is defined using two independent parameters that completely determine the tangent and normal vectors at an arbitrary point on the body surface. In the contact model presented in this study, the points of contact are determined on line during the dynamic simulation by solving the non-linear differential and algebraic equations of the constrained multibody system. The augmented form of the equations of motion expressed in terms of the generalized coordinates and non-generalized surface parameters is presented in this paper.

1. INTRODUCTION

A new generation of flexible multibody tools is needed for the analysis of modern, high-speed, light-weight multibody system applications. Existing multibody simulation tools suffer from

serious limitations and are not suited for modeling the dynamic phenomena that are encountered in the analysis of modern systems. These existing tools are designed to solve problems of mutlibody systems that consist of rigid components or flexible components that experience small deformations. Furthermore, the existing algorithms fail to produce efficient and accurate solutions for some basic vehicle elements, such as *leaf springs*, and flexible cables used in rescue operations and heavy load handling. Most existing flexible multibody computational algorithms, with few exceptions, employ two different dynamic formulations. The first formulation is based on the classical *Newton-Euler* or *Lagrangian equations* for rigid bodies, while the second formulation is based on the *floating frame of reference approach*. In the rigid body formulation, six independent coordinates are initially used to describe the body configuration. These six coordinates include three translation coordinates that define the location of the origin of a centroidal body reference, and three orientation coordinates that define the orientation of the body reference. The generalization of this formulation to study the dynamics of flexible bodies that experience small deformations required introducing an additional set of generalized coordinates in order to be able to define the body deformation with respect to its reference. In the early eighties, this generalization led to the development of a new generation of general-purpose flexible multibody computer codes that are currently widely used in industry and research laboratories. Such codes have been used as the basis for developing new computational design and analysis approaches. These multibody dynamics codes have been used in the design of many mechanical and aerospace system applications, and have resulted in tremendous saving of resources that would have been otherwise wasted. Preliminary designs are made in a computer environment before building the actual prototypes, while existing designs are continuously improved by utilizing the first generation of flexible multibody computer codes.

The general treatment of the rigid body contact problem requires the use of a set of parameters that describe the geometry of the contact surfaces. Two parameters are introduced for each surface. Using the four surface parameters associated with each contact, five algebraic contact constraint equations are formulated. The kinematic contact constraint equations are expressed in terms of the generalized coordinates of the two bodies as well as the non-generalized surface parameters. In order to be able to satisfy the nonlinear contact constraint conditions at the position, velocity, and acceleration levels, third partial derivatives of these constraint equations with respect to the surface parameters must be evaluated.

2.   GENERALIZED COORDINATES

The first step in developing a new formulation, is to select the system coordinates. While in most formulations, one coordinate type is used, in this study, it is proposed to develop a new non-incremental methodology that utilizes different coordinate types in order to achieve efficiency and generality while maintaining accuracy. Different components in the system, depending on whether they are rigid, flexible or very flexible, will be modeled using different types of coordinates. That is, the choice of coordinates will be determined by the degree of flexibility of the components of the system. Such a choice of coordinates introduces many interesting fundamental and numerical problems that include the coupling between the coordinates due to the joint constraints; the definition of different generalized forces associated with different sets of coordinates; the structure of the equations of motion in terms of different sets of coordinates; and

229

the scaling and numerical problems that arise as the result of using different coordinates with different magnitudes.

The new generation of flexible multibody algorithms must incorporate the following different sets of generalized coordinates; *reference coordinates, elastic coordinates* for small deformations, and *absolute nodal coordinates* for large deformations. In this study, the reference coordinates are used to define the location and orientation of a selected body reference. In the case of rigid bodies, a centroidal body coordinate system is used. In the three dimensional analysis, the reference coordinates consist of three translation coordinates and three or four orientation parameters depending on whether Euler angles or Euler parameters are used. This set of coordinates can be used to develop efficient models for bulky components that can be treated as rigid bodies. The elastic coordinates used for the small deformation problem define the body deformation with respect to the body coordinate system. Such a choice of a coordinate set allows using deformation modes in order to reduce the number of the system degrees of freedom. By using this set of elastic coordinates and the floating frame of reference formulation, an efficient algorithm for solving small deformation problems in multibody systems that takes into account the nonlinear coupling between the reference motion and the elastic deformation can be developed. This formulation, which leads to a nonlinear mass matrix and a simple expression for the elastic forces, can be effectively and efficiently used to model flexible components in many multibody system applications. In the floating frame of reference formulation, the global position vector of an arbitrary point on a body i in the system can be written as follows:

$$\mathbf{r}^i = \mathbf{R}^i + \mathbf{A}^i (\overline{\mathbf{u}}_o^i + \mathbf{S}^i \mathbf{q}_f^i)$$

where $\mathbf{R}^i$ is the global position vector of the origin of the body coordinate system, $\mathbf{A}^i$ is the transformation matrix that defines the orientation of the body coordinate system, $\overline{\mathbf{u}}_o^i$ is the position vector of the arbitrary point in the undeformed state, $\mathbf{S}^i$ is the shape function matrix, and $\mathbf{q}_f^i$ is the vector of elastic coordinates that define the body deformation with respect to the body coordinate system. Note that the preceding equation can be used also to describe the rigid body kinematics by setting the last term equal to zero. In this special case, the rigid boy kinematics is described using the reference translation coordinates $\mathbf{R}^i$ and the orientation coordinates 2^i that define the transformation matrix $\mathbf{A}^i$.

The third set of generalized coordinates used to describe the large deformations will be introduced using the absolute nodal coordinate formulation. This set of generalized coordinates consists of global displacement and slope coordinates and does not include any infinitesimal or finite rotations. By using the absolute nodal coordinates, exact modeling of the rigid body dynamics can be obtained. Furthermore, the absolute nodal coordinate formulation leads to a constant mass matrix in two- and three-dimensional problems. In this formulation, the global position vector of an arbitrary point on the flexible body is defined as

$$\mathbf{r}^i = \mathbf{S}_a^i \mathbf{q}_a^i$$

where $\mathbf{S}_a^i$ is a shape function matrix, and $\mathbf{q}_a^i$ is the vector of absolute coordinates that consist of global displacement and slope coordinates. It can be shown that the preceding equation can be

230

used to describe an arbitrary rigid body motion and can also be effectively and efficiently used to describe the large deformation of beams, plates and shells.

Using the different sets of coordinates above described, the vector of the generalized coordinates of the multibody system that contains rigid, flexible, and very flexible components can be described using the following set of system generalized coordinates:

$$\mathbf{q} = \begin{bmatrix} \mathbf{R}^T & \theta^T & \mathbf{q}_f^{\ T} & \mathbf{q}_a^{\ T} \end{bmatrix}^T$$

where $\mathbf{R}$ and 2 are the reference coordinates of the rigid or flexible bodies in the system, $\mathbf{q}_f$ is the vector of elastic coordinates that define the small deformations of the bodies with respect to the body coordinate system, and $\mathbf{q}_a$ is the vector of absolute nodal coordinates used to describe the motion of bodies in the system that undergo large deformations. The preceding equation can be written in terms of three distinct sets of coordinates as follows:

$$\mathbf{q} = \begin{bmatrix} \mathbf{q}_r^{\ T} & \mathbf{q}_f^{\ T} & \mathbf{q}_a^{\ T} \end{bmatrix}^T$$

where $\mathbf{q}_r = [\mathbf{R}^T \quad 2^T]^T$ is the vector of reference coordinates of the system.

3.   NON-GENERALZED COORDINATES

The general treatment of the rigid body contact problem requires introducing a set of parameters **s** that describe the geometry of the contact surfaces. In the augmented form of the equations of motion, there is no inertia or generalized forces associated with these parameters, and for this reason, they are referred to as non-generalized coordinates. Using these surface parameters, the tangents and normal to a surface at the contact point can be determined, and used to define the contact conditions. By using this approach, the contact points can be determined on line, and the coupling between the generalized and non-generalized surface parameters can be taken into consideration. By introducing the surface parameters for the rigid body contact, the vector of the system coordinates can be written as follows:

$$\mathbf{p} = \begin{bmatrix} \mathbf{q}_r^{\ T} & \mathbf{q}_f^{\ T} & \mathbf{q}_a^{\ T} & \mathbf{s}^T \end{bmatrix}^T$$

In the following section, the formulation of the constrained dynamic equations of motion in terms of the generalized coordinates and non-generalized surface parameters is discussed.

4.   DYNAMIC EQUATIONS

A new general flexible multibody algorithm must allow joint connectivity between rigid bodies, flexible bodies, and very flexible bodies as well as the general treatment of the contact problem. In this case, the joint constraints must be expressed in terms of the reference, elastic and absolute nodal coordinates. Considering also *driving constraints* that can depend explicitly on time, the vector of nonlinear constraint functions can be expressed in terms of the system reference, elastic and absolute nodal coordinates as well as the non-generalized surface parameters as follows:

231

$$C(\mathbf{q}_r, \mathbf{q}_f, \mathbf{q}_a, \mathbf{s}, t) = 0$$

As demonstrated in the multibody dynamics literature, the floating frame of reference formulation leads to highly nonlinear expressions for the joint constraints as the result of using the body coordinate system that introduces geometric nonlinearities. The formulation of many of these joints, however, becomes much simpler when the absolute nodal coordinate formulation is used. Nonetheless, since slopes are used as coordinates in the absolute nodal coordinate formulation, the formulations of some joints require the development of new special techniques for defining the kinematics of selected reference frames at the joint definition points in terms of the absolute nodal coordinates.

The kinematic constraints that describe mechanical joints, contact conditions and specified motion trajectories can be adjoined to the system differential equations of motion using the technique of Lagrange multipliers. This leads to the following augmented form of the system equations of motion:

$$
\begin{bmatrix}
\mathbf{M}_{rr} & \mathbf{M}_{rf} & 0 & 0 & \mathbf{C}_{\mathbf{q}_r}^{\mathrm{T}} \\
\mathbf{M}_{fr} & \mathbf{M}_{ff} & 0 & 0 & \mathbf{C}_{\mathbf{q}_f}^{\mathrm{T}} \\
0 & 0 & \mathbf{M}_{aa} & 0 & \mathbf{C}_{\mathbf{q}_a}^{\mathrm{T}} \\
0 & 0 & 0 & 0 & \mathbf{C}_{\mathbf{s}}^{\mathrm{T}} \\
\mathbf{C}_{\mathbf{q}_r} & \mathbf{C}_{\mathbf{q}_f} & \mathbf{C}_{\mathbf{q}_a} & \mathbf{C}_{\mathbf{s}} & 0
\end{bmatrix}
\begin{bmatrix}
\ddot{\mathbf{q}}_r \\
\ddot{\mathbf{q}}_f \\
\ddot{\mathbf{q}}_a \\
\ddot{\mathbf{s}} \\
\lambda
\end{bmatrix}
=
\begin{bmatrix}
\mathbf{Q}_r \\
\mathbf{Q}_f \\
\mathbf{Q}_a \\
0 \\
\mathbf{Q}_c
\end{bmatrix}
$$

where $\mathbf{M}$ refers to a mass sub-matrix, subscripts r, f, a, and s refer respectively to reference, elastic, absolute nodal coordinates, and non-generalized surface parameters, $\mathbf{C}_{\mathbf{q}}$ is the constraint Jacobian matrix associated with the generalized coordinates, $\mathbf{C}_{\mathbf{s}}$ is the constraint Jacobian matrix associated with the non-generalized surface parameters $\mathbf{s}$, 8 is the vector of Lagrange multipliers, $\mathbf{Q}_r$, $\mathbf{Q}_f$, and $\mathbf{Q}_a$ are the generalized forces associated with reference, elastic, and absolute nodal coordinates, and $\mathbf{Q}_c$ is a quadratic velocity vector that results from the differentiation of the kinematic constraint equations twice with respect to time, that is

$$\mathbf{C}_{\mathbf{p}} \ddot{\mathbf{p}} = \mathbf{Q}_c$$

The augmented form of the equations of motion can be solved in order to obtain the second time derivative of the vectors of reference, elastic, absolute nodal coordinates and surface parameters as well as the vector of Lagrange multipliers. Lagrange multipliers can be used to determine the generalized constraint forces associated with the reference, elastic, and absolute nodal coordinates. The reference, elastic, absolute nodal accelerations and the time derivatives of the surface parameters can be integrated forward in time in order to determine the coordinates and velocities. The numerical algorithm used in this investigation ensures that the algebraic constraint equations are not violated.

The vector of Lagrange multipliers can also be used to determine the normal contact forces. These normal contact forces can be used to determine the creep forces required for accurate modeling of railroad vehicle system applications.

5. CHOLESKY COORDINATES

Since the mass matrix $\mathbf{M}_{aa}$ associated with the absolute nodal coordinates is constant, a Cholesky transformation can be used to obtain a generalized identity mass matrix. This will lead to an optimum sparse matrix structure for the augmented form of the equations of motion of the system. The resulting augmented form of the equations of motion can be written as follows:

$$\begin{bmatrix} \mathbf{M}_{rr} & \mathbf{M}_{rf} & \mathbf{0} & \mathbf{0} & \mathbf{C}_{\mathbf{q}_r}^{\mathrm{T}} \\ \mathbf{M}_{fr} & \mathbf{M}_{ff} & \mathbf{0} & \mathbf{0} & \mathbf{C}_{\mathbf{q}_f}^{\mathrm{T}} \\ \mathbf{0} & \mathbf{0} & \mathbf{I} & \mathbf{0} & \mathbf{C}_{\mathbf{q}_{ch}}^{\mathrm{T}} \\ \mathbf{0} & \mathbf{0} & \mathbf{0} & \mathbf{0} & \mathbf{C}_{\mathbf{s}}^{\mathrm{T}} \\ \mathbf{C}_{\mathbf{q}_r} & \mathbf{C}_{\mathbf{q}_f} & \mathbf{C}_{\mathbf{q}_a} & \mathbf{C}_{\mathbf{s}} & \mathbf{0} \end{bmatrix} \begin{bmatrix} \ddot{\mathbf{q}}_r \\ \ddot{\mathbf{q}}_f \\ \ddot{\mathbf{q}}_{ch} \\ \ddot{\mathbf{s}} \\ \lambda \end{bmatrix} = \begin{bmatrix} \mathbf{Q}_r \\ \mathbf{Q}_f \\ \mathbf{Q}_{ch} \\ \mathbf{0} \\ \mathbf{Q}_c \end{bmatrix}$$

where $\mathbf{I}$ is an identity matrix, and subscript ch refers to Cholesky coordinates.

SOLUTION OF REDUNDANT MUSCLE FORCES IN HUMAN LOCOMOTION WITH MULTIBODY DYNAMICS AND OPTIMIZATION TOOLS

M.P.T. SILVA AND J.A.C. AMBRÓSIO
IDMEC/Instituto Superior Técnico
Av. Rovisco Pais 1, 1049-001 Lisboa
e-mail: pcms@alfa.ist.utl.pt and jorge@dem.ist.utl.pt

1. Introduction

Multibody-based methodologies are currently being used to simulate and analyze a wide variety of mechanical systems. In biomechanical applications, in particular, these methodologies present several advantages since they provide a way of calculate the internal forces developed by a specific biomechanical model during the execution of a specified task, without using intrusive force measuring devices. In particular when associated with proper optimization tools, these methodologies can be used to solve the 'redundant problem in biomechanics' [1], calculating the muscle forces produced by a specified muscle apparatus.

It is the purpose of this work to present a multibody based methodology that together with the use of optimization tools, allows for the calculation of the redundant muscle forces, generated in a particular muscle apparatus of the human body. The proposed methodology uses a multibody formulation with natural coordinates where rigid bodies and kinematic joints are modeled using the Cartesian coordinates of a set of anatomical points and unit vectors [2,3]. Using this general-purpose methodology, a whole-body-response biomechanical model is constructed.

Two different types of actuators are used to drive the biomechanical model through a previously acquired motion: joint actuators, that drive the degrees-of-freedom of the biomechanical model associated with joints where muscles are not modeled, and muscle actuators that drive the degrees-of-freedom of the joints crossed by the muscles forming the muscle apparatus under analysis. The use of muscle actuators to drive the mechanical model generates a mechanical system with a redundant nature, with more unknowns to determine then available equations of motion.

Optimization tools are used to resolve this indeterminate problem. These tools consider that muscle forces are generated according to the minimization of some performance criteria and that any optimal solution obtained for the muscle forces must satisfy the equations of motion of the biomechanical system. These performance criteria are analytical expressions that simulate the decisions taken by the central nervous system when executing of the prescribed task.

To each muscle actuator is associated a muscle model that simulates the muscle activation-contraction dynamics [9,10,11]. In the present work, a Hill type muscle model is applied, being the force produce by the muscle contractile element calculated as a function of the muscle activation, maximum isometric peak force, muscle length and muscle shortening rate [23,24].

2. Multibody Formulation and System Equations of Motion

A multibody formulation, using natural or fully Cartesian coordinates, is applied to the study and analysis of the human body movement. With this formulation, rigid bodies are constructed using the Cartesian coordinates of a set of points and unit vectors. These points and unit vectors, usually located at the joints and extremities of the model, are used not only to define the kinematic structure of the rigid bodies, but also, when shared by different rigid bodies, to define in a natural way simple kinematic joints such as the spherical and revolute joints.

A vector of generalized coordinates is constructed with the Cartesian coordinates of the points and vectors used in the definition of the mechanical system:

$$\mathbf{q} = \left\{ q_1 \ q_2 \ q_3 \cdots q_n \right\}^\mathrm{T} \tag{1}$$

where $n=3(np+nv)$ is the total number of natural coordinates and np and nv are, respectively, the total number of points and unit vectors of the model.

The set of natural coordinates, presented in equation (1), is necessary to the definition of the mechanical system, but it is not sufficient. In order to completely define its kinematic structure and topology, some kinematic constraint equations must be supplied. There are several types of constraint equations that are used in formulations using natural coordinates: rigid body constraints, joint constraints and driving constraints. Rigid body constraints, however, are the most common type since the number of natural coordinates that defines a rigid body is always larger then the number of its degrees-of-freedom [2,3]. This means that not all the coordinates are independent and that kinematic constraint equations need to be added

to express these dependences. Rigid body constraints, express physical properties of rigid bodies such as the constant distance between two points, the constant angle between two segments or the constant length of a vector. Mathematically these physical properties are supported by the scalar product equation, given by:

$$\Phi^{(SP,1)}(\mathbf{q},t) = \mathbf{v}^T\mathbf{u} - L_v L_u \cos(\langle \mathbf{v},\mathbf{u}\rangle(t)) = 0 \qquad (2)$$

where $\mathbf{v}$ and $\mathbf{u}$ are two generic vectors used in the definition of rigid bodies, L_v and L_u are the respective norms and $<\mathbf{v},\mathbf{u}>(t)$ is the angle between them. Equation (2) is also applied to the definition of kinematic joints and driving constraints. In the case of driving constraints, used to prescribe the motion of the system, this angle is a function of time.

There are other types of kinematic constraints, such as the linear combination constraint or the cross product constraint that, are also used when modeling with natural coordinates [2]. All the constraint equations associated with the mechanical system are assembled in a single vector and written as:

$$\Phi(\mathbf{q},t) = \mathbf{0} \qquad (3)$$

The equations of motion of a general multibody system, with relative motion between rigid bodies constrained by kinematic joints and acted upon by external applied forces are given by:

$$\mathbf{M}\ddot{\mathbf{q}} + \Phi_q^T\lambda = \mathbf{g} \qquad (4)$$

where $\mathbf{M}$ is the global mass matrix of the system, Φ_q the Jacobian matrix of the constraints, $\ddot{\mathbf{q}}$ the vector of generalized accelerations, $\mathbf{g}$ the generalized force vector and λ the vector of Lagrange multipliers [2,13,14]. When performing inverse dynamic analyses in mechanical systems, the Lagrange multipliers vector, directly associated with the reaction forces and with driving forces and moments, such as muscle forces and net moments of force at the joints of a biomechanical model, is the only unknown present in equation (4). All other quantities are calculated from kinematic data and force measuring devices.

3. The Biomechanical Model

In this work, a three-dimensional, whole-body response biomechanical model of the human body is used [3,5,6,12]. The model, presented in Figure 1, is described using the general multibody formulation presented before. It has a kinematic structure made of thirty-three rigid bodies, interconnected by revolute and universal joints, adding to the sixteen anatomical segments, described in Table 1.
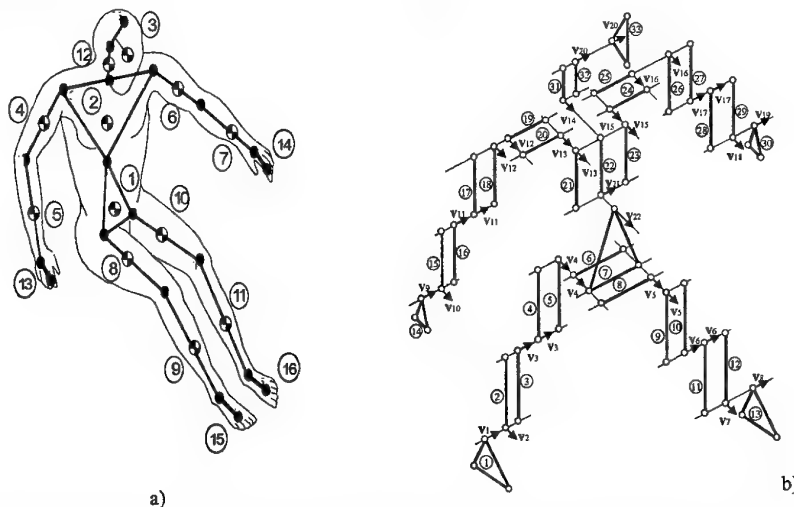
Figure 1. a) Sixteen anatomical segments; b) Kinematic structure of rigid bodies and kinematic joints.

A collection of physical characteristics is associated to each anatomical segment of the biomechanical model. The most important are: mass, principal moments of inertia, segment lengths and distance of its center of mass from the proximal joint. The properties mentioned before are obtained from the literature, relative to the 50th-percentile human male [4,5,15]. However, in order to improve the biofidelity of the data with respect to the anthropometrics of the subject under analysis, these physical properties are scaled using proper non-dimensional scaling factors [4,5].

In order to perform the inverse dynamic analysis, the motion of the subject needs to be acquired. For this

235

purpose, the trajectories of a set of points, located at the joints and extremities of the biomechanical model [16] are obtained using three-dimensional motion reconstruction techniques [18,19,20,21]. After reconstruction, these trajectories are filtered in order to reduce the noise levels introduced during the motion reconstruction procedure [15,19] and they are corrected to be consistent with the kinematic structure of the biomechanical model [16,17]. Velocity and acceleration curves are calculated, for each point, using the time differentiation of the cubic spline trajectory curves.

TABLE 1. Anatomical segments description with rigid bodies topology.

Segment Nr.	Description	Rigid Body Nr.
1	Lower torso	6,7,8
2	Upper torso	19,20,21,22,23,24,25
3	Head	33
4	Right upper arm	17,18
5	Right lower arm	15,16
6	Left upper arm	26,27
7	Left lower arm	28,29
8	Right upper leg	4,5
9	Right lower leg	2,3
10	Left upper leg	9,10
11	Left lower leg	11,12
12	Neck	31,32
13	Right hand	14
14	Left hand	30
15	Right Foot	1
16	Left foot	13

Another important input data are the externally applied forces over the biomechanical model. In this work, the feet ground reaction forces at collected using three force plates.

In order to drive the biomechanical model throughout the inverse dynamic analysis, joint actuators such as the one represented in Figure 2 for the knee joint, must be specified. This means that for each degree-of-freedom, a joint actuator equation is added to the equations of motion of the system.

Figure 2. Joint actuator associated with the knee

Joint actuator equations are kinematic constraints, of scalar product type as presented in equation (2), in which the angle between the two vectors is a function of time and describes, for each time step, the motion of the kinematic joint associated with that degree-of-freedom. These additional equations are added to the constraints in such a way that the number of non-redundant constraint equations becomes equal to the number of natural coordinates describing the model. It should be noted that the inverse dynamics problem, as stated here, is determined, i.e., equation (4) has a solution and that solution is unique.

4. Redundant Muscle Forces and Optimization Techniques

In complex biomechanical systems such as the human body, almost every joint is crossed by several muscles or muscle groups. This means that different muscle activation patterns can generate forces that produce the same net moments-of-force at the joints and as result a same posture or movement. It is the central nervous system that, depending on the task being performed and/or the objectives to be achieved, selects and activates the set of muscles that best fulfill some physiological criteria.

Historically termed 'the redundant problem in biomechanics' [1], this redundancy results, from a mathematical point of view, from the fact that the number of load-transmitting elements at a joint usually exceeds the number of available equilibrium equations and consequently a unique solution for the analytical determination of those forces cannot be obtained [7]. Optimization techniques are applied to resolve the indeterminate problem and to choose, from an infinite set of solutions, the optimal solution that minimize one or more cost functions.

4.1. MUSCLE ACTUATORS IN MULTIBODY SYSTEMS

Muscles are introduced in the equations of motion of the multibody system as point-to-point kinematic

236

driver actuators. Depending on their complexity, muscle actuators can be defined using two or more points. In Figure 3, two muscles of the lower extremity muscle apparatus are presented to illustrate the two types of muscle definition: the *semimembranosus* and the *tensor fasciae latea* [22]. The first one is a two-point muscle defined only with an origin and an insertion point, while the second one, due to a more complex path, uses two additional via points for a more accurate definition.
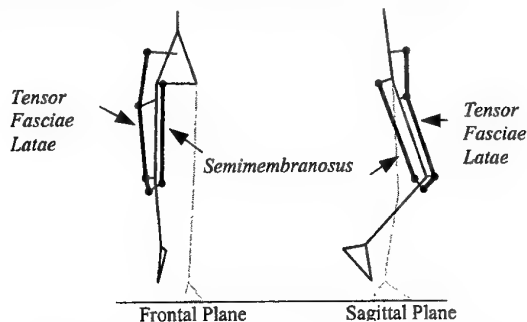

Figure 3. Muscle actuators defined with two or more points.

To each muscle actuator is associated a constraint equation that specifies the muscle action during the analysis period. These expressions, constrain the distance between two generic points, of different rigid bodies, to vary according to a specified length change history, calculated before hand. Considering a two-point muscle actuator, with an origin located in point n of rigid body i, and an insertion located in point m of rigid body j, the mathematical expression used to define the constraint is written as:

$$\Phi^{(MA,1)}(\mathbf{q},t) = (\mathbf{r}_m - \mathbf{r}_n)^T(\mathbf{r}_m - \mathbf{r}_n) - L_{nm}^2(t) = 0 \qquad (5)$$

where $\mathbf{r}_m$ and $\mathbf{r}_n$ are respectively the global position vectors of the origin and insertion points and $L_{nm}(t)$ is the muscle total length, calculated for each time step of the analysis. Note that n and m are two generic points of rigid bodies i and j and are used only to define the muscle actuator. This means that a coordinate transformation needs to be applied in order to explicitly express this equation in terms of the natural coordinates used in the construction of rigid bodies i and j [28].

To each muscle actuator a Lagrange multiplier is associated. When considering this type of actuators, the physical meaning of this multiplier is of a force per unit of length. In order to obtain muscle forces or muscle activations, these multipliers must be multiplied by proper scalar factors [28].

It should be noted that muscle driver actuator equations are introduced in the Jacobian matrix of the constraints together with the kinematic constraint equations defining the kinematics of the biomechanical model and the kinematic joints. This means that an integrated solution is obtained for the inverse dynamics problem in terms of muscle and reaction forces.

4.2. DYNAMICS OF MUSCLE TISSUE

The dynamics of muscle tissue can be divided into activation dynamics and muscle contraction dynamics [9], as schematically indicated in Figure 4.

Figure 4. Dynamics of muscle tissue.

Activation dynamics generates a muscle tissue state that transforms the neural excitation produced by the central nervous system, into activation of the contractile apparatus. Activation dynamics, although not implemented in this work, describes the time lag between neural signal and the corresponding muscle activation [11] and it is usually represented in a microscopic level by first order differential equations [10,11].

Muscle contraction dynamics corresponds to the transformation of muscle activation in muscle force, as represented in Figure 4. To simulate this process, a mathematical model of the muscle needs to be introduced. In the present work, a Hill-type muscle model is applied to the simulation of the muscle contraction dynamics. This model is nowadays extensively applied to the study of intermuscular coordination of biomechanical systems [9].

The model, depicted in Figure 5, is composed of an active Hill *contractive element* (CE) and a *passive element* (PE). Both elements contribute to the total muscle force $F^m(t)$. In the present work, a *series elastic element* (SEE) usually associated with cross-bridge stiffness is not included in the model since it can be

237

neglected, with little inaccuracy, in coordination studies not involving short-tendon actuators [9].

In a Hill-type muscle model, the contractile properties of the muscle tissue are controlled by its current length $L^m(t)$, rate of length change $\dot{L}^m(t)$ and activation $a^m(t)$ in such a way that the force produced by the active Hill *contractile element*, for muscle m, is written as:

$$F_{CE}^m(a^m(t), L^m(t), \dot{L}^m(t)) = \frac{F_L^m(L^m(t))F_{\dot{L}}^m(\dot{L}^m(t))}{F_0^m} a^m(t) \qquad (6)$$

where F_0^m is the maximum isometric force and $F_L^m(L^m(t))$ and $F_{\dot{L}}^m(\dot{L}^m(t))$ are two functions that represent the muscle force-length and force-velocity dependency, respectively [9,11].

The passive element is independent of activation and it only starts to produce force when the muscle is stretched beyond its resting length L_0^m. It should be noted that force produced by the passive element is only function of the muscle length, being its value perfectly determined during the total time of the analysis. Therefore, the force produced by the passive element is treated as an external force, applied directly to the rigid bodies interconnected by the muscle.
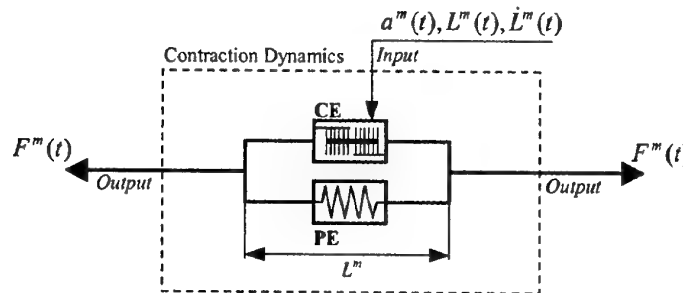

Figure 5. Contraction dynamics using a Hill-type muscle model.

A muscle apparatus of thirty-five muscle actuators is used to simulate the right lower extremity intermuscular coordination. The physiological information regarding muscle definition is obtained from literature [23,24] and compiled in a muscle database. This information consists in the maximum isometric force, resting length, attachment and wrap-around bodies and the local coordinates of the origin, insertion and via points. The whole muscle apparatus is presented in Figure 6.
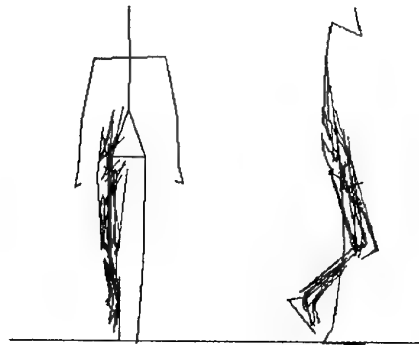

Figure 6. Lower extremity muscle apparatus.

4.3. STATIC OPTIMIZATION: COST FUNCTIONS AND CONSTRAINTS

Indeterminate systems present an infinite set of possible solutions, being the aim of optimization techniques to find, from all the possible solutions, the one that minimize a prescribed objective function, subjected to a certain number of restrictions or constraints. Mathematically optimization problems can be stated as follows:

$$\text{minimize } F_0(u_i) \qquad \text{subject to:} \begin{cases} f_j(u_i) = 0 & j = 1,\ldots,n_{ec} \\ f_j(u_i) \geq 0 & j = (n_{ec}+1),\ldots,n_{ic} \\ u_i^{lower} \leq u_i \leq u_i^{upper} & i = 1,\ldots,n_{sv} \end{cases} \qquad (7)$$

where u_i are the state variables bounded by u_i^{lower} and u_i^{upper}, $F_0(u_i)$ is the objective or cost function to minimize and $f_j(u_i)$ are constraint equations that restrain the state variables. In equation (7), n_{st} represents the total number of state variables and n_{ic} the total number of constraint equations in which n_{ec} are of equality type.

238

The minimization of cost functions, simulate physiological criteria adopted by the central nervous system when deciding which muscles to recruit as well as the level of activation that produce the adequate motion or posture for the task being undertaken. Several cost functions have been used by researchers in the study of the redundant problem in biomechanics [1,7,8]. The principle of minimization of the sum of the cube of the individual muscle stresses [8], used in applications involving human locomotion, is adopted in the present work. This principle is expressed by the following cost function:

$$ F_0 = \sum_{m=1}^{n_{ma}} \left(\sigma_{CE}^m \right)^3 = \sum_{m=1}^{n_{ma}} \left(\bar{\sigma} \frac{F_L^m F_L^m}{F_0^{m^2}} a^m \right)^3 \tag{8} $$

where n_{ma} are the number of muscle actuators and $\bar{\sigma}$ is the specific muscle strength with a constant value of 31.39 N/cm^2 [23,24]. Note that only state variables associated with muscle actuators are used to evaluate the cost functions, although the complete set of state variables also include the Lagrange multipliers associated with the rest of the kinematic constraints. Using these cost functions, the state variables associated with muscle actuators represent muscle activations and, for that reason, can only assume values between 0 and 1. For all other state variables no bounds are specified.

The optimal solution, obtained by the optimization routine for the state variables, must fulfill the equations of motion of the mechanical system, given by equation (4). Therefore, these equations are supplied to the optimizer as constraint equations for the state variables.

5. Application Case

The methodologies and the biomechanical model described before are applied to the gait analysis of a subject performing a normal cadence stride period. The subject under analysis is a 25-year-old male with a height of 1.70 m and a total body mass of 70 kg. The subject is wearing running shoes. The trial starts at the time step just before right heel contacts the floor, and continues until the subsequent occurrence of the same foot. During the stride period, the subject has to walk over three force plates that measure the ground reaction forces for both feet [5,6]. A total number of 66 frames are recorded using four cameras with a sampling frequency of 60 Hz.

The net moments of force developed at the joints of the biomechanical model are calculated. In particular, the net moments of force for the joint actuators of the right ankle, knee and hip joints are presented in Figure 7. These results are within the expected values reported in the literature for a normal cadence stride [27].

The muscle forces developed in the right leg during the stride period are calculated using the procedures described before. The results obtained with two optimization packages [25,26], are presented in Figure 8 for the muscle *Gluteus Minimus*, an abductor of the hip and for *Gluteus*, a powerful plantar flexor of the ankle [22].
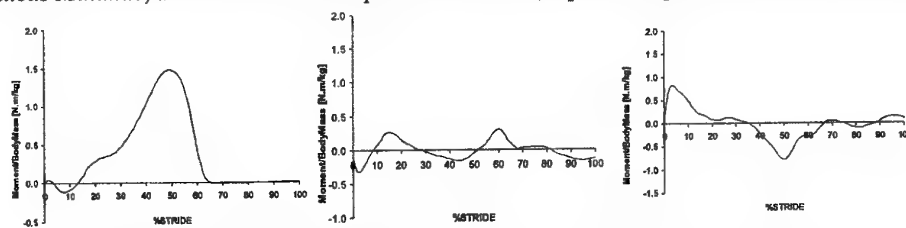

Figure 7. Net moment-of-force (scaled by the body mass) for the right ankle, knee and hip joints.
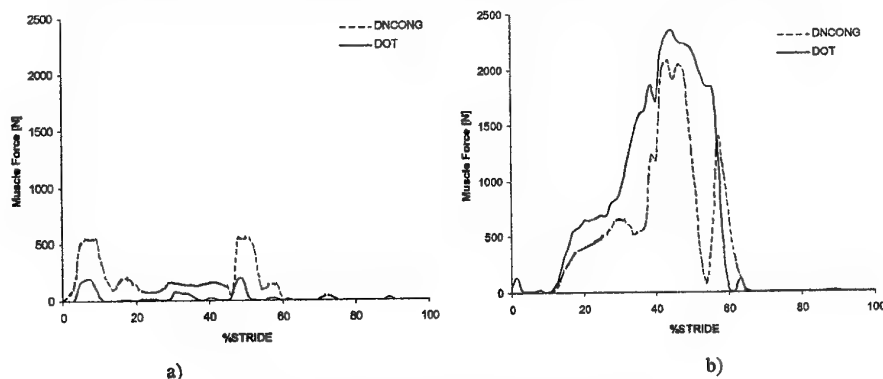
Figure 8. Muscle Forces: a) *Gluteus Minimus*, b) *Soleus*.

The results present a good correlation between both optimization routines. In general terms, the forces present almost the same behavior although different force levels can be identified. It should be noted that the results presented in Figure 8 are two possible solutions obtained by different optimization packages and that both solutions fulfill the equations of motion of the system.

239

6. Conclusions

In this work, a methodology was presented that allows for the calculation of the net moments-of-force and reactions at the joints, and also for the calculation of the muscle forces developed in a specific muscle apparatus of a subject describing a prescribed motion. The subject is simulated using a whole-body-response biomechanical model constructed using a multibody formulation with natural or fully Cartesian coordinates.

The model is driven through the prescribed motion using kinematic driver actuators of two types: joint driver actuators and muscle driver actuators. To each driver actuator is associated a Lagrange multiplier that, depending on the actuator type, represents, for the case of a joint actuator, the net moment-of-force produced by all the muscles crossing the specified joint, or, in the case of the muscle actuator, the muscle force associated with a specified muscle or muscle complex.

It was showed that the use of muscle actuators usually introduces indeterminacy in the equations of motion of the biomechanical system. When this occurs, optimization techniques present a powerful tool that allows for the selection, among an infinite set of possible solutions, of the one that minimizes a specific cost-function associated, from the physiological point of view, with the criteria used during the trial by the central nervous system of the subject.

8. References

1. Yamaguchi, G.T., Moran, D.W. and Si, J. (1995) A computationally efficient method for solving the redundant problem in biomechanics, *J. Biomechanics*, **28** (8), 999-1005.
2. Jalon, J. G. and Bayo, E. (1994) *Kinematic and Dynamic Simulation of Mechanical Systems – The Real-Time Challenge*, Springer-Verlag, Berlin, Germany.
3. Silva, M.P.T., Ambrósio, J.A.C. and Pereira, M. (1997) Biomechanical Model with Joint Resistance for Impact Simulation, *Multibody System Dynamics*, **1**(1), 65-84.
4. Laananen, D., Bolokbasi, A. and Coltman, J. (1983) *Computer simulation of an aircraft seat and occupant in a crash environment – Volume I: technical report*, US Department of Transportation, Federal Aviation Administration, Report n DOT/FAA/CT-82/33-1.
5. Ambrósio, J.A.C., Silva, M.P.T. and Abrantes, J. (1999) Inverse Dynamic Analysis of Human Gait Using Consistent Data, *Proc of the IV Int. Symp. on Computer Methods in Biomechanics and Biomedical Engng*, October 13-16, Lisbon, Portugal.
6. Silva, M.P.T. and Ambrósio, J.A.C., (2001) Sensitivity of the Results Produced by the Inverse Dynamic Analysis of a Human Stride to Perturbed Input Data, *Journal of Biomechanics* (submitted).
7. Collins,J.J. (1995) The redundant nature of locomotor optimization laws, *J. of Biomechanics*, **28**, 251-267.
8. Crowninshield, R.D. and Brand, R.A. (1981) Physiologically Based Criterion of Muscle Force Prediction in Locomotion, *J. Biomechanics*, **14** (11), 793-801.
9. Zajac, F. E. (1989) Muscle and tendon: properties, models, scaling, and application to biomechanics and motor control', *Critical Reviews in Biomedical Engineering*, **17** (4), 359-411.
10. Hatze, H. (1984) Quantitative analysis, synthesis and optimization of human motion', *Human Movement Science*, 3, 5-25.
11. Kaplan, M.L. (2000) *Efficient Optimal Control of Large-Scale Biomechanical Systems*, Ph.D. Dissertation, Stanford University.
12. Silva, M., Ambrósio, J. and Pereira, M. (1997) A multibody approach to the vehicle and occupant integrated simulation, *Int. J. of Crashworthiness*, **2**(1), 73-90.
13. Nikravesh, P.E. (1988) *Computer-Aided Analysis of Mechanical Systems*, Prentice Hall, Englewood-Cliffs, New Jersey.
14. Haug, E. (1989) *Computer Aided Kinematics and Dynamics of Mechanical Systems*, Allyn and Bacon, Neeham Heights, Massachusetts.
15. Winter, D. A. (1990) *Biomechanics And Motor Control Of Human Movement*, 2nd Ed., John Wiley & Sons, Toronto, Canada.
16. Silva, M.P.T. and Ambrósio, J.A.C. (2001) Kinematic Data Consistency in the Inverse Dynamic Analysis of Biomechanical Systems, *Multibody System Dynamics* (accepted for publication).
17. Celigüeta, J.T. (1996) Multibody Simulation of Human Body Motion in Sports, in *Proceedings of the XIV International Symposium on Biomechanics in Sports*, 81-94, Ed. FMH, Technical University of Lisbon.
18. Addel-Aziz, Y. and Karara, H. (1971) Direct linear transformation from comparator coordinates into object space coordinates in close-range photogrammetry, *Proceedings of the Symposium on Close-range Photogrammetry*, Falls Church, Virginia, pp. 1-18.
19. Ambrósio, J., Silva, M. and Lopes, G. (1999) Reconstrução do movimento humano e dinâmica inversa utilizando ferramentas numéricas baseadas em sistemas multicorpo, In *Acta do IV Congreso de Métodos Numéricos en Ingeniería*, Sevilha, Spain, June 7-10.
20. Nigg, B. and Herzog, W. (1999) *Biomechanics of the Musculo-skeletal System*, John Wiley & Sons, New York, New York.
21. Allard, P., Stokes, I. and Blanchi, J. (1995) *Three-Dimensional Analysis of Human Movement*, Human Kinetics, Urbana-Champagne, Illinois.
22. Richardson, M. L. (2001) *Lower Extremity Muscle Atlas*, in http://www.rad.washington.edu/atlas2/ , University of Washington - Department of Radiology, last update October 2001.
23. Yamaguchi, G.T. (2001) *Dynamic Modeling of Musculoskeletal Motion*, Kluwer Academic Publishers, Boston, Massachussetts.
24. Carhart, M.R. (2000) *Biomechanical Analysis of Compensatory Steping: Implications for paraplegics Standing Via FNS.*, Ph.D. Dissertation, Department of Bioengineering, Arizona State University.
25. Vanderplaats R&D (1999) *DOT – Design Optimization Tools – USERS MANUAL – Version 5.0.*
26. Numerics, V., (1995) IMSL *FORTRAN Numerical Libraries – Version 5.0*, Microsoft Corp.
27. Winter, D. A. (1991) *The biomechanics and motor control of human gait: Normal, elderly and pathological*, 2nd Ed., University of Waterloo Press, Waterloo, Canada.
28. Silva, M.P.T. and Ambrósio, J.A.C. (2002) A Multibody Based Methodology for the Solution of the Redundant Nature of the Muscle Forces Using Static Optimization, in *Proc V Congreso de Métodos Numéricos en Ingeniería*, Madrid, 3-6 June.

KNOWLEDGE SUPPORT OF
VIRTUAL MODELLING AND SIMULATION

P. STEINBAUER, M. VALÁŠEK, Z. ZDRAHAL*, P. MULHOLLAND*, Z. ŠIKA,
Department of Mechanics
Faculty of Mechanical Engineering
Czech Technical University in Prague
Karlovo nám. 13, 121 35 Praha 2, Czech Republic
Knowledge Media Institute
*The Open University
Milton Keynes, UK
E-Mail: valasek@fsik.cvut.cz , z.zdrahal@open.ac.uk

1. Introduction

The paper deals with the description of knowledge support of virtual modelling and simulation. The design methodology based on multidisciplinary virtual modelling and subsequent simulation is essential for nowadays any engineering design [1], but specifically for design of complex mechatronic machines [2]. Besides that current engineering design is multidisciplinary and therefore based on team work. The team work often uses the possibility and benefits of geographic distribution and internet communication within the team. Engineering design draws heavily on previous experience and therefore it is essentially to build and maintain the archives of previous cases. It is done in some way also for simulation models.

Engineering design is in nature a knowledge intensive activity, but analysing the resulting documentation of such activities shows that there is a significant loss of knowledge for team communication and future reuse. The simulation of dynamic systems, in particular the nonlinear virtual multibody system, is a prime example. The resulting simulation models do not include the majority of knowledge which was necessary and which was used for their development.

The simulation models include a large amount of knowledge, which is related to the development and usage of dynamic simulation models. However, there are no tools for storing, retrieving, reusing, sharing and communicating such knowledge. Therefore special tools are being developed for enriching traditional dynamic simulation models by the corresponding accompanying knowledge.

2. Knowledge Life Cycle of Virtual Modelling and Simulation

The development of a virtual model and then its simulation typically goes through a number of tasks. These tasks are illustrated in Figure 1, the light arrows represent mappings between the different elements and the black arrows represent transformation processes between the tasks. The development of a simulation, as shown in Figure 1, involves five steps.

The first step is the analysis of the real world, since when it is started to develop a simulation there exists some real world object (either actual or hypothesised). This real world object is investigated within certain experimental frame concentrated on the interested behaviour in order to answer some question, the objective of object investigation. It forms the real world system (either actual or hypothesised). From this real world system we want to create a model to use to answer a modelling question (question), such as how a real-world system would respond to particular stimuli. The real world task has three elements, these elements are the real world system, the question (modelling question) and finally the solution:

- The real world system (either actual or hypothesised), of which we want to create a model to use to answer a modelling question, such as how a real-world system would respond to particular stimuli.
- The question (modelling question) is a question that is based within the real world and is to be answered using simulation.
- The solution is the interpretation of the interpreted output of the simulation task, this will be left blank until there is a set of results.
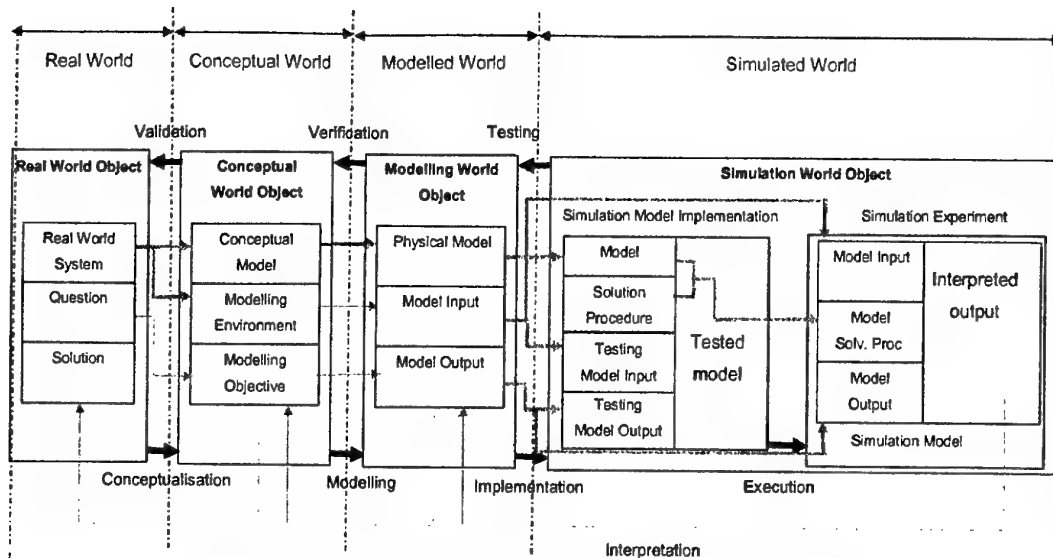
Figure 1. Knowledge life cycle of virtual modelling and simulation

The second step is the conceptual task, where the conceptual model is developed. The transformation from real world into conceptual world consists of creating hierarchical break-down of the real world system being investigated (e.g. hierarchical description of real product components and its environment). This scheme should be accompanied by the description of function (physical interaction) as it is the basis of causal and functional explanation. As soon as this description is completed the conceptualisation is completed. Certainly there are raised different assumptions about the granularity of the modelling being provided. It is the way of "thinking about" and representing the real world system in a conceptual manner. A crucial design decision is determination of what factors influence system behaviour and what system behaviours are to be incorporated into this task. The result of the conceptualisation is the conceptual model investigated within the modelling environment in order to answer the modelling objective:

- The conceptual model is an abstracted view of the real world system.
- The modelling objective is the conceptualisation of the question and form the objectives for the simulation task (i.e. what behaviour we are interested in? and how we will know that we have the correct answer from the results?)
- The modelling environment is the conceptualisation of the inputs of the real world systems, providing a simulation environment to work within in the simulation task, typically the inputs are specified here.

The process of determining whether the conceptual model is an adequately accurate representation of the real world task is the validation.

The next task is the physical modelling. The third step is the transformation from conceptual world into physical world. It consists of replacement of each element on conceptual level by corresponding element on physical level. The elements of physical model are the so-called ideal modelling elements (e.g. rigid body, ideally flexible body, ideal gas, ideal incompressible fluid, ideal capacitor etc.). The engineering sciences deal exactly with the ideal objects. The mathematically described exact prediction of the behaviour is available only for ideal objects. The art of engineering modelling and simulation is the capability to translate the behaviour of real world objects into the behaviour of system consisting of ideal objects.

Again as soon as this replacement is completed the physical modelling is completed. Exactly here the majority of modelling assumptions is raised and exactly here many modelling modifications are being done. It is the way of "modelling it" and representing the real world system in a physical modelling manner. For example two typical modifications are provided: *Either* an element is decomposed into more elements (a small subsystem) (e.g. a body cannot be treated as rigid body and it is modelled as flexible body being modelled as subsystem) *or* several elements are replaced by one element as the detailed treatment of interactions is neglected (e.g. the influence of a suspension mechanism can be neglected and the model consists only of chassis and wheels with flexibility of tyre and suspension spring). The modelling task results into the physical model, its input and the investigated output:

- The physical model is an accurate physical view of the conceptual model.
- The model input is the modelling conceptualisation of the inputs of the real world systems, providing a physical modelling of the real world stimuli to the investigated system, i.e. detailed physical description of modelling environment from conceptual task.
- The model output is the modelling conceptualisation of the objectives for the simulation task (i.e. how the

242

interested behaviour is measured and evaluated ?)

The process of determining whether the physical model is an adequately accurate representation of the conceptual model is the verification.

The results of modelling task are implemented in the form of a computer-executable set of instructions known as the simulation model. It is the transformation from physical world into simulation world. It consists of replacement of each element on physical modelling level by corresponding element on simulation level. Usually this replacement can be straightforward as simulation packages are trying directly contain the ideal objects of physical models. However, always some modifications are necessary. The simulation task consists of two stages. The first stage deals with the implementation of the physical model using particular simulation environment (simulation language and simulation software). The second stage deals with the simulation experiment, i.e. proper usage of the developed simulation model for the solution of the real world problem. Testing is the process of determining whether the implemented version of the model is an accurate representation of the physical model.

Between the models from different worlds there are many relations. The main relations are connected with the described transformations. They represent the relation "consist of" from real world to conceptual world, the relation "is modelled as" from conceptual world to modelling world and the relation "is implemented as" from modelling world to simulation world and finally the relation "is simulated by" and "is answered by" from real world to simulation world. The development of objects of these relations is accompanied by many iterations (*Fig. 2*).
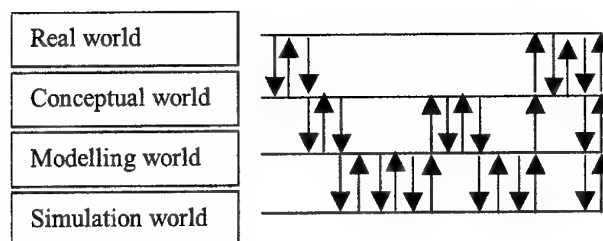

Figure 2. Iterative process of simulation model development

3. Knowledge Support of Virtual Modelling and Simulation

The above described process of creating of virtual models and simulation experiments with them is accompanied with supporting knowledge that is vital for knowledge sharing and reuse within the design team. It is believed that the supporting knowledge for the modelling and simulation process comes in two forms, informal and formal knowledge. Informal knowledge is typically concerned about relationships and knowledge about models using natural language. Formal knowledge is also concerned with the establishment and representation of knowledge about the model, but this knowledge is typically more structured using knowledge modelling technology. Both of these types of knowledge will be associated with each world object as shown in *Figure 3*.
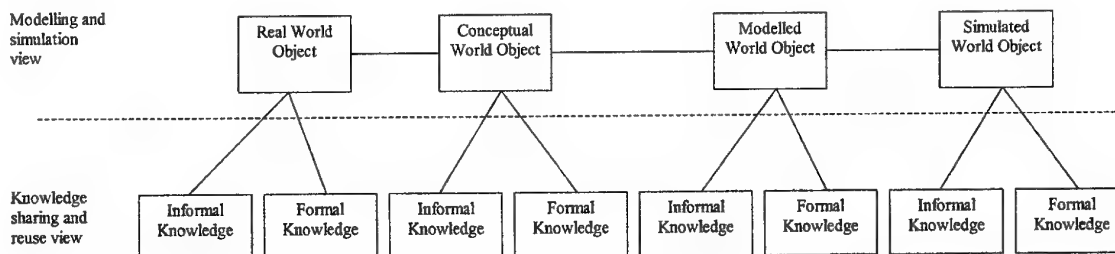

Figure 3. Supporting knowledge for the modelling and simulation process

Based on the methodology of Enrich project [3] the modelling and simulation objects are work documents of engineering activity, the informal knowledge can be captured by annotations and the formal knowledge by semantic indexing using concepts from related ontologies (*Fig. 5*).

Each world model is associated with informal and formal knowledge (*Fig. 4*) on the level of model components as well on the level of complete models and besides that each transition between worlds is also associated with informal and formal knowledge. The informal knowledge about world object components and complete world object is describing the function, behaviour and any other useful information about the

243

component or object in question. The formal knowledge represents the most valuable informal knowledge in terms of corresponding ontologies (*Fig. 5*). However, only the ontologies from the lowest level are formally dscribed and used for semantic indexing. The informal knowledge of the world transitions describes the structural changes of the model with related assumptions raised during particular transformation, the formal knowledge of these transitions describes the relationships of modelling processes.
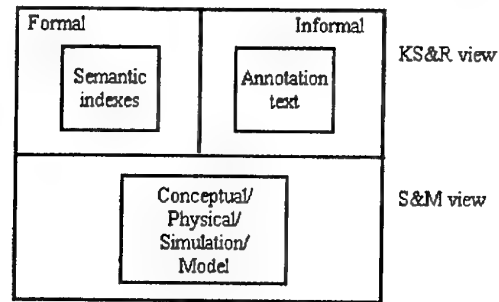

Figure 4. Model with semantic indexes and textual annotation

The particular relationships between cases of world models and their components can be also generalized into more abstract knowledge about development of virtual models and their simulation (general rules) (*Fig. 6*).

Figure 5. Ontology hierarchy
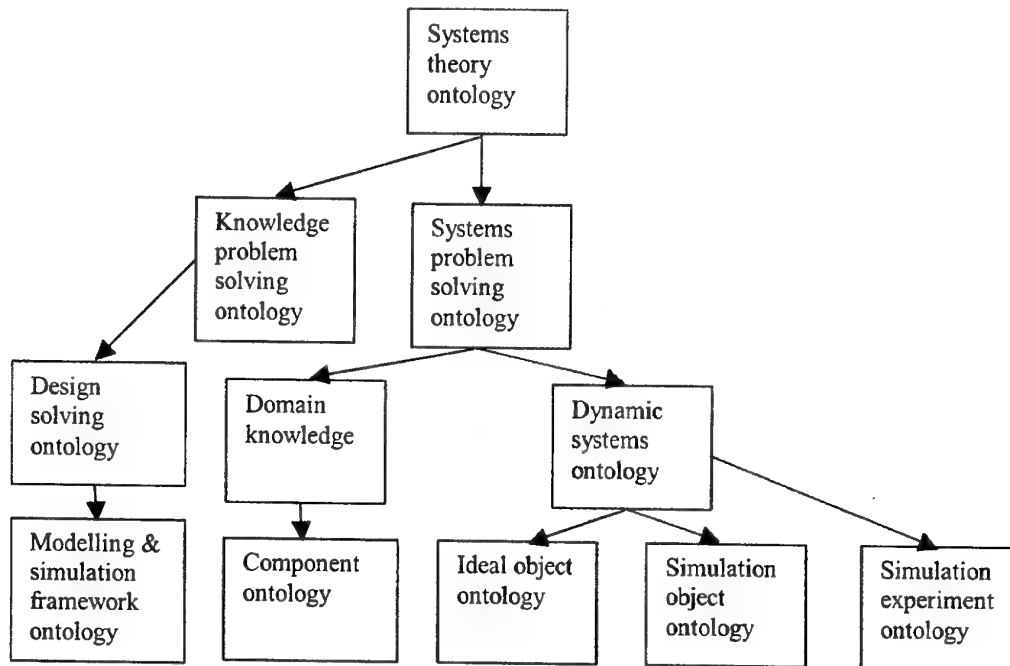
4. Knowledge Tools for Knowledge Support of Virtual Modelling and Simulation

The above described analysis has shown that the process of modelling can be described on the level of each world by three descriptors:
i. Conceptual/physical/simulation model depending on the world (CWO/MWO/SWO),
ii. Annotation text (informal knowledge), and
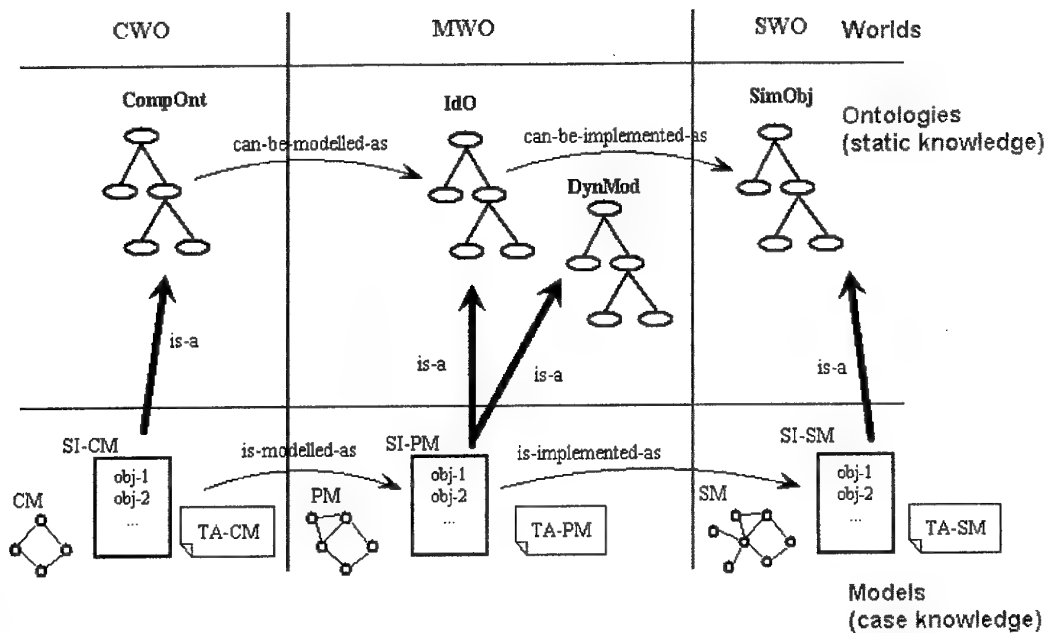iii. Semantic indexes (formal knowledge).

Figure 6. Models, ontologies and their relationships

In order to support these descriptors for each of the worlds, the transitions between them and the whole project data there have been created and resused many tools. They are:

1. Modelling tools: Simulation package for Simulation World and Modelling tool for Conceptual and Modelling Worlds (any primitive tools like drawing creator can be used instead).

2. Tools for informal knowledge: Annotation tool for simulation models (and similarly for further models in modelling tool), Knowledge management tool for supporting descriptions of all objects in Knowledge life cycle (*Fig. 1*).

3. Tools for formal knowledge: Ontology interface tool for semantic indexing and semantic retrieval.

4. Life cycle management tools: Knowledge management tool for supporting all descriptions and related files on all stages of Knowledge life cycle (*Fig. 1*) and Database tool for storing/retrieving all data.
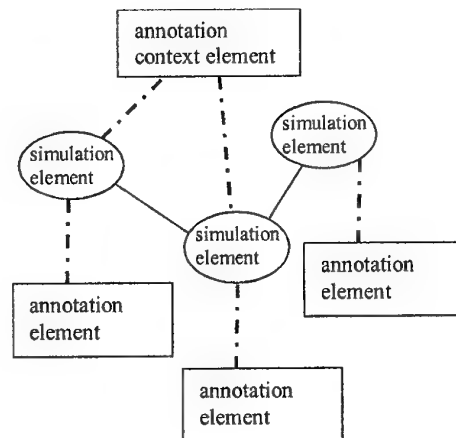
Figure 7. Annotation tool for simulation models (AT)

Specifically new tools are the Annotation tool (AT) and Knowledge management tool (KMT). In order to support the structure of models, especially of simulation models the annotation texts are directly associated with model elements (*Fig. 7*). It is the Annotation tool of models [4]. Then there is proposed another tool for Knowledge management on the level of whole models and worlds. It supports the annotations of whole models and transitions between worlds, the semantic indexing of all objects and hierarchical relations between objects of different worlds (*Fig. 8*).

The knowledge management tool has three parts. One is related to the description of model and annotations

245

of the particular world. The other comprises the hierarchy of world objects and their formal description. The third one involves the discussion space as the tool for internet-based communication and team work.

Navigate	World	Discussion
Hierarchy of worlds Ontology Search engine	Title Specification Picture-s Model of the world Assumptions Further world components List of Files List of Documents List of following worlds	Discussion

Figure 8. Knowledge management tool (KMT)

The usual process of application of these tools is following. One way of usage is just creating of simulation project cases. The problem in the real world is formulated. The slots in the new item of the KMT are filled in according to *Fig. 1*. The problem is semantically indexed using the upper concepts of component ontology. The new item of the KMT on the conceptual layer is created. The Conceptual model is created using the Modelling tool. It may be annotated. Nevertheless the slots in the KMT item are filled in. The concept is semantically indexed using the concepts of component ontology. The new item of the KMT on the modelling layer is open. The Physical model is created using the modelling tool. It may be annotated. The slots in the KMT item are filled in. The physical model is semantically indexed using the concepts of ideal object ontology. Then the implementation of simulation model starts. The new item of the KMT on the simulation layer is created. The Simulation model is created using the simulation package and it is annotated using AT. The slots in the KMT item are filled in. The simulation model is semantically indexed using the concepts of simulation object ontology. If the tested simulation model is finished then the real simulation experiments start. The corresponding item in the KMT is created and filled in with description of contents and results of simulation experiments. They are also semantically indexed using simulation experiment ontology. Their interpreted results are described and semantically indexed in the item of the real world as the solution to the initial question.

The other way is creating of simulation project case but with usage of reuse of previous cases. The process is similar to that one above described, but at the each step the user can look for similar previous case using the semantic search based on the semantic indexes from the appropriate ontologies to the solved step (*Fig. 5*).

5. Conclusions

The paper describes the concepts and tools for knowledge support of virtual modelling and simulation. These techniques are important for virtual modelling used in teams and for reuse typical for any engineering methodology. The developed tools have been tested on cooperative development of simulation models and are being currently tested on the reuse of simulation models. The accumulated experience seems to suggest to apply the developed methodology and tools for other engineering design tasks dealing with other kinds of virtual modelling.

6. References

1. Zdráhal, Z., Valášek, M. (1996) Modeling Tasks in Engineering Design, *Cybernetics and Systems* **27**, 105-118.
2. Valášek, M. (1998) Mechatronic System Design Methodology - Initial Principles Based on Case Studies, in J. Adolfsson and J. Karlsen (eds.), *Mechatronics 98*, Pergamon, Amsterdam, 501-506.
3. ENRICH consortium: The ENRICH Methodology, Technical Report D54, The Open University, Milton Keynes 2000
4. Valášek, M., Steinbauer, P., Zdráhal, Z. (2001) Knowledge supported conceptual control design Methodology of Mechantronic Systems, In: Proc. of 2nd Int. Conf. on Advanced Engineering Design, AED 01, Univ. of Glasgow, Glasgow, pp. 237-242

DESIGN OF NONLINEAR CONTROL OF NONLINEAR MULTIBODY SYSTEMS

M. VALÁŠEK
Department of Mechanics
Faculty of Mechanical Engineering
Czech Technical University in Prague
Karlovo nám. 13, 121 35 Praha 2, Czech Republic
E-Mail: valasek@fsik.cvut.cz

1. Introduction

Multibody systems are the most usual models of mechatronic systems. Mechatronic systems use the synergy achieved by the combination of properties of mechanical (hardware) systems and control (software) systems applied by electronic devices. Therefore the control of multibody systems is very important topic for mechatronic design. Multibody systems have several crucial problems compared with general controlled systems. They make their control to be a challenge in many cases. Its general origin is the usual nonlinearity of multibody systems.

This paper deals with the description of these specific difficulties and with the description of main current approaches for their solutions.

2. Main Problems of Control of Multibody Systems

Multibody systems are the most often models of mechanical systems being controlled. They concentrate the mechanical functionality of machines to be enough precise on one hand and simultaneously to be enough concise for control on the other hand. The main difficulties of control of mechanical (multibody) systems are following:

- Mechanical (multibody) systems are usually nonlinear systems. The well established control methods are developed for linear systems, only recently there have been developed methods for control of nonlinear systems, however still not being so general and powerful as for linear systems.
- Nonlinearity is sometimes essential for the control of multibody systems. There exist multibody systems (e.g. nonholonomic systems) that being linearized about operation point become uncontrollable.
- Multibody systém undergo large displacements where linearization about operation point is impossible. The control problem is quite often not just stabilization around working (equilibrium) point, but the motion from one state into another one.
- Mechanical (multibody) systems in many cases have different number of inputs and outputs, or different number of inputs and degrees of freedom (DOFs). The inputs are operated by actuators (drives). Therefore it can be spoken about under-actuated, equal-actuated and over-actuated systems. This is causing especially problems in combination with nonlinearity of mechanical systems.
- Multibody systems are quite often suitably described by redundant coordinates. Then the models are described by differential-algebraic equations (DAE). DAE cannot be generally and easily transformed into ordinary differential equations (ODE). Only ODE can be described by state space models. The absolute majority of current control methods suppose that the dynamic system being controlled is described by ODE and thus the traditional control methods are difficult to be applied.

Let us summarize the usual control problems to be solved for the control of multibody systems:

- The first fundamental problem is to stabilize the motion of multibody system around its equilibrium. An important subproblem is just to check the stability of some proposed control.
- The next problem is to move the multibody system from one position into another. This problem is transformed into other problems. The problem can be stated as the global stabilization of the system from the initial position around the final position as the stabilized equilibrium. By this way the problem is transformed into previous problem. The other problem statement is to stabilize the system around the given trajectory connecting both positions. It is well known trajectory tracking. For nonlinear multibody systems it can be a serious problem just to construct admissible trajectory connecting initial and final positions.

247

- The previous problem can be formulated as the determination of optimal trajectory with respect to some performance index.
- The problem could be just to find any admissible trajectory of the system connecting two positions of multibody system.

The stabilizing problems are addressed by several groups of methods:
- There were developed methods that exactly linearized the nonlinear system and thus enable after the linearizing transformation to apply standard control methods for linear systems.
- Another approach is to propose a control law based on some insight into the system and then to carry out the synthesis of control parameters for the nonlinear plant as control gain optimization by the technique of multiobjective parameter optimization (MOPO).
- Very promising method is to rewrite the nonlinear system into the form of linear system and then to apply the standard control methods for linear systems however for position (state) dependent system. It is another way for transforming the nonlinear system into linear-like one.

The problem of constructing suitable trajectory is formulated
- either directly as the optimal control problem that is generally not quite easy to be solved
- or in specifically difficult cases of under-actuated systems as time planning problem that requires first to construct the missing control actions in order to modify the system into equal-actuated one.

3. Simple Demonstrational Example

The above stated problems and further described solution methods can be demonstrated on the following simple problem. Despite its simplicity this example includes all serious problem of control of multibody systems.

The exemplary multibody system (*Fig. 1*) consists of two bodies connected by revolute joints in plane. It has two DOFs. The first joint is always actuated by controlled action M_1. The second joint can be or can be not actuated by the torque M_2. If it is actuated then the system is equal-actuated and methods for exact linearization can be applied. It is a case of rigid planar robot manipulator. If the second joint is not actuated then the system is under-actuated and there are problems of its control. If this not-actuated joint is equipped with spring and damper then it is a model of flexible robotic arm. If there is no spring in this not-actuated joint then it is a model of mechatronic toy with different control challenges.

The multibody system can be described by the independent coordinates (e.g. φ_1 and φ_2) or by the dependent coordinates (e.g. the cartesian coordinates of centre of mass and angles of links with respect to the frame or natural Cartesian coordinates of ends of links). According to that the control is formulated as traditional control of ODE or control of DAE.
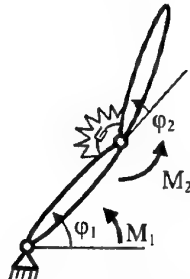
Figure 1. Example of simple multibody system with different control problems

4. Description of Nonlinear Multibody Systems

The (nonlinear) multibody systems including the control action are generally described by Lagrange equations of mixed type (e.g. [1])

$$M(s)\frac{d^2s}{dt^2} - \Phi^T\lambda = Q(s,\frac{ds}{dt}) + T(s,\frac{ds}{dt})u \qquad (1)$$

$$F(s,\frac{ds}{dt}) = 0 \qquad (2)$$

where s are the coordinates describing the multibody system, u the vector of input control variables, M is the mass matrix, Q are the generalized forces, F are the kinematic (holonomic or nonholonomic) constraints, Φ is

the Jacobian corresponding to the kinematic constraints, λ are the Lagrange multipliers, $\mathbf{u}$ the control inputs (forces) acting through transmissions $\mathbf{T}$. This fact that the general description of multibody systems uses differential-algebraic equations (DAE) is one of difficult problem of control synthesis for multibody systems.

These equations of motion for the purposes of control must be often transformed into the state space description. There are two possible ways how to do it. The first approach preserves the same variables $\mathbf{s}$ from original description and only eliminates the Lagrange multipliers λ. The kinematic constraints $\mathbf{F}$ in (2) are twice differentiated with respect to time

$$\Phi \frac{d^2 \mathbf{s}}{dt^2} = -(\Phi \frac{d\mathbf{s}}{dt})_s \frac{d\mathbf{s}}{dt} \tag{3}$$

where subscript s means partial differentiation with respect to the coordinates $\mathbf{s}$. The accelerations are expressed from the equations of motion (1) by multiplying it by the inverse of mass matrix M and they are substituted into (3). The equations for the Lagrange multipliers are thus derived. Solving for them and substituting back it is obtained the formulation of equations of motion of multibody system (1) in seemingly ordinary differential equations (ODE) only.

$$\frac{d^2 \mathbf{s}}{dt^2} = \mathbf{M}^{-1}(\mathbf{I} - \Phi^T(\Phi\mathbf{M}^{-1}\Phi^T)^{-1}\Phi\mathbf{M}^{-1})(\mathbf{Q}+\mathbf{Tu}) - \mathbf{M}^{-1}\Phi^T(\Phi\mathbf{M}^{-1}\Phi^T)^{-1}(\Phi\frac{d\mathbf{s}}{dt})_s\frac{d\mathbf{s}}{dt} \tag{4}$$

Hence the state space description with state vector [s, d/dt s] in dependent coordinates s can be obtained. However, in such case the resulted equations are after linearization not controllable. It follows from the fact that in such case the dependent coordinates on the level of acceleration are related by the quadratic terms in velocities as follows from the second derivatives of kinematic constraints $\mathbf{F}$ in (3). Such equations are after linearization not controllable in usual positions with zero velocities. Nevertheless this simple formulation is sometimes useful, e.g. for optimal control in section 8.

The other approach is based on the description of multibody systems in independent coordinates $\mathbf{q}$. The coordinates must be independent, e.g. the independent coordinates $\mathbf{q}$ are selected (constructed) from s generally

$$\mathbf{s} = \mathbf{r}(\mathbf{q})$$
$$\frac{d}{dt}\mathbf{s} = \mathbf{R}\frac{d}{dt}\mathbf{q} \tag{5}$$
$$\frac{d^2}{dt^2}\mathbf{s} = \mathbf{R}\frac{d^2}{dt^2}\mathbf{q} + \frac{d}{dt}\mathbf{R}\frac{d}{dt}\mathbf{q}$$

Substituting from (5) into the first time derivative of the kinematic constraint it is found out that this matrix $\mathbf{R}$ is the null space of the Jacobian Φ

$$\Phi\mathbf{R} = 0 \tag{6}$$

Thus multiplying the equations of motion (1) by RT eliminates again the Lagrange multipliers. Then using the state vector $\mathbf{x}=[\mathbf{q}, d\mathbf{q}/dt]$ the equations of motion can be transformed into the state space model

$$\frac{d}{dt}\mathbf{q} = \dot{\mathbf{q}}$$
$$\frac{d}{dt}\dot{\mathbf{q}} = (\mathbf{R}^T\mathbf{MR})^{-1}(\mathbf{R}^T\mathbf{g} - \mathbf{R}^T\mathbf{M}\dot{\mathbf{R}}\mathbf{q}) + (\mathbf{R}^T\mathbf{MR})^{-1}\mathbf{R}^T\mathbf{Tu} \tag{7}$$

The theory of multibody systems and the solution of corresponding DAE describes several methods for deriving and obtaining the null space matrix $\mathbf{R}$ (e.g. [1]).

Now the dynamics of multibody systém can be described in the form of general nonlinear system in state space description

$$\frac{dx}{dt} = f(x) + g(x)\,u \tag{8}$$

where $x(nx1)$ is the state vector, $u(mx1)$ is the control vector and generally $f(0)=0$. For the purpose of control it must be stated which variables y can be measured and used as the input to the control system. It is supposed their general dependence

$$y = h(x) \tag{9}$$

Thus there is the output variable vector $y(px1)$.

5. Exact Feedback Linearization of Nonlinear Systems

One of the fundamental approaches towards the control of nonlinear systems is the exact feedback linearization [2-5]. Its idea is simple. Considering the system (8) it is investigated the existence and the construction of a suitable (static) state feedback control

$$u = \alpha(x) + \beta(x)\,w \tag{10}$$

and a transformation of variables

$$z = T(x) \tag{11}$$

that together transform the original system (8) into a linear one

$$\frac{dz}{dt} = Az + Bw \tag{12}$$

The same problem can be investigated for the existence of a suitable dynamic state feedback control

$$u = \alpha(x, p) + \beta(x, p)w$$
$$\frac{dp}{dt} = \phi(x) + \eta(x)\,u \tag{13}$$

with a transformation of variables (11) that again transform the original system into a linear one (12). These problems are called input-state (exact feedback) linearization. And finally both these problems can be investigated for output feedback where instead of state variables x in feedbacks (10) or (13) there are used only output variables y (9). Then these problems are called input-output (exact feedback) linearization.

Then after transforming the original system into the equivalent linear one (12) there are applied the control techniques for linear systems like pole placement, LQR etc.

5.1 INPUT-OUTPUT EXACT FEEDBACK LINEARIZATION

The solution of the problem of input-output exact feedback linearization is simpler. The construction of possible linearizing feedback for the system (8)-(9) is the recursive application of the time differentiation rule

$$y^{(1)} = \frac{\partial h}{\partial x}(f(x) + g(x)\,u) = f_1(x) + g_1(x)\,u = L_f h + L_g h\,u =_{def} \dot{z}_1 =_{def} z_2$$

$$y^{(k+1)} = \frac{\partial z_k}{\partial x}(f(x) + g(x)\,u) = f_{k+1}(x) + g_{k+1}(x)\,u =_{def} \dot{z}_{k+1} =_{def} z_{k+2} \tag{14}$$

There is supposed besides necessary smoothness that $g_i = 0$ for $i=1,\ldots,r\text{-}1$ and $g_r \neq 0$ enabling to express

250

$$\mathbf{f}_r(\mathbf{x}) + \mathbf{g}_r(\mathbf{x})\mathbf{u} = \mathbf{w}$$

$$\mathbf{u} = \frac{\mathbf{w} - \mathbf{f}_r(\mathbf{x})}{\mathbf{g}_r(\mathbf{x})} \tag{15}$$

and this leads to

$$\mathbf{y}^{(r)} = \mathbf{w} \tag{16}$$

This means that the original system is first transformed into the Brunovsky canonical form (14) and then into the Frobenius canonical form (16). These canonical forms prove the controllability of the system and enable to stabilize the system easily by pole placement.

The transformation (11) is

$$\mathbf{z} = \mathbf{T}(\mathbf{x}) = [(\mathbf{h}(\mathbf{x}))^T, (L_\mathbf{f}\mathbf{h}(\mathbf{x}))^T, \ldots, (L_\mathbf{f}^{r-1}\mathbf{h}(\mathbf{x}))^T]^T \tag{17}$$

Here and in previous expressions there is used the formalism of Lie algebra

$$L_\mathbf{f}\mathbf{h}(\mathbf{x}) = \frac{\partial \mathbf{h}}{\partial \mathbf{x}}\mathbf{f}(\mathbf{x}), \quad L_\mathbf{f}^{i+1}\mathbf{h}(\mathbf{x}) = L_\mathbf{f}L_\mathbf{f}^{i}\mathbf{h}(\mathbf{x})$$

$$[\mathbf{f},\mathbf{g}](\mathbf{x}) = \frac{\partial \mathbf{g}}{\partial \mathbf{x}}\mathbf{f}(\mathbf{x}) - \frac{\partial \mathbf{f}}{\partial \mathbf{x}}\mathbf{g}(\mathbf{x}), \quad ad_\mathbf{f}^{0}\mathbf{g}(\mathbf{x}) = \mathbf{g}(\mathbf{x}), \quad ad_\mathbf{f}^{1}\mathbf{g}(\mathbf{x}) = [\mathbf{f},\mathbf{g}](\mathbf{x}), \quad ad_\mathbf{f}^{i+1}\mathbf{g}(\mathbf{x}) = [\mathbf{f},ad_\mathbf{f}^{i}\mathbf{g}](\mathbf{x}) \tag{18}$$

It can happen and it happens that r<n. In that case there is another dynamics in the system (8) besides (16). It is so called zero dynamics that is expressed from the original system stating the condition $y=y^{(1)}=\ldots=y^{(r)}=0$. The zero dynamics is not influenced by the transformation (17) and the control (15). The stability of this zero dynamics is decisive for the stabilizability of the whole system just by stabilizing the input-output dynamics (16) by the feedback (15) and pole placement.

5.2 INPUT-STATE EXACT FEEDBACK LINEARIZATION

This is the problem whether there exists such function y=h(x) for which the input-output exact feedback linearization gives r=n. This means that the system is completely linearized and there is no zero dynamics with the danger of destabilizing the system. There have been proved the necessary and sufficient condition for its existence. This is the full rank (equal n) of the vector field [g, ad$_f$g,...,ad$_f^{n-1}$g] and the set [g, ad$_f$g,...,ad$_f^{n-2}$g] is involutive (this means that if two vectors k_1 and k_2 are from this set then $[k_1,k_2]$ is also from this set). However, the construction of such h(x) is not so easy as the computation of the input-output exact feedback linearization (14).

In all these derivations it is supposed that the dimension of y is equal to the dimension of u and w. This is certainly often violated that prevents to apply this method for the control of under-actuated systems.

5.3 DYNAMIC STATE EXACT FEEDBACK LINEARIZATION

There has been proved that the existence of dynamic exact feedback linearization is equivalent to the special property of the system (8)-(9) called flatness [6-8]. A dynamic system is flat if the system (8)-(9) can be transformed into the relation between states and outputs and inputs and outputs in the form

$$\mathbf{x} = \Phi(\mathbf{y},\mathbf{y}^{(1)},\ldots,\mathbf{y}^{(\alpha)}) \tag{19}$$

$$\mathbf{u} = \Psi(\mathbf{y},\mathbf{y}^{(1)},\ldots,\mathbf{y}^{(\alpha)},\mathbf{y}^{(\alpha+1)}) \tag{20}$$

The equation (19) is inverted and substituted into (20) together with excessive derivatives of output variables y that are replaced by new subsystems of the form (16). This approach enable decide what kind of trajectories are admissible for the control of the investigated system.

Again in all these derivations it is supposed that the dimension of y is equal to the dimension of u and w. This is also violated for corresponding under-actuated systems (e.g. inverse pendulum). Thus only certain class of under-actuated systems can be controlled by this approach (e.g. crane with control of the cable length is flat [8-9], but crane without control of the cable length is not flat).

251

5.4 EXACT FEEDBACK LINEARIZATION OF DAE SYSTEMS

Interesting problem is the way of application of exact feedback linearization to DAE systems. The input-output exact feedback linearization can be applied immediately after elimination the Lagrange multipliers (4). One natural condition is that the output variables (9) must be selected as independent from the point of view of constraints (2). Therefore it is important to consider the choice of outputs based on the DOFs of the multibody system. However, the checking of condition for existence of input-state exact feedback linearization must be based on independent coordinates otherwise the transformation can loos full rank.

Another problem is what is the influence of exact feedback linearization constructed for independent coordinates on the remaining redundant ones [11]. The linearization of the input-output dynamics (16) means the establishment of superposition for nonlinear system. If two controls $\mathbf{w}_1$ and $\mathbf{w}_2$ cause two motions $\mathbf{y}_1$ and $\mathbf{y}_2$ of the multibody system described in independent variables then its linear combination $\alpha \mathbf{w}_1 + \beta \mathbf{w}_2$ leads to the motion $\alpha \mathbf{y}_1 + \beta \mathbf{y}_2$. This is not valid for the dependent output variables $\mathbf{y}_d$ because the constraint (2) is usually nonlinear

$$F(y, y_d) = 0, \quad y_d = F^{-1}(y), \quad F^{-1}(\alpha y_1 + \beta y_2) \neq \alpha F^{-1}(y_1) + \beta F^{-1}(y_2) \tag{21}$$

Nevertheless, if the linear combination $\alpha y_1 + \beta y_2 = y_{des}$ moves to the desired position y_{des} then also the motion of dependent variables y_d ends in the corresponding desired position $y_{d, des}$ as follows from (21). This fact is important for determining the suitable admissible (suboptimal) trajectories (e.g. extension of [10] for DAE in [11]).

6. Multiobjective Parameter Optimization

This method of control synthesis is the least restrictive one regarding the requirement on the description of nonlinear (multibody) system and the form of control law. However, the strength of claims about the properties of the synthetized control is relatively low. The synthesis procedure is following:

The Multi-Objective Parameter Optimization (MOPO) [12] is based on the design-by-simulaton. There is available the nonlinear simulation model of the controlled plant including the control law, the performance index usually in the form of integral performance index or maximum value and selected set of considered excitations. The control law is described in parametric form and its parameters are determined by the numerical optimization of the performance index evaluated by the simulation response of the plant to the considered excitations. Thus, by means of the MOPO approach the nonlinear models and models, which cannot be analytically treated, can be used. This approach enables not only to find parameters of nonlinear control of nonlinear plant, but it allows one also to find a satisfactory compromise among the performance criteria despite the fact that they conflict with each other. The MOPO approach is based on a search in the parameter space (Pareto optimality) by model simulation.

"Free system parameters", the tuning parameters, e.g. control coefficients, mass properties or installation positions, are varied within their given limits until an "optimal compromise" is found. In doing so the performance criteria (also called objective functions) $\mathbf{c}$ are weighted by user-defined weighting factors, the design parameters $\mathbf{d} \geq \mathbf{c}_{start}$. The optimization strategy is to minimize all weighted criteria $c_i(\mathbf{p})/d_i(\mathbf{p})$ in such a way that the currently *worst* criterion with the maximal value will be reduced: optimization tries to decrease the weighted criterion $c_i(\mathbf{p})/d_i(\mathbf{p}) \to 0$. The tuning parameters $\mathbf{p}$ are determined by solving a minmax-optimization problem with constraints and parameter restrictions

$$\alpha^* = \min_p (\max_i c_i / d_i) \tag{22}$$

$$c_i(\mathbf{p}) \leq d_i \text{ for } i \in \Psi \tag{23}$$

$$p_k^- \leq p_k \leq p_k^+ \tag{24}$$

The performance criteria (objective functions) may be free to be optimized or may be partially limited by a set Ψ of performance constraints, e.g. mechanical, hydraulic or electronic restrictions like power, pressure, current and voltage. The weighting factors or design parameters enable the user to adapt the criteria to adequate sizes and to determine the direction of optimization process by weighting some criteria more important $(c_i(\mathbf{p})/d_i(\mathbf{p}) = 1)$, others less important $(c_j(\mathbf{p})/d_j(\mathbf{p}) < c_i(\mathbf{p})/d_i(\mathbf{p}))$. The parameter optimization is

252

finished, when the maximum of all weighted criteria cannot be further decreased. The result is a point on the Pareto-optimal boundary (*Fig. 2*).

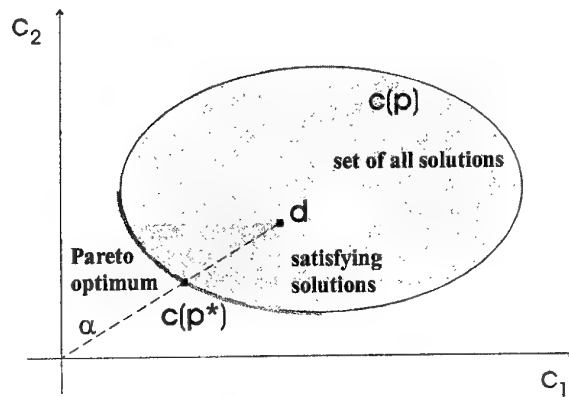Example of application of MOPO synthesis for vehicle suspensions is in [13].

Figure. 2 Pareto-Optimum for Two Objective Functions

7. Nonlinear Linearization of Nonlinear Systems

This is another way of transforming a nonlinear system into a linear form where methods of linear control can be applied [14-19]. The dynamics of the nonlinear system is described by the equations (8). The multibody system must be described by independent coordinates, otherwise further described decomposed system is uncontrollable. The quadratic performance index of the control which is to be synthesized is the infinite horizon control

$$J = \int_0^{\infty} (\mathbf{x}^T \mathbf{Q}\, \mathbf{x} + \mathbf{u}^T \mathbf{R}\, \mathbf{u})\, dt \qquad (25)$$

If there exists the decomposition of the system dynamics

$$\mathbf{f}(\mathbf{x}) = \mathbf{A}(\mathbf{x})\mathbf{x} \qquad (26)$$

and if the following assumptions [14] are valid
- The matrixes $\mathbf{Q}$ and $\mathbf{R}$ are positive definite.
- The matrixes $\mathbf{A}$ and $\mathbf{g}$ are analytic valued functions.
- There exists the control function $\mathbf{u}(t)$ and corresponding state trajectory $\mathbf{x}(t)$ for $t \in <0, \infty>$ which satisfy the system dynamics (8) and the performance index (25) is finite.
- The pair of marixes $(\mathbf{A}(\mathbf{x}), \mathbf{g}(\mathbf{x}))$ is controllable and stabilizable for each $\mathbf{x}$ in the linear system sense, i.e.

$$rank[\mathbf{g}(\mathbf{x}), \mathbf{A}(\mathbf{x})\mathbf{g}(\mathbf{x}), \ldots, \mathbf{A}^{n-1}(\mathbf{x})\mathbf{g}(\mathbf{x})] = n \qquad (27)$$

- The state vector $\mathbf{x}$ is fully measured.

then there exists the control

$$\mathbf{u} = -\mathbf{K}(\mathbf{x})\mathbf{x} \qquad (28)$$

which minimizes the performance index (25). However, it has been shown that this control is only suboptimal.

The nonlinear gain matrix $\mathbf{K}(\mathbf{x})$ is determined as

$$\mathbf{K}(\mathbf{x}) = \mathbf{R}^{-1}\mathbf{g}^T(\mathbf{x})\mathbf{P}(\mathbf{x}) \qquad (29)$$

where $\mathbf{P}(\mathbf{x})$ is the solution of the Riccatti equations

253

$$A^T(\mathbf{x})P(\mathbf{x}) + P(\mathbf{x})A(\mathbf{x}) + Q - P(\mathbf{x})g(\mathbf{x})R^{-1}g^T(\mathbf{x})P(\mathbf{x}) = 0 \qquad (30)$$

This control approach is called Nonlinear Quadratic Regulator (NQR) [17] or State Dependent Riccatti Equation (SDRE) control [15, 16].

The key problem is the computation of the decomposition $A(\mathbf{x})$. There have been derived some formulas for the computation of this decomposition, like [16]

$$A(\mathbf{x}) = \int_0^1 \frac{\partial \mathbf{f}}{\partial \mathbf{x}}\bigg|_{\mathbf{x}=\lambda\,\mathbf{x}} d\lambda \qquad (31)$$

But the computation of this formula for the multibody systems is very difficult because it requires the symbolic manipulation with the equations of motion which might be very large and complex and might include rational and trigonometric functions. Therefore it is not realistic to suppose to compute (31) for multibody systems.

Therefore there have been developed efficient algorithms [17] for computation of this decomposition that moreover enables to use the non-uniqueness of the decomposition (26) for control synthesis. The simplest procedure among them is following. Its idea is based on the following decomposition described for scalar function f of three variables x_1, x_2, x_3

$$f(x_1, x_2, x_3) = \frac{f(x_1, x_2, x_3) - f(0, x_2, x_3)}{x_1} x_1 +$$
$$+ \frac{f(0, x_2, x_3) - f(0,0, x_3)}{x_2} x_2 + \qquad (32)$$
$$+ \frac{f(0,0, x_3) - f(0,0,0)}{x_3} x_3$$

This decomposition must certainly solve the division by zero and it is dependent on the order of variables. The division by zero is equal according to l'Hospital rule in the limit to the corresponding derivative which for smooth functions exists and can be numerically computed by division for magnitudes of numerical accuracy of the computer.

The computation of this decomposition is not unique. It depends on the order of variables and besides that there are some free parameters for decomposition parametrization [17]. The influence of this ambiguity can be described and investigated by the recursive decomposition (32) applied to each addend of the previous decomposition step. There are 2^n such addends at the end for n variables which is very natural for polynomial functions f. However, the problem is that any addend f_i in any level of decomposition can be split into convex sum $f_i\lambda + f_i(1-\lambda)$ where λ can be any function. This makes the decomposition fully ambiguitious. The level of recursive decomposition and-or the free functions λ can be selected in order to improve controllability of decomposed system (8) with (26).

The main problem with NQR is that first it is not the optimum control of general nonlinear system as it has been shown in [18] and second there is still missing a proof of global stability of the control law (28) despite partial results [19]. There has not been found any case of unstable NQR control but general proof is missing. The practical experience is excellent and the stability can be checked for individual cases using the computed solution of the Riccatti equation (30). The Lyapunov function V is proposed as

$$V = \mathbf{x}^T P(\mathbf{x})\mathbf{x} \qquad (33)$$

It is positive definite according to the properties of the solution of Riccatti equation and the negativeness of its time derivative can be checked similarly in the same grid as the computed values of the gain $K(\mathbf{x})$ deriving into

$$\frac{dV}{dt} = -\mathbf{x}^T(Q + P(\mathbf{x})g(\mathbf{x})R^{-1}g^T(\mathbf{x})P(\mathbf{x}) - \frac{d P(\mathbf{x})}{d\mathbf{x}}(A(\mathbf{x}) - g(\mathbf{x})K(\mathbf{x}))\mathbf{x})\,\mathbf{x} \le 0 \qquad (34)$$

The first two terms are proving stability and the third term is usually small.

An important practical issue of NQR is the implementation of the synthetized control law. One approach can be the real-time computation of Riccatti equation and the whole control. It is certainly very

demanding of computational power but for some small systems reasonable. The other approach is based generally on the look-up tables. It means that the solutions of NQR control are computed for some values of states off-line and for the on-line application the pre-computed gains are either retrieved or interpolated. Such approaches were already used for gain scheduling approaches. The problem is certainly the efficient choice of suitable states for off-line computation and the on-line interpolation between them. This approach is applicable even for large multibody systems.

Another important advantage of NQR approach is that the control can be extended into incorporating different limitations of admissible control sets (e.g. asymmetric interval of control variable for semi-active systems [20]).

This approach of NQR is applicable to all under-actuated (certainly equal-actuated) systems that satisfy the condition that the linearized system about the equilibrium $x=0$ is controllable. Even this condition is violated for important classes of under-actuated systems (e.g. some nonholonomic multibody systems). For this class of multibody systems the control is very difficult. The stabilizing control were developed for such systems having $f(x)=0$, but for general systems with $f(x)\neq0$ it is still an open problem.

8. Optimal Control of Multibody Systems

The optimal control in the formulation of Pontryagin principle of maximum is applied for nonlinear multibody systems especially for the purpose of trajectory synthesis. The traditional formulation of Pontryagin principle of maximum for ODE of the system (8) is well known. However, its formulation for DAE systems is quite new problem. There were several approaches to extend the maximum principle straightforward from ODE to DAE systems, however with incorrect results. Only recently [21] it has succeeded to derive the correct proven extension. It is based on the idea that the DAE system (1)-(2) is transformed into the ODE system (4) just for the formulation of optimality conditions. In other words it means that the optimality conditions raised on the Hamiltonian must not involve the Lagrange multipliers λ. The optimality conditions are formulated using the equivalent ODE problem, but the problem solution is done within DAE problem. Thus the efficient and/or convenient formulation of multibody model is maintained and only the optimality conditions are formulated based on ODE.

9. Cyclic Control

The control, but just the synthesis of suitable admissible trajectory for under-actuated systems that are not flat, being linearized around equilibrium are loosing controllability or simply the system states go over the boundary of singularities, is a difficult problem. Then there is possible the approach of cyclic or invariant control [22].

Let solve the equation (15) for input variables u of the system (8) in the number equal to the number of output variables y in (9). The corresponding subsystems i and j will have the form (16) and (14)

$$
\begin{aligned}
& \mathbf{y}_i^{(r_i)} = \mathbf{w} \\
& \mathbf{y}_j^{(r_j)} = \mathbf{f}_{j,r_j}(\mathbf{x}) + \mathbf{g}_{j,r_j}(\mathbf{x})\,\mathbf{u} = \mathbf{f}_{j,r_j}(\mathbf{x}) + \mathbf{g}_{j,r_j}(\mathbf{x})\frac{\mathbf{w} - \mathbf{f}_{i,r_i}(\mathbf{x})}{\mathbf{g}_{i,r_i}(\mathbf{x})}
\end{aligned}
\tag{35}
$$

The new input variables w can be divided into two parts – arbitrary w_A and cyclic (invariant) w_I control

$$
\mathbf{w} = \mathbf{w}_A + \mathbf{w}_I
\tag{36}
$$

The arbitrary control is used for the control of subsystem i and the cyclic (invariant) control is used for the control of those subsystems j that cannot be linearized as the subsystem i. The invariant control is constructed based on periodic functions $\{w_{I,m}\}$ with period T in such way that it does not influence the state of subsystem i in times kT

$$
\begin{aligned}
& w_I = \sum_m k_m w_{I,m} \\
& \int_0^T w_{I,m}\,dt = 0, \quad \iint w_{I,m}\,dtdt = 0, \dots, \int\dots\int_0^T w_{I,m}\,dt\dots dt = 0
\end{aligned}
\tag{37}
$$

By this way there are constructed new control variables w_l that influence only other subsystems than the subsystem i. Such control can be used for the path across the boundary of singularity etc. This control can be then combined with NQR control around the vicinity of equilibrium iff the system is controllable after linearization.

10. Conclusions

There have been developed many very powerful control approaches for general nonlinear systems. A special case are nonlinear multibody systems. Despite many new control methods there still remain open problems (e.g. stabilization of nonholonomic systems with offset). Further there are specific problems of application of control methods for multibody systems if they are described by redundant coordinates and DAE.

11. References

1. Stejskal, V., Valasek, M. (1996) *Kinematics and Dynamics of Machinery*, Marcel Dekker, New York
2. Isidori, A. (1989) *Nonlinear Control Systems*, Springer-Verlag, Berlin.
3. Slotine, J.J., Li, W. (1991) *Applied Nonlinear Control*, Prentice Hall, New Jersey
4. Fliess, M. (ed.) (1992) *Nonlinear Control System Design*, Pergamon Press.
5. Khalil, H.K. (1996) *Nonlinear Systems*, Prentice Hall, New Jersey.
6. Fliess, M. et al. (1995) Flatness and Dynamic Feedback Linearizability: Two Approaches, In: *Proc. Of 3rd European Control Conference*, Rome, pp. 649-654.
7. Delaleau, E., Rudolph, J. (1998) Control of Flat Systems by Quasi-static Feedback of Generalized States, *Int. J. of Control* 71 (1998), 5, pp. 745-765.
8. Rudolph, J., Delaleau, E. (1998) *Some Examples and Remarks on Quasi-Static Feedback of Generalized States*, Automatica 34 (1998), 8, pp. 993-999.
9. Woernle, Ch. (2002) *Control of Robotic Systems by Exact Linearization Methods*, In: P. Maisser, P. Tenberge (eds.), Advanced Driving Systems, Chemnitz
10. Valasek, M. (1986) Synthesis of Optimal Trajectory of Industrial Robots, Kybernetika 22 (1986), pp. 409-424
11. Bastl, P. (2002) Optimal Control of Multibody Systems Described by Redundant Coordinates, PhD Thesis, Czech Technical University in Prague.
12. Joos, H.D. (1992) Informationstechnische Behandlung des mehrzieligen optimierungsgestutzten regelungstechnischen Entwurfs, PhD Thesis, Univ. of Stuttgart.
13. Valasek, M. et al. (1998) Development of Semi-Active Road-Friendly Truck Suspensions, *Control Engineering Practice* 6(1998), pp. 735-744
14. Banks, S.P., Mhana, K.J. (1992) Optimal control and stabilization for nonlinear systems, *SIAM Journal of Mathematical Control and Information*, 9(1992), pp. 179-196
15. Cloutier, J.R. (1997) *State-Dependent Riccati Equation Techniques: An Overview*, Proc. of 1997 American Control Conference, Albuquerque 1997, pp. 932-936
16. Langson, W., Alleyne, A. (1997) Inifinte horizon optimal control of a class of nonlinear systems, *Proc. of the IEEE American Control Conference* 1997, pp. 3017-3022
17. Valasek, M., Steinbauer, P. (1999) Nonlinear Control of Multibody Systems, In: Ambrosio, J., Schiehlen, W. (eds.): *Proc. of Euromech Colloquium 404, Advances in Computational Multibody Dynamics*, Lisabon, pp. 437-444
18. Cloutier, J. R. et al. (1999) On the recoverability of nonlinear state feedback laws by extended linearization control techniques, *Proc. of the 1999 American Control Conference*, San Diego, pp. 1515-1519.
19. Erdem, E.B., Alleyne, A. (1999) Globally stabilizing second order nonlinear systems by SDRE control, *Proc. of the 1999 American Control Conference*, San Diego, pp. 2501-2505.
20. Valasek, M., Kejval, J. (2000) New Direct Synthesis of Nonlinear Optimal Control of Semi-Active Suspensions, In: Proc. of Advanced Vehicle Control AVEC 2000, Ann Arbor, pp. 691-697.
21. Roubicek, T., Valasek, M. (in print) Optimal Controil of Causal Differential-Algebaric Systems, *JMAA*
22. Valasek, M. (1993) Control of Elastic Industrial Robots by Nonlinear Dynamic Compensation, *Acta Polytechnica* 33, 1, (1993), pp. 15-30.

MULTIBODY SYSTEM CONTACT DYNAMICS SIMULATION

Evtim Zahariev
Institute of Mechanics, Bulgarian Academy of Sciences,
Acad. G. Bonchev St., bl. 4
1113 Sofia, BULGARIA
evtimvz@bas.bg

Abstract: In the present article a numerical approach for modeling impact and unilateral contact constraints of multibody systems is presented. The discontinuous Coulomb friction is taken into account. The explicit form dynamic equations and impulse – momentum equations without kinematics constraints are the basis of the dynamic model. Generalized coordinates and impulses are parameters of the dynamic equations. The contact effects: stiction, sliding, the transition sliding-stiction-sliding are included in the simulation. An approach of analysis of the contact point velocities in the tangential plane, as well as, of the normal and tangential impulses is applied for numerical estimation of the motion in the contact points and of the whole system. Rigid and flexible multibody systems are considered. For the rigid bodies, the contact laws of Newton and Poisson are applied. It is pointed out that, either for rigid or for flexible multibody systems, the theory of the coefficient of restitution does not present reliable results. In the treatment a novel approach is suggested in which, as a result of existence of contact, transformation of the dynamic equations is implemented. The normal impulses and/or the normal reactions become parameters of the linear equation system. Simultaneous contact (impact and surface contact) in multiple points is discussed and, in this case, a numerical algorithm for system motion simulation is presented. Several examples of impact of rigid and flexible mechanical systems and existence of unilateral constraints are displayed.

1. Introduction

In the treatment multibody systems are considered mechanical systems built of rigid and flexible bodies. The possible motions are subject of kinematic and force constraints that are imposed by joints, springs, prescribed motions and etc. The main subject is the contact that occurs as a result of the system motion and is not guarantied by the design scheme. That is contact as a result of impact and surface unilateral constraints. The discontinuous nature of this motion makes the dynamic model and the simulation procedure complicated problem and requires specific approaches for its solution.

Mainly two approaches have been used in the scientific literature. These are:

- classical approach of the constrained dynamics and analysis of the Lagrange's multipliers using complimentary conditions and coefficient of restitution;

- approach of estimation of the contact forces as a result of possible penetration of the contact surfaces and consequential integration of the dynamic equation using numerical methods and/or penalty functions.

In the classical theory existence of contact means additional kinematic constraints [1]. The inclusion or exclusion of algebraic constraints that correspond to contact phenomena transforms the dynamic equations where the amplitudes of the contact forces are included. The sign of the Lagrange's multipliers defines the direction of the contact forces and, respectively, existence of contact or separation of the contacting points. The contact problem solution becomes more complicated if nonlinear friction in the tangential plane is assumed. One unilateral constraint could have four different states: separation of the contact; sliding, continuous stiction; transition stiction - sliding. The stiction phenomenon and possible transition stiction - sliding causes branching of the calculations and requires additional transformations of the dynamic equations. A complicated problem is the definition of the sliding direction after stiction in the tangential plane. This branching implies the necessity of solution of combinatorial task. The aforementioned problems are discussed in details and successfully solved in a consequence of scientific investigations of Glocker and Pfeiffer [2, 3], Seyfferth and Pfeiffer [4]], Wosle and Pfeiffer [5].

The distance at the very beginning or end of the contact defines the normal direction and the tangential plane in the contact points. During the impact process it becomes zero and the next stage, called compression phase, transformation of the kinetic energy of the system into potential energy of the elastic deformations is achieved. The process of restitution of the stored potential energy into kinetic and separation of the bodies is called restitution phase. The process of regeneration of kinetic energy is the reason for experimental investigations of the so-called "coefficient of restitution". The most frequently used definitions of the coefficient of restitution are based on (Hunt and Grossley [6] , Brach [7], Keller [8], Wang and Mason [9]): the Newton's theory of the ratio between the relative velocities of the contact points after and before the impact; the Poisson's theory of the ratio of the impulses in the contact point during the phases of restitution and compression.

The coefficient of restitution provides one step solution of the velocity problem and is widely applied for analysis of impact. The basic hypotheses have been used in many treatments. Glocker and Pfeiffer [10] presented a two-dimensional impact model based on Poisson's hypothesis and Coulomb friction. The problem of multiple impacts of multibody systems is regarded using nearly identical conditions during the two impact phases, compression and restitution. In their recent book Pfeiffer and Glocker [11] developed this methodology in case of impact of multibody systems with unilateral constraints. Schiehlen [12] regarded different approaches of multibody contact dynamics and multi-rate integration methods are proposed to enhance the efficiency of the calculation procedures. Lankarani and Pereira [13] made a detailed review of the studies concerning this topic. The authors solved the rigid multibody systems frictional impact and described seven phases of possible motion of colliding bodies that are to be analyzed for estimation of the real motion.

In the second approach of contact and impact simulation the distance (or the gap) between the contact surfaces plays significant role. For modeling of impact an approach is used [14, 15] where the contact points are loaded by forces. The parameters of the forces correspond to the stiffness properties of the body materials and shapes and their values are calculated using linearized data obtained by contact Hertz' theory [16]. The dynamic equations of motion are then numerically integrated. Similar approach is this of the penalty functions [17 - 19]. In [19] the convergence of the penalty function method and the reduced – integration penalty methods are discussed.

In the article a numerical algorithm for modeling of impact of rigid and flexible multibody systems taking into account the nonlinear Coulomb friction is suggested. A modified dynamic model using Lagrange's equations is suggested. The possible motions along the normal directions of the contact point tangential planes are considered coordinates and parameters in the dynamic equations. Transformation of the dynamic equations is implemented, where the motions appear as parameters if no contact exists or, in case of contact, the reaction forces are parameters of the dynamic equations. Using this approach the size and

257

the number of the parameters is constant. The parameters of multiple contact points (unilateral contact an impact points) are included in the dynamic equations.

The algorithm is consequently applied, if rigid bodies are considered, to the two phases of the impact - compression and restitution. In every phase the possible events sliding, reverse sliding, stiction and sliding-stiction are analyzed satisfying the impulse-momentum equations. The algorithm is developed in case of hypotheses of Newton and Poisson for the coefficient of restitution. A new definition for "dominant tangential jump" is developed for analysis of the stick-slip process in the tangential plane at the time of impact. The same numerical procedure is applied in case of flexible systems discretized using finite elements in relative coordinates. The jumps of the velocities are obtained as a result of vanishing of the normal coordinates between the colliding nodes. The resulting global deflections of the flexible system are obtained integrating the dynamic equations with the initial velocities so obtained. The reaction forces in the contact points are calculated. The numerical algorithm is analyzed solving several examples of rigid and flexible multibody systems in case of multiple contact and impact of flexible elements and nodes.

2. Theoretical Background

The theoretical background of the multibody system dynamics is well developed and studied. The analytical form of a multibody system dynamic equations with kinematic constraints, as a common, are presented by second order Differential Algebraic Equations (DAE)

$$M \cdot \ddot{Q} = G(Q, \dot{Q}) \tag{1}$$

$$\Phi(Q) = \mathbf{0}_m \tag{2}$$

with respect to $n \times 1$ matrix - column $\ddot{Q}$ of the second time derivatives of all coordinates of motion $Q = \begin{bmatrix} q_1 & q_2 & \cdots & q_n \end{bmatrix}^T$. For a common case the analytical solution cannot be provided. The numerical solution requires discretization of the equations (1, 2). Using the Lagrange's equations and after transformations one obtains the linear $(n+m) \times (n+m)$ equation system with respect to the unknown $\ddot{Q}$ and coefficient of Lagrange, m sized matrix - column Λ, i. e.:

$$M \cdot \ddot{Q} - \Phi_Q^T \cdot \Lambda = G(Q, \dot{Q}) \tag{3}$$

$$\Phi_Q(Q) \cdot \ddot{Q} + \dot{\Phi}_Q(Q) \cdot \dot{Q} = \mathbf{0}_m \tag{4}$$

that provides solution of the initial value problem (with given Q and $\dot{Q}$). The solution of the DAE (3, 4) should also satisfy the discretized position constraint equations, as well as, their first time derivatives, i. e.:

$$\Phi(Q) = \mathbf{0}_m \tag{5}$$

$$\Phi_Q(Q) \cdot \dot{Q} = \mathbf{0}_m \tag{6}$$

In equations (1 – 6) M is $n \times n$ mass-matrix; G is n sized matrix - column of the applied and velocity dependent inertia forces; $\Phi_Q = \dfrac{\partial \Phi}{\partial Q}$ is $m \times n$ matrix of the partial derivatives of the constraint equations; $\mathbf{0}_m$ is m sized zero matrix-column ($\mathbf{0}^n$ and $\mathbf{0}_m^n$ are n sized row zero matrix and $m \times n$ zero matrix, respectively).

For constraint dynamics the IME in case of impact in a point are as follows [1]:

$$M \cdot \Delta\dot{Q} - \Phi_Q^T \cdot I_\lambda = \dfrac{\partial s}{\partial Q}^T \cdot I_s \tag{7}$$

$$\Phi_Q \cdot \Delta\dot{Q} = \mathbf{0}_m \tag{8}$$

$$s_Q \cdot \Delta\dot{Q} = -(1+e) \cdot s_Q \cdot \dot{Q}^{(-)} \tag{9}$$

where $s = s(Q)$ is the distance between the colliding surfaces at the time of impact; $s_Q = \dfrac{\partial s}{\partial Q}$; $\Delta\dot{Q} = \dot{Q}^{(+)} - \dot{Q}^{(-)}$ is the jump of the velocities after (superscript +) and before (-) the impact; I_λ is m sized matrix – column of the impulses caused by the constraints; and e is the coefficient of restitution for the specific body shapes and materials in the points of impact. Here the coefficient of restitution is defined according to the Newton's hypothesis. As one could see from equations (7 – 9) the existence of impact adds to equations (7, 8) one constraint (9) and one parameter – the impulse I_s in the point of impact. So, the IME (7 - 9) are $n+m+1$ linear equation system with respect to $n+m+1$ unknown parameters - velocities jumps $\Delta\dot{Q}$, impulses of the constraints I_λ and impulse in the contact point I_s.

The Poisson's hypothesis could be applied for the restitution phase only, calculating first the impulse during the compression phase applying the Newton's hypothesis with coefficient of restitution $e = 0$. For the restitution phase the impulse I_s in equation (7) is known parameter, i. e., $I_s = I_s^r = e \cdot I_s^c$, since I_s^c is computed at the compression stage. The solution for the velocity jumps $\Delta\dot{Q} = \dot{Q}^{(+)}$ and the impulses of the constraints I_λ^r at the restitution phase are obtained solving the linear system of equations (7, 8).

258

3. Kinematics of the Contact

In Fig. 1 a multibody system is shown when one of its body approaches the surface of another one at the time of possible contact. The problem of contact point detection is considered in many papers (Eberhard and Jang [20]) and is not subject of this paper. The both tangential planes in the colliding points, respectively, their normal directions coincide. If contact occurs, as a result of active kinematic restrictions, the motion along the normal direction of the contact tangential plane vanishes and the number of the coordinates decreases with one. If stiction occurs the restrictions become two more (in case of three-dimensional motion) and, respectively, two more coordinates become dependent. The possible small translations s_{τ_1}, s_{τ_2} in the tangential plane, and s along its normal direction, as well as, the possible small rotations θ_{τ_1}, θ_{τ_2}, θ_n along the orthogonal directions τ_1, τ_2, n are also presented in the figure. In the article the friction forces imposed on the possible rotations are not regarded and only friction along the translations and the corresponding reactions will be considered. Reaction forces appear along the normal direction, as well as, along both directions of the tangential plane in case of stiction. Friction forces appear in the tangential plane if sliding occurs. The friction forces depend on the friction coefficient and the normal reaction, while their directions are in the opposite direction of the velocities in the tangential plane.

In Fig. 2 two bodies of a multibody system at the moment of incoming impact are shown. The axis defined from the tangential plane and the normal direction in the point of contact are shown. Similarly of Fig. 1, the three possible translations are q_i, q_{i+1}, q_{i+2} that obviously coincide with the translations s, s_{τ_1}, s_{τ_2}, respectively. The corresponding impulses are I_i,
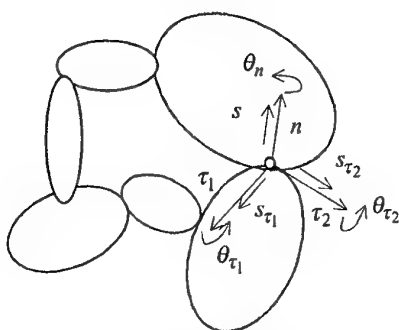

Fig 1: Kinematic presentation
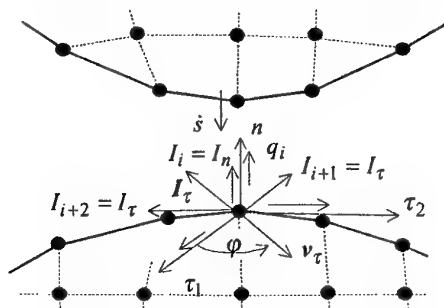of impact points of a multibody system

Fig. 2: Generalized coordinates and
impulses in case of spatial impact

I_{i+1}, I_{i+2}, where I_i corresponds to the normal impulse ($I_i = I_n$) while the other are components of the impulse $I_\tau = \begin{bmatrix} I_{i+1} & I_{i+2} \end{bmatrix}^{\mathrm{T}}$ in the tangential plane. In case of sliding in the tangential plane the frictional impulse is along the opposite direction of the tangential velocity $v_\tau = \begin{bmatrix} \dot{q}_{i+1} & \dot{q}_{i+2} \end{bmatrix}^{\mathrm{T}}$ while its magnitude depends on the friction coefficient and the impulse along the normal direction. The new notations of these possible translations are to point out that we include them as elements of matrix Q and the indexes show the number of the elements. As well as, the impulses in the contact points are stored in a matrix – column of the contact impulses I that differs from the impulses I_λ of the constraints, equation (7). So, if contact occurs in a point or node the possible translations along the normal direction and in the tangential plane will be stored in matrix Q consequently, in order, as it was presented above. So it is for the impulses in the point of contact.

The dynamic equations (3, 4) could be rewritten in matrix form as follows:

$$\begin{bmatrix} M & -\Phi_Q^{\mathrm{T}} \\ \Phi_Q & 0_m \end{bmatrix} \cdot \begin{bmatrix} \ddot{Q} \\ \Lambda \end{bmatrix} = \begin{bmatrix} G \\ -\dot{\Phi}_Q \cdot \dot{Q} \end{bmatrix} = F(Q, \dot{Q}) \tag{10}$$

The kinematic constraints, equations (4 – 6), are assumed invariant in numbers and forms. They do not present the constraints as a result of possible contact. Existence of contact adds additional constraints that, for a single contact point for which the parameter q_i is the motion along the normal in the contact point, could be expressed as follows:

$$\Phi_{m+1} = q_i = a_i = const \tag{11}$$

$$\dot{\Phi}_{m+1} = \dot{q}_i = 0 \tag{12}$$

$$\ddot{\Phi}_{m+1} = \ddot{q}_i = 0 \tag{13}$$

The partial derivatives of the additional constraint Φ_{m+1} is $\dfrac{\partial \Phi_{m+1}}{\partial Q} = \dfrac{\partial q_i}{\partial Q} = \begin{bmatrix} 0 & 0 & \cdots & 0 & 1 & 0 & \cdots & 0 \end{bmatrix}$ where the place of the unity in this matrix - row coincides with the place of the corresponding coordinate q_i in matrix Q. If impact occurs the distance s between the colliding points coincides with the corresponding coordinate (motion along the normal direction) that, in this case is the ith element of matrix Q. The partial derivatives of s are stored in matrix – row

259

$\frac{\partial s}{\partial Q} = \frac{\partial \dot{q}_i}{\partial Q} = \begin{bmatrix} 0 & 0 & \cdots & 0 & 1 & 0 & \cdots & 0 \end{bmatrix}$. The jump of the velocity $\Delta \dot{s} = \dot{s}^{(+)} - \dot{s}^{(-)} = \Delta \dot{q}_i$ (Newton's hypothesis) is also element of matrix $\Delta \dot{Q}$. So, the choice of the possible motions in the points of contact to be elements of the matrix of the coordinates Q simplifies significantly the expressions of the corresponding constraints, as well as, of their partial derivatives.

4. Transformation of the Contact Dynamic Equations

Existence of an additional constraint (11) and having in mind its derivatives, and after substitution of equation (13) in equation (10) one obtain the dynamic equations in case of contact along the coordinate i, i. e.:

$$\begin{bmatrix} M & -\Phi_Q^T \\ \Phi_Q & 0_m \end{bmatrix} \cdot \begin{bmatrix} \ddot{Q} \\ \Lambda \end{bmatrix} - \left(\frac{\partial \Phi_{m+1}}{\partial Q} \right)^T \cdot \lambda_{m+1} = \begin{bmatrix} \underline{M} & -\Phi_Q^T \\ \underline{\Phi}_Q & 0_m \end{bmatrix} \cdot \begin{bmatrix} \underline{\ddot{Q}} \\ \Lambda \end{bmatrix} = F \tag{14}$$

where matrix $\underline{\Phi}_Q$ is composed of matrix Φ_Q for which all elements of row i are zero; matrix $\underline{M}$,

$$\underline{M} = \begin{bmatrix} m_{1,1} & m_{1,2} & \cdots & 0 & m_{1,i+1} & \cdots & m_{1,n} \\ m_{2,1} & m_{2,2} & \cdots & 0 & m_{2,i+1} & \cdots & m_{2,n} \\ \cdots & \cdots & \cdots & \cdots & \cdots & \cdots & \cdots \\ m_{i,1} & m_{i,2} & \cdots & -1 & m_{i,i+1} & \cdots & m_{i,n} \\ \cdots & \cdots & \cdots & \cdots & \cdots & \cdots & \cdots \\ m_{n,1} & m_{n,2} & \cdots & 0 & m_{n,i+1} & \cdots & m_{n,n} \end{bmatrix} \tag{15}$$

is composed of matrix M for which the ith diagonal element is equal 1 and all other elements of ith column are 0; for matrix $\underline{\ddot{Q}}$,

$\underline{\ddot{Q}} = \begin{bmatrix} \ddot{q}_1 & \ddot{q}_2 & \cdots & \lambda_{m+1} & \ddot{q}_{i+1} & \cdots & \ddot{q}_n \end{bmatrix}^T$ the element $\ddot{q}_i$ is substituted by λ_{m+1}. This simple substitution gives the possibility, in case of contact and if the conditions (11 – 13) are fulfilled, the dynamic equations to be solved directly for the accelerations and for the normal reaction λ_{m+1} in the contact point using the latter as a parameter instead of $\ddot{q}_i$. So, the size of the differential equations and the number of the parameters are not changed. The sign of λ_{m+1} defines the direction of the reaction in the contact point and if it is negative the reaction coincides with the positive direction of the normal, which means that the solution of the transformed dynamic equations is true. If the reaction is negative the solution is not real. Separation of the contact points follows and the corresponding constraint must be excluded from the DAE.

If impact occurs and using the motion along the normal direction in the contact point as a coordinate (in this case the ith element of matrix Q) one can rewrite the IME (7 – 9) as follows:

$$\begin{bmatrix} M & -\Phi_Q^T \\ \Phi_Q & 0_m \end{bmatrix} \cdot \begin{bmatrix} \Delta \dot{Q} \\ I_\lambda \end{bmatrix} - \begin{bmatrix} \dfrac{\partial s}{\partial Q}^T \\ 0_m \end{bmatrix} \cdot I_i = 0_{n+m} \tag{16}$$

$$\Delta \dot{q}_i = -(1 + e) \cdot \dot{q}_i^{(-)} \tag{17}$$

which means that with given coefficient of restitution the velocity jump of the ith parameter $\Delta \dot{q}_i$ is calculated explicitly from (17) and could be excluded from equation (16). In equation (16) I_i is the impulse along the normal direction that coincides with the ith coordinate. The resulting IME are as follows:

$$\begin{bmatrix} \underline{M} & -\Phi_Q^T \\ \underline{\Phi}_Q & 0_m \end{bmatrix} \cdot \begin{bmatrix} \Delta \underline{\dot{Q}} \\ I_\lambda \end{bmatrix} + \begin{bmatrix} M_i \\ 0_m \end{bmatrix} \cdot \Delta \dot{q}_i = 0_{n+m} \tag{18}$$

In equation (18) the matrices $\underline{\Phi}_Q$ and $\underline{M}$ are the same matrices as described above in equation (14, 15); M_i is the ith column of matrix M. In matrix $\Delta \underline{\dot{Q}}$, similarly to matrix $\underline{\ddot{Q}}$, the ith element is substituted by I_i, i.e.:

$\Delta \underline{\dot{Q}} = \begin{bmatrix} \Delta \dot{q}_1 & \Delta \dot{q}_2 & \cdots & I_i & \Delta \dot{q}_{i+1} & \cdots & \Delta \dot{q}_n \end{bmatrix}^T$. This selection of the coordinates results in transformation of the mass matrix and the matrix of the partial derivatives modifying only the columns that correspond to the coordinates (motions) in the contact point. This transformation is independent for every contact point and is achieved simultaneously for all contact points.

5. Frictional Contact of Rigid Multibody Systems

5.1. FRICTIONAL UNILATERAL CONTACT
If friction is taken into consideration additional friction force in the tangential plane appears. As the magnitude of the reaction force in the contact point is equal of the Lagrange's coefficient λ_{m+1} we denote this coefficient as a contact force $R_i = \lambda_{m+1}$

that corresponds to the coordinate i. The friction forces in the tangential plane are denoted F_{i+1}, F_{i+2}. If stiction occurs the values and directions of the friction forces are calculated as follows:

$$F_{i+m} = -\mu \cdot \frac{v_{\tau_m}}{\|v_\tau\|} \cdot R_i = -\mu \cdot \frac{\dot{q}_{i+m}}{\sqrt{\dot{q}_{i+1}^2 + \dot{q}_{i+2}^2}} \cdot R_i = -\mu_{i+m} \cdot R_i \, ; \, m = 1, 2 \tag{19}$$

where μ is the coefficient of friction, while with μ_{i+1}, μ_{i+2} directional frictional coefficients are pointed out. The transformation of the DAE (14), respectively of matrix M, taking into account the friction in the contact point is as follows:

$$\underline{M}\langle i_{sl} \rangle = \begin{bmatrix} m_{1,1} & m_{1,2} & \cdots & 0 & m_{1,i+1} & \cdots & m_{1,n} \\ m_{2,1} & m_{2,2} & \cdots & 0 & m_{2,i+1} & \cdots & m_{2,n} \\ \cdots & \cdots & \cdots & \cdots & \cdots & \cdots & \cdots \\ m_{i,1} & m_{i,2} & \cdots & -1 & m_{i,i+1} & \cdots & m_{i,n} \\ m_{i+1,1} & m_{i+1,2} & \cdots & \mu_{i+1} & m_{i+1,i+1} & \cdots & m_{i+1,n} \\ m_{i+2,1} & m_{i+2,2} & \cdots & \mu_{2+1} & m_{i+2,i+1} & \cdots & m_{i+2,n} \\ \cdots & \cdots & \cdots & 0 & \cdots & \cdots & \cdots \\ m_{n,1} & m_{n,2} & \cdots & 0 & m_{n,i+1} & \cdots & m_{n,n} \end{bmatrix} \tag{20}$$

where the notation $\underline{M}\langle i_{sl} \rangle$ points out that column i of matrix M is transformed according to the conditions for sliding in case of contact for i^{th} coordinate (element) of Q. the modified matrix of the accelerations is

$$\underline{\ddot{Q}}\langle i_{sl} \rangle = \begin{bmatrix} \ddot{q}_1 & \ddot{q}_2 & \cdots & R_i & \ddot{q}_{i+1} & \cdots & \ddot{q}_n \end{bmatrix}^{\mathrm{T}} \tag{21}$$

In the modified matrix Φ_Q - $\underline{\Phi}_Q\langle i_{sl} \rangle$ all the elements of column i are equal zero.

If stiction occurs constraints, in the form of equations (11 – 13), are imposed of the motions in the tangential plane, q_{i+1} and q_{i+2}. In this case the modified matrix M is as follows:

$$\underline{M}\langle i_{sl} \rangle = \begin{bmatrix} m_{1,1} & m_{1,2} & \cdots & 0 & 0 & 0 & m_{1,i+3} & \cdots & m_{1,n} \\ m_{2,1} & m_{2,2} & \cdots & 0 & 0 & 0 & m_{2,i+3} & \cdots & m_{2,n} \\ \cdots & \cdots & \cdots & \cdots & \cdots & \cdots & \cdots & \cdots & \cdots \\ m_{i,1} & m_{i,2} & \cdots & -1 & 0 & 0 & m_{i,i+3} & \cdots & m_{i,n} \\ m_{i+1,1} & m_{i+1,2} & \cdots & 0 & -1 & 0 & m_{i+1,i+3} & \cdots & m_{i+1,n} \\ m_{i+2,1} & m_{i+2,2} & \cdots & 0 & 0 & -1 & m_{i+2,i+3} & \cdots & m_{i+2,n} \\ \cdots & \cdots & \cdots & \cdots & \cdots & \cdots & \cdots & \cdots & \cdots \\ m_{n,1} & m_{n,2} & \cdots & 0 & 0 & 0 & m_{n,i+3} & \cdots & m_{n,n} \end{bmatrix} \tag{22}$$

while the modified matrix – column of the accelerations is

$$\underline{\ddot{Q}}\langle i_{sl} \rangle = \begin{bmatrix} \ddot{q}_1 & \ddot{q}_2 & \cdots & R_i & R_{i+1} & R_{i+2} & \ddot{q}_{i+3} & \cdots & \ddot{q}_n \end{bmatrix}^{\mathrm{T}} \tag{23}$$

R_{i+1}, R_{i+2} are the reactions in the tangential plane as a result of the existing stiction. In the modified matrix Φ_Q - $\underline{\Phi}_Q\langle i_{sl} \rangle$ all the elements of columns i, $i+1$, $i+2$ are equal zero. An important task of the contact analysis is that of verification of the conditions for stiction. If the tangential velocity in the point of contact is equal zero there exists two possibilities, i. e.: sliding or stiction.

The algorithm proposed in the article provides easily implemented numerical algorithm for transformation of the DAE without changing the number of the differential equations and parameters in case of contact. Especially convenient the approach is if applied for multiple contact problem solution. The matrices M, Φ_Q, $\ddot{Q}$ are modified using simple and independent substitution of the elements of the columns that correspond to the coordinates describing the motions in the points of contact. For multiple contact points a combinatorial task of all the possible contact events (sliding and stiction) in every contact point should be compiled and every combination should be checked for fulfilling of the contact conditions and for the conditions for stiction and sliding.

5.2. FRICTIONAL IMPACT

In terms of the mathematics the IME do not regard the kind of the velocity jump, i.e. compression or restitution - they are identical for these two phases. The separate investigation of the two phases of the impact process is applied in several treatments [10, 13]. Here, according to the positive direction of the normal in the contact point (Fig. 1, 2), the normal velocity at the stage of compression is negative. The tangential velocity could be negative or positive. The normal impulse for both the stages is positive and the tangential impulse depends on the direction of the tangential velocity. The impact laws for the compression and restitution phases are identical and the solution of the IME is quite the same for both stages.

261

5.2.1. Stiction with zero and non-zero approach tangential velocity

Newton's hypothesis. At the beginning of impact the configuration of a multibody system and the coefficient of friction impose conditions that prevent any kind of sliding, i.e. instant stiction occurs. With given normal $\Delta \dot{q}_i^c = 0 - \dot{q}_i^{(-)}$ and tangential $\Delta \dot{q}_{i+1}^c = 0 - \dot{q}_{i+1}^{(-)}$, $\Delta \dot{q}_{i+2}^c = 0 - \dot{q}_{i+2}^{(-)}$ jumps of the velocities at the compression (superscript "^{c}") phase the impulses I_i^c, I_{i+1}^c, I_{i+2}^c and the other jumps of the generalized velocities could be obtained solving the modified linear equation system of the IME. The superscripts for compression and restitution "^{r}" will be used if it is needed for the explanations. The IME in case of stiction for the ith coordinate are:

$$
\begin{bmatrix} \underline{M}\langle i_{st} \rangle & -\boldsymbol{\Phi}_Q^{\mathrm{T}} \\ \underline{\boldsymbol{\Phi}}_Q \langle i_{st} \rangle & \boldsymbol{0}_m \end{bmatrix} \cdot \begin{bmatrix} \Delta \underline{\dot{Q}}\langle i_{st} \rangle \\ I_\lambda \end{bmatrix} + \begin{bmatrix} M_i & M_{i+1} & M_{i+2} \\ \boldsymbol{0}_m & \boldsymbol{0}_m & \boldsymbol{0}_m \end{bmatrix} \cdot \begin{bmatrix} \Delta \dot{q}_i \\ \Delta \dot{q}_{i+1} \\ \Delta \dot{q}_{i+2} \end{bmatrix} = \boldsymbol{0}_{n+m}
\tag{24}
$$

The modified matrices $\underline{M}\langle i_{st} \rangle$ and $\underline{\boldsymbol{\Phi}}_Q \langle i_{st} \rangle$ coincides with the same matrices in Section 5.1. The matrix of the velocity jumps $\Delta \underline{\dot{Q}}$ is transformed to matrix of the unknown parameters that includes the impulses in the point of impact, i. e.:

$$
\Delta \underline{\dot{Q}}\langle i_{st} \rangle = \begin{bmatrix} \Delta \dot{q}_1 & \Delta \dot{q}_2 & \dots & I_i & I_{i+1} & I_{i+2} & \Delta \dot{q}_{i+3} & \dots & \Delta \dot{q}_n \end{bmatrix}^{\mathrm{T}}
\tag{25}
$$

The free part of the linear equation system (24) is obtained by simple multiplication of columns i, $i+1$, $i+2$ of matrix M by the known jumps of the velocities in the contact point. The inertia and mass parameters of the system are the reason for tangential impulse I_τ,

$$
I_\tau = \sqrt{I_{i+1}^2 + I_{i+2}^2}
\tag{26}
$$

calculated from equation (24) that is the maximal possible tangential impulse the system could produce. The conditions for stiction are:

$$
\begin{aligned}
&\left| I_\tau \right| \le \mu_0 \cdot \left| I_i \right|, \; \left\| v_\tau \right\| = 0 \\
&\left| I_\tau \right| \le \mu \cdot \left| I_i \right|, \; \left\| v_\tau \right\| > 0
\end{aligned}
\tag{27}
$$

Using the Newton's coefficient of restitution the velocity jumps $\Delta \dot{q}_i^r = e \cdot \Delta \dot{q}_i^c$, $\Delta \dot{q}_{i+1}^r = e \cdot \Delta \dot{q}_{i+1}^c$, $\Delta \dot{q}_{i+2}^r = e \cdot \Delta \dot{q}_{i+2}^c$ are calculated and the same IME (24) is solved for the restitution phase.

Poisson's hypothesis. The hypothesis of Poisson defines the coefficient of restitution by the ratio

$$
e_p = \frac{I_i^r}{I_i^c}
\tag{28}
$$

between the accumulated normal impulses I_i^r and I_i^c corresponding, respectively, to the phases of restitution and compression. In the same way the coefficient of restitution for the tangential impulses could be defined in case of stiction in the tangential plane. Obviously, both hypotheses demand the solution of common modified IME (24) for the compression phase. Solving equation (24) for the compression phase we obtain the impulses I_i^c, I_{i+1}^c, I_{i+2}^c and using the data for the Poisson's coefficient of restitution we obtain the impulses $I_i^r = e_p \cdot I_i^c$, $I_{i+1}^r = e_p \cdot I_{i+1}^c$, $I_{i+2}^r = e_p \cdot I_{i+2}^c$ for the restitution phase. The impulses in the point of contact that should be reversed at the restitution phase build the free part of the following IME

$$
\begin{bmatrix} M & -\boldsymbol{\Phi}_Q^{\mathrm{T}} \\ \boldsymbol{\Phi}_Q & \boldsymbol{0}_m \end{bmatrix} \cdot \begin{bmatrix} \Delta \dot{Q} \\ I_\lambda \end{bmatrix} - \begin{bmatrix} \boldsymbol{0}_{i-1} \\ I_i \\ I_{i+1} \\ I_{i+2} \\ \boldsymbol{0}_{n+m-i-2} \end{bmatrix} = \boldsymbol{0}_{n+m}
\tag{29}
$$

for the unknown velocity jumps $\Delta \dot{Q}$ and impulses I_λ of the constraints.

5.2.2. Sliding

Newton's hypothesis. If sliding occurs, the tangential frictional impulses either at the compression or at the restitution stage depend on the normal impulse I_i and the kinetic coefficient of friction μ. The directions of the tangential impulses I_{i+1}, I_{i+2} depend on the relative tangential velocity and the kinetic coefficient of friction, i. e.:

$$
I_{i+m} = -\mu \cdot \frac{v_{\tau_m}}{\left\| v_\tau \right\|} \cdot I_i = -\mu \cdot \frac{\dot{q}_{i+m}}{\sqrt{\dot{q}_{i+1}^2 + \dot{q}_{i+2}^2}} \cdot I_i = -\mu_{i+m} \cdot I_i; \; m = 1, 2
\tag{30}
$$

262

With know jump $\Delta \dot{q}_i^c$ of the normal velocity at the compression phase the IME are modified as follows:

$$\begin{bmatrix} \underline{M}\langle i_{sl}\rangle & -\Phi_Q^{\mathrm{T}} \\ \underline{\Phi}_Q\langle i_{sl}\rangle & 0_m \end{bmatrix} \cdot \begin{bmatrix} \Delta\underline{\dot{Q}}\langle i_{sl}\rangle \\ I_\lambda \end{bmatrix} + \begin{bmatrix} M_i \\ 0_m \end{bmatrix} \cdot \Delta\dot{q}_i = 0_{n+m} \tag{31}$$

The modified matrices $\underline{M}\langle i_{sl}\rangle$ and $\underline{\Phi}_Q\langle i_{sl}\rangle$ are the same as defined by the equations (20) and in Section 5.1. The modified matrix of the parameters

$$\Delta\underline{\dot{Q}}\langle i_{sl}\rangle = \begin{bmatrix} \Delta\dot{q}_1 & \Delta\dot{q}_2 & \cdots & I_i & \Delta\dot{q}_{i+1} & \cdots & \Delta\dot{q}_n \end{bmatrix}^{\mathrm{T}} \tag{32}$$

is similar to matrix $\underline{\ddot{Q}}\langle i_{sl}\rangle$ of equation (21). The solution of equation (31) gives as a result the velocity jumps of the coordinates, the normal impulse I_i^c at the compression phase, and the impulses of the constraints.

Using the coefficient of restitution the jump of the normal velocity $\Delta\dot{q}_i^r$ at the restitution phase is calculated and used as known parameter in the same linear equation system (31) which is to be solved for $\Delta\underline{\dot{Q}}^r$ of the unknown velocity jumps and normal impulse I_i^r at the restitution phase.

Poisson's hypothesis. The normal impulse I_i^c obtained solving the linear system (31) and the coefficient of restitution of Poisson are used for calculation of the normal impulse I_i^r at the time of the restitution that, in its turn, as know parameter built the free part of the IME

$$\begin{bmatrix} M & -\Phi_Q^{\mathrm{T}} \\ \Phi_Q & 0_m \end{bmatrix} \cdot \begin{bmatrix} \Delta\dot{Q} \\ I_\lambda \end{bmatrix} - \begin{bmatrix} 0_{i-1} \\ I_i \\ 0_{n+m-i} \end{bmatrix} = 0_{n+m} \tag{33}$$

that should be solved for the unknown velocity jumps $\Delta\dot{Q}^r$.

5.2.3. Dominant velocity jump in the tangential velocity. A phenomenon we shall discuss here is the case if reverse sliding with non-zero approach tangential velocity. This event could be obtained either in the compression or in the restitution phase. Having in mind that we use here common numerical algorithm for both the stages, the case of dominant tangential velocity jump will be regarded for single discrete value of the normal velocity jump or normal impulse.

The physical nature of the problem stated here could be easily understood if impact is regarded in two-dimensional space, which means that the tangential velocity has only one component along one tangential axis. If this velocity at the beginning of impact is non zero, there is no condition for instant stiction, and solving IME (31) for given normal velocity jump (Newton's hypothesis) or normal impulse (Poisson's hypothesis) respectively, one could obtain resultant tangential velocity with different sign of the initial one. This means that the tangential velocity jump is greater than the initial tangential velocity and with different sign, i.e. during the impact the tangential velocity becomes zero and changes it sign afterwards.

In case of spatial impact, if dominant tangential jump should be considered, the modified IME are as follows:

$$\begin{bmatrix} \underline{M}\langle i_{tj}\rangle & -\Phi_Q^{\mathrm{T}} \\ \underline{\Phi}_Q\langle i_{tj}\rangle & 0_m \end{bmatrix} \cdot \begin{bmatrix} \Delta\underline{\dot{Q}}\langle i_{tj}\rangle \\ I_\lambda \end{bmatrix} + \begin{bmatrix} M_{i+1} \\ 0_m \end{bmatrix} \cdot \Delta\dot{q}_{i+1} = 0_{n+m} \tag{34}$$

where $\underline{M}\langle i_{tj}\rangle$ is the mass matrix modified according to the known jump for the tangential velocity. Solving the IME (34) we obtain only a part of the whole normal velocity jump (Newton's hypothesis) or the a part of the whole normal Impulse (Poisson's hypothesis). The remaining part of the normal velocity jump (or the normal impulse) should be realized checking, because of zero tangential velocity so obtained, for stiction and if not then solving the IME in case of sliding.

5.3. NUMERICAL ALGORITHM FOR IMPACT PROBLEM SOLUTION

The compression and restitution phases have its own initial and final velocities. The initial velocities for the restitution phase are the final velocities for the compression phase. The solution of the rigid-body system impact problem will be achieved using consequently one and the same numerical algorithm for the two phases, compression and restitution of the impact event. Three-step numerical procedure is developed.

Step A. With the initial normal and tangential velocities (Newton's hypothesis) or normal impulse (Poisson's hypothesis) the modified IME are solved for the case of stiction. If the conditions for stiction are:

- fulfilled, then *the solution so obtained is the final solution*;
- not fulfilled, then the next step follows.

Step B. With the same initial tangential and normal velocities or normal impulse, the modified IME are solved in case of sliding. If the condition for dominant tangential jump is:

- not fulfilled, then *the solution so obtained is the final solution*;

263

- fulfilled, then the modified IME are solved in case of dominant tangential velocity jump and the impact analysis continues with the next step.

Step C: The solution so obtained is used the new values of the initial normal velocity or impulse to be updated and with the tangential velocity equal zero involved in a new cycle of calculations starting with Step A.

By the algorithm presented here all possible impact events are numerically simulated, i. e.:

(a) compression phase
- instant stiction with no relative approach tangential velocity;
- instant stiction with relative approach tangential velocity;
- sliding with no relative approach tangential velocity;
- sliding;
- sliding and reverse sliding;
- sliding and stiction;
(b) restitution phase
- continuos stiction;
- continuous sliding;
- continuous sliding and reverse sliding;
- continuous sliding and stiction.

Simulation of the dynamics of multibody system in case of multiple impact point is similar of the case of multiple contact points. The transformation of the matrices $\underline{M}\langle i_{sl}\rangle$, $\underline{M}\langle i_{st}\rangle$, $\underline{M}\langle i_{ij}\rangle$ is independent for every coordinate in which impact event occurs. Every coordinate causes transformations of the corresponding column of matrix M.

6. Frictional Contact of Flexible Multibody Systems

Flexible bodies are discretized of flexible elements and nodes. If finite element theory is used for discretization the nodes and their position approximate the shape of the flexible bodies. In Fig. 3 the definition of the tangential plane and normal is presented schematically. But this task is specific for each case because the variety of elements as shells, beams, tetrahedrons, prisms and etc. Although detection of contact is not a subject of this article, some examples of definition of the tangential plane and its normal in the contact points will be presented in order the contact dynamics simulation to be implemented in terms of the numerical algorithm suggested above.

The most simplest way to define the contact point and its tangential plane and normal is the contact of flexible body, respectively a node, to a rigid body (Fig. 3 a). The contact point of the rigid body, if detected, defines uniquely the plane and its normal. The nodes of tetrahedron (Fig 3 b, c) or prismatic elements (Fig. 3 d) that are over the surface of the flexible body define a mash of hyper-surface patches. If the elements are tetrahedrons the surfaces of this patches are planes and the normal direction is one and the same for the all patch. The corresponding nodes could be used to define the tangential plane and direction of the normal (Fig. 3 b), and in this case, the possible relative translations in the tangential plane are non-orthogonal. In the figure the node of the other element that approaches the contact surface is not shown. If the elements are prismatic surfaces which form is defined by the shape function of the corresponding element. The normal could be obtained differentiating the shape function in the contact point detected. Significant simplification of the procedure for contact detection, as well as, estimation of the tangential plane and normal, could be achieved if the coordinate systems that pertain to the flexible elements are fixed in the nodes that build the body surface (Fig. 3 c, d, e). So, for tetrahedron, prismatic and shell elements, one of the coordinate system plane (in the figure it is XY plane) coincides with the patch of the body surface. For prismatic and shell elements, although the patch is nonlinear-surface, it also could be assumed coincident with XY plane as the relative flexible deflections of the element nodes are assumed small. The situation, in case of beam elements (Fig. 3 f), is a little bit more complicated, because contact is implemented in a point that, in the general case, does not coincide with a node. So, the unity vectors of the beam axes define the tangential plane while the normal is defined by their cross product. The readers familiar with
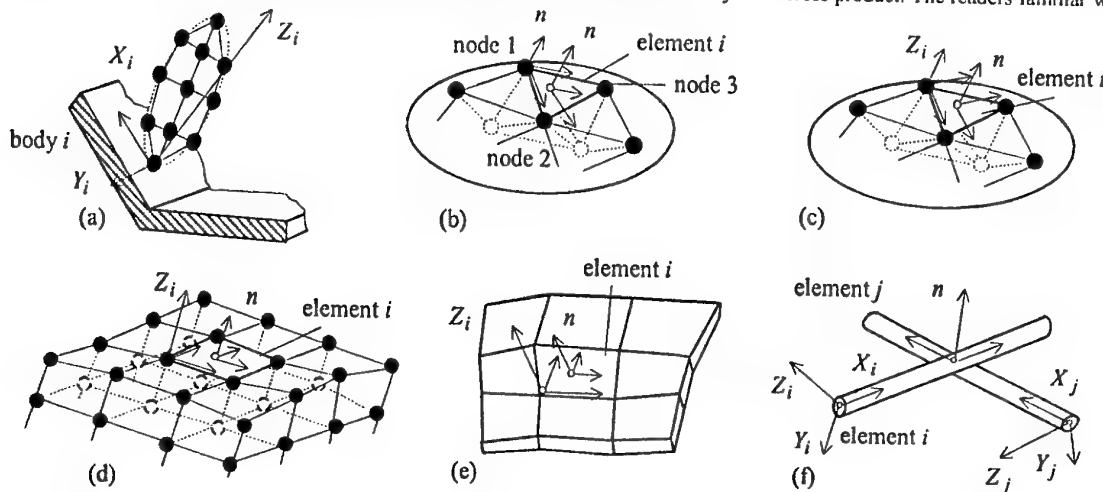

Fig. 3: Flexible elements and definition of contact point tangential planes

264

the contact problems and using the possible penetration for estimation of contact forces will conclude that there is many common definitions of the normal penetration and the normal in the tangential plane. Of course, there are many difficulties and one of it is if the contact point goes from one element to another.

In the finite element theory the deflections of the nodes are with respect to the inertial reference frames. Absolute coordinates are very appropriate if a flexible body comes into contact with a body that coincides with the inertial reference frame. But if contact occurs between two moving bodies, the contact should be described in terms of relative coordinates. The author of this treatment suggested in [21] an approach of relative coordinates for modeling of rigid and flexible multibody system dynamics. This method defines at every time step the position of the body or element coordinate system, respectively the contact tangential plane and its normal. So, the contact of flexible systems could be described as a contact of a node of a flexible body with an element of another body. Respectively, the possible motions of this node are with respect to the coordinate system of the element of the other body (Fig. 4) and these motions are included in matrix – vector Q of the coordinates. It could be easily verified that this presentation allows the algorithm suggested here to be directly applied for simulation of contact of flexible bodies. In case of contact of flexible beam elements (Fig. 5) the coordinates that describe the possible motions in the contact point are the translations along the beam axes and the common normal.
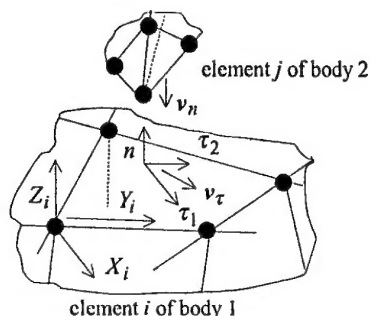
Fig. 4: Incoming contact of a node with an element of flexible bodies
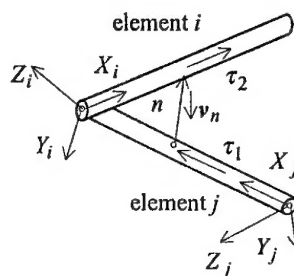
Fig. 5: Incoming contact of two beams

6. Examples

In Figure 6 an example of double pendulum rigid body system is presented. This example is well studied in the scientific literature [13] and it is presented here to verify the results obtained by the method suggested. In Figures 7 and 8 two examples of impacts of slender beam and thin wall ring with the ground are presented.
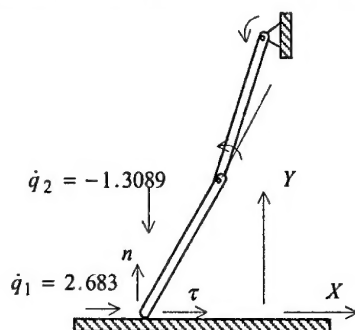
Fig. 6: Impact of rigid body double pendulum
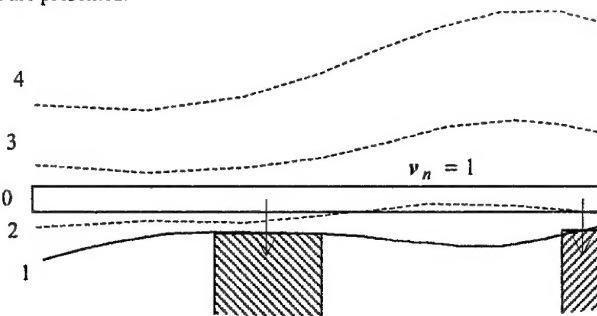
Fig. 7: Impact and large flexible deflections of slender beam
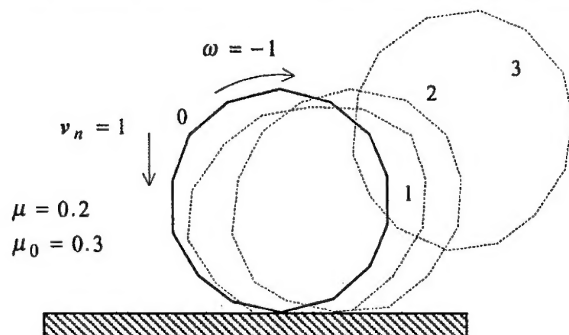
Fig. 8: Impact and multiple node contact of thin flexible ring

265

References

1. E.J. Haug, S.C. Wu and S.M.Yang (1986) "Dynamics of Mechanical Systems with Coulomb Friction, Stiction, Impact and Constraint Addition-Deletion. Part 1: Theory", *Mechanism and Machine Theory*, **21**, No. 5, 401-406.
2. Ch. Glocker and F. Pfeiffer (1992) "Dynamical systems with unilateral contacts", *Nonlinear Dynamics*, No. 3, Vol. 9, 245 - 259.
3. Ch. Glocker and F. Pfeiffer (1994) "Stick - slip phenomena and application, In: Nonlinearity and Chaos in Engineering Dynamics", *IUTAM Symposium, UCL*, John Wiley, New York, 103 - 113.
4. W. Seyfferth and F. Pfeiffer (1994) "Modeling of Time - Variant Contact Problem in Multibody systems", *In: Proc. of 12ᵗʰ Symposium on Engineering Applications of Mechanics, Montreal*, June 27 - 29, 579 - 588.
5. M. Wosle and F. Pfeiffer (1996) "Dynamics of Multibody Systems Containing Dependent Unilateral Constraints with Friction", *Journal of Vibration and Control*, **2**, 161 - 192.
6. K.H. Hunt and F.R.E. Grossley (1975) "Coefficient of Restitution Interpreted as Damping in Vibroimpact", *ASME Journal of Applied Mechanics*, 440-445.
7. R.M. Brach (1989) "Rigid body collision", *ASME Journal of Applied Mechanics*, **56**, 133-138.
8. J.B. Keller (1986) "Impact with Friction", *ASME Journal of Applied Mechanics*, **53**, 1-4.
9. Y. Wang and M.T. Mason (1992) "Two Dimensional Rigid-Body Collisions with Friction", *ASME Journal of Applied Mechanics*, **59**, 635-642.
10. C. Glocker and F. Pfeiffer (1995) "Multiple Impacts with Friction in Rigid Multibody Systems", *Nonlinear Dynamics*, **7**, No. 4, 471-497.
11. F. Pfeiffer and C. Glocker (1996) *Multibody Dynamics with Unilateral Contacts*, JOHN WILEY & SONS, INC,.
12. W. Schiehlen (1998) "Unilateral Contacts in Machine Dynamics", *IUTAM Symposium Unilateral Multibody Dynamics*, Munich, August 3-7, Kluwer Academic Publishers, 1-12.
13. H.M. Lankarani and M.F.O.S. Pereira (1999) "Treatment of Impact with Friction in Multibody Mechanical Systems", *Proc. of EUROMECH Colloquium 404 Advances in Computational Multibody Dynamics* (Eds. Jorge A.C. Ambrosio and Werner O. Schiehlen), IDMEC/IST, Lisbon, Portugal, September, 20-23.
14. A.C.J. Ambrosio and M.S. Pereira (1997) "Flexible Multibody Dynamics with Nonlinear Deformations: Vehicle Dynamics and Crashworthiness Application", In: *Computational Methods in Mechanical Systems: Mechanism Analysis, Synthesis and Optimization* (Eds. J. Angeles and E. Zakhariev), NATO ASI, Ser. F, **161**, Springer Verlag, Berlin, 382-419.
15. W.J. Stronge (1994) "Planar Impact of Rough Compliant Bodies", *Int. J. Impact.Eng.*, **15**, No. 4, 435 – 450.
16. W.J. Stronge (1995) "Theoretical Coefficient of Restitution for Planar Impact of Rough Elasto-Plastic Bodies", *AMD - Vol. 205, Impact, Waves, and Fracture* (Eds. R.C. Batra, A.K. Mal, G.P. MacSithigh), Book H00952, 351-362.
17. N. Kikuchi (1982) "A Smoothing Technique for Reduced Integration Penalty Methods in Contact Problems", *Int. Journal of Numerical Methods in Engineering*, Vol. 18, 343 – 350.
18. J.T. Oden and N. Kikuchi (1982) "Finite Element Methods for Constrained Problems in ", *Int. Journal of Numerical Methods in Engineering*, **18**, 701 – 725.
19. G. Yagawa and Y. Kanto (1993) "Finite Element Analysis of Contact Problems using the Penalty Function Method", *In: Computational Methods in Contact Mechanics* (Eds. M.H. Alibadi and C.A. Brebbia), Computational Mechanics Publications, Elsevier Applied Science, 127-153.
20. P. Eberhard and S. Jiang (1997) "Collision Detection for Contact Problems in Mechanics", *Institutsbericht IB - 30*, Institute B of Mechanics, University of Stuttgart.
21. E.V. Zahariev (2002) "Relative Finite Element Coordinates in Multibody System Simulation", *Multibody System Dynamics*, Vol. 7, 51 – 77.

AUTHORS INDEX